

8 Copies 98  
NASA CR-66599

# APOLLO APPLICATIONS PROGRAM CREW MOTION EXPERIMENT PROGRAM DEFINITION AND DESIGN DEVELOPMENT

By C. H. Murrish and G. W. Smith

Distribution of this report is provided in the interest of information exchange. Responsibility for the contents resides in the author or organization that prepared it.

Prepared under Contract NAS1-7276 by  
MARTIN MARIETTA CORPORATION  
Denver, Colorado

for

NATIONAL AERONAUTICS AND SPACE ADMINISTRATION

N68-22151

FACILITY FORM 602

(ACCESSION NUMBER)

456

(PAGES)

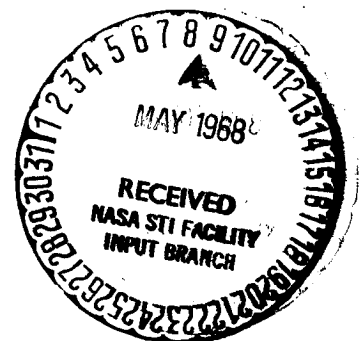
01-66599

(NASA CR OR TMX OR AD NUMBER)

(THRU)

(CODE)

(CATEGORY)



$$\begin{array}{r} 445 \\ .65 \\ \hline 22.25 \end{array}$$



APOLLO APPLICATIONS PROGRAM CREW MOTION EXPERIMENT  
PROGRAM DEFINITION AND DESIGN DEVELOPMENT

By C. H. Murrish and G. W. Smith

Distribution of this report is provided in the interest of  
information exchange. Responsibility for the contents  
resides in the authors or organization that prepared it.

Prepared under Contract NAS1-7276 by  
MARTIN MARIETTA CORPORATION  
Denver, Colorado

for

NATIONAL AERONAUTICS AND SPACE ADMINISTRATION

## FOREWORD

This report is submitted in accordance with Part III A-6 of the statement of work for Contract NAS1-7276.

This report is the result of a team effort in close cooperation with the NASA Technical Monitor, Mr. Bruce Conway. The Martin Marietta Corporation's Denver Division effort was managed by Mr. George W. Smith and the technical direction was provided by Dr. Charles H. Murrish.

The implementation of the Optimum Math Model and Ground Simulation was carried out by Charles H. Johnson. The Force Measuring System design was developed by Tom Jacob. The Limb Motion Sensing System Development was done by Pierre Corveleyn and Steve Hagberg. The Astronaut Position/Attitude System Study was carried out by Wayne Faber. The Digital Attitude and Rate System design effort was done by Robert G. Brown and Richard L. Sazpansky. The Experiment Data System Concepts and design were the creative effort of William J. Maes. The Overall Experiment Design was under the supervision of Joseph Spencer.

# CONTENTS

	Page
FOREWORD . . . . .	ii
CONTENTS . . . . .	iii
LIST OF ILLUSTRATIONS . . . . .	v
LIST OF TABLES . . . . .	xii
SUMMARY . . . . .	1
INTRODUCTION . . . . .	2
SYMBOLS AND ABBREVIATIONS . . . . .	3
MATHEMATICAL MODEL OF EXPERIMENT AND GROUND SIMULATION	
PROGRAMS . . . . .	9
Restrained Crew Activity Program . . . . .	10
Physical Simulations . . . . .	11
Digital Simulations . . . . .	13
Correlation and Conclusions . . . . .	16
Restrained Crew Activities . . . . .	23
Translational Crew Activity Program . . . . .	32
Translational Crew Activities . . . . .	38
LIMS DESIGN . . . . .	42
ASTRONAUT POSITION AND ATTITUDE SYSTEM . . . . .	47
Ultrasonic-Radio Frequency Triangulation . . . . .	48
Inertial Measuring Units . . . . .	51
Photographic Method . . . . .	52
DIGITAL ATTITUDE AND RATE SYSTEM . . . . .	55
System Analysis . . . . .	57
System Tests and Evaluation . . . . .	86
Design, Build Procedures, Component Selection, Reliability, and Operation Aspects of DARS . . . . .	88
FORCE MEASURING SYSTEM . . . . .	94
DATA SYSTEM . . . . .	103
System Design . . . . .	103
T013 System Operation . . . . .	110
Subsystem Description . . . . .	111
RF Link . . . . .	117
System Data Synthesizer . . . . .	126
OVERALL EXPERIMENT DESIGN . . . . .	134
Hardware Requirements and Location . . . . .	134
System/Vehicle Interfaces . . . . .	138
Experiment Constraints, Assumptions, and Setup . . . . .	142
Crew Activity Time Line . . . . .	146
CONCLUSIONS . . . . .	155
APPENDIX A -- GROUND SIMULATION RESULTS . . . . .	157
Part I - Restrained Crew Activity Simulation Results . . . . .	157
Part II - Translational Crew Activity Simulation Results . . . . .	265

	Page
APPENDIX B -- PERTINENT EXCERPTS FROM REFERENCE 4 . . . . .	281
List of Symbols . . . . .	281
Basic Equations of Motion . . . . .	283
Equations of Motion for Hybrid Simulation . . . . .	289
Equations of Motion for Digital Simulation . . . . .	302
General Transformations . . . . .	308
Expanded Forms . . . . .	314
APPENDIX C -- DATA SMOOTHING PROCEDURE . . . . .	338
APPENDIX D -- ANTHROPOMETRIC DATA . . . . .	342
APPENDIX E -- DETERMINATION OF SAMPLING RATE FOR FLIGHT EXPERIMENT . . . . .	354
APPENDIX F -- ANTHROPOMETRIC MEASUREMENTS OF TEST SUBJECT .	363
APPENDIX G -- MATHEMATICAL AND ERROR ANALYSIS OF APAS TECHNIQUES . . . . .	366
APPENDIX H -- DESIGN DRAWINGS REFERENCED IN TEXT . . . . .	397
APPENDIX I -- GYROSCOPE SYSTEMS . . . . .	442
REFERENCES . . . . .	444

# LIST OF ILLUSTRATIONS

Figure		Page
1	Restrained Crew Activity Simulation Plan . . . . .	10
2	Physical Simulation of In-Place Motions . . . . .	12
3	Analog Computer Resolution of Load Cell Outputs . . . . .	12
4	Mathematical Model of Man . . . . .	14
5	Crew Disturbance Digital Program . . . . .	17
6	Arm Motion in Each of Three Planes . . . . .	18
7	Apollo Cluster Vehicle . . . . .	25
8	Heartbeat Data . . . . .	28
9	Spacecraft Disturbance from Heartbeat Data . . . . .	29
10	Spacecraft Disturbances from Modified Load Cell Forces and Moments (Right Arm Motion in Each of Three Planes) S/C Axes . . . . .	30
11	Spacecraft Disturbances from Calculated Forces and Moments (Right Arm Motion in Each of Three Planes) S/C Axes . . . . .	31
12	Artist's Concept of SOS Facility . . . . .	33
13	EAI 8900 Hybrid Computing System . . . . .	34
14	Total View of Motion Simulator . . . . .	36
15	Closeup View of Attitude Head . . . . .	36
16	Artist's Sketch of EVA Flow Diagram . . . . .	37
17	Handrail Translation Mockup . . . . .	39
18	Forces and Moments Resulting from Handrail Translation, Man's Axes . . . . .	40
19	Free Soaring Mockup . . . . .	41
20	LIMS Motion Sensing System . . . . .	43
21	Joint Rotation Transducer - Hinge Joint Design . . . . .	44
22	LIMS Shoulder Yoke . . . . .	46
23	LIMS Hinge and Axial Joint Details, Laboratory Model . . . . .	46
24	APAS Ultrasonic Schematic . . . . .	50
25	APAS Ultrasonic Concept . . . . .	50
26	APAS Photographic Concept . . . . .	53
27	Digital Attitude and Rate System (DARS) . . . . .	58
28	Rate Gyro System (RGS) . . . . .	58
29	RGS Block Diagram . . . . .	60
30	Frequency Response of Rate Gyro System . . . . .	62
31	RGS Mounted on the Three-Axis Servo-Driven Gimbal System . . . . .	63
32	Adjustable dc Bias Supply . . . . .	65
33	Voltage Regulator Block Diagram . . . . .	66

Figure		Page
34	Voltage Regulator Schematic . . . . .	66
35	Definition of Regulator Performance Parameters .	67
36	Transistor Preregulator Versus CRD Preregulator .	69
37	Null Meter . . . . .	70
38	Voltage-to-Frequency Converter . . . . .	71
39	CAD Current Versus Pulse Output . . . . .	74
40	Positive Five-Volt Supply . . . . .	74
41	Digital Output Circuitry . . . . .	75
42	Digital Control Unit Logic Diagram . . . . .	77
43	Input Circuitry to Fairchild 951 One-Shot Multivibrator . . . . .	79
44	One-Shot Input Clamping Circuit . . . . .	80
45	RC Shaping Network . . . . .	80
46	Up/Down Counter . . . . .	82
47	NAND GATES . . . . .	83
48	Buffer Register . . . . .	85
49	DARS Output Versus Input Current Rate Gyro System . . . . .	87
50	DARS Assembly . . . . .	91
51	Wood Mockup of DARS . . . . .	93
52	FMS Orthogonal Force System . . . . .	94
53	FMS Load Cell Array Configurations . . . . .	96
54	FMS Flight Model Configuration . . . . .	96
55	FMS Typical Load Cell Design . . . . .	98
56	JP-100 Load Cell for Flight Model FMS . . . . .	98
57	FMS Compound Emery Flexure . . . . .	99
58	Load Cell Array Assembly . . . . .	100
59	Triple-Channel Recording . . . . .	105
60	Single-Channel Recording . . . . .	105
61	T013 Experiment Data System . . . . .	106
62	T013 Experiment Data System Format . . . . .	109
63	LIMS Data Acquisition Subsystem . . . . .	112
64	Programmer Signals . . . . .	114
65	DC Level and Clock Pulse Control . . . . .	114
66	Programmer Signals . . . . .	116
67	A/D Converter Waveforms . . . . .	116
68	Energy Output Comparison of Battery Systems . . .	117
69	RF Transmitter . . . . .	118
70	Possible Antenna Configurations on Astronaut . .	119
71	Dipole and Loop Radiation Pattern for Induced Orientations . . . . .	121
72	RF Receiver . . . . .	123
73	Receive Antenna Coverage in Experiment Area . . .	124
74	Antenna Configurations . . . . .	125

Figure		Page
75	System Data Synthesizer . . . . .	127
76	Bit Synchronizer . . . . .	127
77	Frame Synchronizer Signals . . . . .	128
78	Frame Sync Detector . . . . .	129
79	Sync Counter and Controller . . . . .	129
80	Astronaut Data System Breadboard . . . . .	133
81	Crew Quarters Floor Plan (Looking Forward) Showing T013 Equipment . . . . .	136
82	Persepctive View of Crew Quarters Showing T013 Equipment . . . . .	137
83	T013 Experiment Layout Concept, Storage Mode in MDA . . . . .	139
84	Random Vibration Spectrum, DARS Rate Gyro System . . . . .	140
85	Estimated Thermal Properties, LIMS . . . . .	140
86	Estimated Thermal Properties, DARS . . . . .	141
87	Estimated Thermal Properties, Experiment Data System . . . . .	141
88	Estimated Thermal Properties, FMS . . . . .	142
89	Crew Activity Time-Line Summary . . . . .	154
A1	150-lb Static Weight, Run 1 . . . . .	161
A2	Heartbeat (No Breathing), Run 2 . . . . .	163
A3	Normal Breathing, Run 3 . . . . .	165
A4	Fast Breathing, Run 4 . . . . .	167
A5	Coughing, Run 5 . . . . .	169
A6	Sneezing, Run 6 . . . . .	171
A7	Head Motion, Run 7 . . . . .	173
A8	Wrist Motion, Run 8 . . . . .	175
A9	Ankle Motion, Run 9 . . . . .	177
A10	Lower Right Arm, Single Pendulum, Sagittal Plane, Run 10 . . . . .	179
A11	Lower Right Arm, Single Pendulum, Sagittal Plane, Run 10 . . . . .	180
A12	Lower Right Arm, Single Pendulum, Sagittal Plane, Run 10 . . . . .	181
A13	Lower Right Arm, Single Pendulum, Sagittal Plane, Run 10 . . . . .	182
A14	Total Right Arm, Single Pendulum, Sagittal Plane, Run 11 . . . . .	184
A15	Total Right Arm, Single Pendulum, Sagittal Plane, Run 11 . . . . .	185
A16	Total Right Arm, Single Pendulum, Sagittal Plane, Run 11 . . . . .	186

Figure		Page
A17	Total Right Arm, Single Pendulum, Sagittal Plane, Run 11 . . . . .	187
A18	Total Left Arm, Single Pendulum, Sagittal Plane, Run 12 . . . . .	189
A19	Total Left Arm, Single Pendulum, Sagittal Plane, Run 12 . . . . .	190
A20	Total Left Arm, Single Pendulum, Sagittal Plane, Run 12 . . . . .	191
A21	Total Left Arm, Single Pendulum, Sagittal Plane, Run 12 . . . . .	192
A22	Total Left Arm, Double Pendulum, Sagittal Plane, Run 13 . . . . .	194
A23	Total Left Arm, Double Pendulum, Sagittal Plane, Run 13 . . . . .	195
A24	Total Left Arm, Double Pendulum, Sagittal Plane, Run 13 . . . . .	196
A25	Total Left Arm, Double Pendulum, Sagittal Plane, Run 13 . . . . .	197
A26	Total Left Arm, Double Pendulum, Sagittal Plane, Run 14 . . . . .	199
A27	Total Left Arm, Double Pendulum, Sagittal Plane, Run 14 . . . . .	200
A28	Total Left Arm, Double Pendulum, Sagittal Plane, Run 14 . . . . .	201
A29	Total Left Arm, Double Pendulum, Sagittal Plane, Run 14 . . . . .	202
A30	Lower Right Leg, Single Pendulum, Sagittal Plane, Run 15 . . . . .	204
A31	Lower Right Leg, Single Pendulum, Sagittal Plane, Run 15 . . . . .	205
A32	Lower Right Leg, Single Pendulum, Sagittal Plane, Run 15 . . . . .	206
A33	Lower Right Leg, Single Pendulum, Sagittal Plane, Run 15 . . . . .	207
A34	Total Right Leg, Single Pendulum, Sagittal Plane, Run 16 . . . . .	209
A35	Total Right Leg, Single Pendulum, Sagittal Plane, Run 16 . . . . .	210
A36	Total Right Leg, Single Pendulum, Sagittal Plane, Run 16 . . . . .	211
A37	Total Right Leg, Single Pendulum, Sagittal Plane, Run 16 . . . . .	212
A38	Right Arm, Console Operation, Run 17 . . . . .	214



Figure		Page
A39	Right Arm, Console Operation, Run 17 . . . . .	215
A40	Right Arm, Console Operation, Run 17 . . . . .	216
A41	Right Arm, Console Operation, Calculated from Load Cell Data, Run 17 . . . . .	217
A42	Right Arm, Console Operation, Calculated from Load Cell Data, Run 17 . . . . .	218
A43	Right Arm, Console Operation, Run 17 . . . . .	219
A44	Lower Right Arm, Single Pendulum, Sagittal Plane, Run 18 . . . . .	221
A45	Lower Right Arm, Single Pendulum, Sagittal Plane, Run 18 . . . . .	222
A46	Lower Right Arm, Single Pendulum, Sagittal Plane, Run 18 . . . . .	223
A47	Lower Right Arm, Single Pendulum, Sagittal Plane, Calculated from Load Cell Data, Run 18 . . . . .	224
A48	Lower Right Arm, Single Pendulum, Sagittal Plane, Run 18 . . . . .	225
A49	Total Right Arm, Single Pendulum, Sagittal Plane, Run 19 . . . . .	227
A50	Total Right Arm, Single Pendulum, Sagittal Plane, Run 19 . . . . .	228
A51	Total Right Arm, Single Pendulum, Sagittal Plane, Run 19 . . . . .	229
A52	Total Right Arm, Single Pendulum, Sagittal Plane, Calculated from Load Cell Data, Run 19 . . . . .	230
A53	Total Right Arm, Single Pendulum, Sagittal Plane, Run 19 . . . . .	231
A54	Total Left Arm, Single Pendulum, Frontal Plane, Run 20 . . . . .	233
A55	Total Left Arm, Single Pendulum, Frontal Plane, Run 20 . . . . .	234
A56	Total Left Arm, Single Pendulum, Frontal Plane, Run 20 . . . . .	235
A57	Total Left Arm, Single Pendulum, Frontal Plane, Run 20 . . . . .	236
A58	Total Left Arm, Double Pendulum, Sagittal Plane, Run 21 . . . . .	238
A59	Total Left Arm, Double Pendulum, Sagittal Plane, Run 21 . . . . .	239
A60	Total Left Arm, Double Pendulum, Sagittal Plane, Run 21 . . . . .	240
A61	Total Left Arm, Double Pendulum, Sagittal Plane, Run 21 . . . . .	241

Figure		Page
A62	Lower Right Leg, Single Pendulum, Sagittal Plane, Run 22 . . . . .	243
A63	Lower Right Leg, Single Pendulum, Sagittal Plane, Run 22 . . . . .	244
A64	Lower Right Leg, Single Pendulum, Sagittal Plane, Run 22 . . . . .	245
A65	Lower Right Leg, Single Pendulum, Sagittal Plane, Run 22 . . . . .	246
A66	Total Left Leg, Double Pendulum, Sagittal Plane, Run 23 . . . . .	248
A67	Total Left Leg, Double Pendulum, Sagittal Plane, Run 23 . . . . .	249
A68	Total Left Leg, Double Pendulum, Sagittal Plane, Run 23 . . . . .	250
A69	Total Left Leg, Double Pendulum, Sagittal Plane, Run 23 . . . . .	251
A70	Right Arm Console Operation, Run 24 . . . . .	253
A71	Right Arm Console Operation, Run 24 . . . . .	254
A72	Right Arm Console Operation, Run 24 . . . . .	255
A73	Right Arm Console Operation, Run 24 . . . . .	256
A74	Both Arms and Legs Exercising, Run 25 . . . . .	258
A75	Both Arms and Legs Exercising, Run 25 . . . . .	259
A76	Both Arms and Legs Exercising, Run 25 . . . . .	260
A77	Both Arms and Legs Exercising, Run 25 . . . . .	261
A78	Both Arms and Legs Exercising, Run 25 . . . . .	262
A79	Both Arms and Legs Exercising, Run 25 . . . . .	263
A80	Both Arms and Legs Exercising, Run 25 . . . . .	264
A81	Compressive Walking, Man's Axes . . . . .	266
A82	Compressive Walking, Spacecraft Axes . . . . .	268
A83	Bounce Walk, Man's Axes . . . . .	271
A84	Bounce Walk, Spacecraft Axes . . . . .	274
A85	Free Soaring, Man's Axes . . . . .	278
B1	Reference Coordinate Systems . . . . .	284
B2	Mathematical Model of Man . . . . .	285
B3	Segment Coordinate Systems . . . . .	287
B4	Load Cell Geometry . . . . .	296
B5	Basic LIMS Elements . . . . .	298
B6	Shoulder or Hip Joint Gimbal . . . . .	299
B7	Hybrid Computational Block Diagram . . . . .	301
D1	Segmental Model of Man . . . . .	343
E1	Definition of T . . . . .	354
E2	Normalized Complex Fourier Integral for Run 19 . .	358
E3	Normalized Complex Fourier Integral for Run 17 . .	359

Figure		Page
E4	Normalized Complex Fourier Integral for Run 19 . .	360
E5	Measured Force Applied in the x Direction, Run 19 . . . . .	361
E6	Calculated Forces Using Reconstructed LIMS Data for Run 19 . . . . .	362
F1	Skeletal Anthropometric Points . . . . .	365
G1	Ultrasonic - RF APAS Geometry . . . . .	366
G2	Implementation of Six-Accelerometers for APAS . .	373
G3	Camera Coordinate Systems . . . . .	381
G4	Simulator-Photo Data Comparison . . . . .	392
I1	Block Diagram Illustrating TARS-RGS Interrelationship . . . . .	442

# LIST OF TABLES

Table		Page
1	Maximum Differences between Physical and Model Motion - Forces and Moments Attributable to Heart-beat and Breathing . . . . .	21
2	Restrained Crew Activities Description . . . . .	24
3	LIMS Properties . . . . .	45
4	OWS Environment . . . . .	47
5	APAS Selection Matrix . . . . .	49
6	Comparison of Apollo Onboard Sensors with T013 Requirements . . . . .	55
7	Specifications, Digital Attitude and Rate System (DARS) . . . . .	56
8	Rate Gyro System Physical Constants . . . . .	60
9	Frequency Response Data of Rate Gyro System . . .	62
10	Experimental Total Pulse Count Data for CAD . . .	64
11	CAD Test Data . . . . .	73
12	NAND GATE Truth Table . . . . .	76
13	Flip-Flop Truth Table . . . . .	78
14	System Output for Test Input Currents . . . . .	86
15	DARS Components . . . . .	89
16	Comparison of Triple- Versus Single-Channel Recording . . . . .	104
17	Original Data Requirements for T013 . . . . .	109
18	Subsystem Characteristics . . . . .	132
19	Training Time . . . . .	143
20	Crew Training Time Line . . . . .	147
D1	Segment Parameters for 140-Pound Man . . . . .	345
D2	Segment Parameters for 150-Pound Man . . . . .	346
D3	Segment Parameters for 160-Pound Man . . . . .	347
D4	Segment Parameters for 170-Pound Man . . . . .	348
D5	Segment Parameters for 180-Pound Man . . . . .	349
D6	Segment Parameters for 190-Pound Man . . . . .	350
D7	Segment Parameters for 200-Pound Man . . . . .	351
D8	Segment Parameters for 210-Pound Man . . . . .	352
D9	Segment Parameters for 220-Pound Man . . . . .	353
F1	Anthropometric Measurements of Subject 1, Weight, 144 Pounds . . . . .	363
F2	Anthropometric Measurements of Subject 2, Weight, 157 Pounds . . . . .	364
G1	Ultrasonic Error Analysis . . . . .	369
I1	Candidate Gyro Parameters . . . . .	443

# APOLLO APPLICATIONS PROGRAM CREW MOTION EXPERIMENT

## PROGRAM DEFINITION AND DESIGN DEVELOPMENT

By C. H. Murrish and G. W. Smith  
Martin Marietta Corporation

### SUMMARY

Under the continuing development of the Apollo Applications Program (AAP) Crew Motion Experiment, Contract NAS1-7276 was awarded to the Martin Marietta Corporation's Denver Division to complete the necessary instrumentation design and development for the flight experiment. The hardware designs were for a flight model Limb Motion Sensing System (LIMS) emphasizing the ease of donning and doffing; a conceptual study of the Astronaut Position/Attitude Sensing System (APAS) to provide continual monitoring of the location of the astronaut as he maneuvers about the spacecraft; a Digital Attitude and Rate System (DARS) to enable the measurement of vehicle attitude perturbations well below the threshold of the onboard sensing systems; a Force Measuring System (FMS) to enable the direct measurement of the forces imposed on the spacecraft by a maneuvering astronaut; and an Experiment Data System (EDS) to enable acquisition of the Crew Motion Experiment (T013) data in a format compatible with the AAP data system to enable ground recovery of all T013 data via a telemetry link.

In addition to the actual hardware designs carried out, a study was made to develop an optimum mathematical model of the man/spacecraft system incorporating extensive physical and digital simulations of basic crew motions.

Further, an intensive review was made of the program plan developed under Contract NAS1-6713 and reported in NASA CR-66277.\* This review resulted in a refinement of the plan and a resultant reduction of in-flight man-minutes from 420 to 231. A conceptual design for the Experiment Components Container (ECC) was made, and an initial effort to meet all interfaces was carried out.

---

\*Tewell, J. R.; and Murrish, C. H.: Engineering Study and Experiment Definition for an Appollo Applications Program Experiment on Vehicle Disturbance Due to Crew Activity. NASA CR-66277, 1966.

As the definition of AAP Missions 1 and 2 becomes clearer and all concepts are firmed up, there will, no doubt, be certain changes of the T013 equipments required. As presently configured, it is anticipated that these changes, in so far as T013 is concerned, will be minimal and readily accomplished.

This report is actually composed of two parts. The present volume including a description of the efforts outlined above and a data supplement in the form of magnetic tapes supplied only to NASA-Langley Research Center.

## INTRODUCTION

The opportunity afforded by the Apollo Applications Program (AAP) to carry out significant engineering experiments in space is unique in the exploitation of man's capabilities in this foreign environment. A prime requirement for any manned space mission is adequate support for man to ensure not only that he be returned safely to earth, but also that he be able to carry out primary mission objectives. Many of these objectives require a stable platform (vehicle) with high precision pointing capabilities ( $\pm 2.5$  arc sec or better) and very low angular accelerations ( $10^{-6}g$  or less). To achieve this degree of stability with reasonable economy, it is necessary to be able to assess, with high accuracy, any disturbing forces. Those disturbances caused by operating equipment such as pumps, circulating fans, valves, etc., can be evaluated analytically. However, studies have shown (ref. 1) that man himself can produce significant attitude disturbances particularly in smaller vehicles and simple extravehicular activity (EVA) maneuvering units. The reliability of analytic methods to assess the nature of the man-induced disturbances is seriously hampered by both the lack of a completely reliable description of the mechanics of man and the random nature of man-induced disturbances. Ground-based simulation techniques also suffer significant deficiencies in that the correlation between 1- and zero-g motion of man's limbs, his contact with an orbiting spacecraft versus his contact with any ground simulation mockups, the psychological effects of existence and behavior in the foreign environment of space, as well as his dynamics under these conditions are unknown.

To remove these deficiencies and to develop a reliable set of engineering data, an AAP experiment has been developed to directly measure the effects of crew motion on the attitude stability of a manned spacecraft. This experiment will generate data that will enable the spacecraft designer to determine the necessary attitude control system thresholds to achieve the degree of attitude stability required for critical tasks, the fuel requirements for stabilization control, and even the thrusting programs for manned interplanetary missions where disturbances occurring during thrust periods could result in significant trajectory perturbations. The development of this experiment (AAP experiment T013) was initiated under Contract NAS1-6713 and continued under the present effort. This present effort resulted in the development of an "optimum" experiment model and the design of a flight configuration Limb Motion Sensing System (LIMS), a Digital Attitude and Rate System (DARS), a Force Measuring System (FMS), and an Experiment Data System (EDS). The actual equipment designs were validated by breadboard configurations of the basic subsystems, and actual laboratory models of the LIMS and FMS were produced. Design drawings and parts lists for all the hardware required were generated.

An investigation was carried out to determine the most feasible method of determining the position and attitude of the astronaut as he maneuvers about the experiment area. This investigation led to the development of a photographic method for achieving the desired result.

In addition, a revised experiment performance program was developed together with astronaut time lines reflecting the advances achieved in equipment concepts including the Experiment Components Container (ECC). These advances in concept resulted in a reduction in estimated performance time from 220 to 86 minutes.

#### SYMBOLS AND ABBREVIATIONS

<u>a</u>	acceleration vector
AAP	Apollo Applications Program
A/D	analog to digital
AM	Apollo Airlock Module

APAS	Astronaut Position/Attitude System
ATM	Apollo Telescope Mount
BMAG	body-mounted attitude gyro system
C	damping coefficient, dyne centimeters-seconds
CAD	controls analog-to-digital converter (voltage to frequency)
C form	code form
C <sub>p</sub>	clock pulse
CRD	current regulating diode
CSM	Apollo Command and Service Module
DARS	Digital Attitude and Rate System
Di	Digital Attitude and Rate System data word
DMS	Apollo Data Management System
ECC	Experiment Components Container
EDC	Experiment Data System
e <sub>i</sub>	input voltage, decibels
e <sub>o</sub>	output voltage, decibels
EVA	extravehicular activities
FET	field effect transistor
Fi	minor frame
FMS	Force Measuring System
FMSi	Force Measuring System data word
FMU	Force Measuring Unit



$f_p$	pulse frequency, cycles/second
FSK	frequency shift keyed
g	Earth's gravitational constant
h	threshold voltage
IF	intermediate frequency
IMU	Inertial Measuring Unit
IVA	intravehicular activities
J	angular moment of inertia, grams-centimeters
K	integrator gain, volts/second
$K_A$	amplifier gain constant, milliamperes/degree
kpbs	kilobits per second
kHz	kilohertz or thousand cycles per second
$K_T$	tachometer voltage constant, dyne centimeters/ radian milliamperes/deg
$\ell$	distance of accelerometer from center of gravity of mass
Li	Limb Motion Sensing System data word
LIMS	Limb Motion Sensing System
LPDTL	low power direct transistor micrologic
MDA	Multiple Docking Adapter
MOS	metal oxide semiconductor
msec	millisecond
M055	Apollo Applications Program Time and Motion Study Experiment designation
N	number of bits in the sync word

NRZ	non-return to zero
OWS	Orbital Workshop
p	pressure
P-C	printed circuit
PCM	pulse code modulation
ppm	parts per million
pps	pulses per second
R	universal gas constant; total rotation
RF	radio frequency
RGP	rate gyro package
RGS	rate gyro system
$\underline{R}_i$	ultrasonic receiver to target vector in vehicle coordinates
$R_r$	radiation resistance, ohms
s	complex variable
S/C	spacecraft
$\underline{S}_i$	ultrasonic receiver position vector in vehicle coordinates
$S_{ix}, S_{iy}, S_{iz}$	components of ultrasonic receiver position vector in vehicle coordinates
$S'_{ix}, S'_{iy}, S'_{iz}$	components of ultrasonic receiver position vector with one receiver ( $S_4$ ) as reference
SOS	Martin Marietta Corporation's Space Operations Simulator
t	time, seconds
$\underline{T}$	target vector with vehicle reference

TARS	three-axis reference system
TC	temperature coefficient
$T'_x, T'_y, T'_z$	components of target vector with ultrasonic receiver coordinates
T013	Apollo Applications Program Crew Motion Experiment designation
US	ultrasonic
US-RF	ultrasonic-radio frequency
VCO	voltage-controlled oscillator
vhf	very high frequency
$V_R$	differential comparator bias voltage
$V_S$	summation junction voltage; velocity of sound
$W_i$	data word
$\gamma$	ratio of specific heat of gas at constant pressure to that at constant volume
$\Delta A$	incremental change in parameter A
$\Delta f_p$	incremental change in pulse frequency
$\Delta h$	incremental change in threshold voltage
$\delta_i$	maximum value of absolute value of incremental change
$\Delta S_i$	incremental change in $\underline{S}_i$
$\Delta T$	incremental temperature change
$\Delta t$	incremental change in time, seconds
$\Delta t_i$	incremental change in time
$\Delta V_S$	incremental change in velocity of sound
$\epsilon$	error

$\lambda$	wavelength
$\mu c$	frequency, megacycles/second
$\mu L$	micrologic
$\rho$	density
$\varphi_1, \varphi_2, \varphi_3$	difference in accelerometer readings along the x, y, or z axis, respectively
$\omega$	angular frequency, radians/second; angular velocity, radians/second
$\Omega_{mx}, \Omega_{my}, \Omega_{mz}$	measured angular velocity about the x, y, or z axis

## MATHEMATICAL MODEL OF EXPERIMENT AND GROUND SIMULATION PROGRAMS

The mathematical models and analytical tools described in this section are those required to **determine** spacecraft (S/C) disturbances caused by the motions of crew members. There are several slightly different mathematical models discussed; however, the basic equations involved are the same. Specific models depend on (1) the type of crew activity being investigated, and (2) whether the model is applied to ground simulation activities or the actual space experiment activities.

Common to all math models are the dynamic equations of motion for the S/C and the astronaut. The S/C is considered to be a rigid body disturbed only by the forces generated by the astronaut. The astronaut is considered to be a segmented man whose segment properties are represented by mathematical equations. Also common to all math models is the requirement for the Limb Motion Sensing System (LIMS), which is a device for measuring the position of man's limb segments relative to the torso. With the information from the segment property equations and from the LIMS, the required dynamics of the astronauts can be calculated.

The crew activities investigated in this study are divided into two categories -- restrained crew activities and translational crew activities. The restrained crew activity program investigates disturbances or activities such as heartbeat and breathing, coughing, sneezing, pure arm motions, and console operations. The translational crew activity program investigates such motions as free soaring, bounce walk, compressive walking, and handrail translation.

Before the actual flight experiment, it is necessary to assure that the mathematical models used to investigate these activities are as complete and accurate as possible and that the computer programs required to obtain numerical results are reliable. The ground simulation programs conducted during this study accomplished this objective in addition to producing realistic values for S/C disturbances caused by the aforementioned crew activities.

In the following subsections, the two ground simulation programs, one for each activity category, are discussed. Results of all activities investigated are presented in Appendix A.

## Restrained Crew Activity Program

Mathematical model accuracy.- An important objective of the restrained crew activity program besides obtaining crew disturbance data is to establish the correctness and accuracy of the equations involved in analytically describing crew motion. Of particular interest is the math model describing the dynamic properties of man and the capability of the LIMS to accurately describe limb segment positions relative to the torso.

The restrained crew activity simulation is, therefore, conducted in two parts -- one called physical simulation that results in experimental test data, and the other called digital simulation that results in calculated data using the mathematical models. These simulations are depicted graphically in figure 1.

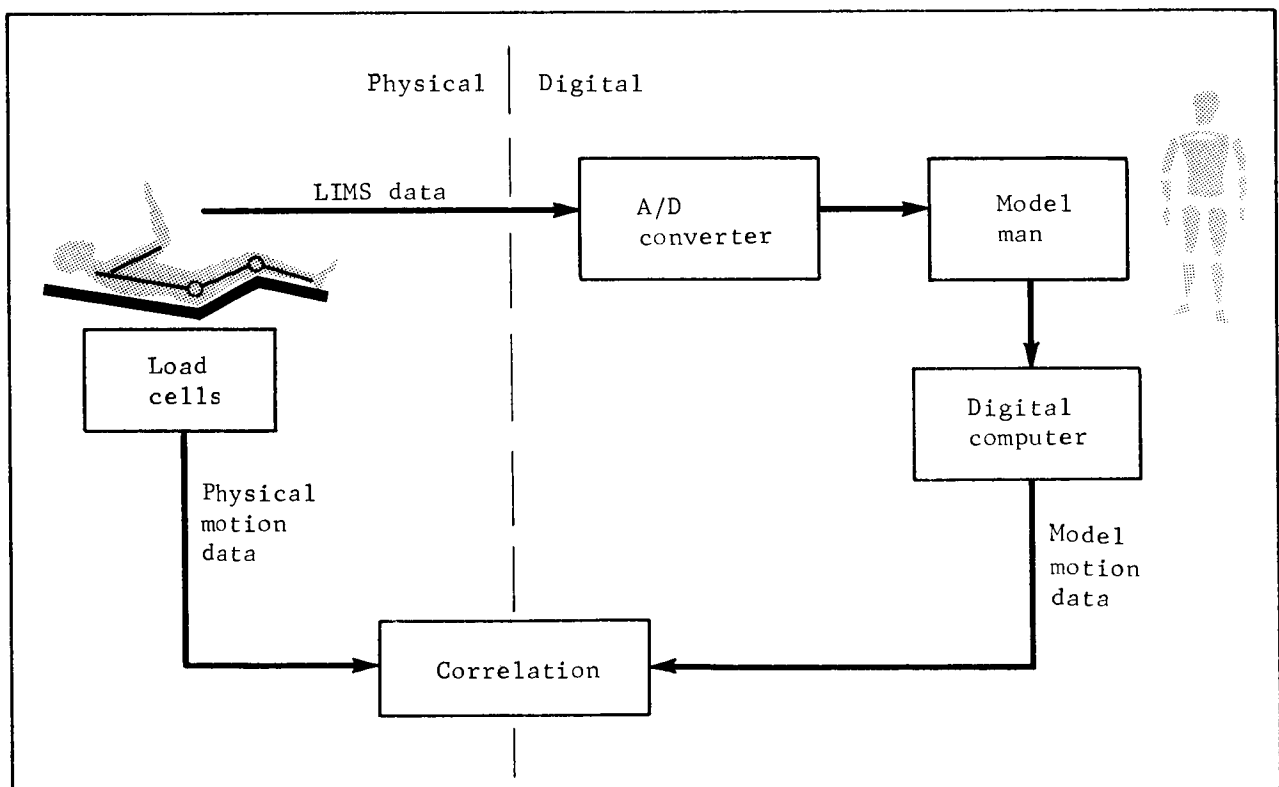


Figure 1.- Restrained Crew Activity Simulation Plan

The physical simulation consists of requiring a human subject to perform the specified activities while lying on a mockup of the Apollo couch. The couch is rigidly attached to a load cell array that measures the forces and moments the man applies to the couch. Data from the physical simulation are termed physical motion data.

While the subject is performing his activities on the couch, the positions of his limbs are continually monitored by the LIMS. These positional data are digitized by an analog-to-digital (A/D) converter for use with digital computers.

The digital simulation consists of feeding the digitized LIMS data into a computer programed with the equations of the math model. Mathematically, it is required that the model man limb motion be exactly the same as the physical test subject, thus allowing the computer to calculate the forces and moments the model man would apply to a couch for the same activities. Results from the digital simulation are termed model motion data.

As explained further in the following subsection along with more details of the restrained activity simulation procedure, the physical motion data and the model motion data can be compared, giving a means of measuring the accuracy of the math model equations and in particular the model man equations and LIMS capability.

### Physical Simulations

The laboratory setup for obtaining the physical motion data is shown in figure 2. The subject is shown lying on the Apollo couch mockup which is rigidly attached to the load cell array. This array, which is more clearly shown in figure 3, consists of six load cells arranged in a geometric array. As the subject moves, the individual load cells produce a voltage directly proportional to the force applied. By resolving the individual outputs of the cells according to the geometric array, three forces and three moments about the orthogonal axis system of the subject are obtained (these axes are shown in fig. 2). The resolution equations are programed on a desk top analog computer shown in figure 3. The forces and moments from the computer resulting from the subject's motions are those that exist at a point corresponding to the load cell array geometric centroid. A further discussion and the resolution equations of the load cell array are presented in Appendix B.



Figure 2.- Physical Simulation of In-Place Motions

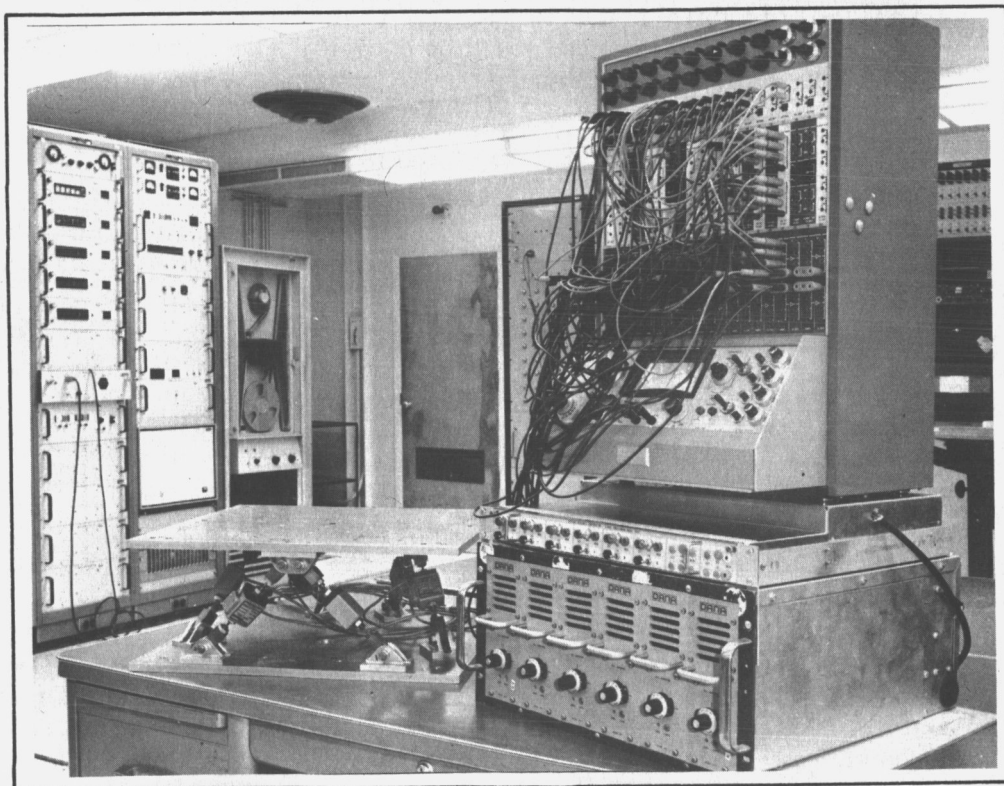


Figure 3.- Analog Computer Resolution of Load Cell Outputs



Also shown in figure 2 is the laboratory model of the LIMS that is worn by the subject while performing all limb motion tasks. The LIMS is a skeletal structure having one or more pivots at the major joints of the human body. Each pivot contains a linear potentiometer whose output voltage is directly proportional to the degree of joint rotation. A total of 16 potentiometers are required to measure all significant limb motions for the required tasks.

The physical simulation test data are taken through the use of an A/D converter and a digital tape recorder. All 16 LIMS potentiometer outputs and the 6 force and moment analog computer outputs are fed directly into the A/D converter, and each is sampled at a rate of 100 sample/sec. These data are then digitally recorded on the magnetic tape. For purposes of monitoring test equipment and to assure good data during the tests, the LIMS angles and load cell forces and moments were recorded on an analog strip-chart recorder.

A simple data reduction program is required to reduce the A/D converter output data to a format acceptable to large digital computers.

### Digital Simulations

Digital simulation of restrained crew activities is accomplished entirely with digital computers. The programed equations of the restrained activity math model, called the Crew Disturbance Program, are used to calculate the model motion data.

Model man.- In the digital simulation of man's activities, it is necessary that the dynamic properties of man's segments be approximated mathematically. A math model for determining segment properties of mass, length, center-of-mass location, and inertia has been developed by Barter (ref. 2) and Woolley (ref 3). The Barter-Woolley equations allow calculation of segment properties knowing only the subject's total weight, and are accurate to within  $\pm 10\%$ . The Barter-Woolley model man consists of nine segments as shown in figure 4. A discussion of the adequacy of the nine-segment model and the accuracy of the segment properties is presented in a subsection entitled "Correlation and Conclusions." The Barter-Woolley equations are given in Appendix D.

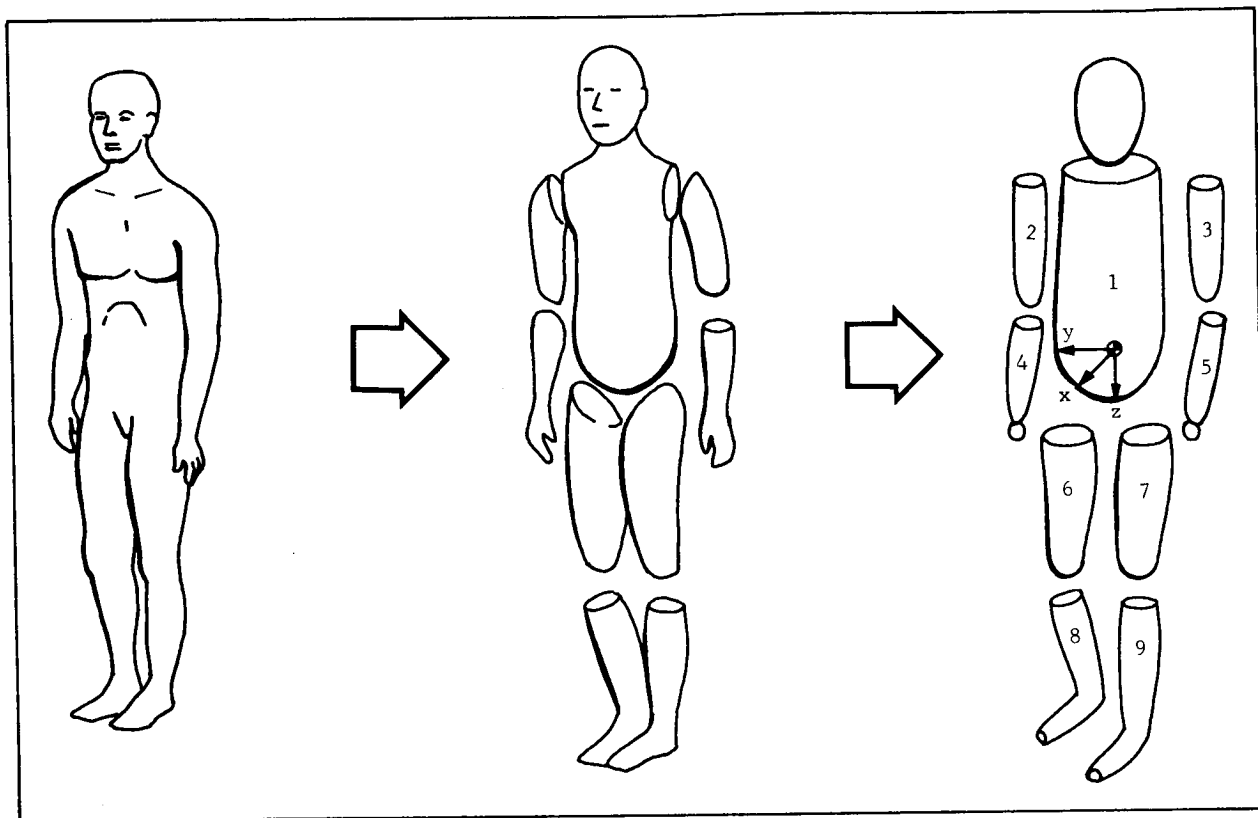


Figure 4.- Mathematical Model of Man

LIMS data.- As previously mentioned, the physical simulation resulted in LIMS data describing how the subject's limbs moved during performance of the restrained crew activities. These data are used by the Crew Disturbance program to calculate the dynamics of the nine-segment model man. Some of the quantities involved in the dynamic equations require that numerical derivatives of the LIMS angles be taken. Because of a small amount of signal noise being generated during the tests, it is required that the LIMS angles be smoothed before being fed into the Crew Disturbance Program. The smoothing technique chosen to accomplish this purpose is the least-squares fit of Tchebycheff polynomials to the data and is one used extensively by the Martin Marietta Titan III personnel for smoothing missile trajectory data. A further description of this smoothing technique is presented in Appendix C.

Digital crew disturbance program.- In the digital simulation of restrained crew activities, both the man and the S/C are integral parts of the math model, and, unlike the physical simulation, S/C disturbances are results of the digital simulation along

with forces and moments caused by man's activities. The crew disturbance equations are derived using the conservation of angular momentum principle as applied to the total man/spacecraft system. The principle states, in this case, that the momentum added to the system by man's activity must be taken out of the system by the S/C. Requiring the LIMS angles as the only inputs, the crew disturbance program can then calculate the S/C disturbances from the model man's motions. The forces and moments produced by the model man that must exist to give the calculated S/C disturbance can then also be determined.

A detailed description of all equations involved in the crew disturbance program are presented in reference 4.

Because one of the purposes of the physical and digital simulations is to verify the math model of man and LIMS capability, it is necessary to assure that the physical and model motion data are directly comparable. One factor that affects both sets of data is the exact point relative to the man's torso at which the forces and moments are calculated. In the physical simulation, the resolved load cell forces and moments are those that exist at a point corresponding to the load cell array geometric centroid. In the digital simulation, it is assumed that the subject is attached to a load cell array in the same manner as in the physical simulation, and that the load cell array is attached to the S/C (this condition is the same as will exist in the actual flight experiment for the restrained crew activities). After forces and moments causing the S/C disturbances are calculated in the digital program, they are transferred to a point in the S/C corresponding to the load cell array geometric centroid. Thus, both the measured and calculated forces and moments are determined at identical locations with respect to man.

Another factor affecting the model motion data is the fact that the magnitude of the forces and moments are a function of the mass and inertia characteristics of the S/C. In the physical simulation, the load cells are effectively attached to an infinite S/C, while in the digital simulation the load cells are attached to a finite but large S/C. Analysis has shown, however, that there is a negligible difference in the forces and moments when considering an infinite or a finite S/C if the finite S/C has mass and inertia characteristics very much greater than those of the man. Because this is the case for the proposed carrier of the crew motion disturbance experiment, physical and model motion data are negligibly affected by S/C size.

Another important factor that affects two of the moments determined from the physical simulation is the gravity environment in which the tests are conducted. In the digital simulation, of course, the moment results are not affected because zero-g conditions are mathematically described. The two moments affected are about the y and z axes of the torso axis system (see fig. 2). As the subject moves his limb segments from an initial position, the combined center of mass (c.m.) of all segments also moves, relative to the fixed torso. The effect then is that static moments about the y and z axes result, which are equal to the subject's weight times the distances along the y and z axes that the c.m. moves. The values of c.m. shift moments can be one order of magnitude greater than the dynamic moments caused by the subjects motions.

The digital crew disturbance program is specifically tailored to account for the above-mentioned factors to assure that calculated and experimental results are directly comparable. The program calculates the static center-of-gravity (c.g.) shift moments from LIMS data and model man equations and adds these results to the calculated dynamic moments. The resulting moments are then the total moments equivalent to those measured by the load cells in the physical simulation. In Appendix A, both the dynamic and total moment results from the crew disturbance program are presented for all motions considered.

To briefly summarize the basic crew disturbance program, a simplified block diagram of the program is shown in figure 5. The model man data and LIMS angles data, obtained as previously described, are used to calculate the angular momentum of the model man's limb segments. Using the conservation of angular momentum principle (and assuming a rigid body S/C and no external forces on the man/spacecraft system), the angular momentum of the S/C can be calculated. From these results, the S/C disturbances such as angular rates and displacements can then easily be determined, as can the forces and moments causing the disturbances. Again, these results are called the model motion data.

### Correlation and Conclusions

In the previous subsections, the methods used to obtain the physical motion data have been described; and it has been explained that the two sets of data are directly comparable. It is the purpose of this subsection to examine the data carefully and attempt to explain any remaining discrepancies or differences between the results of each simulation.

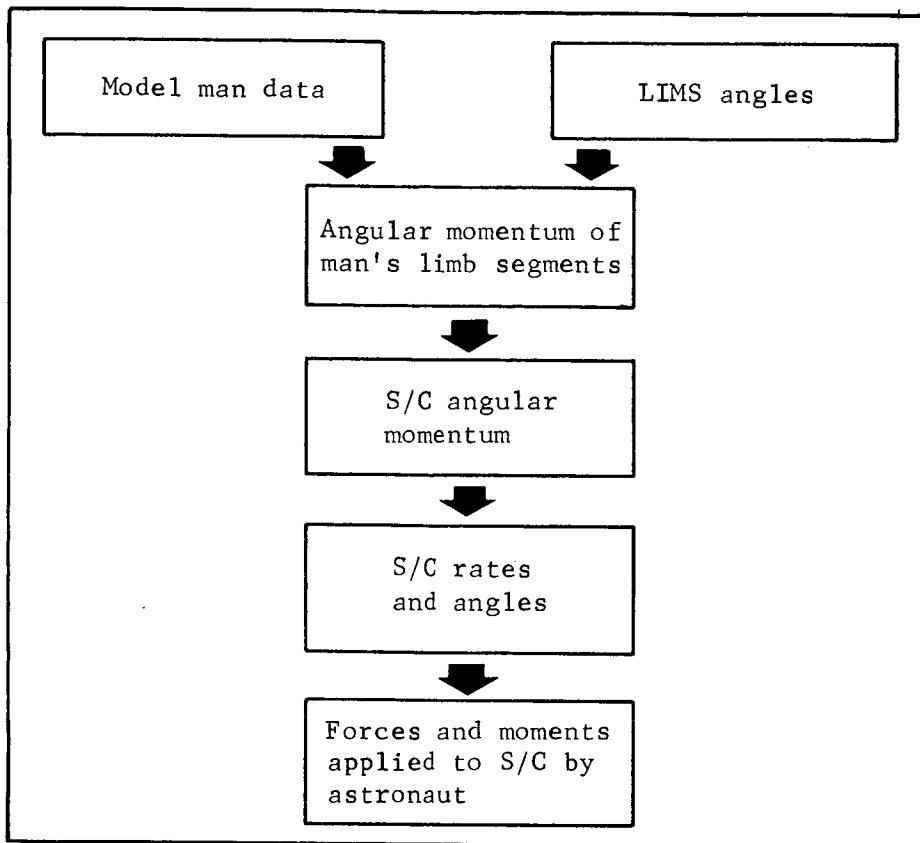
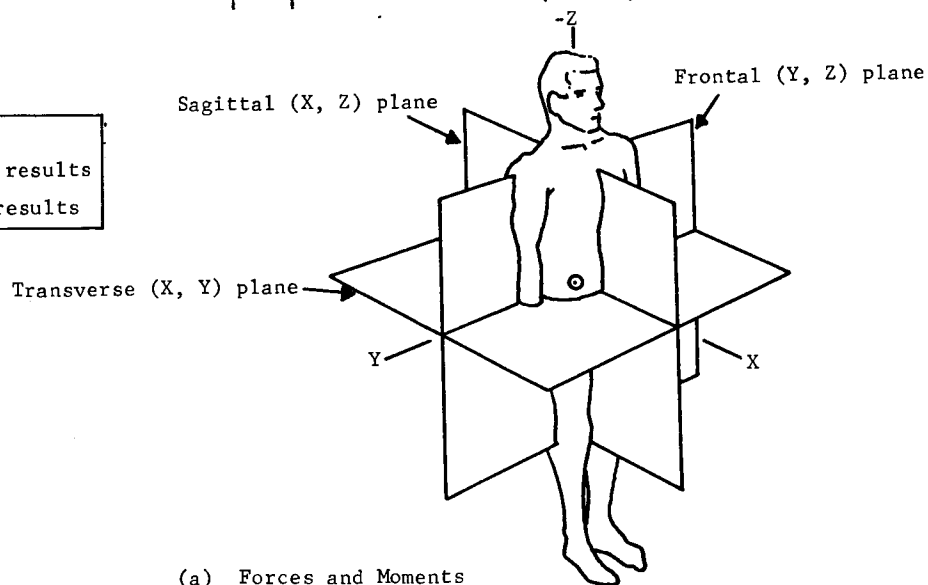
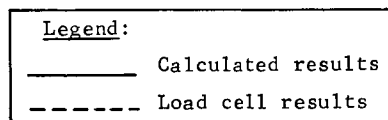
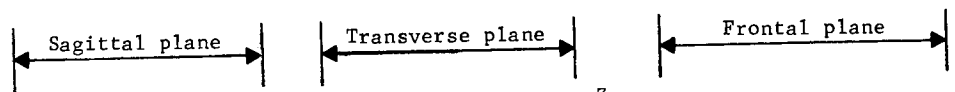
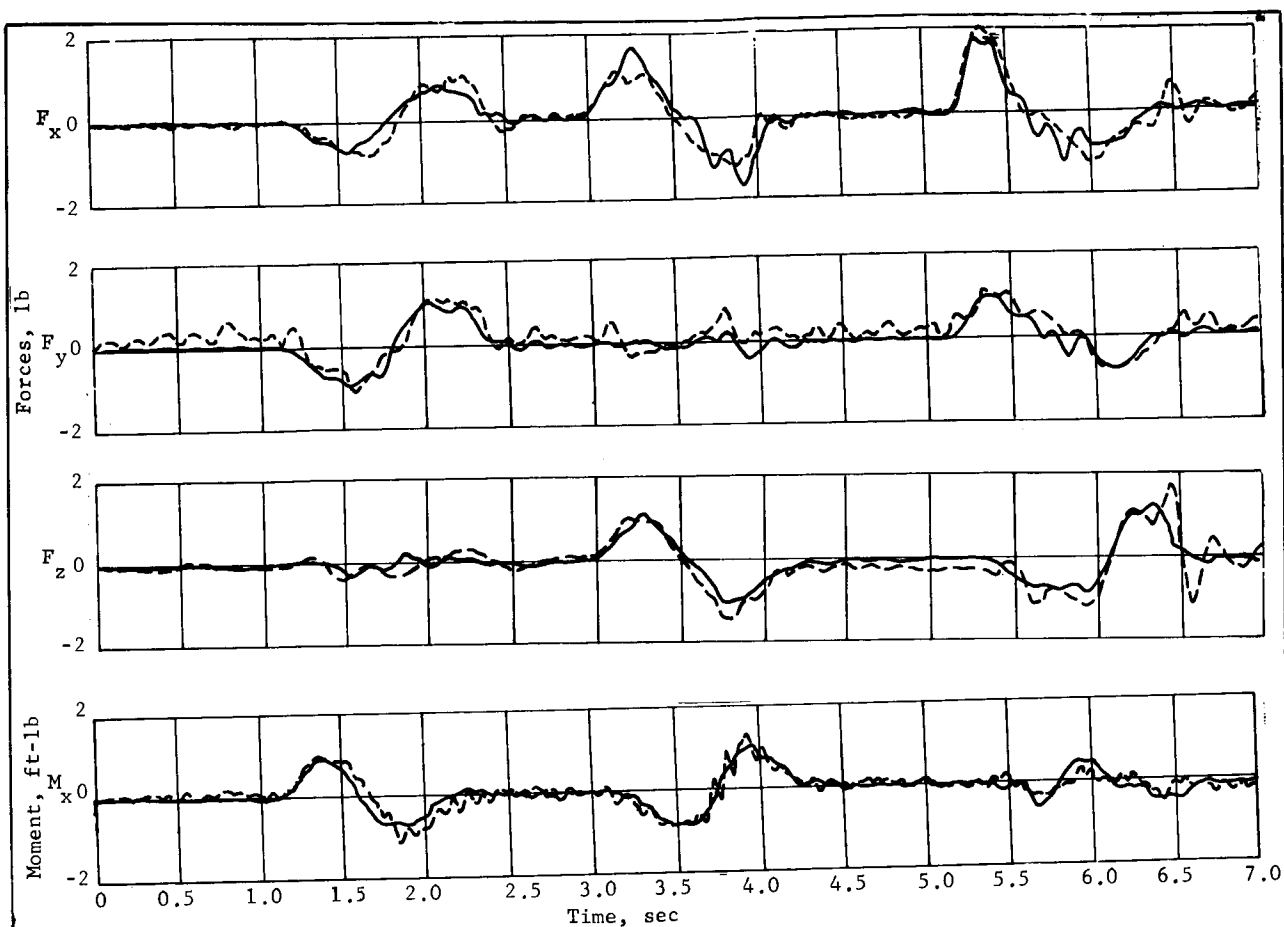


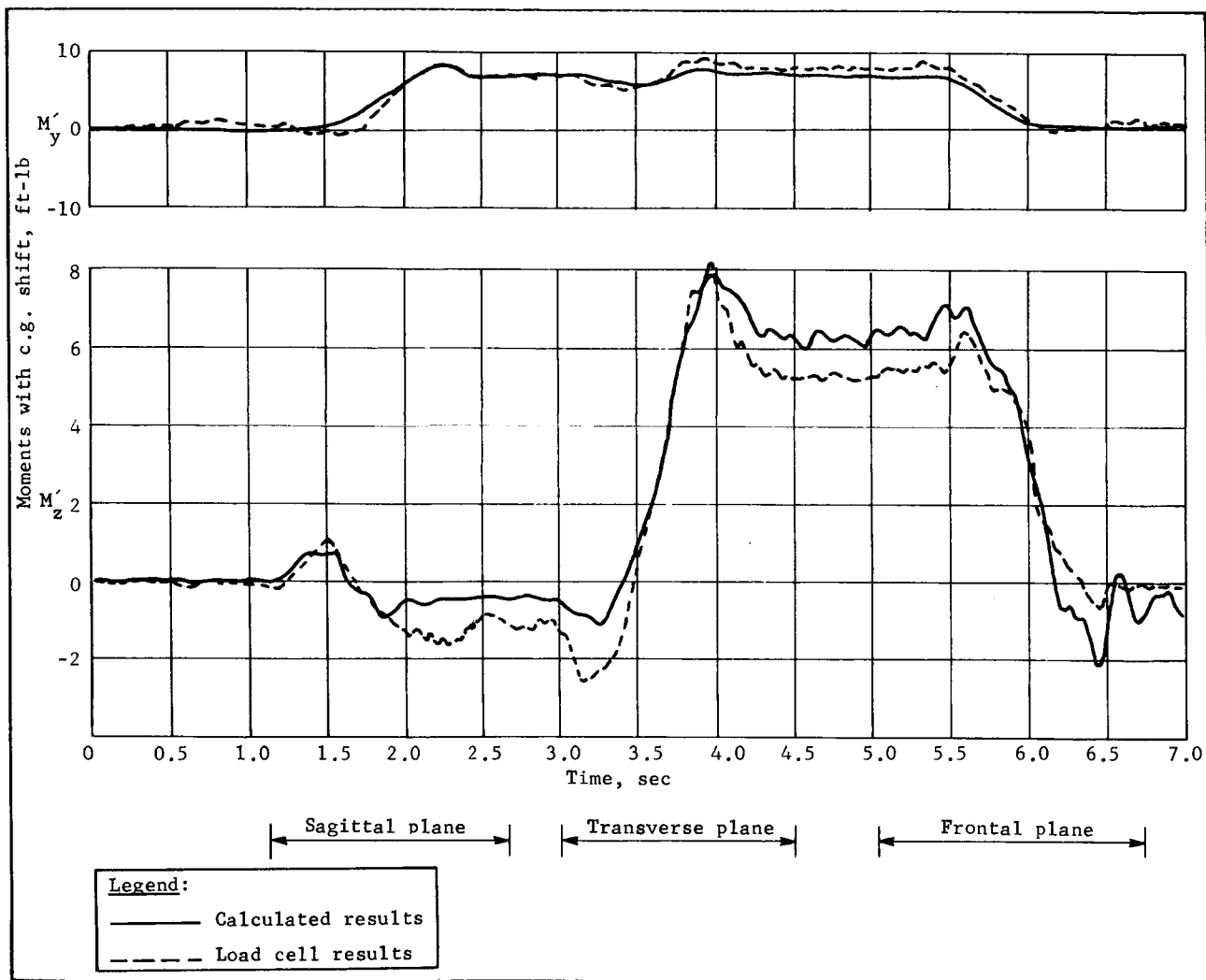
Figure 5.- Crew Disturbance Digital Program

Model motion data and physical motion data for a specified motion are shown in figure 6. The physical motion data are plotted directly from digitized load cell data; the model motion data, plotted on the same graph, are obtained from the digital crew disturbance program. The calculated y and z moments include the static moments due to c.m. shift. The particular motion shown in figure 6 is a right-arm movement of approximately 90° rotation in each of the three planes of man's axis system. Beginning with the right arm at the subject's side, the first movement is approximately a 90° swing in the sagittal plane; the second approximately a 90° swing in the transverse plane, and the third approximately a 90° swing in the frontal plane back to the original position. These motions and when they occur are indicated in figure 6. For approximately 1/2 sec after each 90° swing, the subject held his arm still so that the y and z moments at these times are pure static moments due only to the c.m. shift. The four right arm angles for this motion are shown in figure 6 (see Appendix A for arm angle nomenclature).



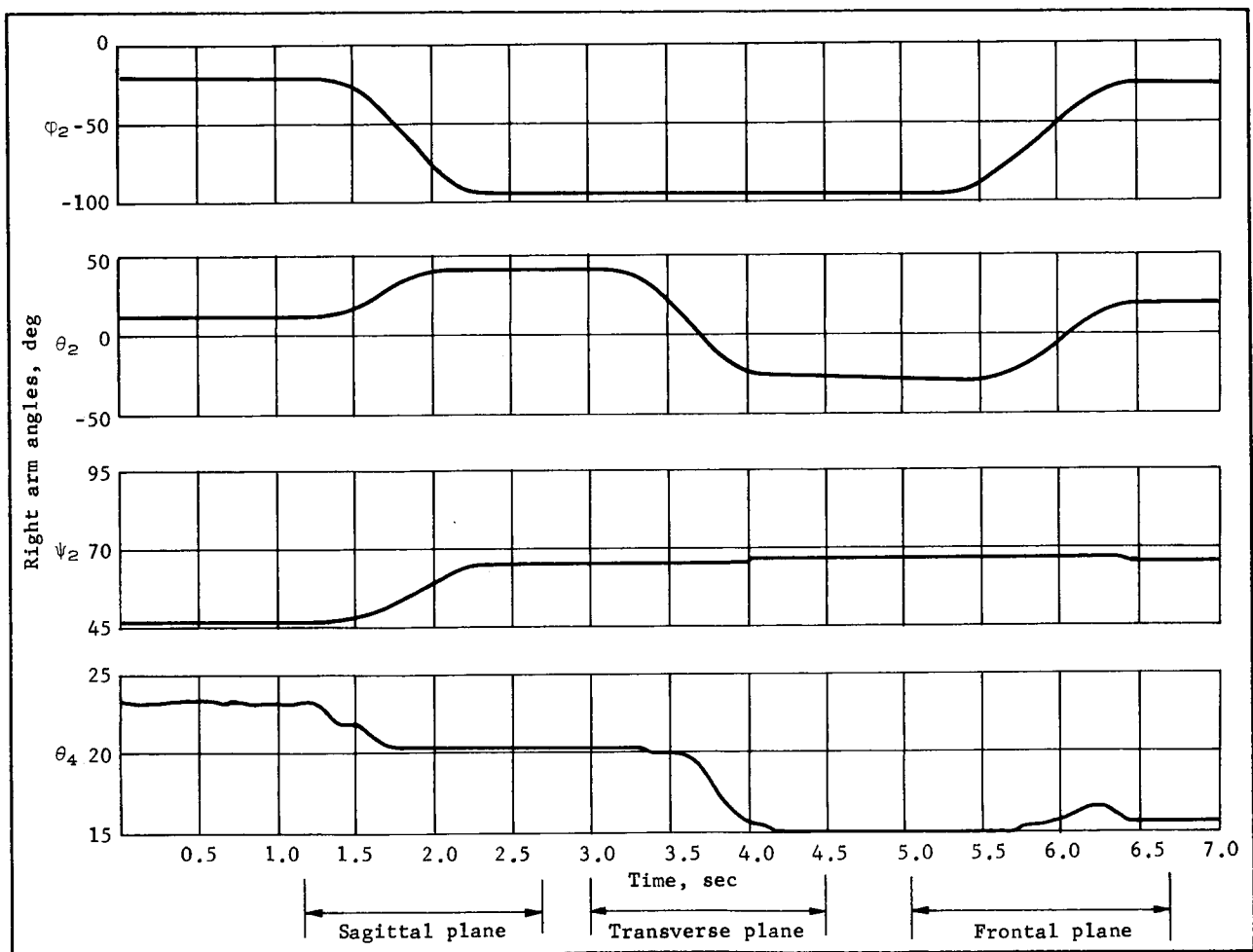
(a) Forces and Moments

Figure 6. - Arm Motion in Each of Three Planes



(a) - Concluded

Figure 6. - Continued



(b) Right Arm Angles

Figure 6. - Concluded



Before discussing possible discrepancies due to model man properties or LIMS angle errors other reasons for differences in the results must be investigated. These are:

- 1) Heartbeat and breathing;
- 2) Nonmeasured segment motions;
- 3) Torso shifting.

Of course, in the physical simulation the disturbances caused by heartbeat and breathing exist simultaneously with forces and moments caused by any limb motions and cannot easily be separated. Normally, however, heartbeat and breathing disturbances are relatively small compared to disturbances from limb motions. Heartbeat and normal breathing disturbance data were taken during the physical simulation tests, and the results are shown in figure A3 of Appendix A. All results for limb motion activity can then be expected to differ from the physical simulation results (where heartbeat and breathing disturbances are not calculated) by at least the approximate values, based on figure A3, Appendix A, listed in table 1.

TABLE 1.- MAXIMUM DIFFERENCES BETWEEN PHYSICAL  
AND MODEL MOTION - FORCES AND MOMENTS  
ATTRIBUTABLE TO HEARTBEAT AND BREATHING

$F_x$	$\pm 0.15$ lb	$M_x$	$\pm 0.15$ ft-lb
$F_y$	$\pm 0.15$ lb	$M_y$	$\pm 0.7$ ft-lb
$F_z$	$\pm 0.4$ lb	$M_z$	$\pm 0.1$ ft lb

Possible extraneous disturbances could also be caused by the effects of nonmeasured segment motions such as head, wrist, and ankle movements. During the performance of the restrained activities, the subject was requested to hold his head, wrists, and ankles as still as possible relative to an inner segment; it is, therefore, believed that the effects of these nonmeasured segments are completely negligible on the results presented in this report. The exception to this may be console operation activity where the subject was allowed to move his wrist.

It is proposed that in the actual flight experiment the astronaut be required to perform the restrained activities in the same manner that the ground activities were performed (i.e., hold his head, wrists, and ankles still). The experiment flight data will then be directly comparable to ground-based data. The prime purpose of this requirement is to simplify the flight experiment as much as possible by reducing the number of segments monitored by

LIMS to only these normally expected to contribute significantly to the forces and moments. It is then established that only eight major limb segments need be monitored by LIMS, and, therefore a nine-segment man (including a torso segment) is used in all calculations.

The above discussion is not meant to imply that exaggerated motion of the head, wrist, or ankle is negligible in comparison to other forces and moments. Data for this type of activity have been obtained and are shown in figures A7 thru A9, Appendix A.

The third factor that affects the physical simulation results is torso shift. For the physical simulation, a form fitting metal backplate was sewed into the subject's suit worn during the tests. This plate was bolted to the couch mockup to minimize torso shifting. Despite this precaution, the torso is still not perfectly rigid when attached to the couch and can move slightly when disturbed by a limb motion. Of course, extraneous forces in both the y and z directions are picked up by the load cells when this occurs. The effect is pronounced at a time during an activity when a limb is suddenly stopped, such as at the end of a swing. A good example of the effect is shown in figure 6(a) at 6.5 sec. The more force that is applied to the torso by a moving limb (such as for leg movements) the greater the effect. The torso shift problem has not been treated analytically, and in the digital simulation the torso is made to be rigidly attached to the S/C. Torso shifting will also occur in the flight experiment.

Based on the previous discussion, it is concluded that the primary discrepancies between physical and model motion data can be explained by heartbeat and breathing disturbances and torso shifting effects. Two other important possible causes for differences are due to model man inaccuracies or limb position errors from the LIMS.

To investigate the effects of model man properties, another math model was substituted in the Crew Disturbance Program for the Barter-Wooley model, and the program was repeated using the same LIMS inputs. The new model is one developed by Hanavan (ref. 5) where segment properties are obtained from anthropometric measurements of the subject and assuming geometric shapes for the segments. The segment masses predicted by both models have been modified slightly to include the mass of the LIMS structure, which is attached to each segment. The results using the Hanavan model were essentially identical (variation was less than 1%) with the results from the Barter-Woolley model. Thus it is concluded that force and moment results are relatively insensitive to segment properties and the math model of man is, therefore, not a critical part of the total math model.

One other discrepancy between the results shown in figure 6(a) is in the y and z moments at points where the arm is in an extended position. This difference is attributed to an inaccuracy in the LIMS program determination of the exact arm position. The discrepancy exists at times when the arm is not moving and is, therefore, caused by inaccurate combined c.g. shift moments. These moments are calculated using the LIMS angles (rather than angle derivatives), whereas the dynamic forces and moments are primarily a function of the angle derivatives. Because the c.g. shift moments are not present in the spaceflight experiment, correlation of calculated and experimental flight data will not experience this problem. Because the three forces and one moment about the x axis correlate very well, it is concluded that the LIMS does an acceptable job of measuring the angular rates of segment motions. The slight inaccuracy of the LIMS program in determining the exact arm position is believed to be caused by the fact that the LIMS was not perfectly aligned on the subject during the physical motion simulation.

#### Restrained Crew Activities

The restrained crew activities are separated into three categories: (1) involuntary motions, (2) voluntary and nonmeasured motions, and (3) voluntary and measured motions. The effects of the motions in all these categories have been investigated in the physical simulation program, however, only the motions in the third category have been studied in the digital simulation program. A brief description of the motions covered in each category is presented in table 2.

All results from the restrained crew activity simulation program are given in Appendix A. The physical simulation forces and moments are presented along with the digitally calculated forces and moments on the same graphs. Also shown are the S/C disturbances calculated from the crew disturbance program. The S/C used in the calculations is the present configuration of the Mission 1/2 S/C, which is the proposed carrier of the Crew Motion Disturbance Experiment. The properties of this S/C and the location of the man relative to the S/C c.m. are shown in figure 7.

TABLE 2.- RESTRAINED CREW ACTIVITIES DESCRIPTION

Motions	Description
Involuntary motions	
Heartbeat and breathing	Heartbeat alone, and normal and fast breathing including heartbeat
Coughing and sneezing	Self-evident
Voluntary and nonmeasured motions	
Head motions	Head rotations about three axes
Wrist motions	Wrist rotations about two axes
Ankle motions	Ankle rotations about two axes
Voluntary and measured motions	
Single pendulum lower arm or lower leg motions	Swinging motion of lower arm or leg with bending only at elbow or knee; sagittal plane
Single pendulum arm or leg motions	Swinging motions of total arm or leg with no bending at elbow or knee; frontal and sagittal plane
Double pendulum arm or leg motions	Swinging motion of arm or leg with bending at elbow or knee and shoulder or hip; sagittal plane
Console operation	Typical motions of right arm reaching for console, turning knobs, flipping switches
Exercising	Motion of both arms and both legs using elastic cord exerciser

Spacecraft properties:

Weight: 105 000 lb

Inertias, slug-ft<sup>2</sup>:

$I_{XX} = 556\ 000$

$I_{YY} = 3\ 270\ 000$

$I_{ZZ} = 3\ 245\ 000$

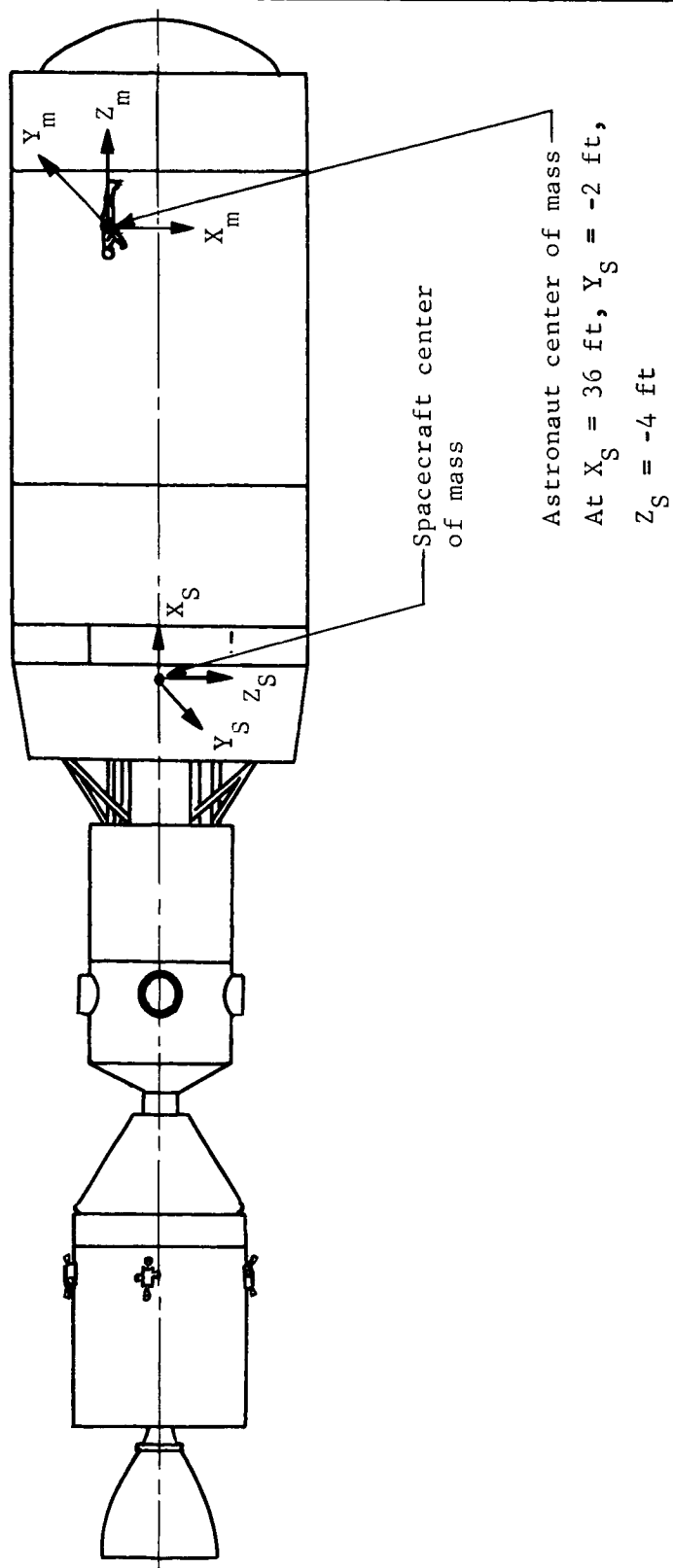


Figure 7.- Apollo Cluster Vehicle

S/C reactions to restrained crew activities can be calculated by two methods, either by the digital crew disturbance program (using LIMS angles and model man equations) or by applying the load cell forces and moments to the S/C. Several problems arise however when attempting to calculate S/C reactions by the latter method. One problem is that the load cell moments include moments due to combined c.g. shift. Using LIMS data and the model man equations, these c.g. shift moments can readily be removed. A special digital program has been written and is available for this purpose.

Another problem that must be corrected is caused by the fact that the load cells cannot be perfectly "zeroed" before recording motion data. Although the small constant bias on the forces and moments is not visible in the figures showing load cell results, it can be of sufficient magnitude to appreciably affect S/C disturbances (this is because the bias, though small, acts as a constant force or moment on the S/C). This bias can easily be removed by digitally subtracting the average value of all data points in a run from each data point. S/C disturbance due to several of the crew activities involving limb motions have been calculated using the load cell forces and moments, and the results are presented and discussed at the end of this section.

Involuntary motions.- The involuntary motions were not monitored in any way other than by the load cell array (the LIMS monitors only limb motions). Therefore, the load cell results include the effects, if any, of the static c.g. shift moments. For the involuntary motion the c.g. shift effects are expected to be small or negligible in comparison to moments generated by limb movements. However, for some involuntary motions the static moments may be of significant magnitude. If such is the case, the involuntary motion results are not applied to a S/C.

Not all involuntary motions contain c.g. shift effects of sufficient magnitude to be concerned about. Such appears to be the case for the heartbeat data and the coughing and sneezing data. The exceptions are the normal and fast breathing data, shown in Appendix A figures A3 and A4, where the c.g. shift is easily seen in the moment  $M_y$ . Comparing figure A2 (heartbeat only) with figure A3 (heartbeat and normal breathing), it is seen that the forces and moments are not noticeably different with the exception of  $M_y$ . Thus it is concluded that the forces and moments from normal breathing are negligible in comparison to disturbances from heartbeat, and that the 1/5 cps frequency content of  $M_y$  is due entirely to static c.g. shift moments.

This is not the case however for the fast breathing data (fig. A4), because a definite frequency (approximately 1/2 cps) is noted in most all forces and moments. Thus the forces and moments from fast breathing are not negligible in comparison to heartbeat alone.

The heartbeat force and moment data, shown in figure 8, has been applied to the S/C and the resulting disturbances are shown in figure 9. The S/C rates and angles can be considered to be disturbances from heartbeat and normal breathing, because, as previously mentioned, the forces and moments due to breathing are negligible in comparison to heartbeat. The rates  $(\omega_x, \omega_y, \omega_z)$  are S/C body axes rates and the angles  $(\phi, \theta, \psi)$  are the conventional Euler angles (sequence is roll, pitch, yaw).

Voluntary and nonmeasured motions.- The voluntary and non-measured motions investigated in the physical simulation are head, wrist, and ankle motions. The forces and moments generated by these motions are shown in Appendix A figure A7 thru A9. Because head, wrist, and ankle motions are not monitored by LIMS, the effects of the combined c.m. shift moments cannot easily be ascertained, and, therefore, the results are not applied to a S/C.

Voluntary and measured motions.- For all limb motions monitored by LIMS, the combined c.m. shift moments can readily be calculated from the LIMS data and model man equations.

This has been done for the same motion considered previously and S/C disturbances from resulting forces and moments are shown in figure 10. For comparison purposes, the S/C rates and angles from calculated forces and moments are shown in figure 11 [load cell and calculated forces and moments are compared in figure 6(a)]. Even though the forces and moments appear to correlate very well, it is apparent that the S/C angles can vary by as much as an order of magnitude. This problem is believed to be related to the one mentioned previously concerning the load cell bias. Although this bias was removed before applying the load cell data to the S/C, it is apparent that the bias is not exactly constant throughout the run. A small amount of friction in the attachment points in the load cell arrays can cause the bias to change slightly as the subject applies positive and negative forces and moments to the load cells. A very slight amount of drift in the load cells or array amplifiers during the run can also cause the same problem. As mentioned previously, unfortunately a very small amount of constant force or moment when applied to a S/C can become the dominate effect even over a short period of time. Because the S/C disturbance from calculated forces and moments do not have this problem, it is concluded that the crew disturbance program S/C disturbances are then a better approximation to the actual S/C disturbances than the disturbances from load cell results.

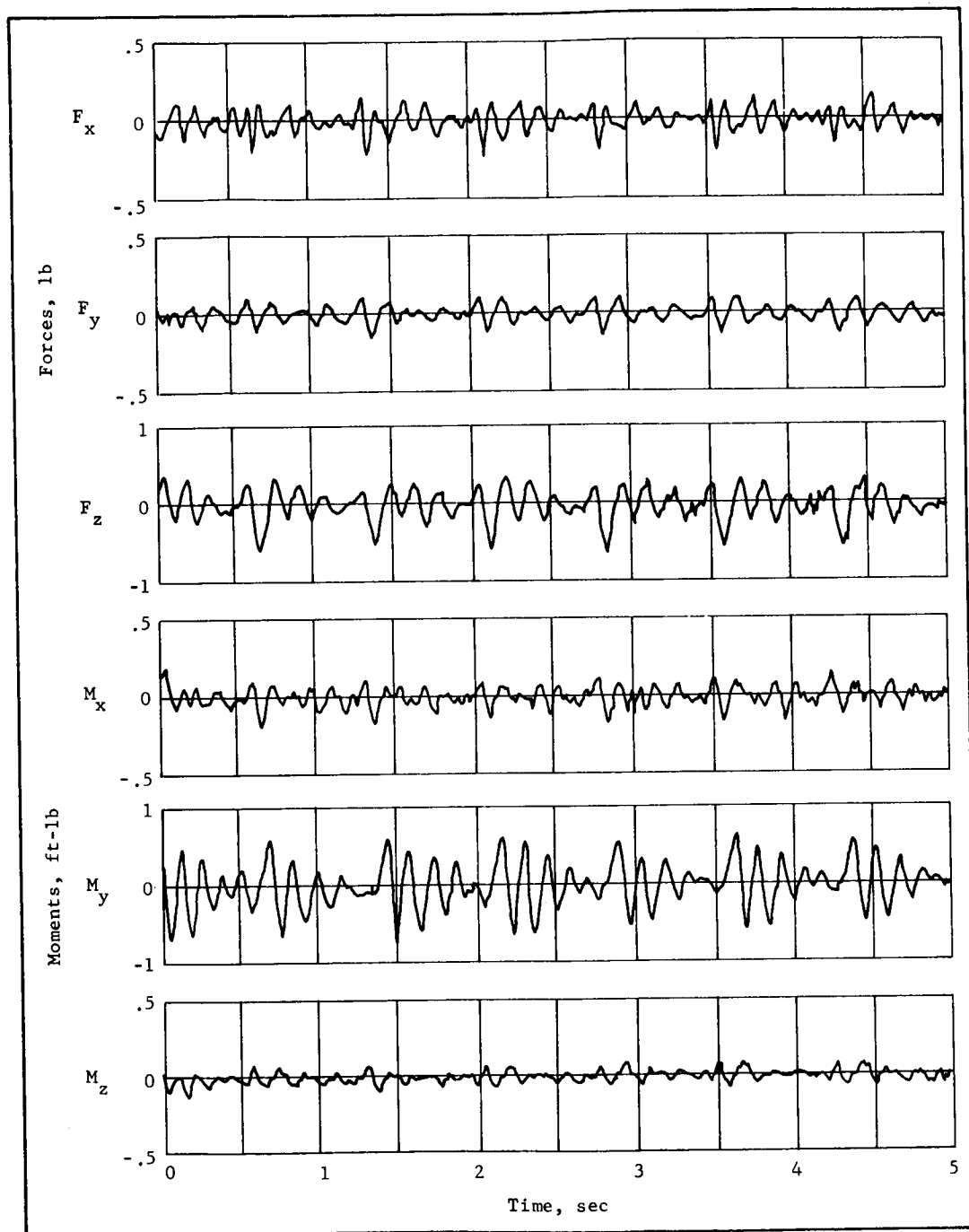


Figure 8.- Heartbeat Data



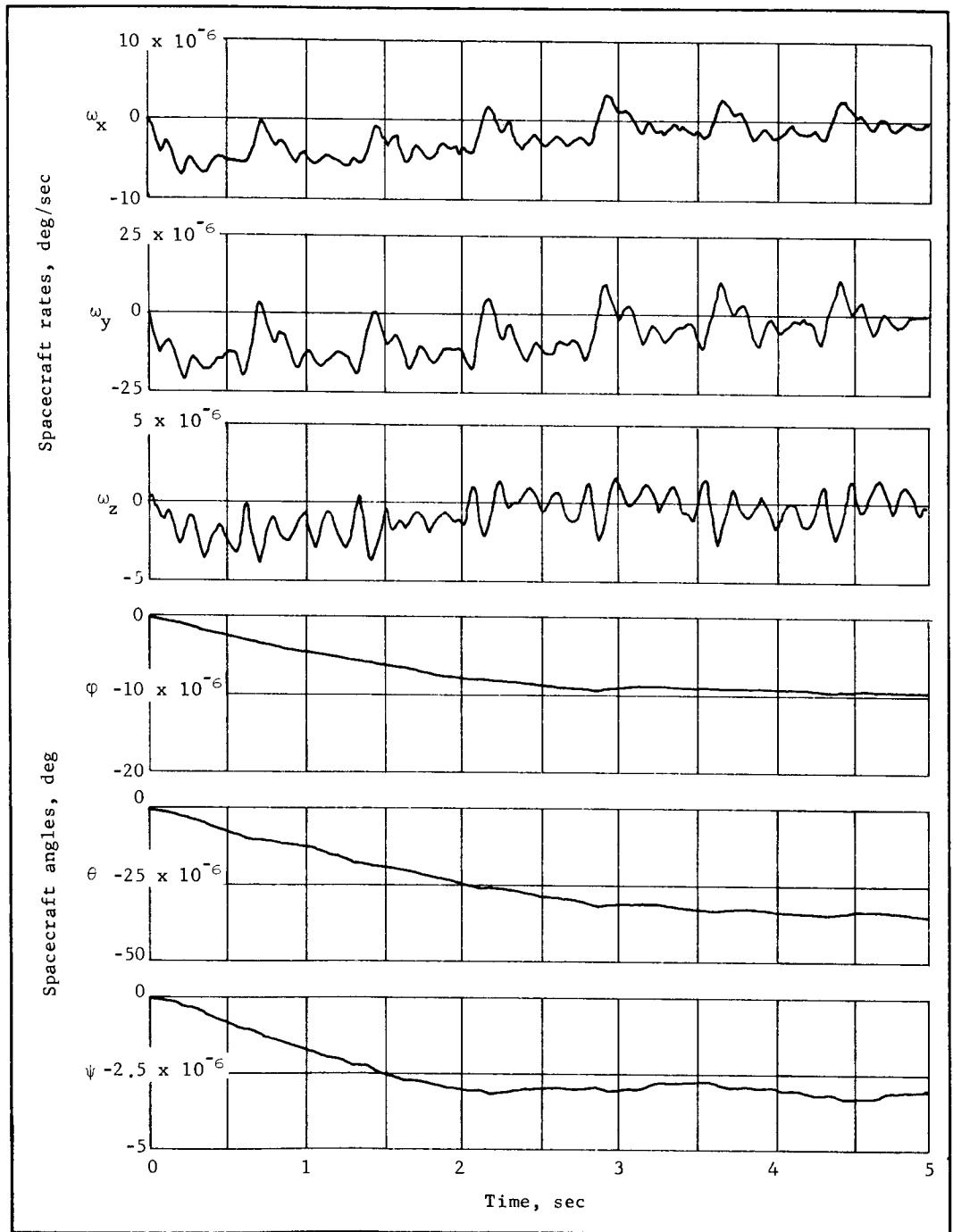


Figure 9.- Spacecraft Disturbance from Heartbeat Data

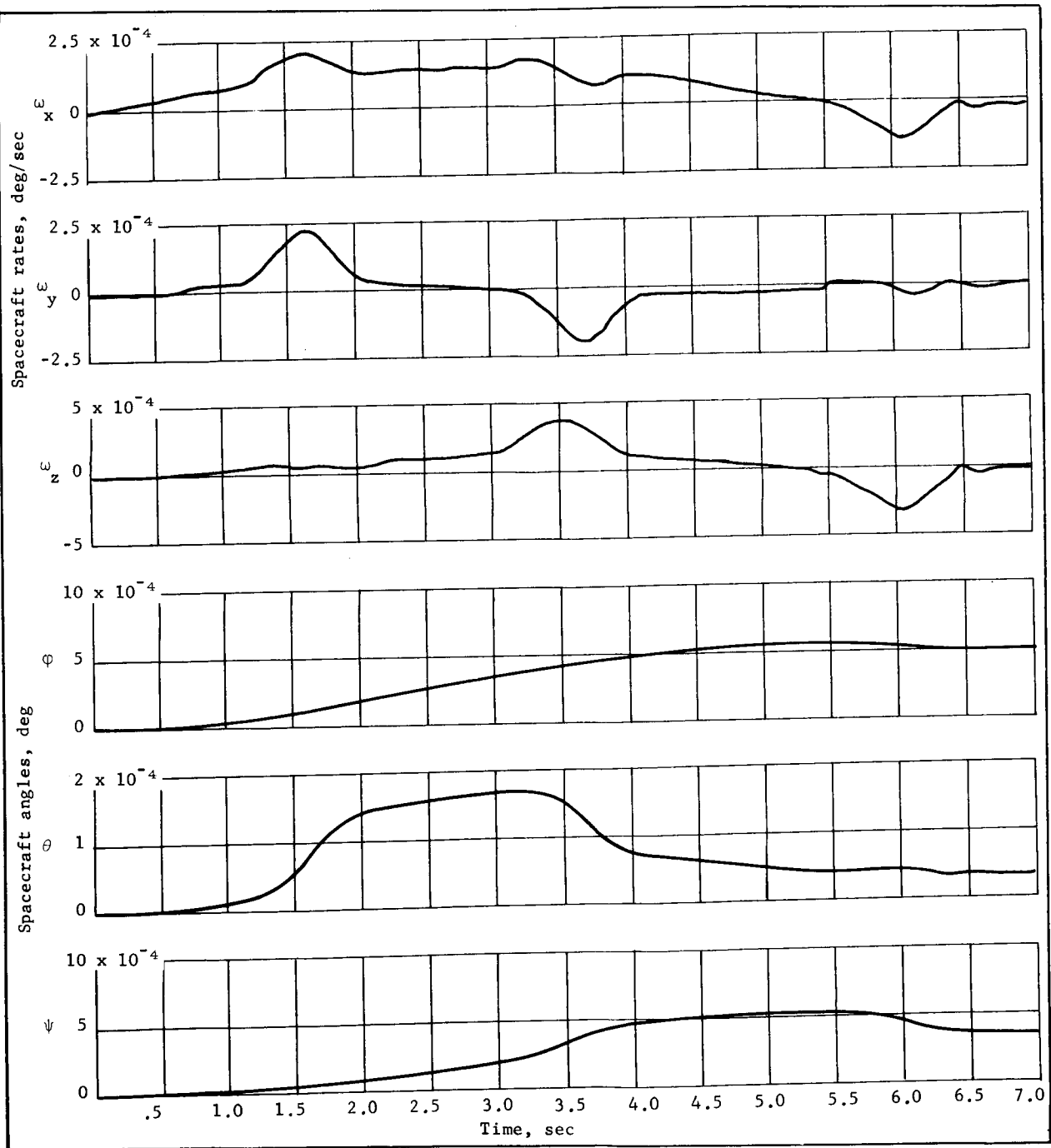


Figure 10.- Spacecraft Disturbances from Modified Load Cell Forces and Moments  
(Right Arm Motion in Each of Three Planes S/C Axes)

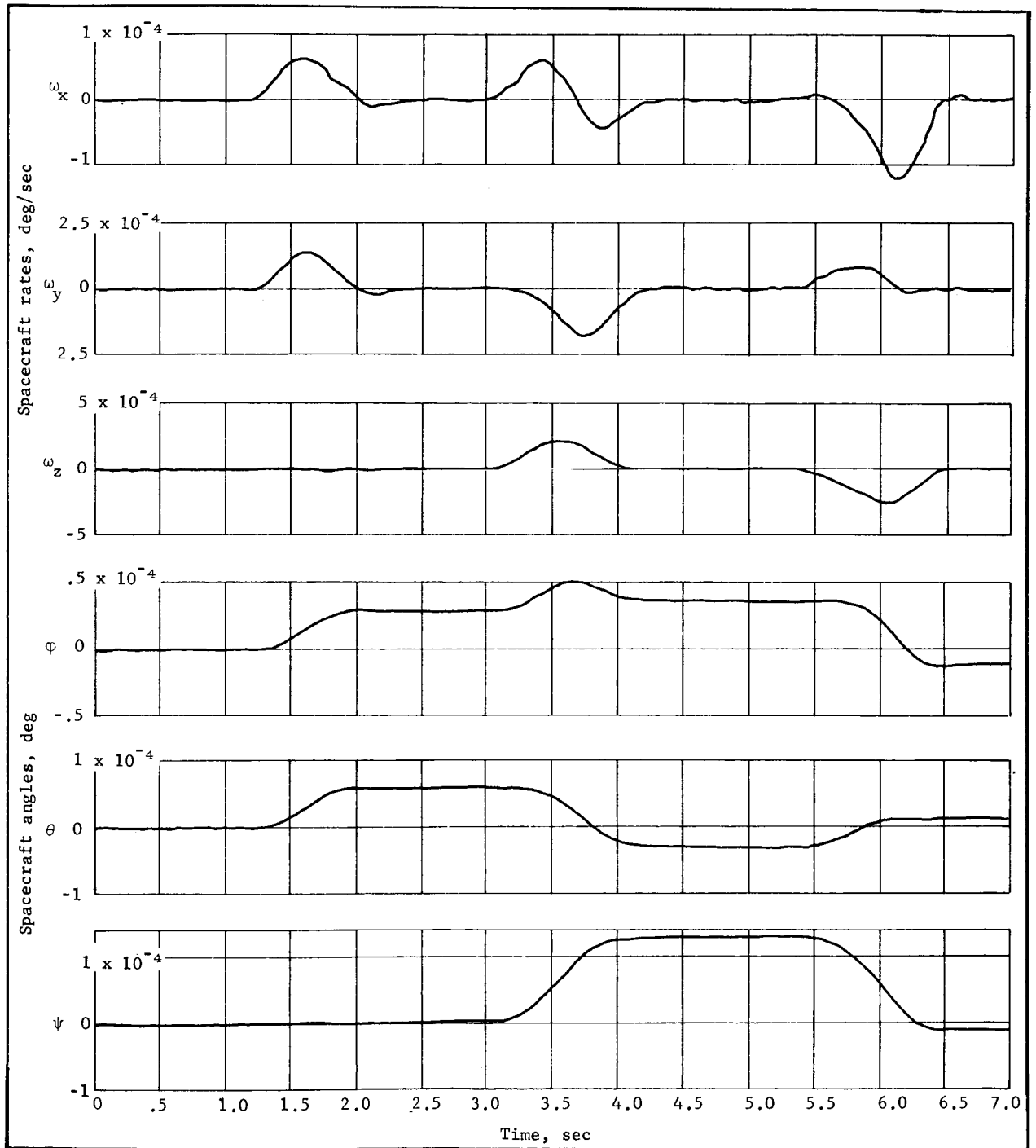


Figure 11.- Spacecraft Disturbances from Calculated Forces and Moments  
(Right Arm Motion in Each of Three Planes) S/C Axes

## Translational Crew Activity Program

In previous discussions of the restrained crew activity program, it was concluded that the Barter-Woolley model man and the limb motion sensor are entirely adequate for use in calculating the dynamic characteristics of a human subject. This model and the LIMS are, therefore, used without reservation in the study of the translational crew activities. The basic equations used in the translational activity math model are the same as in the restrained crew activity math model; however, they are used in a different form. A detailed description of these equations as derived for the hybrid computer are given in Appendix B.

For the actual crew motion flight experiment, the translational activities will be analyzed with a math model more closely resembling the restrained activity math model, i.e., the **conservation** of angular momentum principle will be used. Instead of requiring the torso to maintain a fixed position with respect to the S/C, it will be allowed to move; however, its position relative to the S/C must be known at all times to obtain a solution to the math model equations. This information will be made available from the astronaut position locating system described later. With the torso position known from APAS data and the limb positions known from LIMS data, sufficient information is available to calculate S/C disturbances from translational activities.

The ground simulation program investigating translational activities was conducted using the Martin Marietta Space Operations Simulator (SOS). An artist's concept of this facility is shown in figure 12. A general description of the simulator and its capabilities are presented in the following section.

Simulator description.- The Space Operations Simulator is a servo-driven computer-controlled motion simulator consisting basically of three interdependent systems; the analog computing system, the control and power distribution system, and the motion simulation system. For most space operations, there are two bodies involved, -- e.g., two rendezvous and docking vehicles, or an astronaut and a work station. For simulation purposes, one of these vehicles is simulated by the motion simulator and the other is represented by the fixed base. The particular hardware represented by the fixed base, as well as that mounted on the motion simulator, depends on the space operation under study.

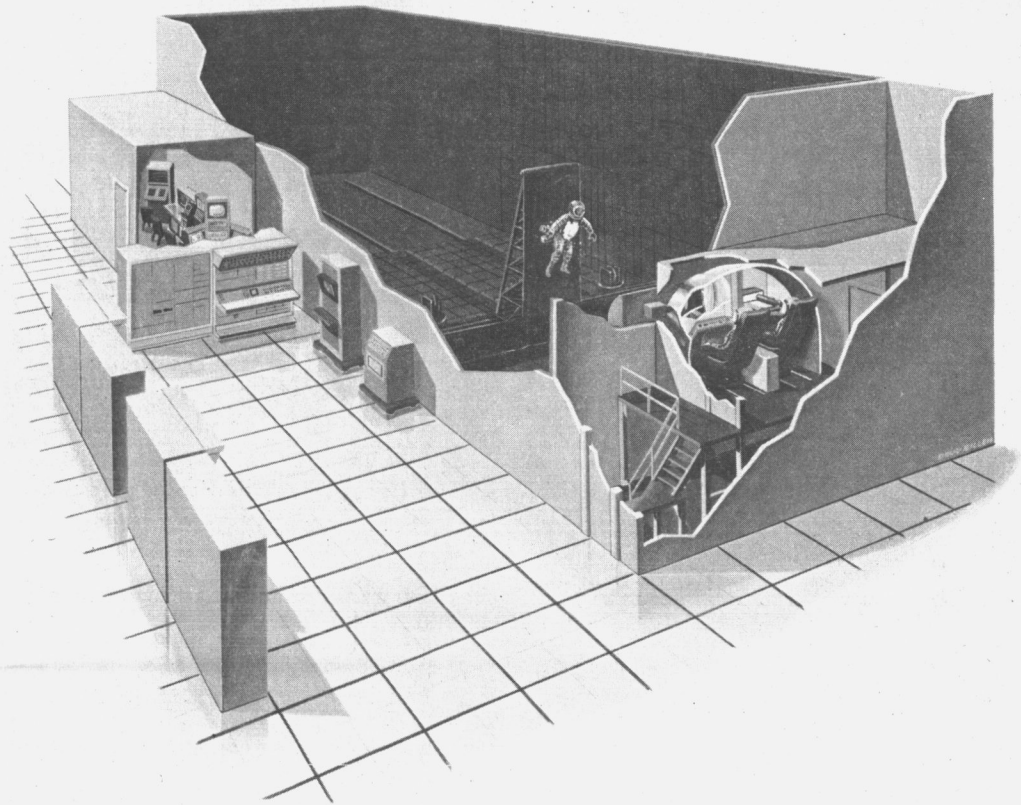


Figure 12.- Artist's Concept of SOS Facility

Computing system.- The computing system available for generating control commands to the motion simulator is an EAI 8900 hybrid computer. This system consists of three EAI 8800 analog computers and an EAI 8400 digital computer with a 32 000 word memory core capacity. The size and versatility of this machine allows the solution of very complicated and involved space operations such as those involving astronaut activities. Associated with this computer are the analog and digital data recording equipment required to store data for subsequent analysis. Part of this computing system is shown in figure 13.

The computing system is used to calculate the motions of spacecraft or astronauts in a zero-g environment by solving the dynamical equations of motion of the body or bodies involved. The computer determines the relative position of one body with respect to the body represented by the fixed base and sends the appropriate positioning commands to the motion simulator.

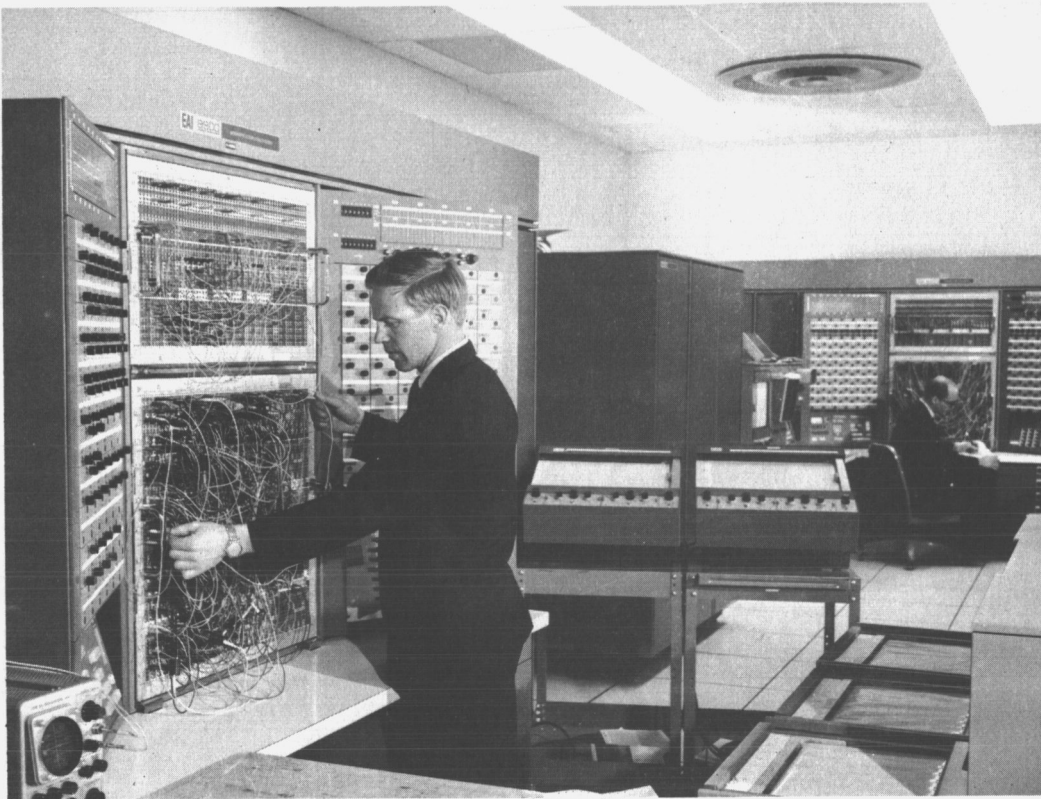


Figure 13.- EAI 8900 Hybrid Computing System

Control system.- The control room houses the power control console, signal patching boards, and some data recording equipment. The power control console furnishes power to the servo systems located on the motion simulator and serves as a monitoring station for all simulation operations. The signal patching boards function as the interface between the computing system and the motion simulator. Computer command voltages pass through the patching boards to the servo systems, and signals from the fixed-base equipment or motion simulator (e.g., from force sensing systems) are likewise returned as inputs to the computer. The data recording equipment located in the control room supplements the computing system.

Motion simulation system.- The motion simulator, shown in figure 14, is housed in a large anechoic chamber (90x32x24 ft) and provides six degrees of motion controlled by servo-motors. The base structure, called the base carriage, moves longitudinally through its 60-ft operating range on three pairs of steel wheels. The V-grooved wheels ride on three stationary tubular tracks, shown in the foreground in figure 14. The base carriage is driven by servomotors that are engaged through sprocket gears to a double strand chain fastened to floor-mounted brackets at each end of the room.

The large structure in figure 14, called the pedestal, moves laterally through an 18-ft operating range on wheels and tracks similar to those of the base carriage. The tracks are rigidly mounted to the top of the base carriage. The pedestal is driven by servomotors in the same manner as the base carriage. The double strand chain in this case is rigidly fastened to structural members at each end of the base carriage where air cylinders have been mounted as safety devices to limit the travel distance of the pedestal.

The structure shown in figure 15 is called the attitude head and moves vertically through its 12-ft operating range on a pair of vertical steel tracks mounted on the pedestal. The attitude head is driven by a single servomotor through a rack and pinion gear. The vertical travel distance of the attitude head is limited for safety reasons by air cylinders mounted on the pedestal.

Also shown in figure 15 are the vertical negator springs used to counterbalance the weight of the attitude head and other simulation equipment mounted on the head. These negator springs exert a nearly constant force independent of extension, and thus relieve the servomotor from the necessity of overcoming the weight of the attitude head.

The three rotational degrees of freedom are obtained with the attitude head. The three servomotors for supplying torque to each axis are similar in design and are geared directly to each gimbal shaft.

Signals to and from the computer, power for the servomotors and associated electronics, and other electrical needs of the equipment mounted on the attitude head are transmitted between the control room and carriage via three large power cables. From the control room, each cable is run through a drive pulley, over a large wheel, and coiled in a drum behind the base carriage. This technique reduces to a minimum cable friction drag over the entire travel distance of the base carriage. For the pedestal, the cables lie in a wide trough on the base carriage and are given sufficient slack to allow free movement of the pedestal from side to side. Power cables required for the attitude head hang in a loop on either side of the head with sufficient slack to allow free vertical motion.



Figure 14.- Total View of Motion Simulator

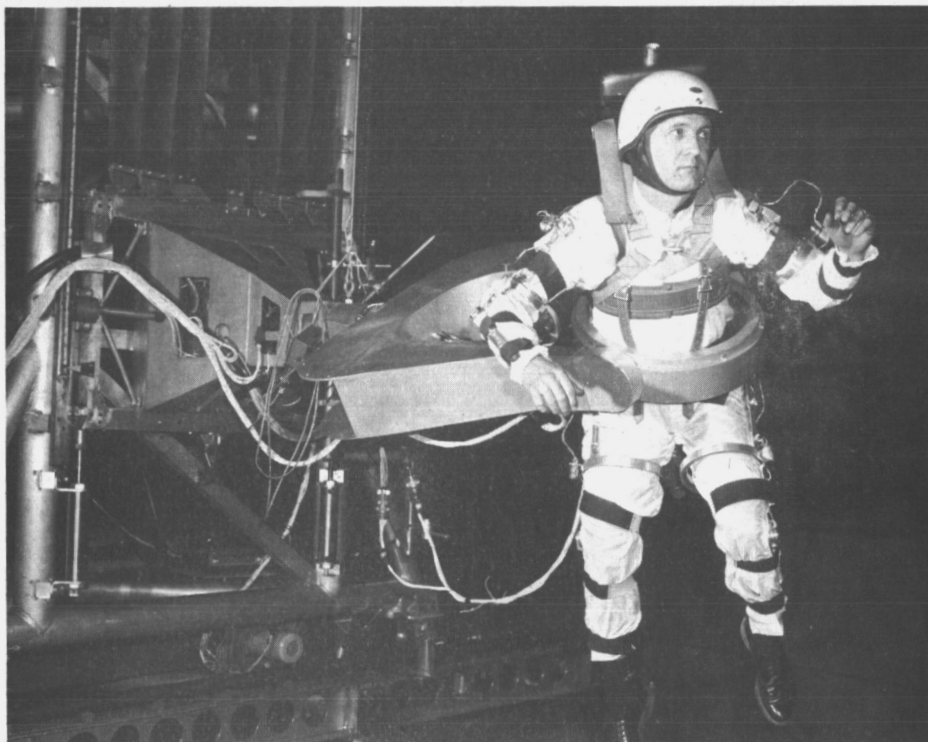


Figure 15.- Closeup View of Attitude Head



EVA simulation.- For the translational activities, the simulator was configured for investigation and analyses of extravehicular activities (EVA). An artist's sketch of the simulation flow diagram is shown in figure 16.

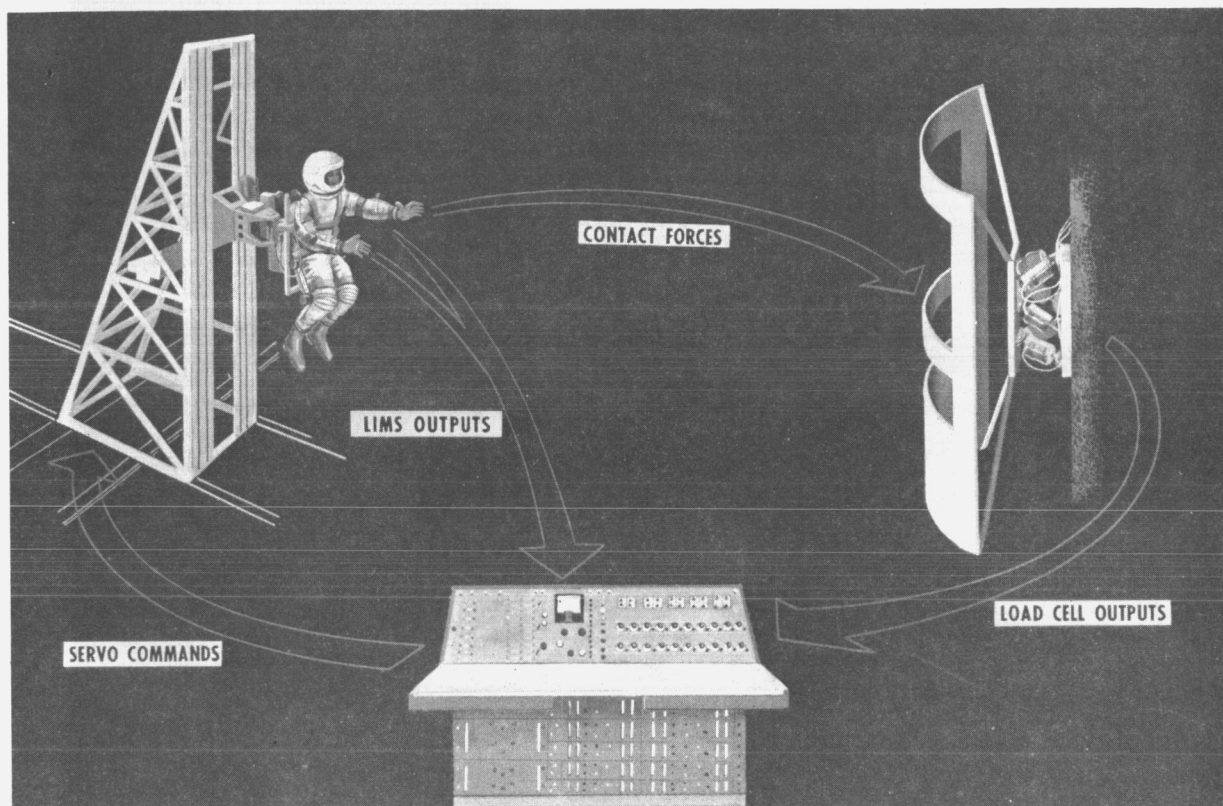


Figure 16.- Artist's Sketch of EVA Flow Diagram

The astronaut is strapped to a seat that is rigidly mounted to the attitude head, giving him three rotational and three translational degrees of freedom. A translational activity mockup is mounted on a load cell array that senses the forces and moments the astronaut applies to the mockup during performance of his task. The load cell forces and moments, which are equal and opposite to those felt by the astronaut, are used by the computer to calculate the correct response the astronaut should have in a zero-g environment relative to the spacecraft. The motion simulator, responding to the computer commands, provides the astronaut with physical motions that realistically simulate those he would encounter in space.

In addition, it is necessary to know as a function of time the position of the astronaut's limbs with respect to his torso. Moving only his arms or legs, for example, will cause rotational reactions of the astronaut about his combined center of mass. The limb position information is supplied by the LIMS and using the anthropometric data from the Barter-Woolley model man for the astronaut's segments, the astronaut's instantaneous inertia properties and c.g. locations are computed to determine the resulting self-induced rotations. These calculated rotations are applied to the astronaut through the simulator servocommands.

Spacecraft disturbances.- In this simulation, the forces and moments measured by the load cell array are the disturbances acting on the spacecraft. These are applied to a spacecraft at a point in the spacecraft where the activity is expected to occur using a digital program containing the actual dynamics associated with the spacecraft. The digital program calculates the resulting spacecraft perturbations.

#### Translational Crew Activities

The translational crew activities investigated using the Space Operations Simulator are:

- 1) Handrail translation - Subject translates along two handrails using only arms and hands;
- 2) Compressive walking - Lateral translation activity between structures where subject can support himself with hands and feet simultaneously;
- 3) Bounce walk - Lateral translation activity between structures where subject touches with only hands or feet at one time;
- 4) Free soaring - Longitudinal translation activity between structures that are several feet (or more) further apart than the subject's reach.

With the exception of the handrail translation results that are presented in this subsection as an example, the load cell forces and moments recorded during the simulation runs are presented in Appendix A. The subject used in the translational activity simulations was Subject 2, whose anthropometric measurements are given in Appendix F.

The load cell forces and moments can be applied directly to a S/C to determine resulting S/C disturbances. This has been done for the compressive walking and bounce walk translational activities where it has been assumed that the subject performs these

activities (between floor and ceiling) in the same location and orientation in the S/C as he was for the restrained activities (see fig. 7). These S/C disturbances are presented in Appendix A. The forces and moments from the handrail translation and free soaring activities have not been applied to a spacecraft because it has not been clearly defined exactly where these activities will take place within the S/C.

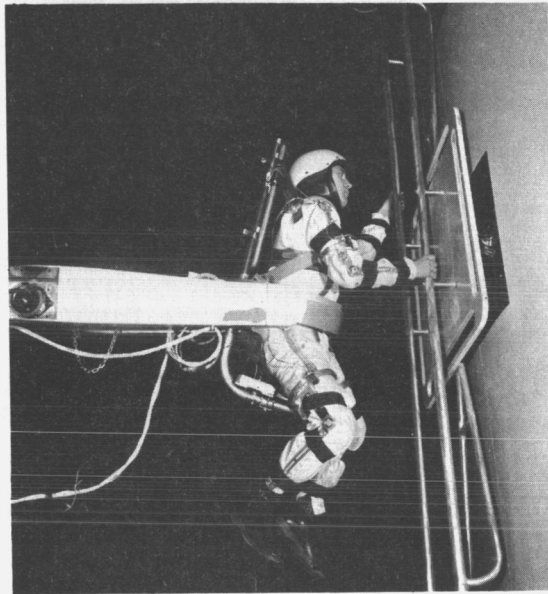


Figure 17.- Handrail Translation Mockup

point near the top he slowed rapidly. Referring to figure 18, the subject stopped and stabilized himself between 11 and 13 sec. For a 1-sec period before this time (between 10 and 11 sec), the subject did not touch the handrails.

Handrail translation.- The handrail translation mockup is shown in figure 17. The subject could maneuver up and down along the handrails using only his arms and hands for locomotion and stabilization. The force and moment data for the handrail translation activity are shown in figure 18. The subject initially stabilized himself near the bottom of the handrails, and data were then taken as he maneuvered himself to a position near the top of handrails and again stabilized himself. The subject began his motion in such a manner that it is not obvious exactly where his motion started. As he translated up the handrail, he gained velocity until at a

Compressive walking.- The mockup used for compressive walking is shown in figure 19 (the mockup configuration shown is for the free soaring task). It consists of two reaction surfaces separated at a distance so the subject could touch both the lower and upper surfaces simultaneously (about 6-ft apart). Both reaction surfaces are joined by a rigid frame that, in turn, is mounted rigidly to the load cell array.

The compressive walking task is to translate laterally (parallel to surfaces) while maintaining contact with both reaction surfaces. The subject could easily translate from one side to the other and back again while maintaining a stable attitude.

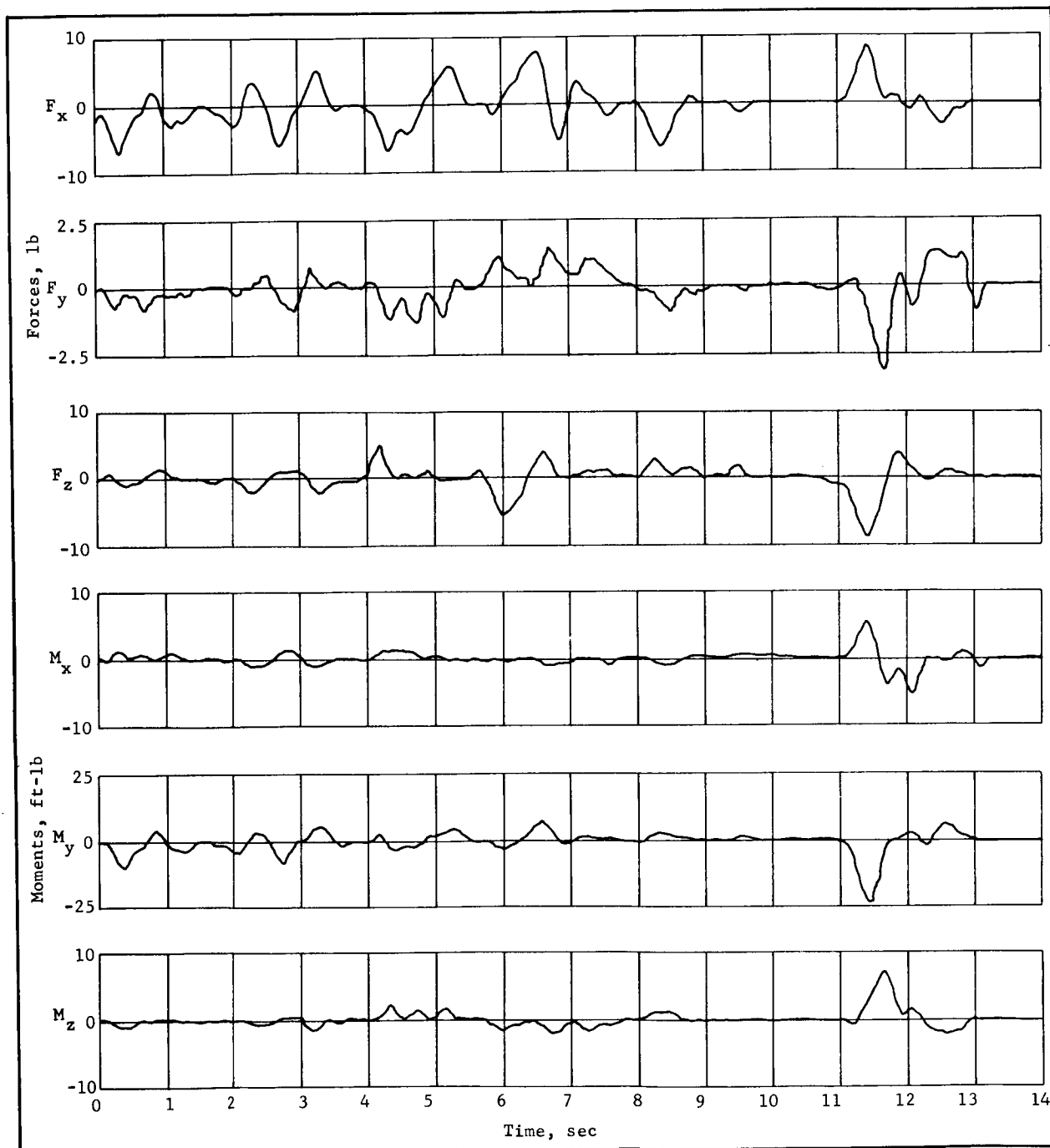


Figure 18.- Forces and Moments Resulting from Handrail Translation, Man's Axes

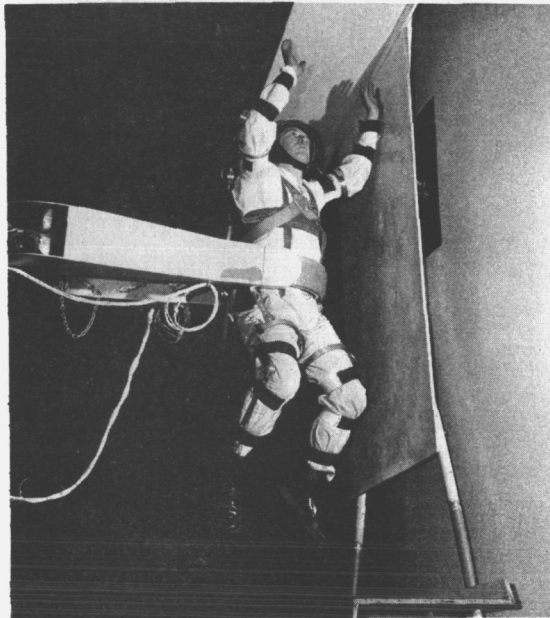


Figure 19.- Free Soaring Mockup

erally (parallel to surfaces) while bouncing between the two reaction surfaces. The subject had little problem maintaining attitude control while translating laterally as long as he kept moving. Of course, without contacting both surfaces at the same time, the subject could not stabilize himself to a condition of no motion.

The load cell forces and moments for the bounce walk are shown in Appendix A figure A83. The S/C angular rate and displacements due to the bounce walk disturbances are shown in figure A84. The bounce walk data were taken while the subject maneuvered from one side of the mockup to the other.

Free soaring.- The free soaring activity was conducted using the same mockup as was used for compressive walking (fig. 19) except the reaction surfaces were separated to a distance of about  $7\frac{1}{2}$ -ft apart. The free soaring task was to translate up and down between the two surfaces with no attempt to translate laterally. When attempting to accomplish this task, the subject found he had difficulty because he could not easily keep his attitude under control. After some practice, however, he learned to control his attitude fairly well. For translation between surfaces further apart than those used in the simulation, it is recommended that hand holds or other stabilization aids be used so that the subject can gain control of his attitude at each surface.

The free soaring force and moment data are shown in Appendix A figure A85 and includes several translations between surfaces.

The load cell force and moment data for the compressive walking is shown in Appendix A, figure A81. These forces and moments have been applied to the cluster S/C, and the resulting S/C disturbances are shown in figure A82. The data were taken while the subject maneuvered from one side of the mockup to the other.

Bounce walk.- The bounce walk activity was investigated using the same mockup as was used for compressive walking (fig. 19). In this case, however, the subject was required to be in contact with only one surface at a time. The bounce walk task is to translate lat-

## LIMS DESIGN

The Limb Motion Sensing System (LIMS) conceived and developed by the Martin Marietta Corporation was developed to enable computation of the dynamics of the human body through knowledge of the mass and inertia properties of the individual body segments. As originally developed, LIMS was designed for use as a laboratory instrument for use in Martin Marietta's Space Operations Simulation Laboratory. As such, it was made adjustable to enable its use on a variety of test subjects. To simplify the structure for use in the AAP Crew Motion Experiment, considerable attention was given to reduce weight, increase reliability, and render it simple to don and doff.

LIMS consists of a stick-figure exoskeleton conforming to the basic human skeletal form with hinge points at the corresponding human joints (fig. 20). To simplify the donning and doffing, the exoskeletal structure has been incorporated in a coverall-type suit. The laboratory model is built into a nylon flight suit and provided with auxiliary velcro straps to ensure proper alignment of the individual joint rotation transducers and the actual human skeletal joints. Preliminary models of the flight unit have been built into a nylon power net fabric that has a tight fitting, three-way-stretch property enabling rapid donning and doffing (under 1 min) while maintaining proper alignment of human and exoskeletal joints.

The joint rotation transducer is a flight-qualified miniature potentiometer -- the case of which forms an integral part of the joint bearing (fig. 21). A battery pack supplies 5 V to each joint potentiometer. The voltage existing between the wiper and one end of the potentiometer is then directly proportional to the angular rotation of the joint.

The limb segments of the laboratory model are adjustable in length and considerably heavier and more rugged than the flight model. The attachment to the suit is through velcro strips and heavy thread hooks permitting easy removal for attachment to another test subject not able to wear the suit provided. The limb segments of the flight model will be of lightweight aluminum tubing attached to the three-way-stretch suit by closely sewn sleeves. All cabling will be run inside the tubing and will terminate in a belt holding the battery pack and astronaut data acquisition system at the waist. The laboratory model is supplied with an umbilical cable for data readout.

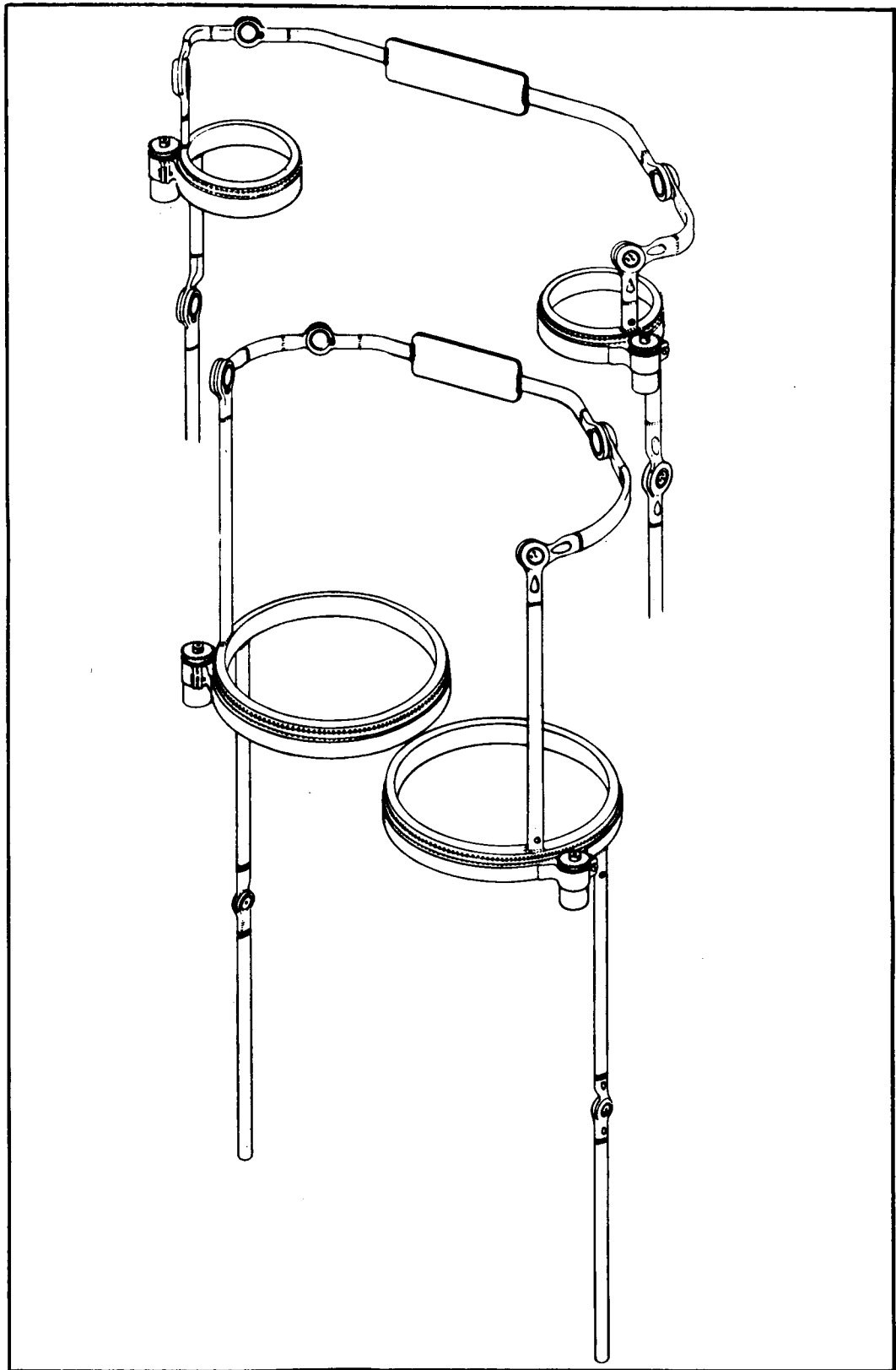


Figure 20.- LIMS Motion Sensing System

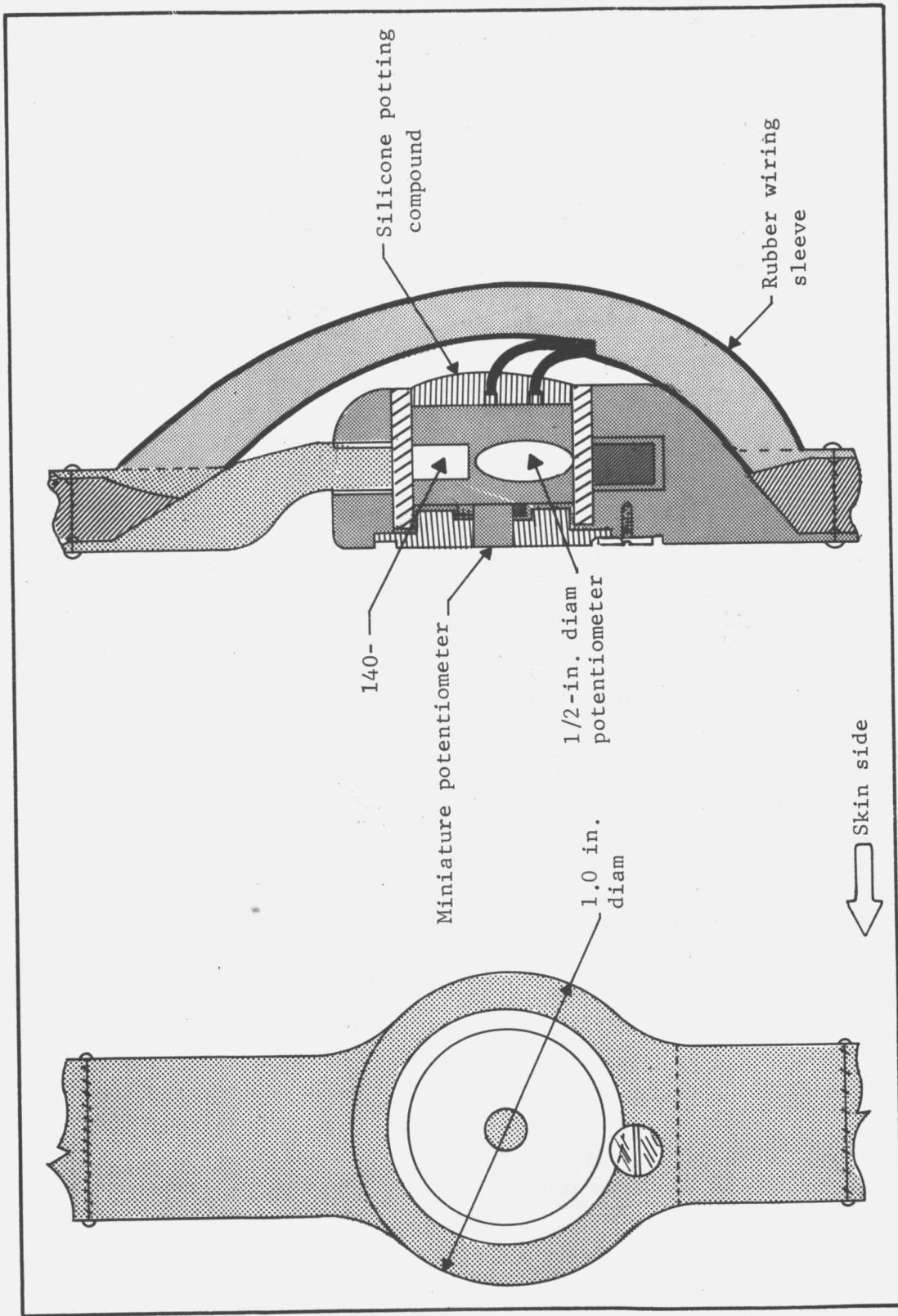


Figure 21.- Joint Rotation Transducer - Hinge Joint Design



The shoulder and hip joints are mechanized by a yoke consisting of four hinge joints -- two each for a shoulder or hip as the case may be (fig. 22 and 23). This mechanization, while not exactly duplicating the shoulder or hip motion, does permit adequate joint rotation while greatly simplifying the exoskeletal structure. To exactly duplicate the shoulder motion, three exoskeletal joints per shoulder joint and three per hip joint are required. Reduction of motion of the leg in the frontal plane and elimination of the capability of 360° rotation of the shoulder reduced these requirements to two exoskeletal joints at each hip and shoulder. This not only greatly simplified the exoskeletal structure, but also the computer requirements necessary to solve the dynamical equations.

The flight model LIMS will add less than 3 in. to the shoulder breadth of the test astronaut, will weigh no more than 12 lb, and will consume 80 mW of power supplied from an integral battery pack; basic properties are included in table 3. During launch and before performance of experiment T013, it will be stored in the experiment components container drawer mounted in the Multiple Docking Adapter (MDA). It can be reactivated at any time following the performance of T013 by the simple replacement of the 5-V battery pack. As desired, LIMS could provide support in terms of making available additional data to any experiment requiring the dynamics of man as an adjunct to the basic experiment purpose.

TABLE 3.- LIMS PROPERTIES

Joint rotation, deg . . . . .	Capable of 320 ±5
Linearity, % . . . . .	±1
Resolution, % . . . . .	0.170
Vibration . . . . .	Acceleration 20 g peak sinusoidal from 5 to 2000 Hz
Shock, g . . . . .	100
Operating temperature range, °C . .	-55 to 125
Life expectancy, joint revolutions . . . . .	250,000 per MIL-R-12934B, p 4.7.20
Noise, ohms . . . . .	100 maximum equivalent noise resistance
Temperature coefficient, PPM/°C . .	±20
Moisture resistance . . . . .	MIL-STD-202B, method 106 A
Salt spray . . . . .	MIL-STD-202B, method 101 A, condition A.
Fungus resistance . . . . .	MIL-E5272C, all materials nonnutrient
<u>Note:</u> Joint rotation potentiometer from Apollo Spacecraft Qualified Parts List, MSC-A-D-66-8 file number 968768.	

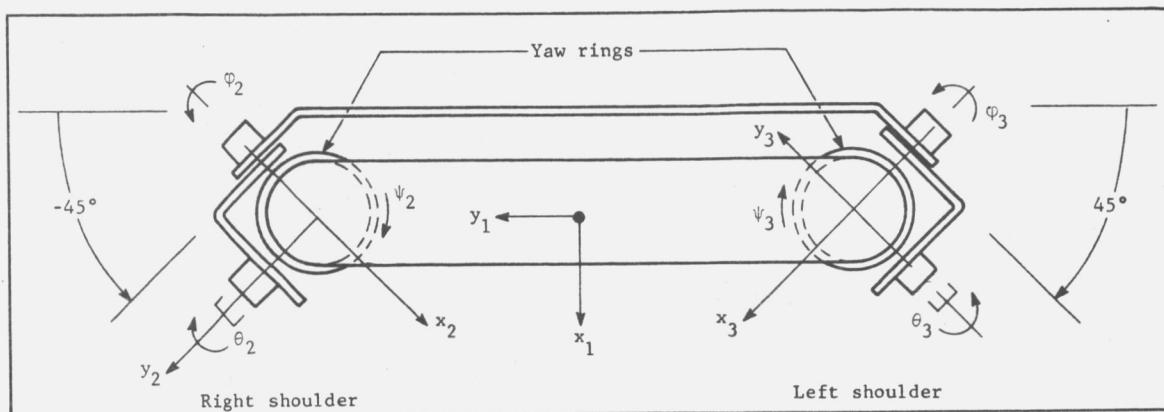


Figure 22.- LIMS Shoulder Yoke



Figure 23.- LIMS Hinge and Axial Joint Details, Laboratory Model

## ASTRONAUT POSITION AND ATTITUDE SYSTEM

In addition to the need for knowledge of the limb position as an input to the dynamical equations for the man/spacecraft system, it is necessary that the torso-centered reference system for all LIMS data also be accurately located with respect to the S/C body-centered reference system. To acquire these data, it is necessary, therefore, to determine, as a continuous function of time, the location of the test subject's torso c.m. and relative attitude during the performance of the experiment.

The performance of T013 will be carried out in two modes. The first involves restrained activities wherein the torso of the test astronaut will be fixed with respect to an arbitrary reference system -- the coordinates of which are presumed known. The second mode involves unrestrained activities such as require translation of the test astronaut. To monitor the position and attitude of the test astronaut during this second mode, an astronaut position/attitude system (APAS) concept must be developed. Continuous use of the APAS provides necessary data during the second mode of experiment performance and backup or redundant data for the force measuring system during the first mode.

The fundamental objective of the APAS is to enable determination of the position of the nominal c.m. of the test astronaut with an error less than 5% and an upper bound of error of 3 in. It is assumed that the astronaut will move about the S/C with velocities in the range of 0 to 3 fps at accelerations in the range of  $10^{-4}$  to 1 g. Because the required attitude accuracy has not yet been defined, it is assumed for this study that a maximum error of 5% will be acceptable.

Because experiment T013 will be performed in the Orbital Workshop (OWS), the environmental constraints imposed on the APAS are those of the OWS environment listed in table 4.

TABLE 4.- OWS ENVIRONMENT

Temperature, °F . . . . .	40 to 100
Pressure, psia . . . . .	5 ± 0.2
Relative humidity, % . . . .	30 to 70 (temperature dependent)
Gas, % . . . . .	69 O <sub>2</sub> , 31 N <sub>2</sub>

The study reported here was not intended to define in detail any of the possible techniques considered, but rather to establish feasibility and develop criteria whereby a near optimum choice of the technique/system could be made. Numerous approaches were considered, but a cursory investigation resulted in elimination of all but three from further study. Table 5 lists those techniques/systems deemed applicable with certain of the criteria highlighted.

### Ultrasonic-Radio Frequency Triangulation

The ultrasonic-radio frequency (US-RF) triangulation scheme makes use of the fact that without ambiguity four spheres can simultaneously intersect only at a single point. The mechanization of this technique involves locating a pair of transmitters -- one ultrasonic (US) and one RF -- on the astronaut (fig. 24 and 25). Automatically keying both transmitters simultaneously results in the radiation of both US and RF signals. The use of multiple receiver pairs (at least four) enables determination of the radius vector from an arbitrary reference, correlated with the S/C reference, to the astronaut-mounted transmitters. The transit time of the RF signal being on the order of  $10^{-6}$  sec ensures that this signal arrives at each receiver  $10^{-3}$  sec before the US signal. This RF signal opens a counting gate enabling a precision pulse generator to deliver pulses to a storage register. The US signal, traveling with a transit time on the order of  $10^{-3}$  sec, will close the counting gate. The number of pulses stored in the register yields an accurate measure of the US transit time, which can be interpreted as the distance from each receiver to the transmitter. Using the formulation derived in Appendix G the position vector can be determined based on an accurate knowledge of the velocity of propagation of the US signal.

The use of a second set of US-RF transmitters/receivers operating on different signal frequencies and located at a different point on the astronaut will enable determination of pitch and yaw. Unfortunately, a roll ambiguity results with this mechanization, which appears incapable of resolution without the use of a third set. A three-set mechanization presents problems with regard to location and mounting on astronaut and vehicle and proper frequency allocations as well as increased complexity, thus attention was directed toward the remaining two concepts.

TABLE 5.- APAS SELECTION MATRIX

	Position accuracy, in.	Weight and volume	System requirements	Development time	Disadvantages	Advantages	Attitude accuracy, deg
IMU			Data handling (all)		Possible development cost significant		
Gimbaled platform	<3	<20 lb 200 in. <sup>3</sup>	Power Mounting mechanism	6 months to 1 year	Equipment mounted on astronaut	Proven technique	<1
Strapdown	<3	<15 lb 350 in. <sup>3</sup>	Computer; Power; Mounting mechanism	6 months to 1 year	Equipment mounted on astronaut	Proven technique	<1
6 accelerometers	<3	<15 lb 1500 in. <sup>3</sup>	Power Mounting mechanism	6 months to 1 year	Equipment mounted on astronaut; APAS data requirement does not justify this complex a mechanism	Low equipment cost	See Appendix B
Triangulation							
Ultrasonic-RF	<3	<15 lb 1000 in. <sup>3</sup>	Power; Data handling; Mounting mechanism on astronaut	3 to 6 months	Requires calibration in space; Equipment mounted on astronaut	Simple concept; Relatively simple to mechanize; Transducers inexpensive and easily obtained	
Photography	<3	*	Power; Camera synchronization with other data	3 to 6 months	Involved data reduction	Simple system; Hardware already being developed for OWS; Very small payload penalty	<4
Tracking							
Radar					Small time measurement $10^{-8}$ - $10^{-9}$ sec		
Laser					Radiation-eyes		
*This equipment will essentially be in the OWS regardless of T013 APAS requirements.							

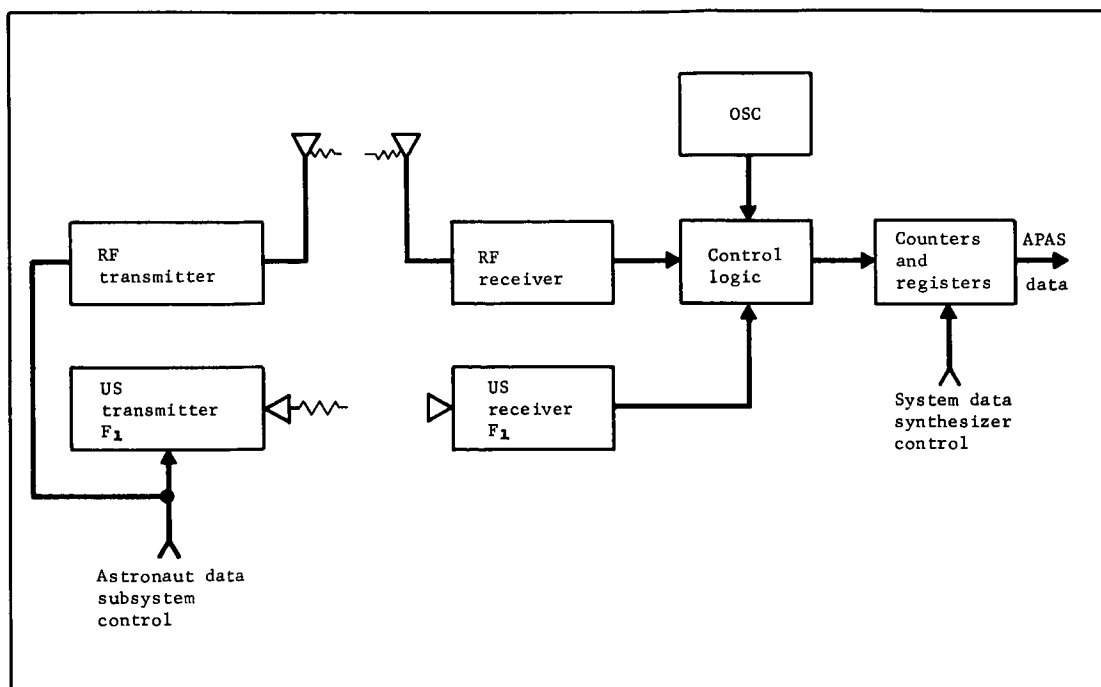


Figure 24.- APAS Ultrasonic Schematic

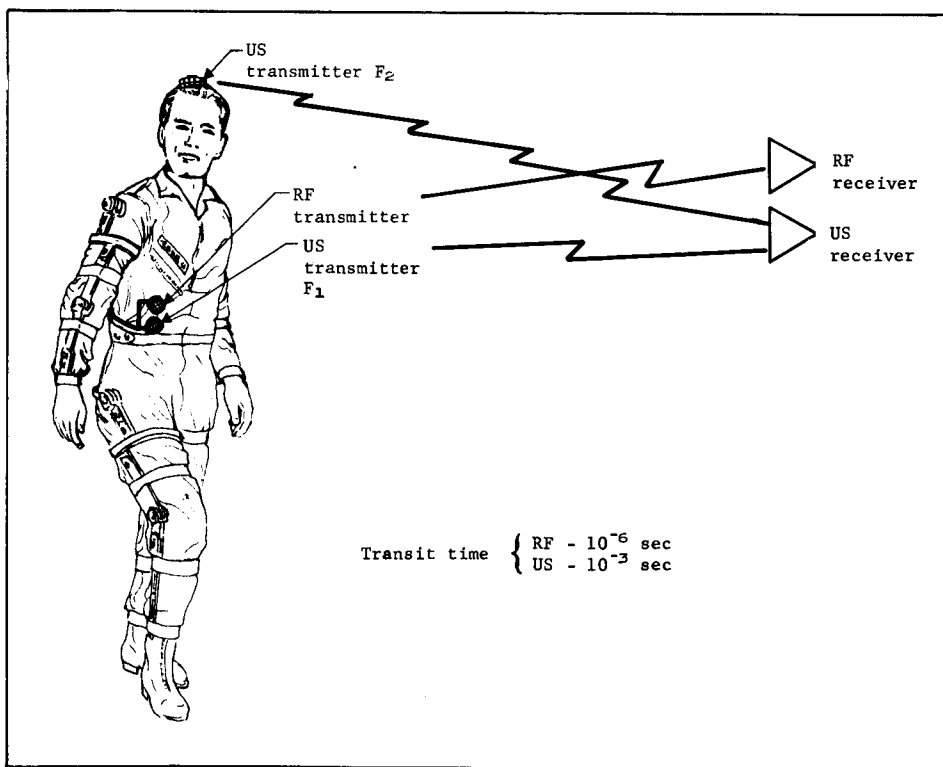


Figure 25.- APAS Ultrasonic Concept

However, a simplified error analysis was carried out on a single US-RF transmitter/receiver pair and appears in Appendix G. The principal conclusion of this preliminary analysis was that this technique for accurate position/attitude determination of the astronaut could be developed provided that an accurate, in-space, calibration or measurement of the velocity of sound were made. Without this calibration or accurate measurement of environmental parameters, the uncertainty of sound velocity would degrade the accuracy below the stated requirements.

The significant problems in applying this technique are:

- 1) Precise location of all receiver sets (at least four);
- 2) Accurate determination of the velocity of sound;
- 3) Provisions for accurate mounting of transmitter pairs on the astronaut;
- 4) Possibly significant power sources required for astronaut-mounted transmitter pairs.

The advantages offered by use of this system are:

- 1) State-of-art hardware is available at low cost;
- 2) Development time is minimum;
- 3) Real-time data can be made available during the performance of the experiment;
- 4) Integration of APAS data into main T013 data stream can be very simply achieved.

#### Inertial Measuring Units

It is well known that inertial measuring units (IMUs) using accelerometers and gyroscopes can measure both position and attitude with a high degree of accuracy. A gimbaled or strap-down system could be employed to mechanize the APAS. However, there are several distinct disadvantages, not the least of which is the requirement that the IMU must be mounted on the astronaut with the attendant problem of coordinate axes alignment and maintenance of this alignment during the performance of T013.

The relatively high cost and extended development time render the gimbale and strapdown systems somewhat less attractive than other mechanizations.

An alternative IMU technique suggested by reference 6 is the use of six accelerometers.

A detailed analysis of this system, included in Appendix G, revealed that, to achieve the required accuracies, accelerometer sensitivities/thresholds on the order of  $10^{-6}$  g for position sensing and  $10^{-9}$  g for attitude sensing is required. Because the same accelerometer is used to sense both parameters, a sensitivity of  $10^{-9}$  g is required. It is not clear, at this writing, whether accelerometers with this sensitivity are available -- although a brief survey indicates that some accelerometers are reputed to have this capability. Obviously at this threshold, evaluation in the Earth environment is greatly influenced by the unavoidable background noise levels existent. Experiments have been proposed for actual orbital evaluation of this capability, but no published results are available.

The uncertainty with regard to the availability of accelerometers capable of yielding the required accuracy and the unduly complex astronaut mounting hardware indicate that this approach is not a particularly desirable one since the photographic approach has been found to be feasible.

#### Photographic Method

The basic photographic technique illustrated in figure 26 uses the principle of photogrammetry to establish position and attitude. The stereography required is obtained through the use of two movie cameras separated by a distance on the order of 4 ft. A well-marked target is placed on the astronaut, and motion pictures are taken as he performs the experiment tasks. A frame-by-frame analysis of the return film is then made using an X-Y plotter with digital readout.

A brief experimental verification of this technique was carried out using two cameras and the Martin Marietta Space Operations Simulator (SOS). Continuous position data were derived from the SOS analog channels, and discrete position data were obtained from analysis of the camera records. Position data can be obtained with errors on the order of 1 in. It appears that through the use of multiple targets mounted on the astronaut, attitude data can be obtained to a similar degree of accuracy.



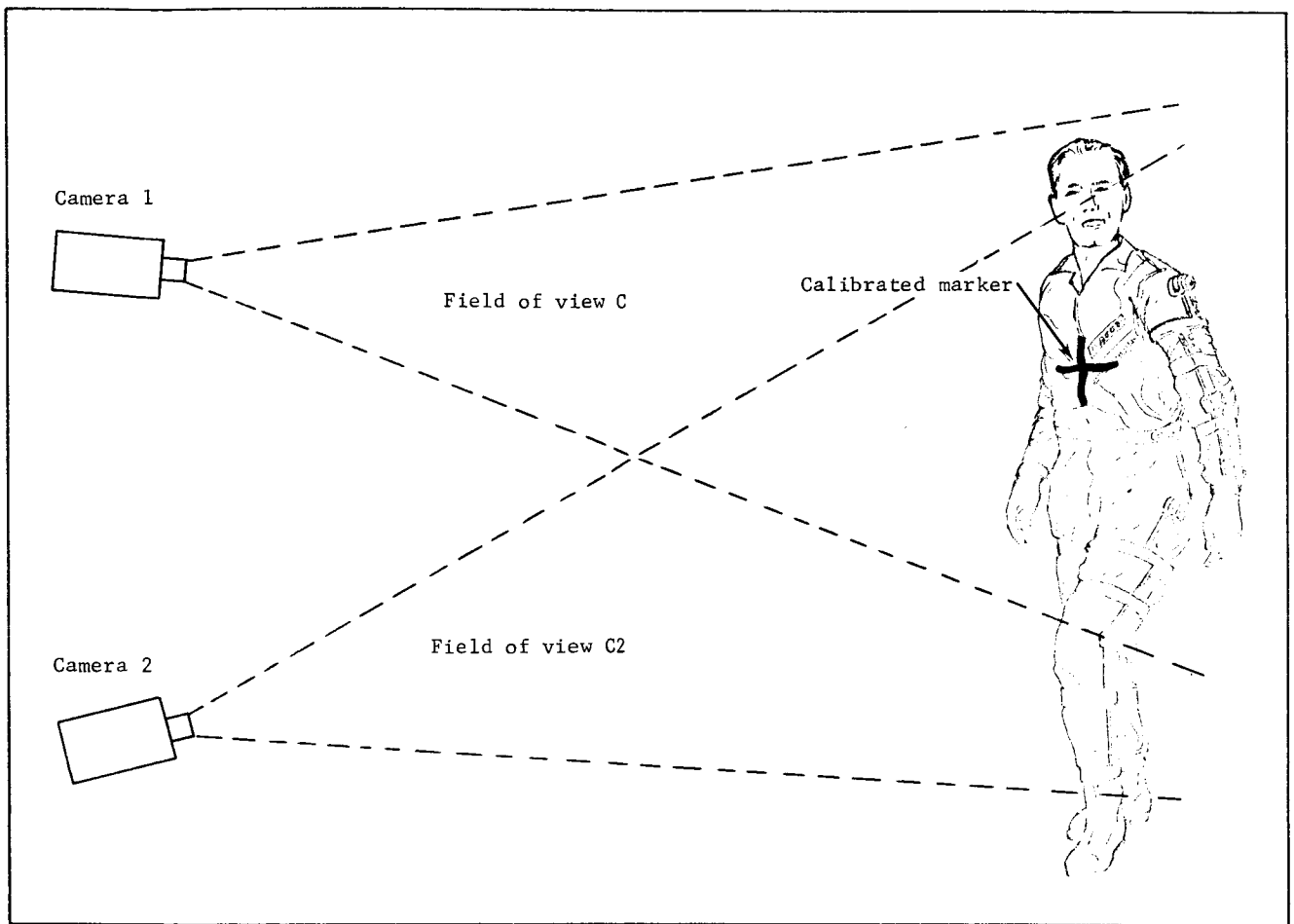


Figure 26.- APAS Photographic Concept

Basic questions relative to this technique that require further study are:

- 1) Definition of lighting requirements;
- 2) Simplification and mechanization of the data reduction;
- 3) Development of infallible astronaut mounted targets;
- 4) Camera synchronization and control;
- 5) Coordination of film and telemetry data.

None of these problem areas appear to be difficult to resolve. Limitations on both time and budgetary allotments simply did not permit their resolution during this study.

The significant advantages to this technique for the mechanization of the APAS lie in the fact that at least two cameras are already planned for use in the OWS and are currently under development. Thus, the only payload requirement for implementing this technique, insofar as T013 is concerned, is the film and any special mounting and control hardware. In addition, the planned for photographic monitoring of the experiment is automatically obtained. The correlated LIMS/APAS data may also prove useful to experiment M055, Time and Motion Study.

A mathematical analysis and error analysis of the photographic technique is included in Appendix G.

## DIGITAL ATTITUDE AND RATE SYSTEM

Paramount to the Crew Motion Experiment is the determination of vehicle attitude perturbations resulting from crew activity. Experimental evidence, based on ground simulations, indicates that crew-motion-induced vehicle angular rates lie in the range from  $0.1^\circ/\text{hr}$  up to  $1200^\circ/\text{hr}$ . In reviewing those sensing systems presently planned for the Apollo Applications Flight 2 (the assigned flight for T013), it was determined that there existed three systems that could conceivably be used to derive the required vehicle data for experiment T013. These are:

- 1) Command and Service Module body mounted attitude gyro package (CSM/BMAG);
- 2) CSM inertial measuring unit rate gyro package;
- 3) Apollo Telescope Mount rate gyro package (ATM/RGP).

A direct comparison of the capabilities of these systems with T013 requirements resulted in the data of table 6.

TABLE 6.- COMPARISON OF APOLLO ONBOARD SENSORS WITH  
T013 REQUIREMENTS

Attitude system	Threshold, deg/hr	Saturation, deg/hr
Experiment T013 requirements	0.1	1 200
CSM/RGP <sup>a</sup>	72	108 000
CSM/BMAG <sup>b</sup>	0.02	72 000
ATM/RGP <sup>c</sup>	0.01	3 600
<sup>a</sup> CSM/RGP - Command and Service Module rate gyro package. <sup>b</sup> CSM/BMAG - Command and Service Module body mounted attitude gyro system. <sup>c</sup> ATM/RGP - Apollo Telescope Mount rate gyro package.		

The CSM/BMAG has a drift rate of  $2^\circ/\text{hr}$ , which is significantly above the required threshold and would result in the acquisition of faulty data (ref. 8). In addition, there has been no provision for outputting rate data (ref. 9). The ATM rate gyro system must be capable of operation without the control moment gyros and must be in a gimbal locked mode to be usable for T013.

A further consideration is the fact that the data processing technique of instantaneous sampling or quantizing of the rate signals of either the CSM or ATM systems followed by ground or onboard integration is not as accurate as is required for T013.

For these reasons, a decision was made to develop an independent attitude sensing system capable of meeting all the T013 requirements. Such a system, the Digital Attitude and Rate System (DARS), based on space-proven hardware was developed and detailed design carried out. The heart of this system, the Rate Gyro System (RGS), has been flown at least 20 times. The analog to digital (CAD) system converting the gyro signals into digital signals for subsequent transmission and analysis will have been subjected to all the environmental and performance tests as the RGS before the time it is required for T013. The additional electronics and control units have been designed to the same reliability and environmental criteria as the RGS and CAD. DARS specifications are given in table 7.

TABLE 7.- SPECIFICATIONS, DIGITAL ATTITUDE  
AND RATE SYSTEM (DARS)

Rate range . . . . .	$0.1^\circ/\text{hr}$ to $40^\circ/\text{hr}$ rate change from nominal inputs of $0^\circ/\text{hr}$ to $1200^\circ/\text{hr}$ absolute range
Attitude range . . . . .	$0.55^\circ \times 10^{-3}/0.05$ sec interval to unlimited angle
Attitude resolution . . . . .	$6.2^\circ \times 10^{-6}$
Output . . . . .	24 bit digital serial (most significant bit first)
Power requirement . . . . .	100 W maximum - operating; 200 W maximum - warmup
Warmup time . . . . .	25 min maximum
Size (height x width x depth) . . . . .	12x12.5x23 in. (maximum)
Weight . . . . .	45 lb (maximum)

The DARS consists of a three-axis rate gyro package together with an adjustable dc bias and null indicator, a voltage-to-frequency converter (CAD), and up/down binary counter, buffer register, and control unit, all interconnected as shown in figure 27.

The rate gyro system (RGS), shown in figure 28, develops a current proportional to input rates. The adjustable dc bias supplies a current to the test torquer winding of the rate gyros to null out residual rates before the performance of experiment TO13. The difference between these signals is converted to a pulse train, the repetition rate of which is proportional to the input current, by the voltage-to-frequency converter.

The up/down binary counter counts the number of pulses for a fixed increment of time. The contents of this counter represent the total angular change occurring during a fixed counting interval. The total number of pulses accumulated during each counting interval is stored in the buffer register.

The buffer register contents are read out into the experiment data system in serial form every 50 milliseconds (msec).

### System Analysis

Rate gyro system\* (fig. 28).— The basic RGS is that used on existing Martin Marietta programs modified to measure the range of 0.1 to 40°/hr input rates. These modifications reduced the frequency pass band of the system minimizing the noise output of the system. Digital filtering techniques employed in the reduction of data will further reduce the noise effects and enhance the system's overall accuracy.

The frequency response of various gyro system electronics and gyro combinations were evaluated to determine the best unit for the DARS application. Two existing systems can be used -- the RGS electronics with an 019 gyro (Martin Marietta designation), and a three-axis reference system (TARS) electronics with the TARS gyro. Selection of the demodulation unit for near-optimum gain and noise characteristics will enhance the system performance.

---

\*See Appendix I for clarification of the TARS and RGS.

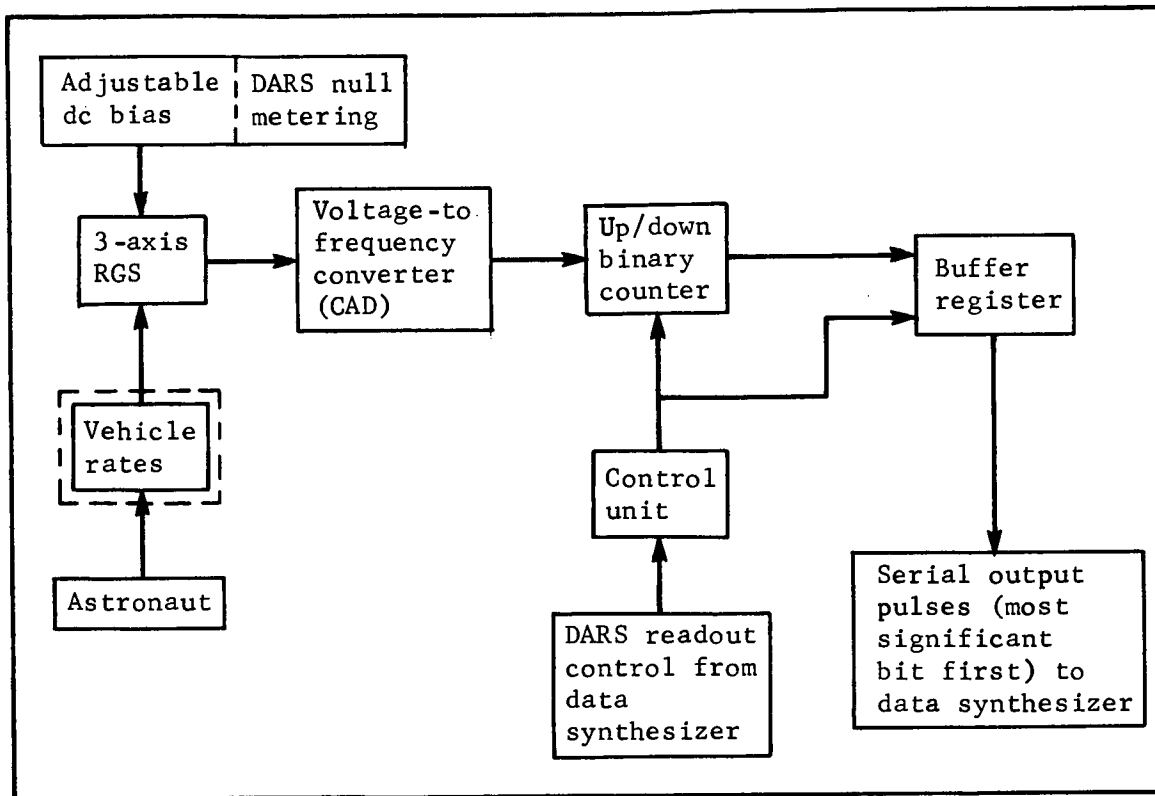


Figure 27.- Digital Attitude and Rate System (DARS)

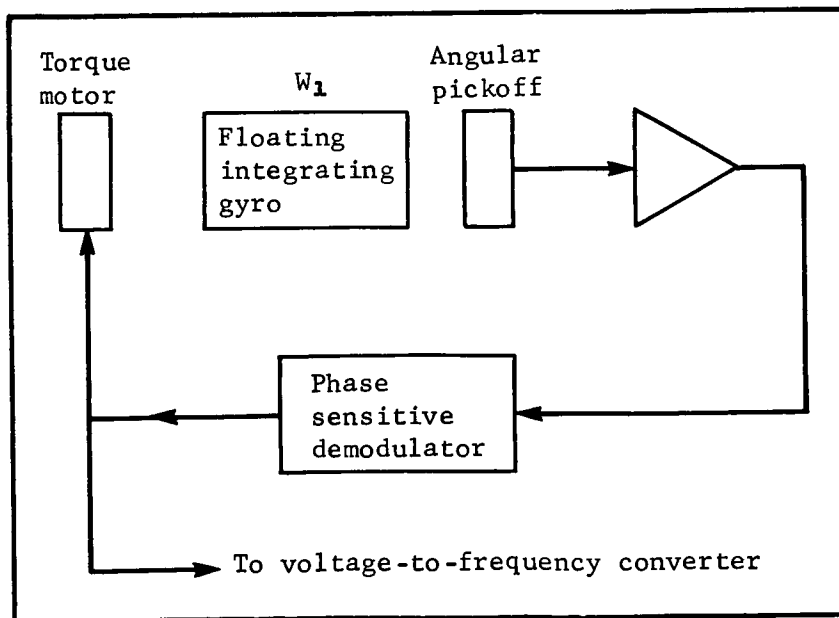


Figure 28.- Rate Gyro System (RGS)

The frequency response of the various gyro system electronics and gyro combinations that were evaluated were calculated to be as follows:

- 1) RGS electronics with rate gyros - First corner frequency = 5 cps;
- 2) RGS electronics with TARS gyros - First corner frequency = 0.5 cps;
- 3) TARS electronics with TARS gyros - First corner frequency = 5 cps.

It was decided to use the RGS electronics with the RGS gyros Martin Marietta Corporation No. 80801030600-019 based on the above frequency response calculations and the signal-to-noise considerations of the candidate systems.

An analysis was made on the gyro system under consideration for the purpose of determining frequency response. The closed-loop block diagram used for the analysis is shown in figure 29.

The characteristics equation to be analyzed is, therefore,

$$Js^2 + Cs + K_A K_T = 0 \quad (1)$$

The system constants are listed in table 8.

Analysis of TARS electronics with TARS gyro: A feedback scale factor of  $(0.15^\circ/\text{sec})/\text{mA}$  corresponds to  $(540^\circ/\text{hr})/\text{mA}$ . However, the maximum vehicle rate to be measured is  $40^\circ/\text{hr}$ . Therefore, the maximum current through the torquer winding will be  $(40^\circ/\text{hr})/(540^\circ/\text{hr}/\text{mA})$  or  $74 \mu\text{A}$ . This current is the input to CAD, which required approximately  $172 \mu\text{A}$  to give its maximum output of 1800 pulses/sec. If a resistor equal in value to the resistance of the torquer winding is placed in parallel with the winding, the output current will double giving more input into CAD as required. Therefore, only approximately half of the current out of the demodulator amplifier passes through the torquer winding and the gain changes from  $57 \text{ mA/mV}$  to about  $29 \text{ mA/mV}$ . The new value for  $K_A K_T$  is therefore reduced to one-half and becomes  $1 \times 10^7 \text{ dyn cm/rad}$ .

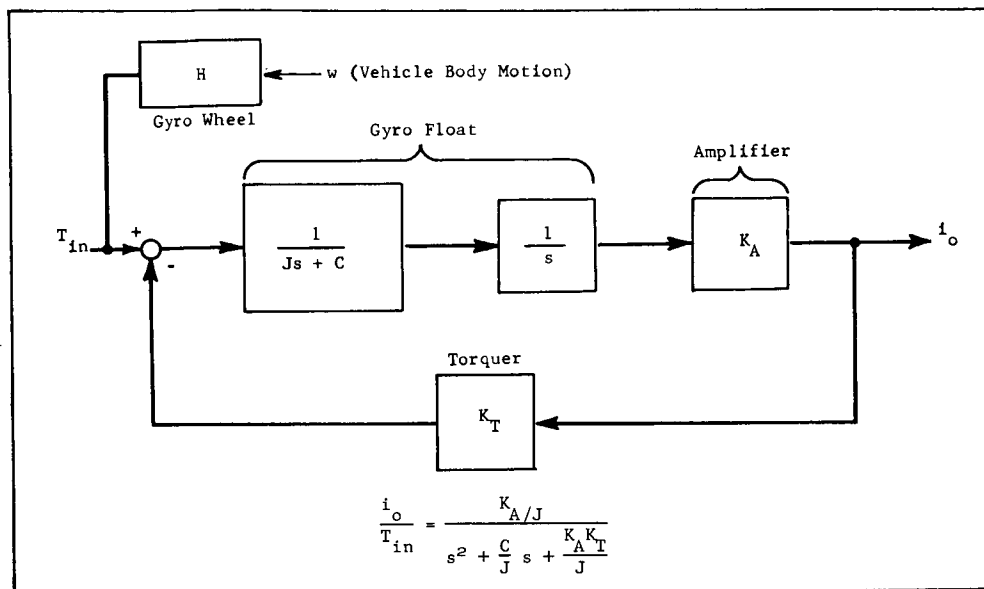


Figure 29.- RGS Block Diagram

TABLE 8.- RATE GYRO SYSTEM PHYSICAL CONSTANTS

Parameter	Angular moment of inertia, J, g-cm <sup>2</sup>	Damping coefficient, C, dyn cm-sec	Amplifier gain constant, K <sub>A</sub> , mA/deg	Torquer voltage constant, K <sub>T</sub> , dyn cm/rad mA/deg	K <sub>A</sub> K <sub>T</sub> , dyn cm/rad	H <sub>g</sub> , dyn cm-sec
Component						
TARS gyro (PD9600010-D10)	86.3	3.16 × 10 <sup>5</sup>	*2500	7700	1.93 × 10 <sup>7</sup>	5.13 × 10 <sup>4</sup>
Rate gyro (PD965008-019)	82.3	2.3 × 10 <sup>4</sup>	232	7700	1.79 × 10 <sup>6</sup>	5.13 × 10 <sup>4</sup>

\*With last stage of amplifier removed to eliminate its dead band.



The characteristic equation of the closed-loop system is then

$$86.3s^2 + 3.16 \times 10^5 s + 1 \times 10^7 = 0 \quad (2)$$

The approximate roots lie at  $s = 31$  and  $s = 4000$ , which is representative of an overdamped second order system with a dominant root in the real frequency domain at  $\omega = 31$  rad/sec or approximately 5 cps. Thus, the first corner frequency, at 5 cps, represents the half-power frequency.

Analysis of rate gyro electronics and TARS gyro: This system consists of a TARS gyro and rate gyro electronics. The torquer winding must be shunted by a resistor of equal value to give the required input to CAD. Therefore, the gain  $K_A K_T$  of  $1.79 \times 10^6$  dyn cm/rad is reduced in half and becomes approximately  $9 \times 10^5$  dyn cm/rad.

The characteristic equation for this system is

$$86.3s^2 + (3.16 \times 10^5)s + 9 \times 10^5 = 0 \quad (3)$$

The dominant root for this system is about 3 rad/sec, which corresponds to a frequency response of 0.5 cps. This system was assembled and tested. Evaluation showed that the frequency response of this system was less than 1 cps indicating close agreement with the analytical results.

Analysis of rate gyro electronics and rate gyro: Based on the preceding discussion, if the system is composed of the rate gyro and the rate gyro package, the characteristics equation becomes

$$82.3s^2 + (2.3 \times 10^4)s + 10^5 = 0 \quad (4)$$

The roots of this equation are  $S = 28$  rad/sec and  $252$  rad/sec.

In the real frequency domain, the breakpoints are located at  $f = 4.5$  cps and 40 cps.

A test was also conducted to determine the frequency response for the rate gyro system with a rate gyro. A signal of variable frequency, from 1 to 15 cps was put into the test torquer and the data recorded in table 9. The curves shown in figure 30 correlate the experimental and theoretical response.

TABLE 9.- FREQUENCY RESPONSE  
DATA OF RATE GYRO SYSTEM

Frequency, cps	$e_o/e_i$ , dB
1	0
1.5	0
2	-0.5
2.5	-0.8
3	-1.0
4	-1.6
5	-3.3
6	-5.2
8	-8.3
10	-12.5
15	-24

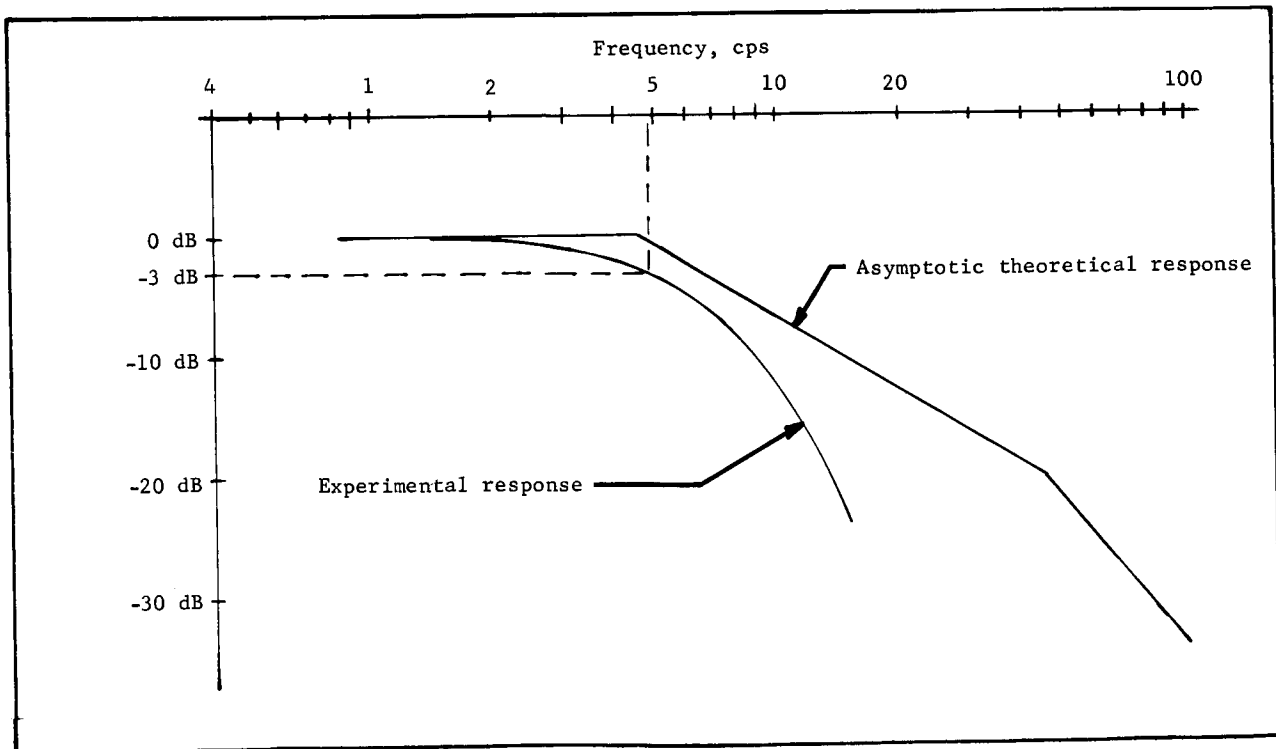


Figure 30.- Frequency Response of Rate Gyro System

Selection of torquer shunt resistor.- As shown previously, a current of  $171.7 \mu\text{A}$  is the required input to CAD for an output of 1800 pulses/sec corresponding to a vehicle rate of  $40^\circ/\text{hr}$ . However, the output current of the rate gyro is only  $74 \mu\text{A}$  for a rate of  $40^\circ/\text{hr}$ .

For the rate gyro that was used (type PD9650008-019, serial number 000007), the resistance of the feedback torquer winding was 96.2 ohms and the resistor of the test torquer winding was 95.6 ohms. A resistance of 68.1 ohms was placed in parallel with the 96.2-ohm torquer winding. Therefore, when the vehicle rate was  $40^\circ/\text{hr}$ ., the current in the torquer remained  $74 \mu\text{A}$ , and the current in the resistor was  $98 \mu\text{A}$ . The total current of  $172 \mu\text{A}$  can then be fed into CAD, which results in an output of 1800 pulses/sec as desired.

The proper shunt resistor was selected experimentally. The rate gyro was mounted on the three-axis servo-driven gimbal system (fig. 31), and angular displacement achieved through the servo drive.



Figure 31.- RGS Mounted on the Three-Axis Servo-Driven Gimbal System

Because the total pulse output of CAD is independent of angular rate, as long as saturation does not occur, a precise measurement (accurate to within 10 sec of arc) of angular displacement correlated with the CAD total pulse count enables the proper selection of the correct CAD input. This input is a function of the gyro torquer shunting resistor. Thus, for an angular rate of 40°/hr to develop a CAD output of 1800 pulses/sec, a 1° angular displacement, independent of rate, should yield a total pulse count of 162 000. Driving the gimbal through an angular displacement of 1° at various rates, the CAD output pulses were fed to a binary counter, accurate to ½%, yielding the data of table 10. Using these data, a shunt resistor of 68.1 ohms yielded a total CAD pulse count of 162 000/deg rotation.

TABLE 10.- EXPERIMENTAL TOTAL PULSE COUNT DATA FOR CAD

Angle displaced, deg	Rate of vehicle, deg/hr	Output pulses of CAD	Number of output pulses of CAD for 1° as interpolated
½	1.7	78 500	157 000
½	3.5	78 500	157 000
½	5.2	79 500	159 000
½	10	80 500	161 000
1	20	165 000	165 000
1	31	163 000	163 000
-½	-5.2	82 500	165 000
-½	-10	80 500	161 000
-1	-20	161 000	161 000
-1	-30	161 000	161 000

It is to be noted here that the shunt resistor must be selected separately for each individual gyro. The resistance of the gyro torquer winding has a specified tolerance of 90 ohms  $\pm$  10%. The shunt resistor may, therefore, vary from approximately 57 to 70 ohms.

DC bias supply.- The adjustable dc bias supply current outputs are used to null out the residual rates on the rate gyro system before the performance of T013. This current is applied to the rate gyro system test torquer windings on each axis (fig. 32).

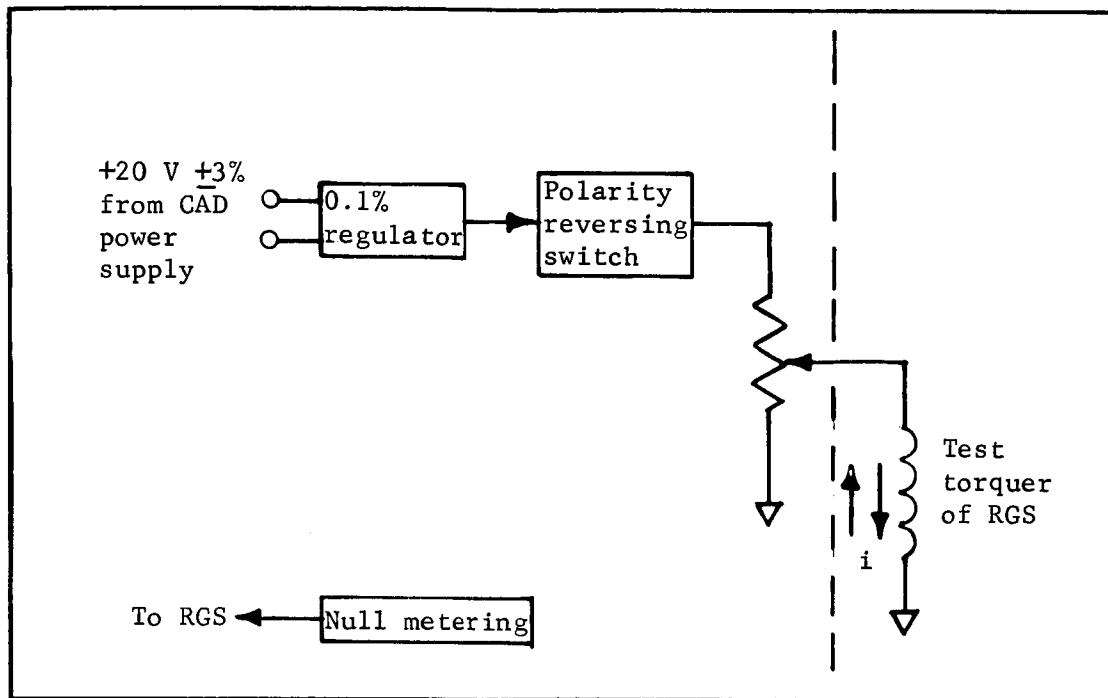


Figure 32.- Adjustable dc Bias Supply

Based on a nominal RGS torquer scale factor of  $540^\circ/\text{hr}/\text{mA}$ , this system can null out rates, in each axis, from  $0.1^\circ/\text{hr}$  up to either  $1370$  or  $1720^\circ/\text{hr}$  with a resolution of  $0.05^\circ/\text{hr}$ . The upper limit dispersion is due to the reference amplifier zener diode tolerance of  $\pm 10\%$ . However, the stability of  $\pm 0.1\%$  is maintained throughout the ranges specified above. The  $\pm 0.1\%$  stability of this supply will contribute errors that are less than  $0.03^\circ/\text{hr}$ .

The input to the dc bias is derived from the  $20\text{ V}, \pm 3\%$  dc, power supply in the voltage-to-frequency converter. Loading effects, caused by the dc bias supply, present no problem to the voltage-to-frequency power supply.

The dc bias supply is a feedback voltage regulator (fig. 33). The circuit diagram is shown in figure 34. The regulator has been designed for an output of  $0$  to  $10\text{ mA}$  at a voltage of  $8.4$  to  $10.5\text{ Vdc}$ . The voltage stability of  $\pm 0.1\%$  includes the effects of (1) line and load regulators, (2) temperature gradient  $0$  to  $40^\circ\text{C}$ , and (3) short-term drift criteria as illustrated in figure 35.

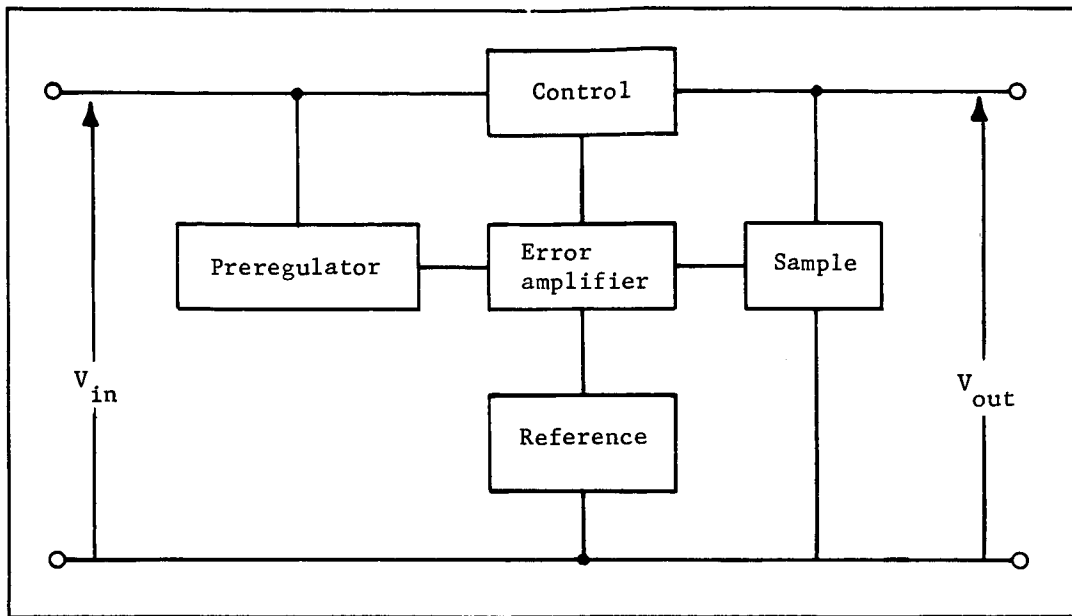


Figure 33.- Voltage Regulator Block Diagram

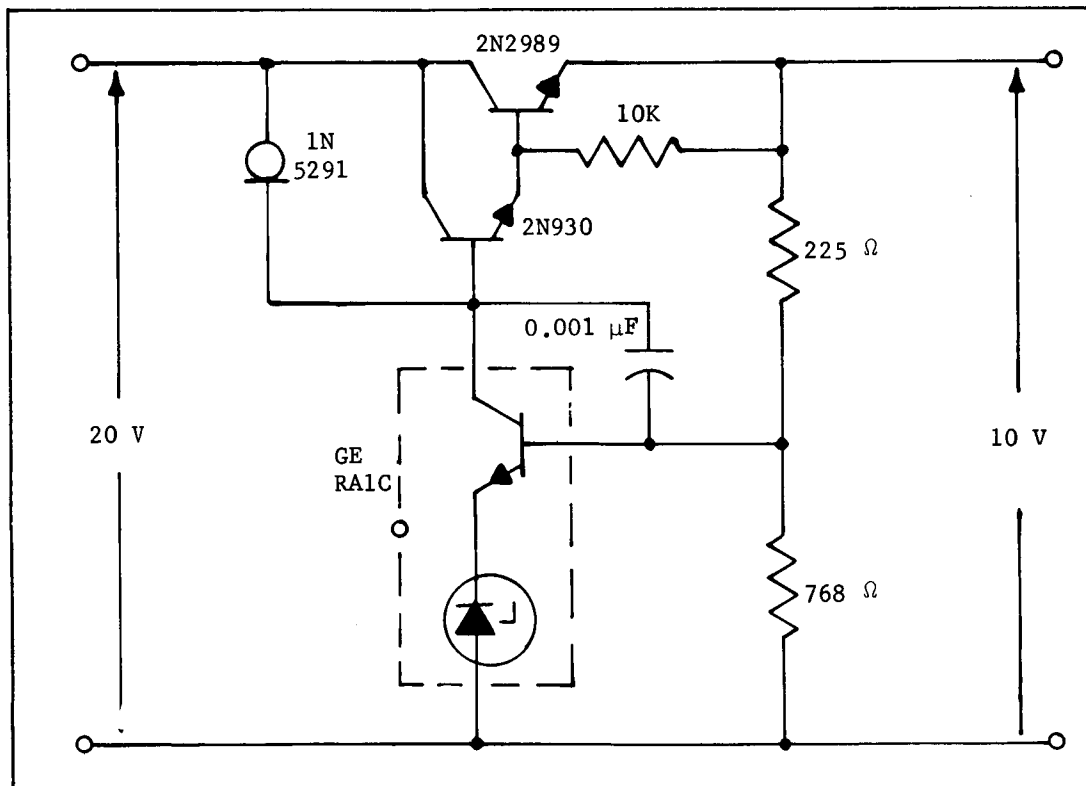


Figure 34.- Voltage Regulator Schematic

$$V_o = f(I_L, V_{in}, T, \tau)$$

$V_o$  = output voltage

$I_L$  = load current       $T$  = temperature

$V_{in}$  = input voltage       $\tau$  = time

$$dV_o = \frac{\delta f}{\delta I_L} dI_L + \frac{\delta f}{\delta V_{in}} dV_{in} + \frac{\delta f}{\delta T} dT + \frac{\delta f}{\delta \tau} d\tau$$

$$\Delta V_o \approx \frac{\Delta f}{\Delta I_L} \Delta I_L + \frac{\Delta f}{\Delta V_{in}} \Delta V_{in} + \frac{\Delta f}{\Delta T} \Delta T + \frac{\Delta f}{\Delta \tau} \Delta \tau$$

where:

$$\frac{\Delta f}{\Delta I_L} = \text{load regulation,} \quad \Delta I_L = 10 \text{ ma}$$

$$\frac{\Delta f}{\Delta V_{in}} = \text{line regulation,} \quad \Delta V_{in} = 2 \text{ V rms}$$

$$\frac{\Delta f}{\Delta T} = \text{temperature stability,} \quad \Delta T = 40^\circ \text{C}$$

$$\frac{\Delta f}{\tau} = \text{short-term drift,} \quad \Delta \tau = 1 \text{ hr}$$

Figure 35.- Definition of Regulator Performance Parameters

The error amplifier and reference are combined in the RA1C reference amplifier to ensure temperature stability. The temperature coefficient of this device is 0.001%/°C maximum, which amounts to a 0.04% change over the full T013 temperature range of 0 to 40°C.

The preregulating diodes (1N-5291) temperature coefficient (TC) has to be specified to lie in the range of 0.1%/°C over the temperature range of 0 to 40°C. The current diode TC coupled with the TC of the reference amplifier will ensure a stability of better than 0.1% in the output voltage over the temperature range of 0 to 40°C.

The output sampling resistors have a temperature coefficient of 20 parts per million (ppm), which results in an 0.08% change over the full-temperature range.

Figure 36 is a schematic comparison of a typical transistor -- zener diode preregulator versus a current regulating diode (CRD) scheme. The main advantages using a CRD as opposed to a typical preregulator are the reduction of the number of components, increased reliability, and reduction in costs. Figure 35 defines the regulator performance parameters.

The output of the dc bias supply is impressed across a potentiometer used to null out the initial vehicle torques, figure 32. Using the potentiometers and polarity reversing switches, the current into the RGS test torquers can be adjusted and monitored on the null meters. The astronaut will be required to manually null to within  $\pm 8 \mu\text{A}$  or 5°/hr (fig. 37). Preliminary tests indicate that the time required to null all three axes, before the performance of the experiment, will be less than 1 min. Upon completion of the nulling procedure, the dial locks located on the potentiometers should be engaged.

Voltage-to-frequency converter (CAD). - The voltage-to-frequency converter will be flight qualified to the same environmental and performance criteria as the rate gyro package.

The input to this converter is the change in vehicle rates after the dc bias has been set. It converts the current into a pulse rate that is proportional to the input. The converter scaling is 1800 pps per 173  $\mu\text{A}$ .



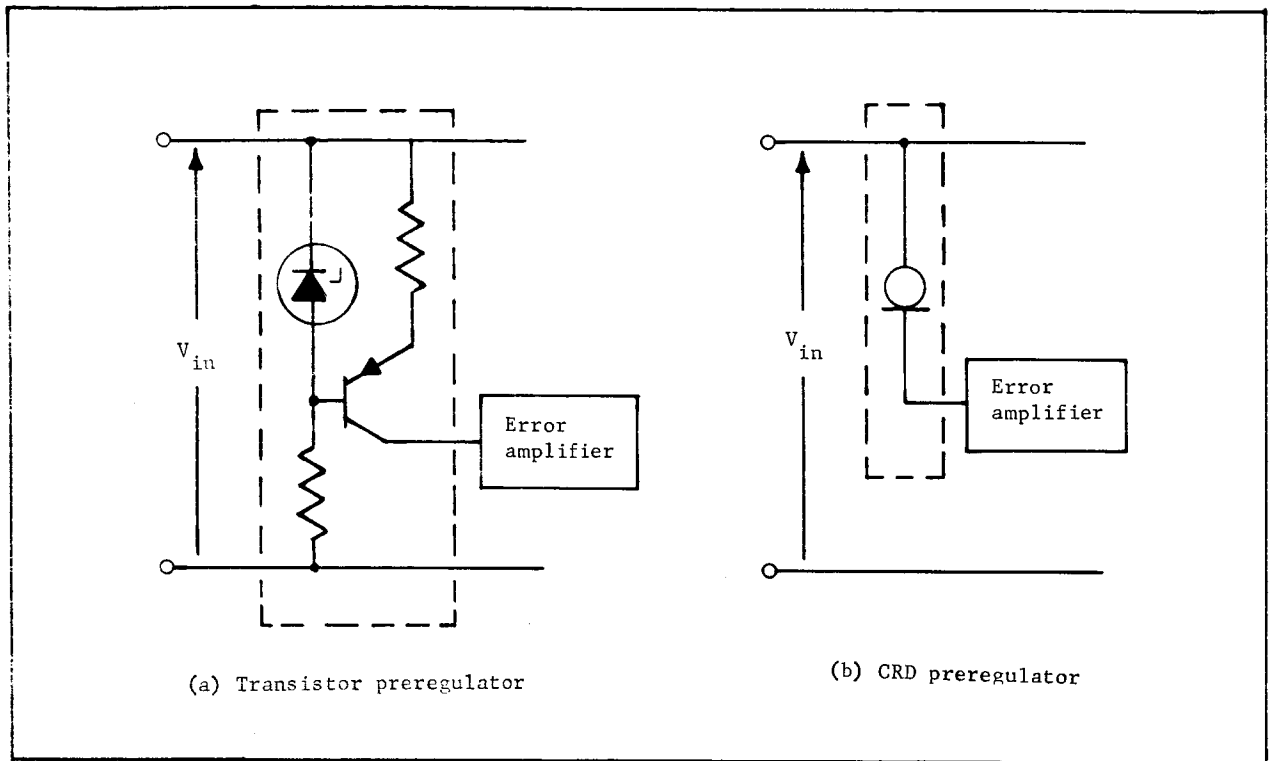
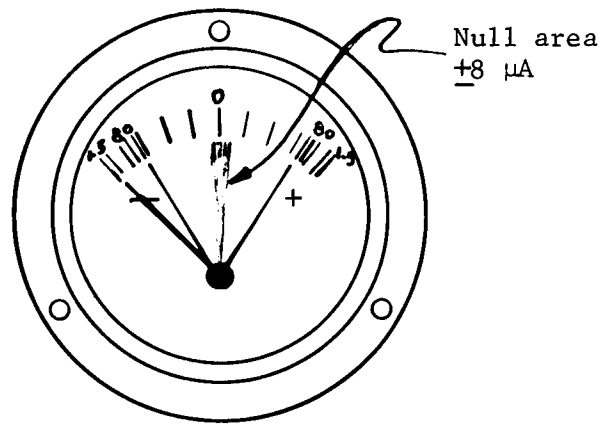


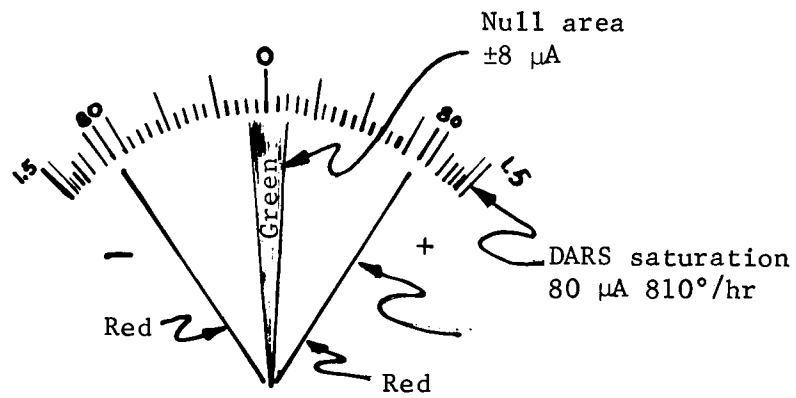
Figure 36.- Transistor Preregulator Versus CRD Preregulator

The converter functions are shown in figure 38. When the integrator ( $1/S$ ) output exceeds the trigger level of the threshold detector, the pulse source is connected through a pulse switch and resistor to the summing junction of the integrator. The pulse switch sets the polarity of the "rebalance" pulse to drive the integrator toward zero.

The ramp output of the integrator is due to  $E_{in}$ , assuming that  $E_{in}$  is constant with respect to the pulse rate output. When the ramp exceeds the threshold voltage of the detector, a monostable multivibrator is triggered from its quiescent state to its timing state. When the one-shot is triggered, it operates solid-state switches to disconnect the pulse generator capacitor from its precision voltage supply and connects it through a resistance to the summing junction of the integrator. As the pulse generator capacitor discharges into the integrator, the output of the integrator falls below the trigger region of the threshold detector and returns to approximately zero. Thus, the pulse frequency is determined by the rate of rise of the integrator output.



Actual size



Twice size

Figure 37.- Null Meter

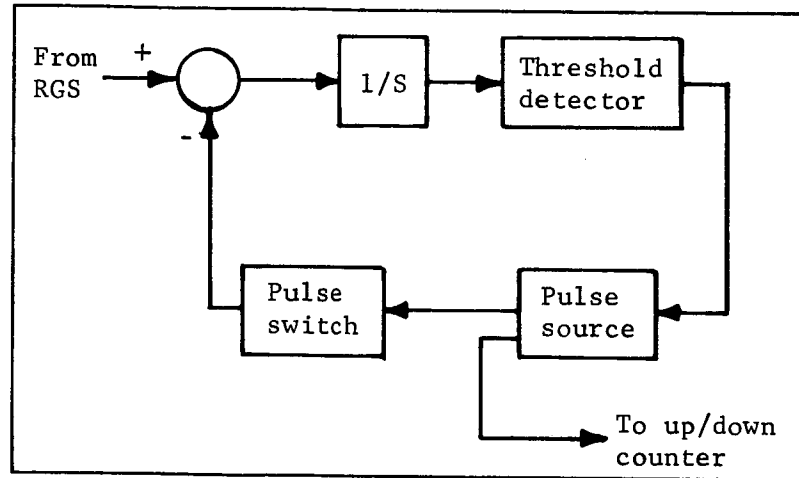


Figure 38.- Voltage-to-Frequency Converter

The pulse frequency per volt is determined by the pulse area, threshold value and the integrator gain. If  $h$  is threshold voltage and  $K$  is integrator gain in volts per second, the time per pulse is:

$$\left. \begin{aligned} Kt &= h \\ t &= \frac{h}{K} \end{aligned} \right\} \quad (5)$$

and the pulse frequency is

$$f_p = K/h \quad (6)$$

We can thus examine the effects of variation in the threshold voltage by expanding  $f_p + \Delta f_p$  in a power series to obtain

$$f_p + \Delta f_p = \frac{K}{h + \Delta h} = K \left[ \frac{1}{h} - \frac{\Delta h}{h^2} + \frac{1}{2!} \left( \frac{\Delta h}{h} \right)^2 - \dots \right] \quad (7)$$

Retaining only first order terms, we have

$$f_p + \Delta f_p = \frac{K}{h} - K \frac{\Delta h}{h^2} \quad (8)$$

and

$$\Delta f_p = -K \frac{\Delta h}{h^2} = -\frac{\Delta h}{h} f_p \quad (9)$$

It is clear, then, that small variations in the threshold have only a slight effect on the pulse frequency. The pulse size is determined by the following equations:

- 1) Maximum output = Pulse amplitude  $\times$  duty cycle  $\times$  scale factor;
- 2) Resolution = Pulse amplitude  $\times$  time per pulse.

The mean voltage out of the integrator is maintained zero so that

$$\int E_{in} dt = \int \text{pulses} dt \quad (10)$$

Then

$$f_p \int_0^{1/f_p} \text{pulses} dt = \text{pulse area} / \frac{1}{\text{pulse rep rate}} \\ = \text{average pulse voltage} \quad (11)$$

The average pulse voltage = 1 V for pulse repetition rates of 1800 pps. Thus, the pulse area = 1 V  $\times$  1/1800 = 1/1800 V sec.

The input resistance to CAD is 5840 ohms yielding a current input of 172  $\mu\text{A}/\text{V}$ . A test was conducted on CAD to determine its scale factor and to see whether it is linear for an input from zero to 1800 pps output. This was done by recording the output of CAD as the input was driven by a precision constant current source. A precision current source was used for the test and found to be accurate to within 0.1%. The input to CAD was varied in steps of 10  $\mu\text{A}$  from 0 A to 220  $\mu\text{A}$ , and the resultant data were recorded in table 11 and plotted in figure 39.

A least-squares approximation shows the CAD scale factor to be 10.49 pps/ $\mu\text{A}$ , approximately 171.7  $\mu\text{A}$  input resulted in an output of 1800 pps.

The frequency response of CAD was measured and found to be flat out to at least 50 cps, well beyond the 5-cps pass band of the rate gyro system.

TABLE 11.- CAD TEST DATA

Input current, A	CAD output, pps
0	0
10	105
20	209
30	314
40	418
50	523
60	627
70	731
80	836
90	941
100	1050
110	1154
120	1258
130	1363
140	1468
150	1573
160	1677
170	1782
180	1887
190	1991
200	2100
210	2205
220	*2271

\*Note that saturation occurred at this point.

Positive five-volt digital logic power supply.- This supply is used to power all the micrologic flat-packs in the digital output circuitry. A 10-turn winding on the CAD inverter provides the input power to this supply. The square wave signal, at an approximate 2.5 kHz rate, from the inverter winding is full wave rectified and filtered in the 5 V supply (fig. 40). This supply is capable of delivering a  $5\text{ V} \pm 10\%$  dc output at a load of 1 A with a maximum ripple of 25 mV at full load. The digital output circuitry operates at an up-level of 4.5 to 5.5 Vdc and draws a total current of 700 mA. The regulation and ripple at this load current is the same or better than that at a load current of 1 A as evaluated using the actual breadboard logic circuitry as a load.

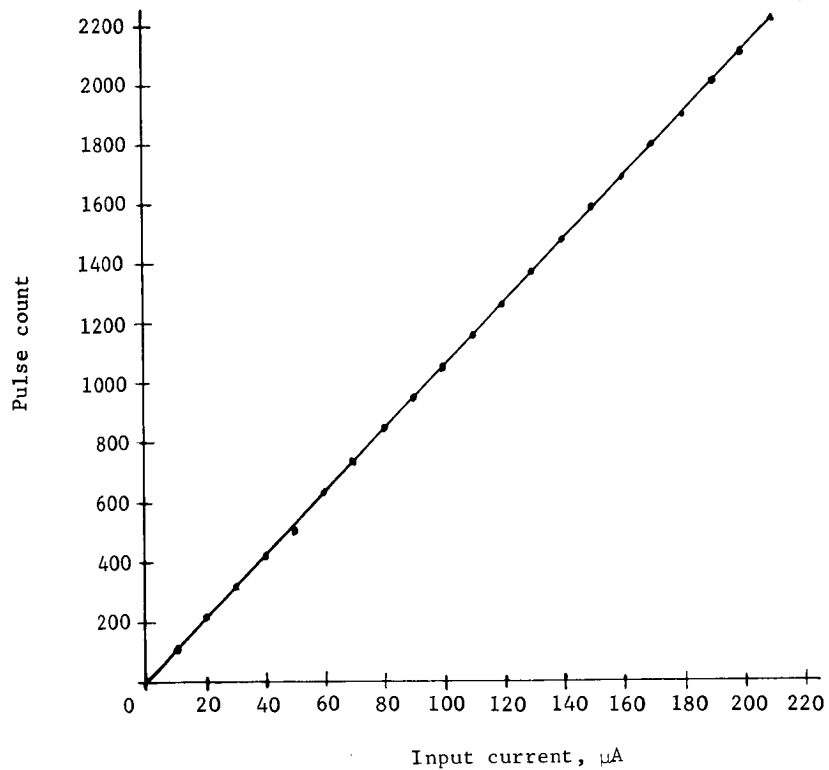


Figure 39.- CAD Current Versus Pulse Output

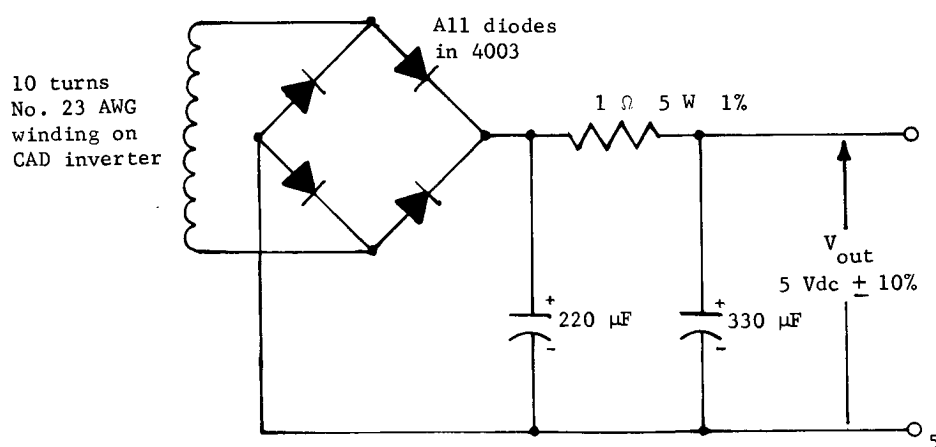


Figure 40.- Positive Five-Volt Supply

Digital output circuitry. - This circuitry counts the pulses from CAD for a time  $\Delta t$  and shifts the total count out to the data synthesizer on command.

A block diagram of the unit is shown in figure 41.

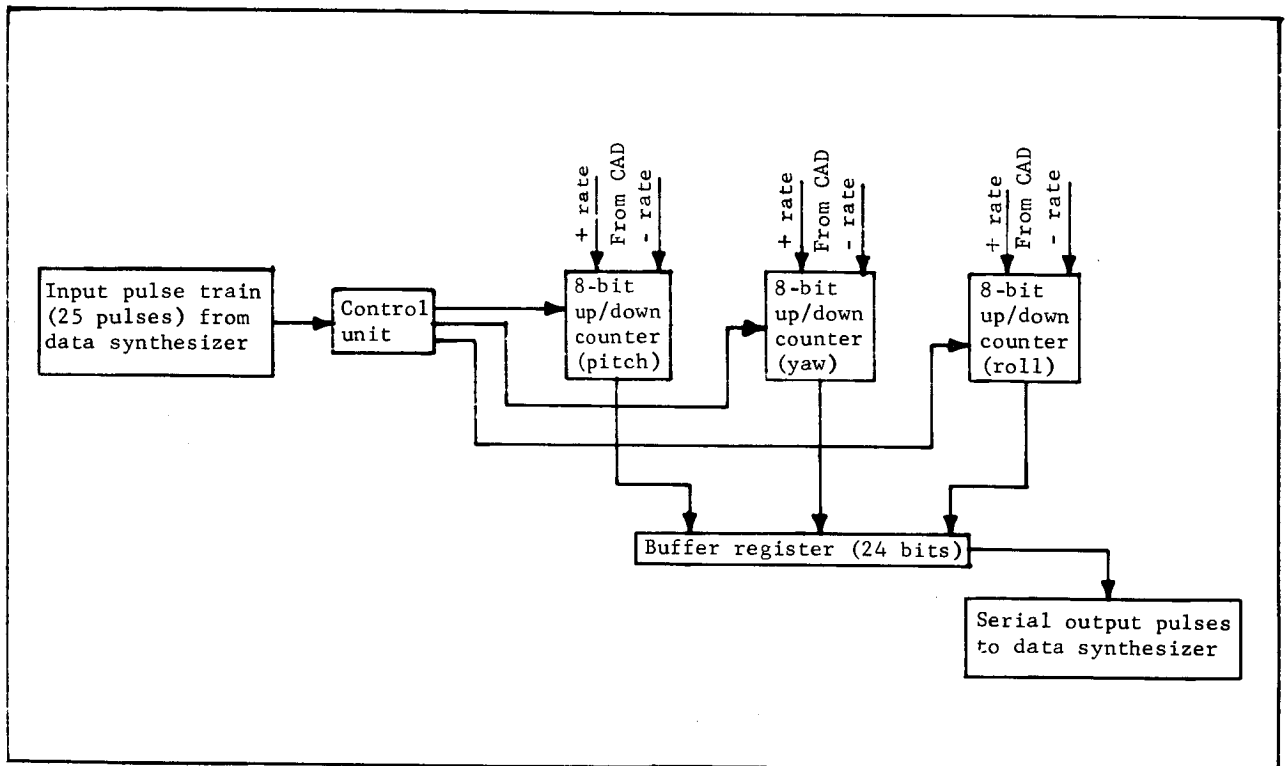


Figure 41.- Digital Output Circuitry

This digital output circuitry, consisting of a control unit, the up/down counter, and the buffer register is housed in a separate assembly called the Electronics Unit. The function of each unit is as follows:

- 1) Control unit,
  - a) Disables up/down counters from CAD,
  - b) Transfers up/down counters to buffer,
  - c) Reset up/down counters,

- d) Enable up/down counters to CAD,
- e) Shift out buffer (24 pulses);
- 2) Up/down counters,
  - a) 8-bit counters are reset to binary 10000000 to provide both up and down counting capability,
    - (1) CAD pulses on + line cause counter to count up from a preset bias,
    - (2) CAD pulses on the negative line cause counter to count down from a preset bias,
    - (3) When counting up, a flip-flop toggles if all lower ordered bits are in one state. The lower ordered bits also toggle;
- 3) Buffer register,
  - a) The buffer register stores counter information from the previous sampling interval,
  - b) Shifts information out serially with 24 pulses from the control unit.

Control unit: The control unit consists of a pulse steering circuit and five monostable timing elements. The pulse steering circuit directs the first pulse of a 25-pulse train to the timing monostable elements (one-shots) and the remaining 24 to the buffer register.

The pulse steering circuit is made up of a one-shot, a flip-flop; and two NAND Gates A and B as shown in figure 42. In the initial state, the output of the input one-shot is low, forcing the outputs of the flip-flop such that Q is low and  $\bar{Q}$  is high. When the first pulse arrives, NAND GATE B goes low and a pulse appears at the output of GATE B.

The truth table for the NAND GATE is shown in table 12.

TABLE 12.- NAND GATE TRUTH TABLE

Input	Output
HH	L
HL	H
LH	H
LL	H
H = high; L = low.	



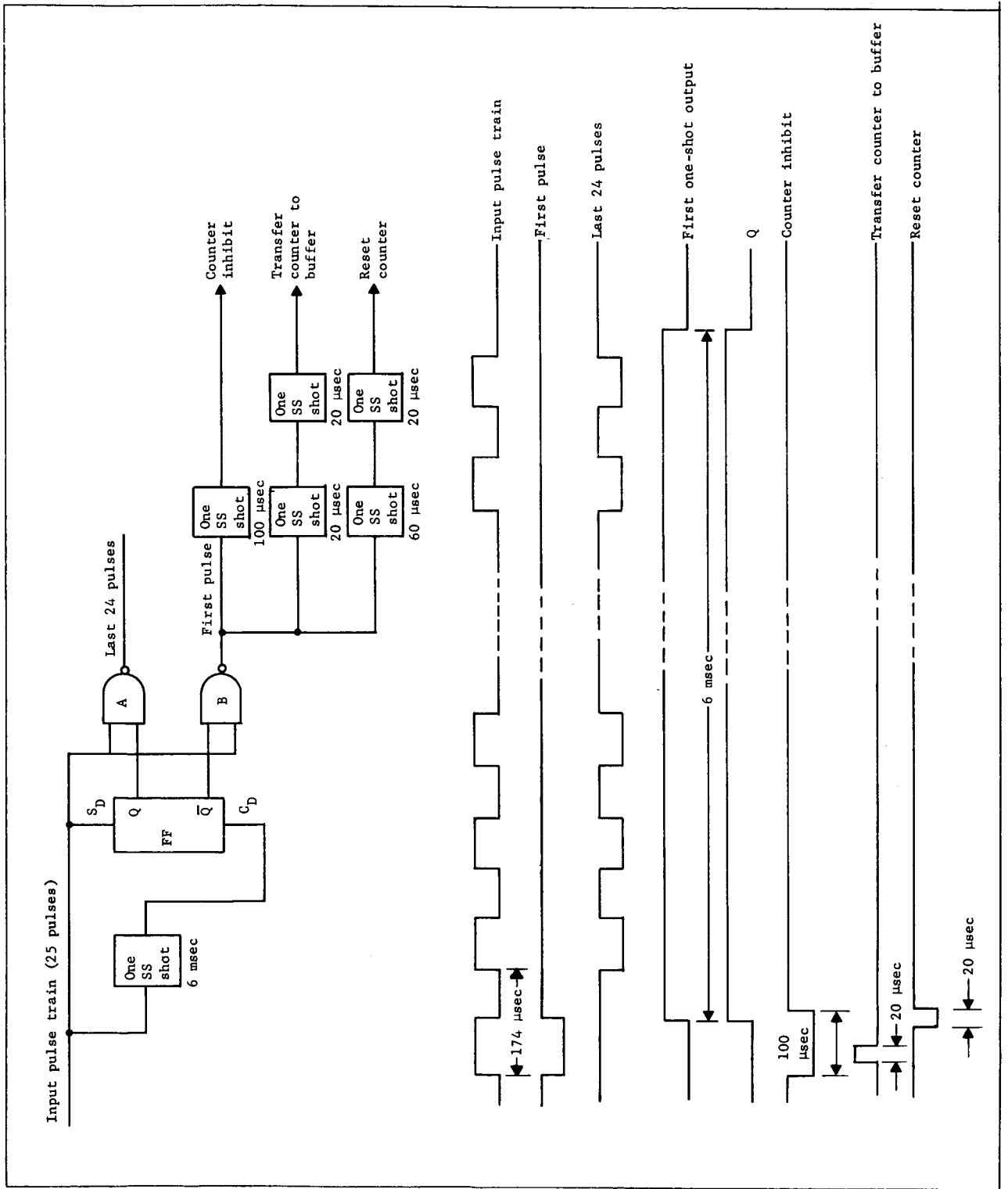


Figure 42.- Digital Control Unit Logic Diagram

Table 13 is the truth table for the flip-flops used in this circuitry

TABLE 13.- FLIP-FLOP TRUTH TABLE

S	C	Q	$\bar{Q}$
H	H	(NC)	(NC)
H	L	L	H
L	H	H	L
L	L	H	H
(NC) = no change.			

When the first pulse drops off, the first one-shot output goes high, and the clear side input to the flip-flop becomes high. Also, at this time, the setside input goes low which causes Q to be high and  $\bar{Q}$  to be low. This disables Gate B and enables Gate A.

The requirements on the one-shot are that its output must remain high for at least the duration of the remaining 24 pulses of the train, and then go low sometime before the next pulse train arrives. The period of each input pulse is approximately 174  $\mu$ sec; therefore, the period for 24 pulses is about 4.2 msec. If the one-shot pulse is set to 6 msec, the flip-flop output remains high during this time, and all 24 pulses are gated through Gate A.

The first pulse is fed into another timing one-shot as shown in figure 42. These one-shots are used to produce other timing pulses used to perform several functions: (1) First the up/down counters are inhibited from receiving pulses from CAD for 100  $\mu$ sec; (2) 20  $\mu$ sec later, a 20- $\mu$ sec pulse transfers the contents of the up/down counters into the buffer register; (3) 20  $\mu$ sec after the transfer pulse drops, another 20- $\mu$ sec pulse resets each counter to binary 10000000; and (4) After the 100  $\mu$ sec counterinhibit pulse falls, pulses from CAD are enabled, and the up/down counters resume counting.

The inhibit pulse duration to the counters was set at 100  $\mu$ sec because this is the approximate pulse width of a pulse from CAD. Thus, the chances for a pulse to be missed or for a pulse to be counted twice are virtually eliminated. It can be noted here that the timing and pulse width of the transfer pulse and

the reset pulse are not critical. It is required that the transfer pulse precede the reset pulse and that both pulses lie within the 100  $\mu$ sec that the counter is inhibited from counting.

The one-shots that are used in the control unit logic present a potential problem that is inherent in all one-shots. The problem is that the one-shot may fire from noise on the input signal. The input circuitry to the Fairchild 951 one-shot is shown in figure 43.

The one-shot is fired when one of the inputs drops with a slope of 0.5 V/10  $\mu$ sec with respect to ground. The magnitude of the drop must be at least the forward voltage drop across the input diode, which is approximately 0.5 V.

Because the circuitry has been designed so that only one input to the one-shot is required, the one input can be used to change the voltage of the other input. Figure 44 shows the clamping circuitry on input 2 of the one-shot.

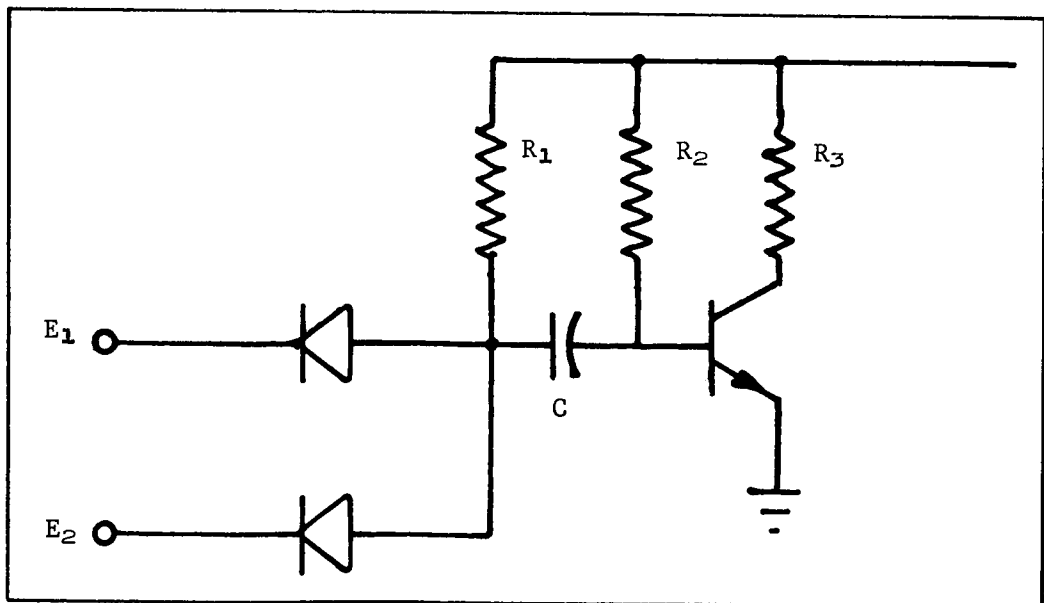


Figure 43.- Input Circuitry to Fairchild 951 One-Shot Multivibrator

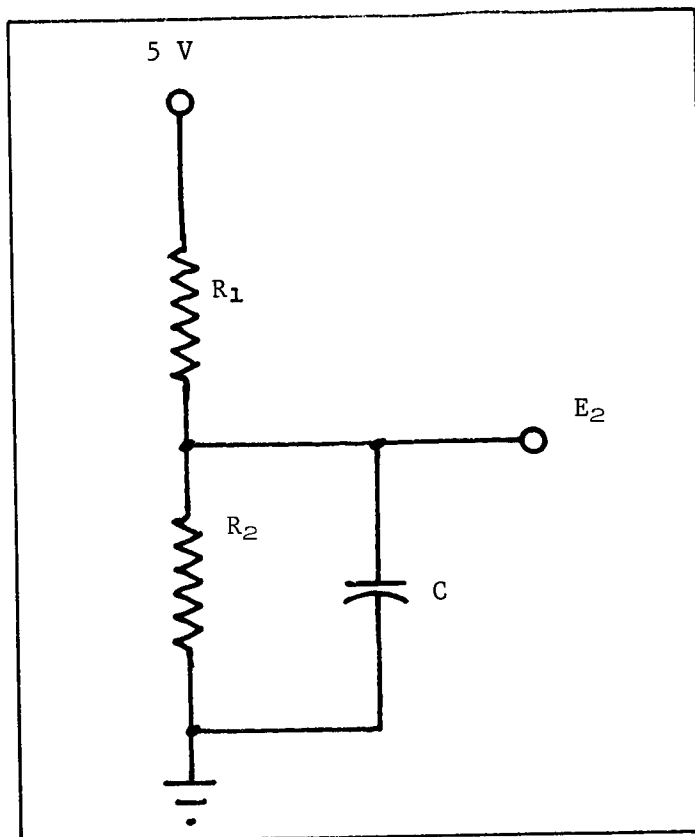


Figure 44.- One-Shot Input Clamping Circuit

The input to the one-shot (input 1) is normally high (5 V). For this case, input 2 of the above circuitry is held at 3 V, and the voltage at the anode of the diode is approximately 3.5 V. For this case, the input voltage must now drop from 5 to 3 V. Therefore, the noise immunity is increased when input 1 is high.

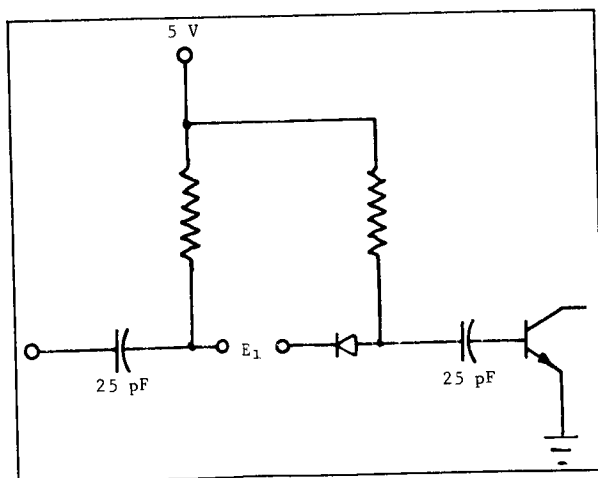


Figure 45.- RC Shaping Network

When the input is low, a voltage drop of 0.5 V can still trigger the one-shot. Figure 45 shows the RC network that was added to input 1 so the voltage level on the input diode is high except for the negative voltage spike required to trigger the one-shot.

The RC time constant can be set so the voltage at input 1 is high by the time the one-shot resets. Also, it is necessary to keep the power and ground lines

on the printed circuit and as noise-free as possible. By making the lines as wide physically as possible, the inductance of the line is low, and hence, the voltage term  $L \frac{di}{dt}$  is also kept to a minimum.

Up/down counters: There are three binary, eight-bit up/down counters in DARS -- one for each of the three axes. The pulse outputs of CAD provide the inputs to the counters as shown in figure 46. Each axis of CAD puts out pulses on either of two lines representing plus or minus rates. Only one of these lines contains pulse data at any particular time. Therefore, pulses on one line indicate rates in one direction, and pulses on the other line indicate rates in the opposite direction. Pulses on one line are used to count the counter up, and pulses on the other line count the counter down.

The maximum differential rate for which the DARS is scaled is 40°/hr. This rate results in a pulse output rate from CAD of 1800 pps. The up/down counters are sampled every 0.05 sec, which corresponds to a maximum pulse count of 90 pulses accumulated in the counter during this period. Ninety pulses corresponds to the binary number of 01011010 in the counter. Initially and after each sampling cycle, the counters are reset to binary 10000000. Thus, the range of the counter output is from binary 00100110 (-40°/hr) to binary 11011010 (40°/hr).

To illustrate the up/down counting scheme, "line one" is used to count the counter up while "line two" is used to count the counter down (fig. 46). "Line one" is used to set a steering flip-flop, which in turn enables all "A" gates used to count the counter up. "Line two" resets the flip-flop and causes the counter to count down by enabling the "B" gates.

The logic for counting up is as follows:

- 1) Look at lowest order bit,
  - a) If it is a zero, toggle it to a one and leave other bits alone,
  - b) If it is a one, go to the first zero bit, toggle it to one, and toggle all lower bits to zeros;
- 2) All high-order bits remain unchanged.

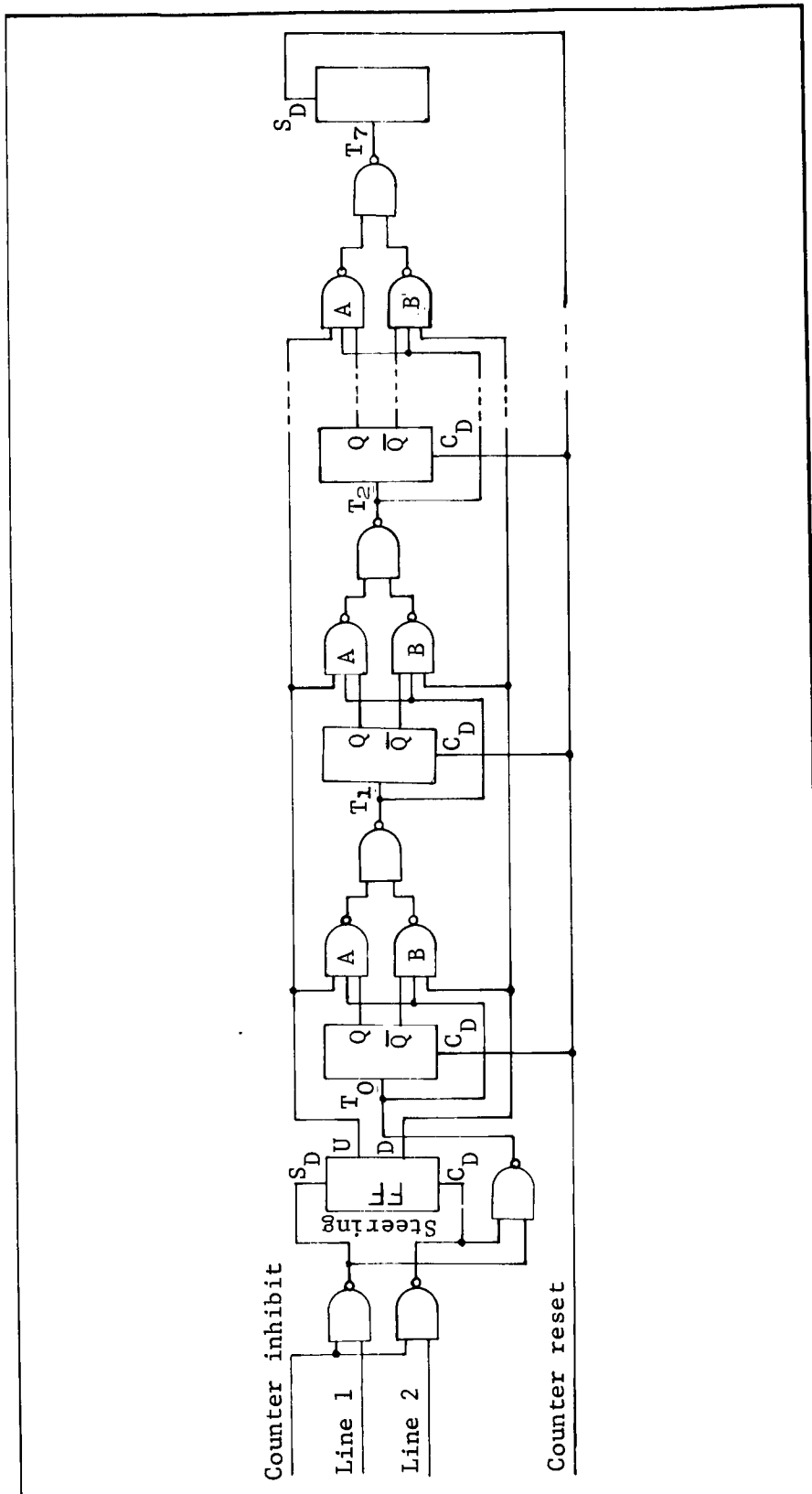


Figure 46. - Up/Down Counter

The logic for counting down is as follows:

- 1) Look at lowest order bit,
  - a) If it is a one, toggle it to a zero and leave other bits alone,
  - b) If it is a zero, go to first non-zero bit, toggle it to zero, and toggle all lower bits to ones;
- 2) All higher order bits remain unchanged.

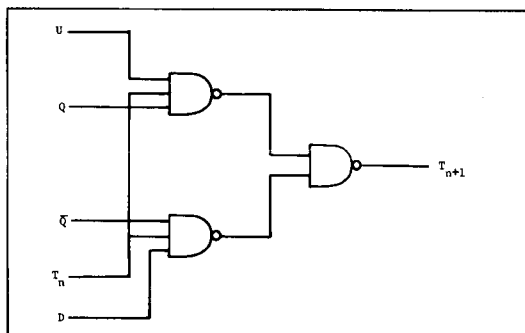


Figure 47.- NAND GATES

Three NAND GATES between each stage are interconnected as shown in figure 47.

When counting up, line 1 has pulses, the steering flip-flop is set, D is a zero, and the lower gate is disabled. An output  $T_{n-1}$  occurs if the top gate  $UTQ$  is made. U is a one if the counter is counting up. Q is a one if the flip-flop preceding the gate is a one.  $T_n$  is a one if all lower order

stages (flip-flops) are in the set state, and a pulse appears on the input to the counter. (Incidentally, if  $T_n$  is a one, then  $T_{n-1}$ ,  $T_{n-2}$  are also in one state.) When the input pulse drops,  $T_{n+1}$ ,  $T_n$ ,  $T_{n-1}$ ,  $T_{n-2}$  also drop. Because a flip-flop toggles on a negative going pulse, all flip-flops fed by these signals will change state. The lower stages will switch from a one to zero, and the last switching stage will switch from zero to one. All single-order stages remain unchanged.

When counting down, D is a one and U is a zero. The upper gate is disabled. The lower gate is enabled when D is a one,  $\bar{Q}$  is a one,  $T_n$  is a one. In this case,  $T_n$  is a one if all lower stages (flip-flop) are in the clear position (Q's are ones in lower flip-flops). In this case, all lower flip-flops switch from zero to one, and the last switching flip-flop changes from one to zero. All higher order stages remain unchanged.

It can be noted here that the trigger line may be eliminated as inputs to the NAND GATES. The delay is increased as it propagates from bit-to-bit. The function of this line is to bypass the flip-flop and eliminate delay of the switching time in the flip-flop.

Buffer register: The buffer register is a 24-bit register that provides intermediate storage between the three 8-bit up/down counters and the output. Contents of the up/down counters are transferred into the buffer register with a 20- $\mu$ sec pulse shown in figure 42. This pulse, which is generated in the pulse-timing circuitry, occurs 20  $\mu$ sec after the leading edge of the 100- $\mu$ sec inhibit pulse to the up/down counter.

The 20- $\mu$ sec pulse enables all NAND GATES shown in figure 48. The gates are wired from the up/down counter stages to the buffer stages in such a way that the flip-flops in the buffer are set in the same state as the flip-flops in the up/down counter.

The buffer register is also wired up as a shift register that works as follows: The set and clear side outputs of each stage are fed to the set and clear side inputs of the next stage, respectively. When a negative going pulse occurs at the trigger input (designed T), the inputs lines are gated in. The new state of a flip-flop becomes what the preceding flip-flop was before the trigger pulse dropped.

The procedure is used to shift all the data information bits into the end flip-flop where they can be gated out serially. The first bit of information is available almost immediately after the transfer pulse rises.

This bit remains available until the first of 24 shift pulses drop (approximately 250  $\mu$ sec). At this time, the second bit becomes available. When the second pulse drops (approximately 170  $\mu$ sec later), the third bit of information becomes available to gate out. This procedure is continued until all bits have been shifted into the end flip-flop.



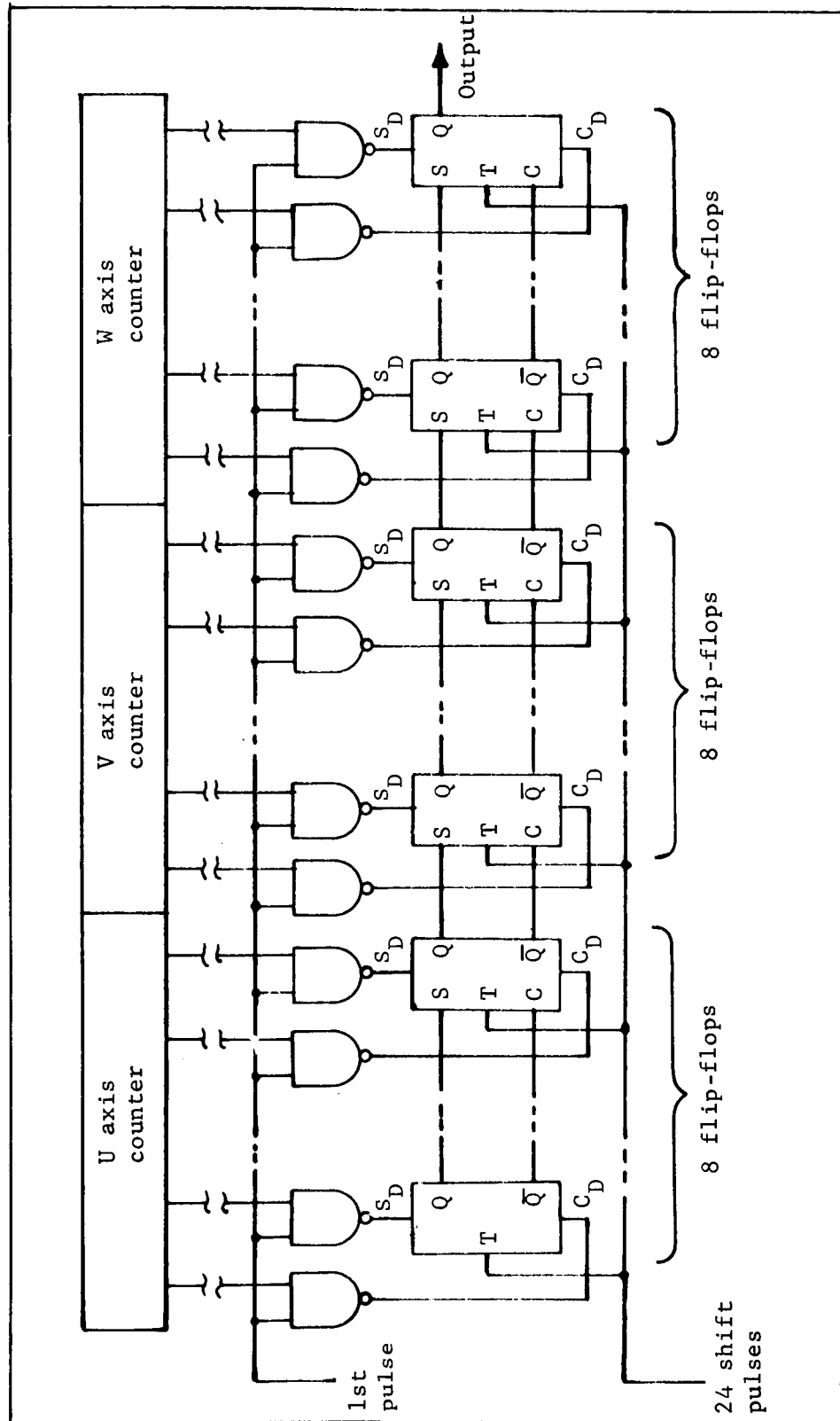


Figure 48.- Buffer Register

## System Tests and Evaluation

Figure 49 is a plot of the system output for input currents to the test torquer. These data were analyzed using a least-squares fit. The slope of the line was 24.56 pps/ $\mu\text{A}$  ( $1 \mu\text{A} = 0.5^\circ/\text{hr}$ ). The rms error or the one-sigma deviation from the fitted line was 2.75 pps. This is equal to a deviation of  $0.11 \mu\text{A}$  or  $0.05^\circ/\text{hr}$ , which is well within the required performance.

Use of the test torquer for an input of equivalent rates is a simplified practical method. The currents driving the test torquer were obtained from a precision dc current supply. The raw data are given in table 14.

TABLE 14.- SYSTEM OUTPUT FOR TEST INPUT CURRENTS

Test torquer current, $\mu\text{A}$	Total pulses per test interval (2 min)	Pulses per second	Least-squares Fit, $y = a_1x + a_0$	Deviation
80.0	233 626	1946.88	1962.7	-15.82
40.0	118 915	990.96	980.1	10.86
20.0	57 548	479.56	488.8	-9.24
10.0	28 772	239.76	243.1	-3.34
2.0	6 096	50.8	46.6	4.20
1.0	2 880	24.0	22.06	1.94
0.2	752	6.26	2.4	3.86
-0.2	592	-4.93	-7.4	2.50
-1.0	3 040	-25.33	-27.0	1.67
-2.0	6 032	-50.26	-51.6	1.37
-10.0	28 780	-239.83	-248.1	8.27
-20.0	57 526	-479.38	-493.8	14.42
-40.0	118 901	-990.84	-985.1	-5.74
-80.0	237 924	-1982.70	-1967.7	15.0

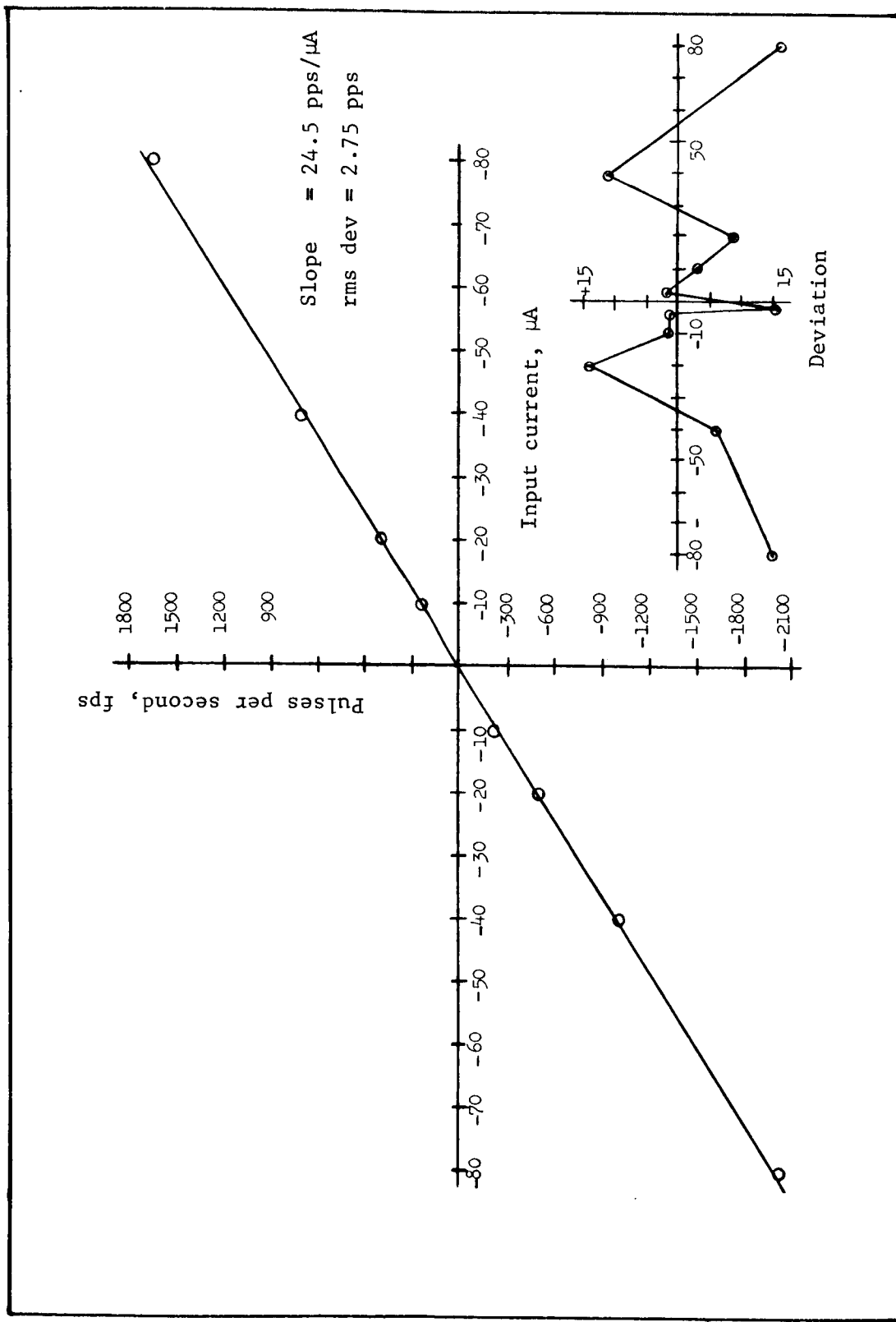


Figure 49.- DARS Output Versus Input Current Rate Gyro System

Design, Build Procedures, Component Selection,  
Reliability, and Operation Aspects of DARS

Component selection.- Throughout the design of DARS, component parts were selected to meet or exceed NASA and/or T013 experiment standards. In practically all cases, these components were selected from the following approved parts lists:

- 1) Approved Parts List, Voyager Program  
Mechanical - Electrical - Electronic.  
Code No. 04236, Document No. 82200000108;
- 2) Apollo Spacecraft Qualified Parts List, November 14,  
1966, No. MSC-A-B-66-8;
- 3) Martin Marietta-Approved Component Parts List for  
Titan III Programs.

Components used in the design of DARS, not on the above lists, were selected on the basis of meeting or exceeding the experiment environmental criteria in regard to reliability, temperature, humidity, vibration, and shock.

Table 15 lists the general DARS components and the three associated specifications or standards. The rate gyro system's individual component parts and the complete system is flight qualified. The voltage-to-frequency converter (CAD) has been developed as part of the Titan III MOL program and will be qualified to the same environment criteria as the RGS. These two subsystems are used intact in the DARS design with but a few modifications. The modifications to these packages will not affect the design or environmental integrity of these DARS subsystems.

Build procedures and packaging - Electronics Unit.- The micro-circuit "flat-packs" used in the digital circuitry are mounted to the printed circuit (P-C) boards by means of a process developed by Martin Marietta to ensure high weld reliability (ref. 8). This process was the result of an extensive study carried out under Martin Marietta's Voyager Programs. Drawings SRD 727610200 and SRD 727610220 (Appendix H) detail a typical board layout together with assembly and build procedures used in the construction of a completed circuit board. The P-C boards along with the 800-cps inverter are housed in the electronics unit package. The construction of this package is similar to the packaging design of the RGS. (SRD 7276 101200 and 10121). The obvious benefits derived by designing the electronics unit similar to the RGS packaging concepts are a high confidence level in regard to shock,

TABLE 15.- DARS COMPONENTS

Component	Type used and/or specification and standards
Meters	MIL-M-10304
Diodes	*
Transistors	*
Micrologic components (digital)	Fairchild 900 series (-55 to 125°C)
Resistors	*
Capacitors	*
Potentiometers	MIL-R22097B and NAS 710
Indicating lights	MIL-E-5272
Connectors	MS3114H and MS3116P
Inverter	MIL-E-5400-B and MIL-E-5272A NPC 200-3 and 200-4
Switches	Microswitch MS toggle type
Relay	Miniature, 6PDT, hermetically sealed (Martin Marietta-approved parts list)
* See items 1), 2), and 3) listed in text under "Component selection" heading	

vibration, temperature, and humidity. It should be mentioned that the bulk of the environmental testing will be accomplished in the following phase of this effort.

The inverter, which is used to power the gyro wheels, has outside dimensions of 2.5x2.5x3.0 in. With a 28 V  $\begin{smallmatrix} +5 \\ -8 \end{smallmatrix}$  dc input, the inverter will supply the following output into a 0.71 to 0.93 lagging power factor load:

- 1) 26-V rms sine wave, 800 cps - single phase;
- 2) Maximum load current = 1.53 A;
- 3) Minimum load current = 0.8 A;
- 4) Line and load regulation =  $\pm 0.5\%$ ;

- 5) Frequency stability =  $\pm 0.4\%$ ;
- 6) Total harmonic distortion = 5% (maximum);
- 7) Ripple and noise =  $\pm 65$  mV (maximum);
- 8) Recovery time (90%) = 1.0 msec.

This inverter is fully flight qualified to NASA standards and complies to NPC 200-4 and 200-3 specifications.

DARS control unit.- The control unit contains the switches, meters, potentiometers, and indicators to initiate and null out the initial vehicle rates (see SRD 727610800 thru 10840 - fig. 50). An interfacing cable to the vehicle, 28 Vdc power, and the data system is also provided on the face of the unit. This cable, containing four wires, is the only interface with the T013 experiment. The detail DARS assembly drawing (SRD 727610000) shows the control panel attached to the main DARS frame. However, by extending the rear cable on the control panel, this panel can be remotely located away from the main DARS assembly.

The lower portion of the control panel contains the necessary switches and indicators to turn the power on the DARS system and to activate the gyros. The upper portion of the panel has the necessary switches, meters, and potentiometers to null the system; decrease the sensitivity; and to activate the digital output circuitry.

The following operational sequence describes the activation and nulling of the DARS (ref. SRD 727610800):

- 1) Initially set switches and potentiometers to,
  - a) PWR to "off" position,
  - b) GYRO to "off" position,
  - c) Sensitivity to "normal" position,
  - d) Null-Operate to "Null" position,
  - e) Potentiometers (3) set to number "5" on dial,
  - f) Polarity switches (3) to "+" position;
- 2) Operate DARS,
  - a) Operate PWR switch to "on" position, power on indicator (Red) will light,
  - b) After approximately 20 min, the GYRO up to temperature indicator (Yellow) will light,

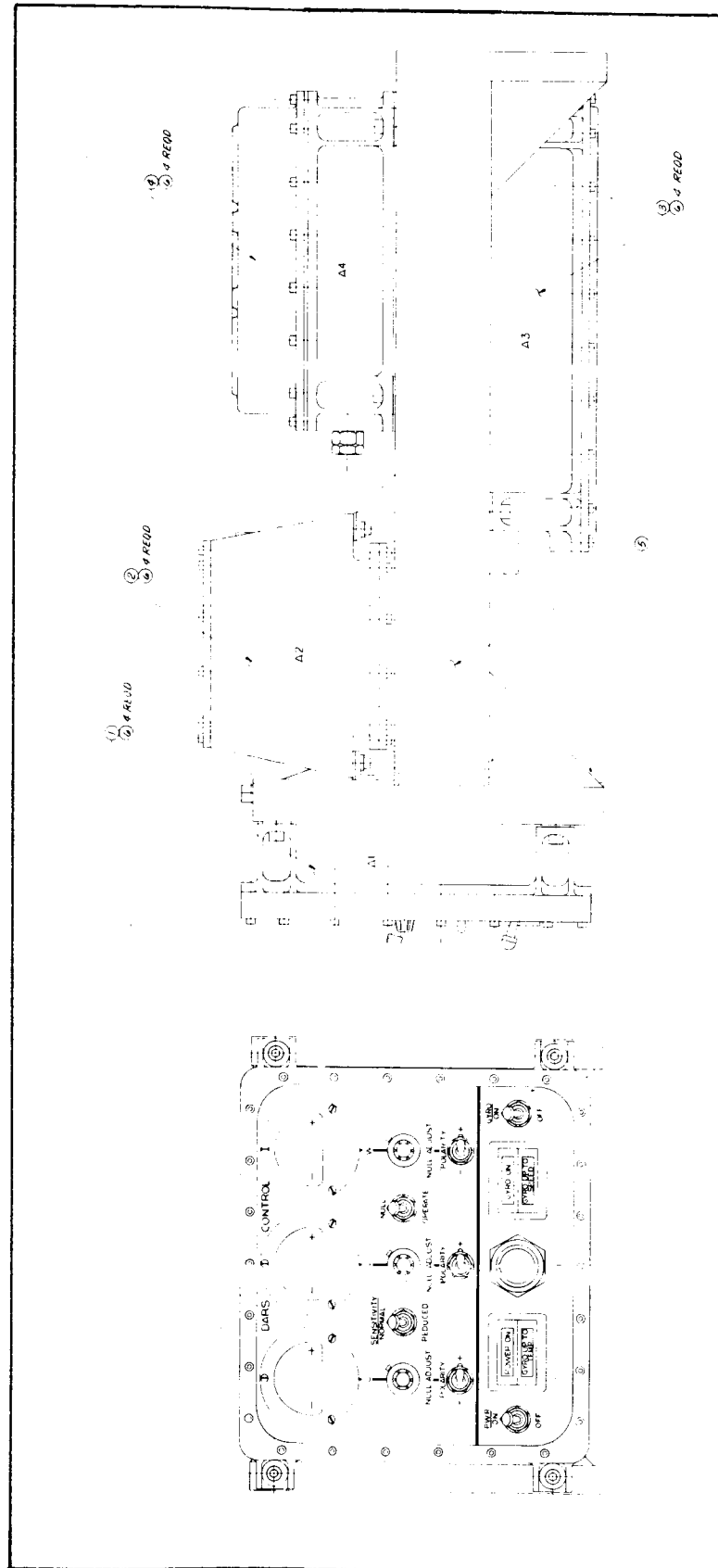


Figure 50.- DARS Assembly

- c) Operate GYRO switch to "on" position; GYRO on indicator (Red) will light,
- d) GYRO up to speed indicator will light in approximately 10 sec;
- e) Using "U" null adjust potentiometer and "U" polarity switch, adjust "U" meter pointer to be within green area of meter (see fig. 38). Lock dial locks on the dial indicators,
- f) Repeat e) for "V" null adjust, using "V" potentiometer, meter and polarity switch,
- g) Repeat e) for "W" null adjust, using "W" potentiometer, meter and polarity switch,
- h) Place Null-Operate switch in the "Operate" position.

The DARS system is now operational and able to measure the differential rates from  $0.1$  to  $40^\circ/\text{hr}$ . In the event of excessive vehicle rates due to astronaut movements or other vehicle disturbances, the sensitivity switch can be moved to the "Reduced" position. This enables the DARS to measure rates from approximately  $0.2$  to  $80^\circ/\text{hr}$ .

The switches used in the control panel are the aerospace-type MS toggle switches. A positive pull-to-unlock feature is incorporated on all the switches excepting the polarity switches.

The indicators conform to the environmental and operational requirements of MIL-E-5272, ABMA-MPD-11023, and 11064. These indicators have two lamps which assure that burnout of one lamp will not result in failure of the indication. Military (MS25237) lamps are used. A press-to-test feature is also incorporated into these indicators. The null adjust potentiometers meet the environmental requirements of MIL-R22097B and NAS 710.

The meters (fig. 37) are nonlinear null meters with a full-scale reading of  $1.5 \text{ mA}$ . This current ( $1.5 \text{ mA}$ ) represents a rate of  $810^\circ/\text{hr}$  or  $0.225^\circ/\text{sec}$ . The meter is also capable of withstanding twice overload (minimum) without permanent damage. The null region ( $0$  to  $60 \mu\text{A}$ ) is linear to better than  $\pm 10\%$ , and this region occupies approximately 65% of the meter scale. The astronaut will only be required to null within  $\pm 8 \mu\text{A}$  (green area) equivalent to a rate of about  $\pm 4^\circ/\text{hr}$ . This nulling operation has been demonstrated on the breadboard DARS and takes about 20 sec/axis. These meters meet the appropriate requirements of MIL-M-10304.



The control unit is packaged with the same design philosophy used in the design of the Electronics Unit Package.

Miscellaneous design considerations.- Miniature MS311411 hermetically sealed connectors are used on the various subsystem packages of the DARS. The cables are constructed using miniature MS3116P type connectors. These cable connectors are supplied with a nylon boot for retention of a potting compound.

Coaxial cable type RG-195/U, terminated in BNC connectors, are used for the digital data interface with the data system of experiment T013. Coaxial cable is used for the pulse data transmission to ensure the integrity of the pulse characteristics regardless of the length of transmission.

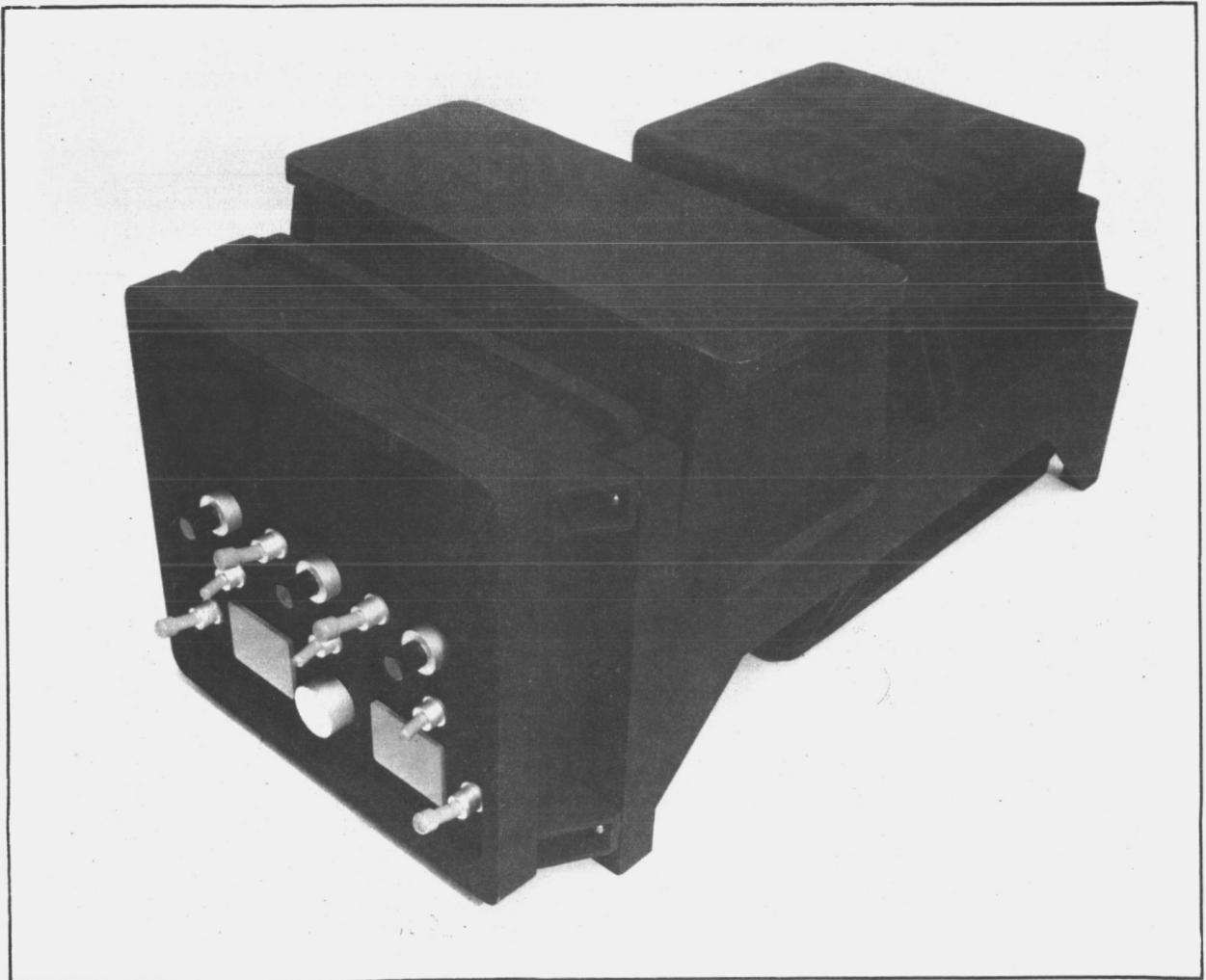


Figure 51.- Wood Mockup of DARS

## FORCE MEASURING SYSTEM

During the performance of both the ground simulation and the orbital experiment, it is necessary to obtain the actual forces and moments imposed on the spacecraft by a maneuvering astronaut. To achieve this goal a Force Measuring System (FMS) has been developed to measure applied forces and local moments. The FMS data will then be correlated with the measured vehicle attitude perturbations resulting from crew activity. Direct comparison of these data with those obtained from the mathematical model of the man/spacecraft system will provide validation of the model.

The maximum forces and local moments to be encountered during the orbital performance have been derived based on actual measurements involving crew activity in the Martin Marietta Space Operations Simulation Laboratory. These force and moment levels have been used to design both a laboratory and a flight configuration of the FMS capable of meeting all the T013 requirements. This system will measure applied forces along three mutually orthogonal axes and, by using a very simple computer program, derive local moments about these same axes. The maximum force to be expected along any one of these axes is 50 lb. The load-bearing platform of the FMS is designed so that this force may exert on a 2-ft moment arm about any axis (see fig. 52).

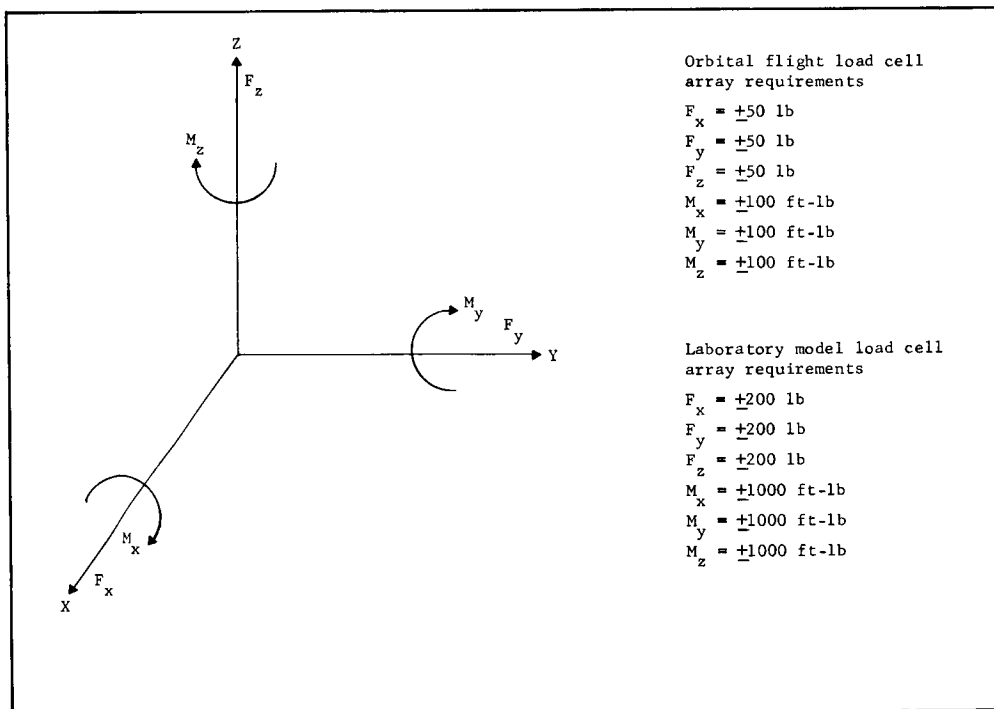


Figure 52.- FMS Orthogonal Force System

Load cell array.- The FMS consists of a load-bearing platform or sensing plate supported by six load cells arranged in a symmetric array and the necessary electronics to obtain usable signals. Each individual load cell will sense both tension and compression forces along its axis. Through the use of the proper transformations, these forces can be resolved into forces along the reference axes and the resulting moments determined. The several geometric arrays investigated are shown in figure 53. Depending on the actual geometry used, the sensitivity of the system may differ from one axis to another and the complexity of the required resolution transformations may vary. The nature of the requirements for T013 dictated a symmetric array resulting in nearly identical sensitivities along each axis and, simply, algebraic resolution transformations. This geometry, shown in figure 54 yields the following transformations:

$$\left. \begin{aligned} F_{Lx} &= 0.7071 F_1 + F_2 + F_3 + F_4 + F_5 + F_6 \\ F_{Ly} &= 0.7071 F_1 - F_2 + 0.5 (-F_3 + F_4 - F_5 + F_6) \\ F_{Lz} &= 0.6124 F_3 - F_4 - F_5 + F_6 \end{aligned} \right\} \quad (12)$$

$$\left. \begin{aligned} M_{Lx} &= 0.3536 - F_1 + F_2 - F_3 + F_4 - F_5 + F_6 \\ M_{Ly} &= 0.3536 F_1 + F_2 - 0.5 (F_3 + F_4 + F_5 + F_6) \\ M_{Lz} &= 0.3062 F_3 + F_4 - F_5 - F_6 \end{aligned} \right\} \quad (13)$$

Where  $F_1$  is the output of each of the individual load, all in pounds,  $F_{Lk}$ ,  $k = x, y, z$ , is the resolved force along the  $k$ th reference coordinate, and  $M_{Lk}$  the resultant moment about the  $k$ th coordinate. Obviously the numerical constants associated with the moment equations are a function of the size of the equilateral triangle formed by the positioning of the load cells that within limits, is arbitrary.

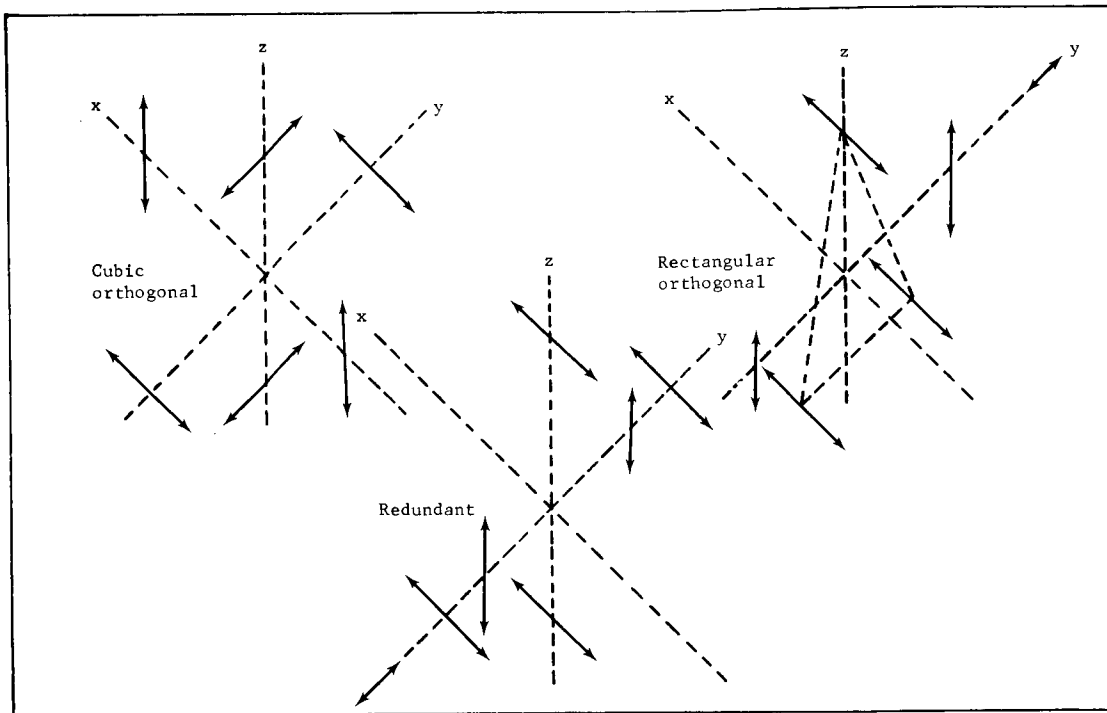


Figure 53.- FMS Load Cell Array Configurations

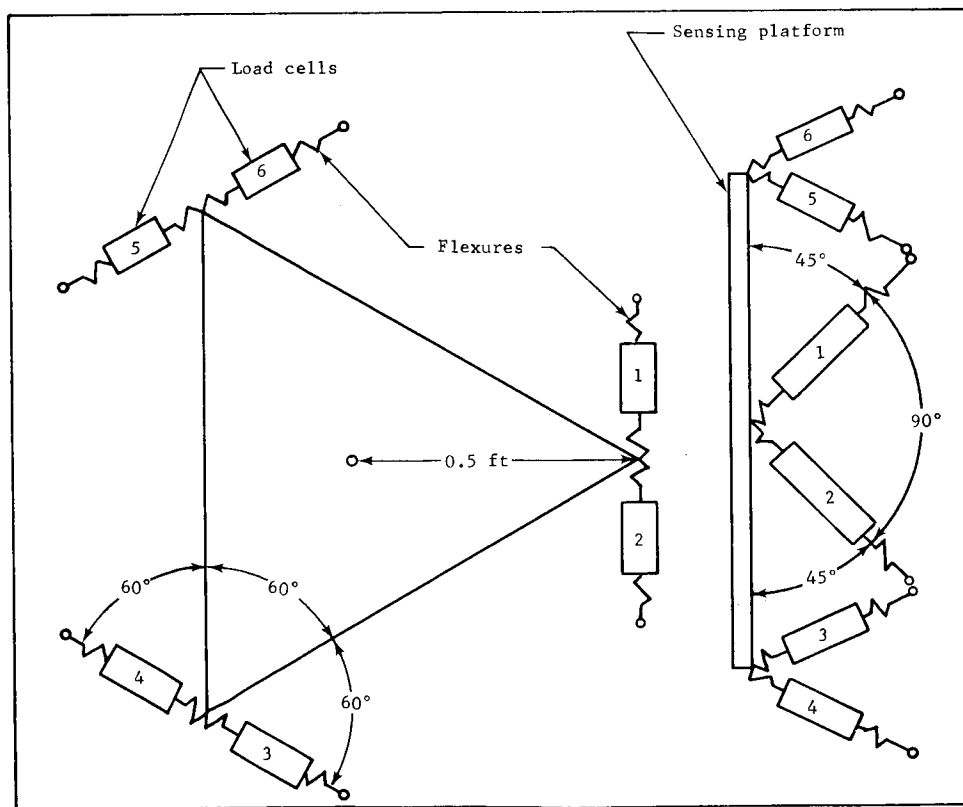


Figure 54.- FMS Flight Model Configuration

The load cells themselves consist of a suitably packaged strain deformation member designed to deflect under strain (tension or compression) in one direction only. This deformation member is then instrumented with bonded strain gages forming the arms of a bridge circuit. The deflection of the strain deformation member produces a change of resistance in the strain gage resulting in an unbalance of the bridge and thus a voltage output from the bridge proportional to the deflection of the strain member or the applied force. Two typical strain deformation members are shown in figure 55.

The strain gages used in the load cells are, typically, one of two types, the foil strain gage and the hybrid semiconductor strain gage. The hybrid semiconductor bridge has a greater output for a given load, better linearity, better repeatability, and better hysteresis characteristics as well as a greater safe overload capacity than foil gages. The overload capacity is somewhat critical to T013 because it influences the physical size of the load cell, as well as the sensitivity. The ability to select a load cell capacity as near the maximum expected force without oversizing the cell to withstand transient overloads results in a smaller, lighter load cell array.

A survey of load cell manufacturers was carried out, and a selection of the load cell to be used in the flight model FMS was made based on physical size, weight, and operational characteristics. The selected cell is shown in figure 56.

Flexures.- An extremely important feature of any load sensing platform is the actual load cell mount. A thorough investigation of this problem resulted in the choice of compound Emery flexures isolating the individual load cells from both the base plate and the load sensing plate. These flexures (fig. 57) are designed to transmit axial forces to the load cell and isolate the cell from transverse forces. This is accomplished by providing, in the flexure, a high degree of stiffness compared to the load cell stiffness in the axial direction and a very low stiffness compared to the load cell in the transverse direction.

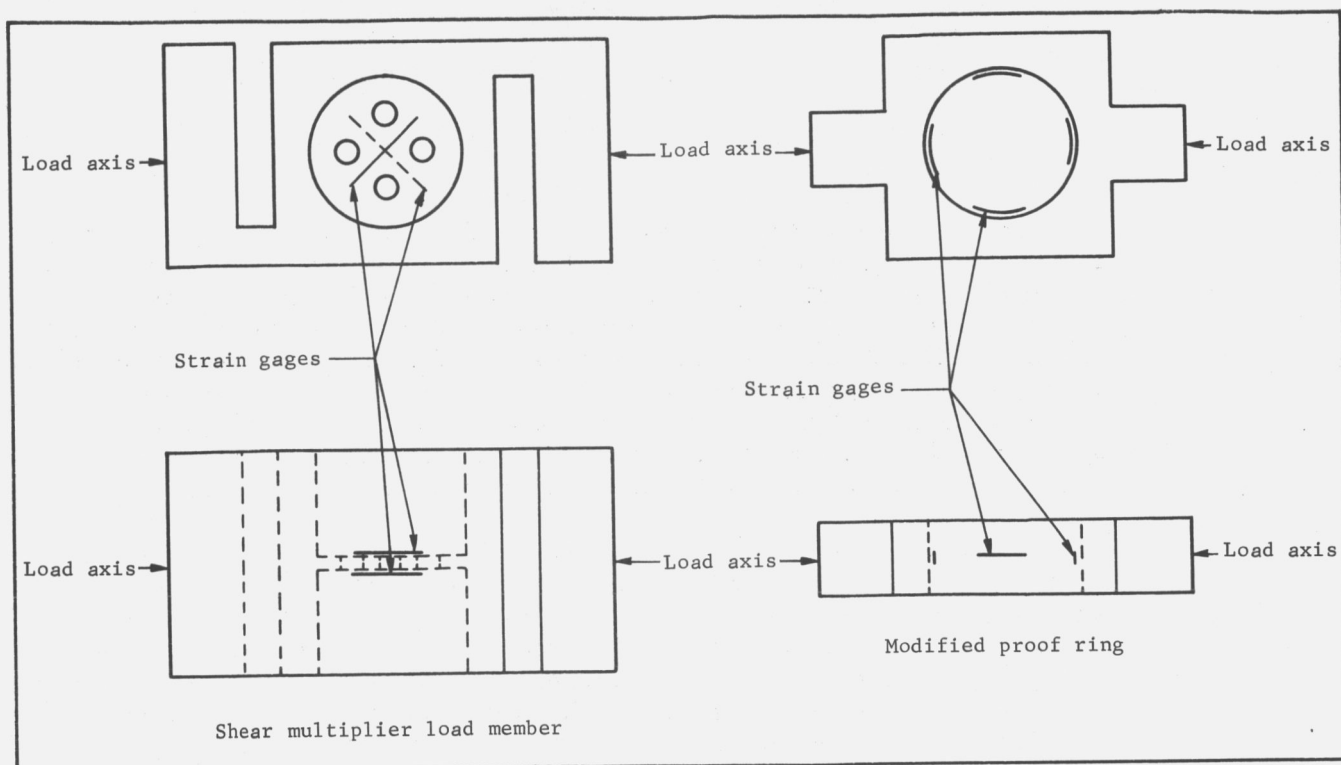


Figure 55.- FMS Typical Load Cell Design

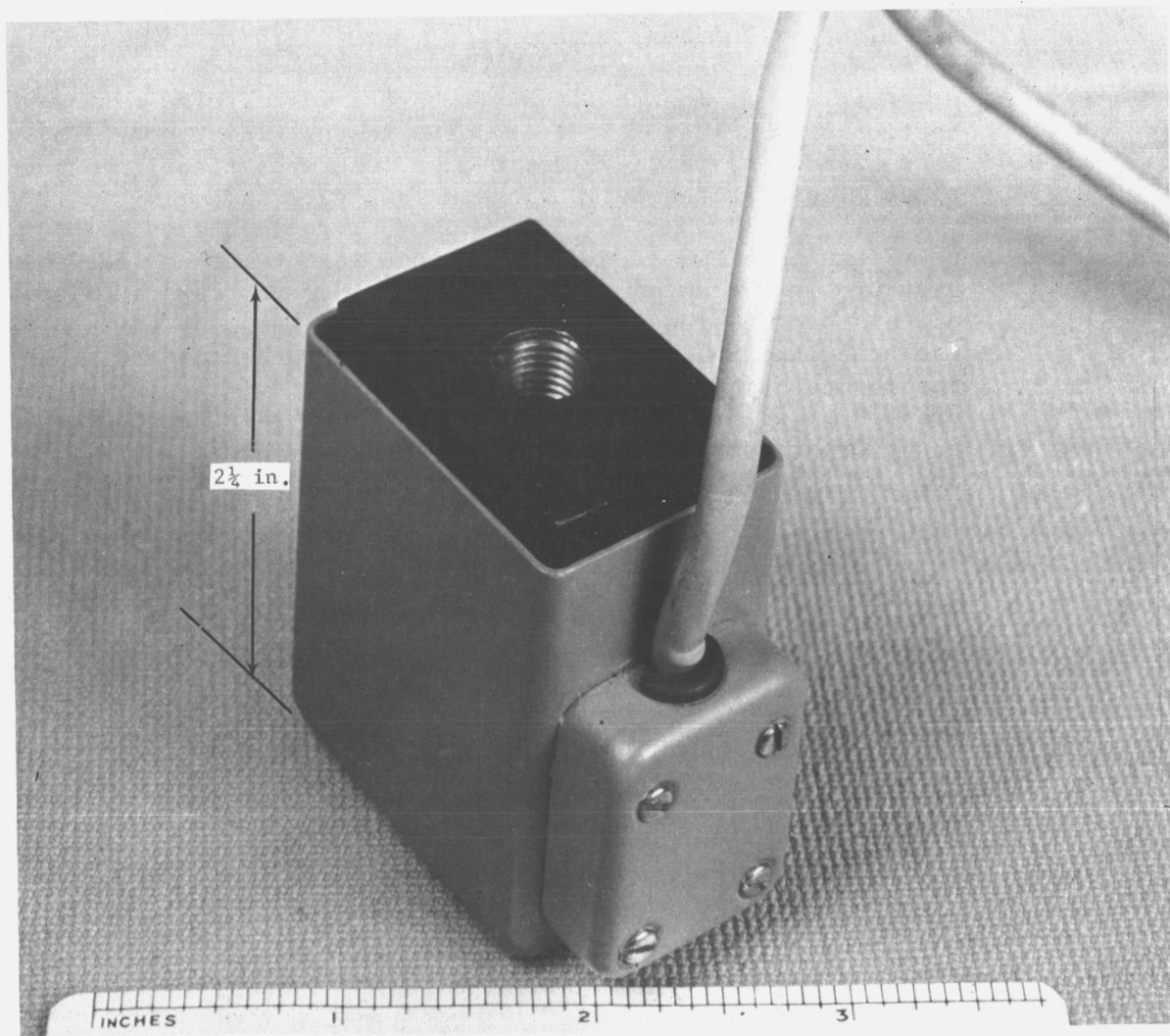


Figure 56.- JP-100 Load Cell for Flight Model FMS

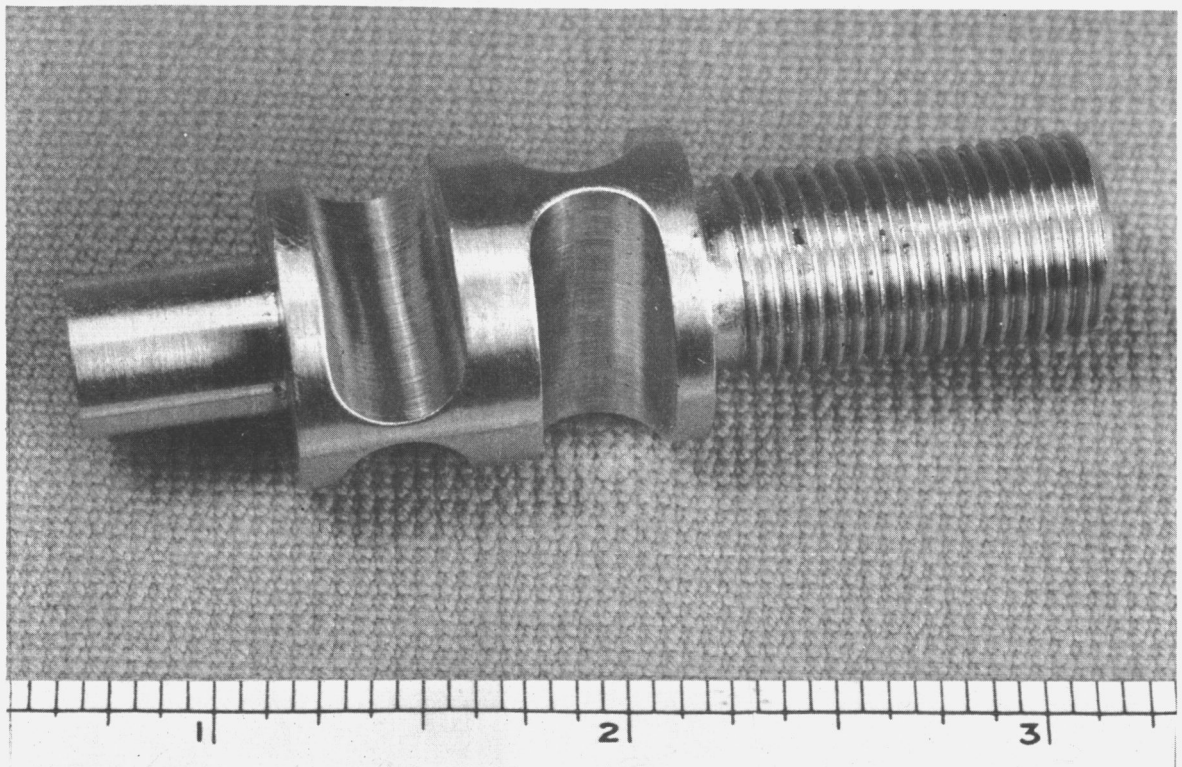


Figure 57.- FMS Compound Emery Flexure

Platform.- The base plate and sensing plates of the load cell array must be as rigid as possible to avoid dissipation of applied forces in the deflection or bending of these plates. To achieve the required stiffness without undue weight, an aluminum honeycomb sandwich with solid mounting inserts were selected (fig. 58). The laboratory model using this construction serves to verify this concept and to develop manufacturing methods for production of the flight model. The particular design selected has a weight density of 1.25 psf compared to the nearly 7 psf of an equally rigid solid aluminum plate.

Electronics.- The necessary electronics for the FMS consists of a power supply for the load cells, the necessary signal-conditioning circuitry and an operational amplifier to increase the 350-mV output of each load cell to the desired 5-V level required for the data system.

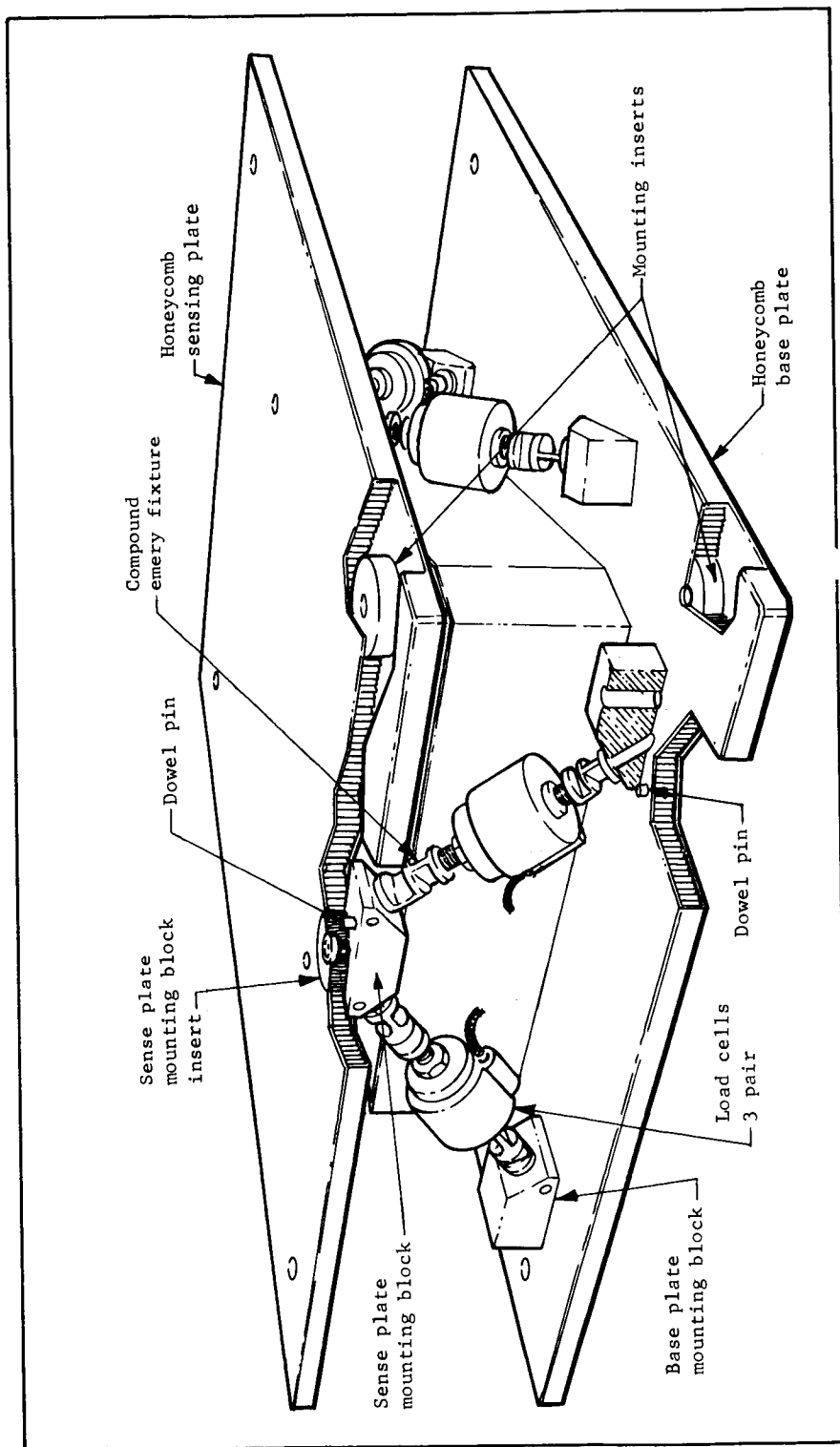


Figure 58.- Load Cell Array Assembly



These electronic components will be packaged within the envelope of the load cell arrays for the flight model and as a separate component for the laboratory model. In the flight configuration, the power supplies for both arrays, the necessary terminals, signal conditioning equipment and amplifiers will be housed in a small enclosure rigidly mounted to the base plate of array number 1. A single power and control cable will interconnect with a similar enclosure mounted to the base plate of array number 2. The signal outputs from each load cell are amplified and transmitted to the T013 data system for subsequent transmission to the ground for reduction and analysis.

Assembly.- The physical assembly of the flight model FMS is such that the arrays may be launched in either the completely assembled form or in a disassembled form. The actual assembly process, should the system be launched disassembled, is particularly simple. One simply inserts each load cell into a mounting block and tightens a lock screw, connects the cables, and the system is operable. The disassembled arrays occupy approximately 80% of the space required for the assembled array. If launched disassembled it is not inconceivable that the assembly task could be incorporated as one of the maintenance and repair tasks of either experiments M508 or D020. However, the present plan is to launch them assembled as an integral part of the Experiment Components Container. The packaging concept here is such that the FMS will not require any special protection during launch.

Performance.- During the actual performance of T013, the two load cells will be mounted to the stringers of the OWS in the crew quarters, separated by a distance of approximately 9 ft 6 in. to allow maneuvering exercises to take place between the two sensing plates. The restrained crew activity will be carried out using only one load cell array. A quick-release restraint will fix the test astronaut to the array so that any contact forces due to the normal crew activities carried out in a crouch, or standing in place in the vehicle, can be measured. Both arrays will also be equipped with suitable handhold and stabilizing grip devices.

Experimental load cell arrays employing the concepts described have been in use in the Martin Marietta Space Operations Simulation Laboratory for a period of two years. The experience gained indicates that accuracies of at least  $\pm 0.5$  lb can be obtained. The zero drift and hysteresis effects are minimal and, if necessary, can be corrected during the experiment performance.

The system will be calibrated and zero balanced before launch. A simple in-flight calibration technique involving static loading will provide data on the ground to permit compensations for any calibration or zero shift occurring before the experiment performance. Thus, no physical adjustment of the controls for the FMS will be required during flight.

## DATA SYSTEM

Phase A Study of the Crew Motion Disturbance Experiment, T013, indicated among other things that the umbilical cable used to acquire data from the Limb Motion Sensors was undesirable in a spaceborne system configuration because of:

- 1) Restriction of astronaut movement;
- 2) Undesired torques imparted to the vehicle by cable stress;
- 3) Probability of creating unsafe conditions to the astronaut during maneuvers.

For these reasons, it was proposed at the end of this study period that an astronaut data acquisition and local telemetry subsystem be used instead of the umbilical cable. At that time an in-house development of a data acquisition and telemetry subsystem for an air-bearing platform was underway, and it was proposed to investigate the modification required to this subsystem to make it compatible with the T013 requirements.

Thus, a study of the modifications required to the original data subsystem, an updated subsystem design, and a demonstration of a laboratory model were carried out. This study included the design of a data multiplexing subsystem that combines data from the three main sensor subsystems (LIMS, DARS, and FMS) into a single data channel for the purpose of achieving simplicity in data recording, transmission, and final reduction by ground stations.

### System Design

All data obtained in the simulation studies were acquired in a parallel mode and transmitted directly to the computer for processing and control. In considering the use of the same methods in the spaceborne version of the system, it was obvious that a computer would not be available in the spacecraft for processing data in the same manner as for the ground simulation. Therefore, it is required that data be recorded in the spacecraft and telemetered to a ground station for subsequent reduction and analysis.

Because of the importance of the T013 data, a requirement existed that the data be made available to the experimenter as soon as possible after the performance of the experiment. This, in turn, established a requirement that the recorded data be in format compatible with the AAP Data Management System and ground telemetry receiving stations. A study performed to examine parallel versus single-channel recording of all T013 data indicated that single-channel recording was more desirable from the standpoint of interface simplicity with the AAP Data Management System, and format generation and compatibility with ground receiving stations. Figures 59 and 60 are block diagrams of the two methods considered. Table 16 shows advantages and disadvantages of both methods.

The single-channel recording method was selected over the triple-channel recording method because it offered more advantages and fewer disadvantages than the latter method. Failure of the astronaut data system or the T013 data synthesizer is not expected to occur because of the simplicity of design and use of proven low-power micrologic elements. A reliability analysis, which will be conducted on these subsystems during the next phase of the study, will indicate the probability of successful operation during the 40- to 80-min experiment time. Redundancy in design will be included if found to be necessary. Figure 61 shows the current T013 data system design.

**TABLE 16.- COMPARISON OF TRIPLE- VERSUS SINGLE-CHANNEL RECORDING**

	Advantages	Disadvantages
Single-channel recording	<p>Simple AAP interface 1 tape channel required</p> <p>All T013 data can be transmitted to ground station during a single pass</p> <p>Only one data format compatible with ground receiving stations is used</p> <p>Only one programmer and sync word generator is used</p> <p>Minimum power, weight, volume, and cost</p>	<p>Requires a T013 data multiplexer</p> <p>Failure of T013 data multiplexer or astronaut data subsystem causes loss of all T013 data</p>
Triple-channel recording	<p>Main data multiplexer not required</p> <p>Retrieval of data from each sensor subsystem is independent</p>	<p>More complex AAP interface</p> <p>Three tape data channels required</p> <p>Method does not permit transmission of all T013 data to ground station during one orbit pass due to tape recorder playback limitations</p> <p>Separate programmers and sync word generators are required for each sensor subsystem</p> <p>Three different data formats required</p> <p>Requires more power, weight, and volume than single-channel recording</p> <p>This method is more expensive</p>

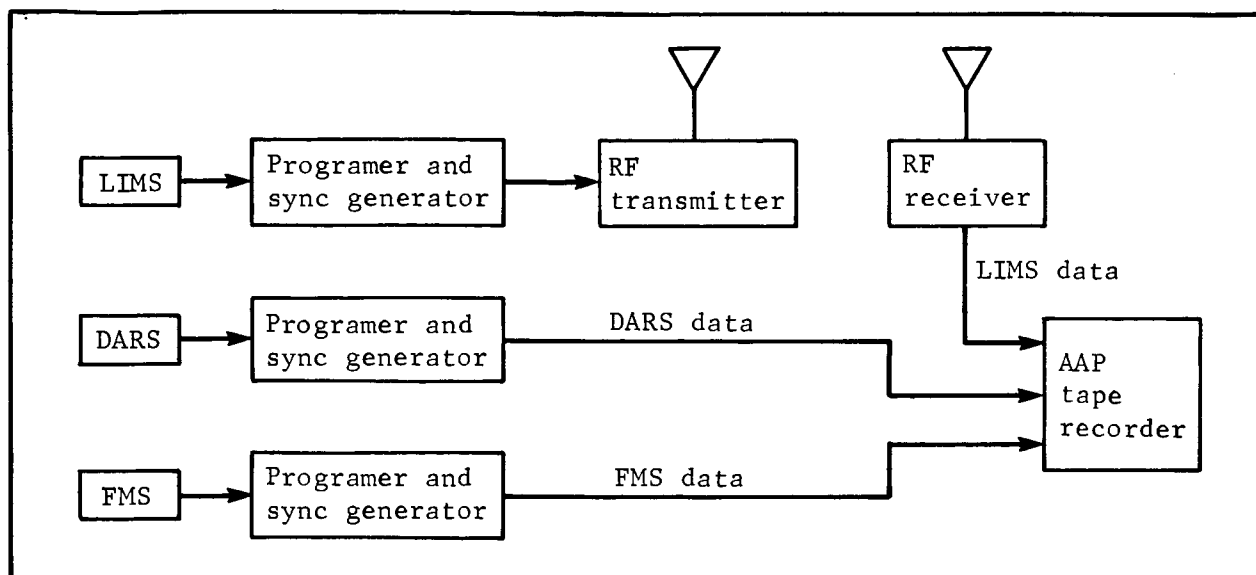


Figure 59.- Triple-Channel Recording

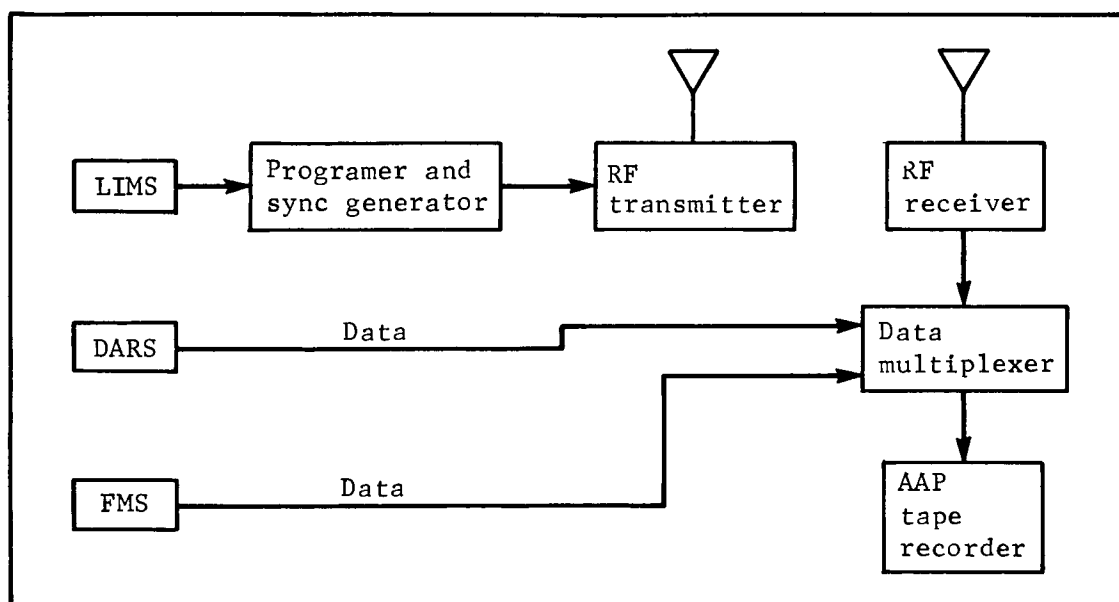


Figure 60.- Single-Channel Recording

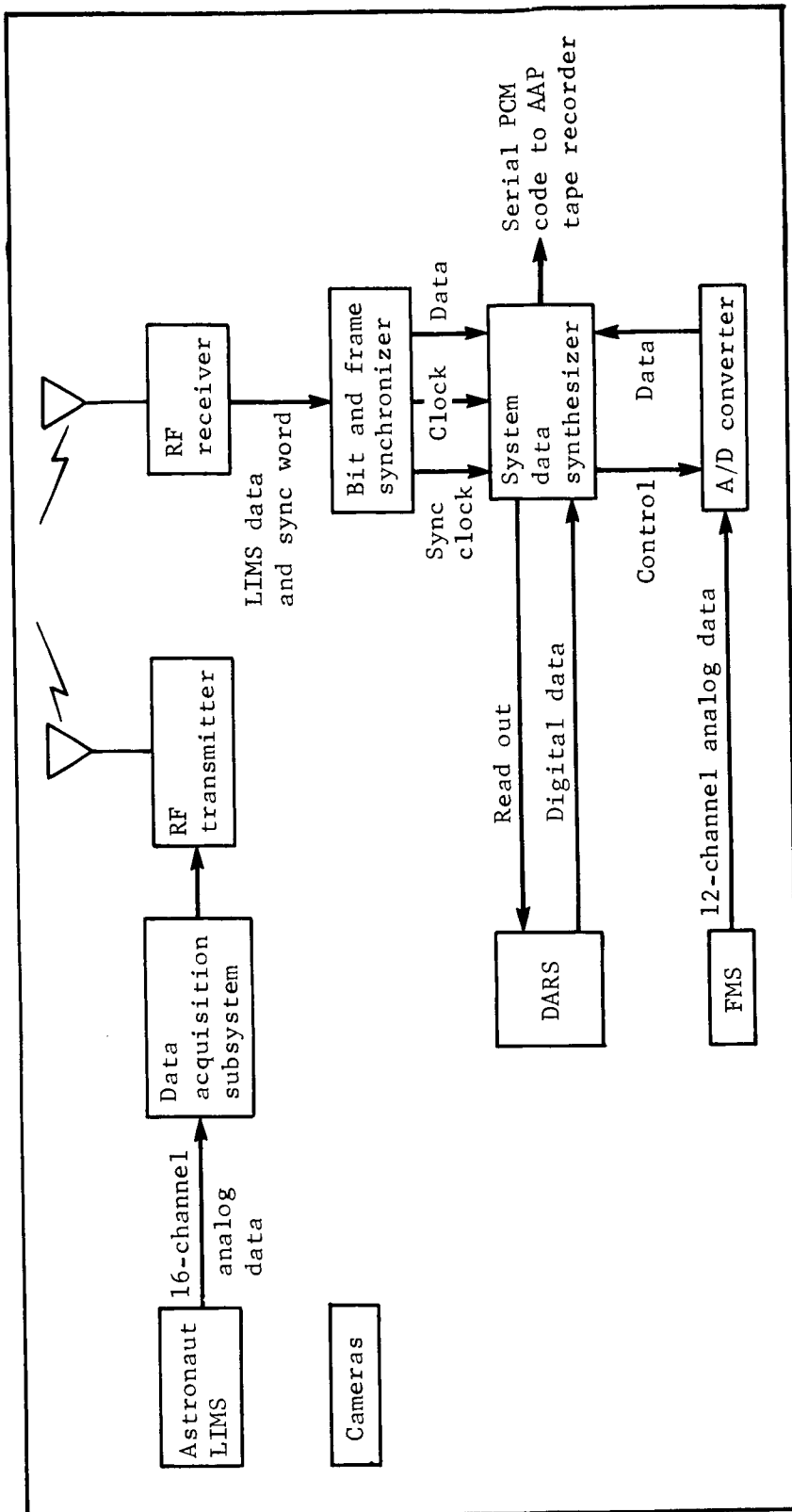


Figure 61.- Experiment Data System

Design requirements.- The design requirements established during this and the previous phase of the crew motion study are as follows:

- 1) The system shall be designed to incorporate simplicity and ease of operation;
- 2) Data accuracy of the system shall be 1% or better;
- 3) The system data format shall be compatible with ground receiving and data reduction stations;
- 4) The sampling rate shall be 20 samples per second for all data;
- 5) The frequency of the RF link shall be selected in a region that will ensure no interference to other AAP systems;
- 6) The transmitter power shall be kept to a minimum to preclude the need for an FCC license and to minimize interference;
- 7) The power consumption, weight, and volume shall be minimized;
- 8) The system shall be designed to ensure a high degree of reliability;
- 9) The system shall provide position and attitude of the astronaut while maneuvering within the experiment area;
- 10) Time information during the performance of the experiment shall be provided by the AAP Data Management System.

Fulfillment of the above-stated requirements have been accomplished as follows:

- 1) Requirement 1) has been met by selecting a single-channel method of data recording and the use of a single data format that is compatible with ground receiving stations;
- 2) Requirement 2) has been met by using proven circuit design principles and an 8-bit digital word to represent LIMS, DARS, and FMS data;

- 3) Requirement 3) has been fulfilled by surveying most commonly used data formats and selecting one that is compatible with ground stations and by complying with current IRIG telemetry standards;
- 4) For requirement 4), the sampling rate of 20 samples per second, established from studies of simulation data (Appendix E), has been set by adjusting the clock frequency of the astronaut data system to run at a rate of 5,760 kilobits per second (kbps). This was computed by multiplying the total number of bits in a major frame (288) by the desired sampling rate (20);
- 5) For requirement 5), the frequency selected for the RF link is 25 Mc. The use of this frequency does not conflict with frequencies presently being planned for use in AAP. These frequencies are in the very high frequency (vhf) and S-band spectrums. MSFC was contacted at the beginning of this phase to verify the fact that the selected frequency would not conflict with other AAP systems;
- 6) Requirement 6) has been met by keeping the radiated power of the transmitter at a level of 10 mW;
- 7) For requirement 7), low power integrated micrologic elements have been used wherever possible to minimize power consumption. Weight and volume have also been minimized by use of these elements;
- 8) Requirement 8), which calls for high reliability of the system has been partially fulfilled by selecting full military temperature range components (-55 to 125°C). These components have been flown in Lunar Orbiter and have undergone extensive evaluation and testing at Martin Marietta Corporation during the past year. A reliability analysis of the system, further testing and evaluation will be required before system reliability can be firmly established;
- 9) Requirement 9) will be fulfilled by the use of cameras. This effort will have to be carried into the next phase of the program to complete the evaluation of the camera system;
- 10) Requirement 10) has been coordinated with the Martin Marietta AAP Data Management Team, and it has been agreed that the DMS will furnish time information for the TO13 experiment.

Other requirements that may become apparent as the overall Apollo Applications Program progresses will have to be fulfilled at that time.



Data Format.- The design of any data handling system has a preliminary requirement of defining the characteristics of the data to be handled, and a second requirement for establishing a data format that accommodates all of the data in a prescribed sequence. Once the format has been established, the design of the data handling system can proceed in an orderly manner.

Because a data format had already been established for the air-bearing platform system, it became necessary only to examine the data that were to be handled for T013 and to modify the format and the data system accordingly. The original data that were to be handled by the system are shown in table 17.

TABLE 17.- ORIGINAL DATA REQUIREMENTS FOR T013

Synchronization	One 24-bit word
LIMS data	Sixteen 8-bit words
Position data	Eight 8-bit words
DARS data	Three 8-bit words
FMS data	Twelve 8-bit words

Position data were eliminated after cameras were selected as the method for obtaining astronaut position data instead of by using the ultrasonic-RF system. The format was then reduced to the form shown in figure 62.

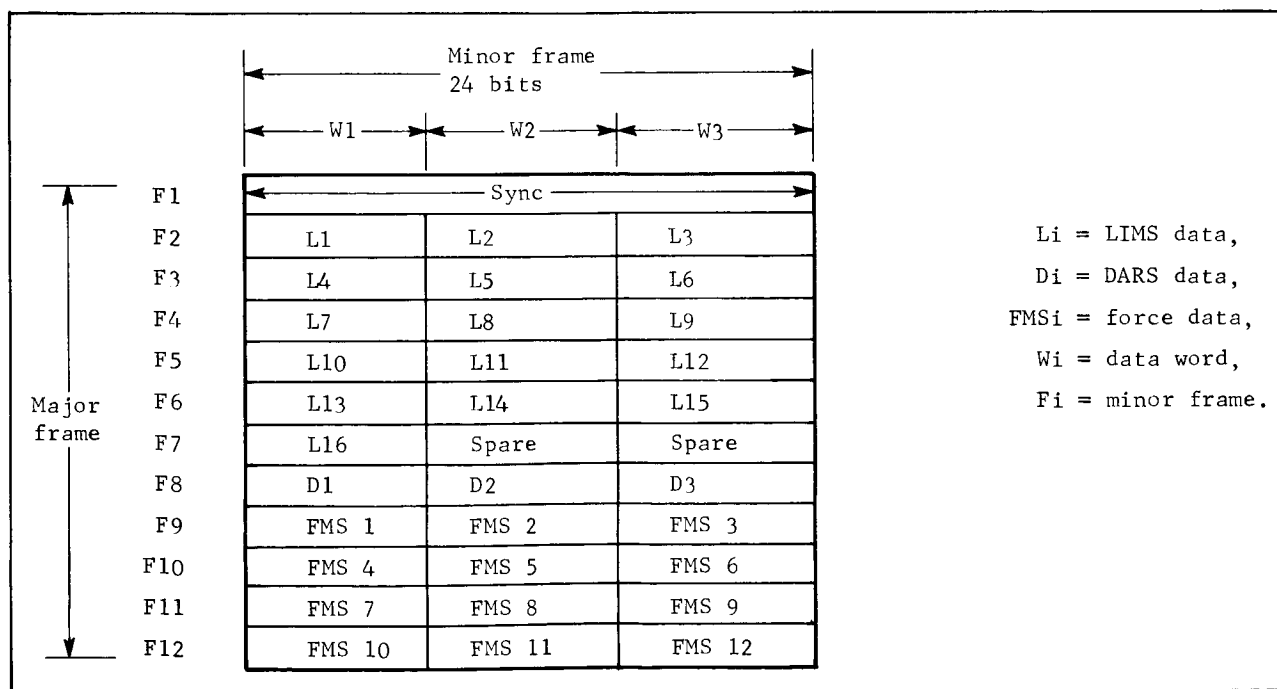


Figure 62.- T013 Experiment Data System Format

This format contains one 24-bit sync word, thirty-one 8-bit data words, and two spare 8-bit word slots for LIMS. The major frame consists of 12 minor frames or a total of 288 bits. The format is repeated in the system at a rate of 20/sec.

### T013 System Operation

The T013 system operates as follows: The astronaut before donning the LIMS suit applies power to the system allowing 30 min for the DARS to warmup. After calibration procedures are complete, the astronaut depresses the system RESET switches located on the receiver-synthesizer and the astronaut data subsystem. Immediately thereafter, he presses the START switch on the astronaut data subsystem. This starts the acquisition and transmission of data from the three sensor subsystems to the AAP tape recorder, which is started sometime before data acquisition starts. The sequence of events that occurs during acquisition and formatting of T013 data is:

- 1) The programmer in the Astronaut Data Subsystem generates a 24-bit major frame synchronization word;
- 2) The programmer generates control signals used to sample and convert sixteen LIMS analog voltages into sixteen 8-bit binary words, which represent LIMS positions;
- 3) The sync word and data are transmitted by the frequency shift keyed (FSK) transmitter located in the astronaut data subsystem;
- 4) The programmer continues to run and to generate synchronization bits that are used at the receiver end for clock frequency synchronization;
- 5) The FSK receiver receives the synchronization word and LIMS data in a PCM NRZ-C form. The information is applied to a phase locked loop where the clock frequency is reestablished;
- 6) The sync word is detected and the data synthesizer programmer is started;
- 7) The programmer then performs the following functions,
  - a) It allows LIMS data to be transmitted to the AAP tape recorder,
  - b) It generates a group of 25 clock pulses that are transmitted to DARS for controlling and shifting its data out,

- c) It receives DARS data and formats it for transmission to the tape recorder immediately following LIMS data,
  - d) It initiates control signals used to operate the FMS A/D converter, and to convert twelve FMS analog channels into twelve 8-bit digital words. These are also formatted with LIMS and DARS data. This completes one major data frame;
- 7) The sync word is checked at the beginning of the second frame to verify synchronization;
  - 8) The sync word is formatted into the main data channel and sent to the tape recorder. Thereafter, the steps outlined above are repeated throughout the performance of the T013 experiment.

In Step 7), if the system loses synchronization it goes into a search mode to reestablish synchronization. If at anytime the astronaut suspects or observes that data are not being transmitted to the AAP tape recorder, he should reset and restart the system.

### Subsystem Description

The subsystems described in this subsection are the astronaut data acquisition; the RF transmitter and receiver; and the system data synthesizer.

Astronaut data acquisition subsystem.- The main functions of the astronaut DAS are to generate a synchronization word; to sample and convert into digital form 16 LIMS analog voltages; and to format these data for transmission to the receiver and system data synthesizer. Figure 63 is a block diagram of the DAS. A brief description of the operation of this part of the T013 data system was given in the previous subsection, System Operation. A more detailed discussion of each of the units will be presented in the following paragraphs. Reference will be made to the block diagrams and to the detailed design drawing included with this report.

Clock pulse generator.- The clock pulse generator (see schematic drawing No. SRD 7276130000 in Appendix H) consists of an astable and a monostable element. The astable element generates a 50-50 duty cycle square wave at a frequency of 5.76 kc/sec.

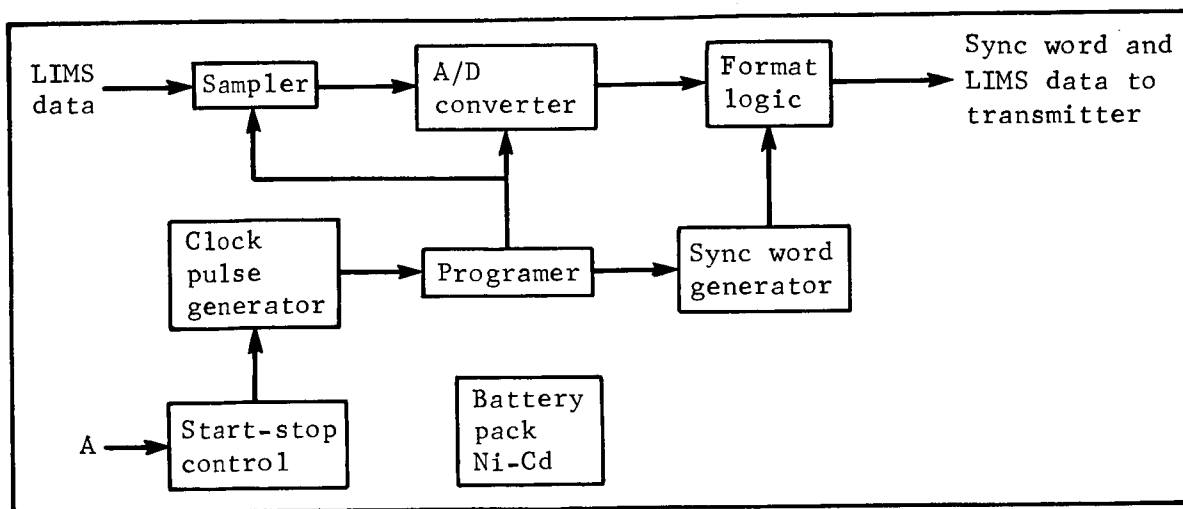


Figure 63.- LIMS Data Acquisition Subsystem

This signal is used to trigger the monostable element after the system is started. The monostable element generates a negative 1  $\mu$ sec clock-pulse, which is applied to an inverter-driver. The positive clock pulse is used to operate the programmer and other logic in the subsystem.

An LPDT  $\mu$ L 9040 bistable element is used to control the gating ON and OFF of the clock pulses to the DAS.

A/D clock pulse generator.- This generator is essentially gating logic that is operated only during the time that conversion of the LIMS data takes place. A total of 144 clock pulses are gated during the A/D conversion period.

Programmer.- The function of the programmer is to generate all of the main control signals required to generate the sync word, and to execute the A/D conversion and formatting functions. The programmer consists of three ring counters designated as the BIT COUNTER, WORD COUNTER, and FRAME COUNTER. The counters consist of 8, 3, and 12 bistable elements, respectively. With this arrangement, the main data format can be generated to accommodate the functions required in the T013 Data System. Each of the LPDT micrologic counter stages has at its output a high-power DTL element to accommodate various loading requirements on each stage. The logic equations are implemented using the outputs

from these stages. The schematic shows the details of all interconnections. Figure 64 shows typical signals from the word counter and one stage of the frame counter. Figure 65 shows the clock pulse and dc level control used in the subsystem.

Synchronization word.-- The synchronization word is used at the receiver end to synchronize the system data synthesizer. The code that has been selected for the sync word is 24 bits long and was selected from a table of synchronization codes prepared by Goddard Space Flight Center. The sync word is generated by the programmer unit during minor frame 1 of the format. The word is composed by logically ORING outputs from the bit counter, which correspond to the desired code. This code is formatted into the main output line at the beginning of every major frame (fig. 66).

A/D converter.-- The A/C converter is used to sample and convert the LIMS analog voltages into digital form during minor frames 2 thru 7. This converter is of the successive approximation type and is designed using Siliconix MOS FET multiplexing gates and gate drivers, and Fairchild micrologic elements. The Siliconix elements are approximately the same size as a Fairchild flatpack and each gate package accommodates 5 analog channels.

Each input to the multiplexing gate has an input filter network to filter noise and provide a smooth average dc value to the gate during the encoding process.

Four multiplexing units are required to accommodate the 16 LIMS channels. The output from these units is combined in a logical OR configuration and fed to a buffer amplifier at the proper time. The output of the buffer is fed to a  $\mu$ A 710 Comparator where the signal is compared to the output of the ladder network. The logical output of the comparator is based on the following criteria:

- 1) If the input sampled voltage is less than the ladder output voltage, the comparator provides a high output level signal. If the opposite is true, a low level output signal is provided by the computer. These signals from the comparator are strobed at clock-pulse-time and the strobed output is used to control the state of the data register during each successive comparison;

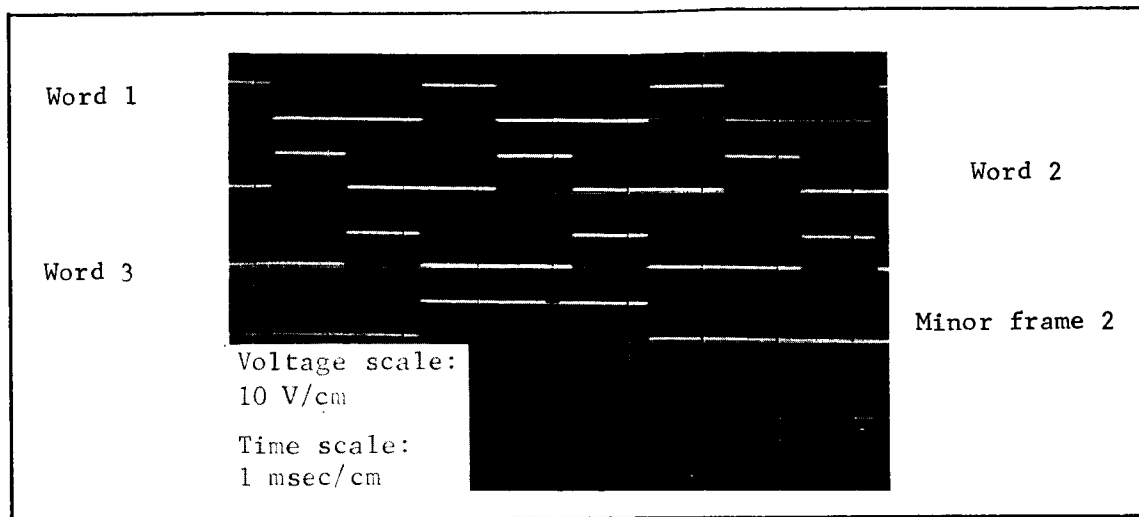


Figure 64.- Programmer Signals

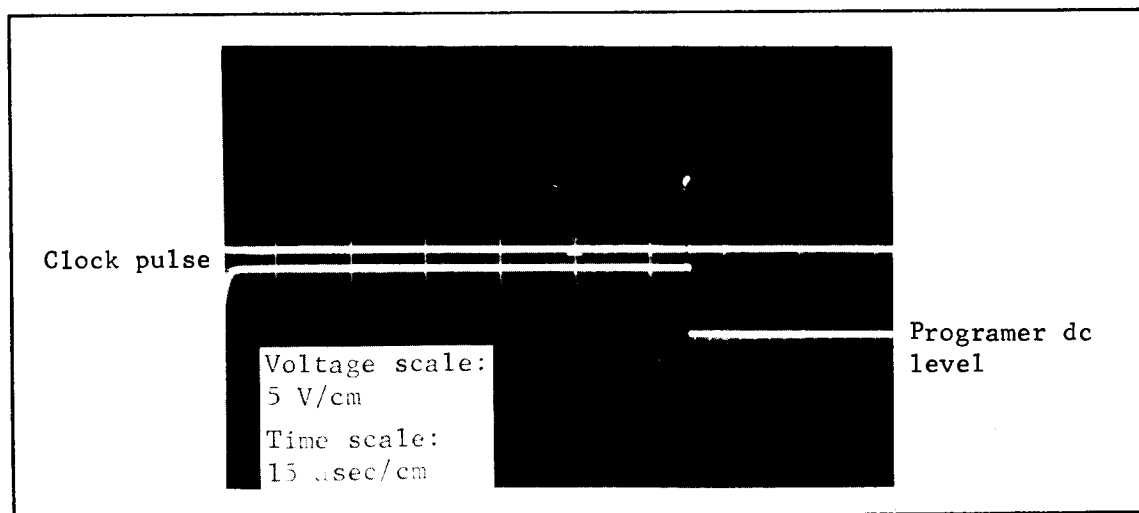


Figure 65.- DC Level and Clock Pulse Control

- 2) The data register output is used to switch in the resistors in the ladder network to either the reference dc voltage or ground. The resulting voltage output of the ladder network always corresponds to the binary number in the register at the end of strobe-time. The data register is always reset after the 8-bit conversion is completed to start the next word conversion in synchronization.

Figure 67 shows waveforms of the output data line, the ladder network, and the sampled simulated LIMS voltage. Bit-time period number 1 is also shown to obtain timing correlation. It may be seen that the final conversion value of the ladder network is equal to the sampled quantity. The output digital code appearing on the top line can be decoded to determine the sampled analog voltage. The ground station computer system will perform the decoding and printout of information during the data reduction phase of the T013 experiment.

Power supply.- The power for the data acquisition subsystem and the transmitter will be supplied by **nickel-cadmium batteries**. These batteries will also supply the reference voltage for the A/D converter and the LIMS sensor potentiometers. Figure 68 shows the results of a tradeoff study conducted to determine what type batteries provide the highest energy to weight ratio. A study will be performed during the next phase to establish an optimum package configuration.

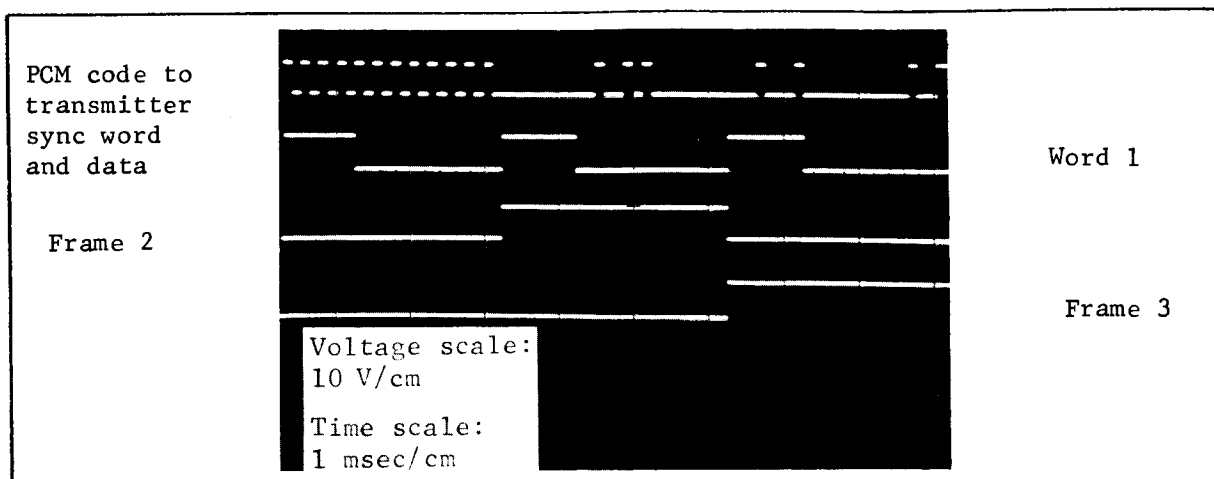


Figure 66.- Programmer Signals

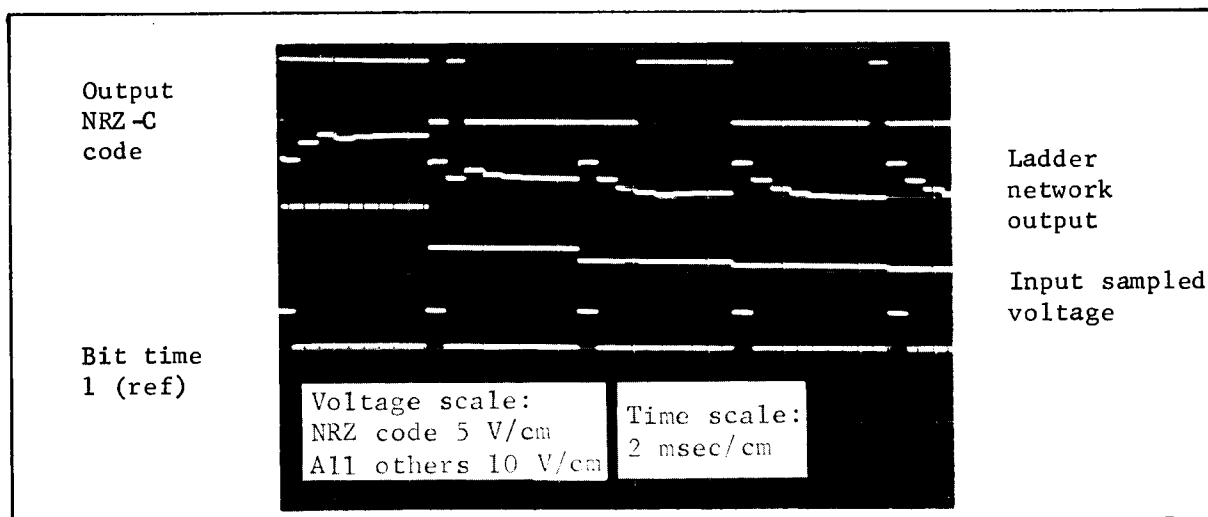


Figure 67.- A/D Converter Waveforms



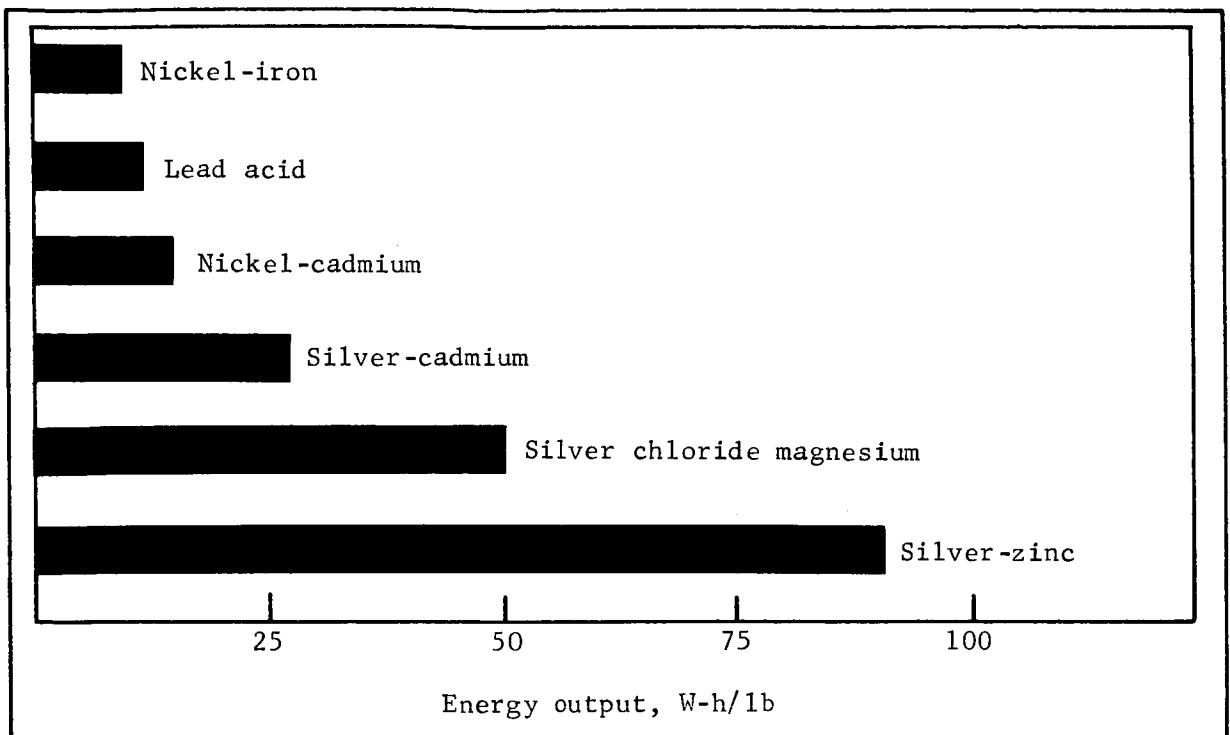


Figure 68.- Energy Output Comparison of Battery Systems

#### RF Link

The RF link consists of the transmitter mounted on the astronaut data package, and the receiver, which is mounted at a remote location in the Orbital Workshop area. Preliminary design requirements for this link were discussed previously. The transmitter and receiver designs are discussed below.

RF transmitter.- The transmitter is of the frequency shift keyed (FSK) type, and operates at two crystal controlled frequencies of 25.925 MHz and 26.075 MHz. The input PCM code is used to key the two crystals. The higher frequency crystal is turned ON by the ONES contained in the code, and the lower frequency crystal is turned ON by the ZEROS contained in the same pulse train. The two frequencies are alternately fed to an RF amplifier and from there to the antenna.

This type of transmitter design was selected because of its simplicity and because it provides a means of redundancy in recovering the data from either frequency channel. Figure 69 shows the block diagram of the transmitter. The circuit details are shown in schematic drawing No. SRD 72613000 (Appendix H).

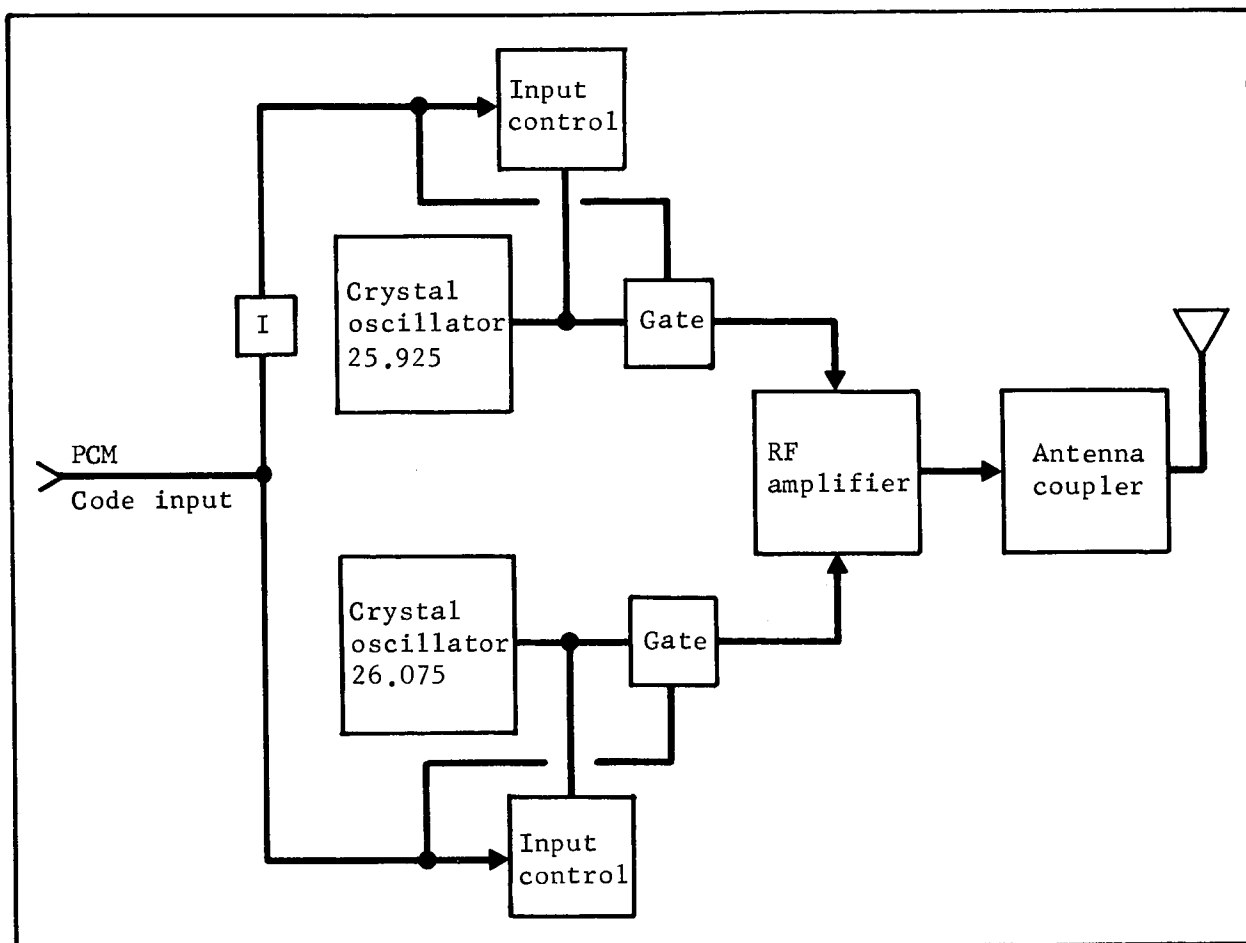


Figure 69.- RF Transmitter

### Transmit antenna.-

Electrical characteristics: Two configurations exist for the transmit antenna located on the astronaut -- the loop antenna or the dipole antenna. The loop would be located around the waist, either in the form of a belt that may be strapped on or in the form of a ribbon or wire that is permanently sewn into the suit the astronaut wears. The dipole would consist of a conductive ribbon sewn into the suit and probably running from the shoulder to the foot down one of the suit legs. The proposed configurations are shown in figure 70.

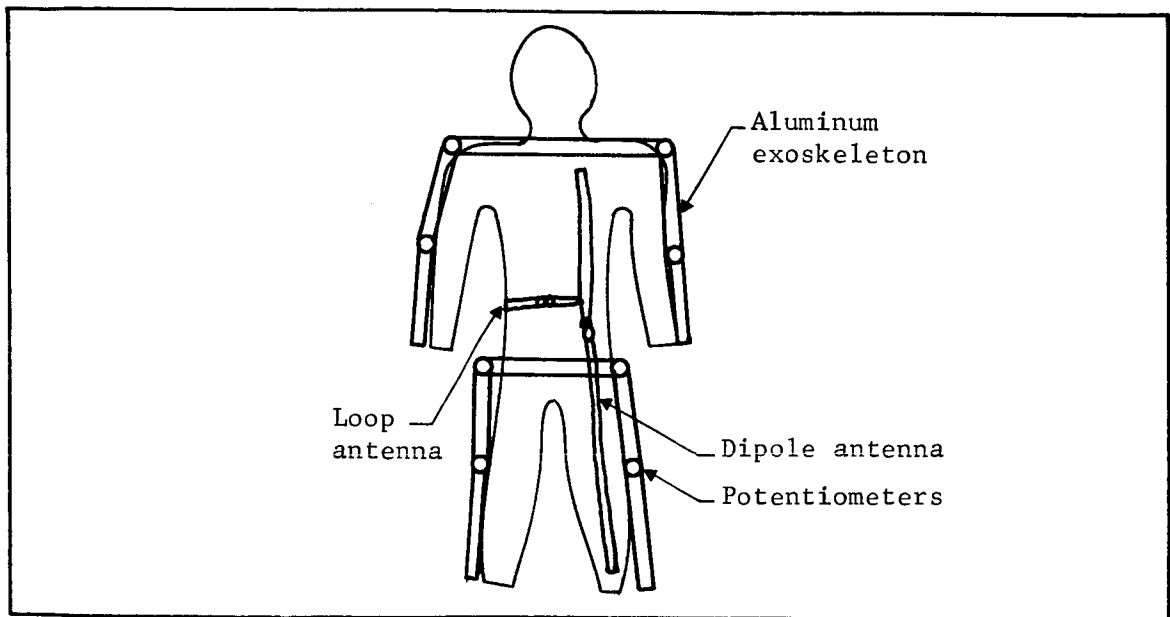


Figure 70.- Possible Antenna Configurations on Astronaut

These antenna types will be discussed together because most of the comments to follow apply to both types. For the sake of discussion, the circumference of the loop will be assumed to be 32 in. The length of the dipole will be taken as 4 ft.

The frequency of operation of the transmitter is given as  $26 \pm 0.075$  MHz. At this frequency the wavelength is  $\lambda = 454$  in. = 37.8 ft, hence both antenna types are electrically small. The electrical length of the dipole is found to be  $L = 0.106$  wavelength, while the loop circumference is  $C = 0.0705$  wavelength. Both antennas will have a low value of radiation resistance, a large reactive impedance component, and low efficiency.

We shall now estimate these values considering first the dipole and then the loop. The dipole radiation resistance may be estimated using the expression

$$R_r = 80 \pi^2 \left( \frac{\ell}{\lambda} \right)^2 \quad (14)$$

where  $\ell$  is the half length of the dipole ( $\ell = L/2 = 0.053\lambda$ ). For the 4-ft dipole, equation (14) gives  $R_r = 2.13$  ohms. The short dipole has a capacitive reactance whose magnitude is given by

$$X_d = -120 \left[ \ell \ln \frac{\ell}{a} - 1 \right] \cot k\ell \quad (15)$$

where  $a$  is the radius of the dipole and  $\ell$  is the same as above. If the dipole consists of a flat conductive ribbon, an equivalent radius may be determined. It will be assumed that the dipole will consist of a ribbon 1.5 in. wide and 1/16 in. thick. This ribbon has an equivalent radius equal to 0.390 in.  $X_d$  is then found to be 1078 ohms. It is necessary to match out this reactance using a coil whose loss resistance will probably exceed the radiation resistance of the dipole. Hence, we may expect an efficiency of only a few percent for the dipole.

Turning now to the loop, the radiation resistance is given by

$$R_r = 31\,171 \left( \frac{nA}{\lambda^2} \right)^2 \quad (16)$$

where  $n$  is the number of turns and  $A$  is the area enclosed by the loop. Using equation (16) gives a radiation resistance of  $R_r = 0.0049$  ohms for the 32-in. loop with one turn. If the number of turns is increased to 20, then  $R_r = 1.96$  ohms, equivalent to the dipole radiation resistance. The reactive component of the loop impedance is inductive. The loop may, therefore, be matched with a capacitor that is essentially lossless when compared to the coil necessary to match the dipole. A resonant condition for the loop may not be possible using a capacitor of reasonable size. However, it is believed that this will not hinder operation of the loop.

Both the dipole and the loop are linearly polarized. When the axis of the dipole is coincident with the loop axes, the radiation patterns for a small (electrical) dipole and a small loop are identical except that the polarizations are everywhere perpendicular. The form of the radiation pattern is a figure eight of revolution with nulls occurring along the axes of the antennas as shown in figure 71. Maximum gain is obtained perpendicular to the axes of the antennas.

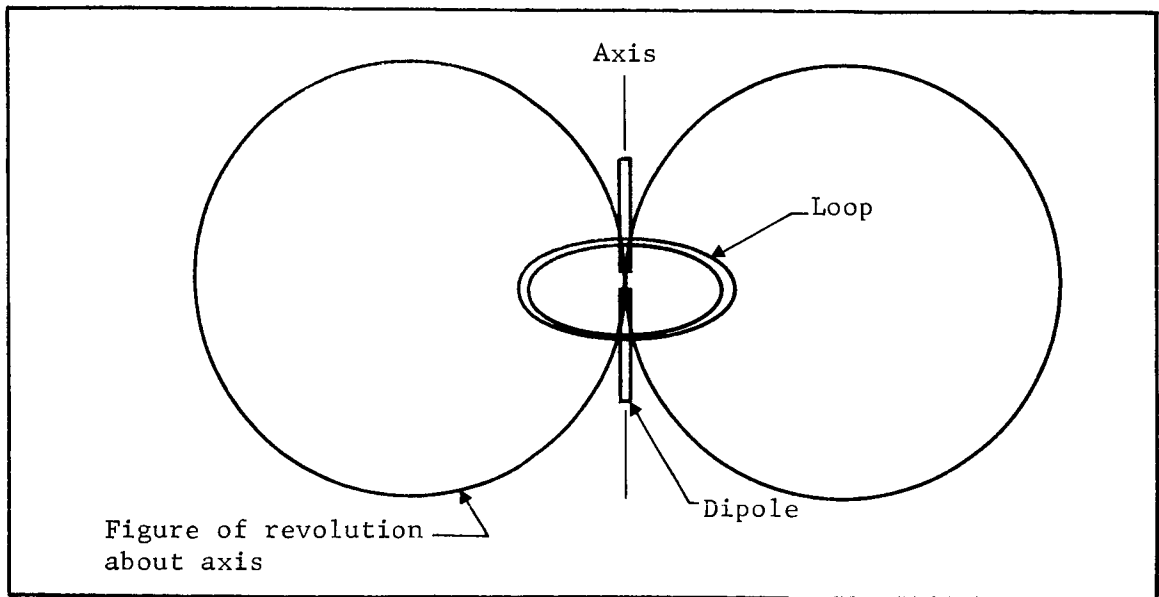


Figure 71.- Dipole and Loop Radiation Pattern for Indicated Orientations

Physical configuration: Both the dipole and loop antennas can be sewn into the suit the astronaut will wear. This approach seems most reasonable from the standpoint of minimizing hinderance to the astronaut when wearing the antenna. The dipole was assumed to be 4 ft long. However, this length would require that it extend from the shoulder to the foot down one of the suit legs. Movement of the astronaut will cause pattern and impedance variations that could be very detrimental to the dipole performance.

The loop antenna can be sewn into the suit in the region of the waist. Pattern behavior for the loop will be much less affected by general astronaut movement. A loop consisting of a few turns is suggested. If the loop is enclosed in an electrostatic shield all parts of the loop will have the same capacitance

to ground, regardless of the loop orientation or of the proximity of various objects. This characteristic is important because the transmit antenna must operate in proximity to the aluminum exoskeleton of the suit. A test was made using a shielded loop 7 in. in diameter in the screen room and there was adequate signal even when the loop was next to the conducting wall. The shielding on the loop could be a braided conductor so that maximum flexibility is maintained. A coaxial connector could be provided at the antenna input so that the transmitter could be attached or detached as desired. It is felt that the loop would provide more reliable performance than the dipole and is, therefore, the more desirable transmit antenna configuration.

Telemetry receiver.- The requirements for an FSK receiver operating in a high-density electronic environment dictate that the receiver have some special features. The first receiver problem encountered is that of unwanted cross-modulation products that may be formed in the front end by mixing with strong undesired signals. These spurious signals could originate either as harmonics of switching devices, such as timers, computers, etc., or directly from adjacent RF systems. To minimize problems, the receiver designed at Martin Marietta Corporation contains a prefilter that passes only the desired input band. The attenuation rapidly falls to -35 dB or greater outside the desired input band and before an active device. This prevents strong adjacent band signals from producing spurs that could affect data reception.

If undesired signals, by some chance, enter into the receiver, higher distortion products will be minimized by the FET RF amplifier and mixer incorporated in the present design. Image problems are reduced by a narrow band input filter. The filter in addition allows a conversion to a lower intermediate frequency (IF) with subsequent higher gain per stage. The receiver design includes an input limiter that begins action at about 0.1 V and limits input signals to less than 0.8 V at the input of the first active device. This is necessary to prevent damage to the front end of the receiver. Normal limiting takes place within the IF stages when the signals reach about 500  $\mu$ V. This is not critical, however, because of the design of the FSK demodulator.

The receiver output is available on two output lines. One output line contains the PCM code corresponding to the true data, and the other contains its complement. Thus, if either data line is lost, the information can still be recovered from the other. Figure 72 is a block diagram of the receiver. The schematic is shown in drawing No. SRD 727613800 (Appendix H).

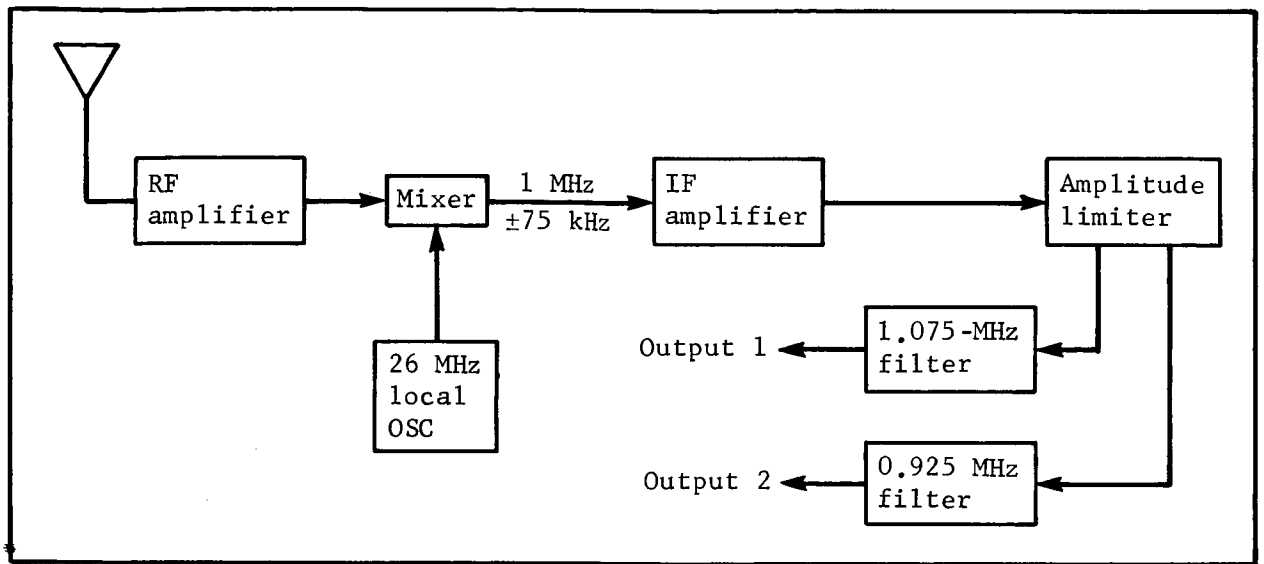


Figure 72.- RF Receiver

Receive antenna.- The transmit antenna described previously is a linearly polarized element. If the receive antenna were also a linearly polarized element, a loss of signal would result when the two linear antennas were cross polarized (perpendicular to one another). To ensure a received signal regardless of the relative orientation of the transmit and receive antennas, it is suggested that the receive antenna be circularly polarized. If we momentarily neglect the effect of the radiation pattern, it may be seen that this scheme will provide a constant signal level that will be 3 dB below the maximum possible level obtained if the receive antenna were linearly polarized and oriented parallel to the transmit antenna.

The radiation pattern of the transmit antenna has been described as a figure eight of revolution possessing two diametrically opposed nulls. If the loop is employed, these nulls occur in the directions of the head and feet. For the dipole, the nulls would also occur in these directions. It is seen that the data signal could be lost if either of these nulls were turned toward the receive antenna. To avoid this loss, it is proposed that two receive antennas be employed. Complete coverage will be obtained if these two antennas were mounted at right angles to each other and at 30° with respect to the plane wall of the experiment area. The proposed arrangement is shown in figure 73.

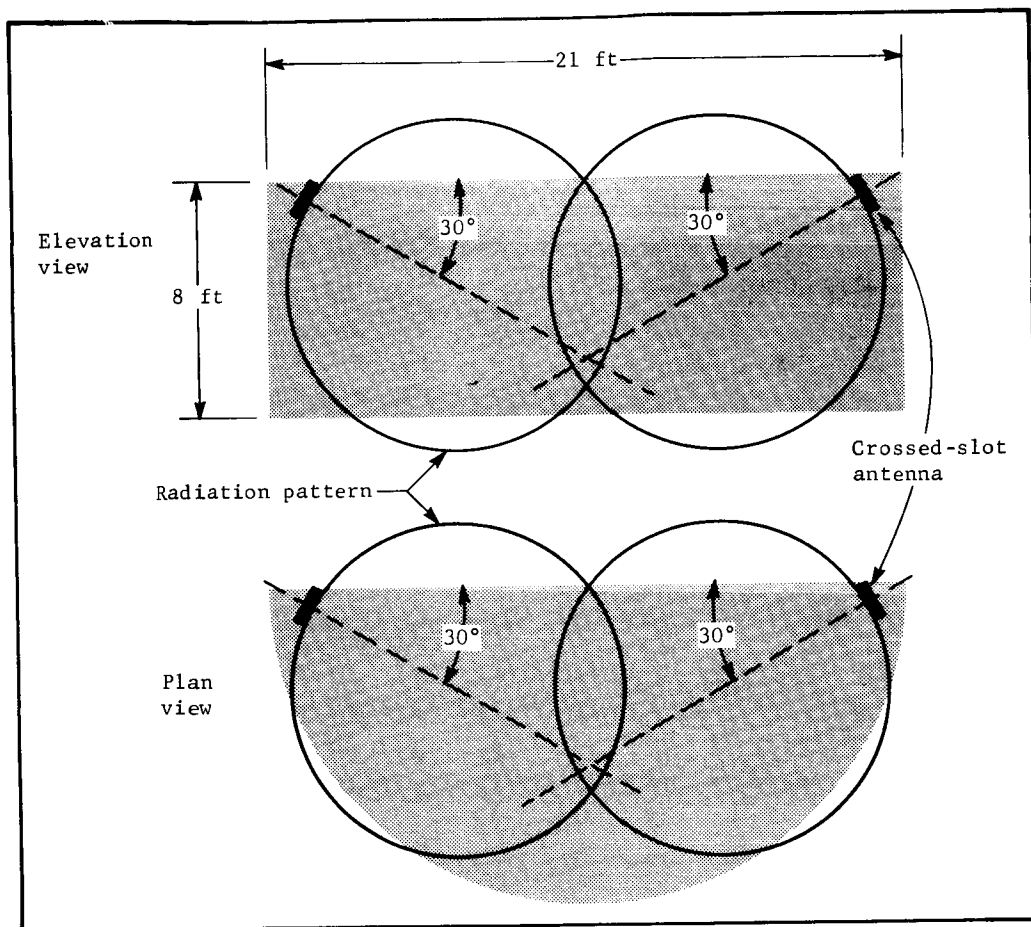


Figure 73.- Receive Antenna Coverage in Experiment Area

It is seen that if a null of the transmit antenna is pointed toward one of the receive antennas then a pattern maximum is pointed toward the second receive antenna. Hence, total coverage is assured. The receive antennas should also be mounted at a  $30^\circ$  angle with respect to the ceiling (or floor) so the pattern maximum is pointed toward the center of the experiment area.

A candidate for the receive antenna is the cavity-backed crossed-slot antenna (fig. 74). A crossed dipole (turnstile) may also be used; however, this element would protrude into the experiment area slightly. To provide protection both for the astronaut and the antenna, a small hemispherical radome should be placed over the antenna. These antennas provide circular polarization and a radiation pattern with a broad main beam (3 dB beamwidth,  $90^\circ$ ). The two crossed elements are fed through a  $90^\circ$  hybrid so that the phase of the elements differs by  $90^\circ$  to provide the required polarization. At 26 MHz, the hybrid may be a lumped element circuit (such as those available from Anzac Electronics, Inc.). It is



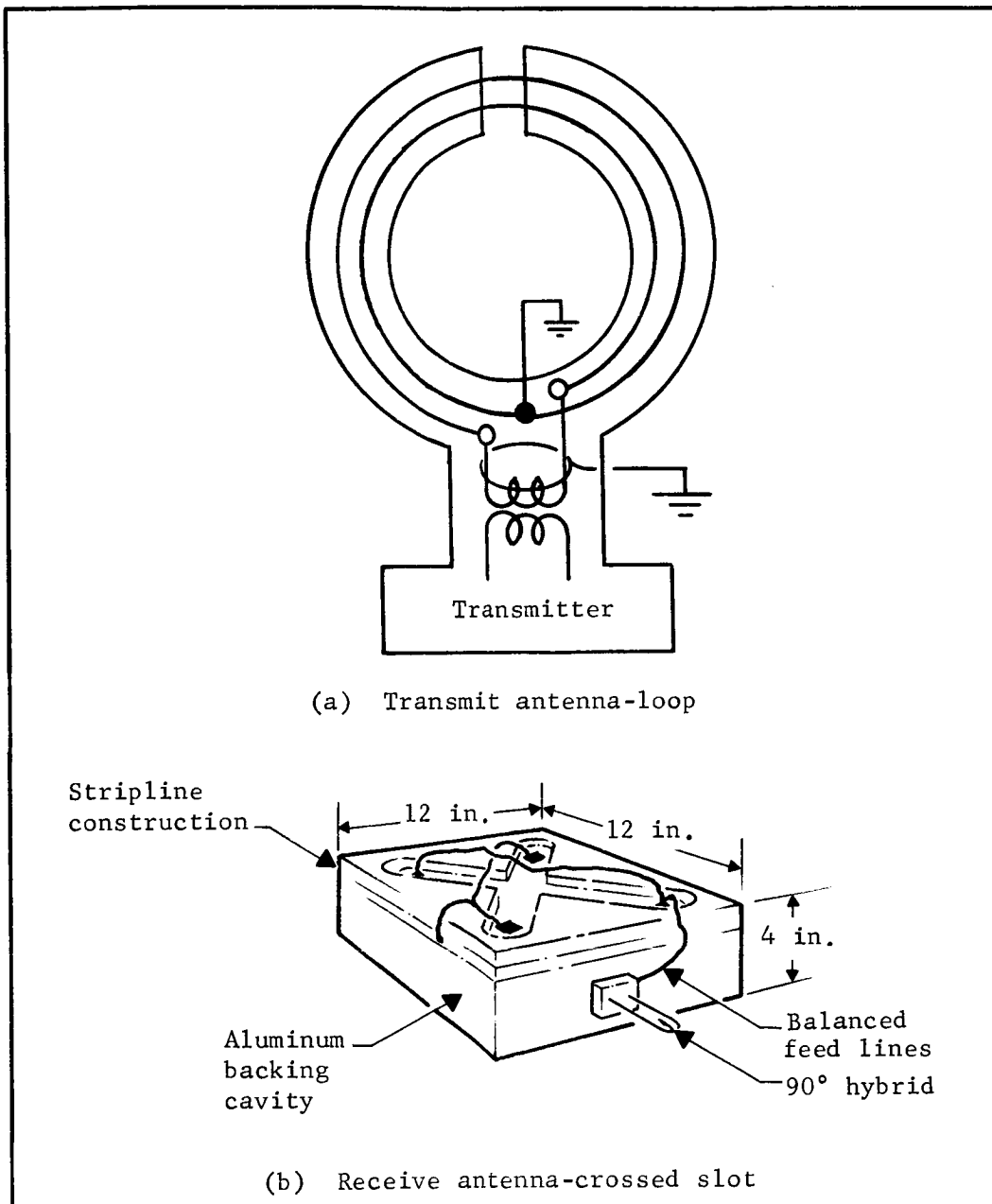


Figure 74.- Antenna Configurations

assumed that the receive antenna configuration should be as small as possible. Therefore, an element length of 12 in. is proposed. To improve the antenna efficiency somewhat, loading techniques could be employed. The effectiveness of end loading of the slot or dipole and dielectric loading of the backing cavity will be evaluated in the laboratory during the next phase of this effort.

## System Data Synthesizer

The system data synthesizer consists of the bit and frame synchronizers, the sync counter, a programmer, an A/D converter, data formatter, and its power supply. A block diagram of this subsystem is shown in figure 75. The details are shown in the enclosed schematic.

Bit synchronizer.- The master clock for the data system is generated in the astronaut data subsystem (transmitter side). In the bit synchronizer, the clock pulse is recovered from the data and is kept in synchronization with the master clock in the transmitter by a phase-locked voltage-controlled oscillator (VCO). The bit synchronizer block diagram is shown in figure 76.

The recovered data from the receiver is applied to a phase comparator along with the output from the VCO TOGGLE FLIP-FLOP. If the TOGGLE FLIP-FLOP frequency into the phase comparator increases with respect to the data frequency, a decrease in the pulse width output of the phase comparator results. The consequence of this decreased pulse width on the integrator output is a decrease in the average value of dc voltage available to the VCO. The VCO characteristics are such that an increase in control voltage increases the oscillator frequency, and a decrease in control voltage decreases the oscillator frequency. As a result of the decrease in voltage from the integrator, the oscillator frequency is pulled back into synchronization. Conversely, a decrease in the VCO frequency causes wider pulse to be generated in the phase comparator. The resultant output of the integrator is a higher average dc control voltage that causes the VCO to speed up and pull back into synchronization. The output of the VCO is also used to trigger a one-shot multivibrator to reduce the duty cycle of the clock pulse of a few microseconds in width. The narrow clock pulse thus generated operates at the same frequency as the master clock in the transmitter. Recovered receiver data is further modified by synchronizing it with the generated clock pulse to realign the edges of the clock pulse with the data bit edges.

The recovered clock pulse,  $C_p$  and edge synchronized data,  $D$  and  $\bar{D}$ , are available for system use at this point.

Frame sync detector.- The purpose of the sync detector is to detect the sync word from the incoming data stream and to provide a coincidence bit,  $C_o$ , whenever the data in a 24-bit shift

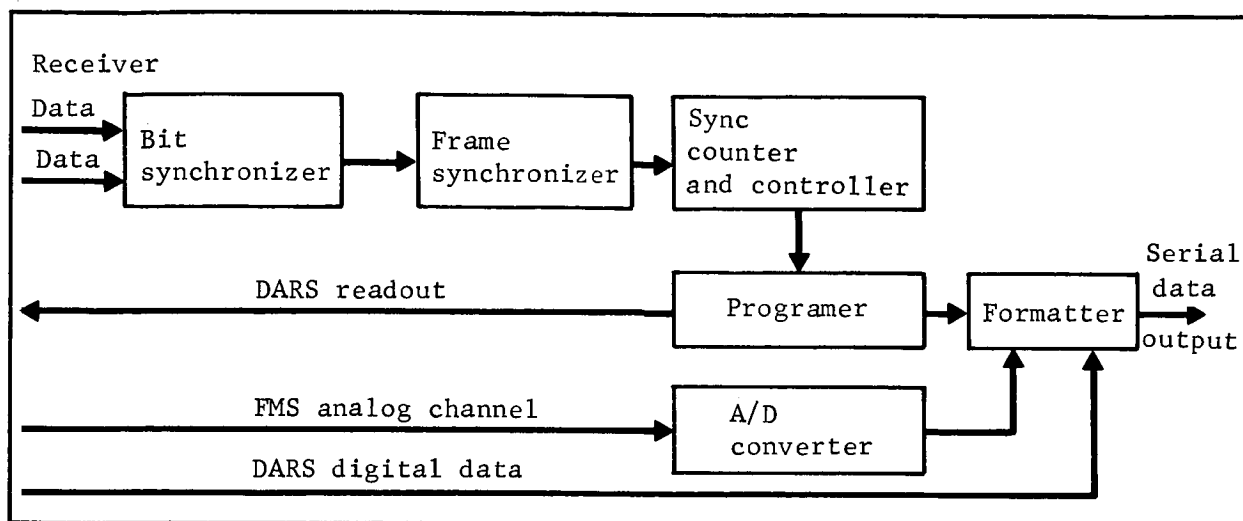


Figure 75.- System Data Synthesizer

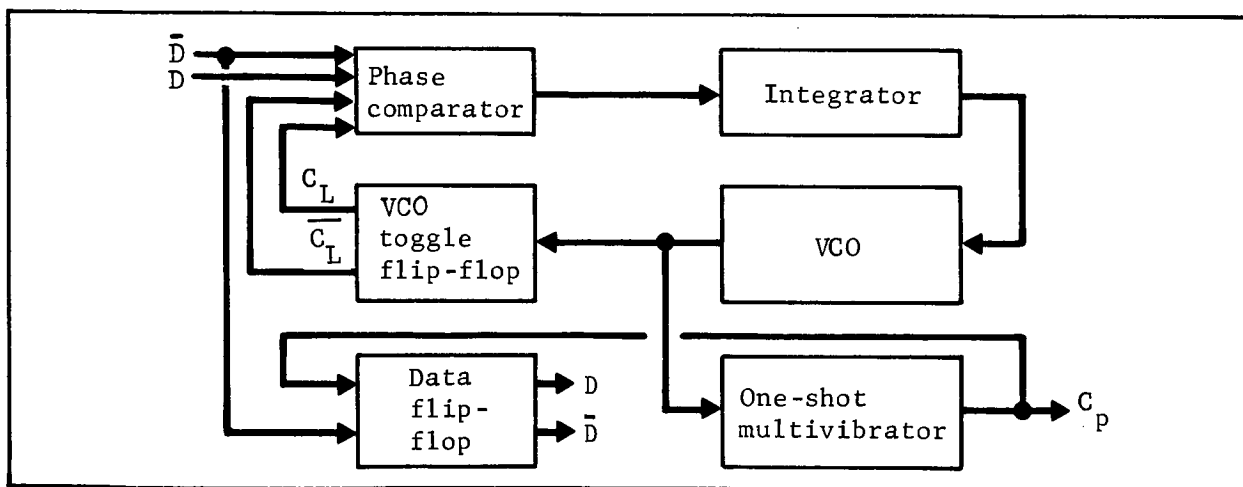


Figure 76.- Bit Synchronizer

register contains the sync word code. The detection of the sync word is accomplished by a differential comparator that is biased to  $V_R$  volts on one of the input terminals. The other terminal of the comparator is tied to the summation junction of a bank of 24 resistors, each of which is driven separately from each of the 24 shift register outputs. The resistors are properly terminated to the respective high side of the register stages,  $Q$  or  $\bar{Q}$ . When the sync word code is stored in the register, the summation junction voltage,  $V_S$ , will achieve the highest possible potential. Furthermore, if  $V_R$  is adjusted so  $V_S > V_R > V_S \left(1 - \frac{1}{N}\right)$ , where  $N$  = no. of bits in the sync word, the differential comparator will produce a high state uniquely at the accumulation of a sync code in the register. In the present system,  $V_S = 5$  V,  $n = 24$  bits, and  $5$  V  $> V_R > 4.8$  V. The latitude of adjustment on  $V_R$  is 0.2 V/bit. The hysteresis of a UA 710 differential comparator is 2 mV; therefore, the detection of a sync word can be assured down to the last bit with a comfortable margin. A photograph of a typical 24-bit sync word, the summation junction voltage waveform, and the subsequent  $C_0$  pulse are shown in figure 77.

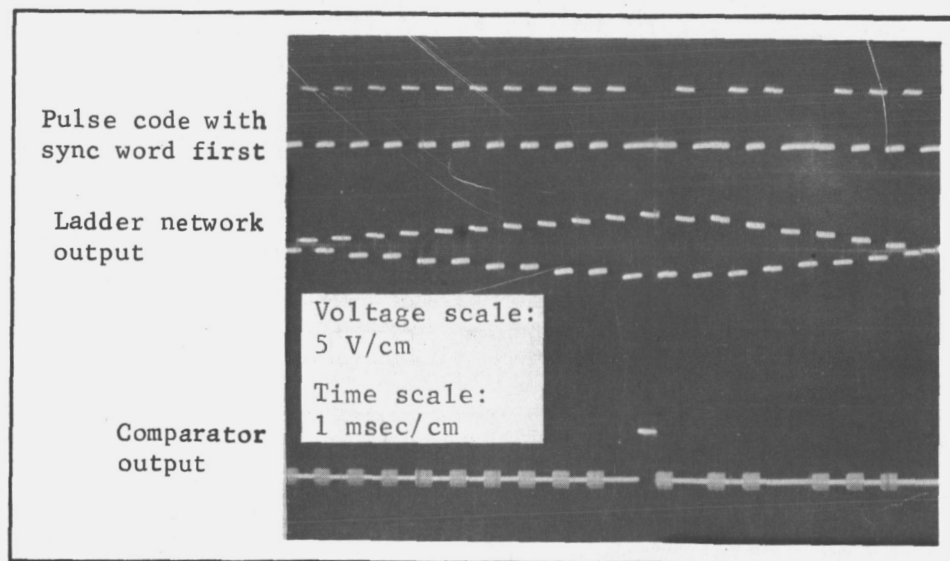


Figure 77.- Frame Synchronizer Signals

Figure 78 shows the sync word detector logic.

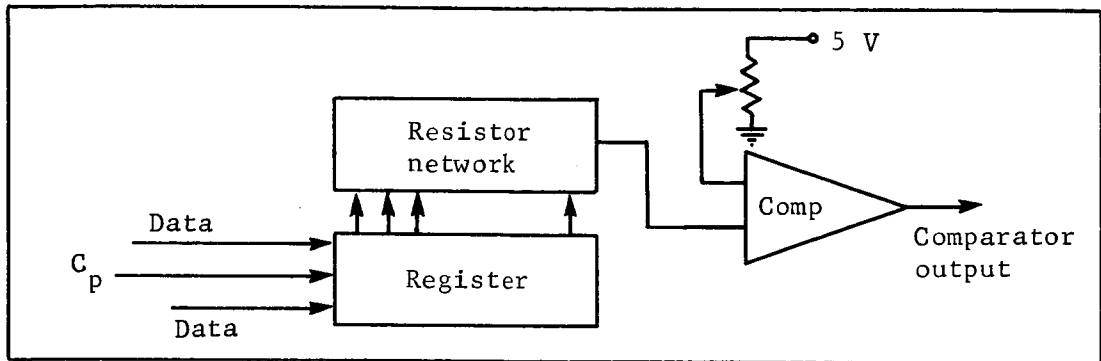


Figure 78.- Frame Sync Detector

The data,  $D$  and  $\bar{D}$ , stream that also contains the sync word is shifted into the 24-bit register and causes a 1-bit time delay. The  $C_o$  therefore appears 1 bit time after  $F_1$  at  $F_2$   $W_1$   $B_1$  and is available to synchronize the slaved receiver programmer at this time.

Sync counter and controller.- Before the data from the transmitter side,  $D$ , and data from the receiver side can be multiplexed into the major frame format in the receiver, assurance must be made that the receiver programmer is in sync with the master programmer in the transmitter. The sync counter and controller performs this function. Figure 79 is a block diagram of the sync counter and controller.

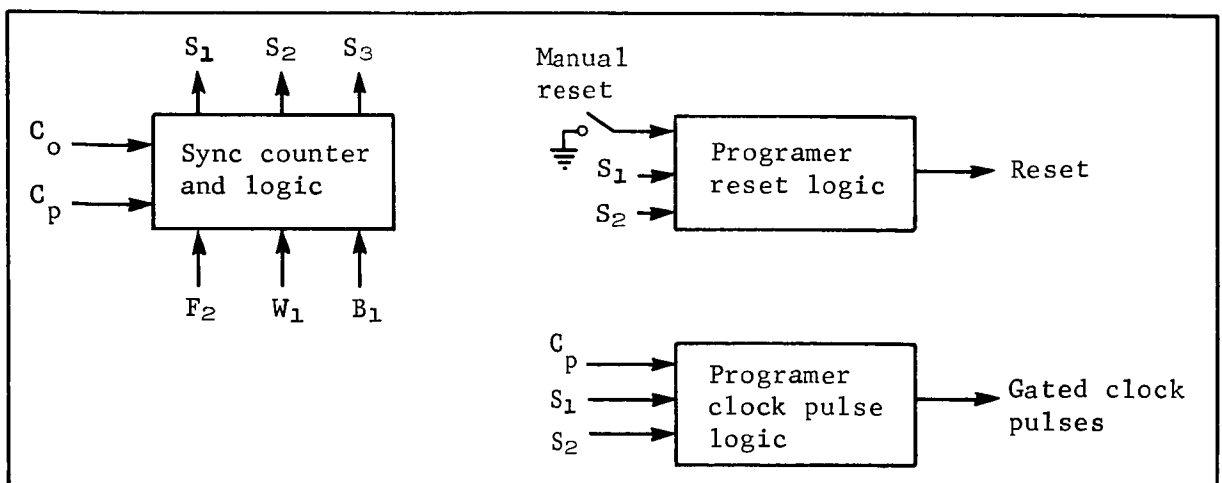


Figure 79.- Sync Counter and Controller

The sync counter's logic philosophy requires that three successive coincidences,  $C_o$ , occur before data can be finally formatted. Once the data are formatted, two successive misses will reset the sync counter and programmer and will cause it to begin another three count up-count sequence. Full synchronization is defined by the logic equation  $S_2 S_3 = 1$ . In operation, the sync counter logic opens a "window" during every  $F_2 W_1 B_1$  time. If the  $C_o$  pulse is not present during this "window" time, the sync counter counts back. If a  $C_o$  pulse is present, the sync counter will either advance a count or stay if it is already at  $S_1 S_2 S_3 = 1$ . The two controlling equations for the forward and back count logic are:

$$\left. \begin{aligned} \text{Forward count} &= \bar{S}_3 C_p C_o \bar{S}_1 \bar{S}_2 \bar{F}_2 \bar{W}_1 \bar{B}_1 + S_1 \bar{S}_2 F_1 W_1 B_1 + S_1 S_2 \bar{S}_3 F_2 W_1 B_1 \\ \text{Backward count} &= C_p \bar{C}_o S_1 F_2 W_1 B_1 \bar{S}_2 \bar{S}_3 + S_2 S_3 + S_2 \bar{S}_3 \end{aligned} \right\} \quad (17)$$

The logic output of the sync counter is used to gate the clock pulses and reset logic in the receiver side programmer and to control the final formatting of the composite data in the system data formatter.

Programmer.— This programmer format is identical to the programmer format in the transmitter with a few minor exceptions. One exception is the reset mode. Whereas in the transmitter programmer all stages except frame one and word one of the programmer are reset to zero; in the receiver programmer all stages but  $F_2$ ,  $W_1$ , and  $B_2$  are reset to zero. These three stages are set by the reset line  $R_p$ , and contain the initial state necessary in a circulating ring counter. Clock pulses  $C_g$ , are prevented from arriving at the programmer until the detection of a  $C_o$  can cause  $S_1$  to achieve a high state. The logic circuits of the  $C_g$  gate in the sync counter and controller then allow the clock pulses to proceed to the programmer. When  $S_1$  achieved the high state, the reset logic gate also removed the reset bias allowing all subsequent  $C_g$  pulses to advance the programmer.

Once the programmer is synchronized, the following functions occur:

- 1) LIMS data are transmitted to the AAP tape recorder;
- 2) DARS shift pulses are generated, and the received DARS data are formatted into the main data stream;

- 3) A/D conversion of the 12 FMS channels takes place, and the resulting digital data are sent to the tape recorder;
- 4) The next major frame is initiated and the sync word is formatted into the main pulse train;
- 5) The format repeats.

For further details, refer to schematic SRD 727613800 (Appendix H).

FMS A/D converter.— The function of this unit is to convert twelve channels of analog data from the force measurement subsystem into twelve 8-bit words. This unit is under the control of the programmer; its design and theory of operation are the same as that of the LIMS A/D converter discussed previously.

Data formatter.— The data formatter unit combines the synchronization word and the data from LIMS, DARS, and FMS into a single PCM pulse train with a 0- to 5-V swing. The schematic shows the logic for this unit.

Power supply.— The power supply requirements for the receiver and data synthesizer are approximately 200 mA at 5 Vdc, 140 mA at 12 Vdc, and 10 mA at -12 Vdc.

During this phase of the program, the use of a battery package similar to that used in the astronaut data acquisition subsystem was considered. The consensus is that batteries should only be used where necessary because the spacecraft can provide the necessary power. Therefore, a dc/dc converter-type of power supply will be used for the receiver and data synthesizer.

The power supply schematic is shown in drawing No. SRD 727613800 (Appendix H). The design of this power supply is standard and the detailed operation description will not be covered here. The only addition that has been made to the standard design is a voltage regulator circuit that uses a Fairchild UA709 to obtain the reference voltage required for the FMS A/D converter.

The characteristics of the data subsystems are summarized in table 18, and figure 80 shows the astronaut data subsystem that was breadboarded in the laboratory.

TABLE 18.- SUBSYSTEM CHARACTERISTICS

## DAS

Input analog channels . . . . .	16, 0 to 5 Vdc
Sampling rate . . . . .	20/sec
Sync word length, bits . . . . .	24
Data word length, bits . . . . .	8
Major frame length, bits . . . . .	288
Clock frequency, cps . . . . .	5760
Clock pulse width, $\mu$ sec . . . . .	1
Output data form . . . . .	NRZ-C
Output signal level, V . . . . .	0 to 5
Battery pack voltages, Vdc . . . . .	12, -12, 5
Power consumption, W . . . . .	4.4
Weight, lb . . . . .	3.0
Batteries . . . . .	8 oz
DAS cards . . . . .	16 oz
Pkg and misc . . . . .	24 oz
Volume (includes transmitter, cu in. . . . .	40 (5x4x2 in.)
Logic elements . . . . .	Low power micrologic

## Transmitter

Type . . . . .	Dual crystal FSK
Frequency, MHz . . . . .	25.925 and 26.075
Power required, mW . . . . .	90
RF power output, mW . . . . .	10
Weight, oz . . . . .	2
Volume, cu in. . . . .	2.0 (2x2x $\frac{1}{2}$ in.)
Antenna . . . . .	Loop

## Receiver

Type . . . . .	FSK
Sensitivity, $\mu$ V . . . . .	20
Selectivity . . . . .	40 dB at 300 kHz >60 dB above 1 Mc
Output . . . . .	Dual filter true and complement
Antennas . . . . .	Two slot, CP
Volume, cu in. . . . .	10 (5x2x1 in.)
Weight, oz . . . . .	8
Power required, W . . . . .	0.5

## System data synthesizer\*

Power required, W . . . . .	2
Volume, cu in. . . . .	40
Weight, lb . . . . .	3
Output . . . . .	Multiplexed NRZ-C data 0 to 5 Vdc

\*Includes bit and frame synchronization logic.



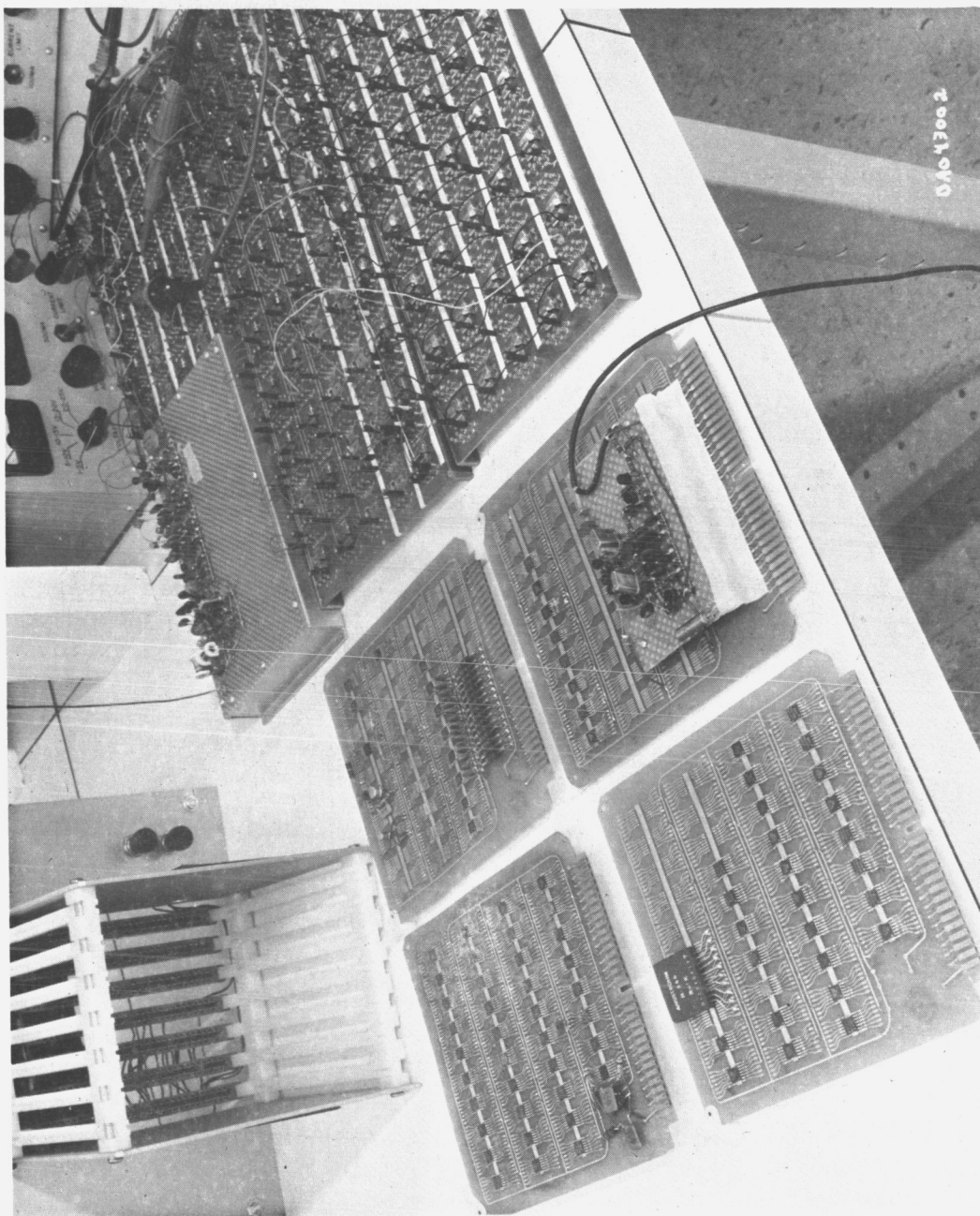


Figure 80.-- Astronaut Data System Breadboard

## OVERALL EXPERIMENT DESIGN

The overall experiment design encompasses the hardware requirements and locations; the T013 system/vehicle interfaces; the experiment constraints, assumptions, and setup; and the crew activity time-line. The prime considerations in developing the overall experiment concepts and accomplishing their design were:

Accuracy	Reliability
Simplicity	Data Transmission
Ease of Operation	Sampling Rate
Interfaces	Format
Weight	Frequency Selection
Volume	Power Consumption

At the completion of this study, it was planned that experiment T013 would be performed in the experiment area, adjacent to the crew quarters in the OWS; that the DARS, with the exception of the DARS control unit, would be operated in its storage location within the MDA.

This report reflects those decisions; however, it appears now that in all likelihood the experiment will be performed in the area just forward of the crew quarters in the OWS, and that DARS will be removed from the MDA and operated in the experiment performance area. The details involving this change in plans will thus be worked out early during the next phase of the T013 program to enable integration into AAP mission 2 without difficulty.

### Hardware Requirements and Location

The flight experiment has essentially two basic modes, i.e., storage and performance. It is planned that the experiment will be contained in two packages for storage. These are the DARS and the Experiment Components Container (ECC). They will be stored before and after performance in the MDA in this configuration. The DARS will remain in the storage position during the performance also, while the experiment package will be moved to the OWS for the actual experiment performance.

Currently planned for the flight experiment are two sets of the following, of which one is a backup set and will not fly:

- |                           |                                    |
|---------------------------|------------------------------------|
| 1 - DARS                  | 1 - Experiment package             |
| 1 - LIMS                  | 1 - DARS control panel             |
| 1 - Data system           | 1 - Set of mounting hardware       |
| 2 - Force measuring units | 1 - Set of interconnecting cabling |

The ECC will contain the hardware necessary to support itself and the FMUs in the OWS. It will also contain:

- 1) LIMS;
- 2) FMS;
- 3) DARS control panel;
- 4) Data system;
- 5) Cabling necessary to connect power, the FMUs, the camera controls, the AM recorder, and the DARS to the data system on the experiment package.

All but the DARS control panel and the data system are separable from the package. Deployment of the separable items will occur in the crew quarters of the OWS during performance.

The location in the OWS for experiment performance is restricted to two possible locations because of limitations in collecting astronaut position data by camera.

If the locations shown in figures 81 and 82 (with an alternative located in the same area but rotated 90° toward quadrant IV) are not available to T013 because of interference with other equipment, the experiment can be performed, as mentioned previously, in the area forward of the crew quarters.

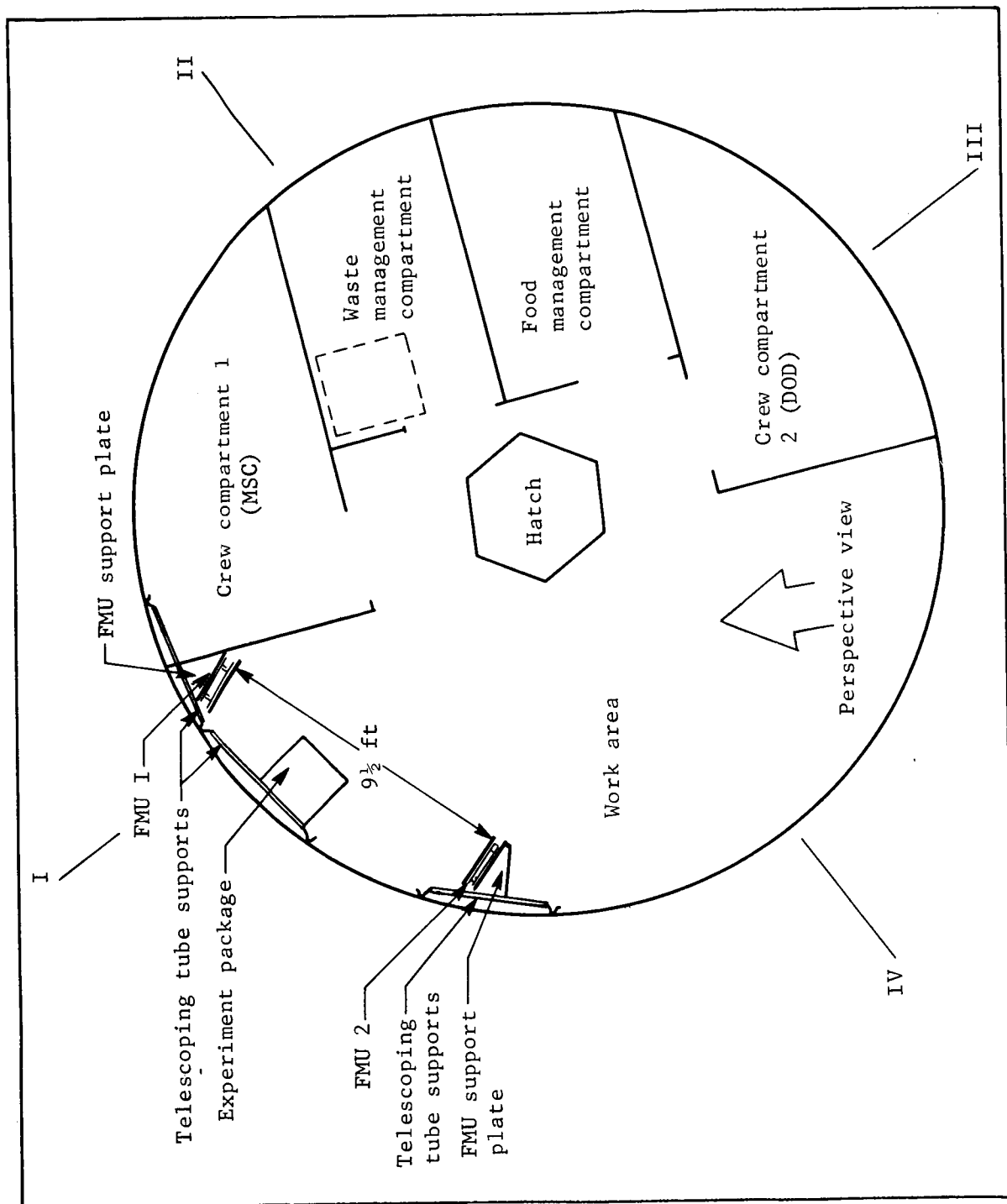


Figure 81.- Crew Quarters Floor Plan (Looking Forward) Showing T013 Equipment

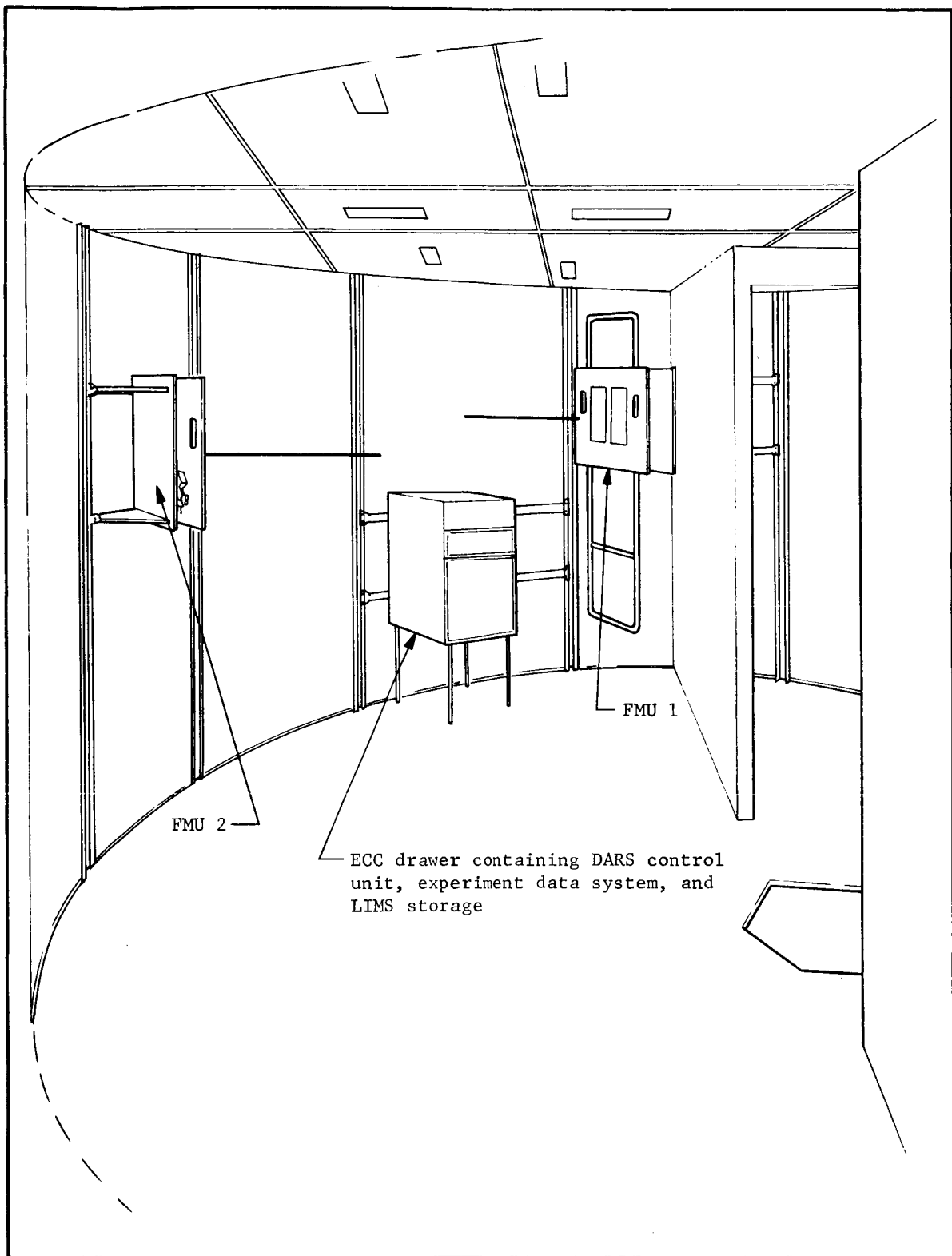


Figure 82.- Perspective View of Crew Quarters Showing T013 Equipment

## System/Vehicle Interfaces

Interfaces between the experiment systems and the vehicle occur during the storage and performance modes.

T013 equipment will be in the storage mode continuously during flight except during the performance time. The mechanical interfaces during storage are the supports in the MDA necessary to hold the DARS and the experiment package in place. Both pieces of equipment will incorporate attachments necessary to mount to the MDA grid support structure. No removal of equipment from the grid structure will be required. The experiment package disconnects from its supporting shelf, which remains attached to the grid structure. The DARS remains in place during the entire flight. Power from the 28-Vdc bus will be required before and during the boost phase of flight.\* No other power requirements exist during the storage mode. The space envelope requirements of the experiments container are shown in figure 83.

During the experiment performance the interfaces are mechanical, space, power, cabling, and data collection. All mechanical support structure is contained as part of the experiment package and presumes attachment points as shown in figure 83. The DARS remains in the MDA in its storage mode position. The power requirements and vibration spectra are detailed in figures 84 thru 88. In addition to the DARS requirement in the MDA, the experiment package requires its power source at the location shown in figure 81. The following interconnecting cabling will be supplied as a part of the experiment and interfaces with the vehicle as stated:

- 1) Power cable to DARS in MDA;
- 2) Power cable to experiment package in OWS;
- 3) Cable between AM recorder (jack point in OWS and AM) and experiment package in OWS;
- 4) Cable between camera controls and experiment package in OWS;
- 5) Cable between FMUs and experiment package in OWS;
- 6) Cable between DARS in MDA and experiment package in OWS (requires jack points on each side of each hatch between MDA and OWS crew quarters).

---

\*The necessity for and satisfaction of this requirement is currently under investigation.

**Note:** Experiment package is stored in storage cabinet.  
Storage cabinet is mounted to MDA structure and remains in place at all times. Experiment package is removed from cabinet and taken to OWS for performance, then returned to storage.

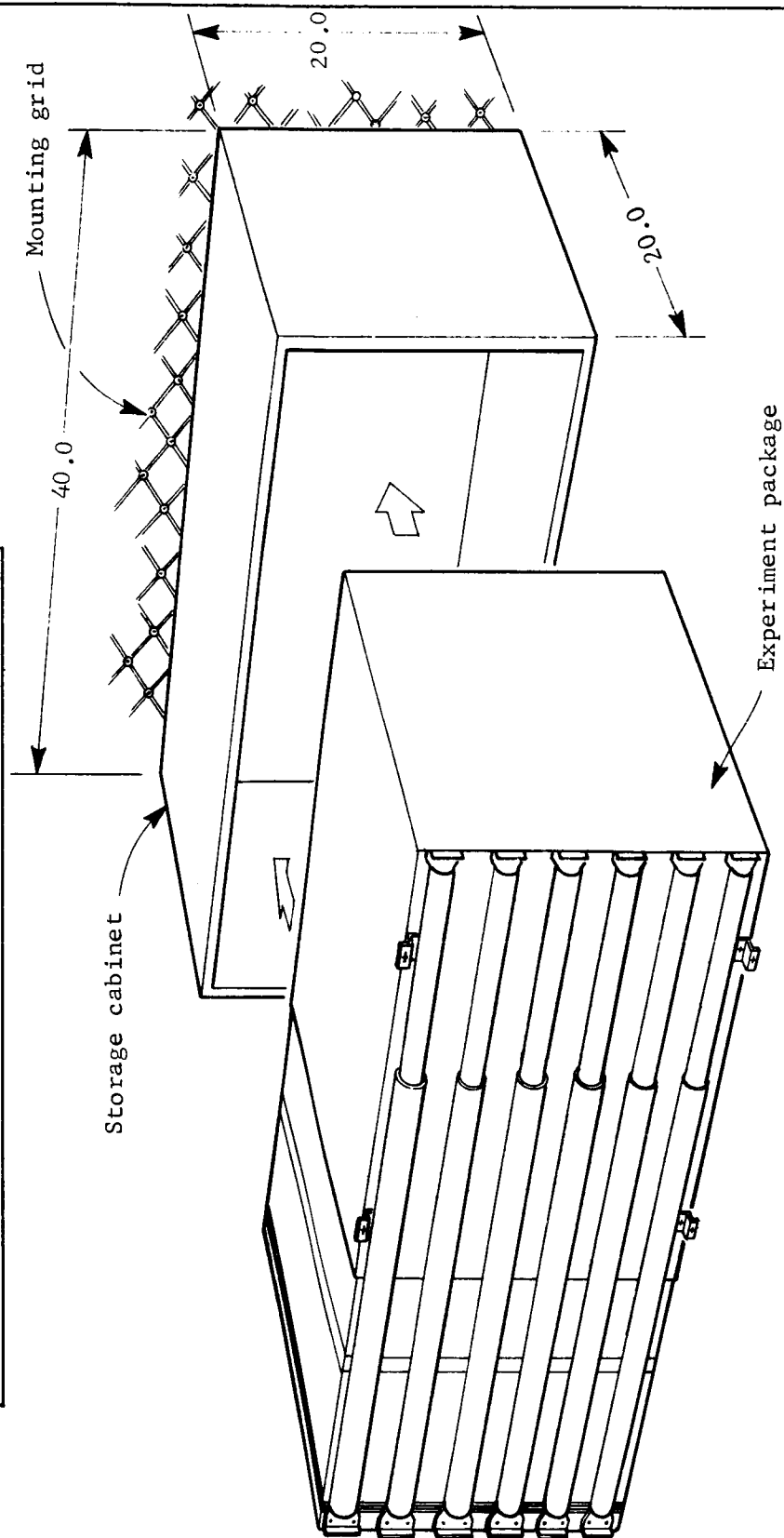


Figure 83.- T013 Experiment Layout Concept, Storage Mode in MDA

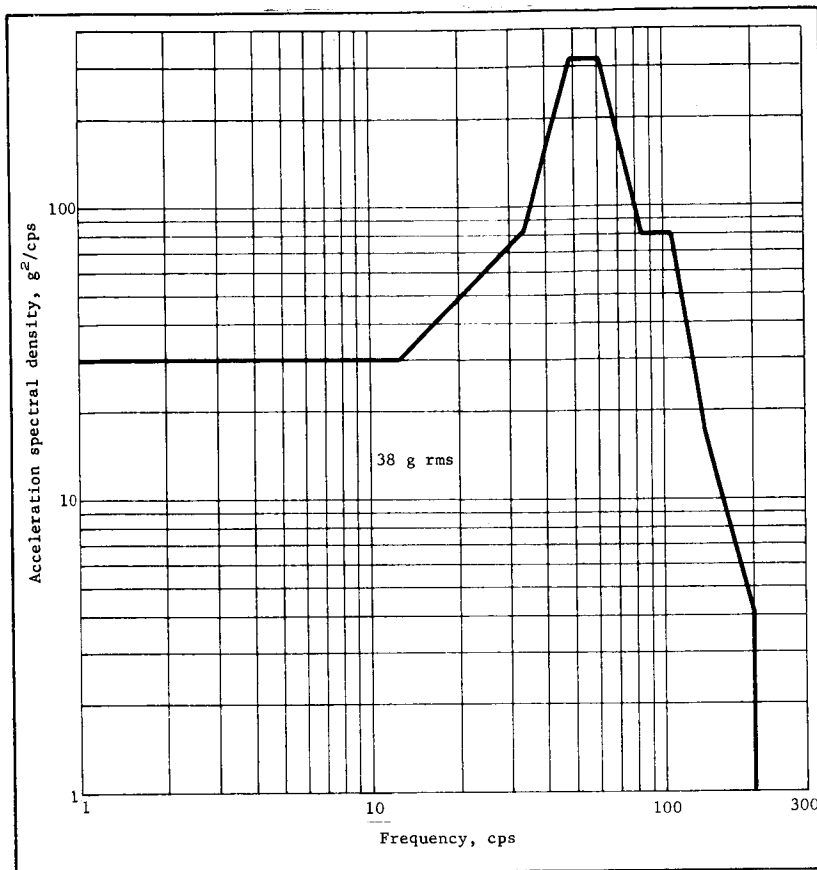


Figure 84.- Random Vibration Spectrum, DARS Rate Gyro System

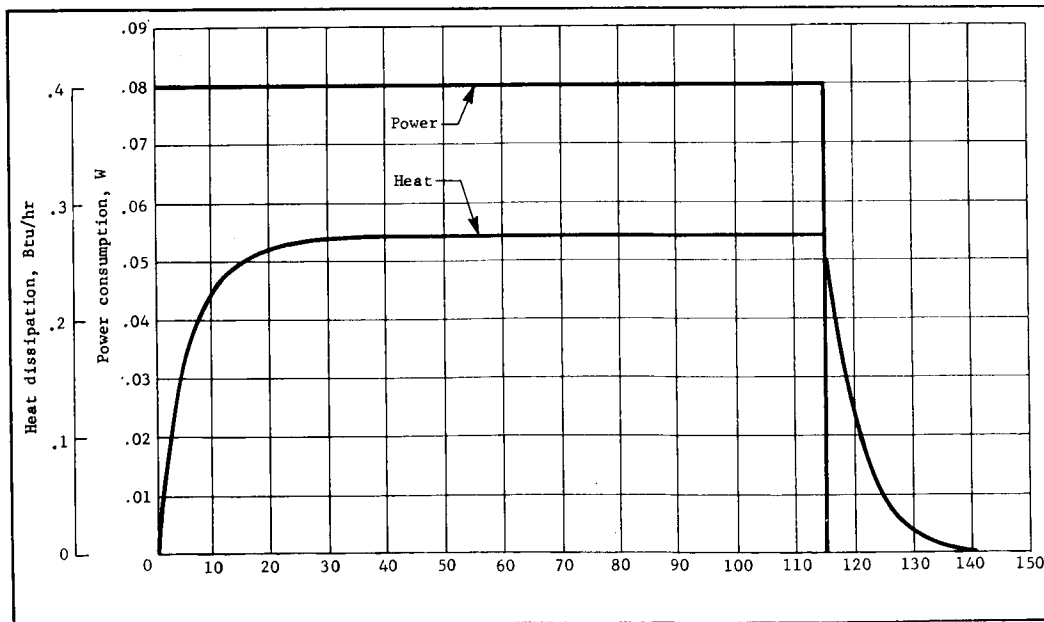


Figure 85.- Estimated Thermal Properties, LIMS



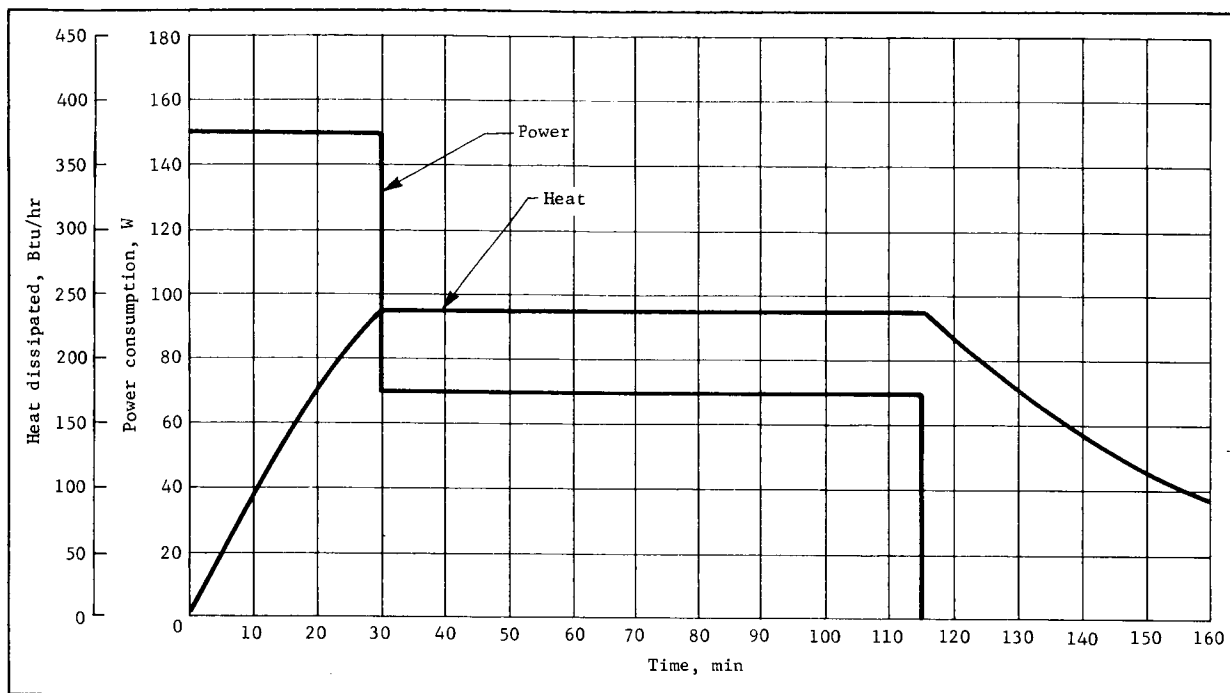


Figure 86.- Estimated Thermal Properties, DARS

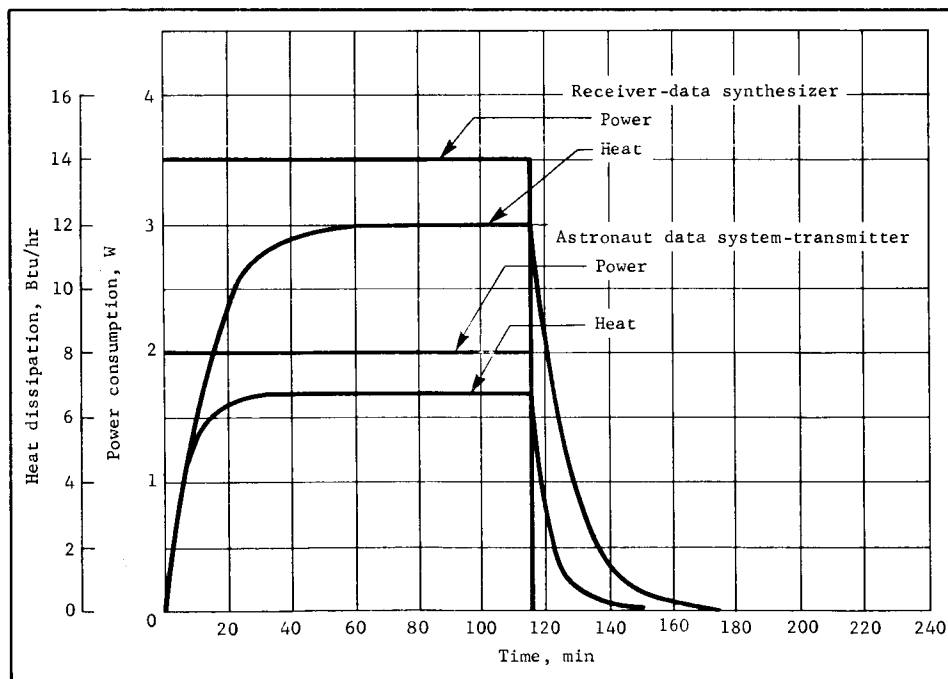


Figure 87.- Estimated Thermal Properties, Experiment Data System

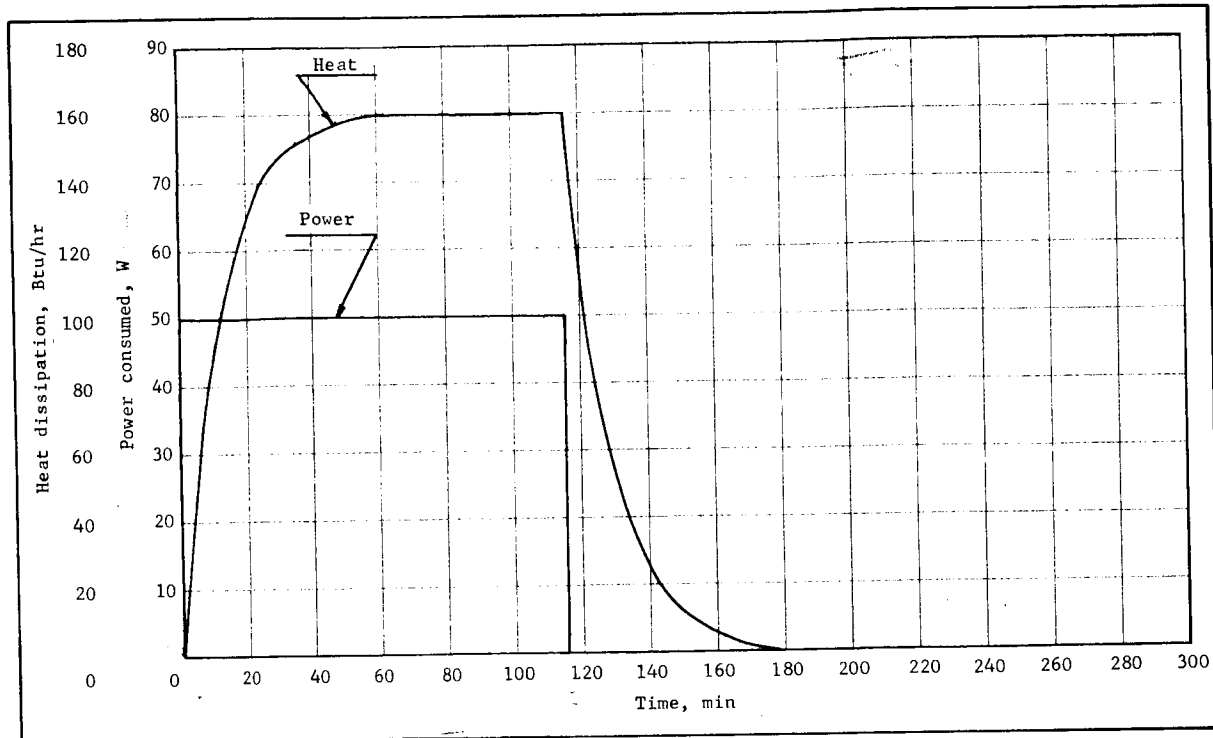


Figure 88.- Estimated Thermal Properties, FMS

Data collection has been detailed in an earlier section of this report. The interface requirements are: one channel of the AM recorder for approximately 55 min, CSM event camera for approximately 5 min, and two OWS cameras with adjustable mounts. Sufficient lighting in the OWS is presumed as is verbal communication between the OWS crew quarters and the CSM.

#### Experiment Constraints, Assumptions, and Setup

The experiment hardware, its setup, and the sequence of operations have been designed to minimize the astronaut participation time and the complexity of operation.

In addition, an evaluation of the possible combination of this experiment with three others (M050, M055, and M509) was made in an attempt to reduce astronaut participation time, total experiment time, and training time. The method of analysis was to first list objectives, equipment, procedures, and subtasks for M050, M055, M509, and T013. The experiments were examined for possibilities of direct combination, and opportunities for increasing the value of data from any of the four experiments were sought.

The number of participating astronauts cannot be reduced because no extraneous motion outside of T013 activities is allowed during its performance. All three astronauts are required by T013 as is shown by the time line. When not actually functioning as a participant, they must remain quiescent.

The use of the LIMS, FMS, and the bulk of the T013 data system is currently under examination for possible incorporation as a part of experiment M509. The principal investigator for experiment M050 has evidenced considerable interest in the combination of T013 LIMS and film data for his use. Other equipment combinations do not appear to be of significant value.

An estimate of required training time has been made following a close look at the operation of the experiment and is shown in table 19.

TABLE 19.- TRAINING TIME

	Classroom and laboratory, time, hr	Simulation time, hr
Astronaut 1 (CSM pilot)	8	
Astronaut 2 (director)	8	8
Astronaut 3 (experimenter)	8	8

This estimate indicates that 40 man-hours per crew is required.

The assumed flight experiment ground rules are:

- 1) Any orbit providing zero-g is acceptable for this experiment;
- 2) The experiment will be conducted in the CSM, the OWS, and the passageway between the MDA and OWS;
- 3) There is no requirement for pressure suits or EVA during this experiment;
- 4) All experiment-peculiar equipment will be stowed initially in the MDA or airlock section;
- 5) This experiment will make the maximum use of equipment assembled in the MDA, AM, and OWS for other experiments; i.e., voice communication links, structural supports, camera (16-mm movies), lights, recorders, electric power, and personnel anchoring tethers;

- 6) The spacecraft attitude control thrusters must be off and remain off throughout the experiment or positive identification of their on-time mode and provisions for renulling DARS must be made. Minimum impulse stability shall be attained before the start of the experiment. The OWS stability system shall be off;
- 7) Voice communication shall be maintained continuously between the CSM and the experiment area;
- 8) Astronauts shall observe the no-motion requirement at the specified times. This necessitates their being restrained at these times.

The assumptions of the initial conditions for experiment performance are:

- 1) Astronaut 1 is in the CSM in the couch;
- 2) The experiment hardware is,
  - a) 1 DARS,
  - b) 1 experiment package composed of
    - (1) 2 force measuring units,
    - (2) DARS control panel,
    - (3) System data synthesizer,
    - (4) LIMS,
    - (5) Film cartridges,
    - (6) Cabling,
    - (7) Mounting hardware for FMUs and experiment package;
- 3) The DARS will remain in the stowed condition in the MDA;
- 4) The two FMUs will remain in the OWS after completion of this experiment;
- 5) Two 16-mm movie cameras are in the OWS but not in the required position for this experiment. The cameras can be controlled and synchronized from a single point. Mounts are available in the proper locations or mounts are movable;
- 6) Astronauts 2 and 3 are in the MDA in shirt-sleeve attire;

- 7) An open-door policy is in effect throughout the cluster interiors;
- 8) The AM recorder is available for use and has pickup jacks at appropriate locations;
- 9) A time reference signal shall be recorded on the data tape to correlate film time and DARS time;
- 10) The AM recorder shall have sufficient capacity and shall be so set to record the entire experiment sequence without attention.

The flight experiment activities to be monitored are described below with a detailed time line following in the next subsection.

The flight experiment will duplicate the ground simulation as closely as possible and will include measurement of the reactions to the following activities (asterisks denote those forces that will be measured by the force measuring units):

- 1) CSM couch activity,
  - a) Breathing and heart actions,
  - b) Coughing and sneezing,
  - c) Three typical couch movements -- reaching, operating controls, and body turning;
- \*2) In-place motions while attached to FMU 1,
  - a) Breathing and heart action,
  - b) Coughing and sneezing,
  - c) Single- and double-arm pendulums in the frontal and sagittal planes,
  - d) Single- and double-leg pendulums in the frontal plane,
  - e) Leg exercises with Gemini-type exerciser;
- \*3) In-place motions while standing on FMU 1,
  - a) Body bending,
  - b) Exaggerated in-place stepping;
- 4) Compressive walking between floor and ceiling from FMU 1 to FMU 2;
- 5) Bounce walking between floor and ceiling from FMU 1 to FMU 2;

- \*6) Free soaring by pushing off from FMU 1 and landing on FMU 2 and reverse;
- 7) Transfer of mass and traversing the OWS-AM-MDA by returning the experiment package to the MDA for storage.

A brief outline of the experiment procedure follows:

- 1) The DARS is turned on in the MDA;
- 2) The experiment package is transported to the OWS by Astronauts 2 and 3, and the hardware is deployed and mounted. Appropriate cabling is deployed and cameras are set up;
- 3) Equipment is turned on and verified;
- 4) The LIMS is donned by Astronaut 3 and he is placed on FMU 1. Astronaut 2 acts as test director and assists Astronaut 3 with setup and performance;
- 5) Astronaut 1 in CSM performs his activities;
- 6) Astronaut 3 performs his activities on the FMU;
- 7) Astronaut 3 performs the free movement activities in the OWS;
- 8) Astronauts 2 and 3 reassemble experiment package and return with it to MDA where the equipment is turned off;
- 9) The LIMS is removed and stored along with the experiment package;
- 10) The experiment film cartridges are stored for return.

#### Crew Activity Time Line

Table 20 is the crew activity time line. Tasks preceded by asterisk are accomplished jointly by Astronauts 2 and 3. Astronaut 1 is the CSM pilot, Astronaut 2 is the experiment director, and Astronaut 3 is the experimenter. Astronaut 1 remains in CSM during entire experiment.

TABLE 20.- CREW ACTIVITY TIME LINE

Cumulative time, min	Astronaut 3	Astronaut 2	Astronaut 1
0	<u>1.0</u> Disconnect experiment package	<u>.25</u> Turn on DARS and verify operation (20 min warmup)	<u>.10</u> Begin minimum impulse stability mode
1			
	<u>*.25</u> Connect cable from experiment package to DARS		<u>.25</u> Load and position event recording camera to film CSM couch movements
1.25			
	<u>*4.0</u> Transport experiment package to OWS and string DARS cable on the way		
5.25			
	<u>*3.0</u> Position experiment package and deploy mounting hardware		
8.25			
	<u>.10</u> Establish voice communications with CSM		
8.35			
	<u>*5.0</u> Set up FMU mount-structures		
13.35			
	<u>*2.0</u> Separate FMUs from experiment package		
15.35			
	<u>2.5</u> Attach FMU 1 including connecting cabling	<u>2.5</u> Attach FMU 2 including connecting cabling	
17.85			
	<u>*.5</u> Mount experiment package		
18.35			
	<u>5.0</u> Reposition Camera, load, and aim	<u>5.0</u> Reposition camera, load, and aim	
23.35			
	<u>1</u> String cable to AM recorder jack	<u>1</u> String cable from SDS to camera controls	
24.35			

TABLE 20.- CREW ACTIVITY TIME LINE - Continued

Cumulative time, min	Astronaut 3	Astronaut 2	Astronaut 1
29.35	<u>*5.0</u> Remove LIMS from experiment package and place on Astronaut 3		<u>.10</u> Turn off attitude thrusters when minimum impulse stability is attained
31.35	<u>*2.0</u> Position Astronaut 3 in FMU 1	<u>1.0</u> Adjust DARS on control panel and verify operation	<u>.25</u> Turn on AM recorder and verify operation
32.35		<u>.25</u> Turn on and verify operation of SDS	<u>.10</u> Turn on CSM/camera
32.60		<u>1.0</u> Secure in OWS	<u>.25</u> Secure in CSM couch
33.60	No motion	No motion	<u>.25</u> No motion - record spacecraft motion as baseline
33.85			<u>.25</u> Breathe hard
34.10			<u>.10</u> Stabilize
34.20			<u>1.0</u> Cough 5 times with 10-sec intervals
35.20			<u>.10</u> Stabilize
35.30			<u>1.0</u> Sneeze 5 times with 10-sec intervals
36.30			



TABLE 20.- CREW ACTIVITY TIME LINE - Continued

Cumulative time, min	Astronaut 3	Astronaut 2	Astronaut 1
36.40	No motion	No motion	<u>.10</u> Stabilize
36.90			<u>.50</u> Reach to control panel and return
37.00			<u>.10</u> Stabilize
37.50			<u>.50</u> Turn knob on panel and return
37.60			<u>.10</u> Stabilize
38.10			<u>.50</u> Turn body in couch and return to nor- mal position
38.20			<u>.10</u> Stabilize
38.30			<u>.10</u> Turn off CSM camera
			<u>1.0</u> Communicate with OWS and transfer experiment con- trol
39.30			
39.40		<u>.10</u> Turn on OWS cam- eras and synchro- nize with DARS	
39.50		<u>.10</u> Secure in OWS	<u>.10</u> Secure in CSM
39.75	<u>.25</u> No motion	No motion	No motion
40.00	<u>.25</u> Breathe hard		
40.10	<u>.10</u> Stabilize		
41.10	<u>1.0</u> Cough 5 times with 10-sec intervals		
41.20	<u>.10</u> Stabilize		
42.20	<u>1.0</u> Sneeze 5 times with 10-sec intervals		

TABLE 20.- CREW ACTIVITY TIME LINE - Continued

Cumulative time, min	Astronaut 3	Astronaut 2	Astronaut 1
42.30	<u>.10</u> Stabilize		
	<u>1.0</u> Perform 3 single-arm pendulums in frontal plane at 10-sec intervals	No motion	No motion
43.30			
43.45	<u>.15</u> Stabilize		
	<u>1.0</u> Perform 3 single-arm pendulums in sagittal plane at 10-sec intervals		
44.45			
44.60	<u>.15</u> Stabilize		
	<u>1.0</u> Perform 3 double-arm pendulums in frontal plane at 10-sec intervals		
45.60			
45.75	<u>.15</u> Stabilize		
	<u>1.0</u> Perform 3 double-arm pendulums in sagittal plane at 10-sec intervals		
46.75			
46.90	<u>.15</u> Stabilize		
	<u>1.0</u> Perform 3 single-leg pendulums in frontal plane at 10-sec intervals		
47.90			
48.05	<u>.15</u> Stabilize		
	<u>1.0</u> Perform 3 double-leg pendulums in frontal plane at 10-sec intervals		
49.05			
49.20	<u>.15</u> Stabilize	↓	↓

TABLE 20.- CREW ACTIVITY TIME LINE - Continued

Cumulative time, min	Astronaut 3	Astronaut 2	Astronaut 1
50.20	<u>1.0</u> Perform leg exercises with ergometer for 30 sec	No motion	No motion
50.45	<u>.25</u> Stabilize		
51.45	<u>1.0</u> Release from FMU 1 and position for compressive walk		
51.70	<u>.25</u> Stabilize		
53.70	<u>2.0</u> Perform compressive walk to FMU 2		
53.95	<u>.25</u> Stabilize		
55.95	<u>2.0</u> Perform compressive walk to FMU 1		
56.20	<u>.25</u> Stabilize		
58.20	<u>2.0</u> Perform bounce walk to FMU 2		
58.45	<u>.25</u> Stabilize		
60.45	<u>2.0</u> Perform bounce walk to FMU 1		
60.70	<u>.25</u> Stabilize		
61.70	<u>1.0</u> Position feet on FMU 1 and extend to soar position		
62.70	<u>1.0</u> Push off with legs and stabilize at FMU 2 with hands only		
62.95	<u>.25</u> Stabilize		

TABLE 20.- CREW ACTIVITY TIME LINE - Continued

Cumulative time, min	Astronaut 3	Astronaut 2	Astronaut 1
63.95	<u>1.0</u> Position feet on FMU 2 and extend to soar position	No motion	No motion
64.95	<u>1.0</u> Push off with legs and stabilize at FMU 1 with hands only		
65.20	<u>.25</u> Stabilize		
66.20	<u>1.0</u> Restrain feet on FMU 1 and extend body		
67.20	<u>1.0</u> Perform body bend at waist and return 3 times with 10-sec intervals		
67.45	<u>.25</u> Stabilize		
68.45	<u>1.0</u> Perform exaggerated stepping on FMU 1 for 30 sec		
68.70	<u>.25</u> Stabilize		
68.95	<u>.25</u> Disconnect SDS cable from recorder and leave loose	<u>.10</u> Stop camera	<u>.10</u> Stop AM recorder
69.95	<u>1.0</u> Disconnect cable from FMU 1 and store in experiment package	<u>1.0</u> Unload cameras and store film in experiment package and return SDS cable to experiment package from camera controls	
70.20		<u>.25</u> Disconnect cable from FMU 2 and store in experiment package	

TABLE 20.- CREW ACTIVITY TIME LINE - Concluded

Cumulative time, min	Astronaut 3	Astronaut 2	Astronaut 1
71.70	<u>*1.5</u> Disconnect experiment package from OWS and store mounting hardware. Move experiment package to hatchway		
	<u>3.0</u> Hold experiment package at hatchway	<u>1.5</u> Take SDS cable to AM recorder jack in AM	
74.70	No motion	<u>1.5</u> Return to OWS	<u>.10</u> Turn on AM recorder
78.70	<u>*4.0</u> Transfer experiment package to MDA and retrieve DARS cable on the way		↓
78.95	<u>*.25</u> Turn off DARS and SDS		<u>.10</u> Turn off AM recorder
83.95	<u>*5.0</u> Remove LIMS from Astronaut 3 and store in experiment package		<u>.10</u> Initiate spacecraft control
84.95	<u>*1.0</u> Store experiment package		
85.45	<u>.50</u> Disconnect DARS cable and store in experiment package	<u>.50</u> Disconnect SDS cable from AM recorder jack and store in experiment package	
85.95	<u>*.50</u> Unload film from experiment package		

The total experiment time is 85.95 min. Astronauts 2 and 3 are involved for the entire period. Astronaut 1 is free except during his above-noted activities and during period requiring no motion.

Figure 89 is a summary of the crew activity time line.

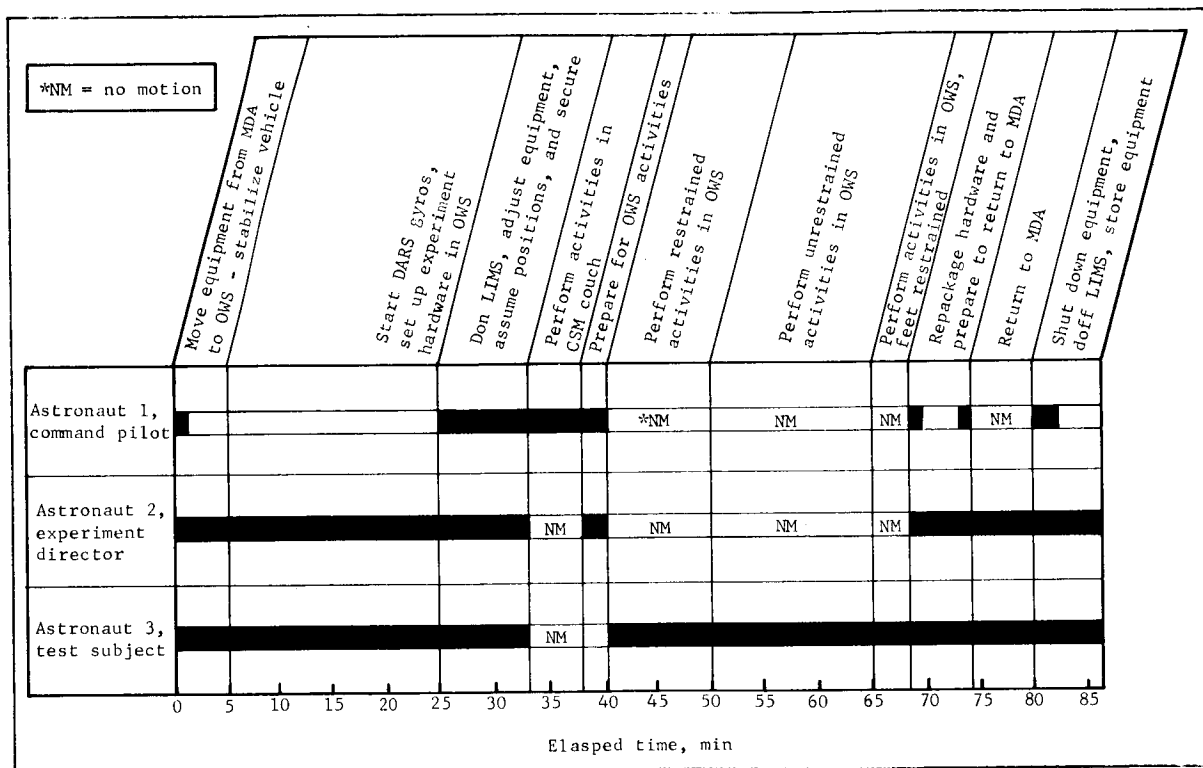


Figure 89.- Crew Activity Time-Line Summary

## CONCLUSIONS

This study has resulted in the design of flight capable instrumentation to enable aquisition of astronaut limb motion history and astronaut induced forces and moments on a spacecraft.

In addition, a strap-down inertial attitude sensing system has been designed to enable measurement of the vehicle attitude perturbations resulting from crew motions.

A data system to organize all the individual sensor outputs in the simplest possible format to interface with the Apollo Applications Program data system has been developed and a preliminary circuit design carried out.

All designs developed under this study have been evaluated, performancewise, in a breadboard configuration. Laboratory models of the Limb Motion Sensing System and the Force Measuring System have been built, tested and delivered to the Langley Research Center.

Preliminary integration of the total experiment T013 into AAP Mission 2 has been carried out based on the then current concepts. Since the writing of this report, certain concepts have altered, and thus integration details will have to be modified to reflect these changes.

A near-optimum model of the experiment has been developed for ground-based simulation of experiment T013 as well as any other manned space mission insofar as crew activity affects vehicle attitude. This model should be exploited to the fullest extent to enable the design of future manned spacecraft control systems to reflect and obviate the possible deleterious effects of crew motion.

Martin Marietta Corporation  
Denver, Colorado, March 6, 1968

This page intentionally left blank.



## APPENDIX A

### GROUND SIMULATION RESULTS

#### Part I - Restrained Crew Activity Simulation Results

Part I of this appendix contains the results of the Restrained Crew Activity Simulation Program. The activities and the page on which the results for each activity begin are tabulated below. The axis system in which the results are resolved is also given. Anthropometric data on the two subjects used are presented in Appendix F.

<u>Run</u>	<u>Activity</u>	<u>Axis</u>	<u>Page</u>
1.	150-lb static weight	Man's	160
	<u>Subject A</u>		
2.	Heartbeat (no breathing)	Man's	162
3.	Normal breathing	Man's	164
4.	Fast breathing	Man's	166
5.	Coughing	Man's	168
6.	Sneezing	Man's	170
7.	Head motion	Man's	172
8.	Wrist motion	Man's	174
9.	Ankle motion	Man's	176
10.	Lower right arm, single pendulum, sagittal plane	S/C	178
11.	Total right arm, single pendulum, sagittal plane	S/C	183
12.	Total left arm, single pendulum, frontal plane	S/C	188
13.	Total left arm, double pendulum, sagittal plane	S/C	193
14.	Total left arm, double pendulum, sagittal plane	S/C	198
15.	Lower right leg, single pendulum, sagittal plane	S/C	203
16.	Total right leg, single pendulum, sagittal plane	S/C	208
17.	Right arm, console operation	S/C	213

## APPENDIX A

<u>Run</u>	<u>Activity</u>	<u>Axis</u>	<u>Page</u>
<u>Subject B</u>			
18.	Lower right arm, single pendulum, sagittal plane	S/C	220
19.	Total right arm, single pendulum, sagittal plane	S/C	226
20.	Total left arm, single pendulum, frontal plane	S/C	232
21.	Total left arm, double pendulum, sagittal plane	S/C	237
22.	Lower right leg, single pendulum, sagittal plane	S/C	242
23.	Total left leg, double pendulum, sagittal plane	S/C	247
24.	Right arm console operation	S/C	252
25.	Both arms and legs - exercising	S/C	257

For activities 1 thru 9, only the load cell forces and moments (in man's axis system defined in figure 2) are given. For activities 10 thru 25, the following information is given.

- 1) Load cell forces and moments;
- 2) Calculated forces and moments (with and without c.g. shift);
- 3) S/C rates and angles from calculated forces and moments;
- 4) LIMS angles for the limb or limbs involved in the motion.

These results are presented in S/C axes (defined in fig. 7). Also, for activities 17, 18, and 19, the S/C rates and angles from load cell forces and moments (modified to exclude c.g. shift and load cell bias effects) are presented.

Legend and nomenclature for all curves.- The following nomenclature is common to all curves:

$F_x$	Force in x direction, lb
$F_y$	Force in y direction, lb

## APPENDIX A

$F_z$	Force in z direction, lb
$M_x$	Moment about x axis, ft-lb, no c.g. shift moment
$M_y$	Moment about y axis, ft-lb, no c.g. shift moment
$M_z$	Moment about z axis, ft-lb, no c.g. shift moment
$M'_x$	Moment about x axis, ft-lb, c.g. shift moment included
$M'_y$	Moment about y axis ft-lb c.g. shift moment included
$\omega_x$	S/C rate about S/C body x axis, deg/sec
$\omega_y$	S/C rate about S/C body y axis, deg/sec
$\omega_z$	S/C rate about S/C body z axis, deg/sec
$\phi$	S/C Euler angle, x axis, deg
$\theta$	S/C Euler angle, y axis, deg
$\psi$	S/C Euler angle, z axis, deg
$\phi_2, \theta_2, \psi_2$	Roll, pitch, yaw angle for right shoulder, deg
$\phi_3, \theta_3, \psi_3$	Roll, pitch, yaw angle for left shoulder, deg
$\theta_4$	Pitch angle for right elbow, deg
$\theta_5$	Pitch angle for left elbow, deg
$\phi_6, \theta_6, \psi_6$	Roll, pitch, yaw angle for right hip, deg
$\phi_7, \theta_7, \psi_7$	Roll, pitch, yaw angle for left hip, deg
$\theta_8$	Pitch angle for right knee, deg
$\theta_9$	Pitch angle for left knee, deg
Time	Real time, sec

On the force and moment plots where two curves appear, the darker line is the calculated results and the lighter line is the load cell results. The moments  $M_x$  and  $M_y$  are calculated.

## APPENDIX A

Run 1, 150-lb static weight.- Figure A1 data are taken with a 150-lb weight lying on the couch mockup and load cells. The force and moment results are the inherent noise generated in the total system. The data show that this noise is sufficiently small to negligibly affect any data generated by the man.

APPENDIX A

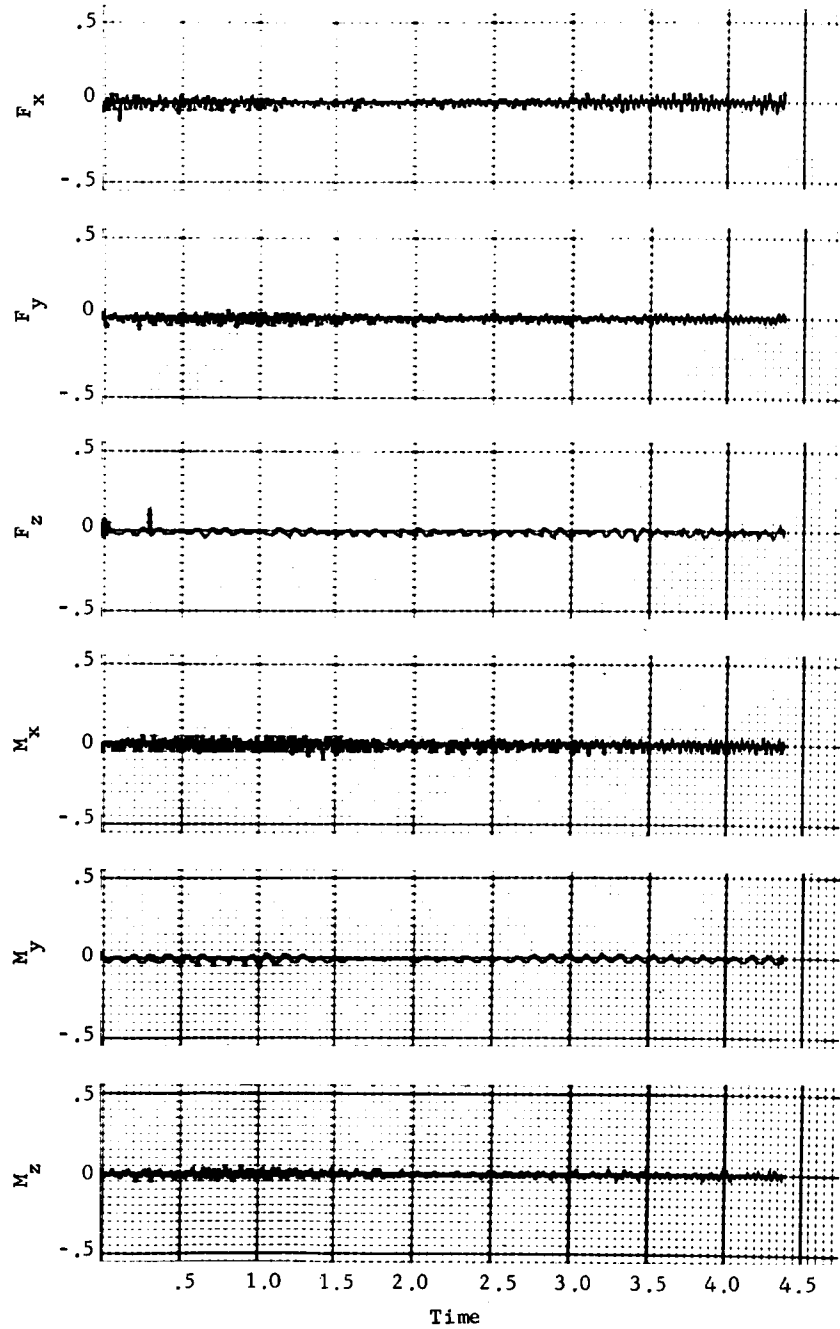


Figure A1.- 150-1b Static Weight, Run 1

## APPENDIX A

Run 2, heartbeat (no breathing).- Figure A2 data were taken with Subject 1 lying on the couch mockup as still as possible, and holding his breath. The data can be considered as inherent noise of the total system including man. Note the well-defined heartbeat occurring at approximately 0.7, 1.5, 2.1, etc., sec.

# APPENDIX A

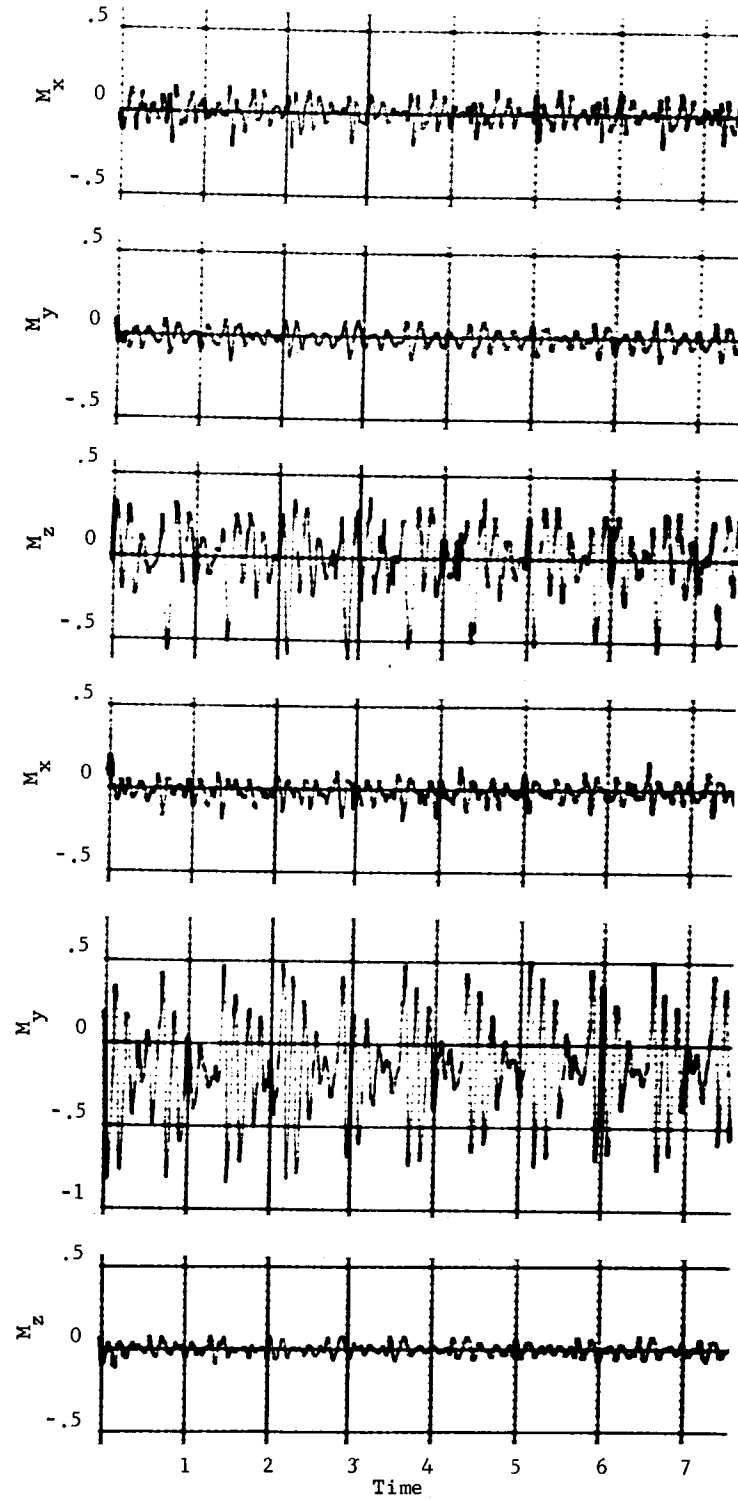


Figure A2.- Heatbeat (No Breathing), Run 2

## APPENDIX A

Run 3, normal breathing.- Figure A3 data were taken with Subject 1 lying on the couch mockup without any limb motion, but allowing normal breathing. The breathing cycle is clearly apparent (approximately 1/5 cps) in the moment  $M_y$ . Again the heart-beat is also well-defined. The change in the moment  $M_y$  is caused by a slight combined c.g. shift from expansion of the chest cavity. No dynamic forces appear to be present from the breathing alone.



# APPENDIX A

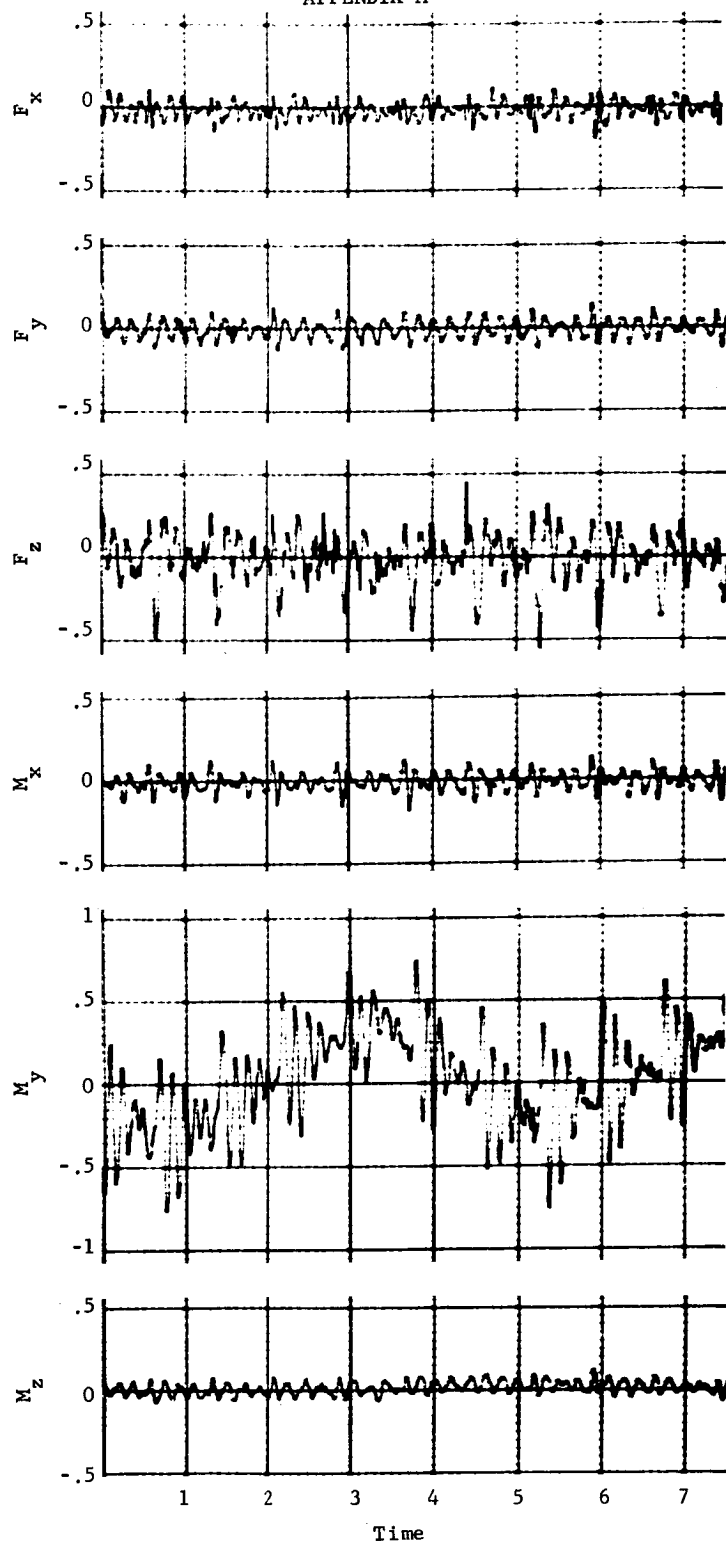


Figure A3.- Normal Breathing, Run 3

## APPENDIX A

Run 4, fast breathing.- Figure A4 data result from the rapid breathing of Subject 1. The heartbeat is apparent, but not so clearly defined, and the fast-breathing cycle (at approximately 1/2 cps) shows up in most forces and moments. Dynamic forces and moments from breathing alone are no longer negligible in comparison to heartbeat alone.

# APPENDIX A

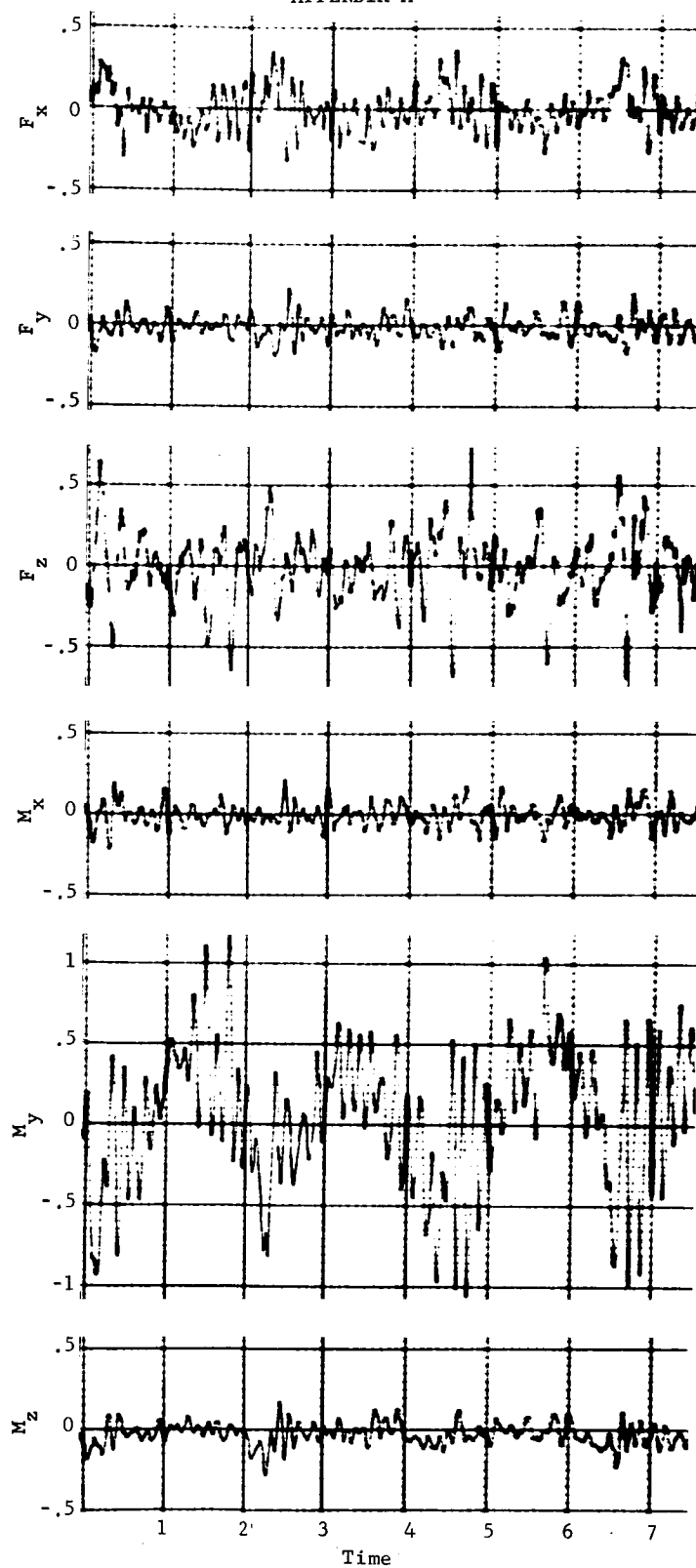


Figure A4.- Fast Breathing, Run 4

## APPENDIX A

Run 5, coughing.- For the data shown in figure A5, Subject 1 was required to lie as still as possible except for head motions associated with coughing. The subject coughed three times and the disturbances are clearly seen at approximately 1.0, 2.5, and 4 sec. Note that the coughing disturbances are relatively large compared to disturbances from other motions.

# APPENDIX A

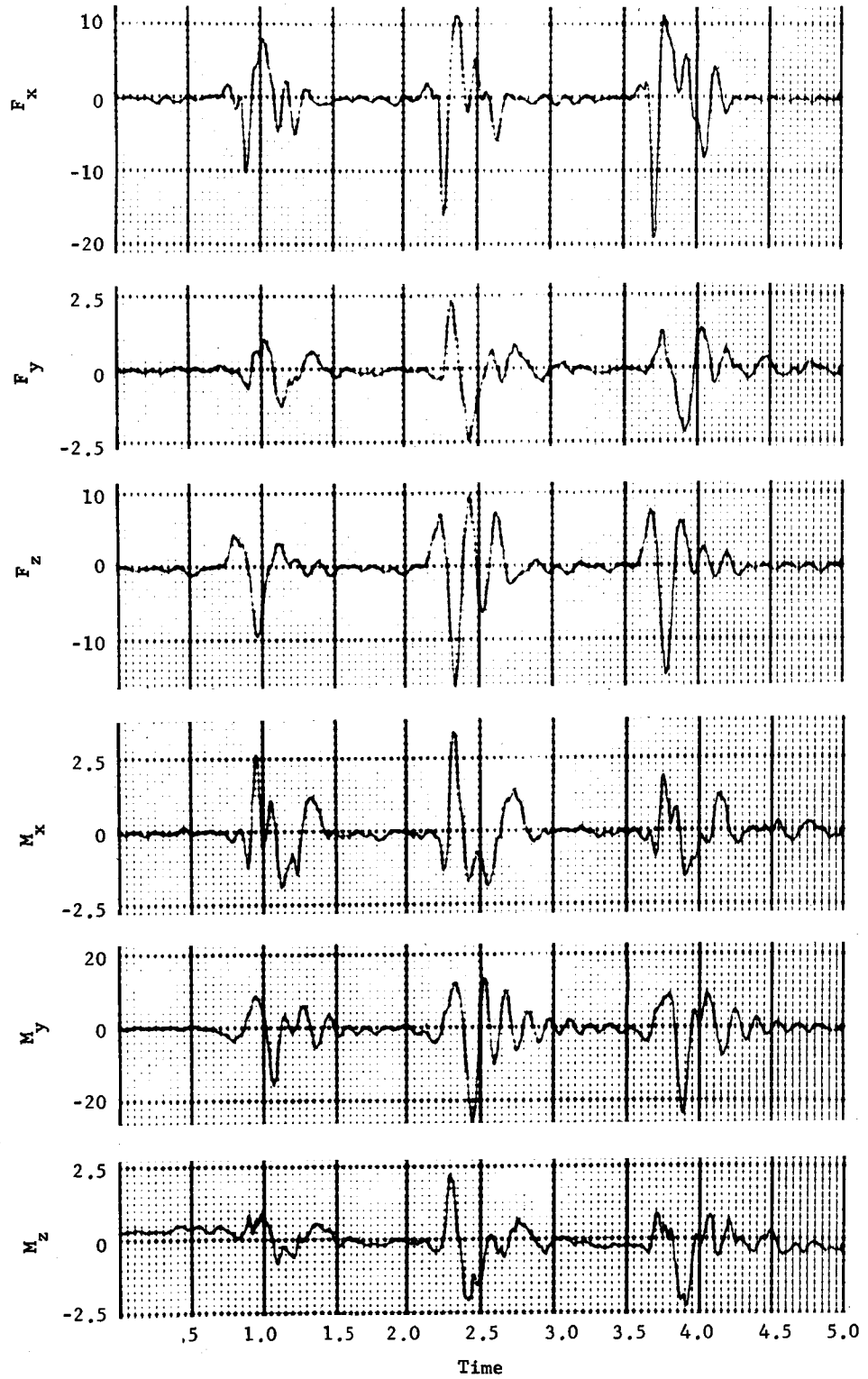


Figure A5.- Coughing, Run 5

## APPENDIX A

Run 6, sneezing.- For the data shown in figure A6, Subject 1 was required to lie as still as possible except for head motions associated with sneezing. The subject sneezed three times and the disturbances are clearly seen at approximately 0.5, 2.5, and 4.5 sec. Disturbances caused by sneezing are very similar to those from coughing.

# APPENDIX A

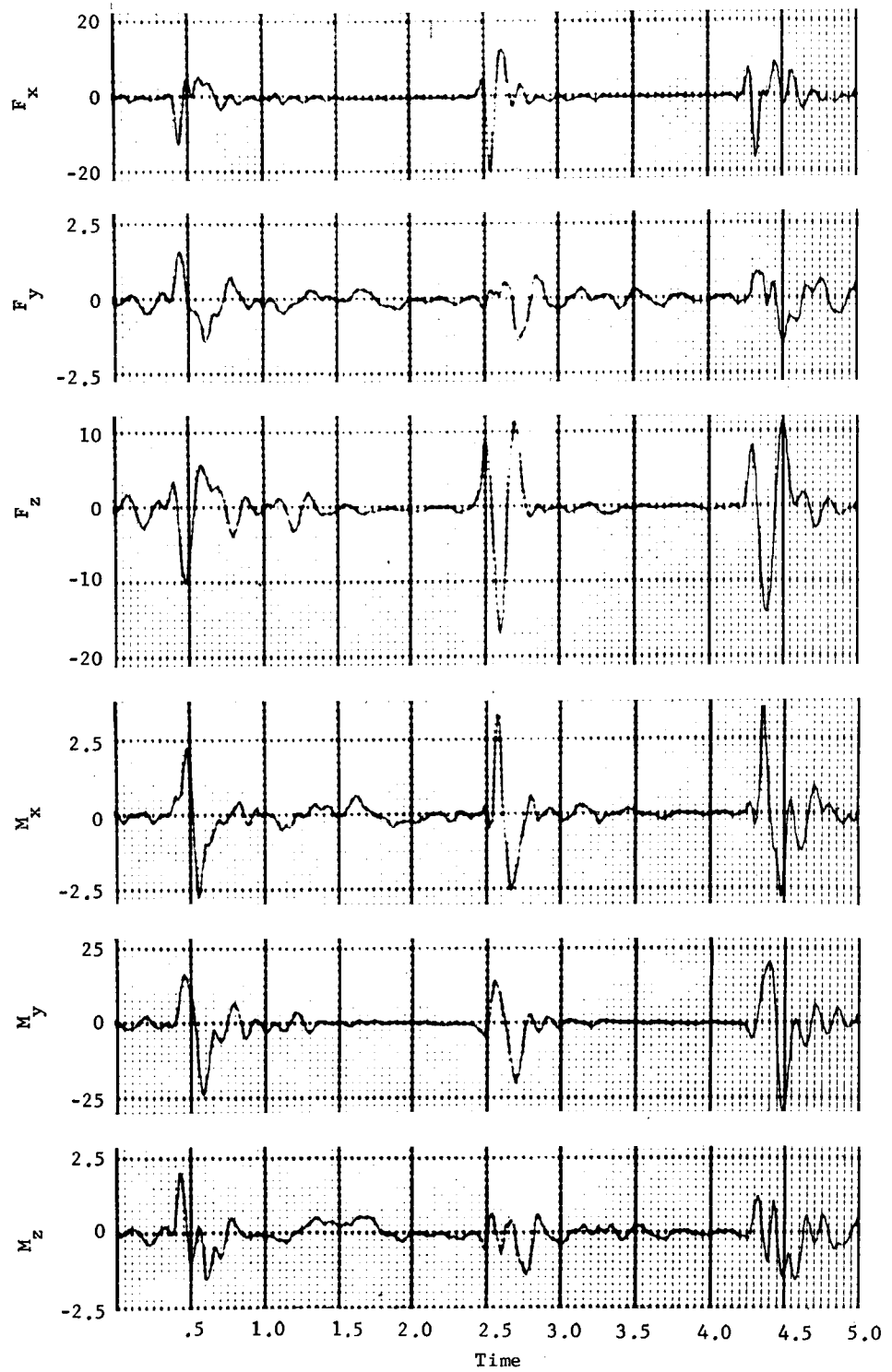


Figure A6.- Sneezing, Run 6

## APPENDIX A

Run 7, head motion.- For the data shown in figure A7, Subject 1 was required to lie as still as possible except for specific head rotations. The first rotations were about the yaw axis (man's z axis) and occur between 1 and 4 sec. The second rotations were about the pitch axes (man's y axis) and occur between 4 and 8 sec. The third rotations were about the roll axis (man's x axis) and occur between 8 and 13 sec. The subject rotated his head three times about each axis.



# APPENDIX A

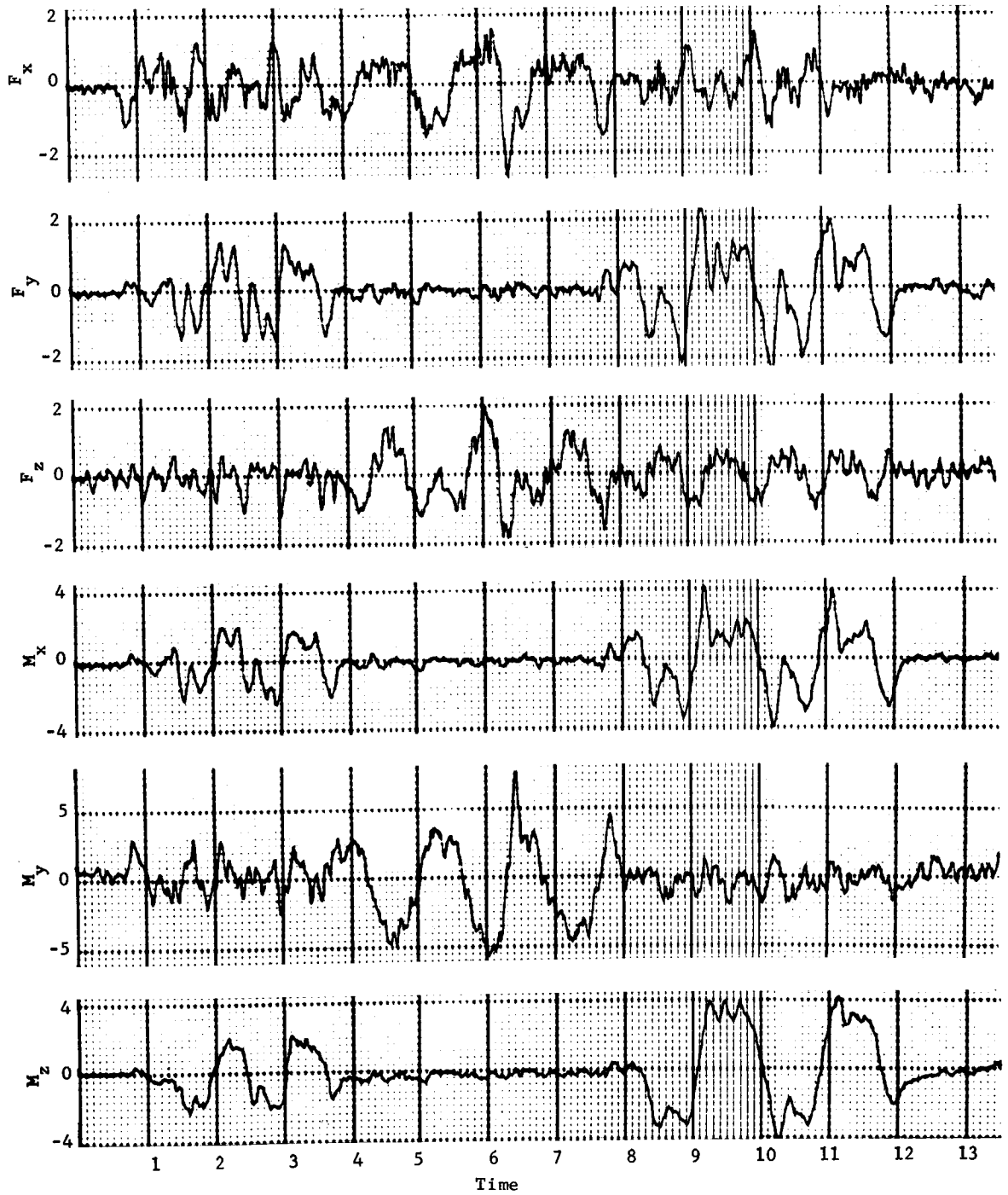


Figure A7.- Head Motion, Run 7

## APPENDIX A

Run 8, wrist motion.- For the wrist motion data shown in figure A8, Subject 1 raised his arm slightly, resulting in the  $M_y$  moment change occurring from 0 to 1 sec. He lowered his arm from 8 to 8.5 sec. This moment change is caused by combined c.g. shift. The subject first rotated his wrist several times about the pitch axis (man's y axis) and then several times about the roll axis (man's x axis). The pitch rotation occurs between 1 and 4.5 sec and the roll between 4.5 and 8 sec.

# APPENDIX A

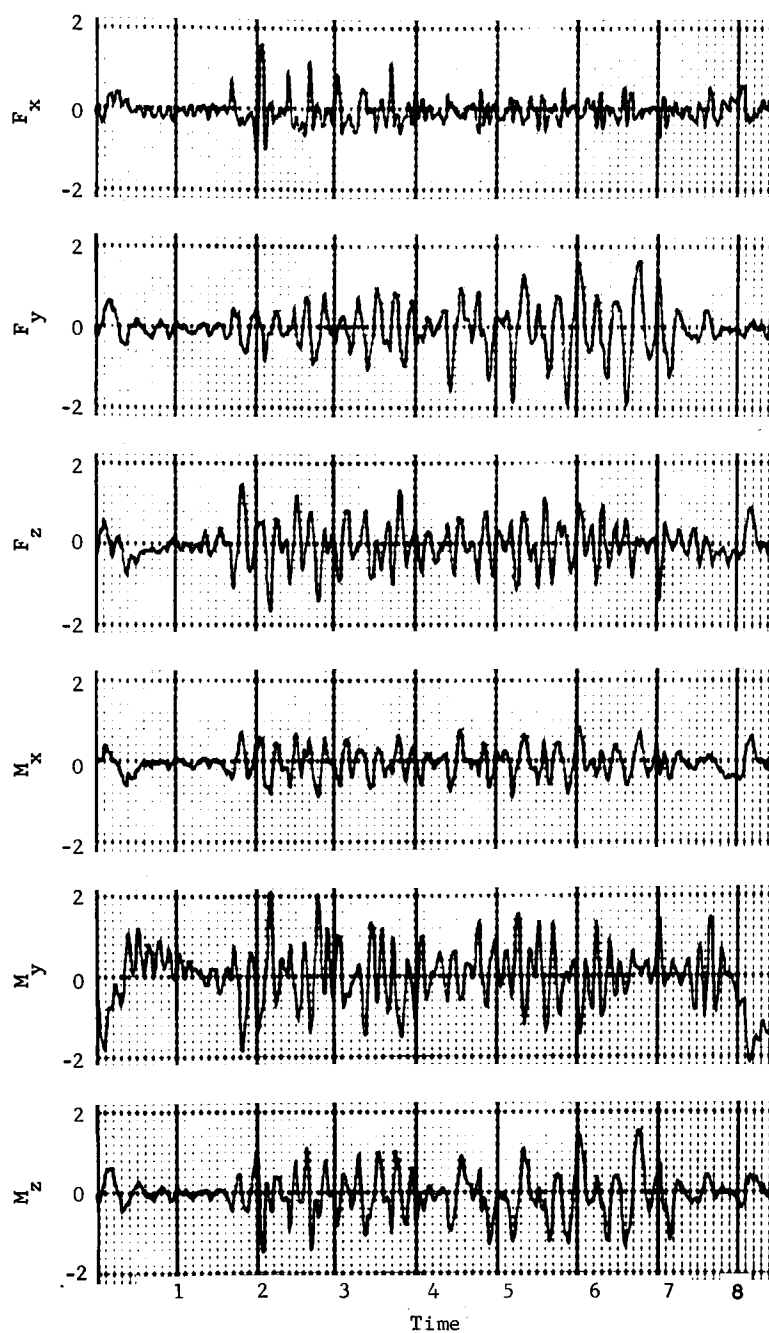


Figure A8.- Wrist Motion, Run 8

## APPENDIX A

Run 9, ankle motion.- For the ankle motion shown in figure A9, Subject 1 raised his lower leg slightly and held it while data were being taken (thus the c.g. shift moment is not seen). The subject first rotated his ankle several times about the pitch axis (man's y axis) and then several times about the **roll axis** (man's x axis). The pitch motion occurs between approximately 0 and 3 sec and the roll between 3 and 6 sec.

# APPENDIX A

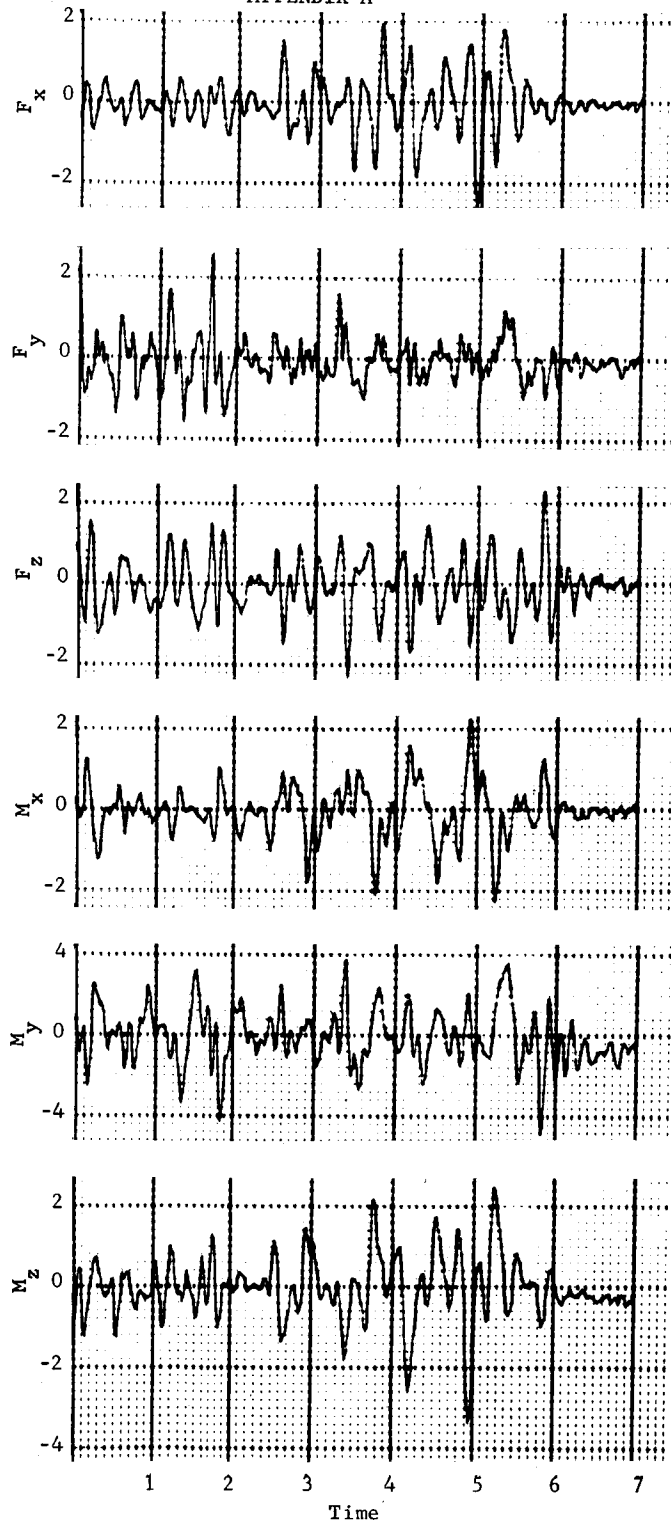


Figure A9.- Ankle Motion, Run 9

## APPENDIX A

Run 10, lower right arm, single pendulum, sagittal plane.-

As shown by the right arm angles in figure A13, this motion is approximately a  $100^\circ$  swing at the lower right arm in the sagittal plane. The motion is performed twice, once between 1.4 and 3.7 sec and once between 4.5 and 7.5 sec. The lower arm is raised between 1.4 and 2.5 sec and lowered between 2.5 and 3.7 sec. All other arm and leg angles are assumed constant throughout the run and were given the following values (average values obtained from LIMS data):

$\phi_3 = -1.15^\circ$	$\phi_6 = -50.88^\circ$	$\phi_7 = 38.16^\circ$
$\theta_3 = -16.22^\circ$	$\theta_6 = 43.72^\circ$	$\theta_7 = 47.61^\circ$
$\psi_3 = -40.51^\circ$	$\psi_6 = 72.00^\circ$	$\psi_7 = -63.26^\circ$
$\theta_5 = 41.85^\circ$	$\theta_8 = -80.64^\circ$	$\theta_6 = -83.61^\circ$

# APPENDIX A

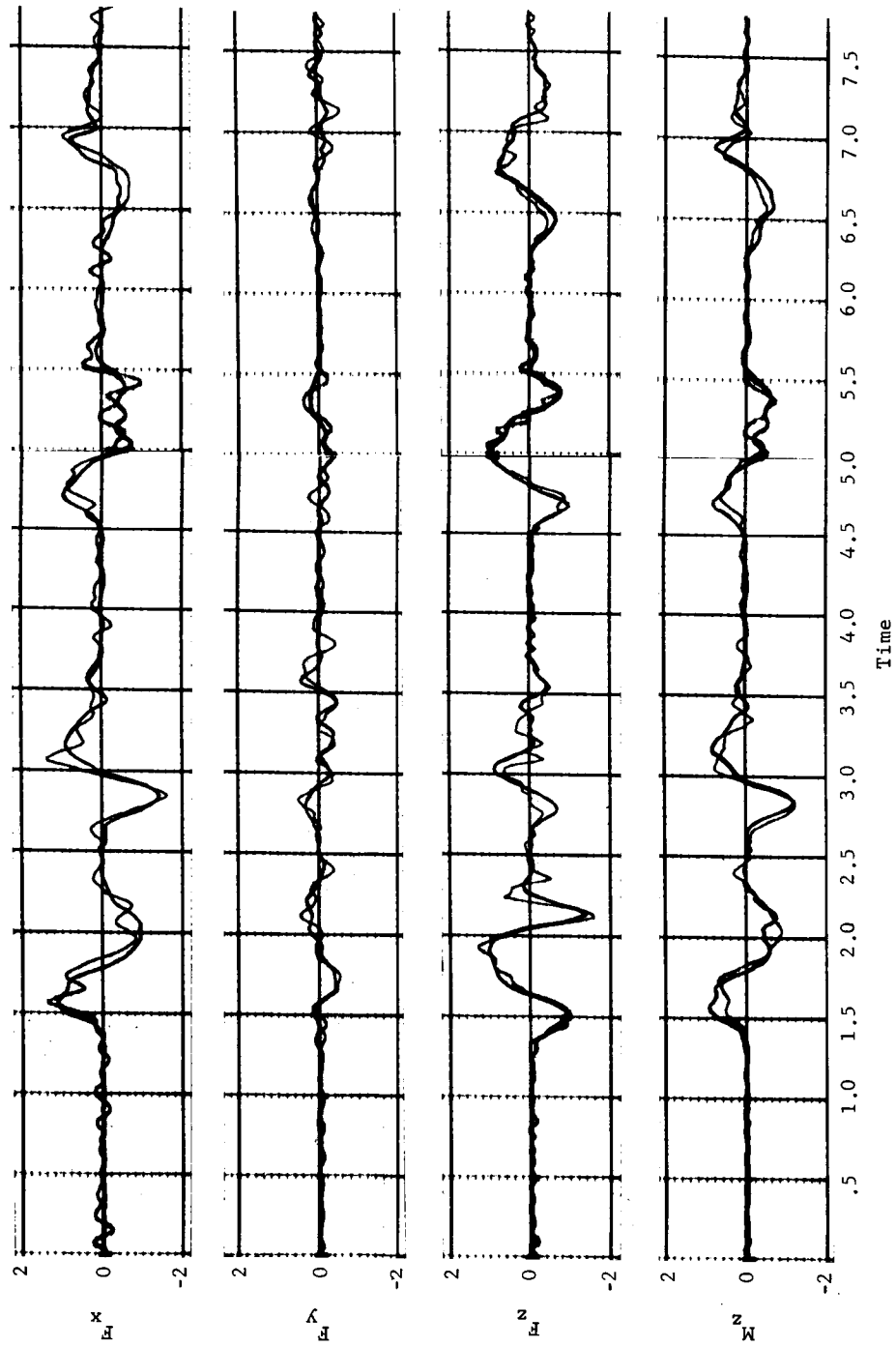


Figure A10.- Lower Right Arm, Single Pendulum, Sagittal Plane, Run 10

# APPENDIX A

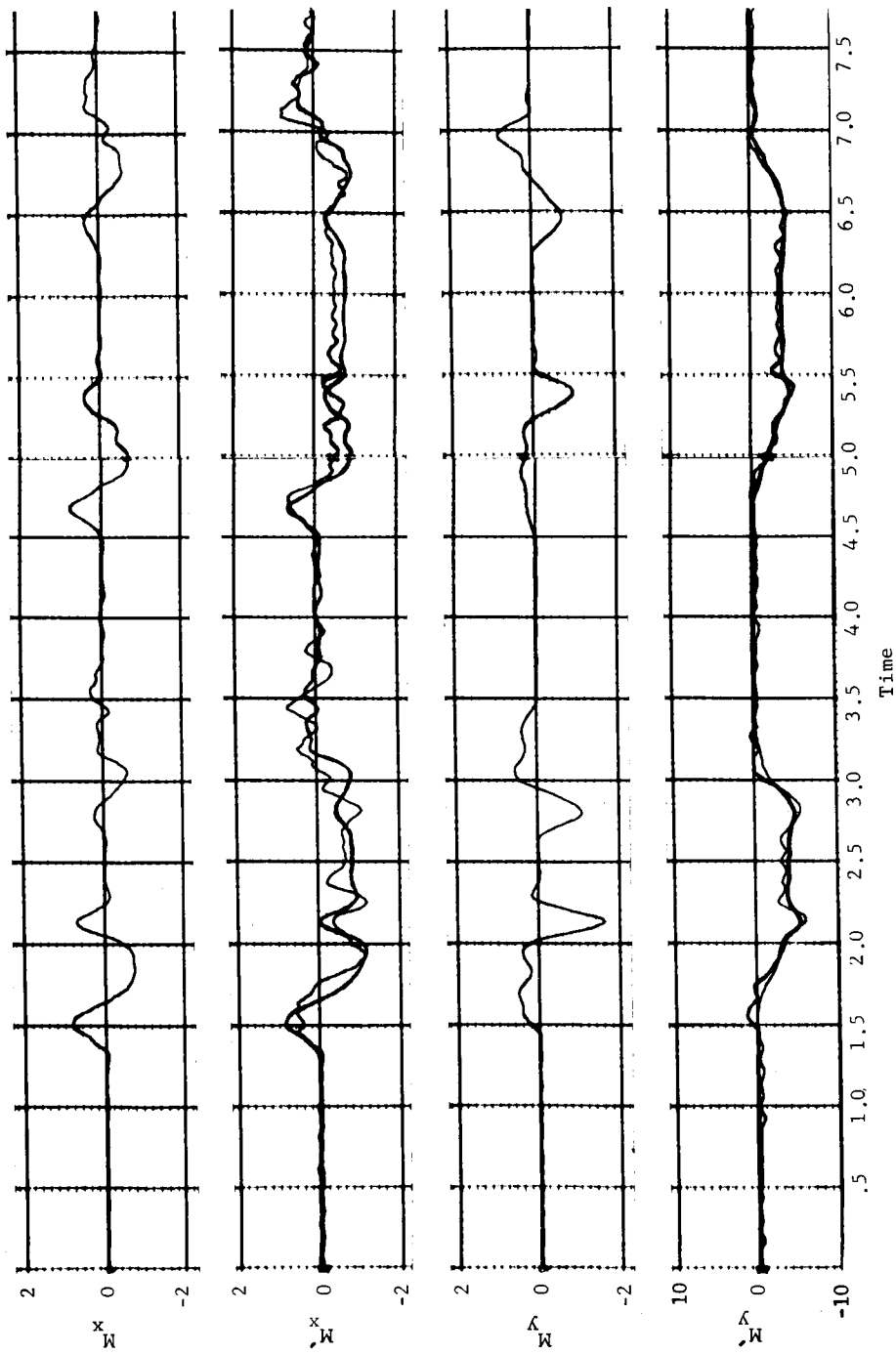


Figure All.- Lower Right Arm, Single Pendulum, Sagittal Plane, Run 10



# APPENDIX A

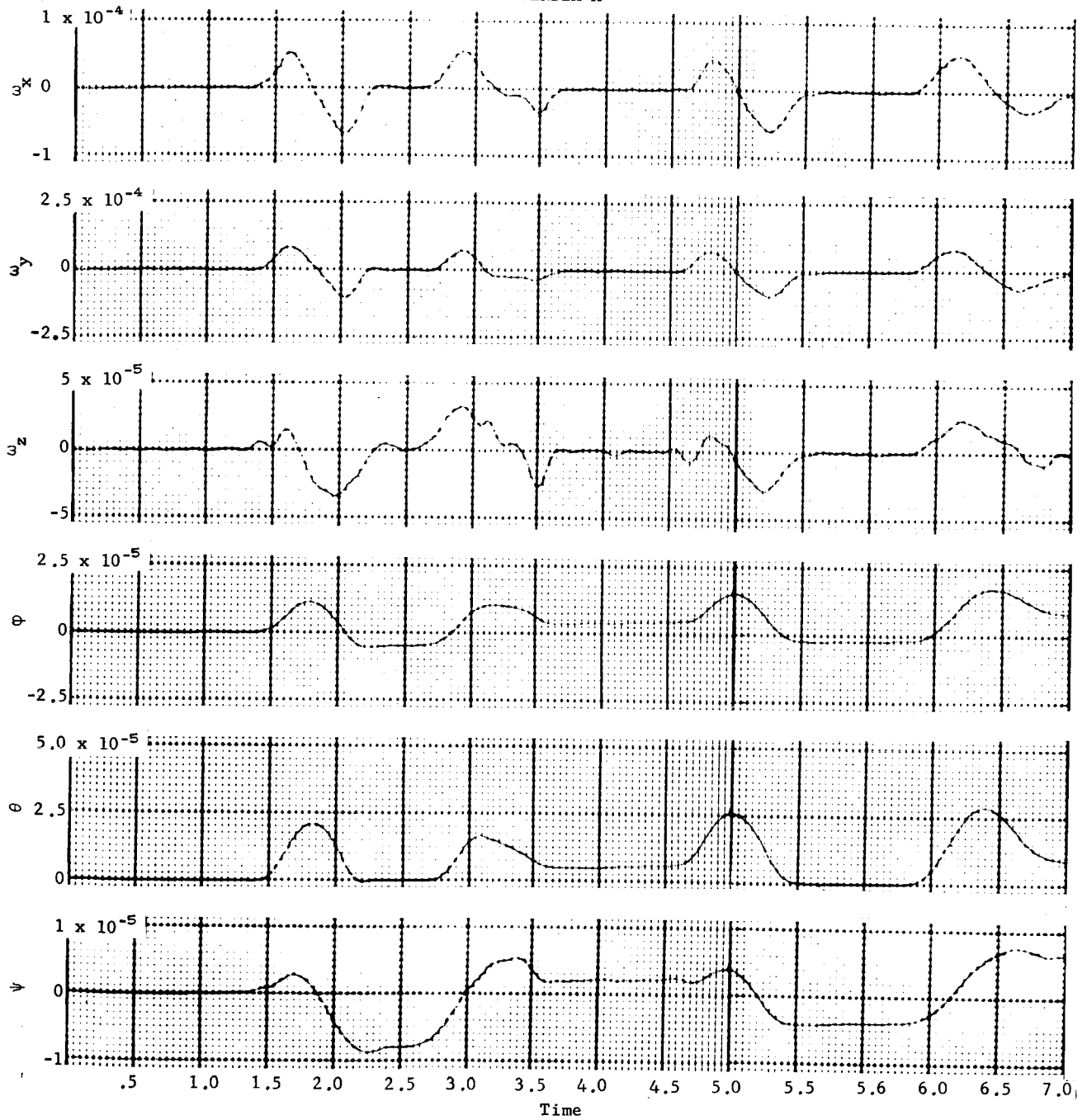


Figure A12.- Lower Right Arm, Single Pendulum, Sagittal Plane, Run 10

# APPENDIX A

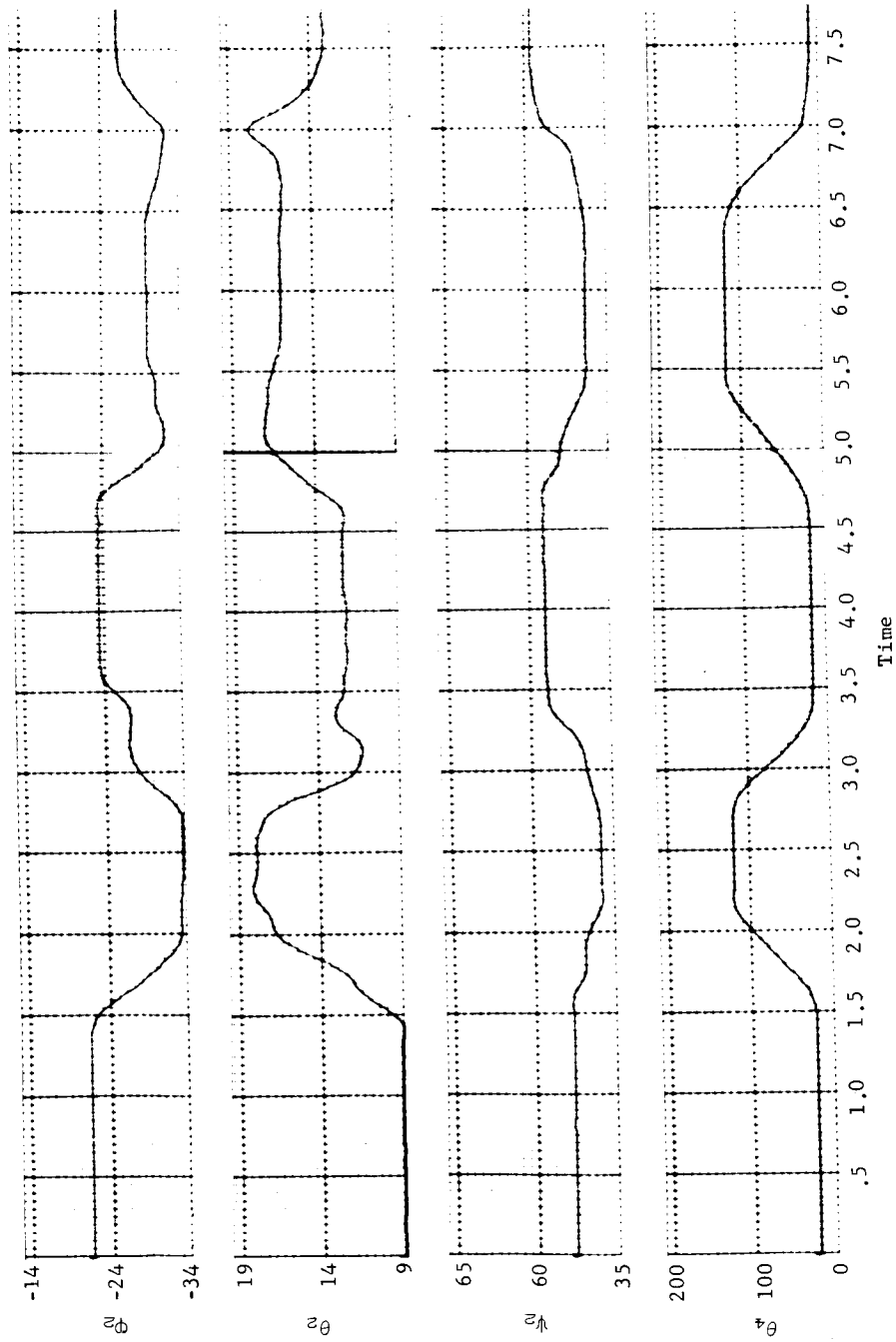


Figure A13.- Lower Right Arm, Single Pendulum, Sagittal Plane, Run 10

## APPENDIX A

### Run 11, total right arm, single pendulum, sagittal plane.-

This motion is approximately a  $90^\circ$  swing of the right arm in the sagittal plane (with little elbow bending). Resulting data are shown in figures A14 thru A17. The motion is performed twice, once between 0 and 4 sec and once between 5 and 8 sec. All other arm and leg angles are assumed constant and were given the same values as for Run 10.

# APPENDIX A

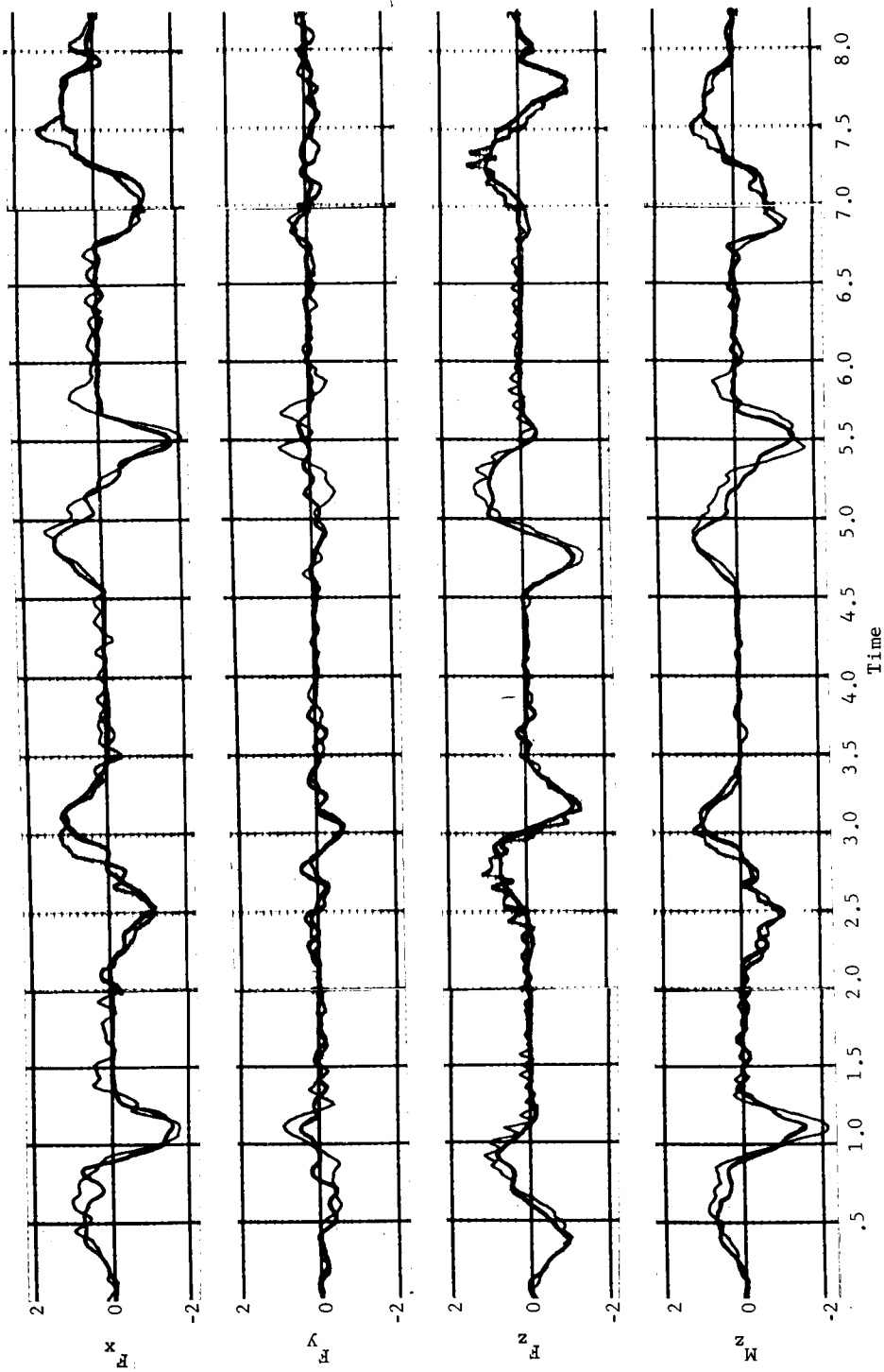


Figure A14.- Total Right Arm, Single Pendulum, Sagittal Plane, Run 11

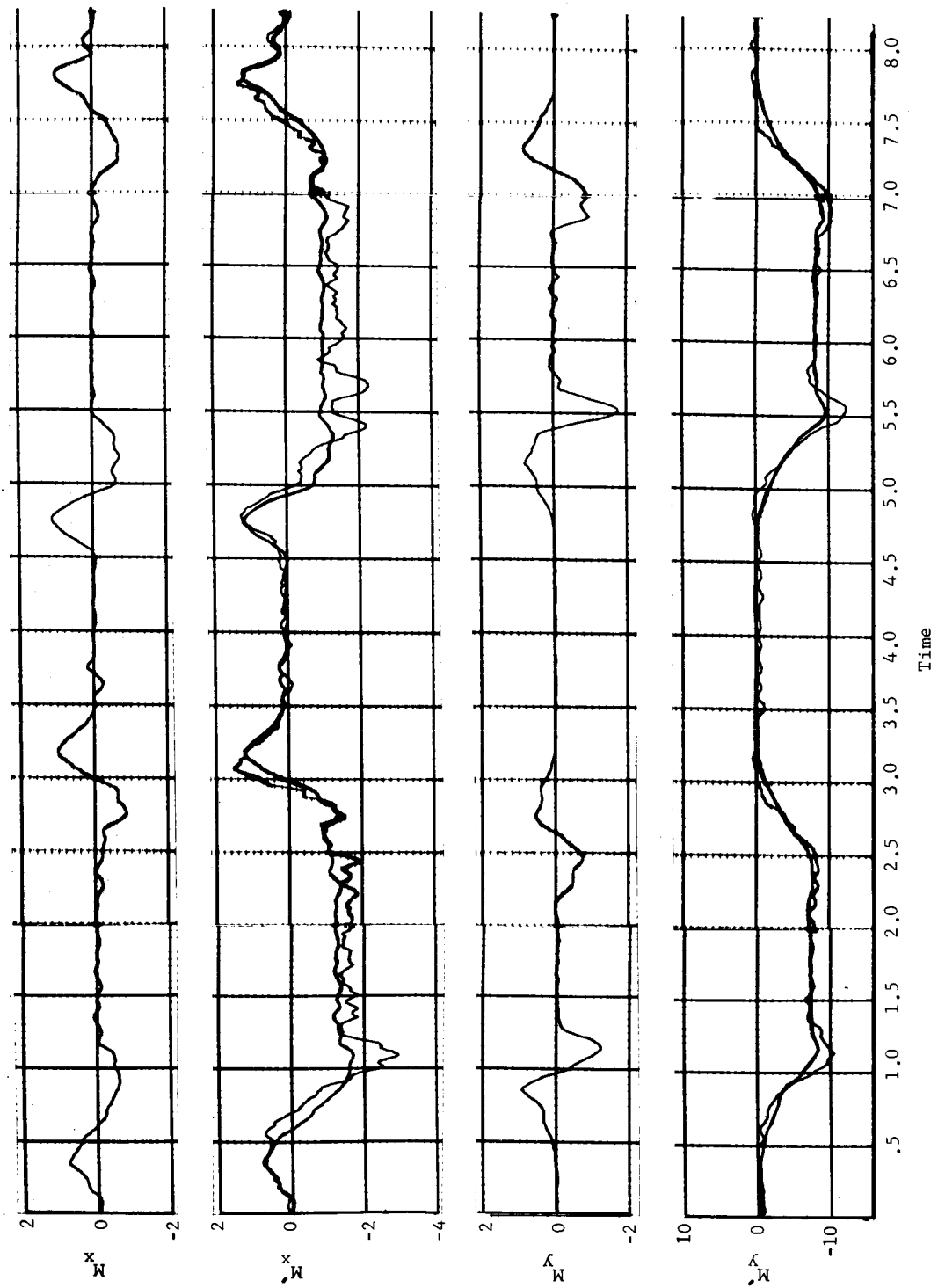


Figure A15-. Total Right Arm, Single Pendulum, Sagittal Plane, Run 11

# APPENDIX A

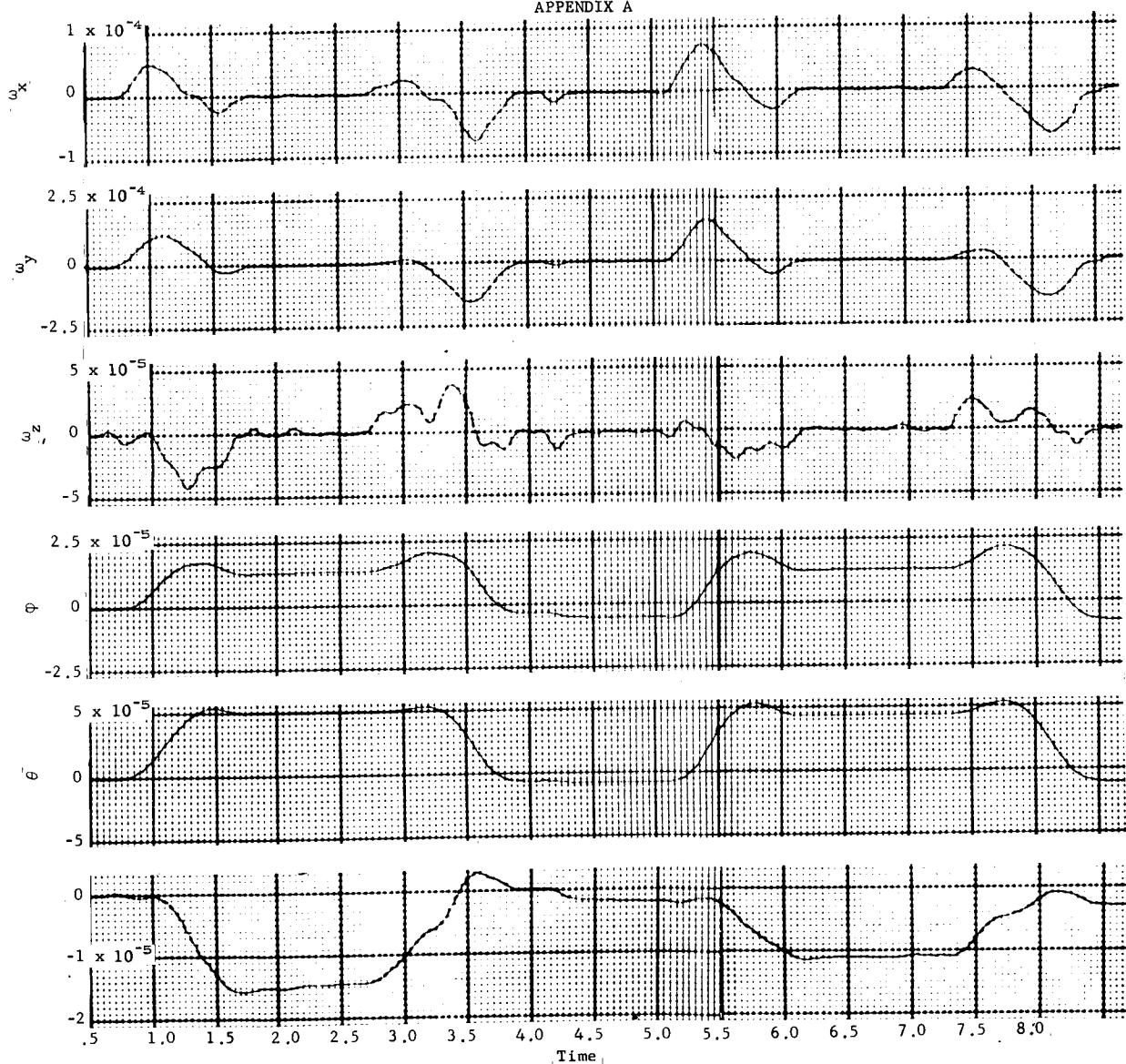


Figure A16.- Total Right Arm, Single Pendulum, Sagittal Plane, Run 11

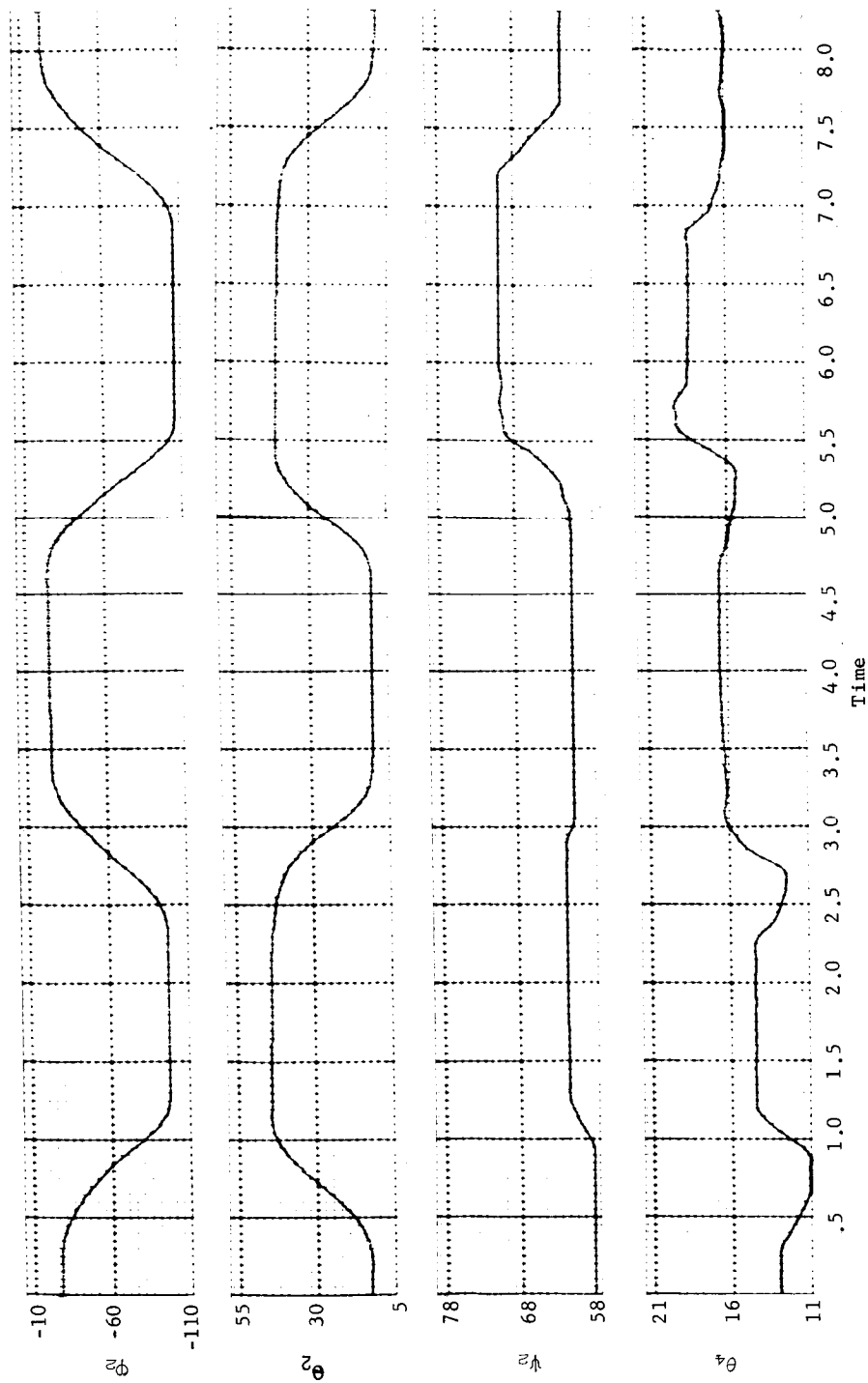


Figure A17.- Total Right Arm, Single Pendulum, Sagittal Plane, Run 11

## APPENDIX A

Run 12, total left arm, single pendulum, frontal plane.- This motion is approximately a  $90^\circ$  swing of the left arm in the frontal plane (with little elbow bending). Resulting data are shown in figures A18 thru A21. The subject raised his arm between 1 and 3 sec and lowered it between 3.3 and 5 sec. All other arm and leg angles are assumed constant throughout the run and were given the following values (average values obtained from LIMS data):

$\phi_2 = -2.38^\circ$	$\phi_6 = -50.20^\circ$	$\phi_7 = 38.16^\circ$
$\theta_2 = -18.55^\circ$	$\theta_6 = 43.24^\circ$	$\theta_7 = 47.23^\circ$
$\psi_2 = 27.16^\circ$	$\psi_6 = 71.32^\circ$	$\psi_7 = -63.16^\circ$
$\theta_4 = 39.84^\circ$	$\theta_8 = -80.54^\circ$	$\theta_9 = -83.42^\circ$

A large deviation in the calculated forces and moments is noted at about 1.7 sec. This is due to the sudden change in the angle  $\psi_3$  in figure A21. Apparently when the subject was performing this motion, the LIMS yaw ring (measuring  $\psi_3$ ) did not follow the motion properly and suddenly slipped into position at about 1.7 sec. This, of course, gives rise to forces not actually existing. Also, the slight consistent discrepancy between the load cell and calculated force  $F_x$  is caused by improperly removing the load cell bias.



# APPENDIX A

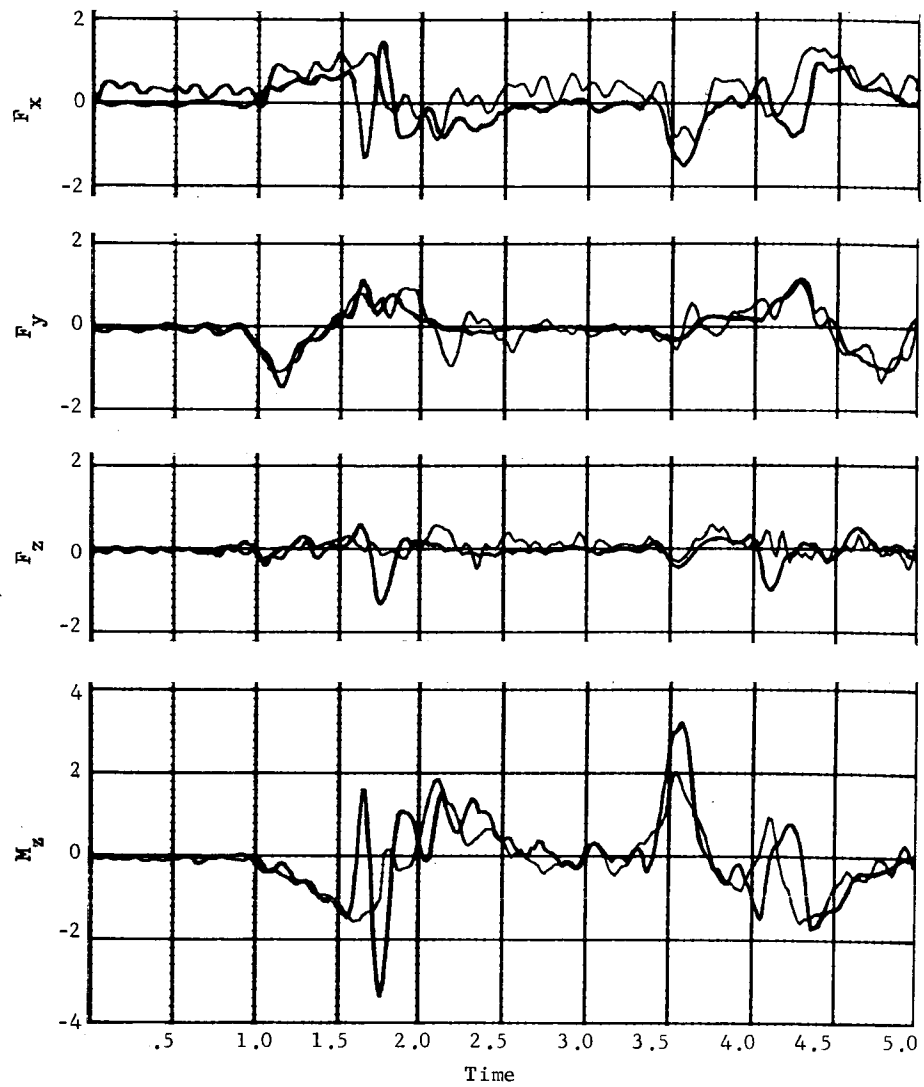


Figure A18.- Total Left Arm, Single Pendulum, Frontal Plane, Run 12

# APPENDIX A

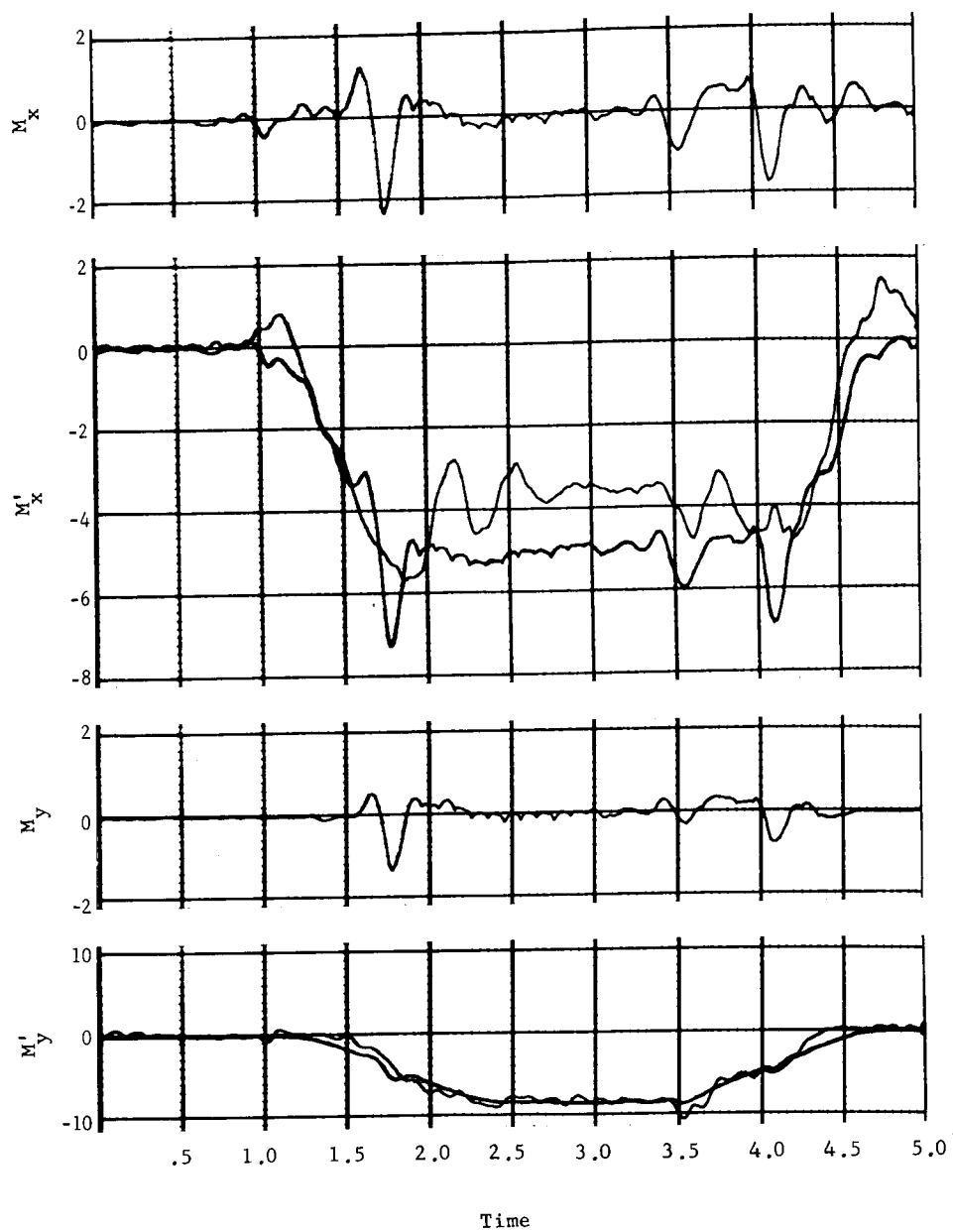


Figure A19.- Total Left Arm, Single Pendulum, Frontal Plane, Run 12

# APPENDIX A

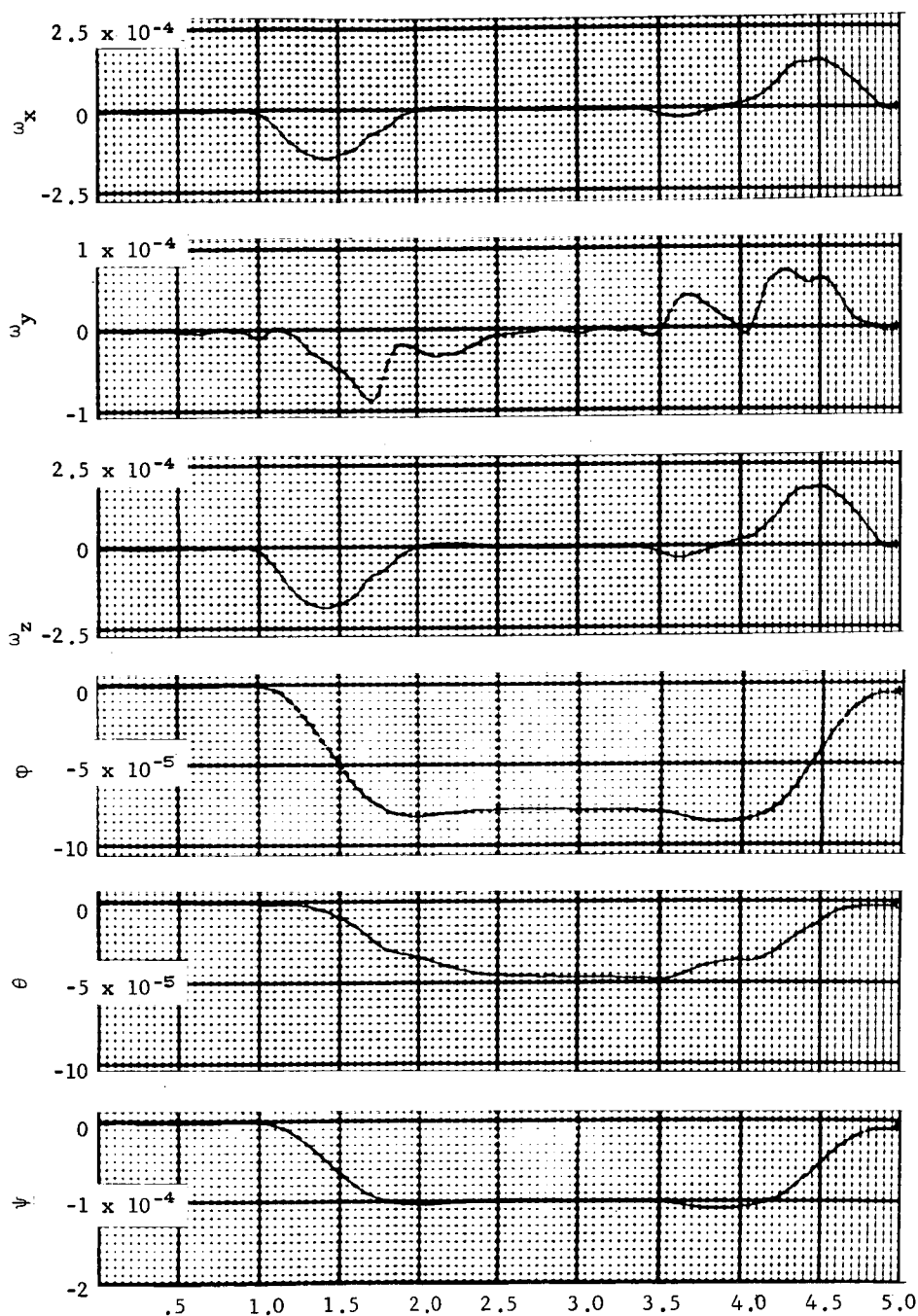


Figure A20.- Total Left Arm, Single Pendulum, Frontal Plane, Run 12

# APPENDIX A

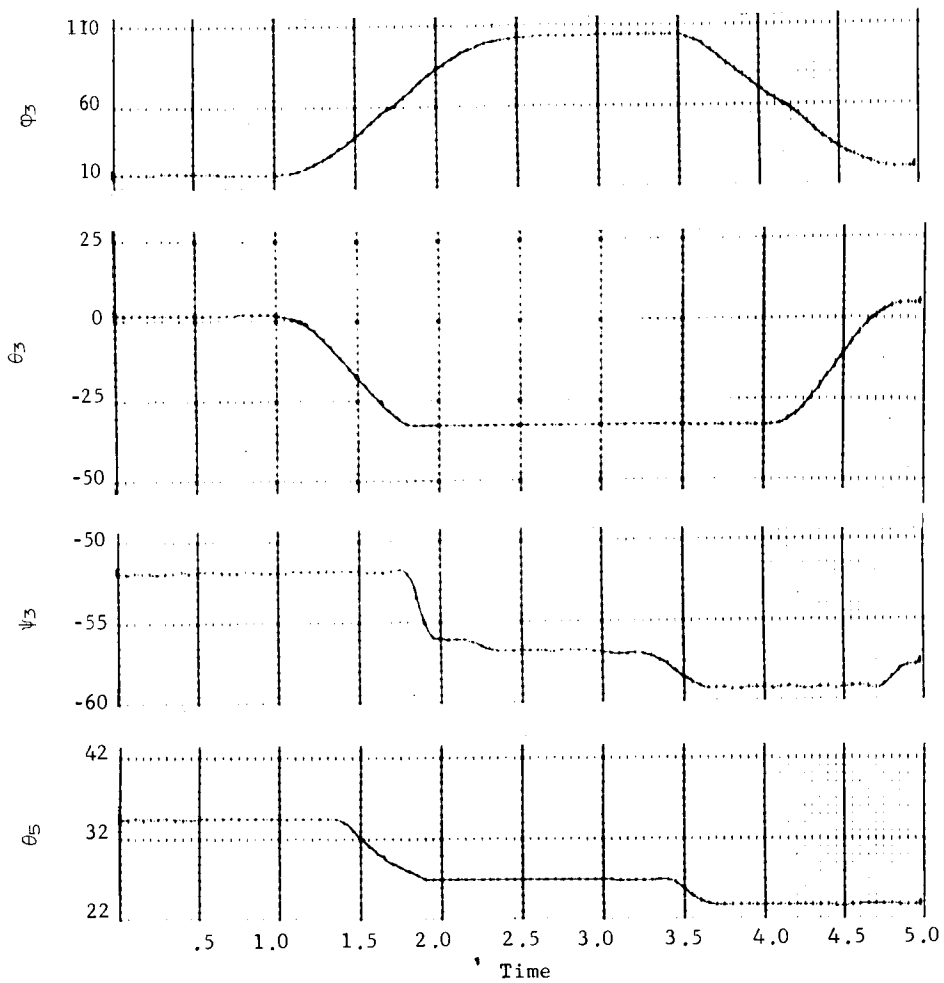


Figure A21.- Total Left Arm, Single Pendulum, Frontal Plane, Run 12

## APPENDIX A

### Run 13, total left arm, double pendulum, sagittal plane.-

This motion is approximately a 90° swing of the left upper arm and a 100° swing of the left lower arm in the sagittal plane. Resulting data are shown in figures A22 thru A25. The subject raised his arm between 0.8 and 2.5 sec and lowered it between 3 and 4.5 sec. Other arm and leg angles are the same as in Run 12. The moment discrepancy between load cell and calculated  $M'_x$  is caused by a slight inaccuracy in the measurement of the limb angles by LIMS. If the arm were raised exactly in the sagittal plane, there would be no moment about x from c.g. shift. The load cell results show that the arm was raised slightly to the outside (towards minus S/C y axis) of the sagittal plane giving a small c.g. shift moment about x. The calculated results show that the LIMS positions the arm slightly closer to the sagittal plane.

# APPENDIX A

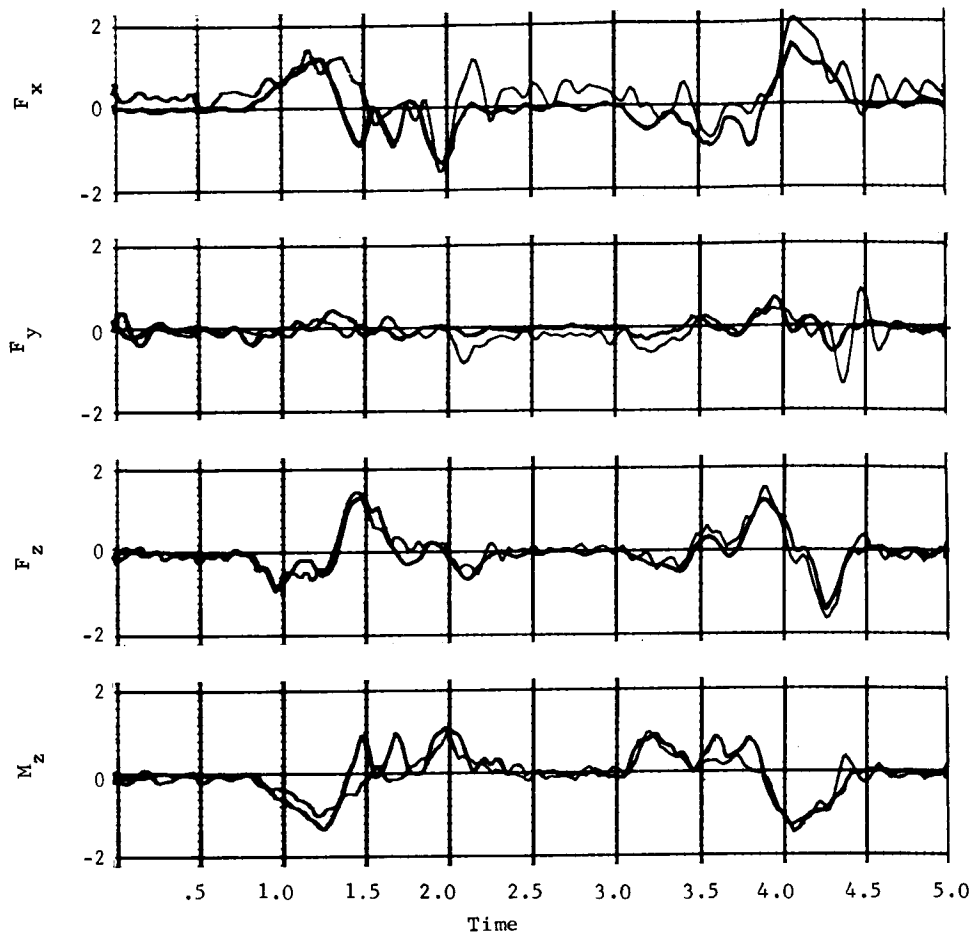


Figure A22.- Total Left Arm, Double Pendulum, Sagittal Plane, Run 13

# APPENDIX A

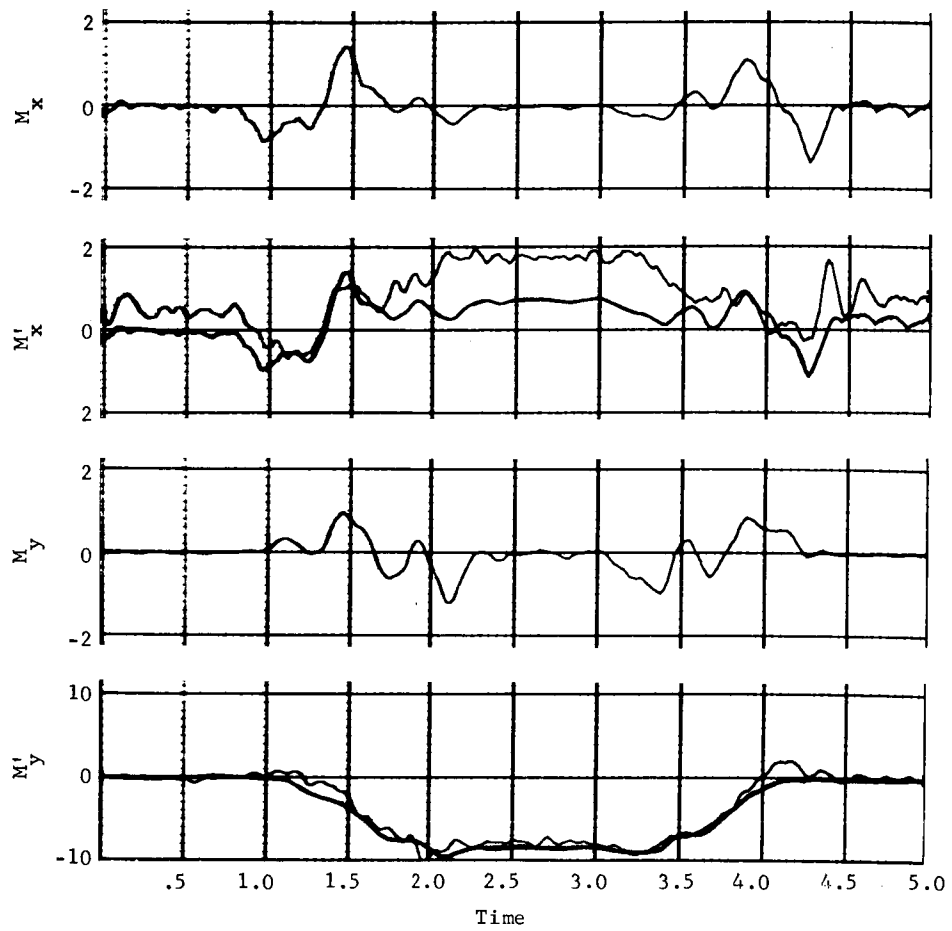


Figure A23.- Total Left Arm, Double Pendulum, Sagittal Plane, Run 13

# APPENDIX A

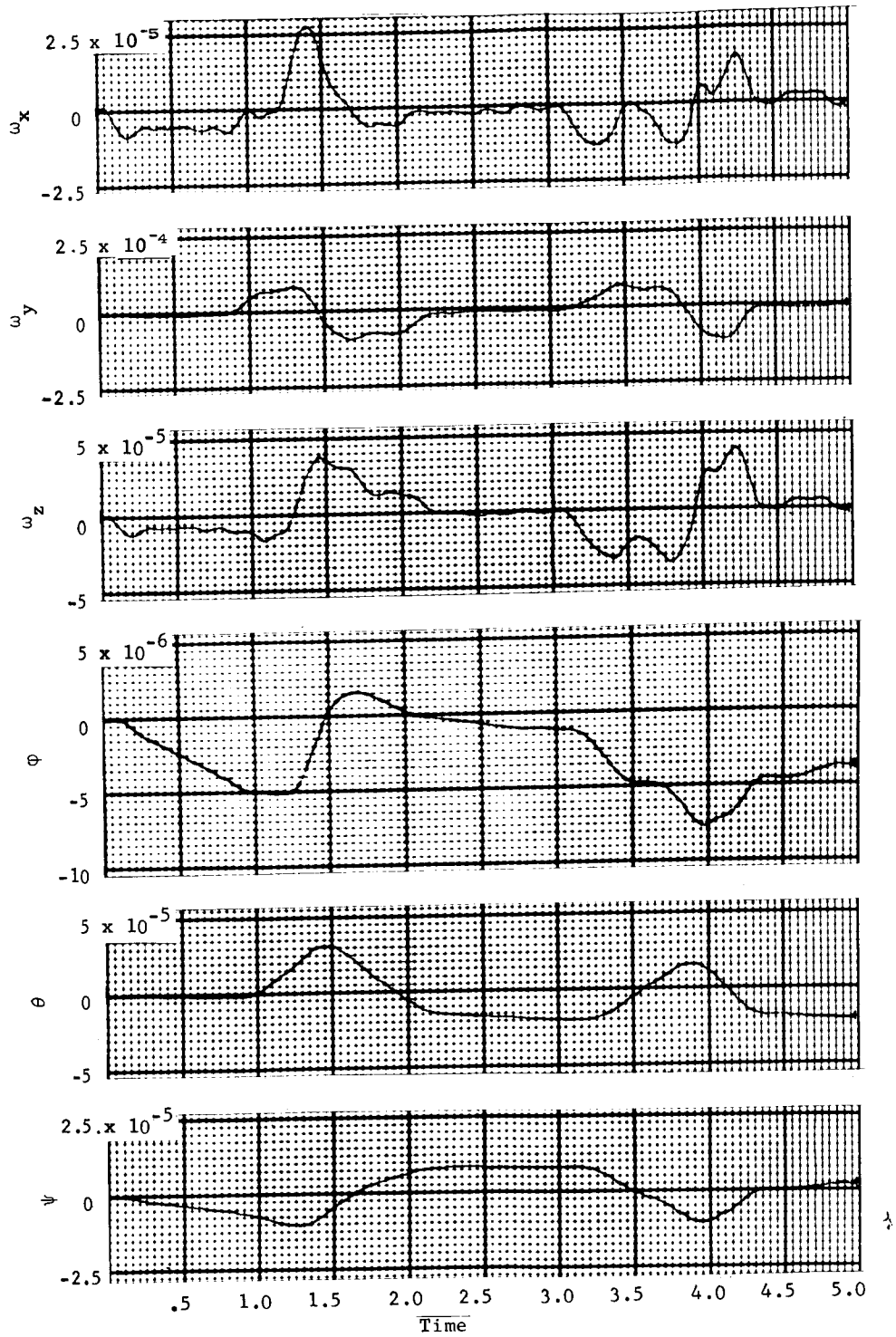


Figure A24.- Total Left Arm, Double Pendulum, Sagittal Plane, Run 13



# APPENDIX A

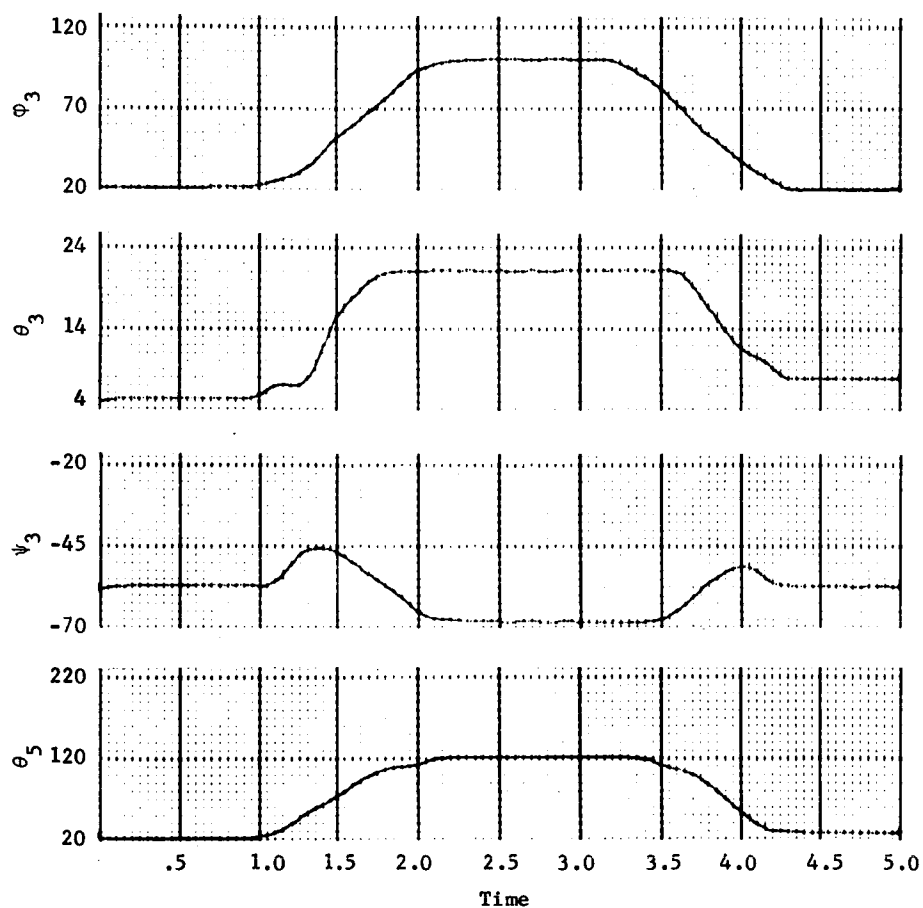


Figure A25.- Total Left Arm, Double Pendulum, Sagittal Plane, Run 13

## APPENDIX A

Run 14, total left arm, double pendulum, sagittal plane.-  
This run is a repeat of Run 13 with the same constant arm and leg angle as Run 12. Note that the results shown in figures A26 thru A29 are very similar.

# APPENDIX A

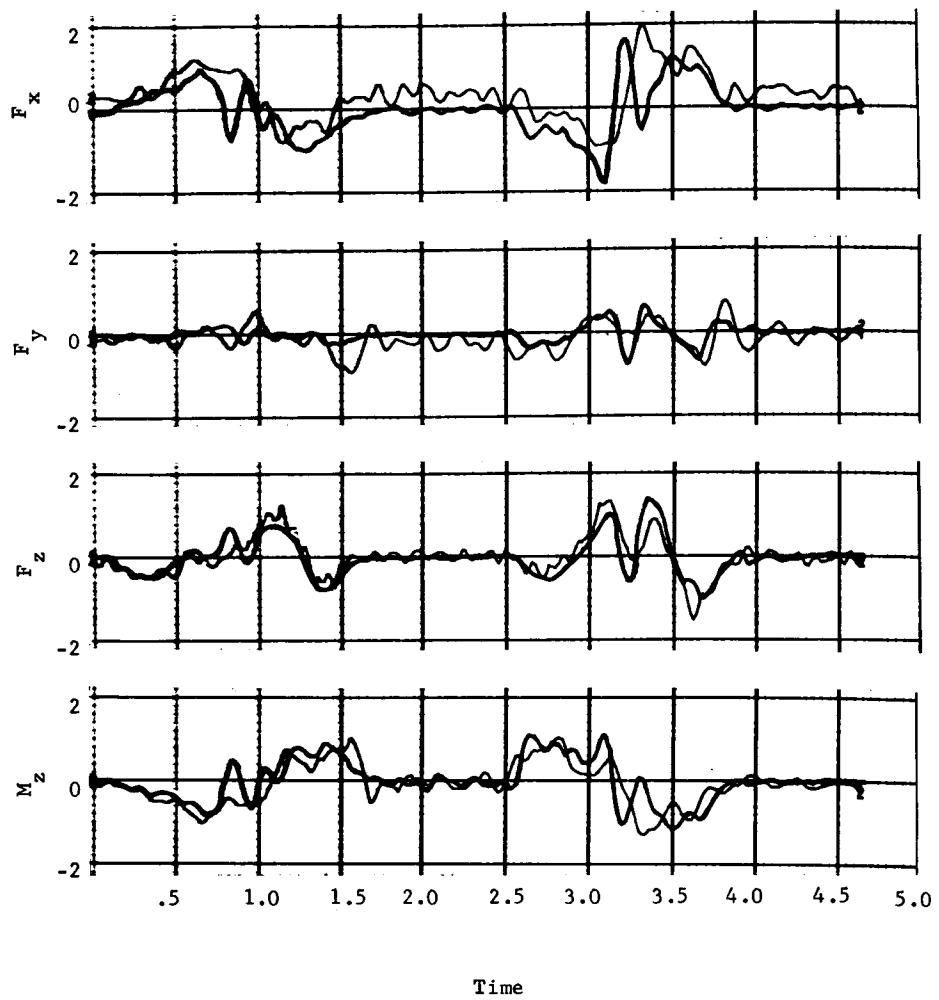


Figure A26.- Total Left Arm, Double Pendulum, Sagittal Plan, Run 14

# APPENDIX A

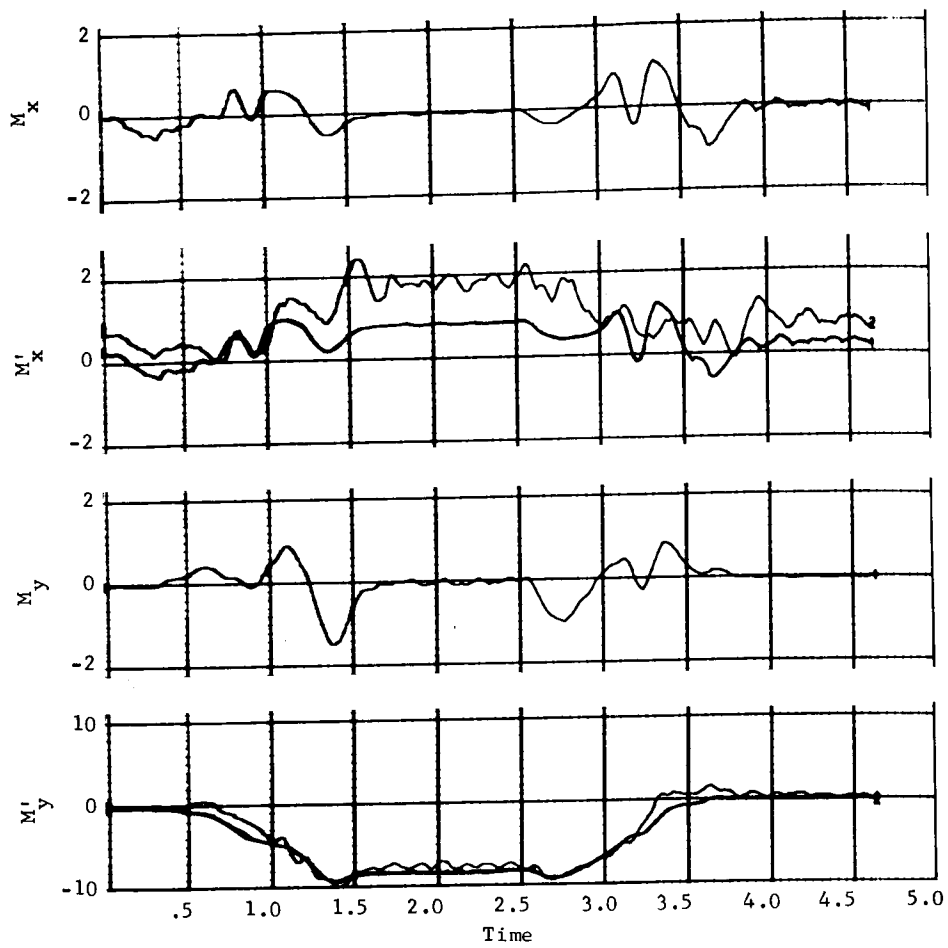


Figure A27.- Total Left Arm, Double Pendulum, Sagittal Plane, Run 14

# APPENDIX A

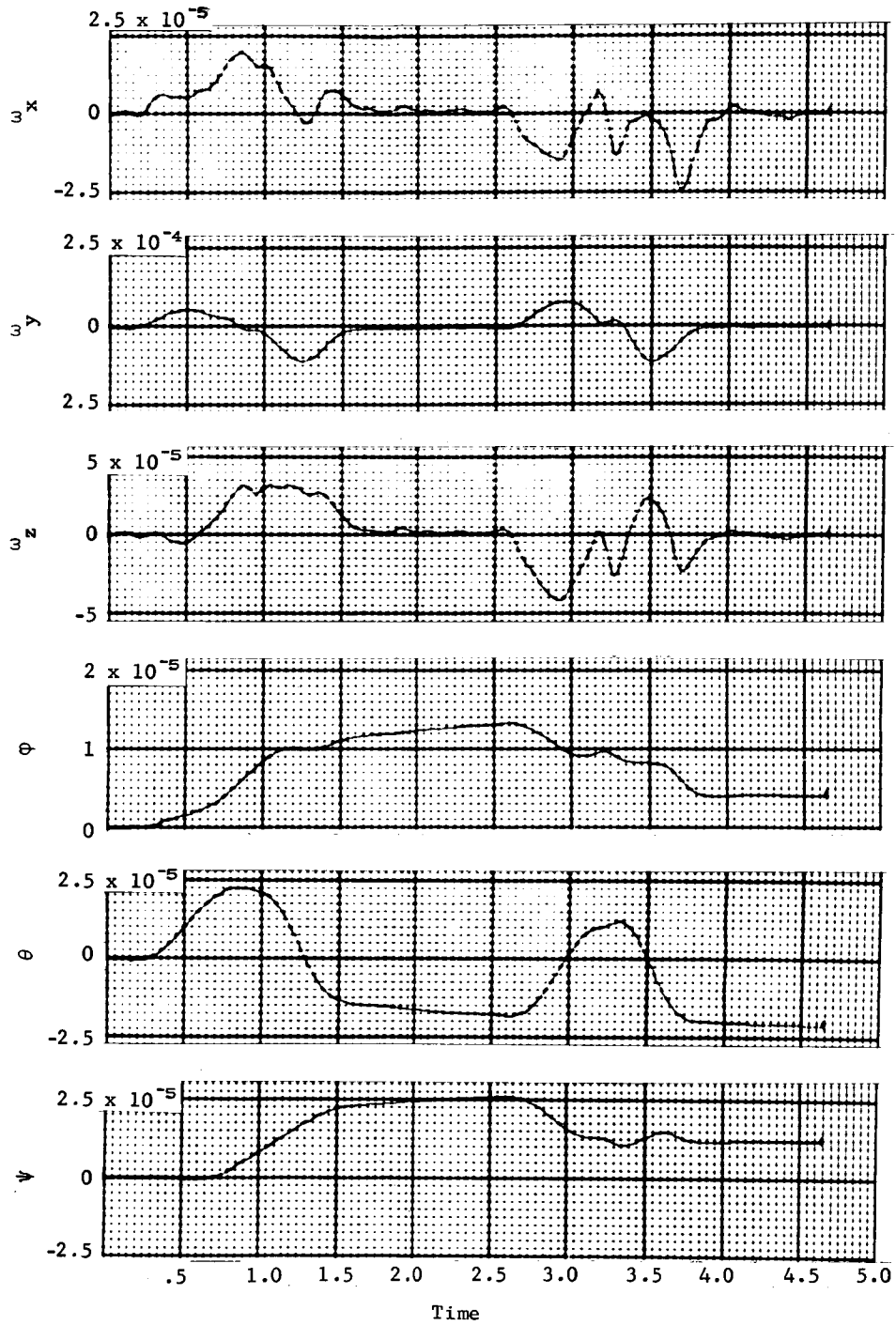


Figure A28,- Total Left Arm, Double Pendulum, Sagittal Plane, Run 14

# APPENDIX A

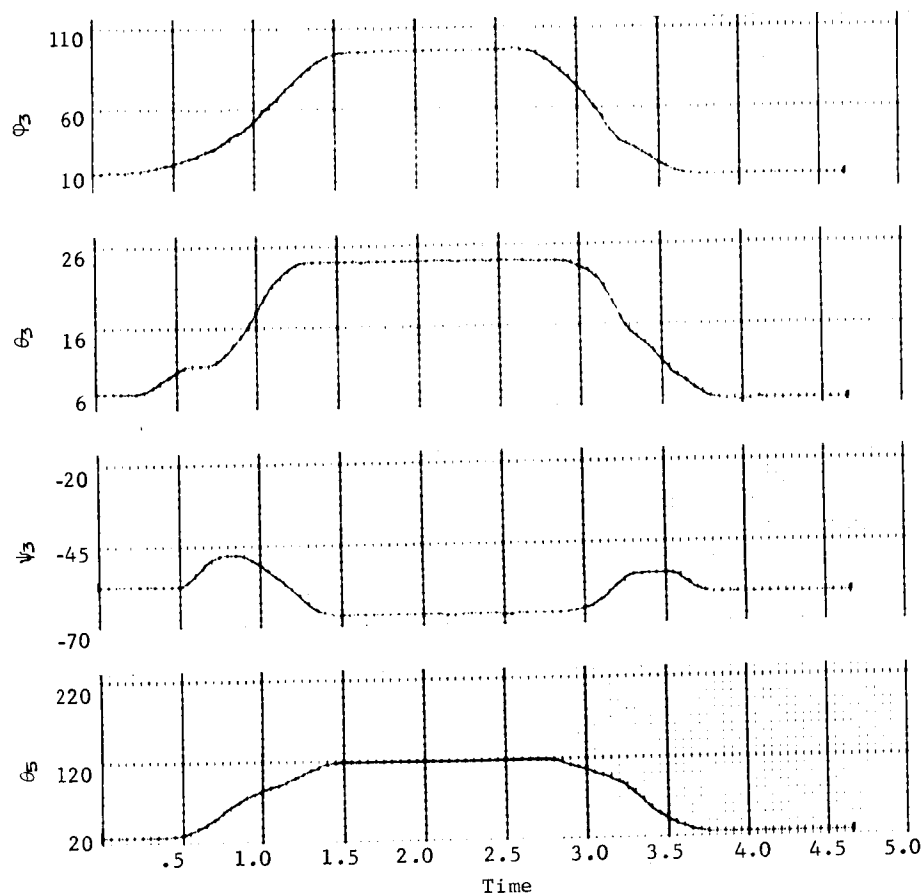


Figure A29.- Total Left Arm, Double Pendulum, Sagittal Plane, Run 14

## APPENDIX A

### Run 15, lower right leg, single pendulum, sagittal plane.-

This motion is approximately a  $60^\circ$  swing of the lower right leg in the sagittal plane. Resulting data are shown in figures A30 thru A33. The lower leg is raised between 1 and 2.5 sec and lowered between 2.5 and 4 sec. All other arm and leg angles are assumed constant and given the following values (average values obtained from LIMS data):

$\phi_2 = -4.34^\circ$	$\phi_3 = 0.57^\circ$	$\phi_7 = 42.51^\circ$
$\theta_2 = -17.95^\circ$	$\theta_3 = -17.20^\circ$	$\theta_7 = 33.28^\circ$
$\psi_2 = 27.02^\circ$	$\psi_3 = -42.24^\circ$	$\psi_7 = -66.91^\circ$
$\theta_4 = 36.09^\circ$	$\theta_5 = 42.38^\circ$	$\theta_9 = -56.53^\circ$

It is apparent from these results that the leg LIMS potentiometers are somewhat noisier than the arm potentiometers and were not satisfactorily smoothed by the smoothing routine. This gives rise to the higher frequency fluctuations shown in the calculated results. The mismatch in the c.g. shift moments  $\left(\begin{smallmatrix} M \\ x \end{smallmatrix}\right)$  are caused by slight inaccuracies in LIMS angular positions and are discussed under Run 13.

# APPENDIX A

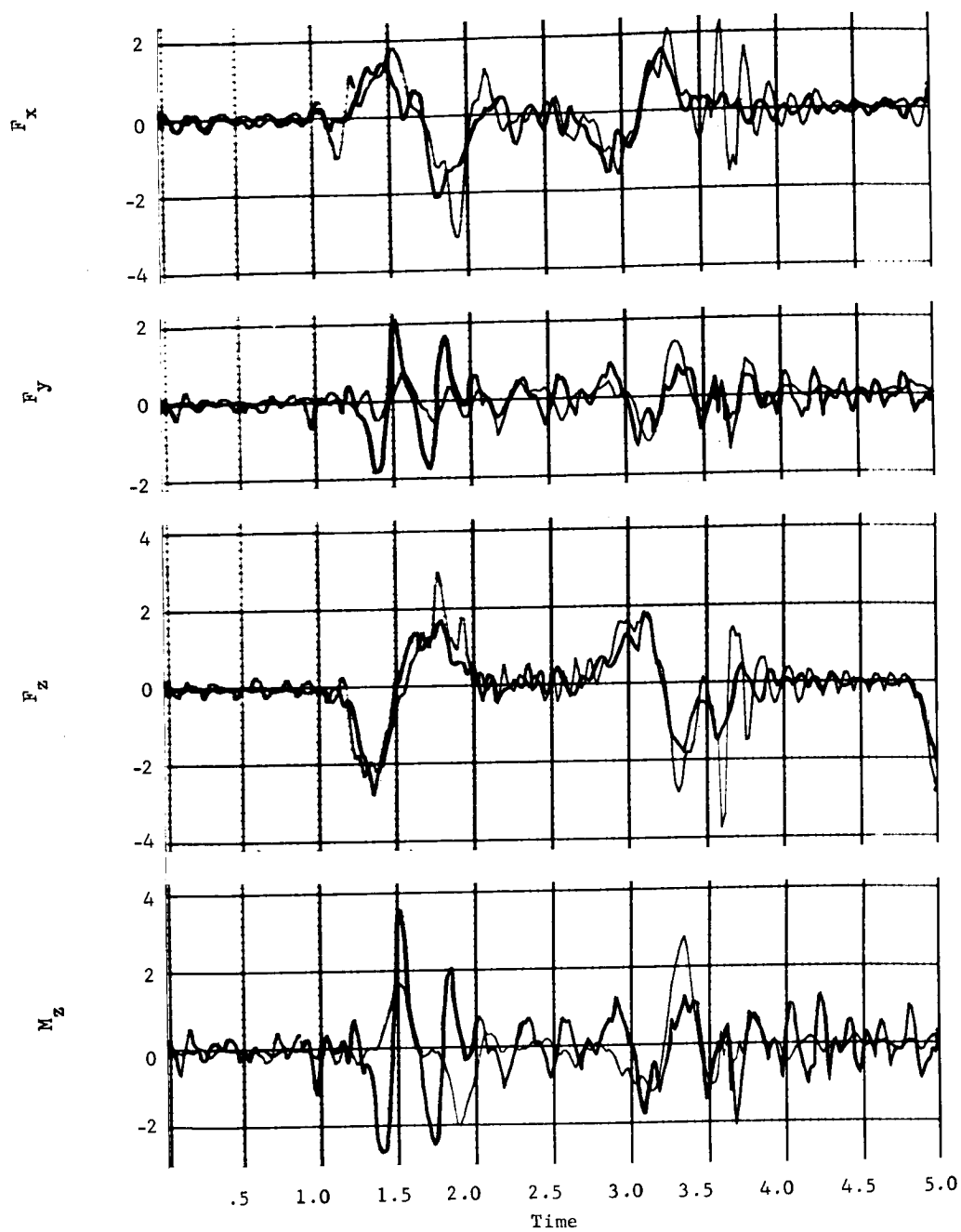


Figure A30.- Lower Right Leg, Single Pendulum, Sagittal Plane,  
Run 15



# APPENDIX A

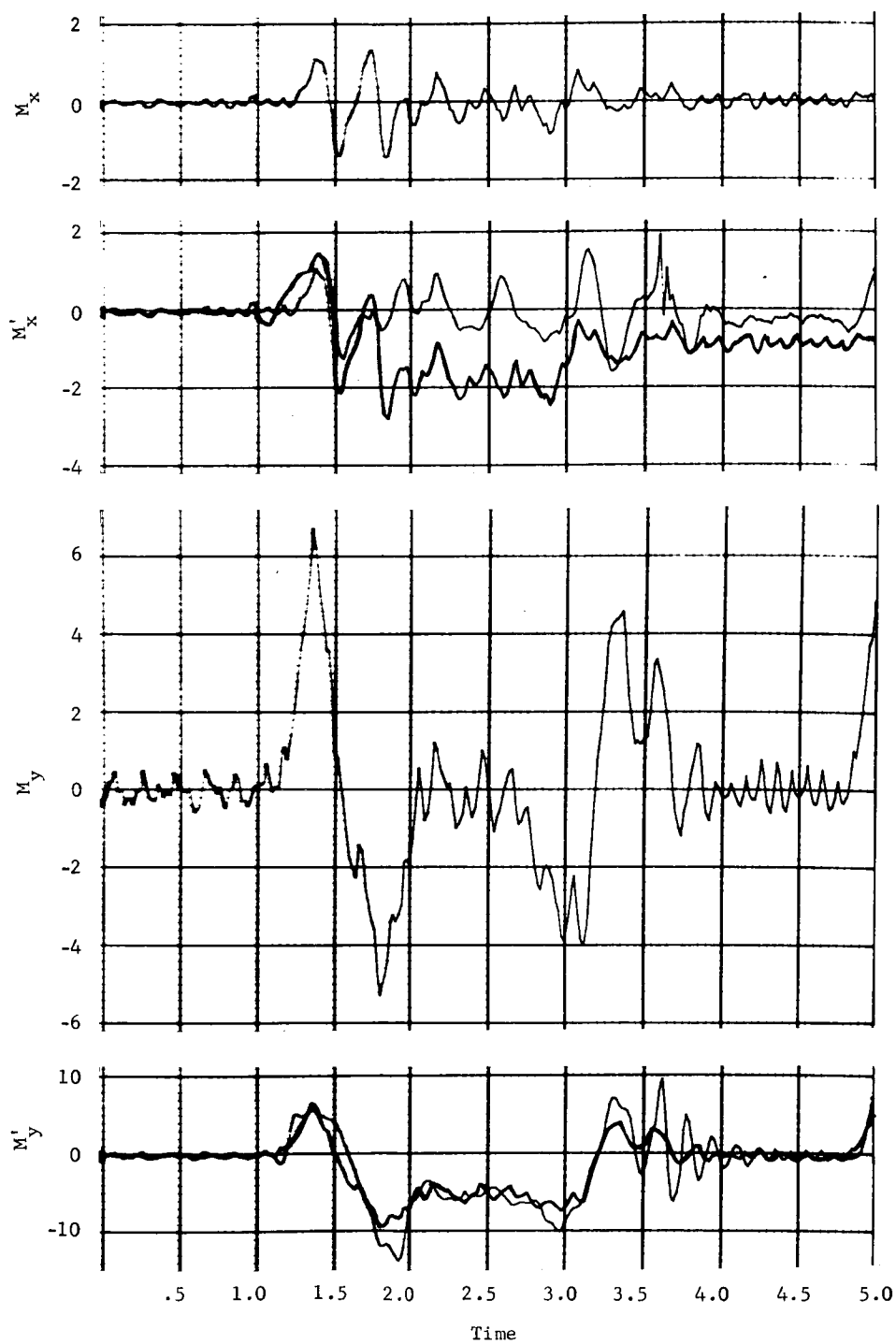


Figure A31.- Lower Right Leg, Single Pendulum, Sagittal Plane,  
Run 15

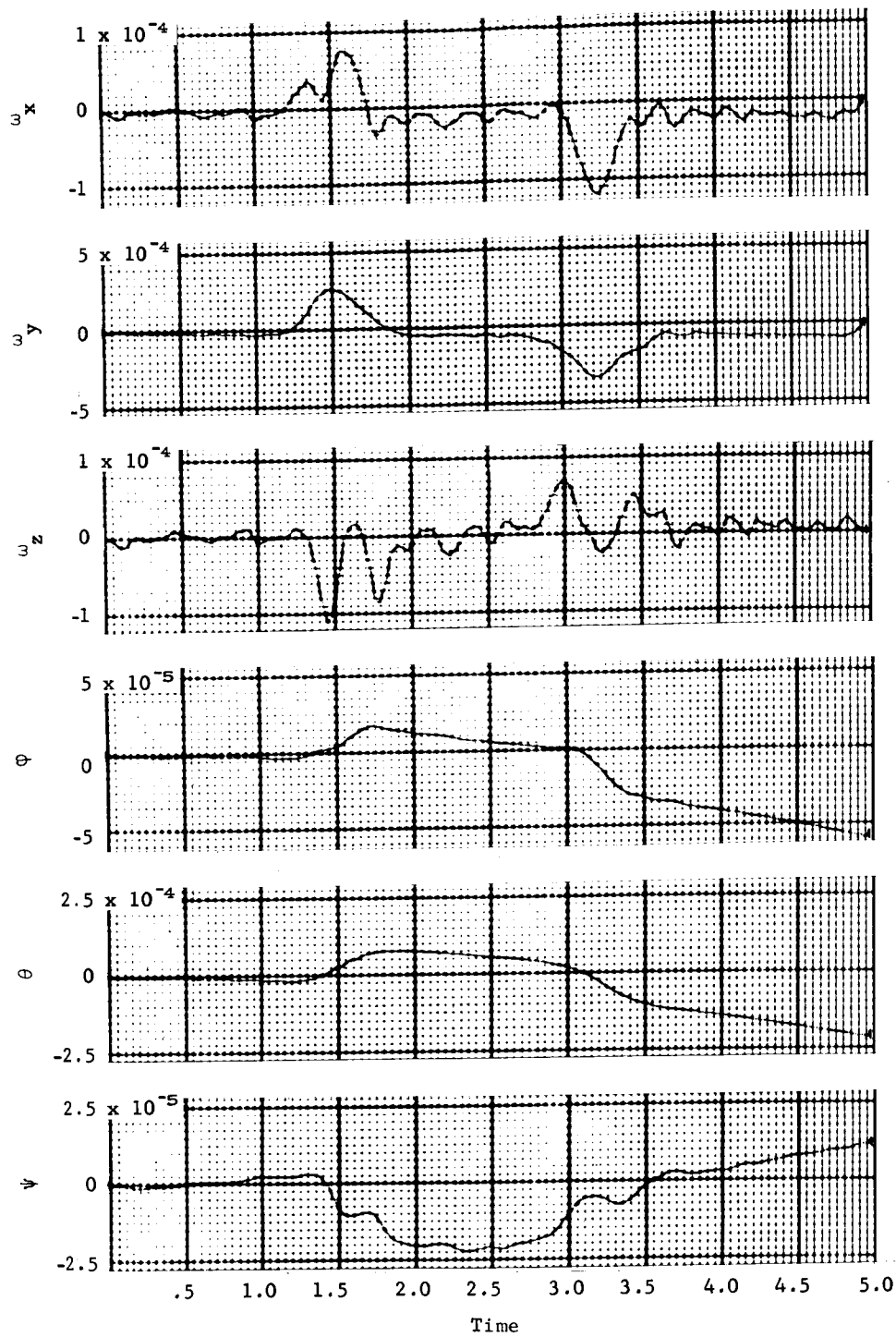


Figure A32.- Lower Right Leg, Single Pendulum, Sagittal Plane,  
Run 15

# APPENDIX A

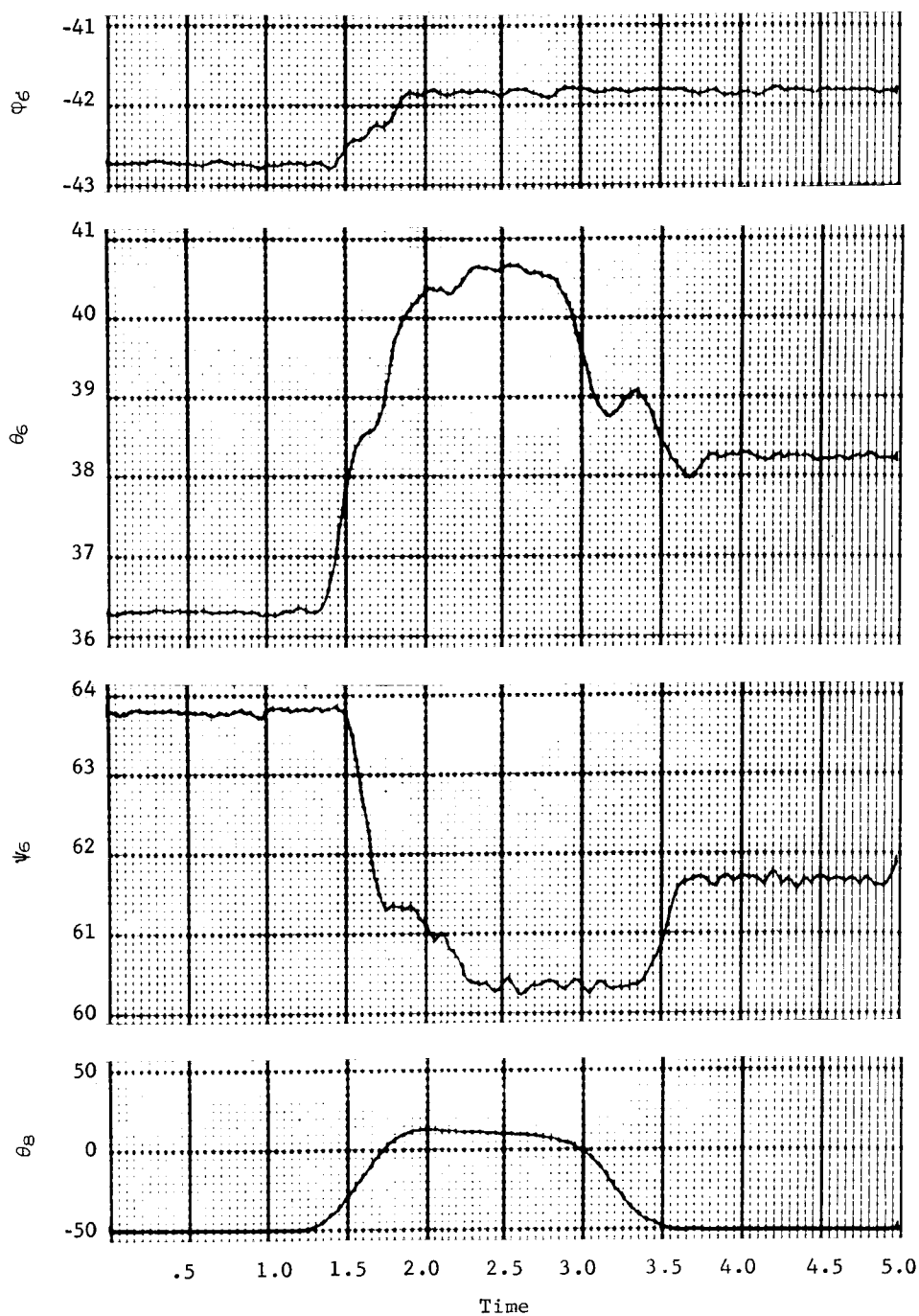


Figure A33.- Lower Right Leg, Single Pendulum, Sagittal Plane,  
Run 15

## APPENDIX A

### Run 16, total right leg, single pendulum, sagittal plane.-

This motion is approximately a 30° swing of the right leg in the sagittal plane (with little knee bending). Resulting data are shown in figures A34 thru A37. The leg is raised between 1.5 and 2.5 sec and lowered between 2.5 and 4 sec. The forces and moments existing between 0 and 1 sec are a result of raising the lower leg from the normal couch position (of approximately -50°) to about 0°. All other LIMS angles are the same as in Run 15.

The force and moment fluctuation caused by inadequate smoothing of LIMS angles is again apparent as in Run 15. Also, the load cell bias in  $M'_x$  has not been removed properly. Other discrepancies are primarily caused by torso shifting, which becomes a significant factor for leg motions. Sufficient torso shifting can occur to appreciably move the combined c.g. giving rise to large load cell c.g. shift moments. This is particularly apparent in the moment  $M'_y$ .

# APPENDIX A

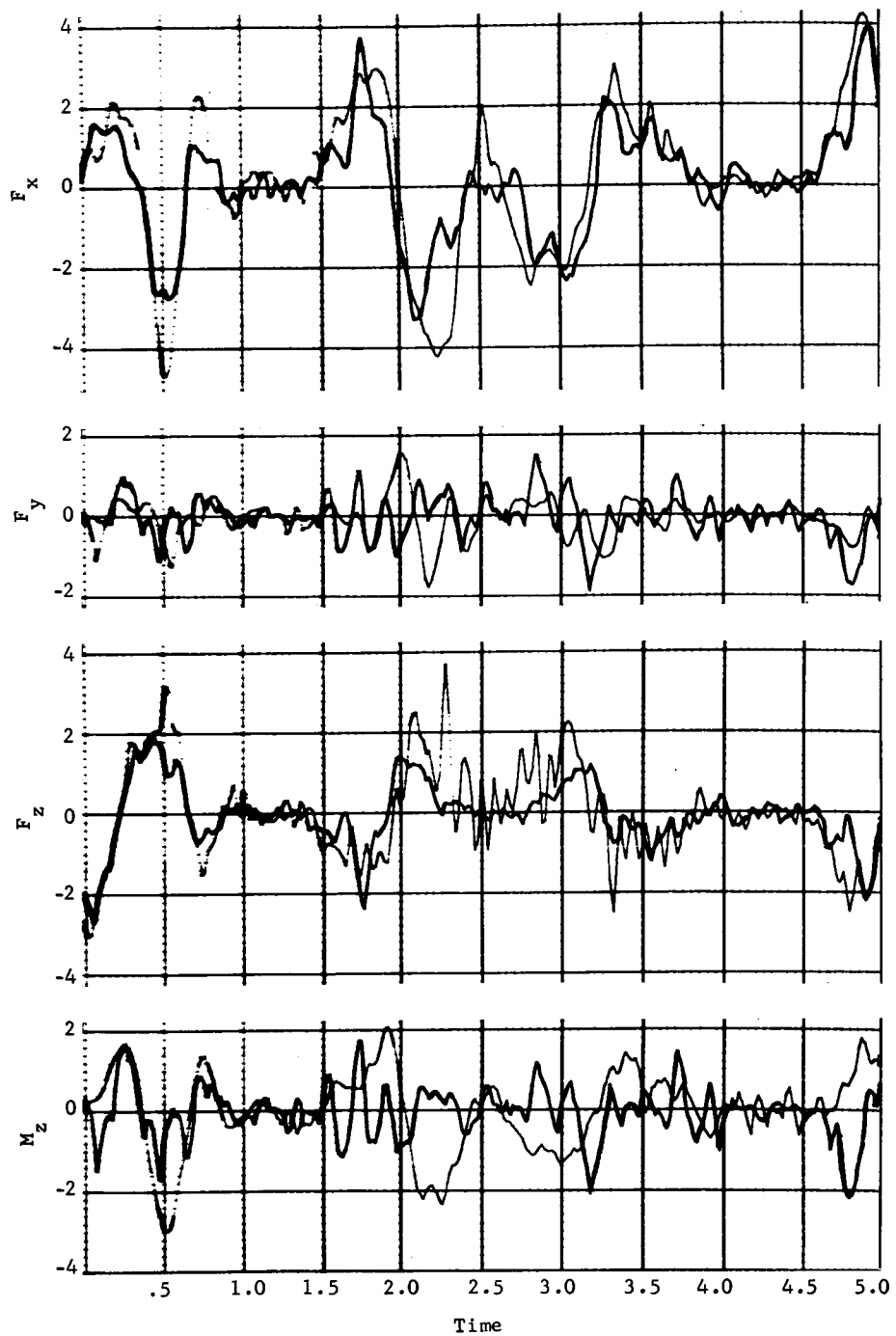


Figure A34.- Total Right Leg, Single Pendulum, Sagittal Plane, Run 16

# APPENDIX A

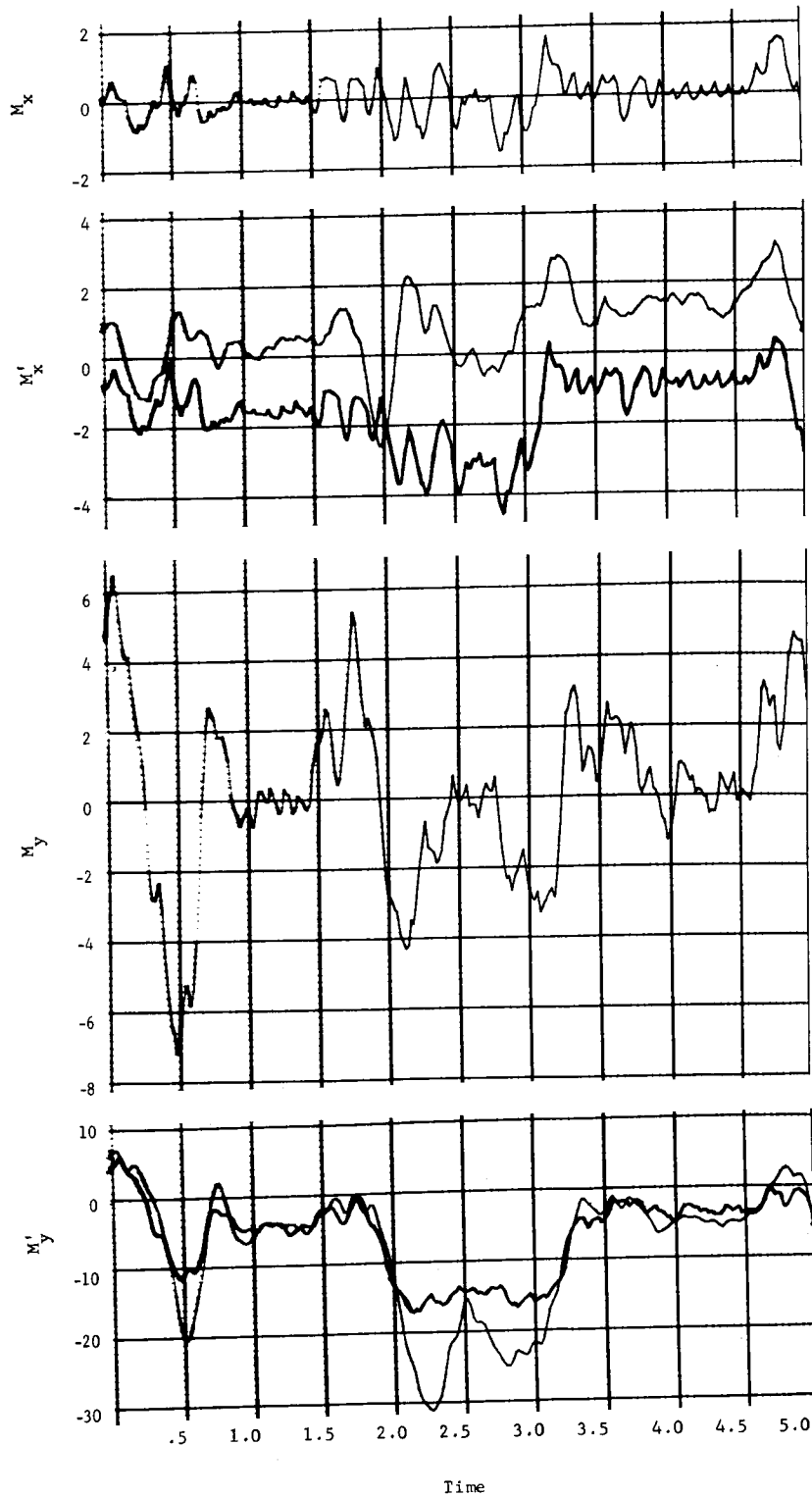


Figure A35.- Total Right Leg, Single Pendulum, Sagittal Plane, Run 16

# APPENDIX A

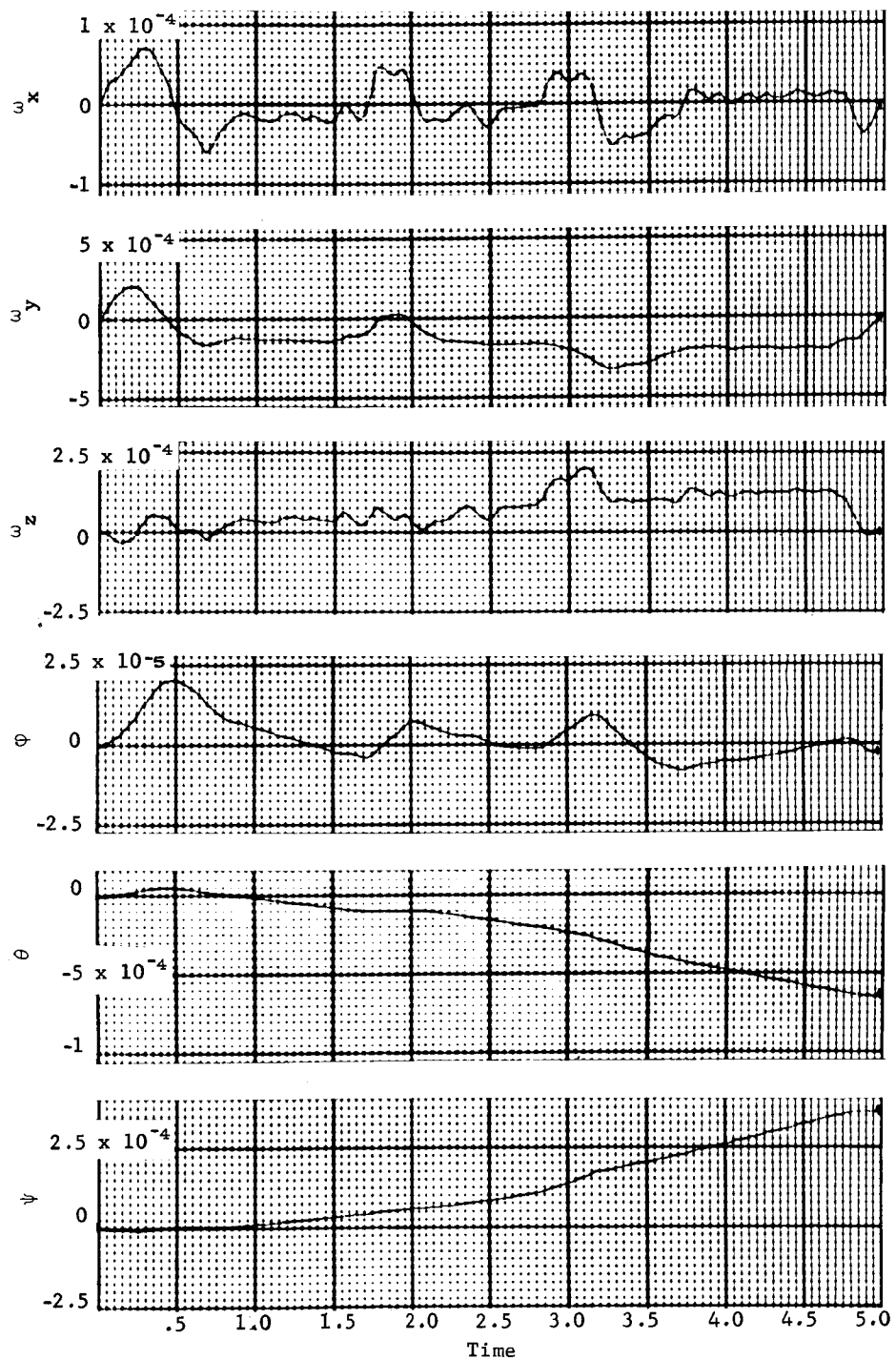


Figure A36.- Total Right Leg, Single Pendulum, Sagittal Plane, Run 16

# APPENDIX D

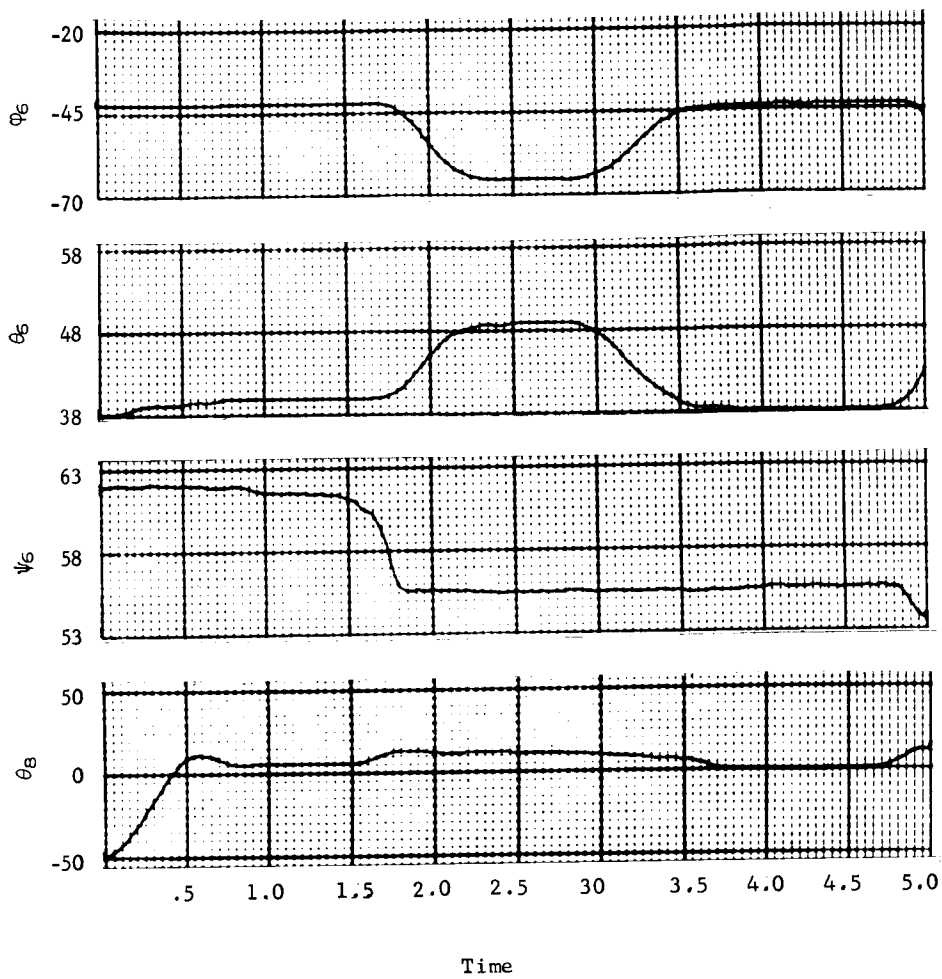


Figure A37.- Total Right Leg, Single Pendulum, Sagittal Plane, Run 16



## APPENDIX A

Run 17, right arm, console operation.- In this run, the subject raised his arm (approximately  $90^\circ$ ), simulated console operations such as turning knobs and flipping switches, and then lowered his arm. Resulting data are shown in figures A38 thru A43. The arm was raised between 1 and 2.5 sec and lowered between 7 and 8.5 sec. Other constant limb angles for this run are:

$\phi_3 = -.31^\circ$	$\phi_6 = -43.24^\circ$	$\phi_7 = 38.83^\circ$
$\theta_3 = -15.27^\circ$	$\theta_6 = 42.81^\circ$	$\theta_7 = 47.85^\circ$
$\psi_3 = -40.36^\circ$	$\psi_6 = 65.37^\circ$	$\psi_7 = -62.11^\circ$
$\theta_5 = 42.85^\circ$	$\theta_8 = -76.41^\circ$	$\theta_6 = -82.46^\circ$

Many of the discrepancies between load cell and calculated results in this run are attributed to wrist motion, which was not monitored. Also, because of the relatively quick arm motions, forces and moments from torso shifting are apparent, particularly in  $F_y$  and  $M_x$ .

The load cell forces and moments (modified to exclude c.g. shift moments and load cell bias) were applied to the S/C for this run and the results are shown in figures A41 and A42.

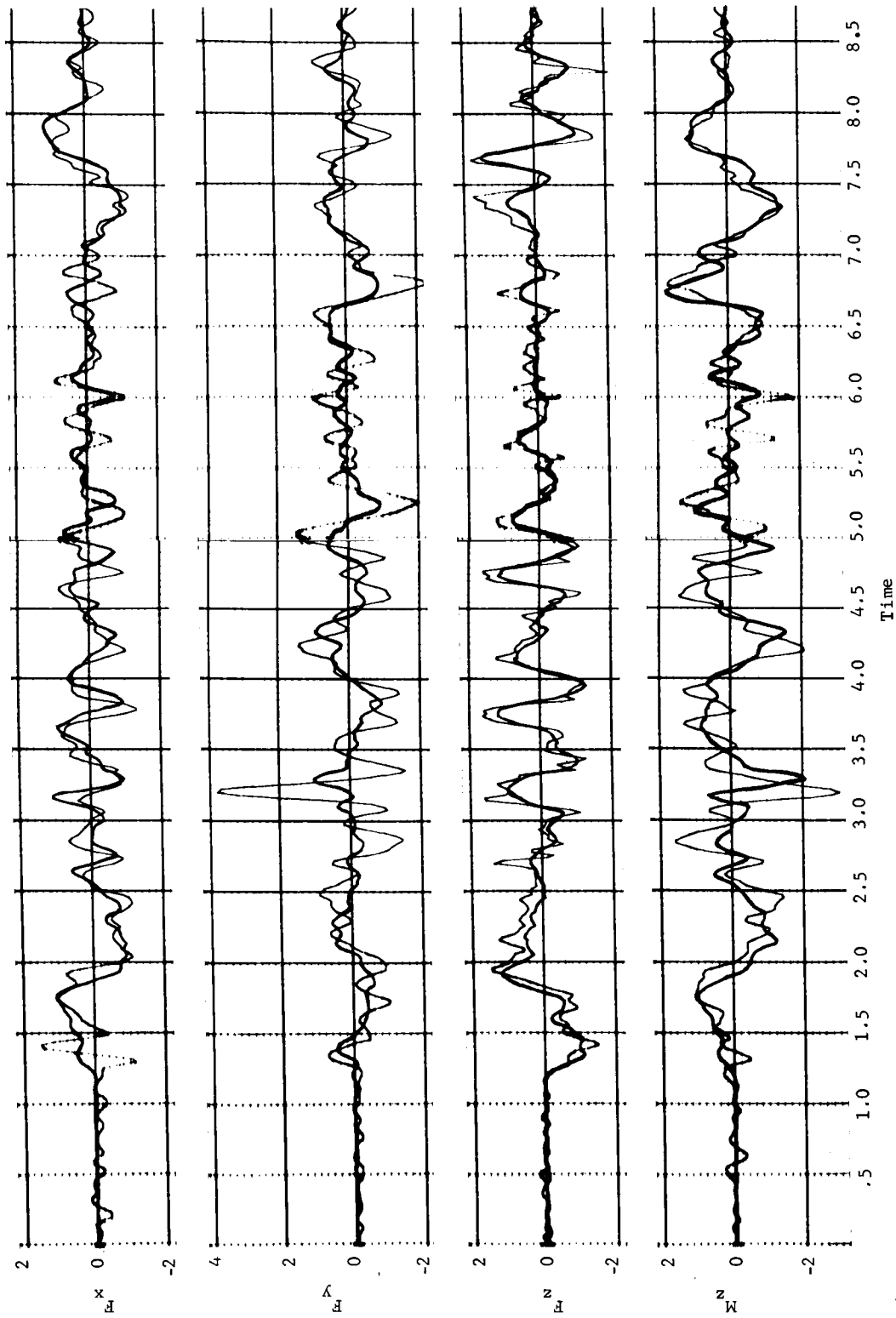


Figure A38.- Right Arm, Console Operation, Run 17

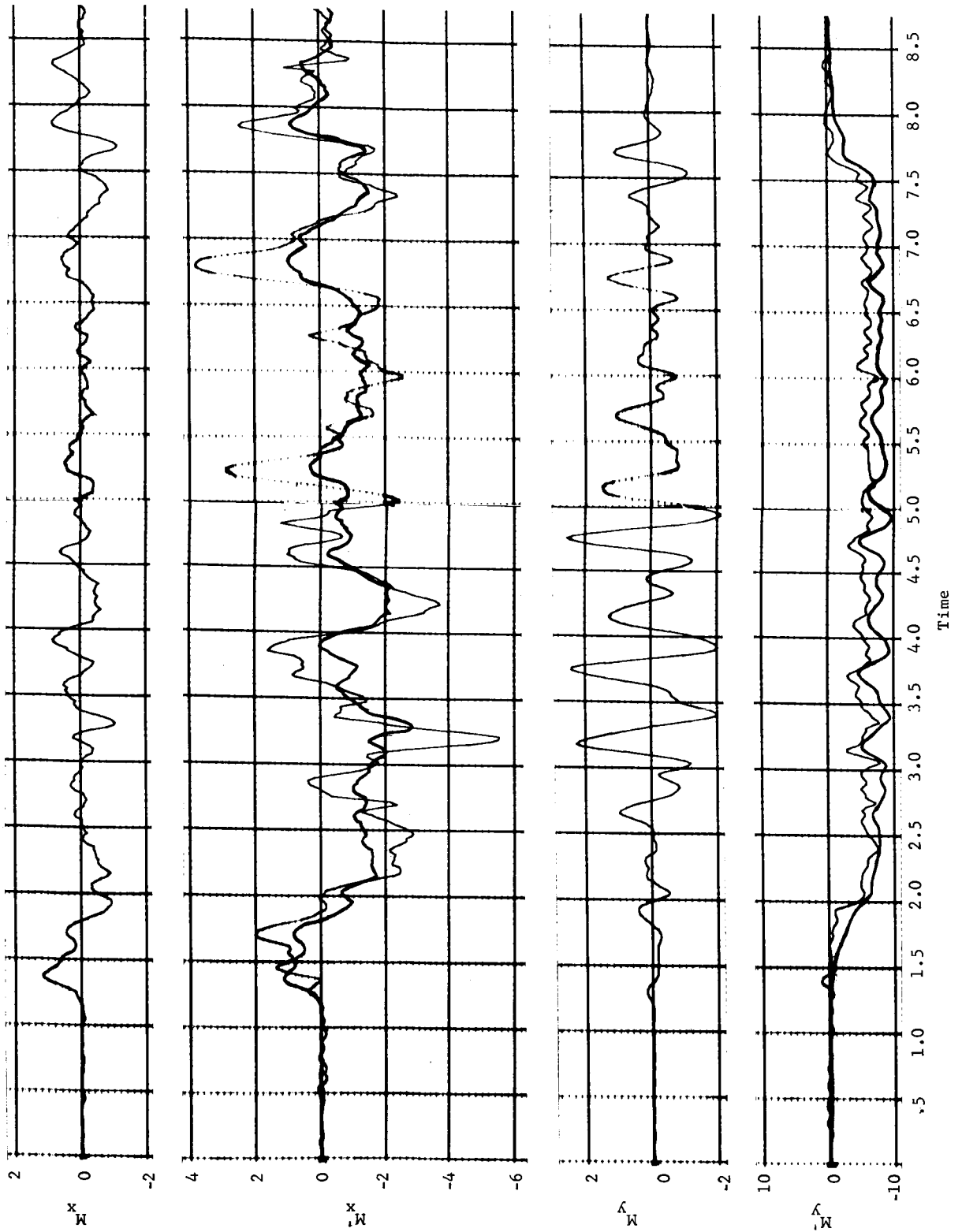


Figure A39.- Right Arm Console Operation, Run 17

# APPENDIX A



Figure A40.- Right Arm, Console Operation, Run 17

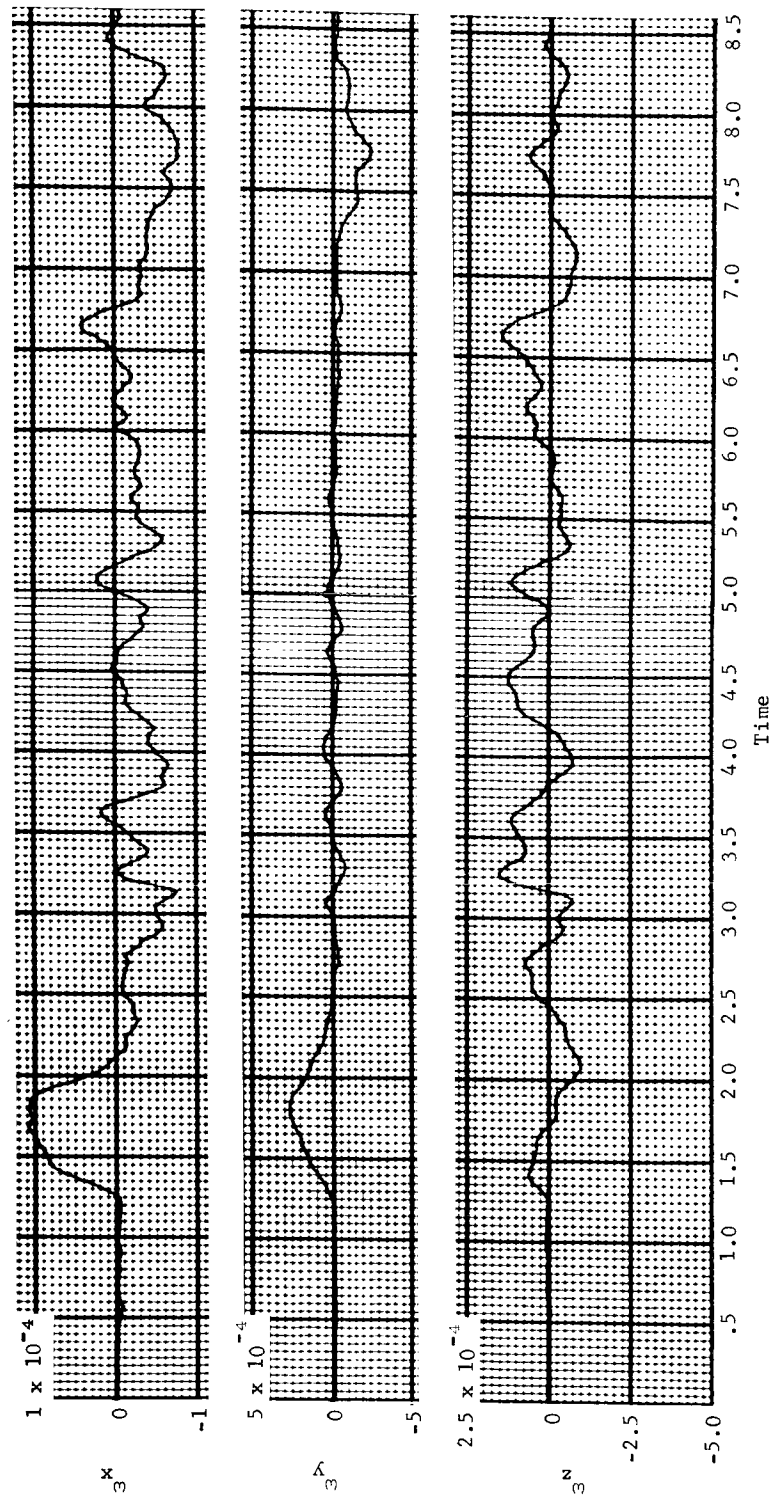


Figure A41.- Right Arm, Console Operation, Calculated from Load Cell Data, Run 17

# APPENDIX A

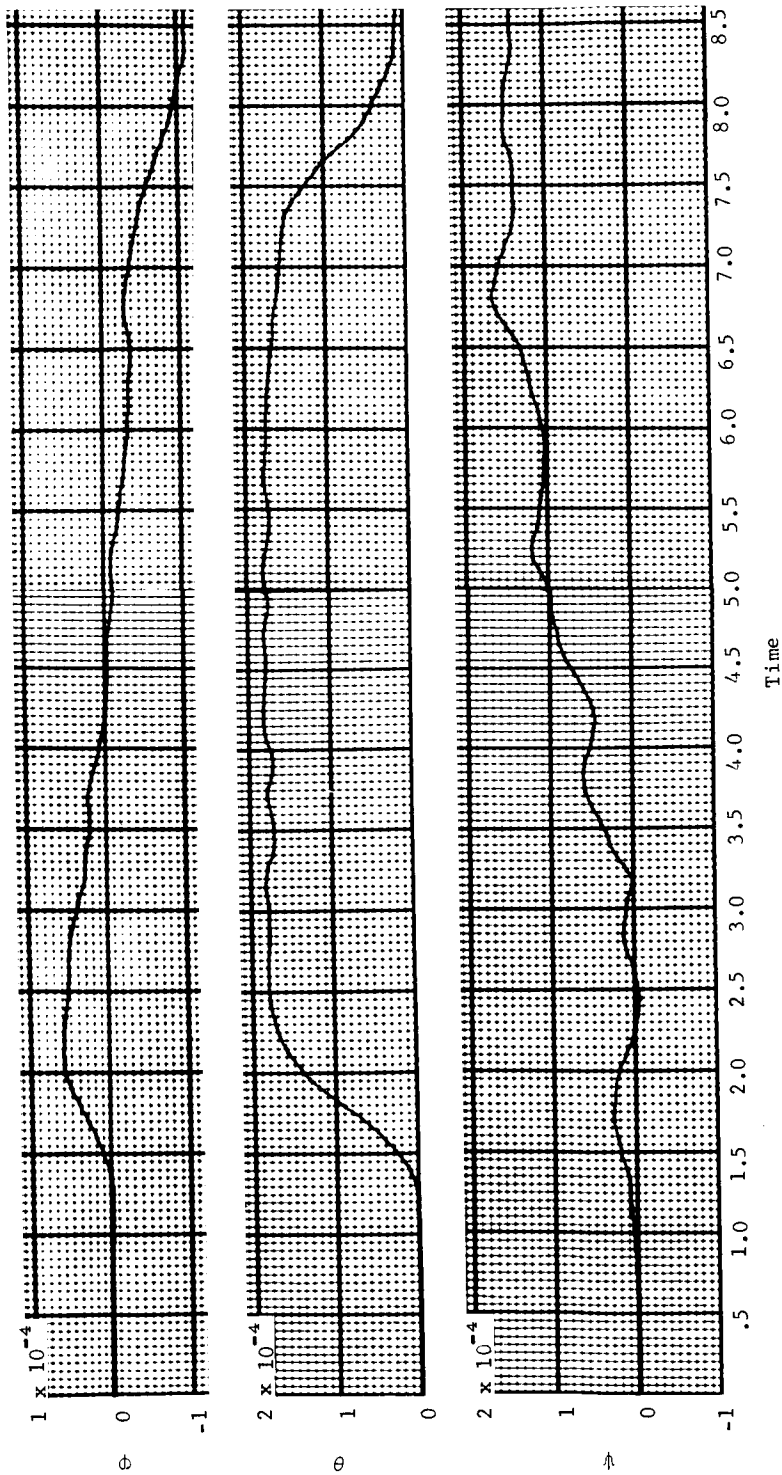


Figure A42.- Right Arm, Console Operation, Calculated from Load Cell Data, Run 17

# APPENDIX A

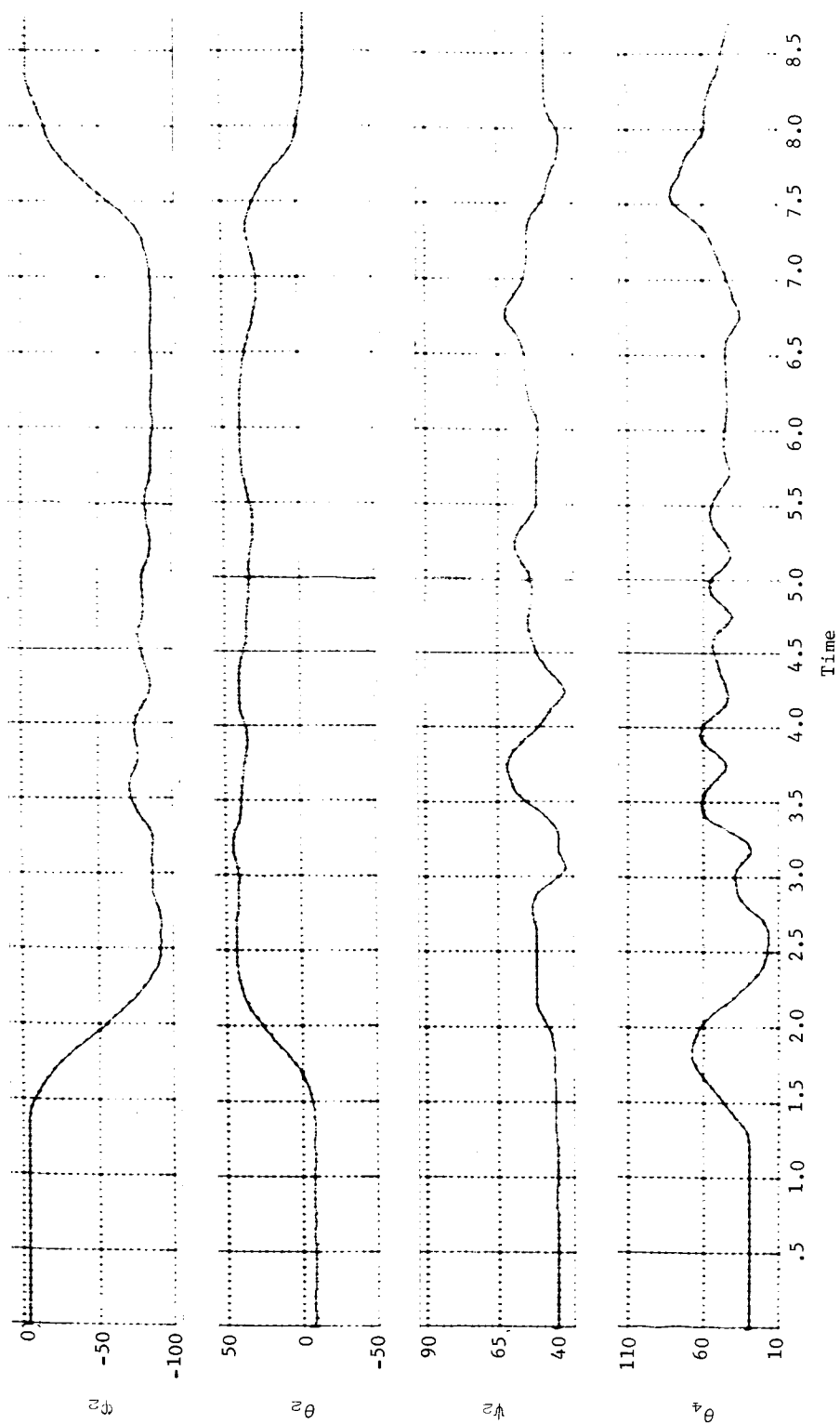


Figure A43.- Right Arm, Console Operation, Run 17

## APPENDIX A

### Run 18, lower right arm, single pendulum, sagittal plane.-

This run is the same as Run 10 except that Subject 2 was used. Resulting data are shown in figures A44 thru A48. The motion is approximately a  $100^\circ$  swing of the lower right arm in the sagittal plane. The motion is performed twice as shown by  $\theta_4$  in figure A48. The other arm and leg angles that are assumed constant are:

$\phi_3 = -24.64^\circ$	$\phi_6 = -25.92^\circ$	$\phi_7 = 28.32^\circ$
$\theta_3 = -11.90^\circ$	$\theta_6 = 27.12^\circ$	$\theta_7 = 32.50^\circ$
$\psi_3 = 13.50^\circ$	$\psi_6 = 45.60^\circ$	$\psi_7 = -47.13^\circ$
$\theta_5 = 60.83^\circ$	$\theta_8 = -59.90^\circ$	$\theta_9 = -61.73^\circ$

The discrepancy between load cell and calculated force  $F_y$  is attributed primarily to torso shift, which is more of a problem in the  $y$  direction. Also, the discrepancies in  $M'_x$  are caused by slight inaccuracies in LIMS angles as discussed under Run 13. Spacecraft rates and angles have been calculated for this motion using load cell forces and moments (less c.g. shift moments and load cell bias). These are shown in figure A47.



# APPENDIX A

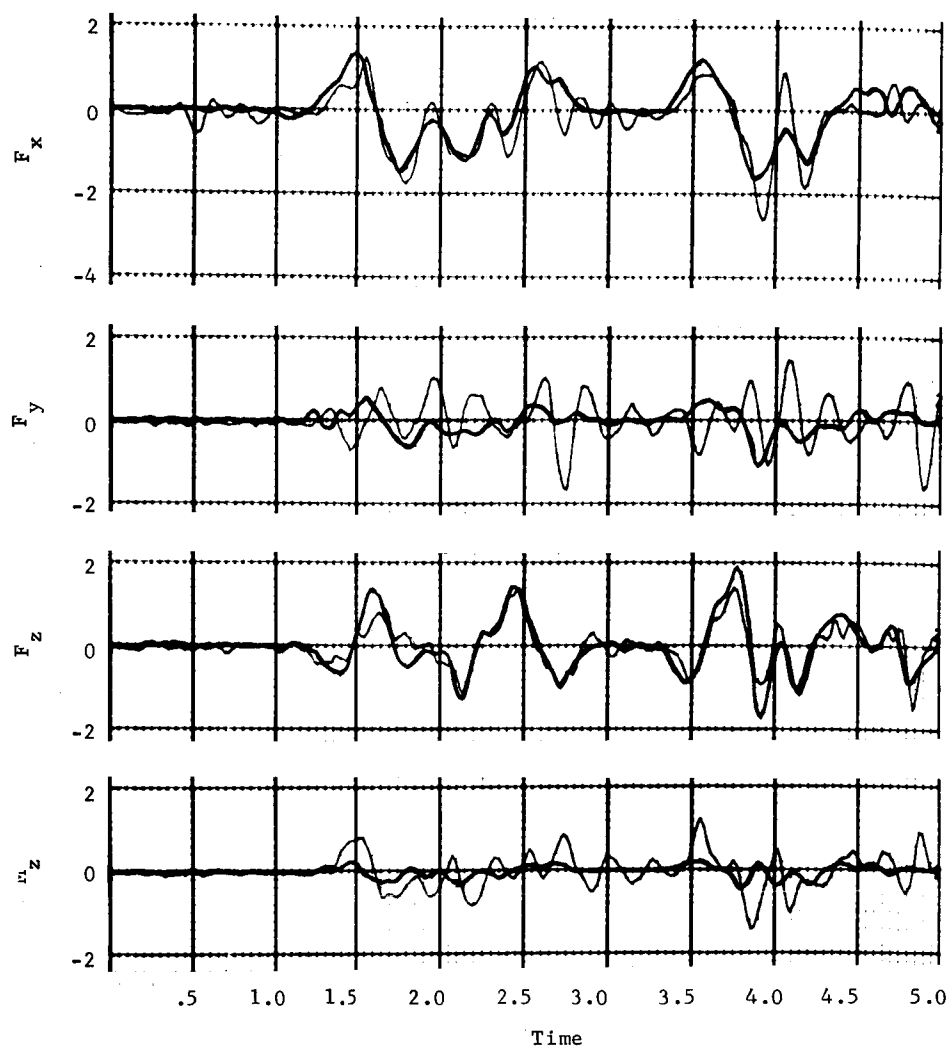


Figure A44.- Lower Right Arm, Single Pendulum, Sagittal Plane, Run 18

# APPENDIX A

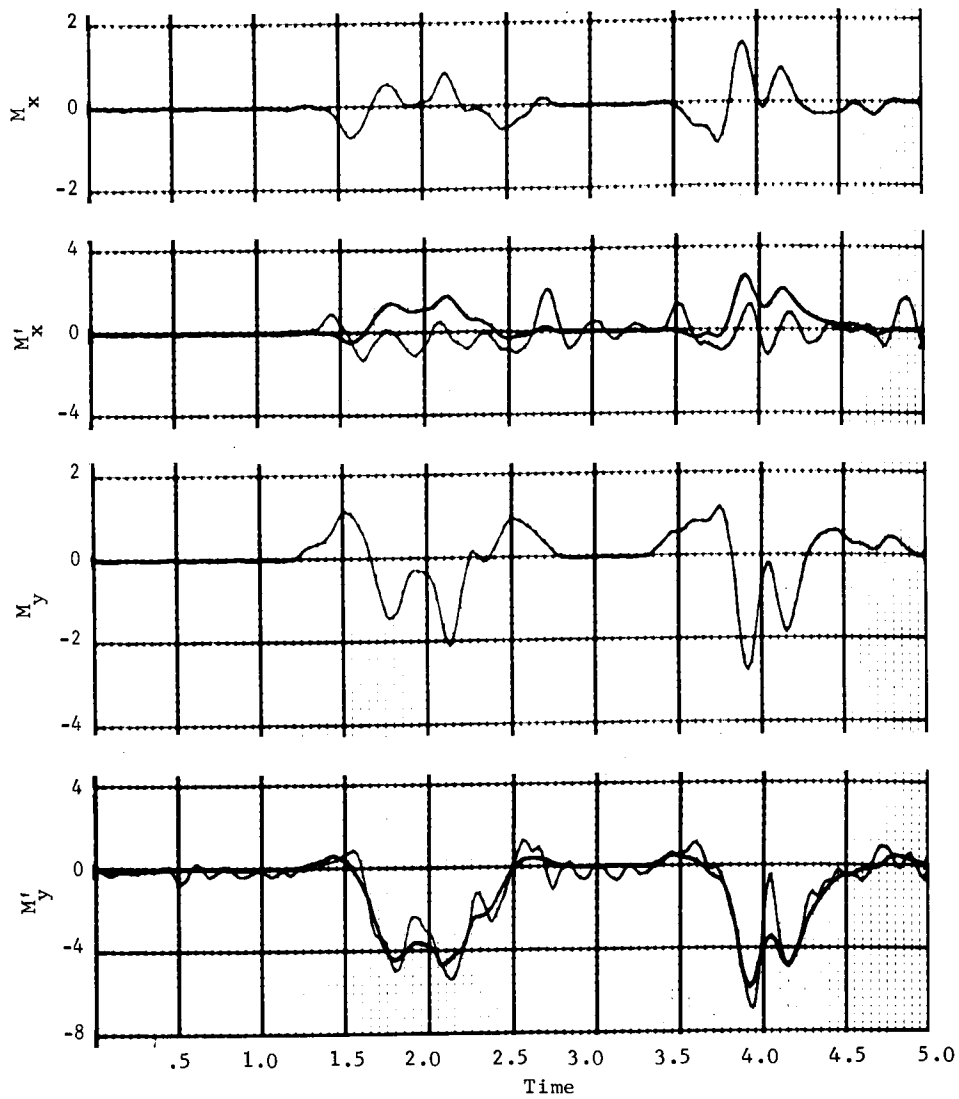


Figure A45.- Lower Right Arm, Single Pendulum, Sagittal Plane, Run 13

# APPENDIX A

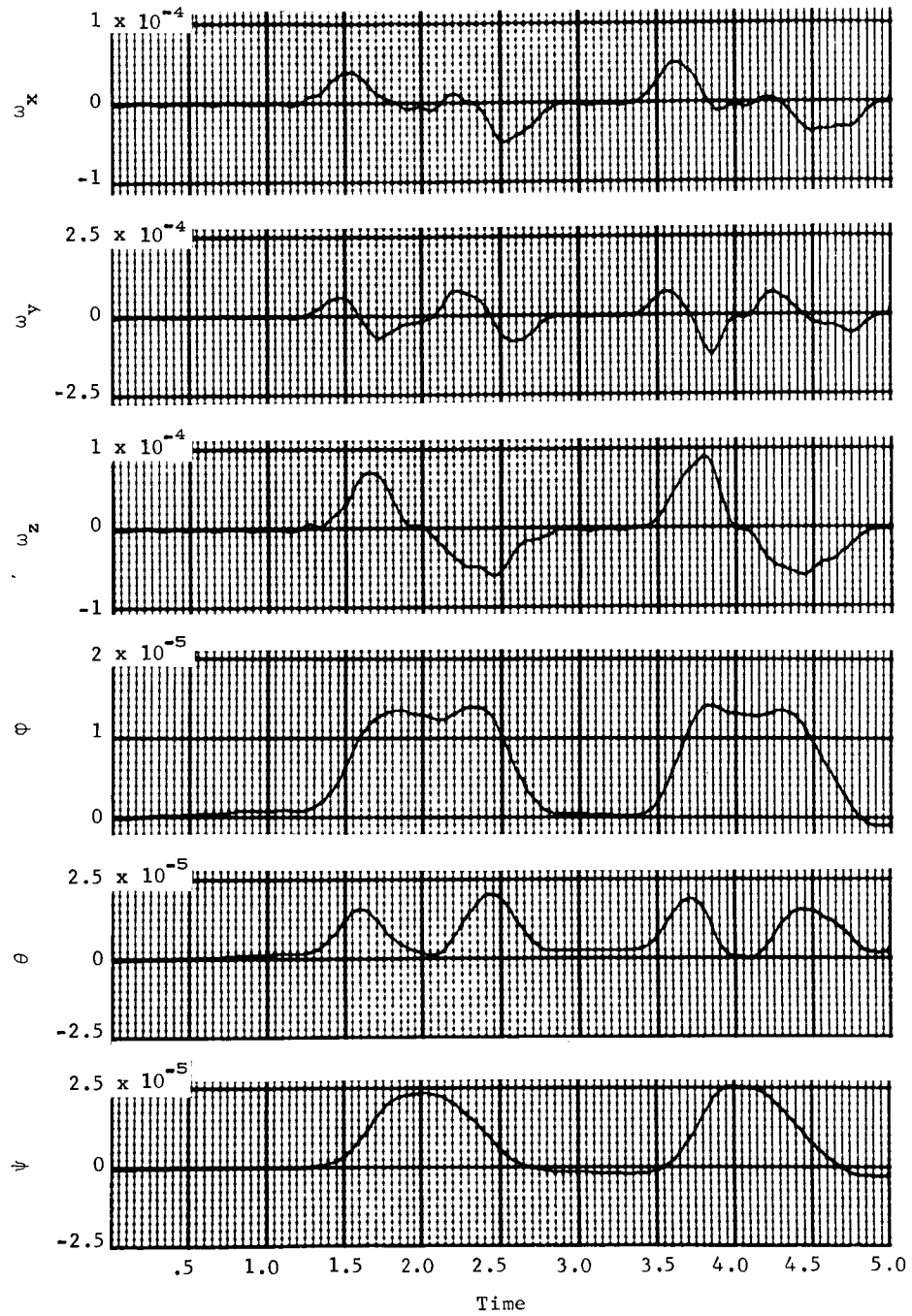


Figure A46.- Lower Right Arm, Single Pendulum, Sagittal Plane, Run 18

# APPENDIX A

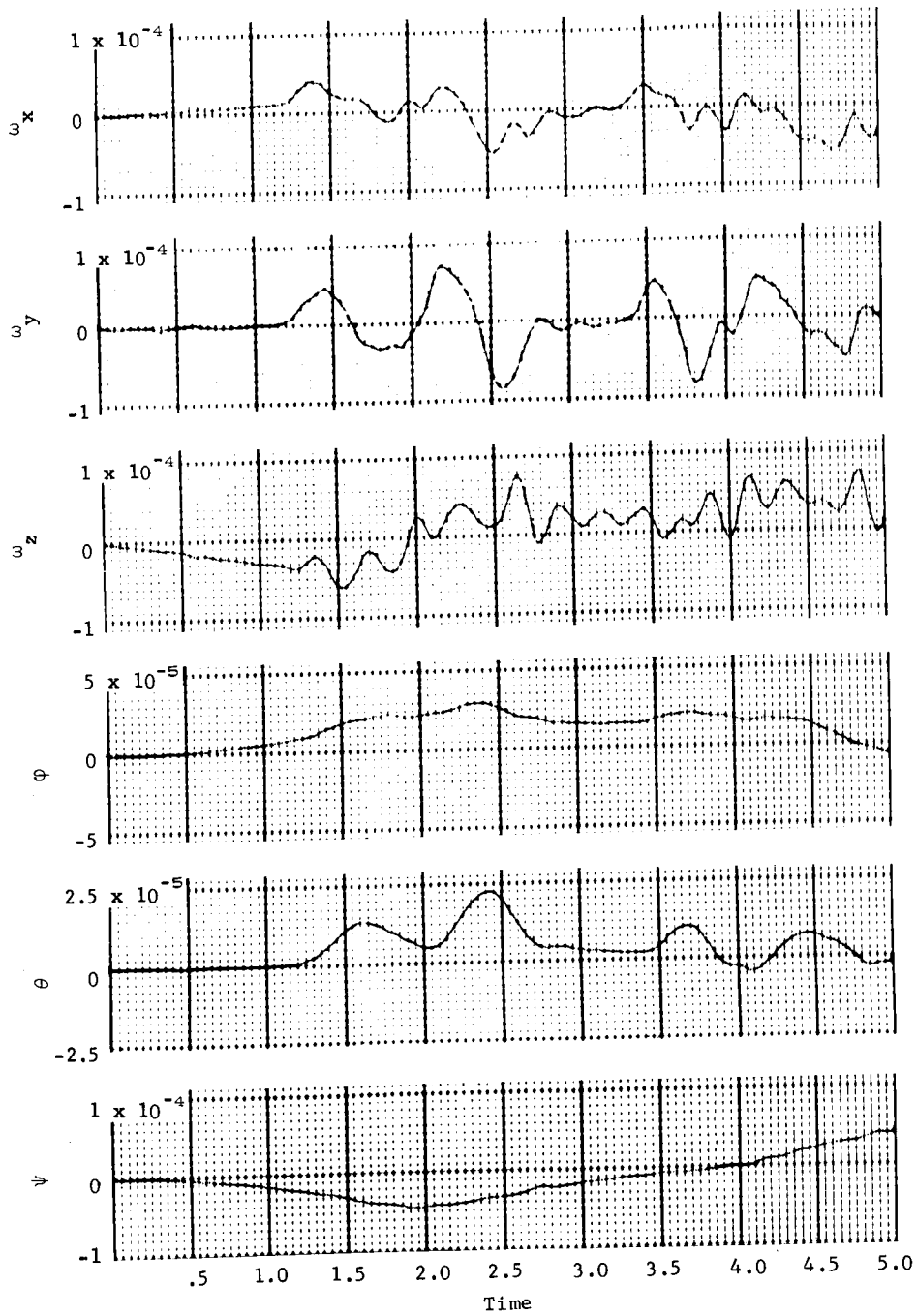


Figure A47.- Lower Right Arm, Single Pendulum, Sagittal Plane, Calculated from Load Cell Data, Run 18

# APPENDIX A

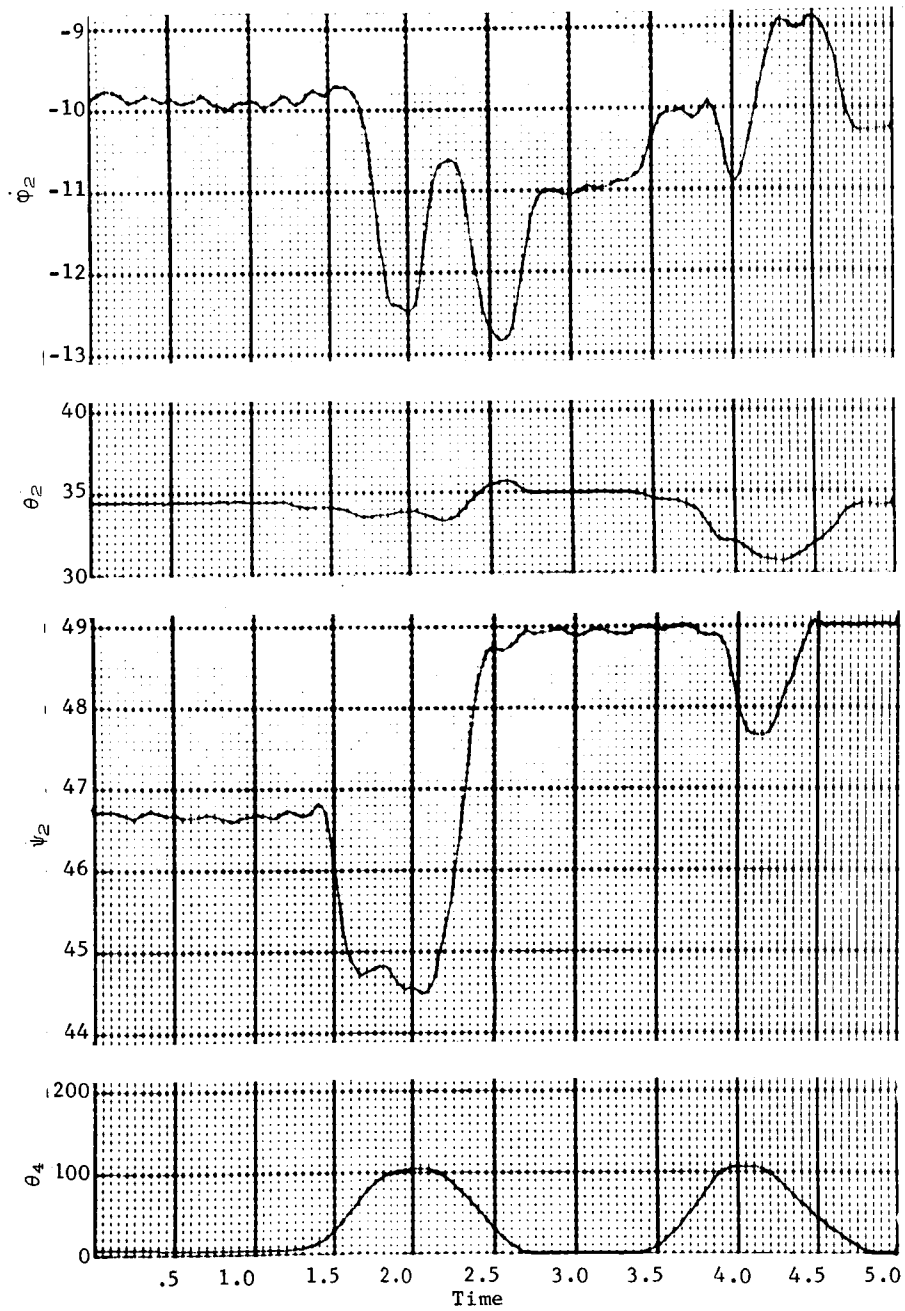


Figure A48.- Lower Right Arm, Single Pendulum, Sagittal Plane, Run 18

## APPENDIX A

### Run 19, total right arm, single pendulum, sagittal plane.-

This run is the same as Run 11 except that Subject 2 was used. Resulting data are shown in figures A49 thru A53. The motion is approximately a  $90^\circ$  swing of the right arm in the sagittal plane (with little elbow bending). The motion is performed twice as shown by the angles in figure A53. The other arm and leg angles that are assumed constant are:

$\phi_3 = -24.67^\circ$	$\phi_6 = -25.87^\circ$	$\phi_7 = 28.46^\circ$
$\theta_3 = -11.90^\circ$	$\theta_6 = 28.46^\circ$	$\theta_7 = 33.21^\circ$
$\psi_3 = 13.51^\circ$	$\psi_6 = 45.60^\circ$	$\psi_7 = -47.08^\circ$
$\theta_5 = 60.86^\circ$	$\theta_8 = -61.53^\circ$	$\theta_9 = -62.72^\circ$

Torso shift problems are also apparent in this run. Note that where torso shift is not a factor (in the  $F_z$  direction) that the correlation is very good. As explained in Run 13, LIMS inaccuracies account for the inaccurate c.g. shift moment calculation shown in  $M'_x$ . Spacecraft rates and angles from load cell forces and moments are also calculated for this run and shown in figure A52.

# APPENDIX A

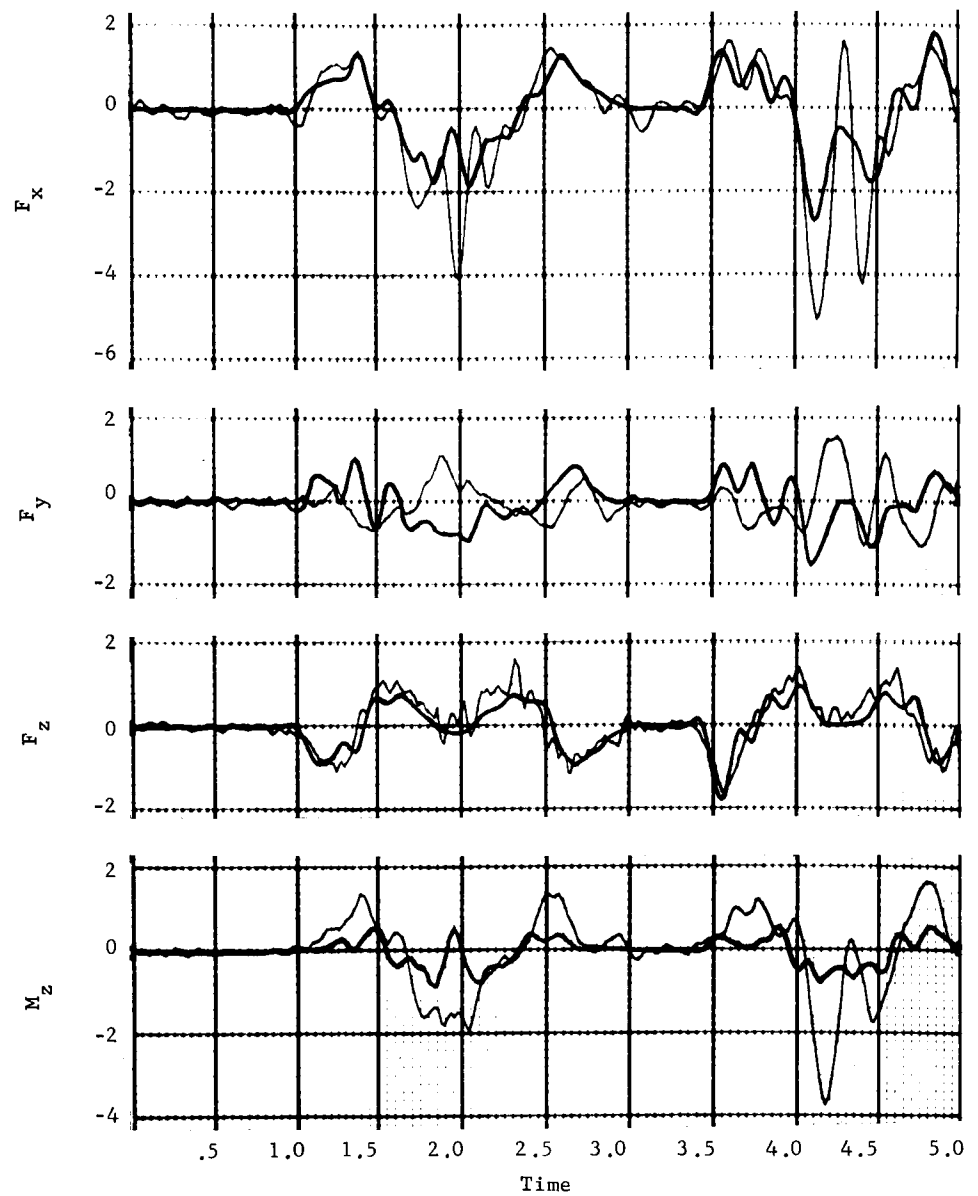


Figure A49.- Total Right Arm, Single Pendulum, Sagittal Plane, Run 19

# APPENDIX A

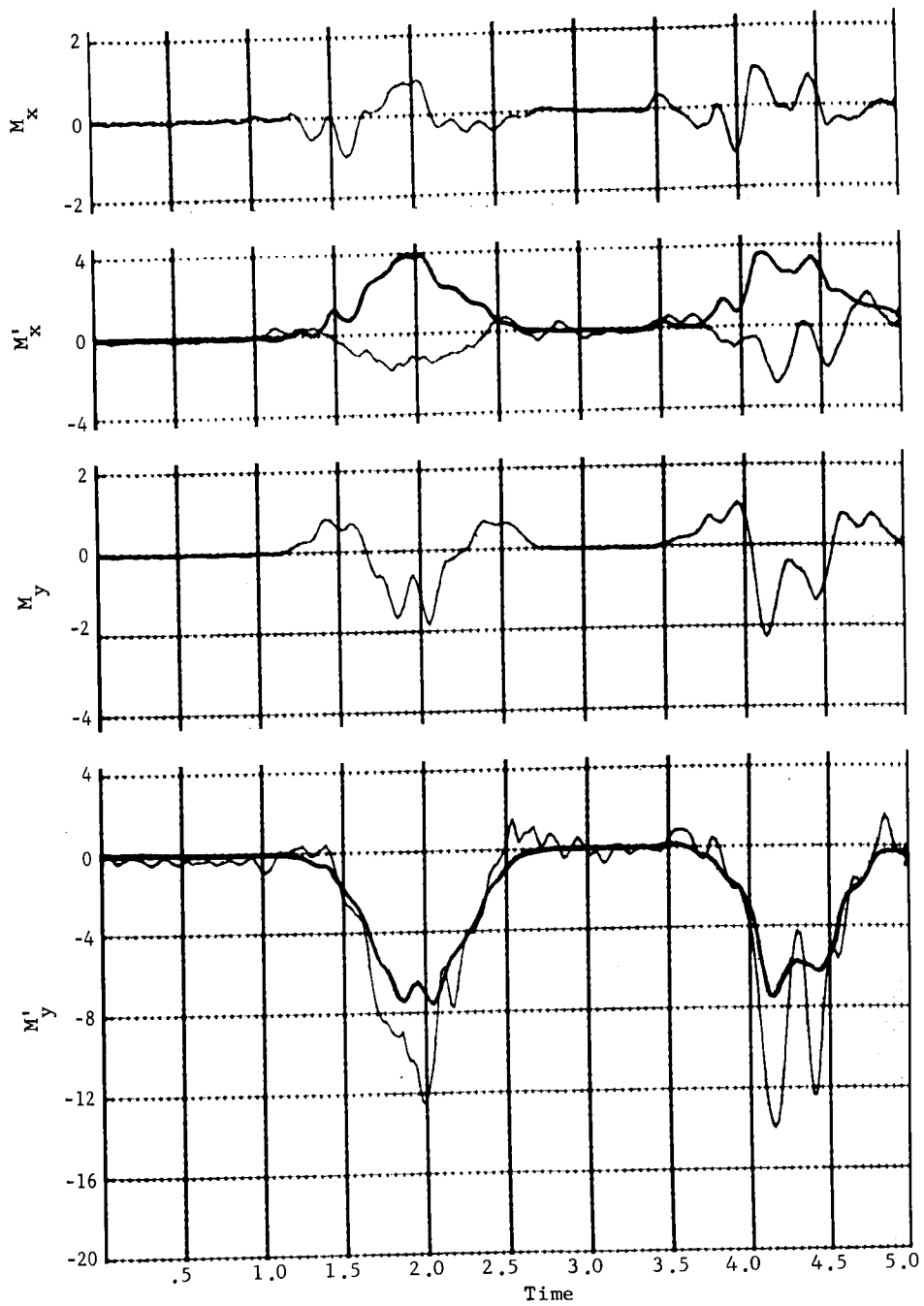


Figure A50.- Total Right Arm, Single Pendulum, Sagittal Plane, Run 19



# APPENDIX A

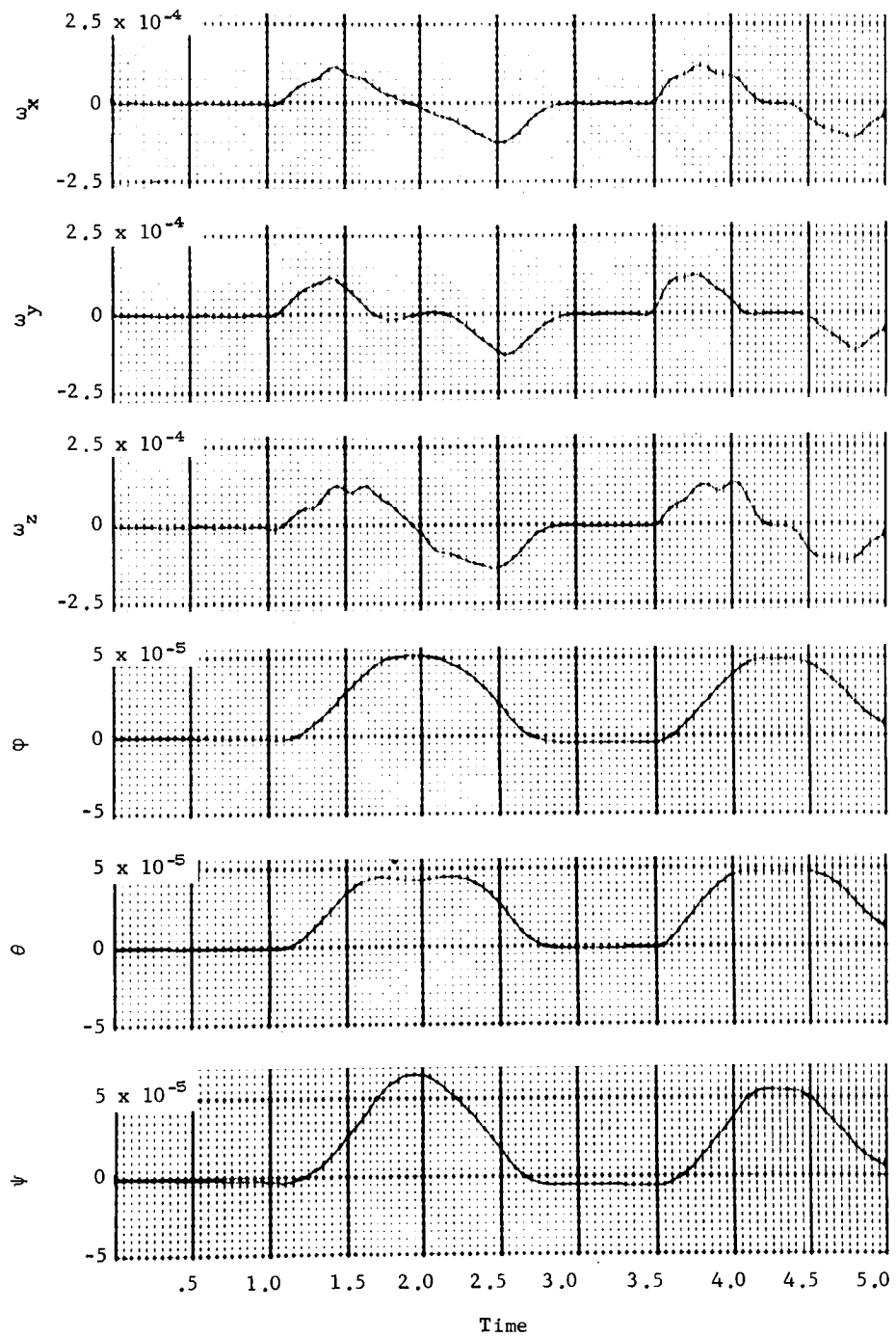


Figure A51.- Total Right Arm, Single Pendulum, Sagittal Plane, Run 19

# APPENDIX A

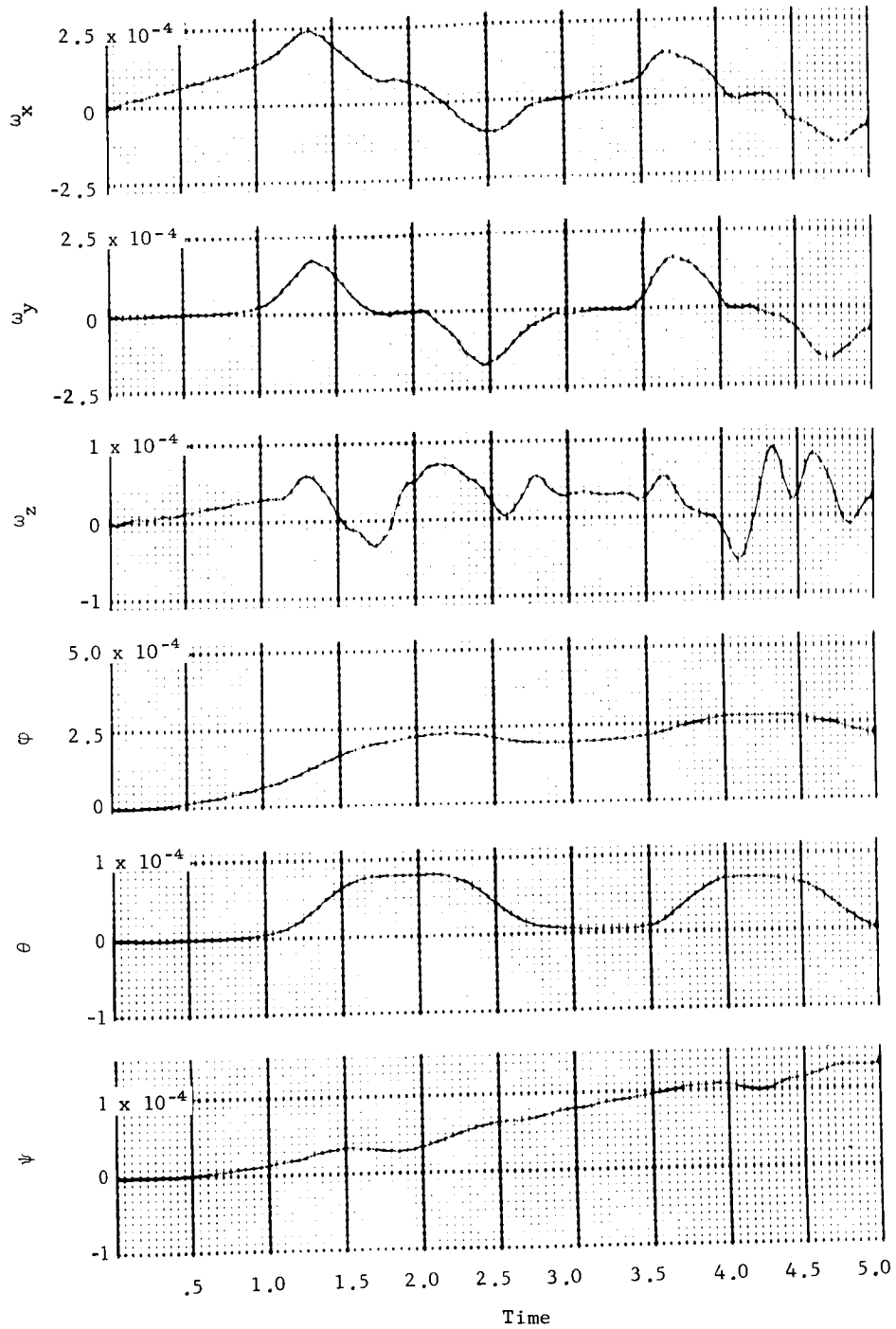


Figure A52.- Total Right Arm, Single Pendulum, Sagittal Plane,  
Calculated from Load Cell Data, Run 19

# APPENDIX A

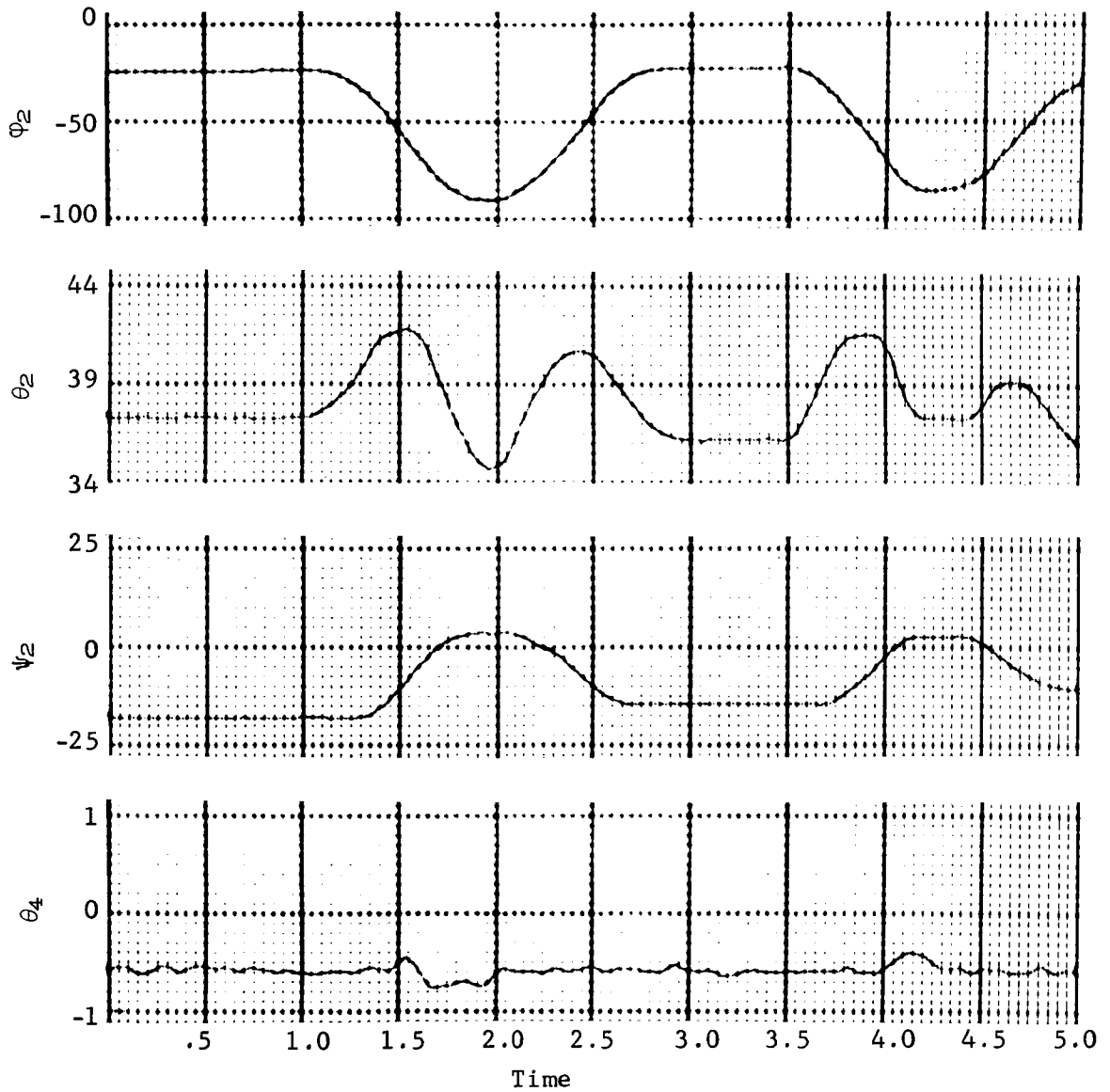


Figure A53.- Total Right Arm, Single Pendulum, Sagittal Plane, Run 19

## APPENDIX A

Run 20, total left arm, single pendulum, frontal plane.- This run is the same as Run 12 except that Subject 2 was used. Resulting data are shown in figures A54 thru A57. The motion, performed twice, is approximately a 70° swing of the left arm in the frontal plane. No elbow bending occurred. The other arm and leg angles held constant are:

$\phi_2 = 15.19^\circ$	$\phi_6 = -25.82^\circ$	$\phi_7 = 31.29^\circ$
$\theta_2 = -0.15^\circ$	$\theta_6 = 26.49^\circ$	$\theta_7 = 33.84^\circ$
$\psi_2 = 5.35^\circ$	$\psi_6 = 45.55^\circ$	$\psi_7 = -47.19^\circ$
$\theta_4 = 33.26^\circ$	$\theta_8 = -65.66^\circ$	$\theta_9 = -57.58^\circ$

Primary discrepancies in this run are caused by torso shift and LIMS angles inaccuracies (in calculation c.g. shift moments) as explained under Run 13.

# APPENDIX A

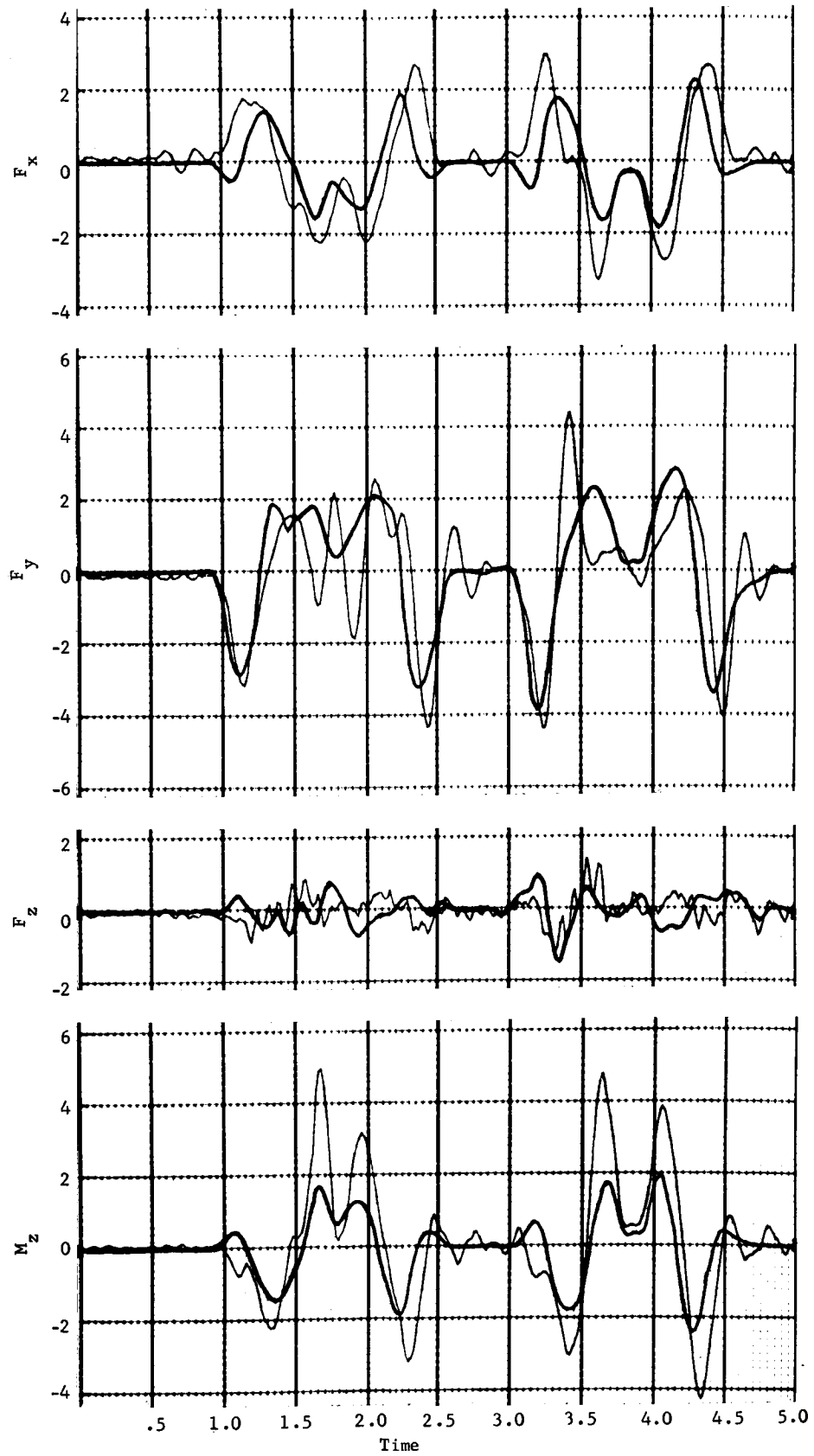


Figure A54.- Total Left Arm, Single Pendulum, Frontal Plane, Run 20

# APPENDIX A

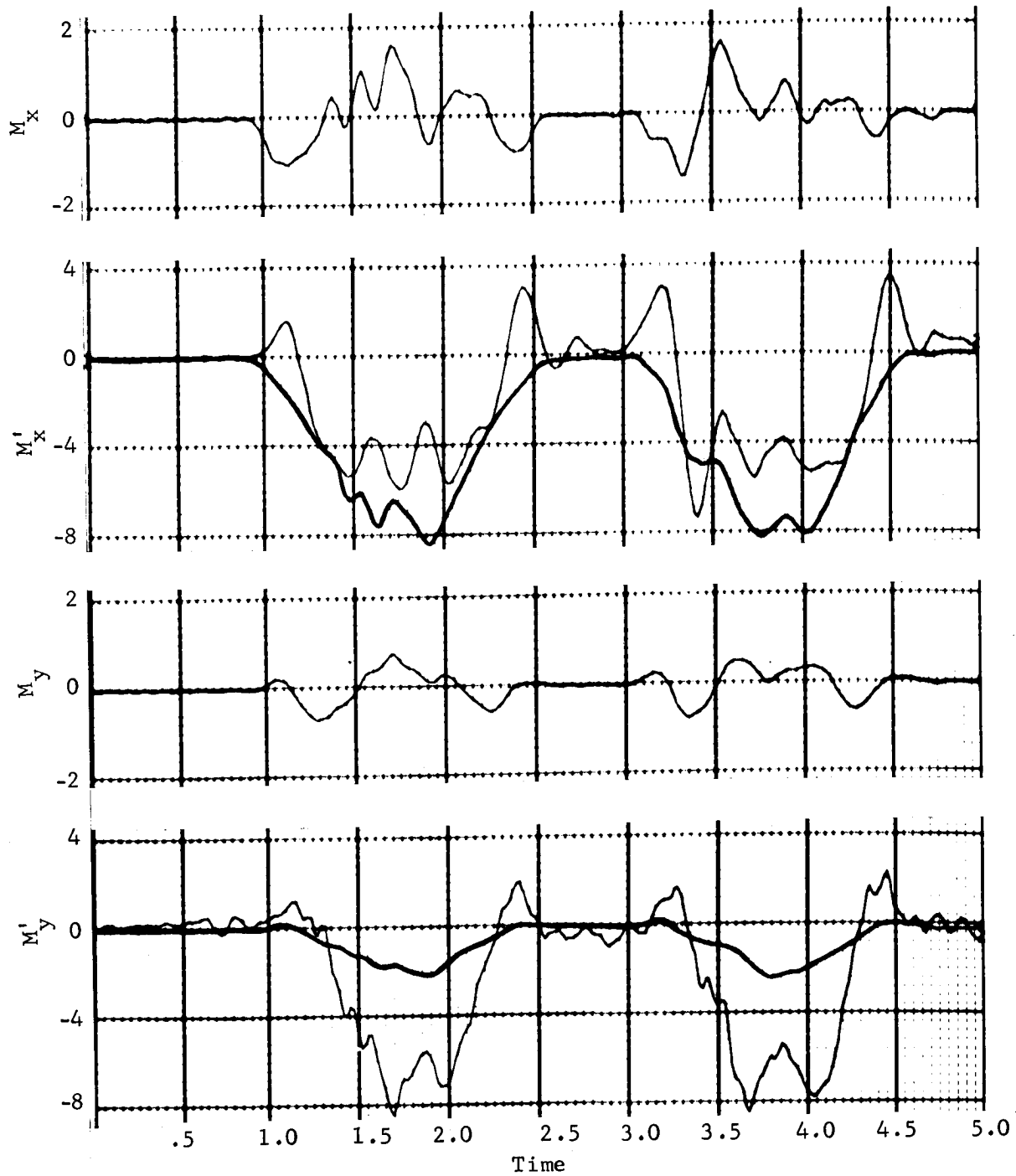


Figure A55.- Total Left Arm, Single Pendulum, Frontal Plane, Run 20

# APPENDIX A

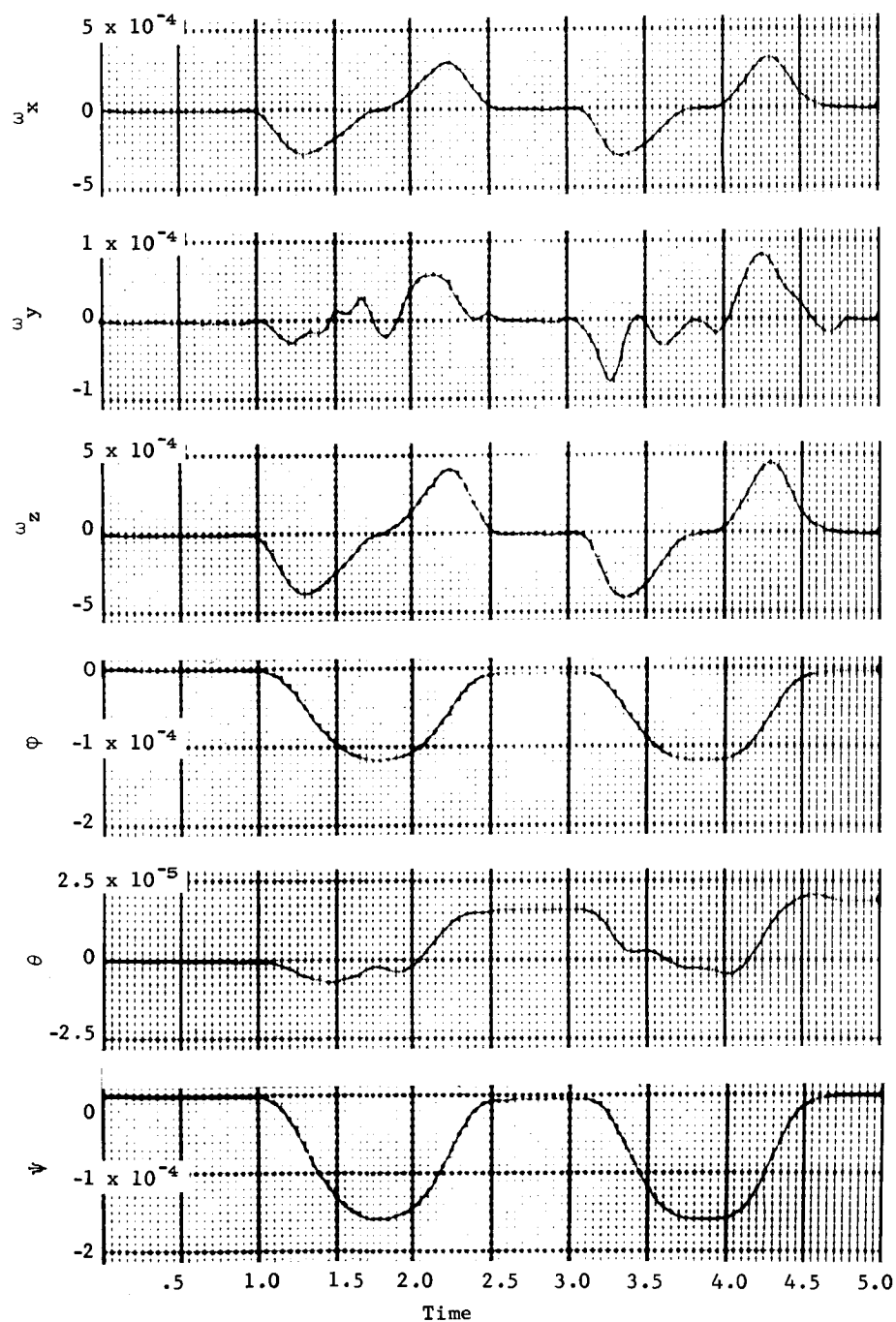


Figure A56.- Total Left Arm, Single Pendulum, Frontal Plane, Run 20

# APPENDIX A

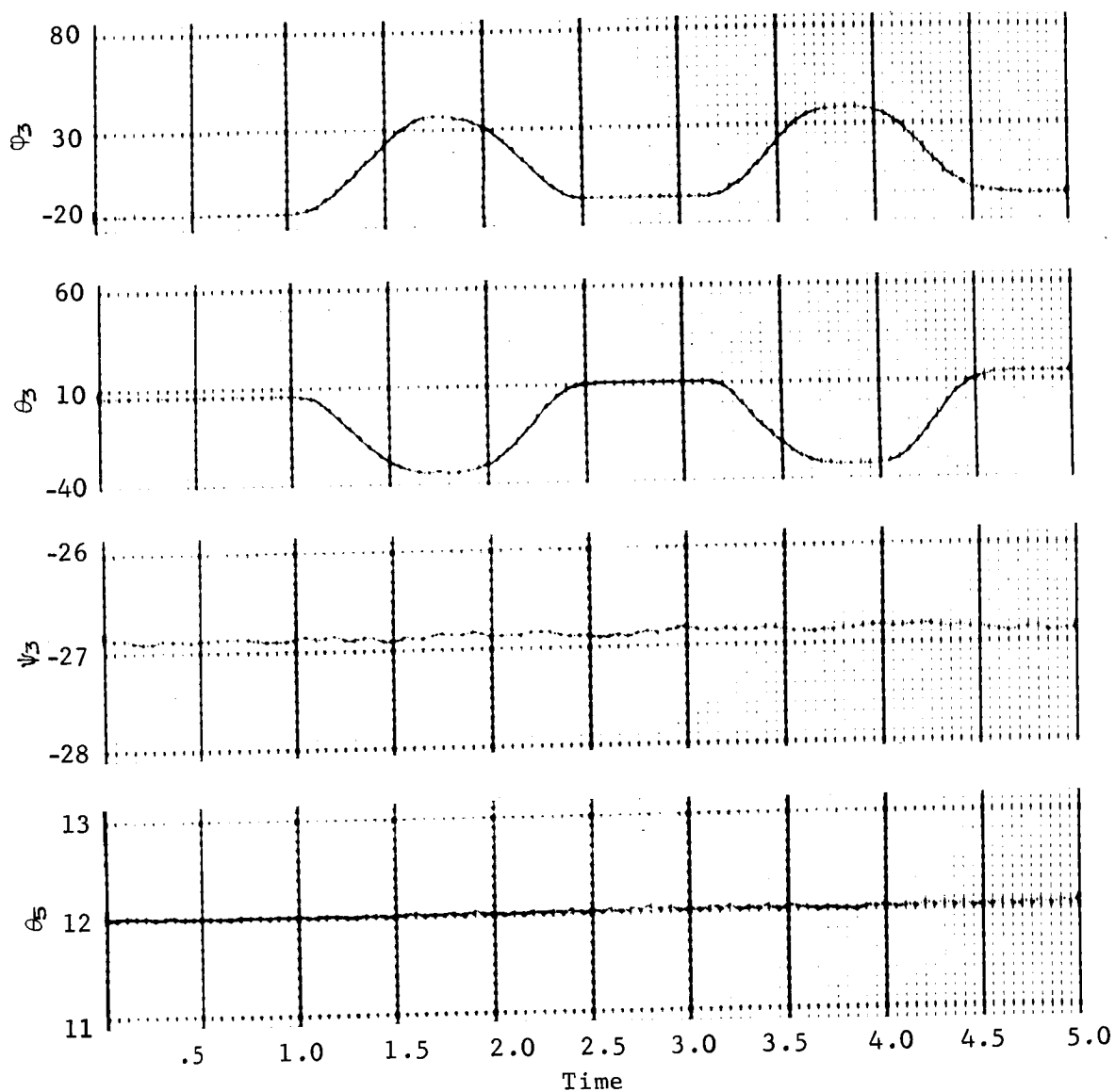


Figure A57.- Total Left Arm, Single Pendulum, Frontal Plane, Run 30



## APPENDIX A

### Run 21, total left arm, double pendulum, sagittal plane.-

This run is a repeat of Run 13, but using Subject 2. Resulting data are presented in figures A58 thru A61. The motion, performed twice, is approximately a  $90^\circ$  swing of the left upper arm and a  $100^\circ$  swing of the left lower arm in the sagittal plane. The other arm and leg angles assumed constant are:

$\phi_2 = 14.35^\circ$	$\phi_6 = -26.73^\circ$	$\phi_7 = 30.91^\circ$
$\theta_2 = -6.26^\circ$	$\theta_6 = 26.64^\circ$	$\theta_7 = 33.69^\circ$
$\psi_2 = 3.49^\circ$	$\psi_6 = 45.50^\circ$	$\psi_7 = -47.42^\circ$
$\theta_4 = 40.51^\circ$	$\theta_8 = -64.41^\circ$	$\theta_9 = -58.40^\circ$

As explained under Run 13, the LIMS inaccuracies in angles result in incorrect c.g. shift moments in  $M'_x$ .

# APPENDIX A

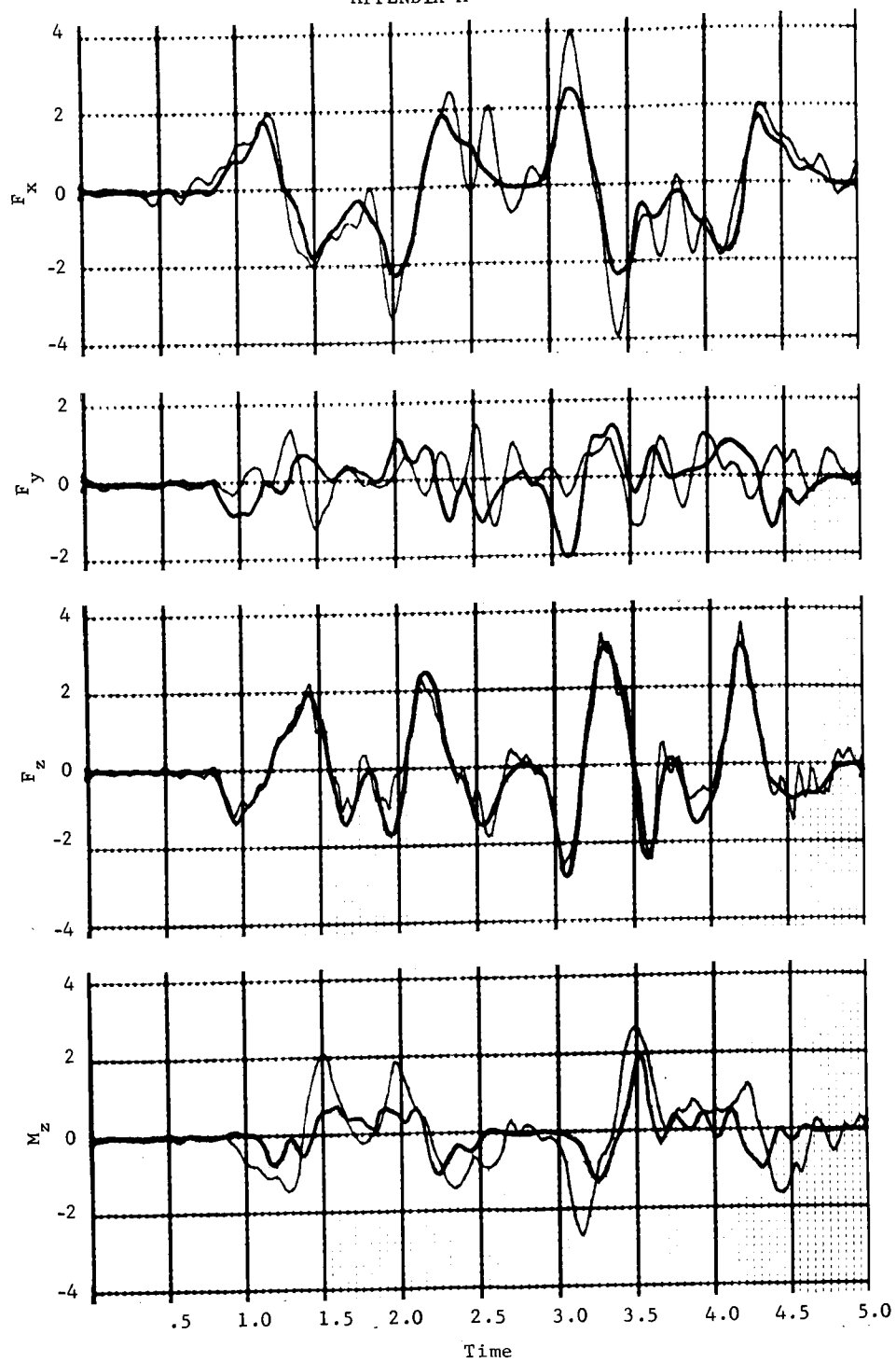


Figure A58.- Total Left Arm, Double Pendulum, Sagittal Plane, Run 21

# APPENDIX A

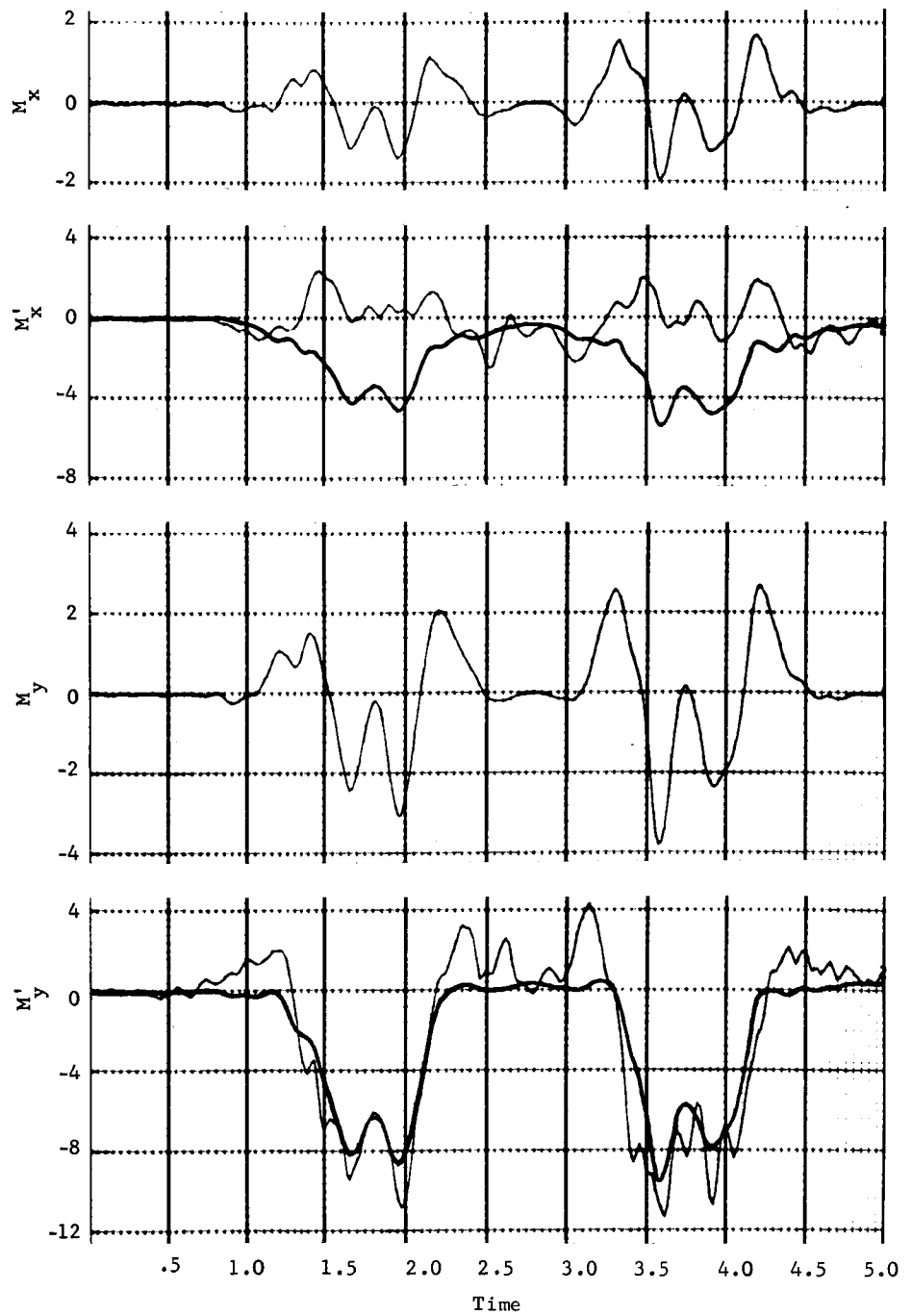


Figure A59.- Total Left Arm, Double Pendulum, Sagittal Plane, Run 21

# APPENDIX A

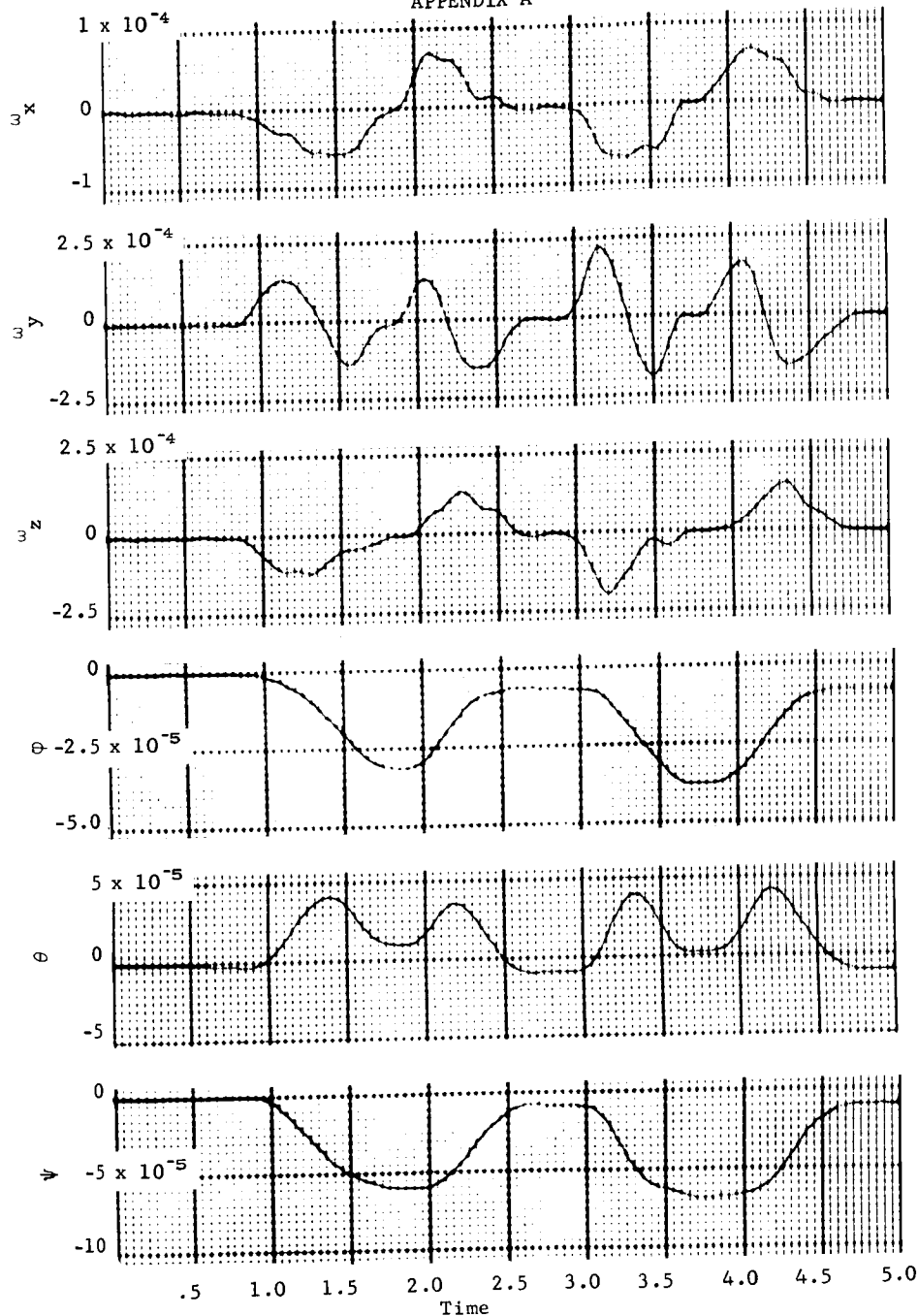


Figure A60.- Total Left Arm, Double Pendulum, Sagittal Plane, Run 21

# APPENDIX A

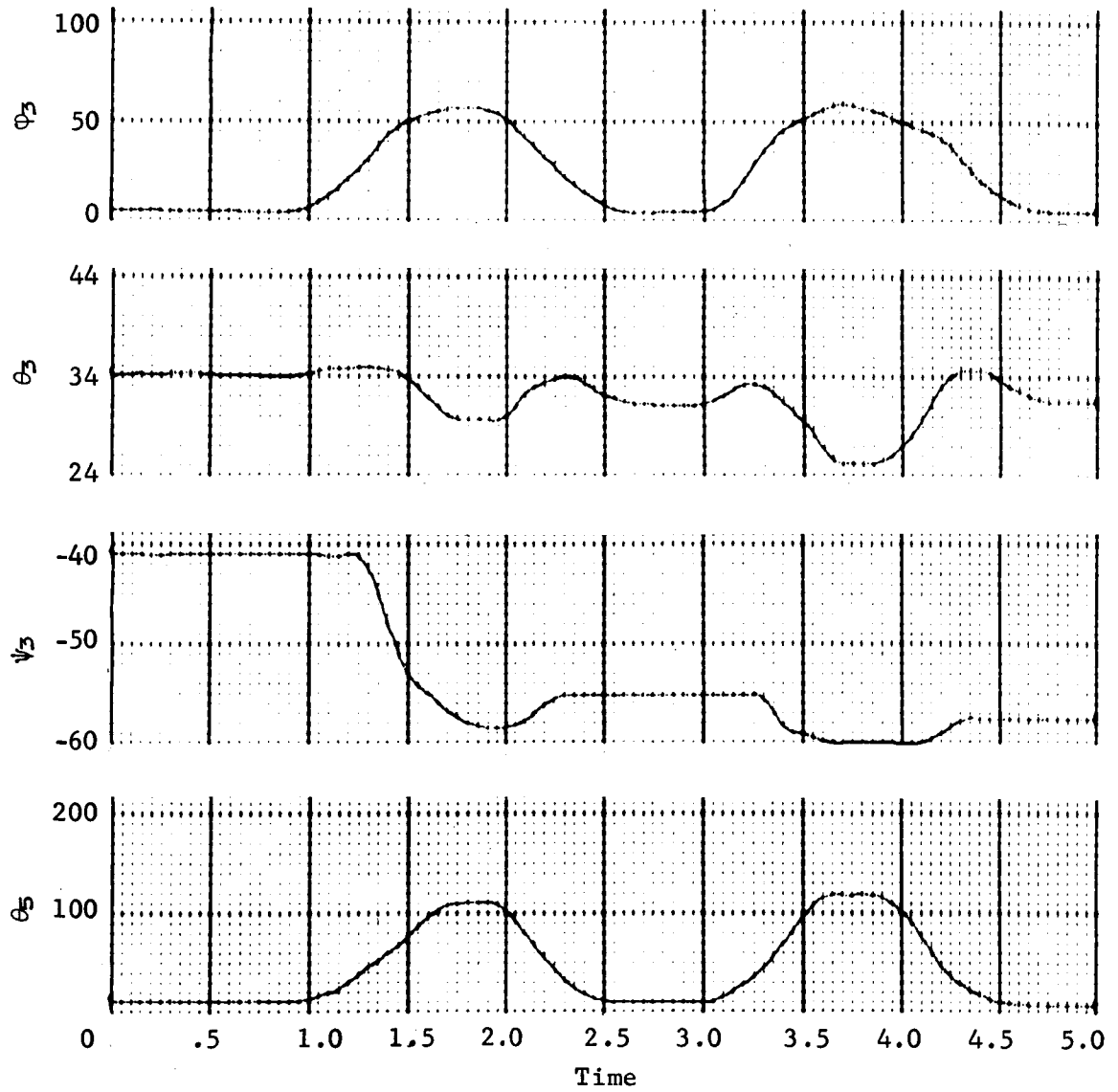


Figure A61.- Total Left Arm, Double Pendulum, Sagittal Plane, Run 21

## APPENDIX A

### Run 22, lower right leg, single pendulum, sagittal plane.-

This run is a repeat of Run 15, but using Subject 2. Resulting data are shown in figures A62 thru A65. The motion, performed twice, is approximately a  $60^\circ$  swing of the lower right leg in the sagittal plane. The other arm and leg angles held constant are:

$\phi_2 = 13.92^\circ$	$\phi_3 = -29.61^\circ$	$\phi_7 = 17.56^\circ$
$\theta_2 = -7.44^\circ$	$\theta_3 = -9.08^\circ$	$\theta_7 = 3.72^\circ$
$\psi_2 = 18.60^\circ$	$\psi_3 = 6.76^\circ$	$\psi_7 = -33.02^\circ$
$\theta_4 = 45.36^\circ$	$\theta_5 = 54.91^\circ$	$\theta_9 = -44.14^\circ$

Except for forces and moments from torso shifting (certainly more of a problem with leg motions), the correlation is very good.

# APPENDIX A

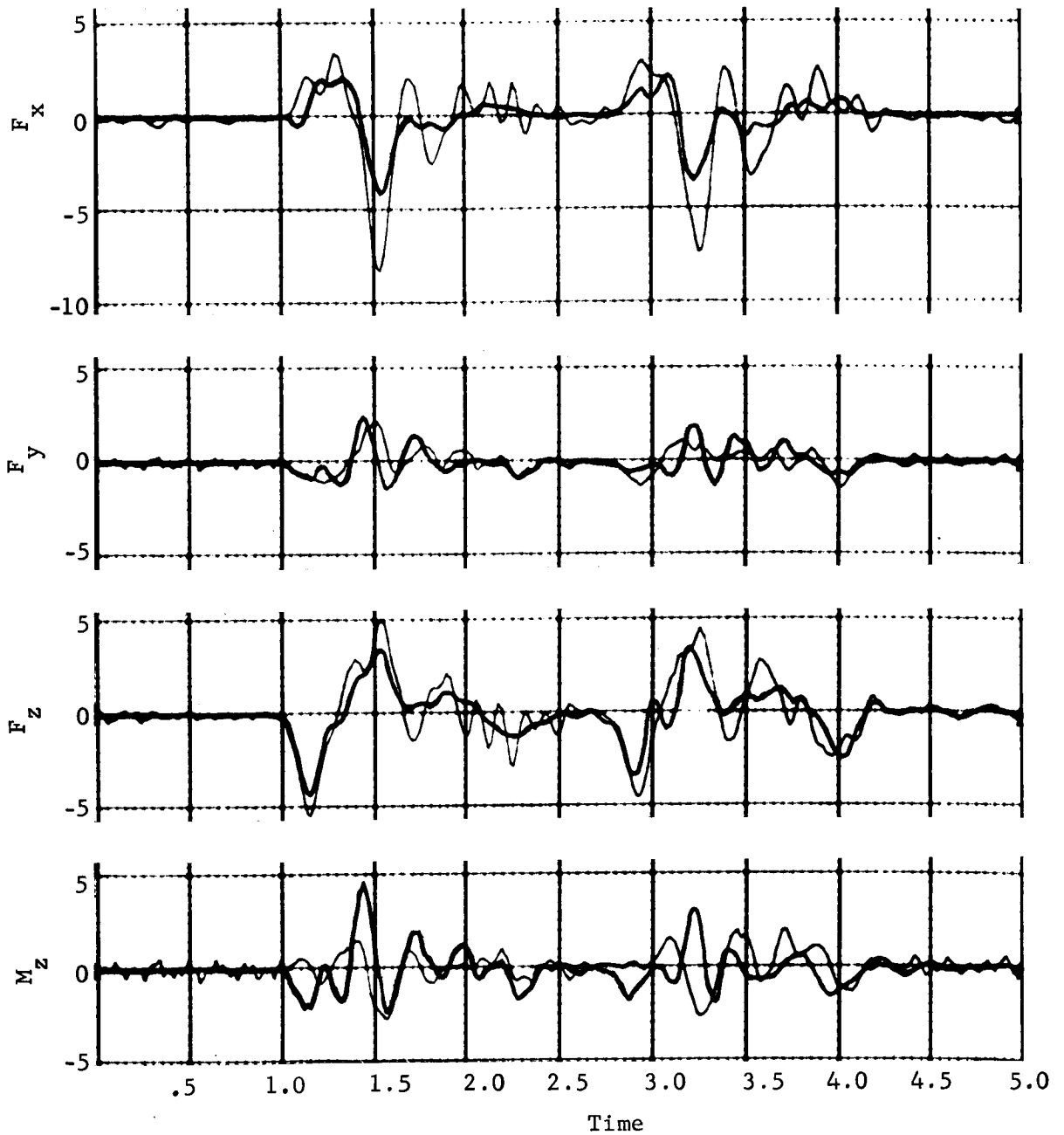


Figure A62.- Lower Right Leg, Single Pendulum, Sagittal Plane, Run 22

# APPENDIX A

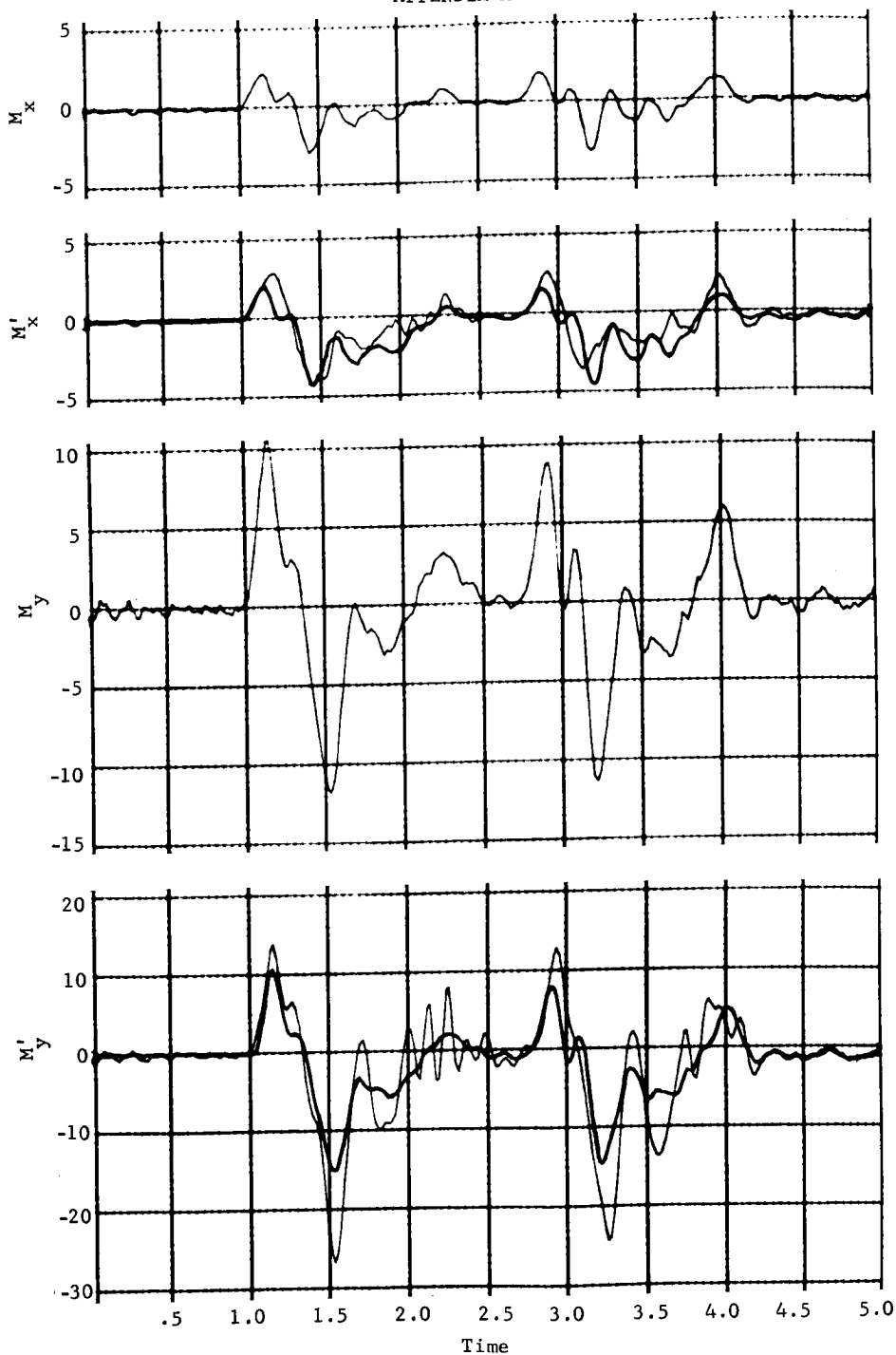


Figure A63.- Lower Right Leg, Single Pendulum, Sagittal Plane, Run 22



# APPENDIX A

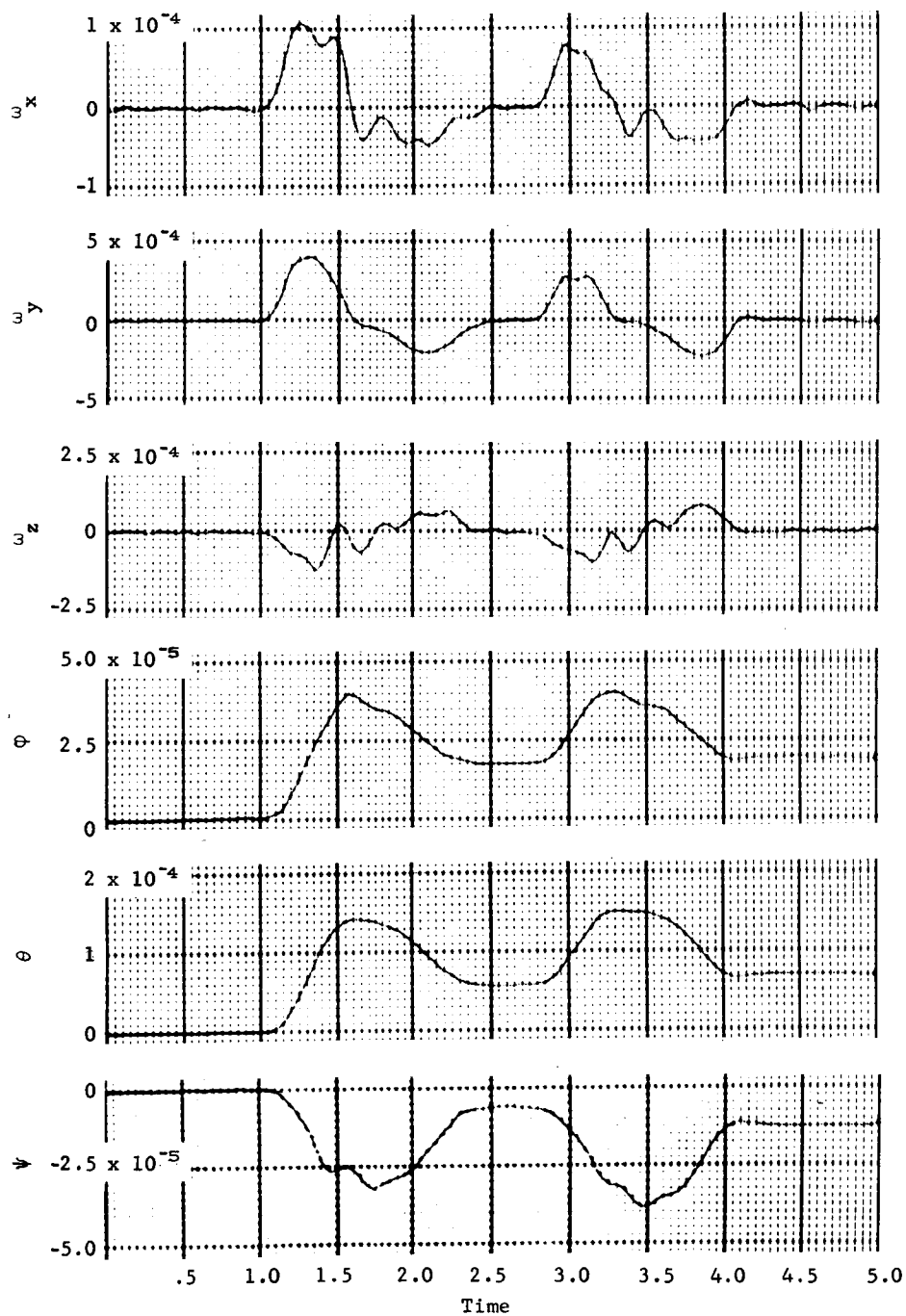


Figure A64.- Lower Right Leg, Single Pendulum, Sagittal Plane, Run 22

# APPENDIX A

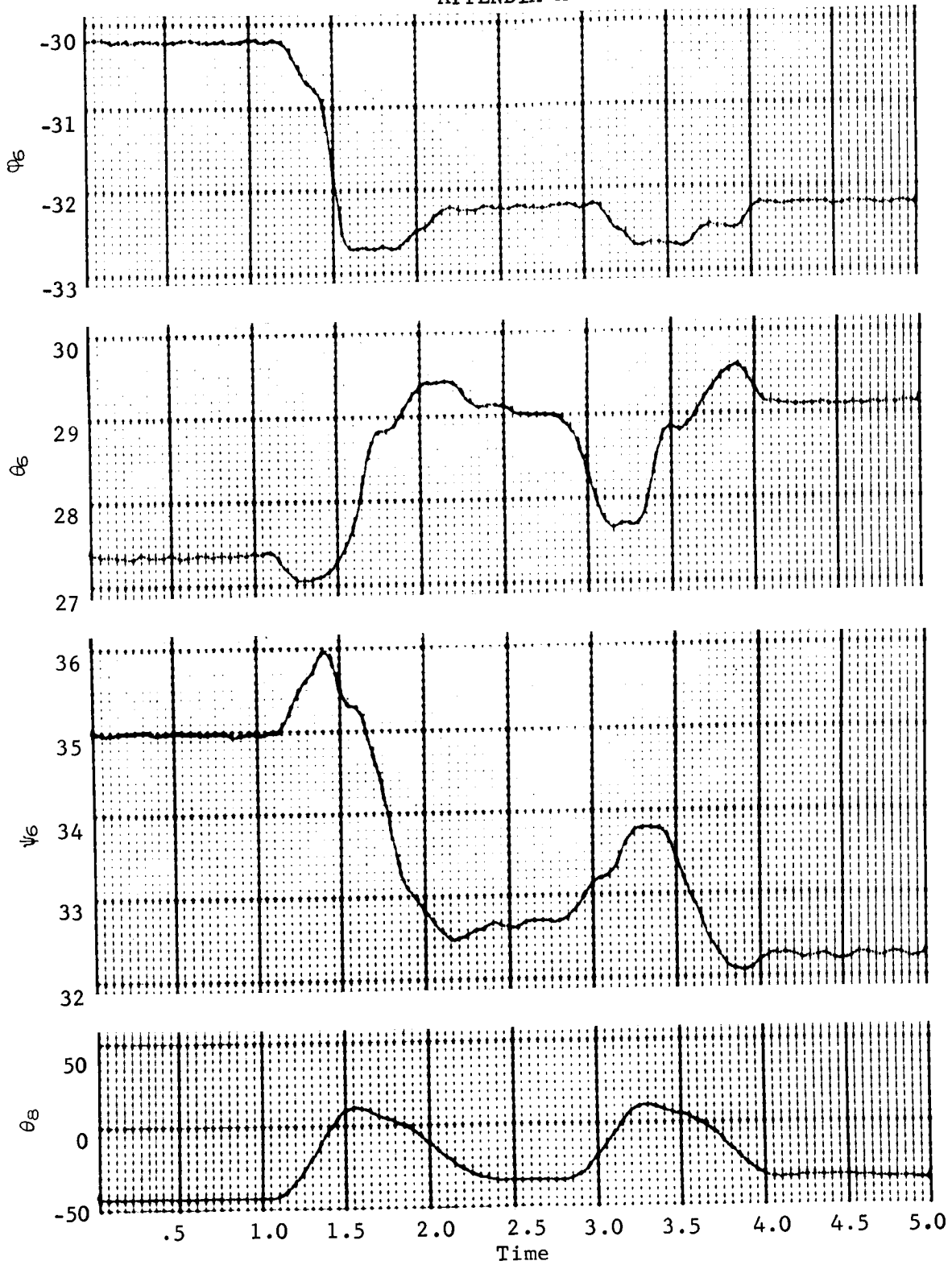


Figure A65.- Lower Right Leg, Single Pendulum, Sagittal Plane, Run 22

## APPENDIX A

### Run 23, total left leg, double pendulum, sagittal plane.-

This motion is approximately a  $30^\circ$  swing of the upper left leg and a  $100^\circ$  swing of the lower left leg, and is performed twice. Resulting data are shown in figures A66 thru A69. The other arm and leg angles held constant are:

$\phi_2 = 17.37^\circ$	$\phi_3 = -31.34^\circ$	$\phi_6 = -33.21^\circ$
$\theta_2 = -4.57^\circ$	$\theta_3 = -9.44^\circ$	$\theta_6 = 31.15^\circ$
$\psi_2 = 16.27^\circ$	$\psi_3 = 0.00^\circ$	$\psi_6 = 45.74^\circ$
$\theta_4 = 41.28^\circ$	$\theta_5 = 54.14^\circ$	$\theta_8 = -60.67^\circ$

As in Run 16, appreciable torso shifting can give rise to large c.g. shift moments as noted in the load cell results of  $M'_y$ .

# APPENDIX A



Figure A66.- Total Left Leg, Double Pendulum, Sagittal Plane, Run 23

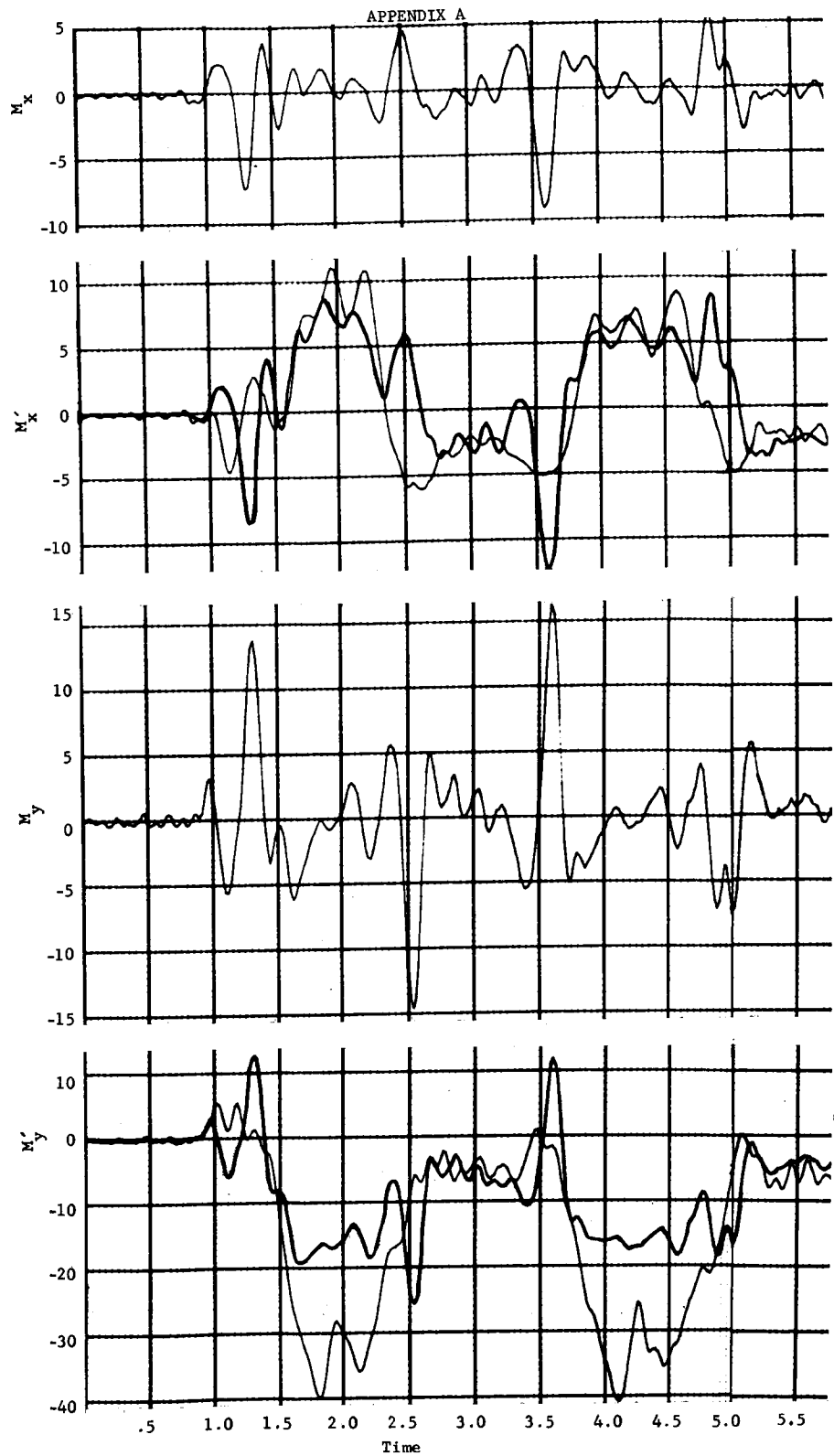


Figure A67.- Total Left Leg, Double Pendulum, Sagittal Plane, Run 23

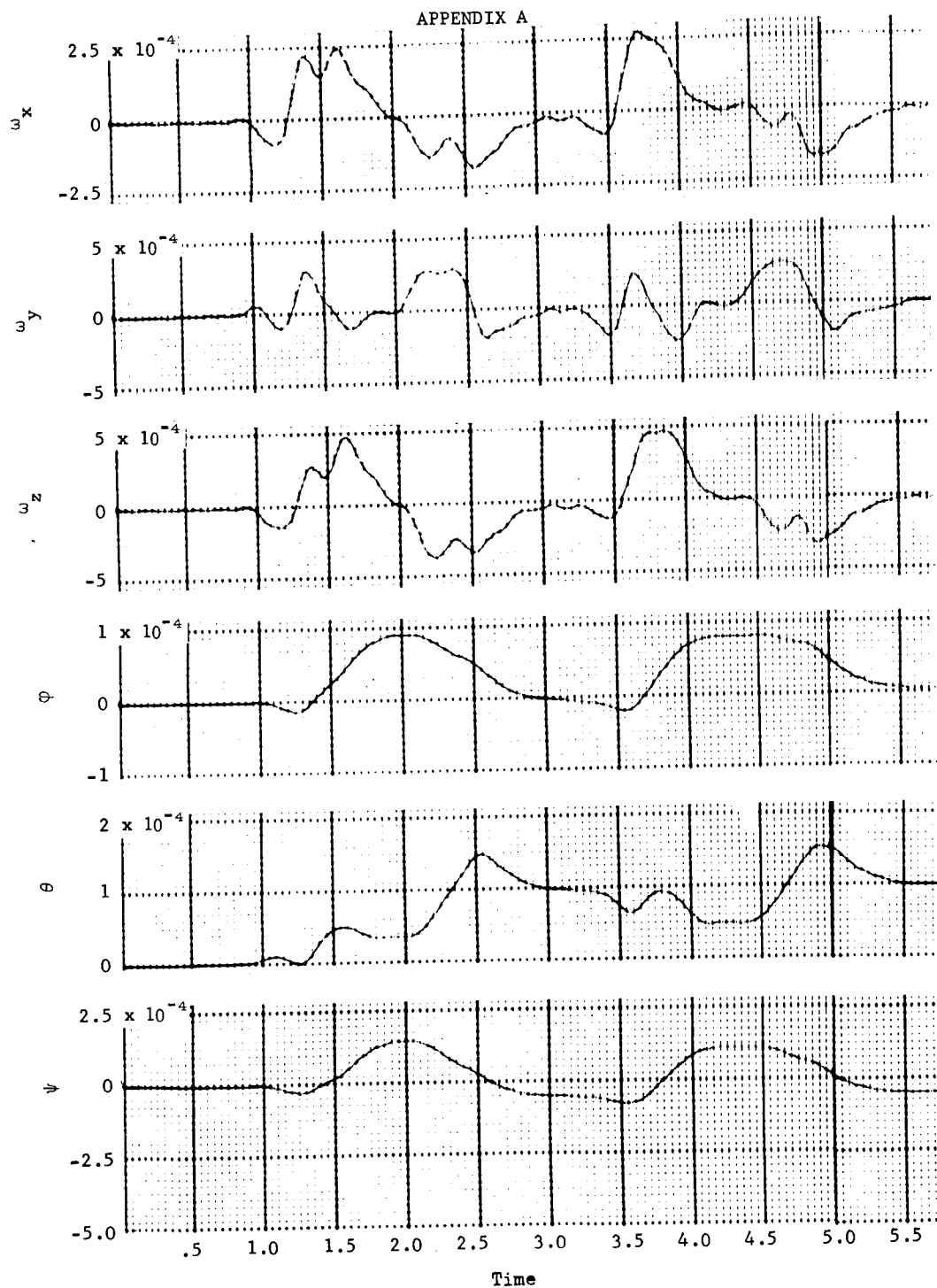


Figure A68.- Total Left Leg, Double Pendulum, Sagittal Plane, Run 23

# APPENDIX A

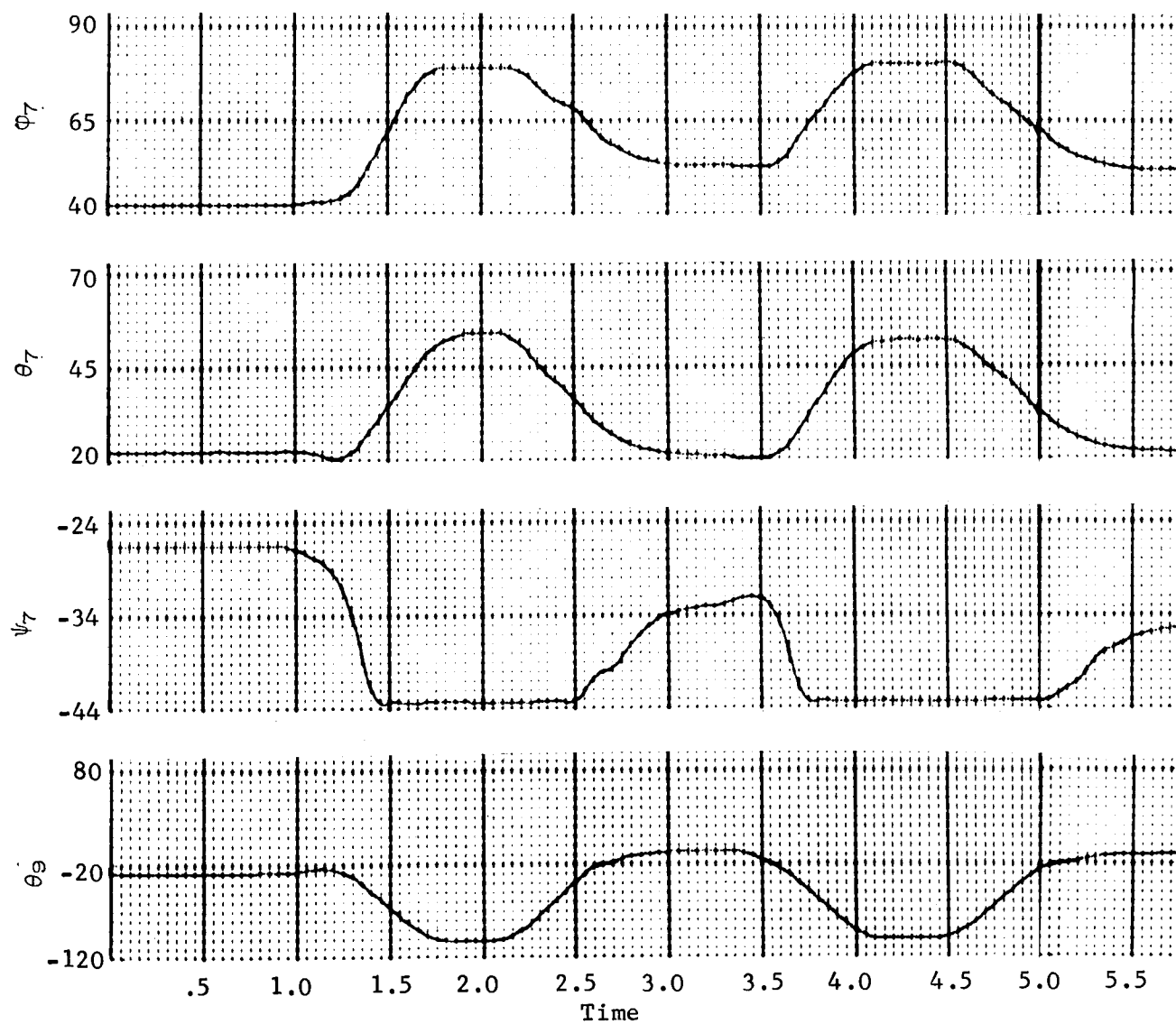


Figure A69.- Total Left Leg, Double Pendulum, Sagittal Plane, Run 23

## APPENDIX A

Run 24, right arm console operation.- This run is a repeat of Run 17 using Subject 2. Resulting data are shown in figures A70 thru A73. The subject raises his arm, simulates turning knobs and flipping switches, and then lowers his arm. The other arm and leg angles held constant are:

$\phi_3 = -29.61^\circ$	$\phi_6 = -26.68^\circ$	$\phi_7 = 31.53^\circ$
$\theta_3 = -7.00^\circ$	$\theta_6 = 24.38^\circ$	$\theta_7 = 27.98^\circ$
$\psi_3 = -8.18^\circ$	$\psi_6 = 45.55^\circ$	$\psi_7 = -47.23^\circ$
$\theta_5 = 41.90^\circ$	$\theta_8 = -49.24^\circ$	$\theta_9 = -51.98^\circ$

As in Run 17, unmonitored wrist actions can account for some of the discrepancies. However, the primary problem appears to be torso shifting (note the good correlation in  $F_z$  where torso shifting cannot occur). Inaccurate LIMS angles account for the inaccurate calculation of the c.g. shift moments in  $M'_x$  and  $M'_y$ .



# APPENDIX A

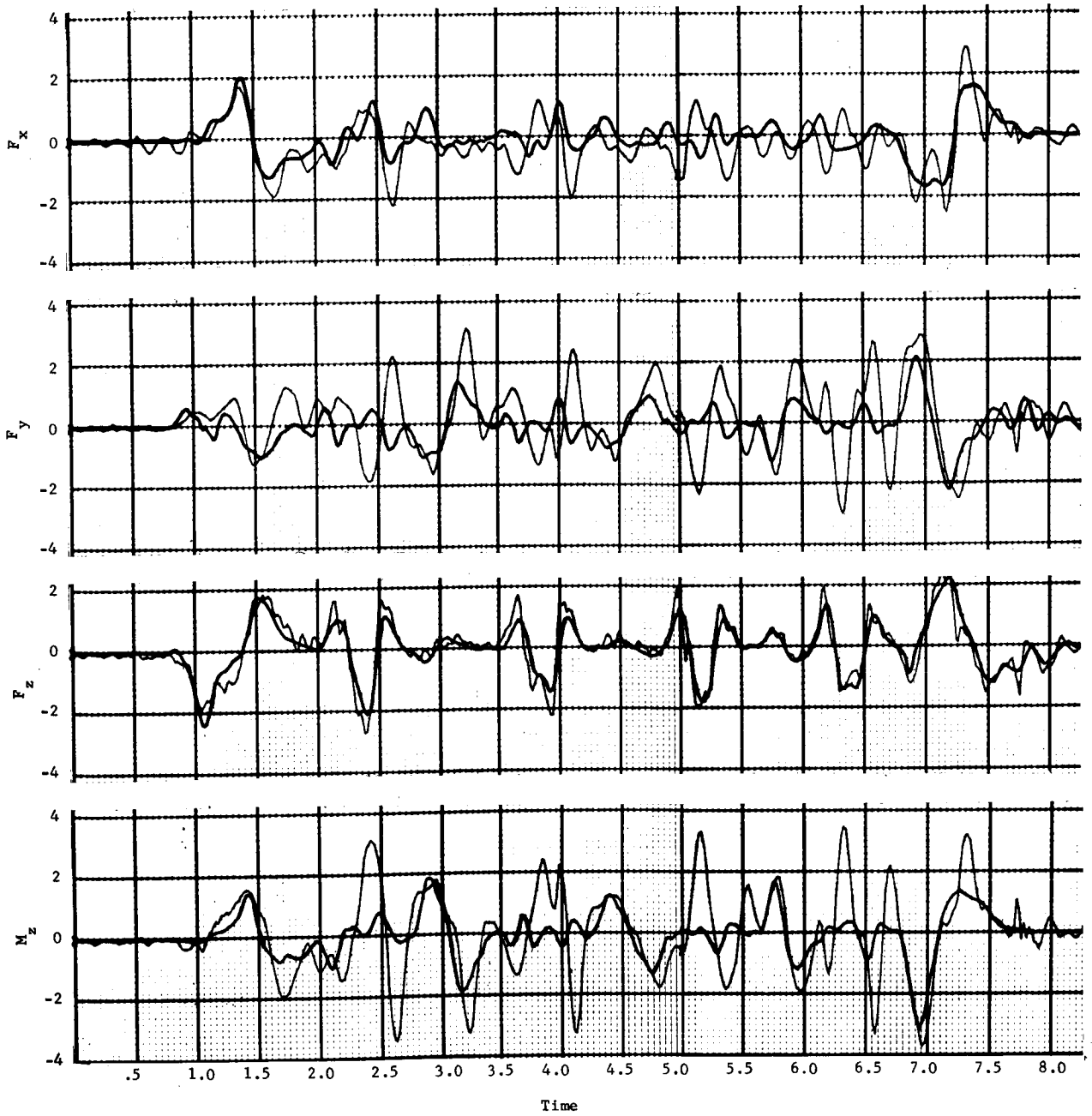


Figure A70.- Right Arm Console Operation, Run 24

# APPENDIX A

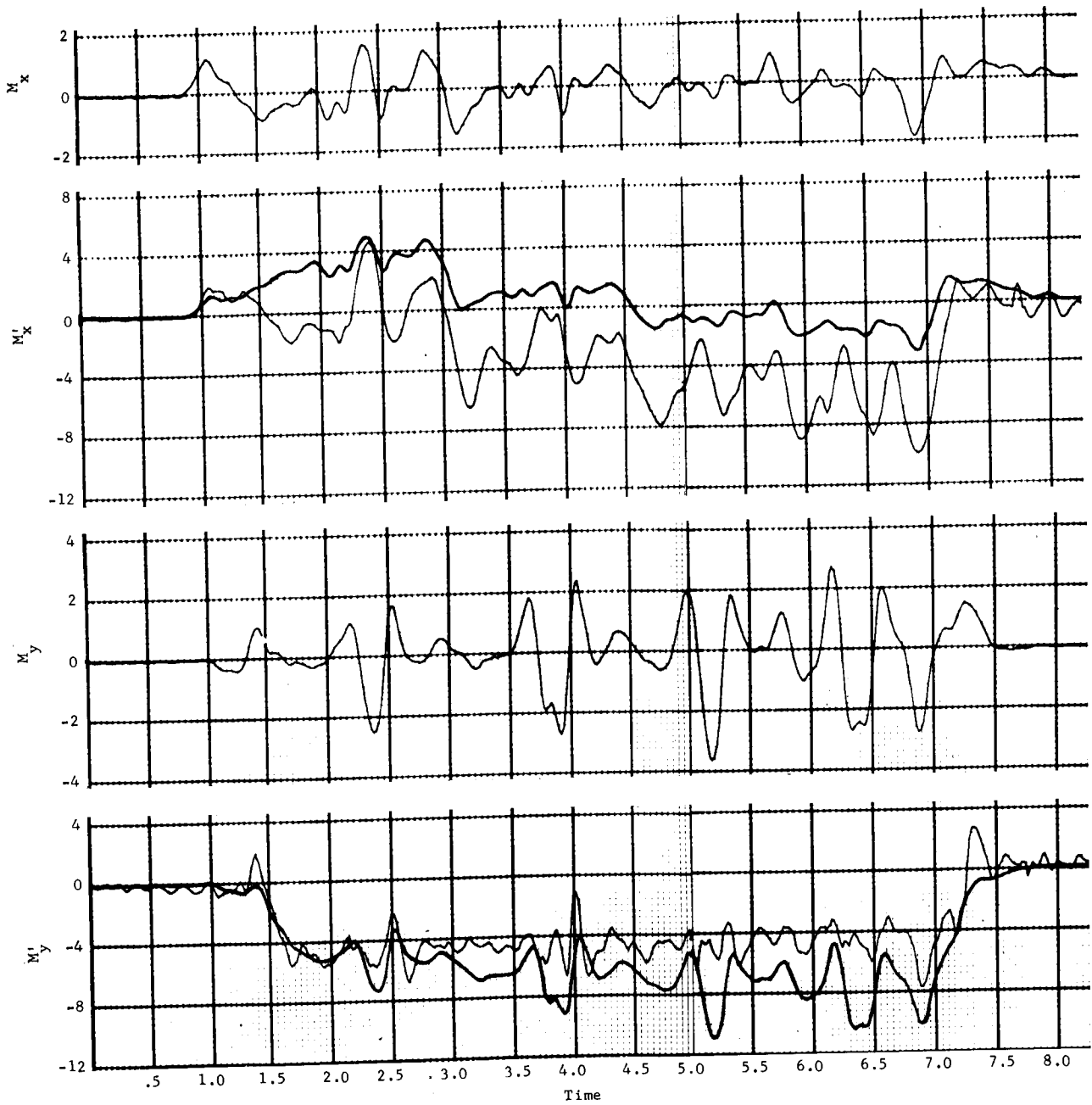


Figure A71.- Right Arm Console Operation, Run 24

# APPENDIX A

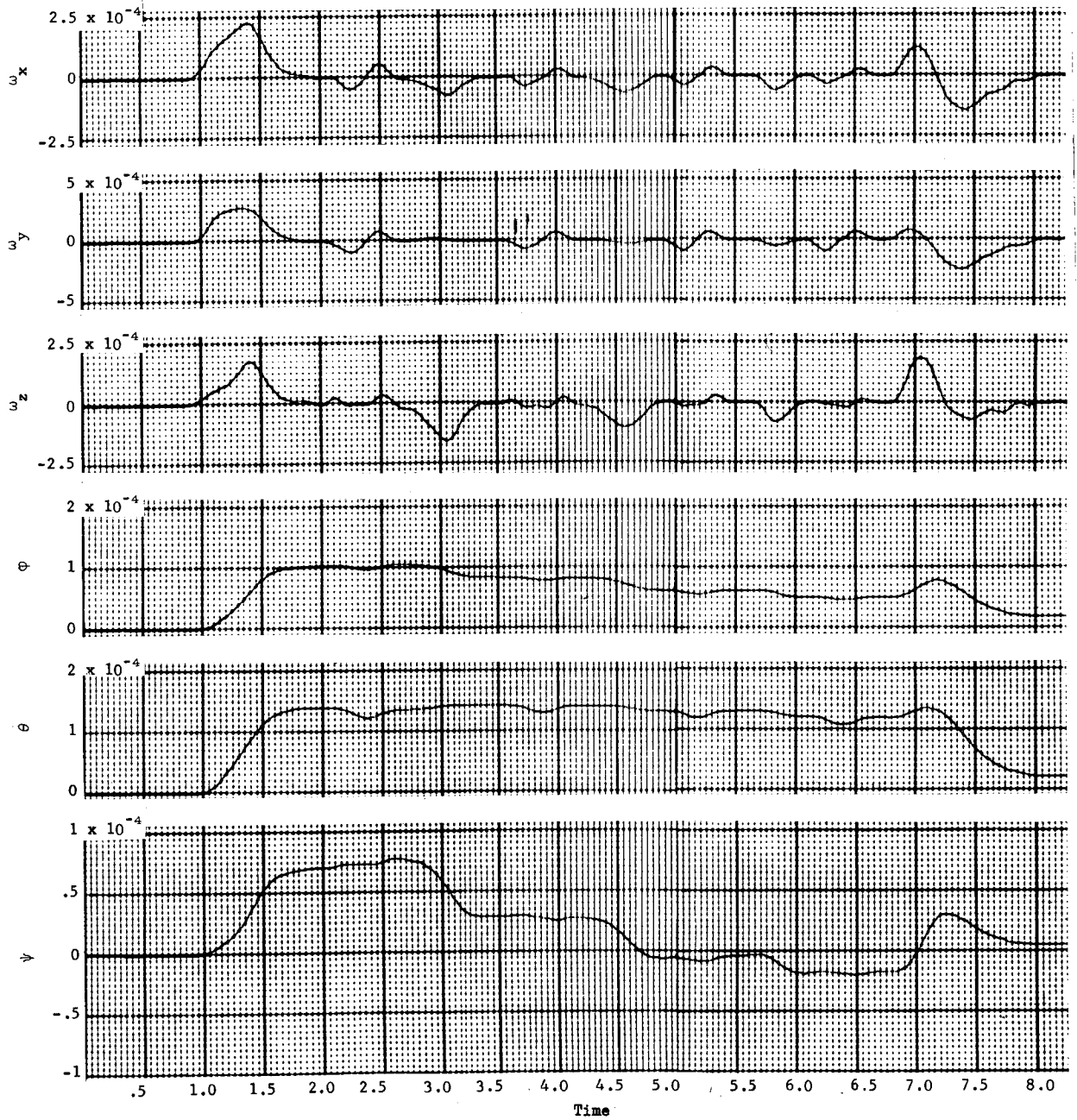


Figure A72.- Right Arm Console Operation, Run 24

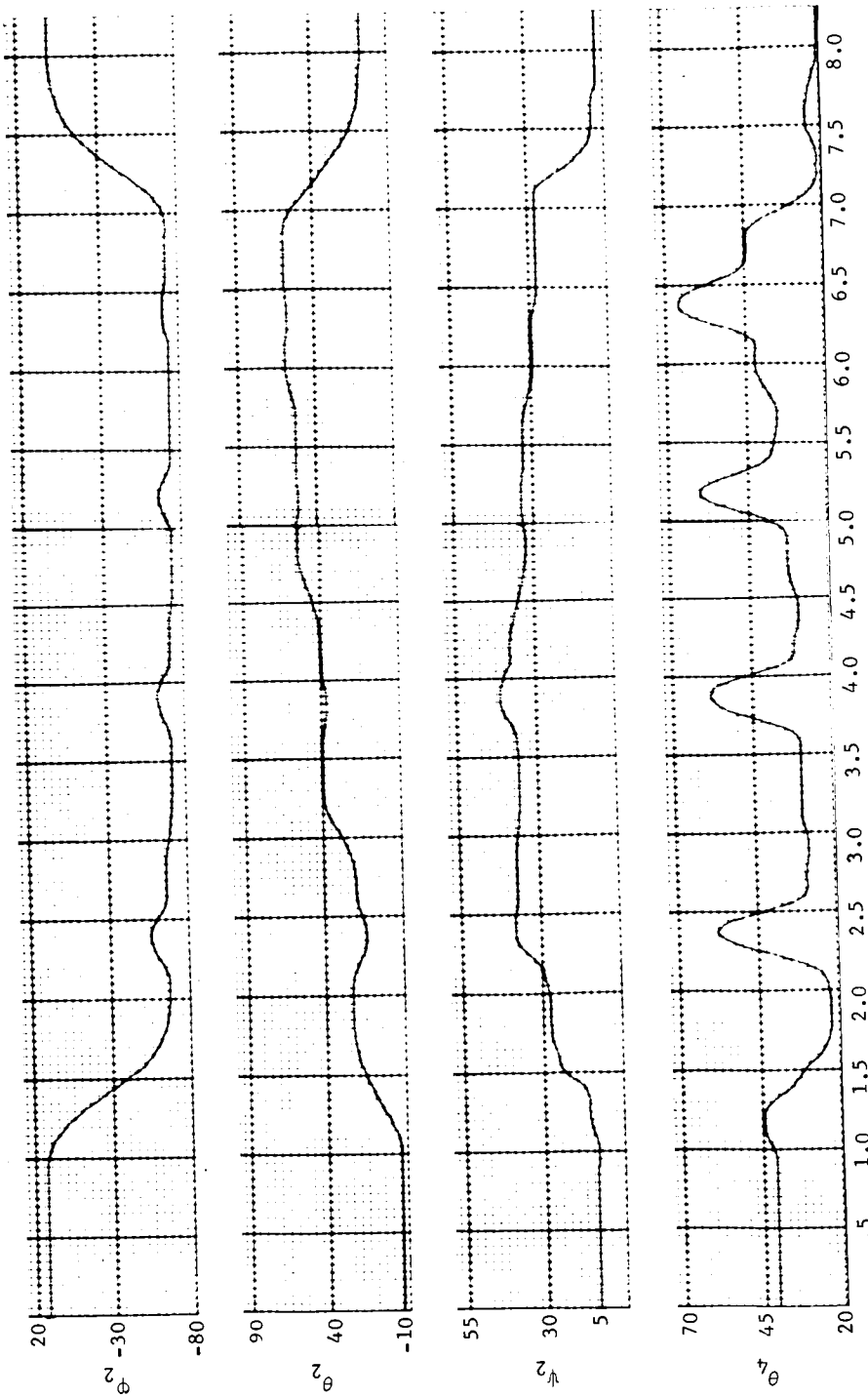


Figure A73.- Right Arm Console Operation, Run 24

## APPENDIX A

Run 25, both arm and legs, exercising.- In this motion, an elastic cord exerciser was used to simulate exercising. Both arm and legs were used (see angles in figs. A74 thru A80). However, most of the motion was caused by the arms and lower legs. Considering the large amount of torso shifting possible in this motion, the correlation is fairly good. The large load cell spikes in the data occurring at 2.3 and 4.6 sec are caused by the yaw rings of the legs hitting the wooden couch mockup as the legs were returned to their rest position.

# APPENDIX A

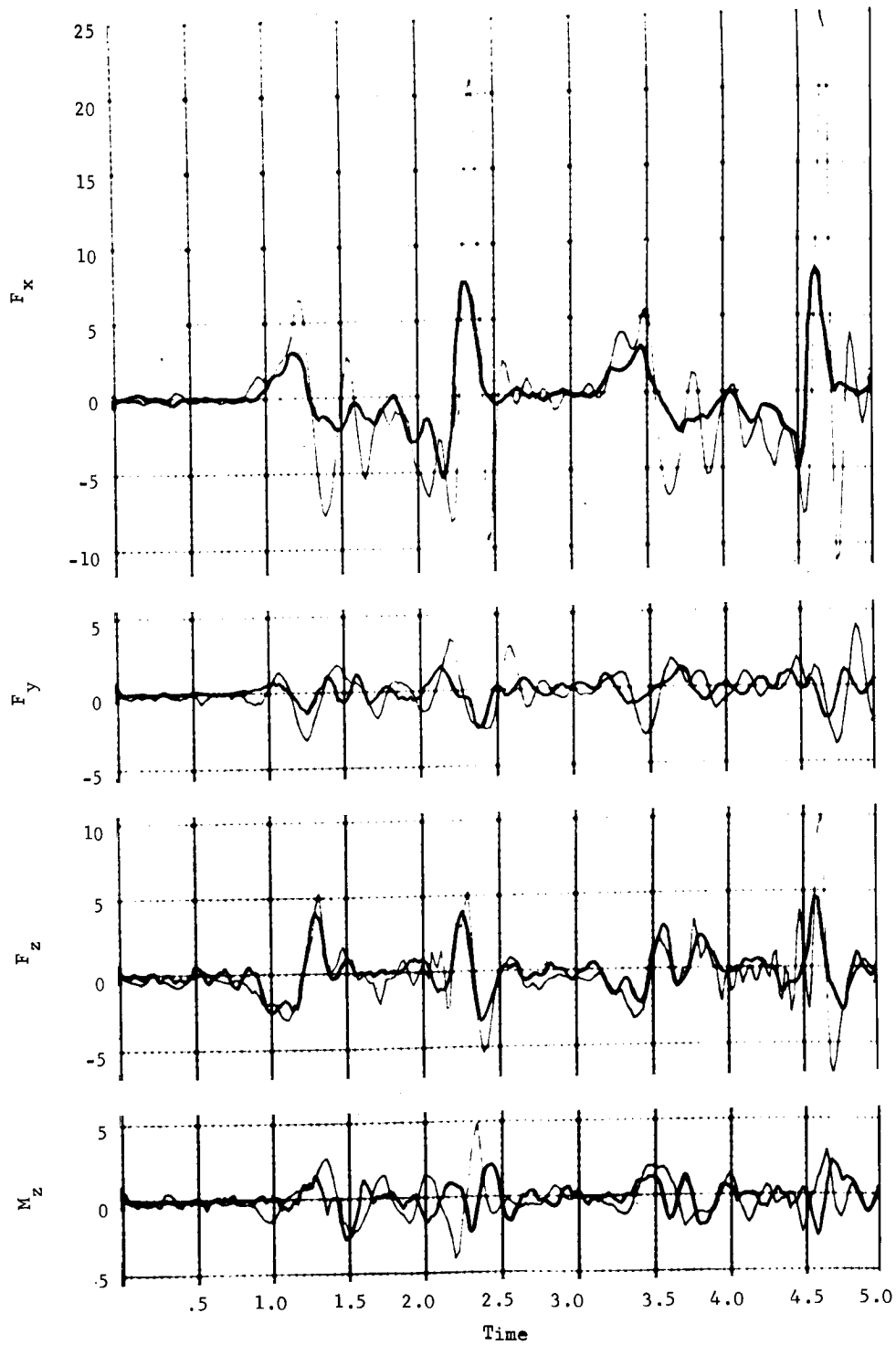


Figure A74.- Both Arms and Legs, Exercising, Run 25

# APPENDIX A

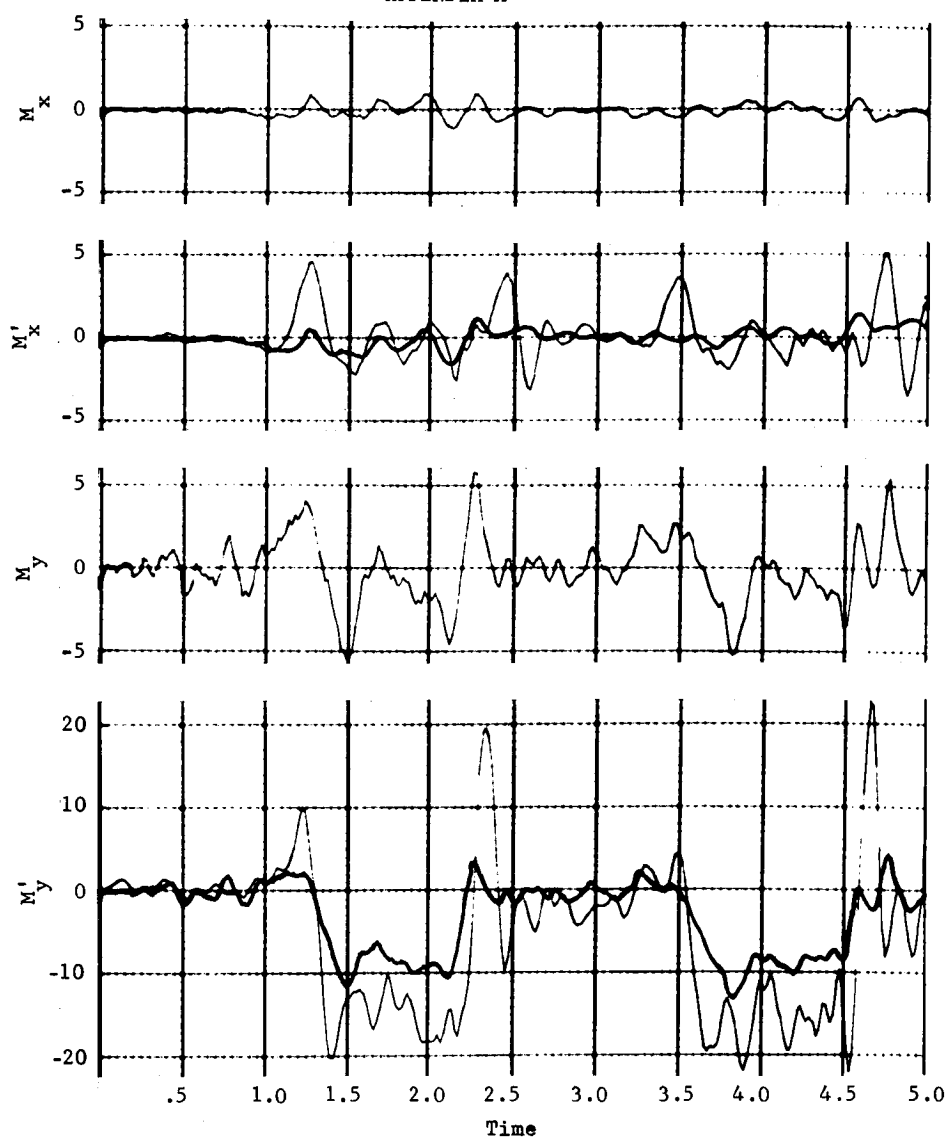


Figure A75.- Both Arms and Legs, Exercising, Run 25

# APPENDIX A

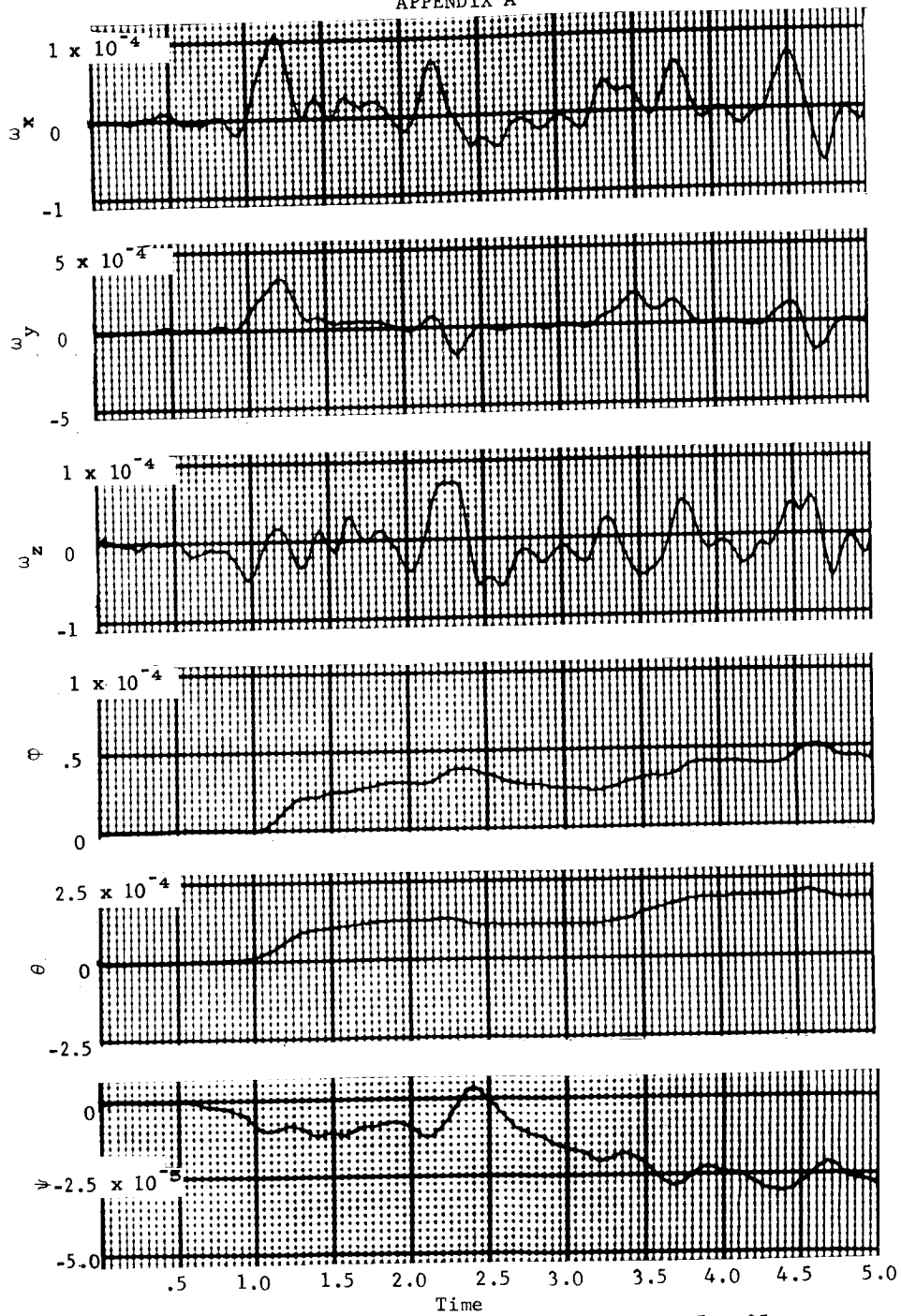


Figure A76.- Both Arms and Legs, Exercising, Run 25



# APPENDIX A

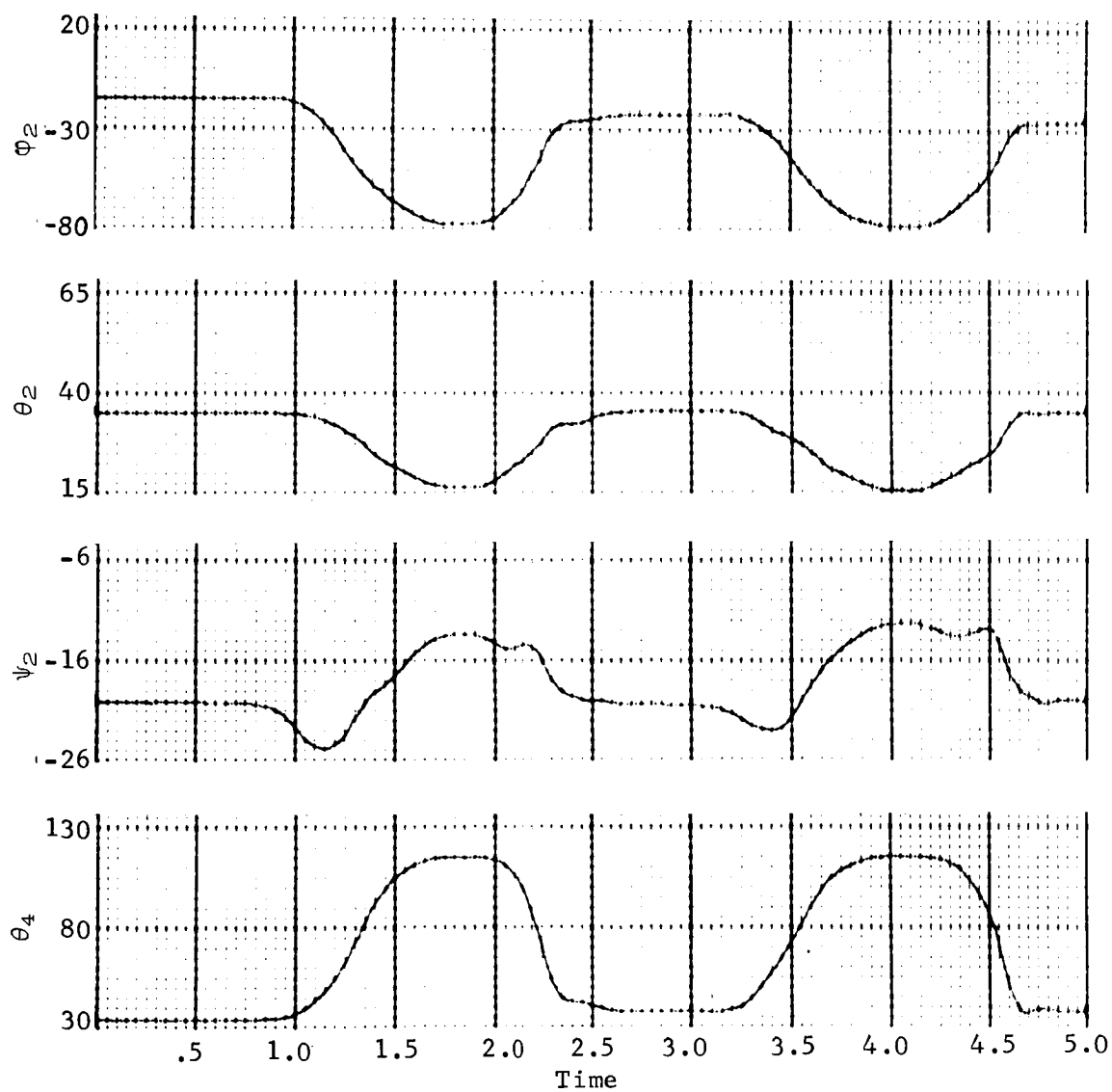


Figure A77.- Both Arms and Legs, Exercising, Run 25

# APPENDIX A

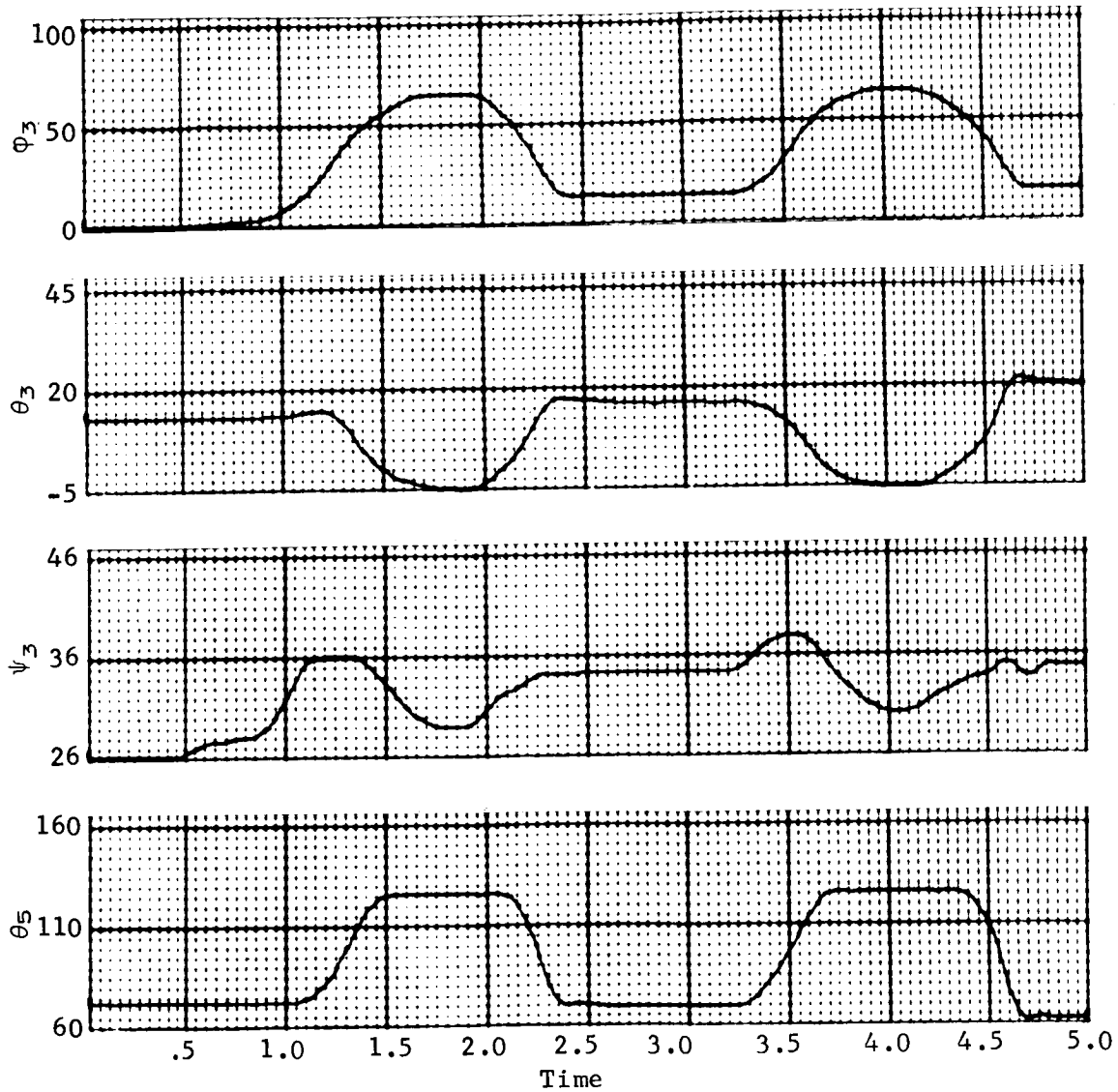


Figure A78.- Both Arms and Legs, Exercising, Run 25

# APPENDIX A

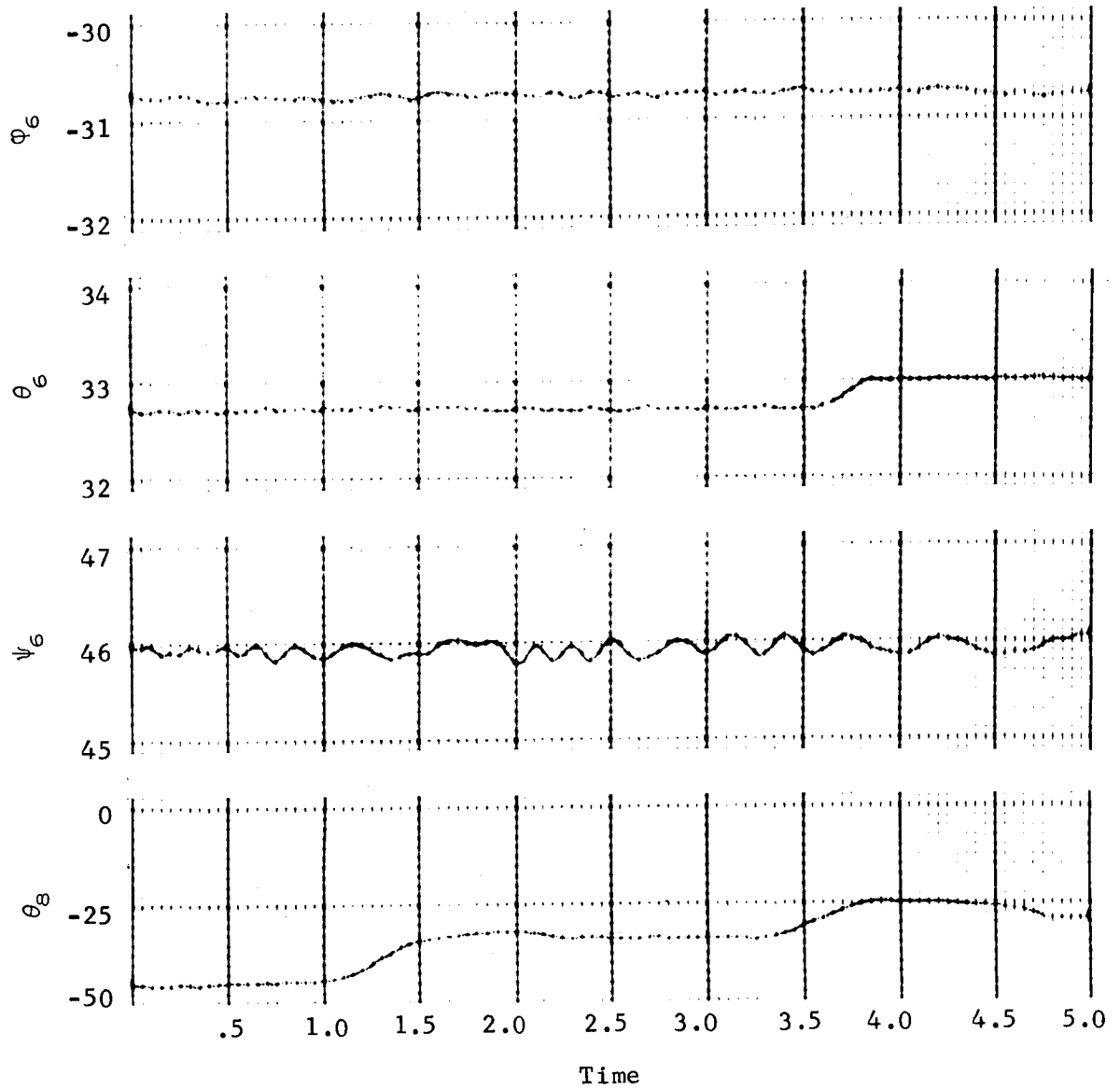


Figure A79.- Both Arms and Legs, Exercising, Run 25

# APPENDIX A

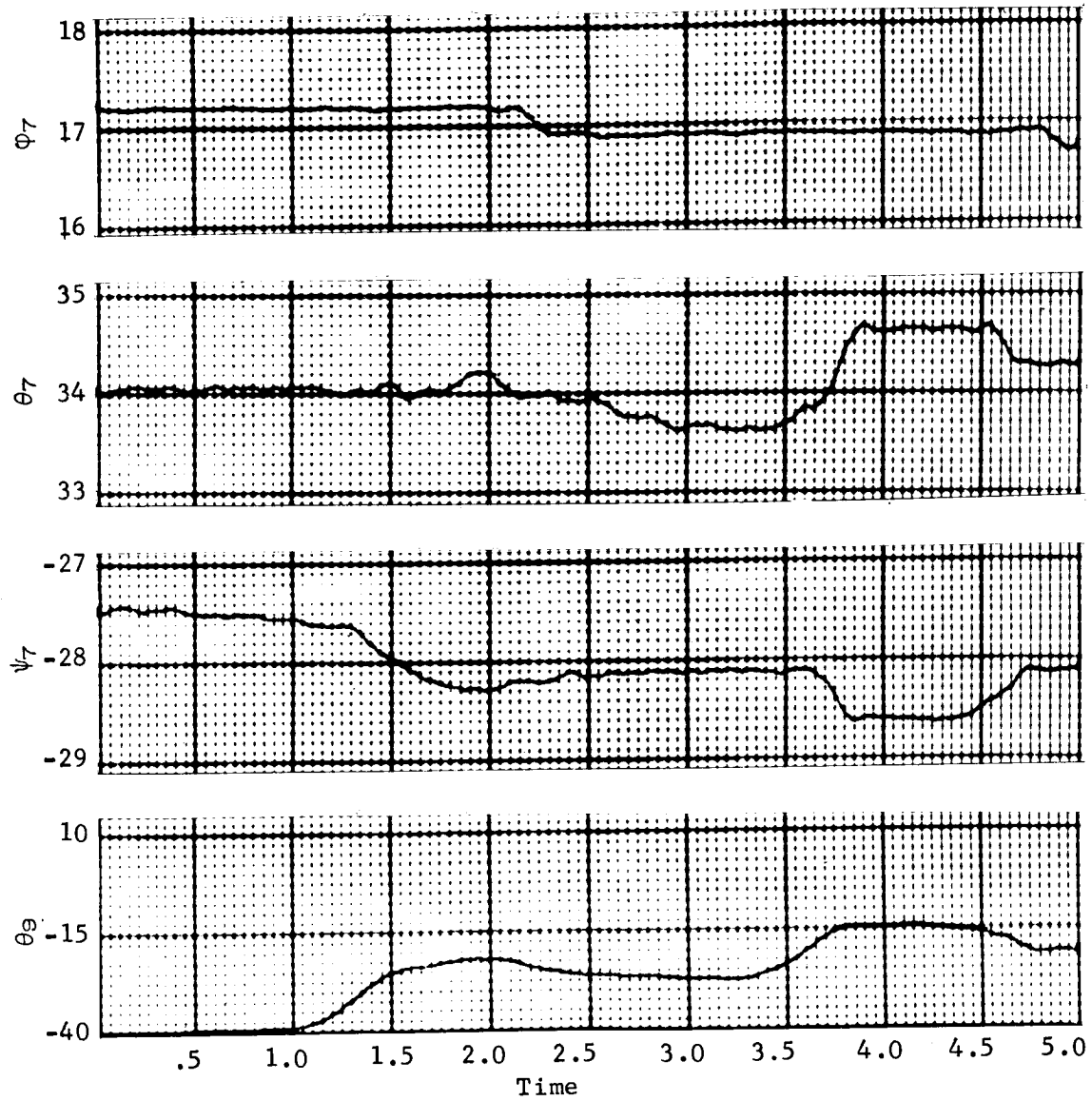


Figure A80.- Both Arms and Legs, Exercising, Run 25

## APPENDIX A

### Part II - Translational Crew Activity Simulation Results

Part II of this appendix contains the results of the translational crew activity program conducted using the Space Operations Simulator (SOS). The load cell forces and moments for the handrail translation activity are presented under the heading Translational Crew Activities in the main text. The other activities and the page on which the results for each activity begin are shown in the following tabulation. The axis system in which the results are resolved is shown on each figure.

<u>Activity</u>	<u>Page</u>
1. Compressive walking	265
2. Bounce walk	270
3. Free soaring	277

For activities 1 and 2, the forces and moments have been applied to the cluster S/C. The nomenclature for the curves is given in Part I of this appendix.

Compressive walking. - The results shown in figures A81 and A82 are the load cell forces and moments and S/C angular rates and displacements resulting from the compressive walking task. The subject remained in contact with both reaction surfaces while maneuvering from one side of the mockup to the other.

# APPENDIX A

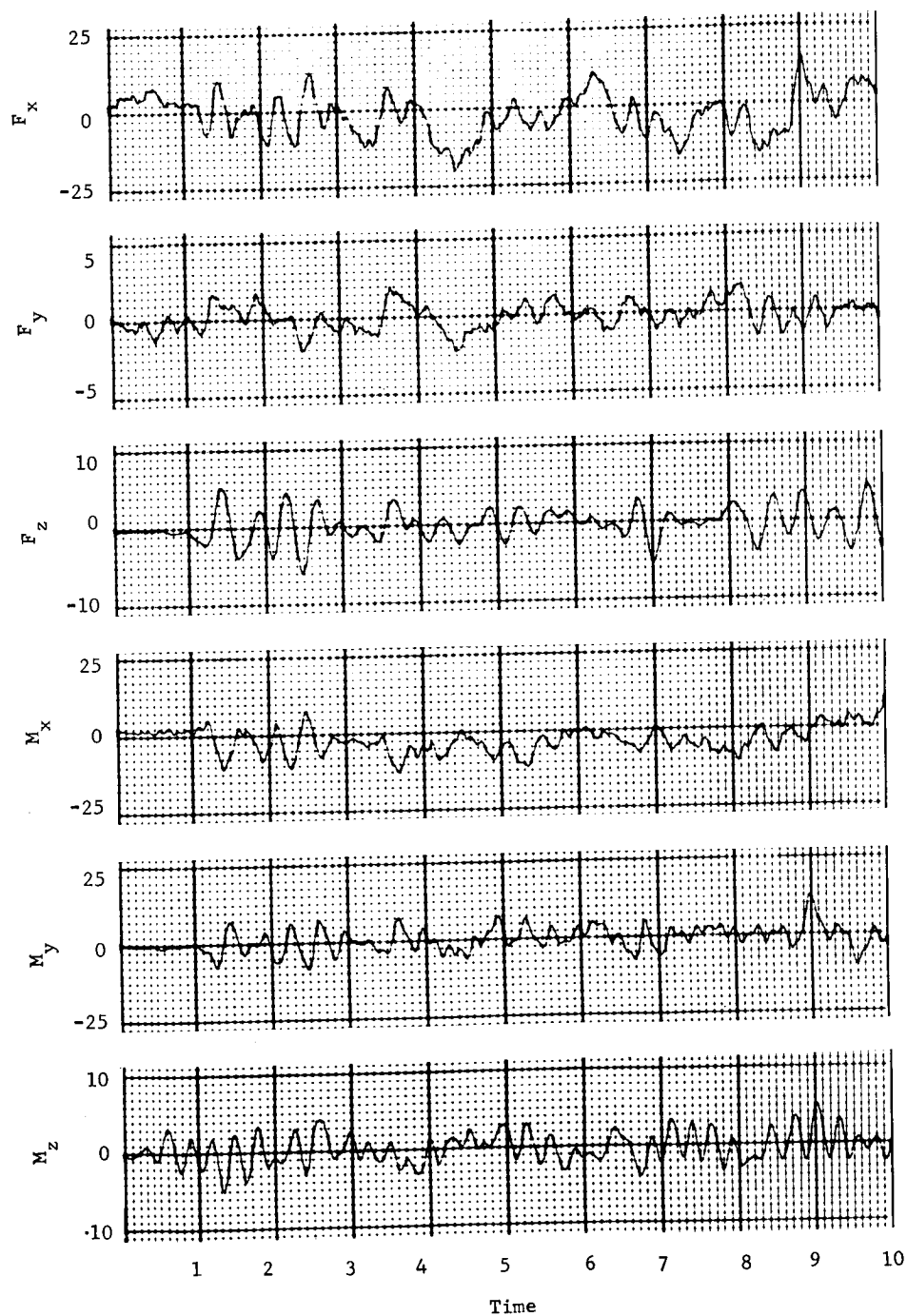


Figure A81.- Compressive Walking, Man's Axes

# APPENDIX A

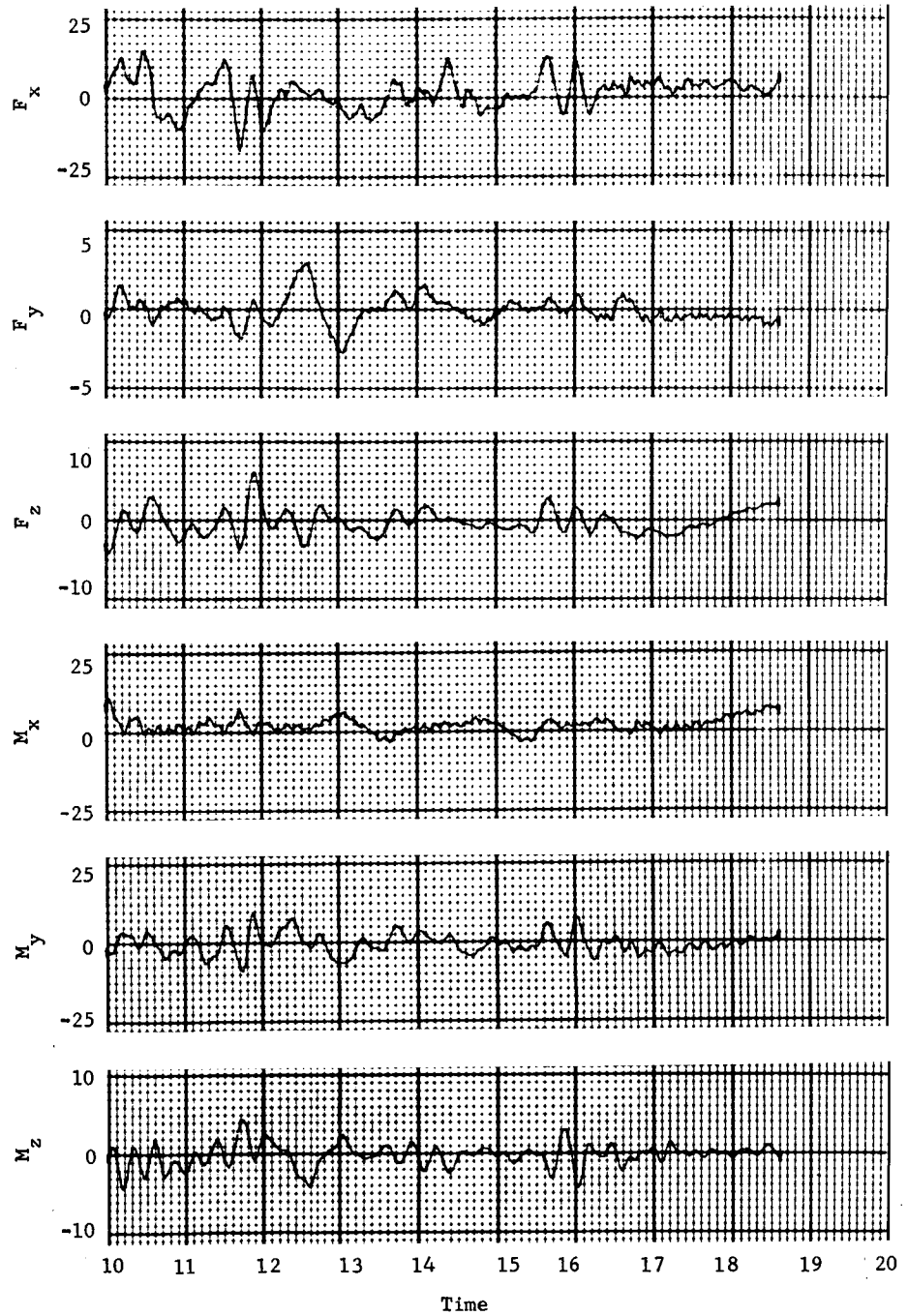


Figure A81.- Concluded

# APPENDIX A

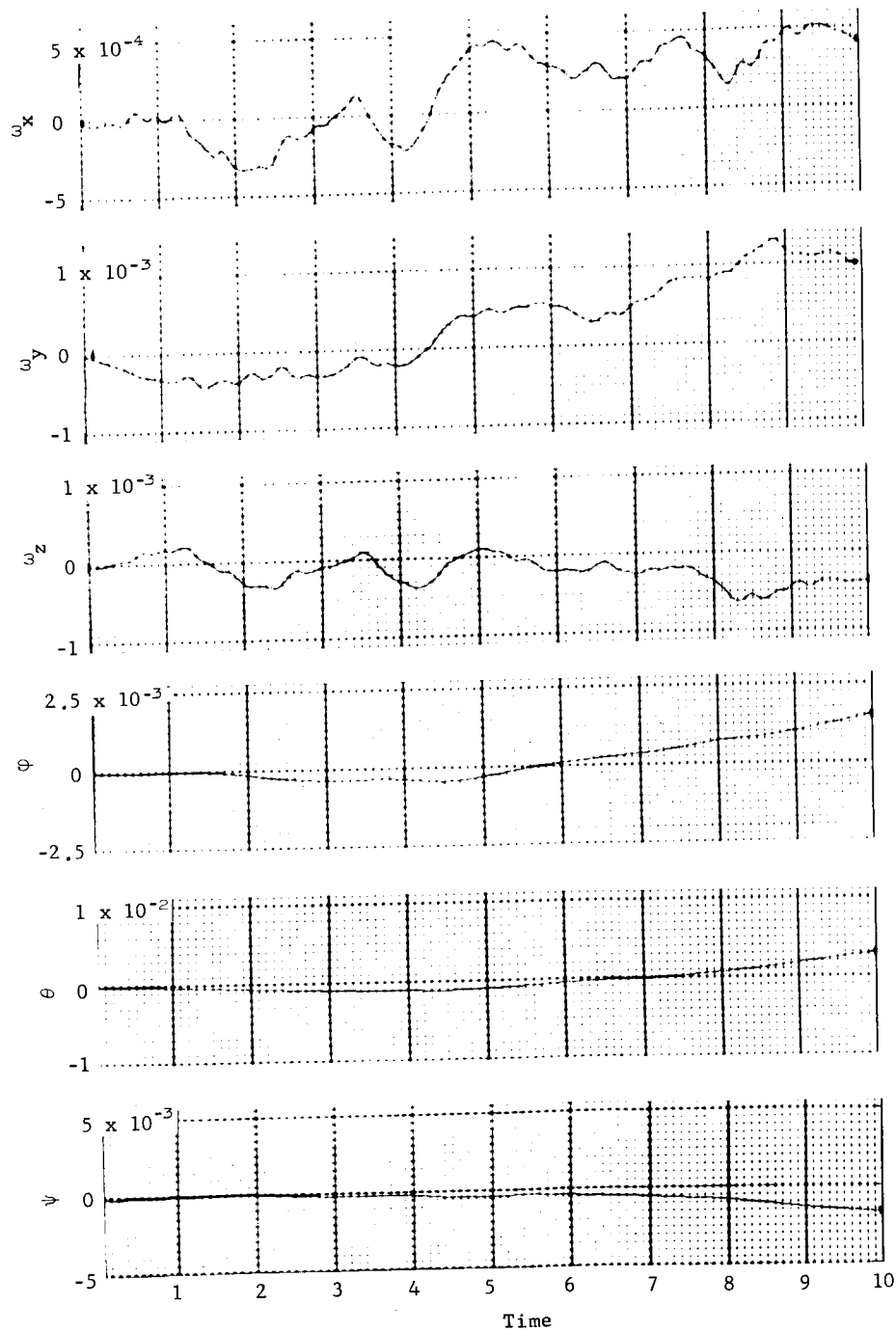


Figure A82.- Compressive Walking, Spacecraft Axes



# APPENDIX A

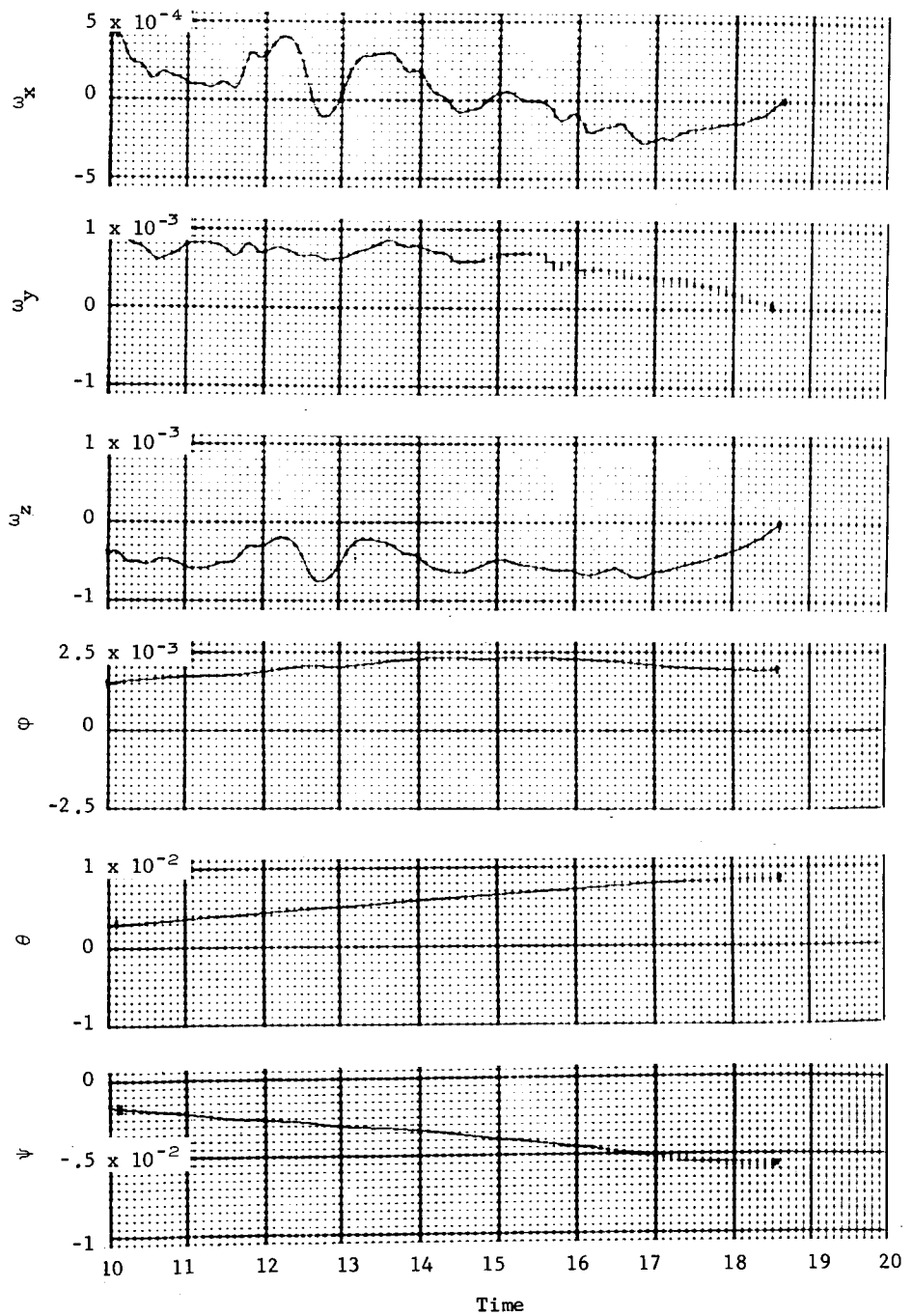


Figure A82.- Concluded

## APPENDIX A

Bounce walk.- The results shown in figures A83 and A84 are the load cell forces and moments and S/C angular rates and displacements resulting from the bounce walk task. The subject remained in contact with only one surface at a time with periods of no contact with either surface (note that forces and moments return to zero periodically). Because of a mockup that was not perfectly rigid, some of the forces and moments show a small amplitude sine wave resulting from the mockup vibration. These extraneous forces and moments are not expected to affect the calculated S/C disturbances.

# APPENDIX A

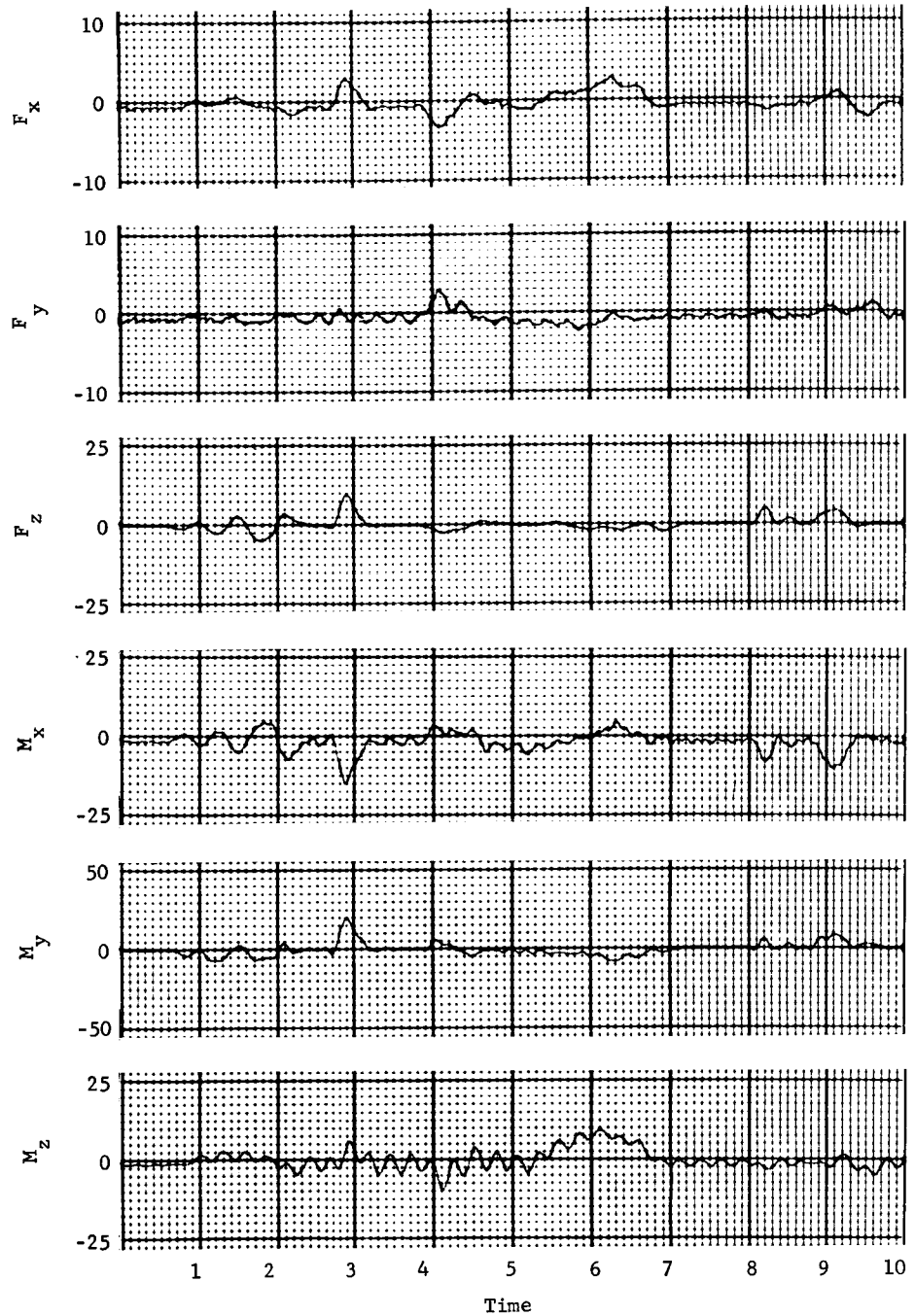


Figure A83.- Bounce Walk, Man's Axes

# APPENDIX A

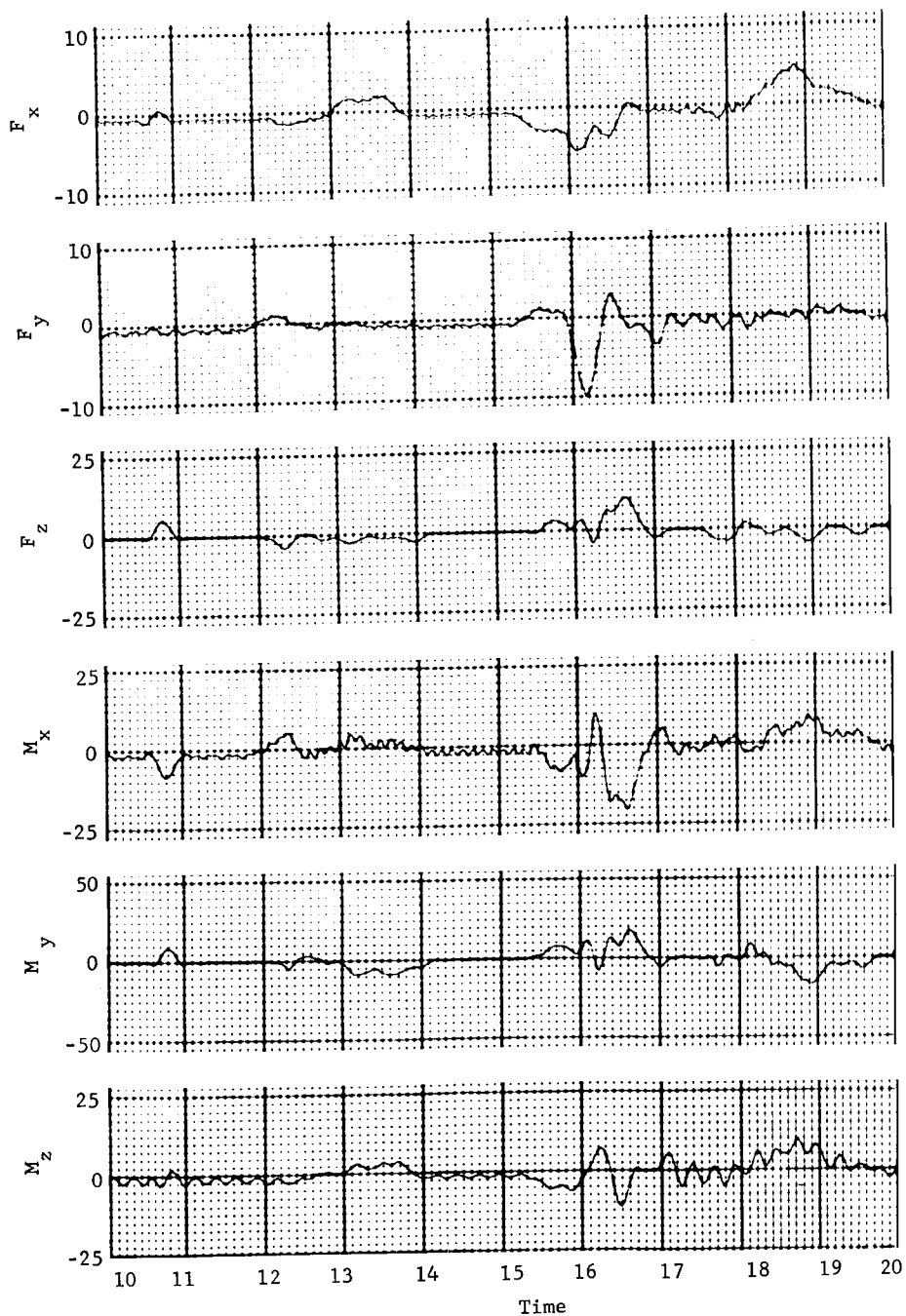


Figure A83.- Continued

# APPENDIX A

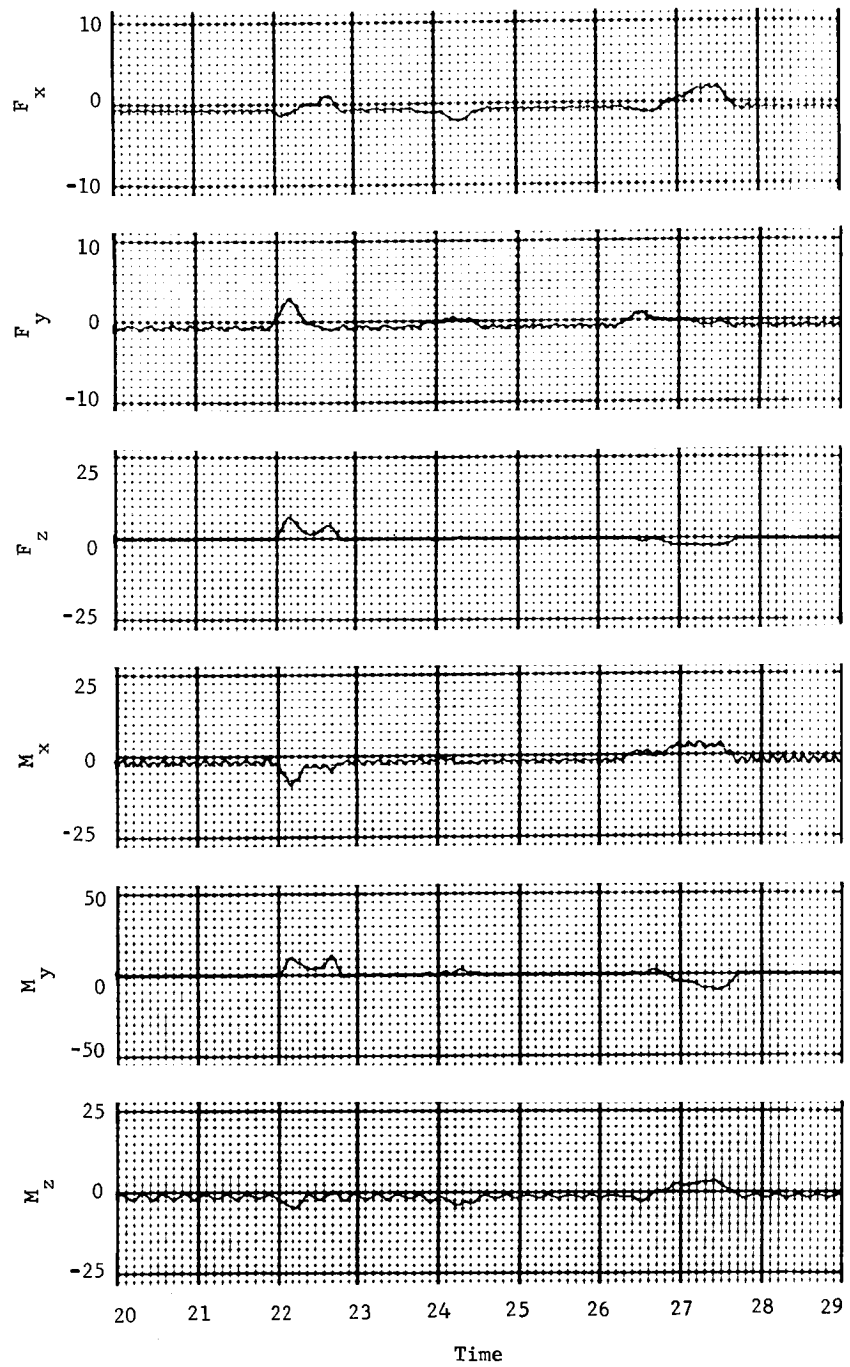


Figure A83.- Concluded

# APPENDIX A

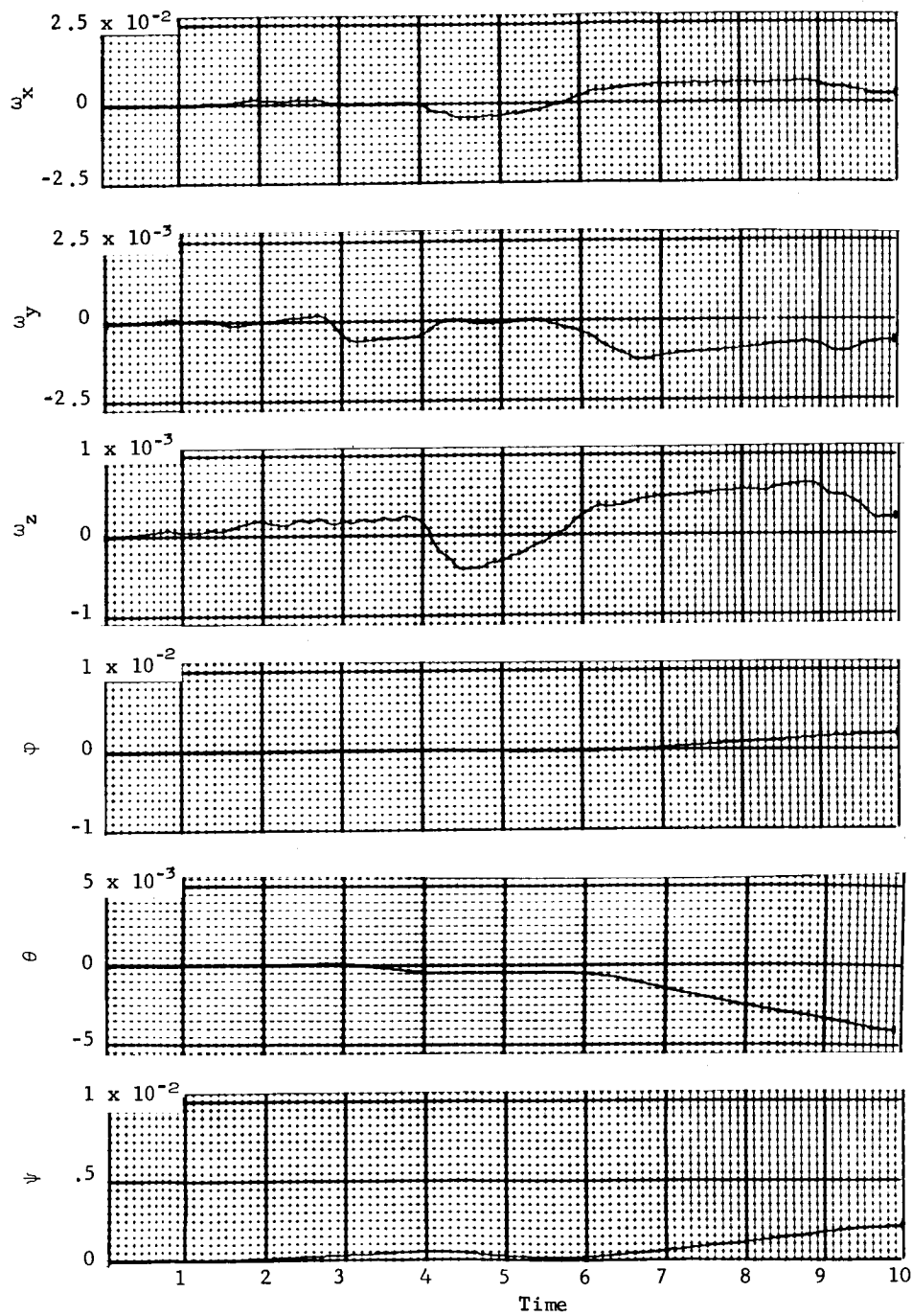


Figure A84.- Bounce Walk, Spacecraft Axes

# APPENDIX A

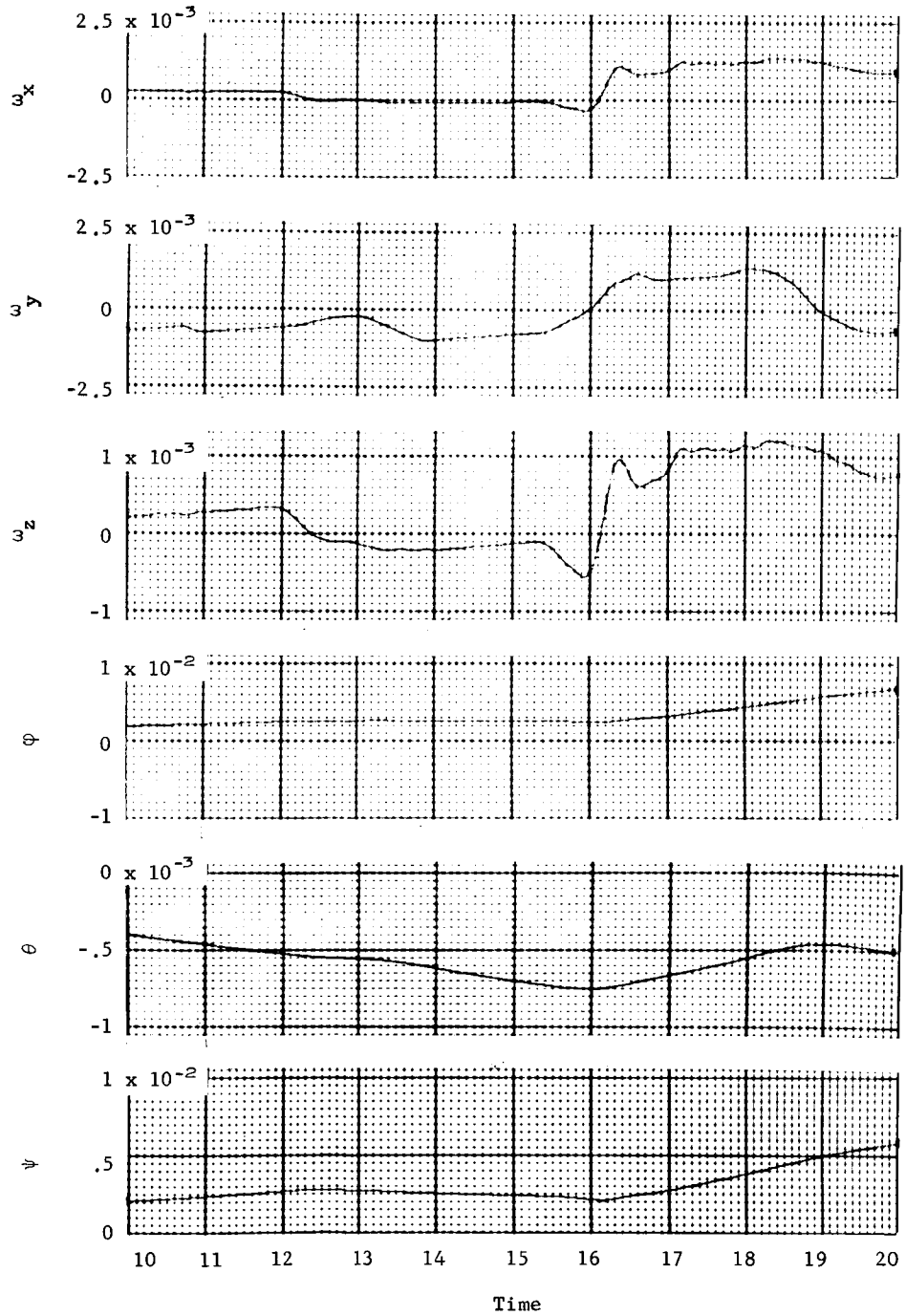


Figure A84.- Continued

# APPENDIX A

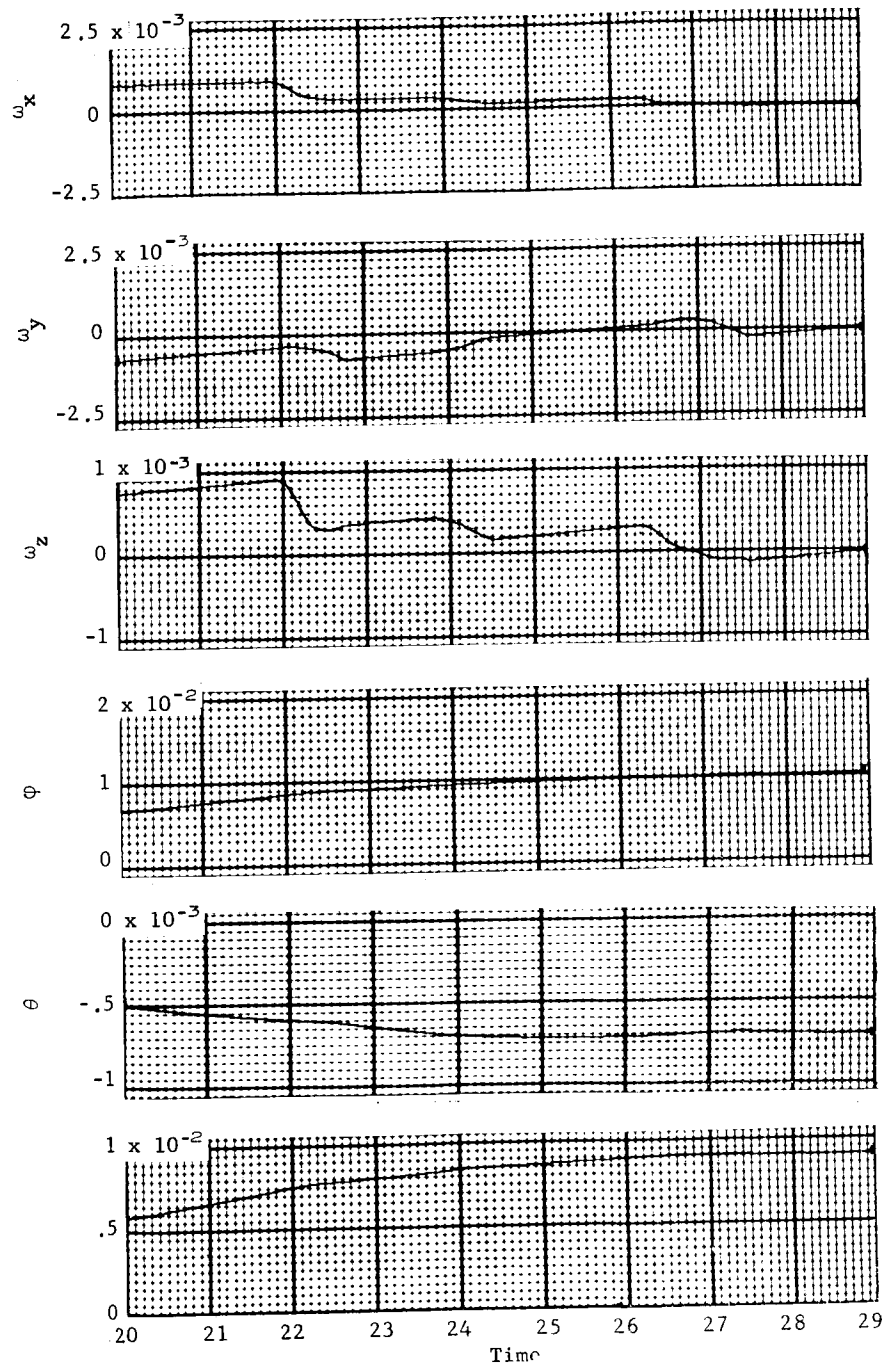


Figure A84.- Concluded



## APPENDIX A

Free soaring.- The results shown in figure A85 are the load cell forces and moments from the free soaring task. The 1- or 2-sec periods where the forces and moments return to zero are where the subject was soaring between surfaces. Apparent in these results, as in the bounce walk result, are the effects of mockup vibration that are more pronounced because of the greater extension distances of the surfaces.

# APPENDIX A

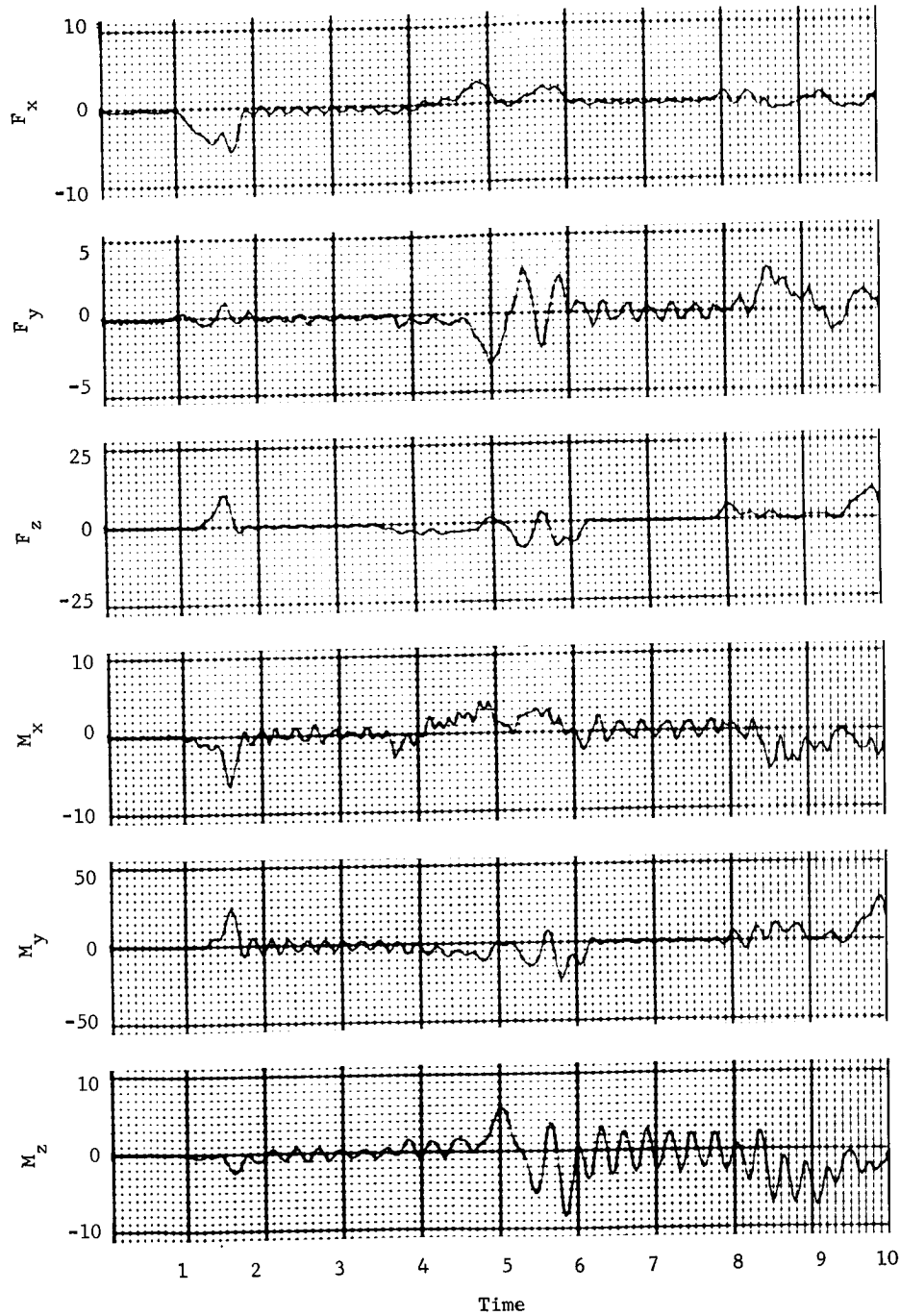


Figure A85.- Free Soaring, Man's Axes

# APPENDIX A

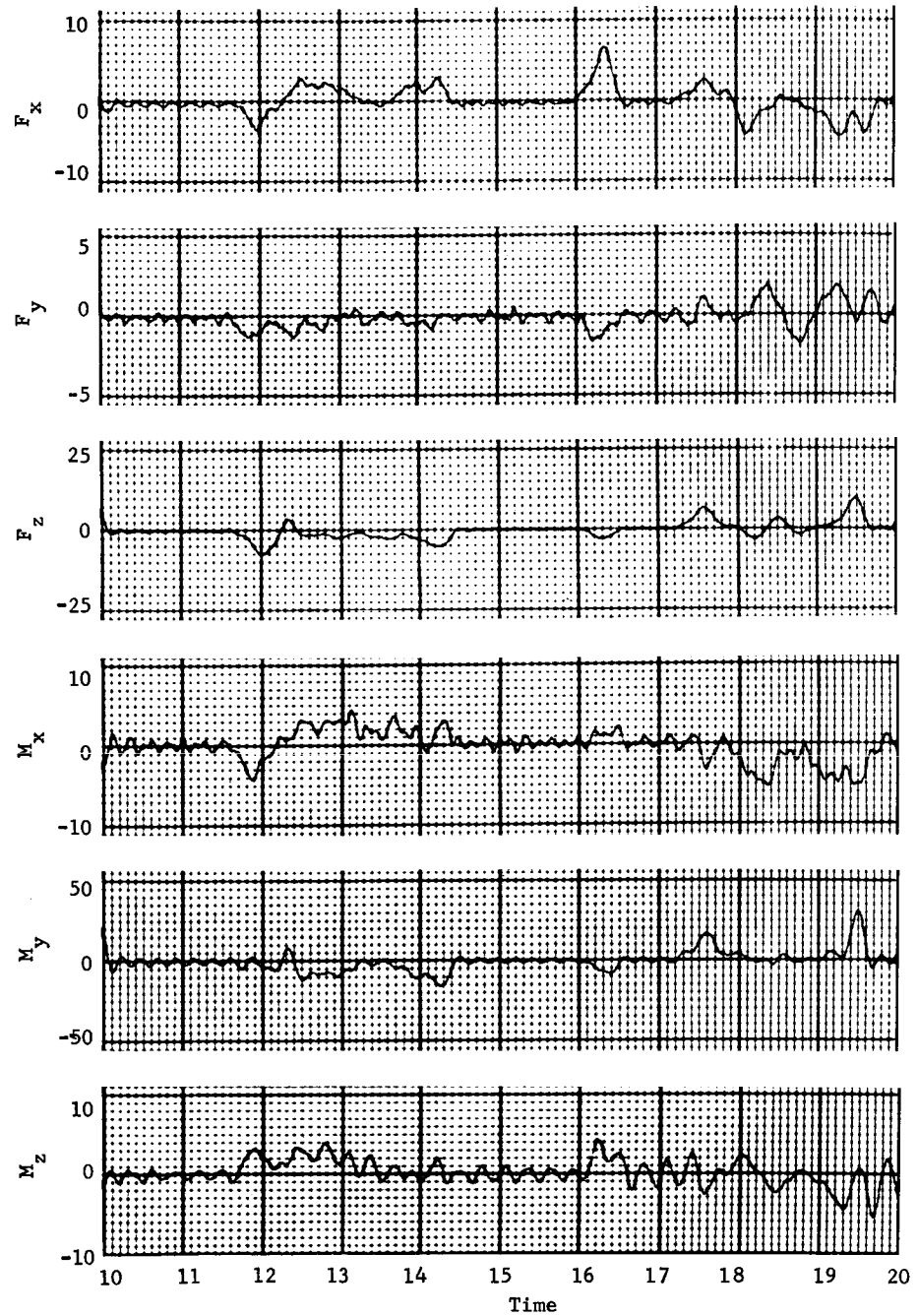


Figure A85.- Continued

# APPENDIX A

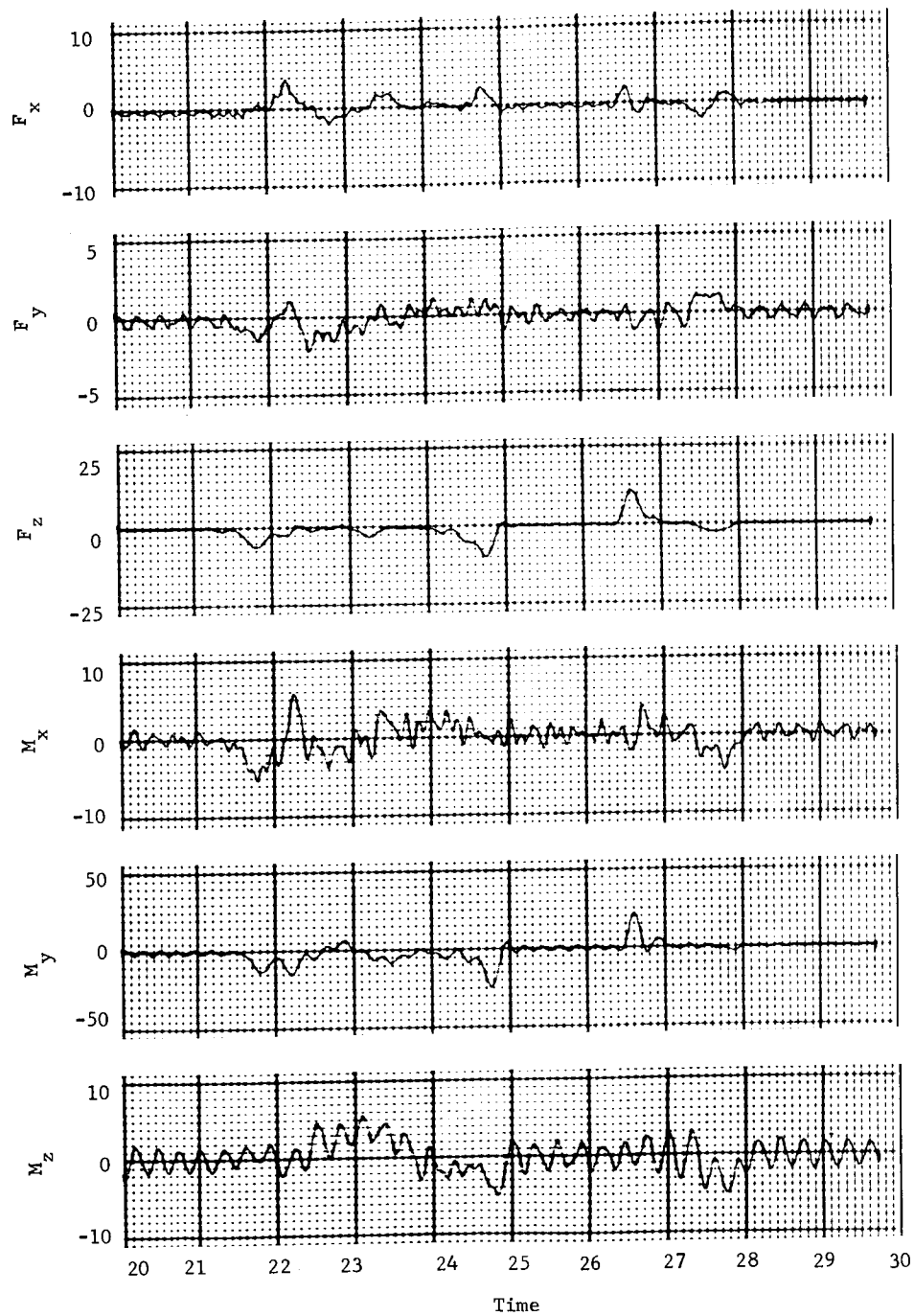


Figure A85.- Concluded

# APPENDIX B

## PERTINENT EXERPTS FROM REFERENCE 4

### List of Symbols

<u>Symbol</u>	<u>Definition</u>	<u>Units</u>
$a$	Component of acceleration vector	$\text{fps}^2$
$\bar{A}$	Angular momentum term defined in equation (B91a)	
$d$	Element of a transformation matrix	
$D$	Transformation matrix	
$\bar{E}$	Unit dyadic	
$\dot{\bar{C}}$	Euler angular rate vector	$\text{rad/sec}$
$\bar{F}$	Force	$\text{lb}$
$\bar{H}$	Angular momentum vector	$\text{slug-ft}^2/\text{sec}$
$\bar{i}, \bar{j}, \bar{k}$	Orthogonal unit vectors	
$\bar{I}$	Inertia dyadic	$\text{slug-ft}^2$
$\bar{J}$	Angular momentum term defined in equation (B26)	
$\bar{K}$	Inertia term defined in equation (B58)	
$K$	Constant used in segment mass definition	
$\ell$	Segment dimension	$\text{ft}$
$L$	Segment dimension	$\text{ft}$
$m$	Mass	$\text{slugs}$
$\bar{M}$	Moment or torque	$\text{ft-lb}$
$p, q, r$	Roll, pitch, and yaw body angular rates	$\text{rad/sec}$

## APPENDIX B

<u>Symbol</u>	<u>Definition</u>	<u>Units</u>
Q	Mass ratio, defined in equation (B34)	
$\bar{r}$	Position vector	ft
$\bar{R}$	Position vector	ft
S	Torso dimension	ft
t	Time	sec
v	Component of velocity vector	fps
W	Weight	lb
x, y, z	Components of position vector	ft
X, Y, Z	Orthogonal coordinate axes	
$\bar{p}$	Position vector	ft
$\phi, \theta, \psi$	Roll, pitch, and yaw Euler angles	rad
$\bar{\omega}$	Angular velocity vector	rad/sec
<u>Subscript</u>	<u>Refers to</u>	
a	Load cell centroid	
i, j	ith or jth segment	
L	Load cells	
m, mm	Astronaut center of mass	
o	Inertial reference	
R	Reference axes	
s	Spacecraft	
T	Total	
x, y, z	Coordinate axes	

## APPENDIX B

<u>Subscript</u>	<u>Refers to</u>
1 thru 9	A specific body segment
1 thru 3	A specific row or column of a transformation matrix
$\epsilon$	A Euler rate transformation

Note: The sine is usually abbreviated by an S and the cosine by a C; i.e.,  $S\theta$ ,  $C\theta$ .

### Basic Equations of Motion

The notation, coordinate systems, and the basic equations describing the general motions of the spacecraft/astronaut system used in the analysis are discussed.

A method of notation for vectors, dyadics, and transformation matrices has been devised to define completely all variables and constants. A single bar or dot appearing above a quantity indicates a vector or a first time derivative, respectively. Two bars or two dots appearing above a quantity indicate a dyadic or second-time derivative, respectively. If the dots appear above the bars, an inertial time derivative is indicated. Dots below the bars indicate that a derivative is to be taken as if seen by an observer in the rotating coordinate system.

A subscript appearing to the left of a quantity (vectors or dyadics) indicates the coordinate system in which the components are resolved. The first subscript to the right of a quantity refers the quantity to either the spacecraft, the astronaut, or a specific body segment. The subscript  $s$  refers to the spacecraft;  $m$  to the astronaut's combined center of mass; 1 thru 9 to the body segments; and  $o$  to the inertial reference, i.e., the combined center of mass of the astronaut and spacecraft. The subscript  $sm$  is used to indicate a position vector locating the astronaut's combined center of mass relative to that of the spacecraft. For example,  ${}_1\bar{R}_4$  is a position vector resolved in the coordinate system of segment 1 and locates segment 4;  ${}_1\bar{I}_2$  is the inertia dyadic of segment 2 resolved in segment 1 coordinates.

A second subscript is used in denoting angular velocity to indicate the reference with respect to which the angular velocity is measured. For example,  ${}_3\bar{\omega}_{21}$  is the relative angular velocity vector of segment 2 with respect to segment 1 and resolved in segment 3 coordinates.

## APPENDIX B

Coordinate transformation matrices, denoted by  $D$ , are subscripted by two numbers to the right, indicating the two segments or bodies between which the transformation is to take place. For example,  $D_{21}$  is the transformation matrix needed to transform vectors in segment 2 coordinates into segment 1 coordinates. The **small letter d is used to denote an element of a matrix. Two** subscripts to the left indicate the specific element. For example,  $_{13}d_{21}$  is the element in the first row, third column of the transformation matrix,  $D_{21}$ .

**Spacecraft.-** The coordinate system in which the governing equations are written and the problem geometry are shown in figure B1. The spacecraft is considered to be a rigid body with mass  $m_s$ . A right-hand set of orthogonal axes,  $X_s Y_s Z_s$ , are rigidly imbedded in the spacecraft with the origin at the spacecraft center of mass.

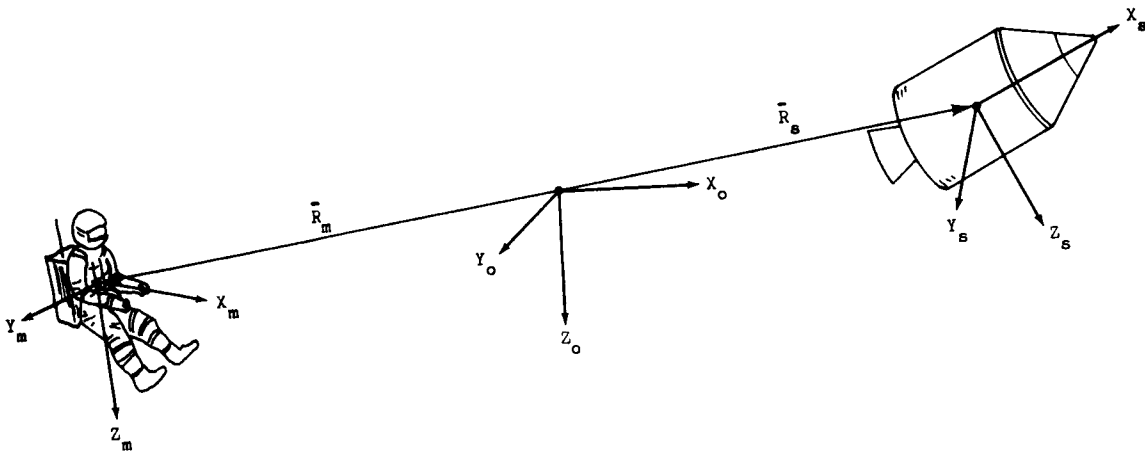


Figure B1.- Reference Coordinate Systems

The vector  $\vec{R}_s$  denotes the location of the spacecraft center of mass with respect to the inertial reference,  $X_o Y_o Z_o$ , and  $\vec{\omega}_{s/o}$  denotes the inertial angular velocity of the spacecraft.



## APPENDIX B

Denoting the spacecraft inertia dyadic by  ${}_s\bar{I}_s$ , the angular momentum,  ${}_s\bar{H}_s$ , of the spacecraft written about the origin of the inertial reference is given by

$${}_s\bar{H}_s = {}_s\bar{I}_s \cdot {}_s\bar{\omega}_{so} + m_s ({}_s\bar{R}_s \times \dot{{}_s\bar{R}}_s) \quad (B1)$$

The first term to the right of the equality sign in equation (B1) represents the angular momentum of the spacecraft about its own center of mass, and the second term represents the angular momentum of the spacecraft center of mass about the origin of the inertial reference.

Astronaut.- For this analysis, the astronaut is approximated by a model man consisting of nine rigid body segments as illustrated by figure B2.

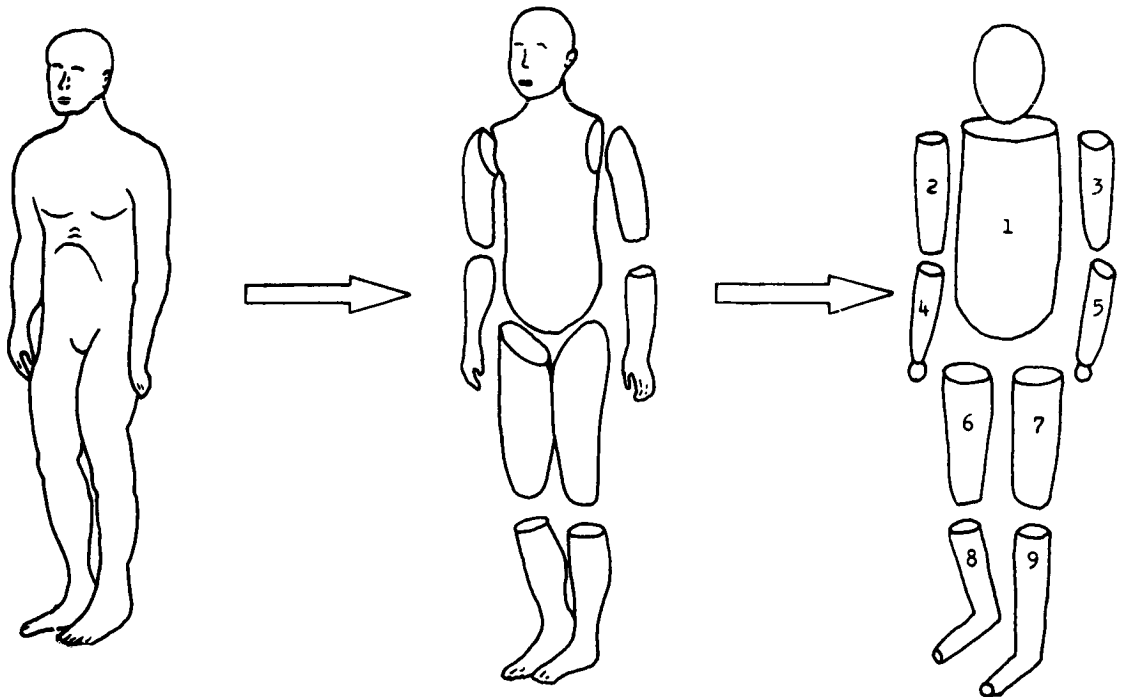


Figure B2.- Mathematical Model of Man

## APPENDIX B

Body segments are identified as follows:

- Segment 1 - Torso and head;
- Segment 2 - Right upper arm;
- Segment 3 - Left upper arm;
- Segment 4 - Right lower arm and hand;
- Segment 5 - Left lower arm and hand;
- Segment 6 - Right upper leg;
- Segment 7 - Left upper leg;
- Segment 8 - Right lower leg and foot;
- Segment 9 - Left lower leg and foot.

A detailed description of the properties of each segment of the model is contained in Appendix D, of this final report, Anthropometric Data.

The coordinate systems for the model man are shown in figure B3. A right hand set of orthogonal axes  $X_i Y_i Z_i$  are rigidly imbedded in the  $i$ th body segment with origin at the center of mass of the  $i$ th segment. In addition, an orthogonal set of axes,  $X_m Y_m Z_m$ , is located at the origin of the astronaut's composite center of mass and always remains parallel to the  $X_1 Y_1 Z_1$  torso axes.

The vector  ${}_1\bar{R}_i$  denotes the  $i$ th segment center of mass location relative to the inertial reference  $\begin{pmatrix} X_o Y_o Z_o \end{pmatrix}$  origin, and  ${}_1\omega_{io}$  denotes the inertial angular velocity of the  $i$ th segment. Denoting the inertia dyadic of the  $i$ th segment by  ${}_1\bar{I}_i$  and the segment mass by  $m_i$ , the angular momentum,  ${}_1\bar{H}_m$ , of the model man written about the origin of the inertial reference is given by

$${}_1\bar{H}_m = \sum_{i=1}^9 \left[ {}_1\bar{I}_i \cdot {}_1\bar{\omega}_{io} + m_i \left( {}_1\bar{R}_i \times {}_1\dot{\bar{R}}_i \right) \right] \quad (B2)$$

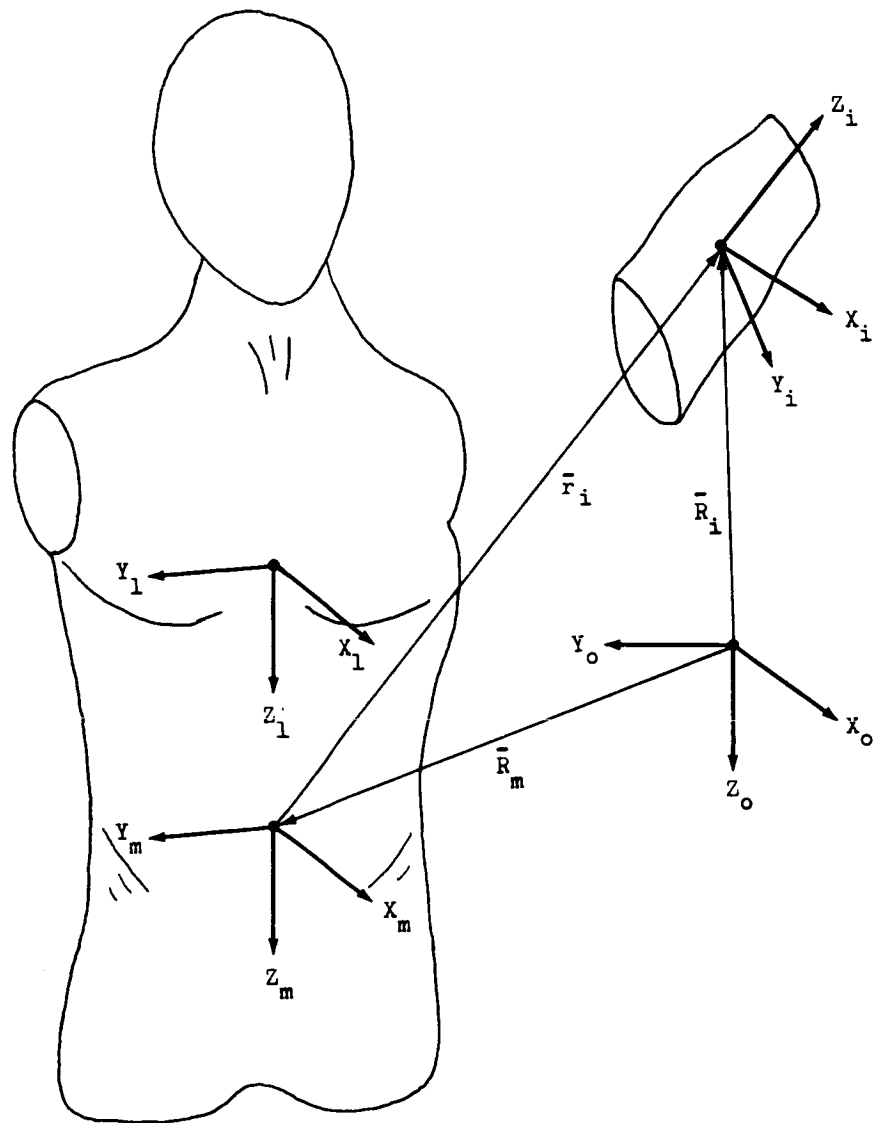


Figure B3.- Segment Coordinate Systems

The first term in brackets in equation (B2) represents the angular momentum of the  $i$ th segment about its own center of mass, and the second term represents the angular momentum of the  $i$ th segment center of mass about the origin of the inertial reference.

## APPENDIX B

The vector  ${}_1\bar{r}_i$  locates the  $i$ th segment center of mass with reference to the model man combined center of mass, and  ${}_1\bar{R}_m$  locates the combined center of mass with reference to the inertial origin. Thus,

$${}_1\bar{R}_i = {}_1\bar{R}_m + {}_1\bar{r}_i \quad (B3)$$

By definition of the model man center of mass,

$$\sum_{i=1}^9 m_i ({}_1\bar{r}_i) = 0 \quad (B4)$$

Also,

$$\sum_{i=1}^9 m_i = m_m \quad (B5)$$

where  $m_m$  denotes the total mass of the model man.

Substituting equations (B3), (B4), and (B5) into equation (B2) gives

$${}_1\bar{H}_m = \sum_{i=1}^9 \left[ {}_1\bar{I}_i \cdot {}_1\bar{\omega}_{io} + m_i ({}_1\bar{r}_i \times {}_1\dot{\bar{r}}_i) + m_m ({}_1\bar{R}_m \times {}_1\dot{\bar{R}}_m) \right] \quad (B6)$$

Equations (B1) and B6) are the basic dynamic equations describing the motion of the spacecraft/astronaut system. These two equations are expanded in the following subsections to obtain those required by the analog and digital simulations. Each simulation requires a different approach. In the analog simulation, the forces and moments are known quantities, and are used to produce spacecraft/astronaut motion. In the digital simulation, astronaut motions are known and are used to determine the forces and moments perturbing the spacecraft.

## APPENDIX B

### Equations of Motion for Hybrid Simulation

This subsection develops the equations of motion of the spacecraft and the astronaut considering each as a separate dynamic system. Then, the equations of relative motion between the spacecraft and astronaut are determined. It is shown that if the forces and moments applied to the spacecraft/astronaut system are known by using a load cell array and if the angular position of the limb segments relative to the torso are obtained from the LIMS, the solution to the dynamical system is possible.

Spacecraft.- The angular momentum of the spacecraft as given by equation (B1) is

$${}_s \bar{H}_s = {}_s \bar{I}_s \cdot {}_s \bar{\omega}_{so} + m_s \left( {}_s \bar{R}_s \times \dot{{}_s \bar{R}_s} \right) \quad (B1)$$

The time derivative of the angular momentum is equal to the net external moment about the inertial origin. Denoting the sum of the moments and forces acting on the spacecraft center of mass by  ${}_s \bar{M}_s$  and  ${}_s \bar{F}_s$ , respectively,

$$\dot{{}_s \bar{H}_s} = {}_s \bar{M}_s + {}_s \bar{R}_s \times {}_s \bar{F}_s \quad (B7)$$

Because the translational properties of the spacecraft are described by

$${}_s \bar{F}_s = m_s \ddot{{}_s \bar{R}_s} \quad (B8)$$

the second term of equation (B7) becomes

$$\left. \begin{aligned} {}_s \bar{R}_s \times {}_s \bar{F}_s &= m_s \left( {}_s \bar{R}_s \times \ddot{{}_s \bar{R}_s} \right) \\ &= m_s \left( \dot{{}_s \bar{R}_s} \times \dot{{}_s \bar{R}_s} \right) \end{aligned} \right\} \quad (B9)$$

Differentiating equation (B1) and equating to equation (B7) using the identity of equation (B9),

$$\left. \begin{aligned} {}_s \bar{M}_s &= \frac{d}{dt} \left( {}_s \bar{I}_s \cdot {}_s \bar{\omega}_{so} \right) \\ &= {}_s \dot{\bar{I}}_s \cdot {}_s \bar{\omega}_{so} + {}_s \bar{\omega}_{so} \times \left( {}_s \bar{I}_s \cdot {}_s \bar{\omega}_{so} \right) \end{aligned} \right\} \quad (B10)$$

## APPENDIX B

The cross product term appears because the quantities are measured in a rotating coordinate system. Rearranging equation (B10) and integrating, the spacecraft angular rate is

$${}_s \bar{\omega}_{so} = {}_s \bar{I}_s^{-1} \cdot \int \left[ {}_s \bar{M}_s - {}_s \bar{\omega}_{so} \times ({}_s \bar{I}_s \cdot {}_s \bar{\omega}_{so}) \right] dt \quad (B11)$$

The attitude of the spacecraft body axes with respect to the inertial reference is described by three Euler angles. The time derivative of the Euler angles,  $\dot{\mathcal{E}}_s$ , may be expressed as

$$\dot{\mathcal{E}}_s = D_{s \in s} {}_s \bar{\omega}_{so} \quad (B12)$$

where  $D_{s \in s}$  is the transformation matrix relating spacecraft body rates to Euler rates and is a function of the Euler angle sequence. Integration of equation (B12) provides the Euler angles that describe the spacecraft attitude.

Equations (B11) and (B12) describe the rotational properties of the spacecraft, while equation (B8) describes the translational properties.

Astronaut. - From equation (B6), the angular momentum of the astronaut is

$${}_1 \bar{H}_m = \sum_{i=1}^9 \left[ {}_1 \bar{I}_i \cdot {}_1 \bar{\omega}_{io} + m_i \left( {}_1 \bar{r}_i \times {}_1 \dot{\bar{r}}_i \right) + m_m \left( {}_1 \bar{R}_m \times {}_1 \dot{\bar{R}}_m \right) \right] \quad (B6)$$

The time derivative of the angular momentum is equal to the net external moment about the inertial origin. Denoting the sum of the moments and forces acting on the astronaut's composite center of mass by  ${}_1 \bar{M}_m$  and  ${}_1 \bar{F}_m$ , respectively,

$${}_1 \dot{\bar{H}}_m = {}_1 \bar{M}_m + {}_1 \bar{R}_m \times {}_1 \bar{F}_m \quad (B13)$$

Because the translational properties of the astronaut's composite center of mass are described by

$${}_1 \bar{F}_m = m_m {}_1 \ddot{\bar{R}}_m \quad (B14)$$

## APPENDIX B

the last term of equation (B13) becomes

$$\begin{aligned} {}_1\bar{\mathbf{R}}_m \times {}_1\bar{\mathbf{F}}_m &= m_m \left( {}_1\bar{\mathbf{R}}_m \times {}_1\ddot{\bar{\mathbf{R}}}_m \right) \\ &= m_m \left( {}_1\bar{\mathbf{R}}_m \times {}_1\dot{\bar{\mathbf{R}}}_m \right) \end{aligned} \quad (\text{B15})$$

Differentiating equation (B6) and equating to equation (B13) using the identity of equation (B15),

$${}_1\bar{\mathbf{M}}_m = {}_1\dot{\bar{\mathbf{H}}}_{mm} \quad (\text{B16})$$

where

$${}_1\bar{\mathbf{H}}_{mm} = \sum_{i=1}^9 \left[ {}_1\bar{\mathbf{I}}_i \cdot {}_1\bar{\boldsymbol{\omega}}_{i0} + m_i \left( {}_1\bar{\mathbf{r}}_i \times {}_1\dot{\bar{\mathbf{r}}}_i \right) \right] \quad (\text{B17})$$

${}_1\bar{\mathbf{H}}_{mm}$  represents the angular momentum of the astronaut about his center of mass.

The inertial angular velocity of each limb segment can be written as

$${}_1\bar{\boldsymbol{\omega}}_{i0} = {}_1\bar{\boldsymbol{\omega}}_{10} + {}_1\bar{\boldsymbol{\omega}}_{i1} \quad (\text{B18})$$

where  ${}_1\bar{\boldsymbol{\omega}}_{10}$  is the inertial torso angular velocity and  ${}_1\bar{\boldsymbol{\omega}}_{i1}$  is the angular velocity of the  $i$ th segment relative to the torso, segment 1. Substituting equation (B18) into equation (B17),

$${}_1\bar{\mathbf{H}}_{mm} = \sum_{i=1}^9 \left[ {}_1\bar{\mathbf{I}}_i \cdot {}_1\bar{\boldsymbol{\omega}}_{10} + {}_1\bar{\mathbf{I}}_i \cdot {}_1\bar{\boldsymbol{\omega}}_{i1} + m_i \left( {}_1\bar{\mathbf{r}}_i \times {}_1\dot{\bar{\mathbf{r}}}_i \right) \right] \quad (\text{B19})$$

The position vector,  ${}_1\bar{\mathbf{r}}_i$ , is resolved in a rotating coordinate system. Therefore,

$${}_1\dot{\bar{\mathbf{r}}}_i = {}_1\bar{\mathbf{r}}_i + {}_1\bar{\boldsymbol{\omega}}_{10} \times {}_1\bar{\mathbf{r}}_i \quad (\text{B20})$$

## APPENDIX B

The last term of equation (B19) expands to

$$m_i (\bar{\mathbf{r}}_i \times \dot{\bar{\mathbf{r}}}_i) = m_i (\bar{\mathbf{r}}_i \times \bar{\dot{\mathbf{r}}}_i) + m_i \left[ \bar{\mathbf{r}}_i \times (\bar{\omega}_{10} \times \bar{\mathbf{r}}_i) \right] \quad (\text{B21})$$

Substituting equation (B21) into equation (B19), and using the vector identity

$$\bar{\mathbf{r}} \times (\bar{\omega} \times \bar{\mathbf{r}}) = [(\bar{\mathbf{r}} \cdot \bar{\mathbf{r}}) \bar{\bar{\mathbf{E}}} - \bar{\mathbf{r}}\bar{\mathbf{r}}] \cdot \bar{\omega} \quad (\text{B22})$$

where  $\bar{\bar{\mathbf{E}}}$  is the unit dyadic defined by

$$\bar{\bar{\mathbf{E}}} = \begin{bmatrix} \bar{i}\bar{i} & 0 & 0 \\ 0 & \bar{j}\bar{j} & 0 \\ 0 & 0 & \bar{k}\bar{k} \end{bmatrix} \quad (\text{B23})$$

then,

$$\begin{aligned} {}_1\bar{\mathbf{H}}_{mm} = & \sum_{i=1}^9 \left\{ {}_1\bar{\bar{\mathbf{I}}}_i + m_i \left[ ({}_1\bar{\mathbf{r}}_i \cdot {}_1\bar{\mathbf{r}}_i) \bar{\bar{\mathbf{E}}} - {}_1\bar{\mathbf{r}}_i {}_1\bar{\mathbf{r}}_i \right] \right\} \cdot {}_1\bar{\omega}_{10} \\ & + \sum_{i=1}^9 \left[ {}_1\bar{\bar{\mathbf{I}}}_i \cdot {}_1\bar{\omega}_{i1} + m_i ({}_1\bar{\mathbf{r}}_i \times \dot{{}_1\bar{\mathbf{r}}}_i) \right] \end{aligned} \quad (\text{B24})$$

Let

$${}_1\bar{\bar{\mathbf{I}}}_m = \sum_{i=1}^9 \left\{ {}_1\bar{\bar{\mathbf{I}}}_i + m_i \left[ ({}_1\bar{\mathbf{r}}_i \cdot {}_1\bar{\mathbf{r}}_i) \bar{\bar{\mathbf{E}}} - {}_1\bar{\mathbf{r}}_i {}_1\bar{\mathbf{r}}_i \right] \right\} \quad (\text{B25})$$

where  ${}_1\bar{\bar{\mathbf{I}}}_m$  represents the instantaneous inertial dyadic of the astronaut, and

$${}_1\bar{\mathbf{J}}_m = \sum_{i=1}^9 \left[ {}_1\bar{\bar{\mathbf{I}}}_i \cdot {}_1\bar{\omega}_{i1} + m_i ({}_1\bar{\mathbf{r}}_i \times \dot{{}_1\bar{\mathbf{r}}}_i) \right] \quad (\text{B26})$$



## APPENDIX B

equation (B24) reduces to

$${}_1\bar{H}_{mm} = {}_1\bar{I}_m \cdot {}_1\bar{\omega}_{10} + {}_1\bar{J}_m \quad (B27)$$

Recall

$${}_1\bar{M}_m = {}_1\dot{\bar{H}}_{mm} \quad (B15)$$

Because these quantities are measured in a rotating coordinate system,

$${}_1\bar{M}_m = {}_1\dot{\bar{H}}_{mm} + {}_1\bar{\omega}_{10} \times {}_1\bar{H}_{mm} \quad (B28)$$

Rearranging equation (B28) and integrating,

$${}_1\bar{H}_{mm} = \int ({}_1\bar{M}_m - {}_1\bar{\omega}_{10} \times {}_1\bar{H}_{mm}) dt \quad (B29)$$

Combining equations (B29) and (B27), and solving for the torso angular rate,

$${}_1\bar{\omega}_{10} = {}_1\bar{I}_m^{-1} \cdot \left\{ \int [{}_1\bar{M}_m - {}_1\bar{\omega}_{10} \times ({}_1\bar{I}_m \cdot {}_1\bar{\omega}_{10} + {}_1\bar{J}_m)] dt - {}_1\bar{J}_m \right\} \quad (B30)$$

The solution to equation (B30) becomes possible when  ${}_1\bar{M}_m$  is generated by the load cells and the LIMS provides the ability to determine  ${}_1\bar{J}_m$  and  ${}_1\bar{I}_m$ .

The torso attitude relative to the inertial reference is obtained in the same manner as the spacecraft attitude.

**Astronaut/spacecraft relative motion.**— The hybrid simulation provides six degrees of freedom to the astronaut. Therefore, realistic motion of the astronaut is obtained by using the equations of relative motion for the astronaut/spacecraft dynamic system.

The relative translational equation is

$$\ddot{{}_s\bar{r}}_{sm} = \ddot{{}_s\bar{R}}_m - \ddot{{}_s\bar{R}}_s = \frac{{}_s\bar{F}_m}{m_m} - \frac{{}_s\bar{F}_s}{m_s} \quad (B31)$$

## APPENDIX B

where  $\bar{r}_{sm}$  is the position vector from the spacecraft center of mass to the astronaut center of mass. If the spacecraft/astronaut system has no means other than through contact to generate forces on each, then

$$\bar{F}_m = -\bar{F}_s \quad (B32)$$

substituting equation (B32) into equation (B31),

$$\ddot{\bar{r}}_{sm} = -\frac{\bar{F}_s}{Q} \quad (B33)$$

where

$$Q = \frac{m_m m_s}{m_m + m_s} \quad (B34)$$

Therefore, the relative linear velocity is

$$\dot{\bar{r}}_{sm} = \int \left[ -\frac{\bar{F}_s}{Q} - \left( \bar{\omega}_{so} \times \dot{\bar{r}}_{sm} \right) \right] dt \quad (B35)$$

and the relative position vector,

$$\bar{r}_{sm} = \int \left[ \dot{\bar{r}}_{sm} - \left( \bar{\omega}_{so} \times \bar{r}_{sm} \right) \right] dt \quad (B36)$$

If the SOS moving base carriage applied motion to the astronaut's composite center of mass, the components of  $\bar{r}_{sm}$  would be the carriage translational commands. However, the astronaut's torso is attached to the gimbale head and is the body segment upon which the motion is effected. Therefore, the translational commands are determined by the components of the vector from the spacecraft center of mass to the torso center of mass. Denoting this vector by  $\bar{r}_{s1}$ ,

$$\bar{r}_{s1} = \bar{r}_{sm} + \bar{r}_1 = \bar{r}_{sm} + D_{1s} \bar{r}_1 \quad (B37)$$

The relative rotational equation is given by the difference between the spacecraft and astronaut inertial angular rates, equation (B11) and (B30), respectively.

## APPENDIX B

Therefore,

$${}_{11s}^{\bar{\omega}} = {}_{110}^{\bar{\omega}} - {}_{1s0}^{\bar{\omega}} = {}_{110}^{\bar{\omega}} - D_{s1} {}_{s0}^{\bar{\omega}} \quad (B38)$$

where  ${}_{11s}^{\bar{\omega}}$  is the angular velocity of the astronaut relative to the spacecraft.

The attitude of the astronaut's torso axes with respect to the spacecraft body axes is described by three Euler angles. The time derivative of the Euler angles,  $\dot{\epsilon}_{s1}$ , is given by

$$\dot{\epsilon}_{s1} = D_{s1\epsilon} {}_{11s}^{\bar{\omega}} \quad (B39)$$

where  $D_{s1\epsilon}$  is the Euler rate transformation matrix and is a function of the Euler angle sequence. Integration of equation (B39) provides the Euler angles that describe the astronaut's attitude with respect to the spacecraft. These angles are used as commands to drive the SOS attitude head to provide the proper attitude to the astronaut.

**Load cell array.**- The load cell array provides the knowledge of the forces and moments applied to the spacecraft and the astronaut as required for the solution of the spacecraft/astronaut system equations. Denoting the forces and moments sensed by the load cell array by  $\bar{F}_L$  and  $\bar{M}_L$ , respectively, their components are determined in terms of the six individual load cell outputs  $F_1$  thru  $F_6$ . By direct resolution from the load cell geometry shown in figure B4,\*

$$\left. \begin{aligned} F_{Lx} &= 0.7071(F_1 + F_2 + F_3 + F_4 + F_5 + F_6) \\ F_{Ly} &= 0.7071[F_1 - F_2 + 0.5(-F_3 + F_4 - F_5 + F_6)] \\ F_{Lz} &= 0.6124(F_3 - F_4 - F_5 + F_6) \end{aligned} \right\} \quad (B40)$$

---

\*Compression of the load cell produces a positive amplifier output voltage.

# APPENDIX B

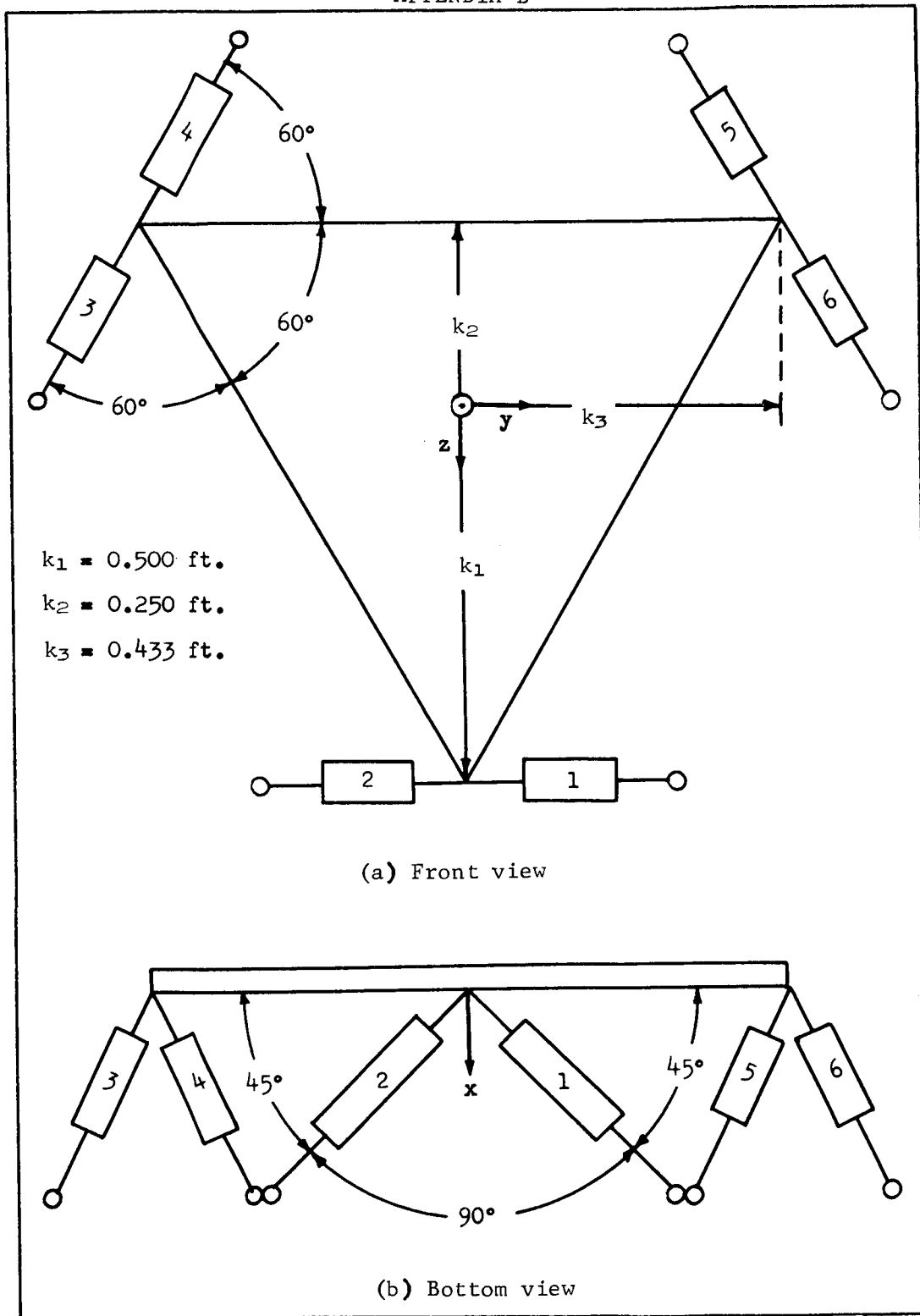


Figure B4.- Load Cell Geometry

## APPENDIX B

$$M_{Lx} = 0.3536(-F_1 + F_2 - F_3 + F_4 - F_5 + F_6)$$

$$M_{Ly} = 0.3536[F_1 + F_2 - 0.5(F_3 + F_4 + F_5 + F_6)] \quad (B41)$$

$$M_{Lz} = 0.3062(F_3 + F_4 - F_5 - F_6)$$

If the load cell centroid is located at the spacecraft center of mass, equations (B40) and (B41) would be the forces and moments on the spacecraft. Generally, only that portion of the spacecraft where astronaut activity is performed is attached to the load cell array. Therefore, denoting the vector from the spacecraft center of mass to the array centroid by  $\bar{r}_a$ , the spacecraft forces and moments are

$$\bar{F}_s = \bar{F}_L \quad (B42a)$$

$$\bar{M}_s = \bar{M}_L + \bar{r}_a \times \bar{F}_L \quad (B42b)$$

The astronaut experiences equal but opposite contact forces and moments. The equivalent set at the astronaut's center of mass when transferred from the spacecraft center of mass become

$$\bar{F}_m = -\bar{F}_s = -\bar{F}_L \quad (B43a)$$

$$\left. \begin{aligned} \bar{M}_m &= -\bar{M}_s + \left( \bar{r}_{sm} \times \bar{F}_L \right) \\ &= -\bar{M}_L - \left( \bar{r}_a \times \bar{F}_L \right) + \left( \bar{r}_{sm} \times \bar{F}_L \right) \end{aligned} \right\} \quad (B43b)$$

and the moments on the astronaut in torso coordinates, as required in equation (B30), are given by

$${}_1\bar{M}_m = D_{s1} {}_s\bar{M}_m \quad (B44)$$

Limb Motion Sensor (LIMS)..- In addition to the load cell outputs, the motion of the astronaut's limbs with respect to his torso are required for the solution of the hybrid equations. The angular positions of the astronaut's limbs are measured by the LIMS potentiometers. The LIMS design is shown in figure B5 for the left arm (other limbs are wired with the same basic design).

## APPENDIX B



Figure B5.- Basic LIMS Elements

The initial axes orientation for each segment is determined from the "zero" position of LIMS, i.e., the position when all potentiometers read zero. This position is attained when the astronaut assumes a normal standing position. For segment 1 the positive  $x$  axis points toward the front of the astronaut, the positive  $y$  toward the right, and the positive  $z$  downward. The axes orientation for segments 2, 3, 6, 7 are shown in figure B6 (The axes for 4 and 5 are parallel to 2 and 3 and 8 and 9 are parallel to 6 and 7). The positive  $z$  axis points toward the lower part of the segment and is coincident with the longitudinal axis of the segment. If the arm assumes an initial position at the astronaut's side, the forearm will rotate about the  $y$  axis at the elbow, which is yawed approximately  $45^\circ$  with respect to the torso axes as shown in figure B6. Therefore, the initial

## APPENDIX B

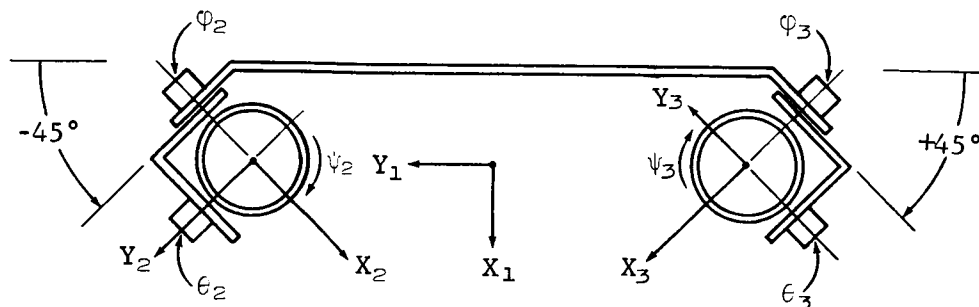


Figure B6.- Shoulder or Hip Joint Gimbal

orientation of the  $x$  and  $y$  axes for segments 2 thru 9 is defined as follows: for segments 2 and 4, and 6 and 8 (right arm and right leg)  $x$  and  $y$  axes are yawed  $-45^\circ$ , and for segments 3 and 5, and 6 and 8 (left arm and left leg)  $x$  and  $y$  are yawed  $+45^\circ$ . Angles in these yawed coordinates are measured by LIMS.

The sequence of Euler angle rotations for the right upper arm, segment 2, and right upper leg, segment 6, going from the torso axes to the segment axes is a yaw of  $-45^\circ$ , roll ( $\phi$ ), pitch ( $\theta$ ), and finally a yaw ( $\psi$ ). The sequence of angle rotations for the left upper arm, segment 3, and left upper leg, segment 7, going from the torso axes to the segment axes is a yaw of  $+45^\circ$ , roll ( $\phi$ ), pitch ( $\theta$ ), and finally a yaw ( $\psi$ ). Segments 4, 5, 8, and 9 rotates only in pitch ( $\theta$ ) relative to an adjacent segment.

With these Euler sequences defined, the following matrices can be written to transform segment quantities into torso coordinates:

$$D_{21} = D(\psi = -45^\circ) D(\phi_2) D(\theta_2) D(\psi_2)$$

$$D_{31} = D(\psi = +45^\circ) D(\phi_3) D(\theta_3) D(\psi_2)$$

$$D_{41} = D_{21} D_{42}$$

$$D_{42} = D(\theta_4)$$

$$D_{51} = D_{31} D_{53}$$

$$D_{53} = D(\theta_5)$$

$$D_{61} = D(\psi = -45^\circ) D(\phi_6) D(\theta_6) D(\psi_6)$$

## APPENDIX B

$$D_{71} = D(\psi = +45^\circ) D(\phi_7) D(\theta_7) D(\psi_7)$$

$$D_{81} = D_{61} D_{86}$$

$$D_{86} = D(\theta_8)$$

$$D_{91} = D_{71} D_{97}$$

$$D_{97} = D(\theta_9)$$

where  $D(\alpha_i)$  is an Eulerian transformation matrix defined later in the subsection entitled, General Transformations.

Summary. - The equations required for the hybrid simulation have been derived. However, all the terms of the basic vector equations must be expanded and written as vectors or dyadics resolved in the torso coordinates. The expanded forms are quite cumbersome because of the resulting member of transformations and component terms. Therefore, a block diagram of the hybrid computational flow is shown in figure B7 while all expanded forms of these quantities are developed later in the subsection entitled Expanded Forms.



# APPENDIX B

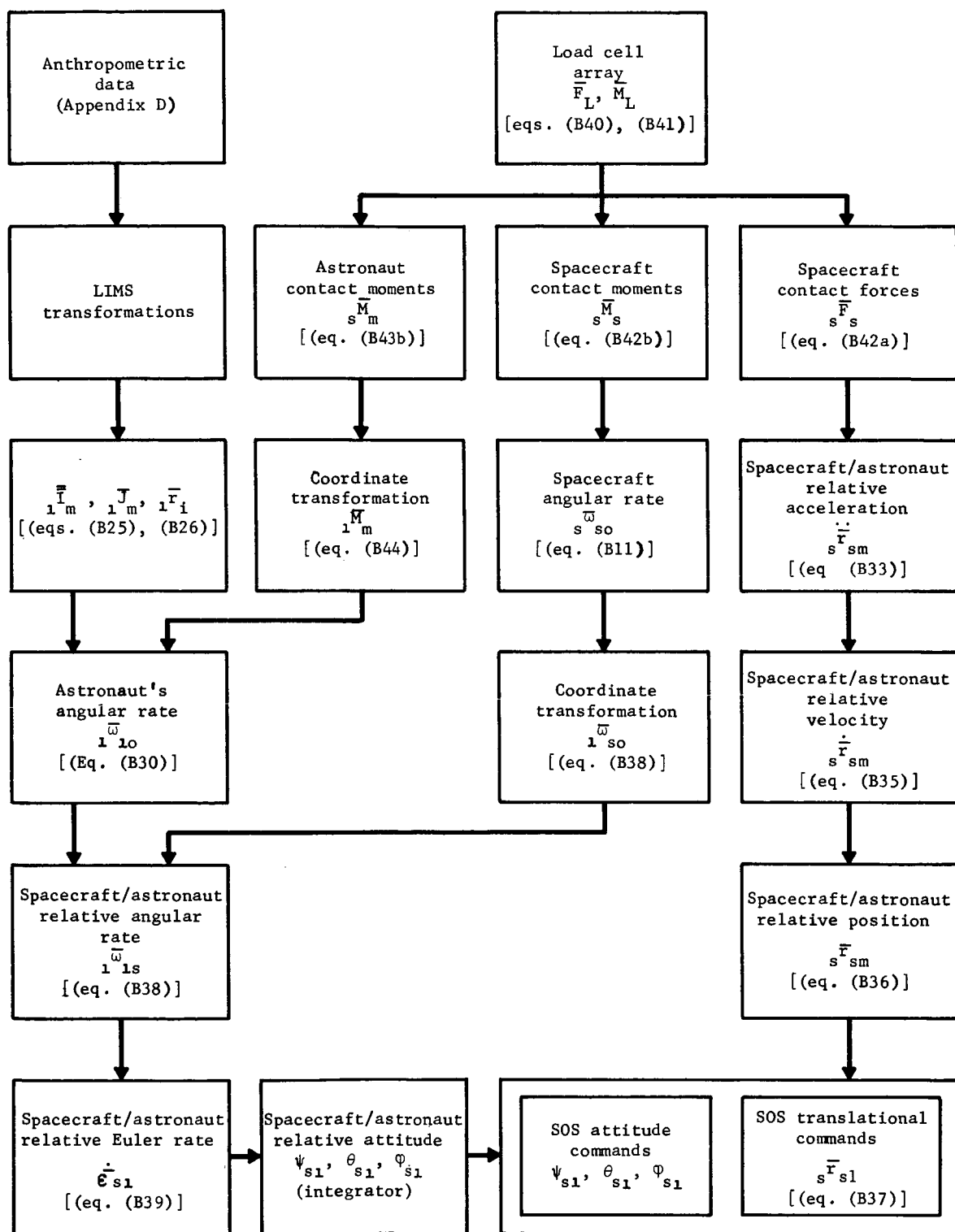


Figure B7.- Hybrid Computational Block Diagram

## APPENDIX B

### Equations of Motion for Digital Simulation

This subsection presents the equations of motion of the spacecraft/astronaut system for solution on a digital computer. It is assumed that no net external forces or moments (e.g., from thrusters) are applied to the system, and thus the combined center of mass of the system is considered the inertial reference. The vector equation of motion is obtained from the conservation of angular momentum principle that states the total angular momentum of the system about the combined center of mass is constant with respect to time.

The angular momentum equations of the spacecraft and astronaut written about the system combined center of mass have been derived previously as

$${}_s \bar{H}_s = {}_s \bar{I}_s \cdot {}_s \bar{\omega}_{so} + m_s \left( {}_s \bar{R}_s \times {}_s \dot{\bar{R}}_s \right) \quad (B1)$$

and

$${}_1 \bar{H}_m = \sum_{i=1}^9 \left[ {}_1 \bar{I}_i \cdot {}_1 \bar{\omega}_{io} + m_i \left( {}_1 \bar{r}_i \times {}_1 \dot{\bar{r}}_i \right) \right] + m_m \left( {}_1 \bar{R}_m \times {}_1 \dot{\bar{R}}_m \right) \quad (B6)$$

Writing equation (B1) in segment 1 coordinates and adding to equation (B6), the total angular momentum of the system is

$$\begin{aligned} {}_1 \bar{H}_T = & {}_1 \bar{I}_s \cdot {}_1 \bar{\omega}_{so} + m_s \left( {}_1 \bar{R}_s \times {}_1 \dot{\bar{R}}_s \right) \\ & + \sum_{i=1}^9 \left[ {}_1 \bar{I}_i \cdot {}_1 \bar{\omega}_{io} + m_i \left( {}_1 \bar{r}_i \times {}_1 \dot{\bar{r}}_i \right) \right] + m_m \left( {}_1 \bar{R}_m \times {}_1 \dot{\bar{R}}_m \right) \end{aligned} \quad (B45)$$

From the definition of the total system center of mass,

$$\left. \begin{aligned} {}_1 \bar{R}_s &= - \left( \frac{m_m}{m_m + m_s} \right) {}_1 \bar{r}_{sm} \\ {}_1 \bar{R}_m &= \left( \frac{m_m}{m_m + m_s} \right) {}_1 \bar{r}_{sm} \end{aligned} \right\} \quad (B46)$$

# APPENDIX B

where  ${}^1\bar{\mathbf{r}}_{sm} = {}^1\bar{\mathbf{R}}_m - {}^1\bar{\mathbf{R}}_s$ . Substituting equations (B46) into equation (B45) gives

$${}^1\bar{\mathbf{H}}_T = {}^1\bar{\mathbf{I}}_s \cdot {}^1\bar{\boldsymbol{\omega}}_{so} + \sum_{i=1}^9 \left[ {}^1\bar{\mathbf{I}}_i \cdot {}^1\bar{\boldsymbol{\omega}}_{io} + m_i \left( {}^1\bar{\mathbf{r}}_i \times {}^1\dot{\bar{\mathbf{r}}}_i \right) \right] + Q \left( {}^1\bar{\mathbf{r}}_{sm} \times {}^1\dot{\bar{\mathbf{r}}}_{sm} \right) \quad (\text{B47})$$

where

$$Q = \frac{m_m m_s}{m_m + m_s} \quad (\text{B48})$$

The inertial angular rotation of each segment can be written as

$${}^1\bar{\boldsymbol{\omega}}_{io} = {}^1\bar{\boldsymbol{\omega}}_{so} + {}^1\bar{\boldsymbol{\omega}}_{ls} + {}^1\bar{\boldsymbol{\omega}}_{il} \quad (\text{B49})$$

where  ${}^1\bar{\boldsymbol{\omega}}_{so}$  is the inertial spacecraft angular velocity,  ${}^1\bar{\boldsymbol{\omega}}_{ls}$  is the angular velocity of segment 1 relative to the spacecraft, and  ${}^1\bar{\boldsymbol{\omega}}_{il}$  is the angular velocity of the  $i$ th segment relative to segment 1. Equation (B47) can now be written as

$${}^1\bar{\mathbf{H}}_T = \left( {}^1\bar{\mathbf{I}}_s + \sum_{i=1}^9 {}^1\bar{\mathbf{I}}_i \right) \cdot {}^1\bar{\boldsymbol{\omega}}_{so} + \sum_{i=1}^9 {}^1\bar{\mathbf{I}}_i \cdot \left( {}^1\bar{\boldsymbol{\omega}}_{ls} + {}^1\bar{\boldsymbol{\omega}}_{il} \right) + \sum_{i=1}^9 m_i \left( {}^1\bar{\mathbf{r}}_i \times {}^1\dot{\bar{\mathbf{r}}}_i \right) + Q \left( {}^1\bar{\mathbf{r}}_{sm} \times {}^1\dot{\bar{\mathbf{r}}}_{sm} \right) \quad (\text{B50})$$

Because the position vectors  ${}^1\bar{\mathbf{r}}_i$  and  ${}^1\bar{\mathbf{r}}_{sm}$  are resolved in the rotating coordinate system of the torso,

$${}^1\dot{\bar{\mathbf{r}}}_i = {}^1\dot{\bar{\mathbf{r}}}_i + {}^1\bar{\boldsymbol{\omega}}_{lo} \times {}^1\bar{\mathbf{r}}_i \quad (\text{B51})$$

and

$${}^1\dot{\bar{\mathbf{r}}}_{sm} = {}^1\dot{\bar{\mathbf{r}}}_{sm} + {}^1\bar{\boldsymbol{\omega}}_{lo} \times {}^1\bar{\mathbf{r}}_{sm} \quad (\text{B52})$$

# APPENDIX B

where

$${}_1\bar{\omega}_{10} = {}_1\bar{\omega}_{s0} + {}_1\bar{\omega}_{1s} \quad (\text{B53})$$

Substituting equations (B51) thru (B53) into equation (B50) gives

$$\begin{aligned} {}_1\bar{H}_T = & \left( {}_1\bar{I}_s + \sum_{i=1}^9 {}_1\bar{I}_i \right) \cdot {}_1\bar{\omega}_{s0} + \sum_{i=1}^9 {}_1\bar{I}_i \cdot \left( {}_1\bar{\omega}_{1s} + {}_1\bar{\omega}_{i1} \right) \\ & + \sum_{i=1}^9 m_i \left( {}_1\bar{r}_i \times {}_1\bar{r}_i \right) + Q \left( {}_1\bar{r}_{sm} \times {}_1\bar{r}_{sm} \right) \\ & + \sum_{i=1}^9 m_i \left( {}_1\bar{r}_i \times {}_1\bar{\omega}_{s0} \times {}_1\bar{r}_i \right) + Q \left( {}_1\bar{r}_{sm} \times {}_1\bar{\omega}_{s0} \times {}_1\bar{r}_{sm} \right) \\ & + \sum_{i=1}^9 m_i \left( {}_1\bar{r}_i \times {}_1\bar{\omega}_{1s} \times {}_1\bar{r}_i \right) + Q \left( {}_1\bar{r}_{sm} \times {}_1\bar{\omega}_{1s} \times {}_1\bar{r}_{sm} \right) \quad (\text{B54}) \end{aligned}$$

Using a vector identity, the vector triple product terms can be written as

$$\bar{r} \times (\bar{\omega} \times \bar{r}) = \left[ (\bar{r} \cdot \bar{r}) \bar{\bar{E}} - \bar{r}\bar{r} \right] \cdot \bar{\omega} \quad (\text{B55})$$

where  $\bar{\bar{E}}$  is the unit dyadic defined by

$$\bar{\bar{E}} = \begin{bmatrix} \bar{i}\bar{i} & 0 & 0 \\ 0 & \bar{j}\bar{j} & 0 \\ 0 & 0 & \bar{k}\bar{k} \end{bmatrix} \quad (\text{B56})$$

# APPENDIX B

Substituting equation (B55) into equation (B54) gives

$$\begin{aligned}
 {}_1\bar{H}_T = & \left\{ {}_1\bar{I}_s + \sum_{i=1}^9 {}_1\bar{I}_i + \sum_{i=1}^9 m_i \left[ \left( {}_1\bar{r}_i \cdot {}_1\bar{r}_i \right) \bar{E} - {}_1\bar{r}_i {}_1\bar{r}_i \right] \right. \\
 & + Q \left[ \left( {}_1\bar{r}_{sm} \cdot {}_1\bar{r}_{sm} \right) \bar{E} - {}_1\bar{r}_{sm} {}_1\bar{r}_{sm} \right] \Big\} \cdot {}_1\bar{\omega}_{so} + \sum_{i=1}^9 {}_1\bar{I}_i \cdot {}_1\bar{\omega}_{il} \\
 & + \sum_{i=1}^9 m_i \left( {}_1\bar{r}_i \times {}_1\bar{r}_i \right) + Q \left( {}_1\bar{r}_{sm} \times {}_1\bar{r}_{sm} \right) \\
 & + \left\{ \sum_{i=1}^9 {}_1\bar{I}_i + \sum_{i=1}^9 m_i \left[ \left( {}_1\bar{r}_i \cdot {}_1\bar{r}_i \right) \bar{E} - {}_1\bar{r}_i {}_1\bar{r}_i \right] \right. \\
 & \left. + Q \left[ \left( {}_1\bar{r}_{sm} \cdot {}_1\bar{r}_{sm} \right) \bar{E} - {}_1\bar{r}_{sm} {}_1\bar{r}_{sm} \right] \right\} \cdot {}_1\bar{\omega}_{ls} \quad (B57)
 \end{aligned}$$

Defining  ${}_1\bar{I}_m$  and  ${}_1\bar{J}_m$  as before,

$${}_1\bar{I}_m = \sum_{i=1}^9 \left\{ {}_1\bar{I}_i + m_i \left[ \left( {}_1\bar{r}_i \cdot {}_1\bar{r}_i \right) \bar{E} - {}_1\bar{r}_i {}_1\bar{r}_i \right] \right\} \quad (B25)$$

$${}_1\bar{J}_m = \sum_{i=1}^9 \left[ {}_1\bar{I}_i \cdot {}_1\bar{\omega}_{il} + m_i \left( {}_1\bar{r}_i \times {}_1\bar{r}_i \right) \right] \quad (B26)$$

and defining  ${}_1\bar{K}_{sm}$  as

$${}_1\bar{K}_{sm} = Q \left[ \left( {}_1\bar{r}_{sm} \cdot {}_1\bar{r}_{sm} \right) \bar{E} - {}_1\bar{r}_{sm} {}_1\bar{r}_{sm} \right] \quad (B58)$$

Equation (B57) can be written as

$$\begin{aligned}
 {}_1\bar{H}_T = & \left( {}_1\bar{I}_s + {}_1\bar{I}_m + {}_1\bar{K}_{sm} \right) \cdot {}_1\bar{\omega}_{so} + {}_1\bar{J}_m + Q \left( {}_1\bar{r}_{sm} \times {}_1\bar{r}_{sm} \right) \\
 & + \left( {}_1\bar{I}_m + {}_1\bar{K}_{sm} \right) \cdot {}_1\bar{\omega}_{ls} \quad (B59)
 \end{aligned}$$

## APPENDIX B

If the astronaut or spacecraft has inertial rotations at time equal to zero, equation (B59) can be used to find the initial total angular momentum. Normally the system is assumed to be at rest at time equal to zero and, therefore, the initial angular momentum is taken as zero. Solving for  ${}_1\bar{\omega}_{so}$  from equation (B59) gives the equation describing the variation of the spacecraft angular rates after time zero.

$${}_1\bar{\omega}_{so} = -\left({}_1\bar{\bar{I}}_s + {}_1\bar{\bar{I}}_m + {}_1\bar{\bar{K}}_{sm}\right)^{-1} \cdot \left[{}_1\bar{J}_m + Q\left({}_1\bar{r}_{sm} \times {}_1\bar{r}_{sm}\right) + \left({}_1\bar{\bar{I}}_m + {}_1\bar{\bar{K}}_{sm}\right) \cdot {}_1\bar{\omega}_{ls}\right] \quad (B60)$$

Equation (B60) is the prime equation involved in the digital solution of the spacecraft/astronaut system dynamics. All the terms to the right of the equal sign are known or can be determined from the constraints of the problem. The quantities  ${}_1\bar{\bar{I}}_m$  [eq. (B25)] and  ${}_1\bar{J}_m$  [eq. (B26)] are specified at every instant of time from the data obtained from LIMS and from the anthropometric data in Appendix D. These quantities are shown later in the subsection entitled Expanded Forms. The quantities  ${}_1\bar{r}_{sm}$  (which also appears in the  ${}_1\bar{\bar{K}}_{sm}$  term) and  ${}_1\bar{\omega}_{ls}$  depend on the type of interface existing between the astronaut and spacecraft. If the astronaut is rigidly attached to the spacecraft by his torso (e.g., strapped to a couch), then  ${}_1\bar{\omega}_{ls} = 0$  and  ${}_1\bar{r}_{sm} = {}_1\bar{r}_{s1} - {}_1\bar{r}_1$ , where  ${}_1\bar{r}_{s1}$  is a constant vector from the spacecraft center of mass to the torso center of mass. If the astronaut is attached to the spacecraft by one or more outer segments (e.g., by handrails or foot holds), then  ${}_1\bar{\omega}_{ls} = {}_1\bar{\omega}_{li} + {}_1\bar{\omega}_{is}$ , where  $i$  refers to any attached outer segment and  ${}_1\bar{\omega}_{is}$  can be obtained by measuring the angular position of the  $i$ th outer segment with respect to the spacecraft. The quantity  ${}_1\bar{r}_{sm}$  can be obtained from the equation  ${}_1\bar{r}_{sm} = {}_1\bar{\rho}_i - {}_1\bar{r}'_i$ , where  ${}_1\bar{\rho}_i$  is the constant vector from the spacecraft center of mass to the point of contact of the  $i$ th segment on the spacecraft, and  ${}_1\bar{r}'_i$  is a vector from the astronaut's center of mass to the point of contact of the  $i$ th segment on the spacecraft and can be obtained from LIMS data. These quantities can also be obtained from an actual analog simulation of the problem as they are merely the angular velocity and

## APPENDIX B

position of the astronaut relative to the spacecraft and are the same quantities used to position the carriage. These quantities can be recorded during the analog simulation, digitized, and fed directly into the digital program just as are the LIMS angles.

Equation (B60) also holds for the case where the astronaut is not touching the spacecraft. In this case, however,  ${}_1\bar{\omega}_{so}$  is either zero or a known constant and  ${}_1\bar{r}_{sm}$  is either a constant or varies linearly and both are known from initial conditions. Equation (B60) can then be used to solve for the angular velocity of the astronaut relative to the spacecraft,  ${}_1\bar{\omega}_{ls}$ .

The solution to equation (B60) provides the information necessary to calculate forces and moments existing at any point in the system as a function of time. Of prime interest are the set of forces and moments that, if acting alone and at the spacecraft center of mass, would cause the calculated spacecraft translations and rotations. In spacecraft coordinates, the forces and moments are given by

$${}_s\bar{F}_s = m_s \left( {}_s\ddot{\bar{R}}_s \right) \quad (B61)$$

and

$${}_s\bar{M}_s = \frac{\dot{{}_s\bar{I}}_s}{{}_s\bar{\omega}_{so}} \quad (B62)$$

where  ${}_s\bar{\omega}_{so} = D_{1s} {}_1\bar{\omega}_{so}$ . From equations (B46) and (B48), equation (B61) can be written as

$${}_s\bar{F}_s = -Q {}_s\ddot{\bar{r}}_{sm} \quad (B63)$$

where  ${}_s\bar{r}_{sm} = D_{1s} {}_1\bar{r}_{sm}$ . Equations (B63) and (B62), because they contain derivatives measured in a rotating coordinate system, become

$${}_s\bar{F}_s = -Q \left[ {}_s\ddot{\bar{r}}_{sm} + {}_s\bar{\omega}_{so} \times {}_s\bar{r}_{sm} + 2 \left( {}_s\bar{\omega}_{so} \times {}_s\dot{\bar{r}}_{sm} \right) + {}_s\bar{\omega}_{so} \times \left( {}_s\bar{\omega}_{so} \times {}_s\bar{r}_{sm} \right) \right] \quad (B64)$$

## APPENDIX B

and

$$\bar{\mathbf{M}}_s = \bar{\mathbf{I}}_s \cdot \bar{\boldsymbol{\omega}}_{so} + \bar{\boldsymbol{\omega}}_{so} \times \left( \bar{\mathbf{I}}_s \cdot \bar{\boldsymbol{\omega}}_{so} \right) \quad (\text{B65})$$

These force and moment equations are also programed for the digital computer along with equation (B60). Because the spacecraft has been assumed to be a rigid body, the forces and moments given by equations (B64) and (B65) can be transferred to any point on or in the spacecraft. For example, if they are transferred to the astronaut/spacecraft contact point, the resulting forces and moments would represent those actually applied to the spacecraft by the astronaut.

### General Transformations

The purpose of this subsection is twofold: first, to provide those transformation matrices required for the expansion of the EVA/IVA simulation equations into component form; and second, to provide a reference of the transformation matrices for use in other problems.

Euler transformation matrices. - One method of obtaining a transformation matrix between two orthogonal sets of coordinate systems is by rotating the reference system successively about each of its own axes so that after three rotations the reference system is parallel to a second specified axis system. This method generates conventional Euler angles defined as follows:

- $\psi$  (yaw) - a positive rotation about the reference z axis;
- $\theta$  (pitch) - a positive rotation about the reference y axis;
- $\phi$  (roll) - a position rotation about the reference x axis.

Transformations from the second system into the reference system for a single rotation about an axis are defined as:



# APPENDIX B

$$\left. \begin{aligned} D(\psi) &= \begin{bmatrix} C\psi & -S\psi & 0 \\ S\psi & C\psi & 0 \\ 0 & 0 & 1 \end{bmatrix} \\ D(\theta) &= \begin{bmatrix} C\theta & 0 & S\theta \\ 0 & 1 & 0 \\ -S\theta & 0 & C\theta \end{bmatrix} \\ D(\phi) &= \begin{bmatrix} 1 & 0 & 0 \\ 0 & C\phi & -S\phi \\ 0 & S\phi & C\phi \end{bmatrix} \end{aligned} \right\} \quad (B66)$$

Equivalent transformations from the reference system into the second system are denoted by  $D^{-1}(\psi)$ ,  $D^{-1}(\theta)$ , and  $D^{-1}(\phi)$  and can be obtained (because these matrices are orthogonal) from:

$$\left. \begin{aligned} D^{-1}(\psi) &= D^T(\psi) = D(-\psi) \\ D^{-1}(\theta) &= D^T(\theta) = D(-\theta) \\ D^{-1}(\phi) &= D^T(\phi) = D(-\phi) \end{aligned} \right\} \quad (B67)$$

where  $-1$  denotes the inverse and  $T$  denotes the transpose.

Because the final orientation of the reference system depends on the sequence of rotations, it is necessary to specify and maintain a specific sequence. Assume the rotational sequence, when going from the reference to the second system, is  $\alpha_1, \alpha_2, \alpha_3$ . Vectors in the reference system are then transformed into the second system by

$${}_2\bar{r} = \left[ D^{-1}(\alpha_3) D^{-1}(\alpha_2) D^{-1}(\alpha_1) \right] {}_R\bar{r} \quad (B68)$$

Likewise, transforming from the second system into the reference the sequence must be  $-\alpha_3, -\alpha_2, -\alpha_1$ , giving

$${}_R\bar{r} = \left[ D^{-1}(-\alpha_1) D^{-1}(-\alpha_2) D^{-1}(-\alpha_3) \right] {}_2\bar{r} \quad (B69)$$

## APPENDIX B

or

$${}_R\bar{F} = \left[ D(\alpha_1) D(\alpha_2) D(\alpha_3) \right] {}_2\bar{F} \quad (B70)$$

The quantity  $D(\alpha_1) D(\alpha_2) D(\alpha_3)$  is expanded for the six possible rotational sequences. Because these matrices are orthogonal, the transformations from the reference system into the second system are simply the transpose of those from the second into the reference.

In addition, the rates of change of the Euler angles, represented as vectors whose components are directed along the axes about which the individual rotation takes place, are functions of the angular rate,  $\bar{\omega}$ , of the second axis system relative to the reference system. Denoting  $p$ ,  $q$ , and  $r$  as the  $x$ ,  $y$ , and  $z$  components of  $\bar{\omega}$  measured in the second system, the transform equation becomes

$$\begin{bmatrix} \dot{\phi} \\ \dot{\theta} \\ \dot{\psi} \end{bmatrix} = D_{\epsilon} \begin{bmatrix} p \\ q \\ r \end{bmatrix} \quad (B71)$$

or

$$\begin{bmatrix} p \\ q \\ r \end{bmatrix} = D_{\epsilon}^{-1} \begin{bmatrix} \dot{\phi} \\ \dot{\theta} \\ \dot{\psi} \end{bmatrix} \quad (B72)$$

where  $D_{\epsilon}$  is the Euler rate transformation matrix. The Euler angular rates are not orthogonal therefore both  $D_{\epsilon}$  and  $D_{\epsilon}^{-1}$  are given for the six possible rotational sequences.

Yaw-pitch-roll sequence: The vector transformation matrix is:

$$\left[ D(\psi) D(\theta) D(\phi) \right] = \begin{bmatrix} C\psi C\theta & C\psi S\theta S\phi - S\psi C\phi & C\psi S\theta C\phi + S\psi S\phi \\ S\psi C\theta & S\psi S\theta S\phi + C\psi C\phi & S\psi S\theta C\phi - C\psi S\phi \\ -S\theta & C\theta S\phi & C\theta C\phi \end{bmatrix} \quad (B73)$$

## APPENDIX B

The Euler rates-to-body rates are:

$$\begin{bmatrix} p \\ q \\ r \end{bmatrix} = \begin{bmatrix} 1 & 0 & -S\theta \\ 0 & C\varphi & S\varphi C\theta \\ 0 & -S\varphi & C\varphi C\theta \end{bmatrix} \begin{bmatrix} \dot{\varphi} \\ \dot{\theta} \\ \dot{\psi} \end{bmatrix} \quad (B74)$$

The body rates-to-Euler rates are:

$$\begin{bmatrix} \dot{\varphi} \\ \dot{\theta} \\ \dot{\psi} \end{bmatrix} = \begin{bmatrix} 1 & S\varphi S\theta/C\theta & C\varphi S\theta/C\theta \\ 0 & C\varphi & -S\varphi \\ 0 & S\varphi/C\theta & C\varphi/C\theta \end{bmatrix} \begin{bmatrix} p \\ q \\ r \end{bmatrix} \quad (B75)$$

Yaw-roll-pitch sequence: The vector transformation matrix is:

$$[D(\psi) D(\varphi) D(\theta)] = \begin{bmatrix} C\psi C\theta - S\psi S\varphi S\theta & -S\psi C\varphi & C\psi S\theta + S\psi S\varphi C\theta \\ S\psi C\theta + C\psi S\varphi S\theta & C\psi C\varphi & S\psi S\theta - C\psi S\varphi C\theta \\ -C\varphi S\theta & S\varphi & C\varphi C\theta \end{bmatrix} \quad (B76)$$

The Euler rates-to-body rates are:

$$\begin{bmatrix} p \\ q \\ r \end{bmatrix} = \begin{bmatrix} C\theta & 0 & -S\theta C\varphi \\ 0 & 1 & S\varphi \\ S\theta & 0 & C\theta C\varphi \end{bmatrix} \begin{bmatrix} \dot{\varphi} \\ \dot{\theta} \\ \dot{\psi} \end{bmatrix} \quad (B77)$$

The body rates-to-Euler rates are:

$$\begin{bmatrix} \dot{\varphi} \\ \dot{\theta} \\ \dot{\psi} \end{bmatrix} = \begin{bmatrix} C\theta & 0 & S\theta \\ S\theta S\varphi/C\varphi & 1 & -C\theta S\varphi/C\varphi \\ -S\theta/C\varphi & 0 & C\theta/C\varphi \end{bmatrix} \begin{bmatrix} p \\ q \\ r \end{bmatrix} \quad (B78)$$

Pitch-roll-yaw-sequence: The vector transformation matrix is:

$$[D(\theta) D(\varphi) D(\psi)] = \begin{bmatrix} C\theta C\psi + S\theta S\varphi S\psi & -C\theta S\psi + S\theta S\varphi C\psi & S\theta C\varphi \\ C\varphi S\psi & C\varphi C\psi & -S\varphi \\ -S\theta C\psi + C\theta S\varphi S\psi & S\theta S\psi + C\theta S\varphi C\psi & C\theta C\varphi \end{bmatrix} \quad (B79)$$

## APPENDIX B

The Euler rates-to-body rates are:

$$\begin{bmatrix} p \\ q \\ r \end{bmatrix} = \begin{bmatrix} C\psi & S\psi C\varphi & 0 \\ -S\psi & C\psi C\varphi & 0 \\ 0 & -S\varphi & 1 \end{bmatrix} \begin{bmatrix} \dot{\phi} \\ \dot{\theta} \\ \dot{\psi} \end{bmatrix} \quad (\text{B80})$$

The body rates-to-Euler rates are:

$$\begin{bmatrix} \dot{\phi} \\ \dot{\theta} \\ \dot{\psi} \end{bmatrix} = \begin{bmatrix} C\psi & -S\psi & 0 \\ S\psi/C\varphi & C\psi/C\varphi & 0 \\ S\psi S\varphi/C\varphi & C\psi S\varphi/C\varphi & 1 \end{bmatrix} \begin{bmatrix} p \\ q \\ r \end{bmatrix} \quad (\text{B81})$$

Pitch-yaw-roll sequence: The vector transformation matrix is:

$$\begin{bmatrix} D(\theta) & D(\psi) & D(\varphi) \end{bmatrix} = \begin{bmatrix} C\theta C\psi & -C\theta S\psi C\varphi + S\theta S\varphi & C\theta S\psi S\varphi + S\theta C\varphi \\ S\psi & C\psi C\varphi & -C\psi S\varphi \\ -S\theta C\psi & S\theta S\psi C\varphi + C\theta S\varphi & -S\theta S\psi S\varphi + C\theta C\varphi \end{bmatrix} \quad (\text{B82})$$

The Euler rates-to-body rates are:

$$\begin{bmatrix} p \\ q \\ r \end{bmatrix} = \begin{bmatrix} 1 & S\psi & 0 \\ 0 & C\psi C\varphi & S\varphi \\ 0 & -C\psi S\varphi & C\varphi \end{bmatrix} \begin{bmatrix} \dot{\phi} \\ \dot{\theta} \\ \dot{\psi} \end{bmatrix} \quad (\text{B83})$$

The body rates-to-Euler rates are:

$$\begin{bmatrix} \dot{\phi} \\ \dot{\theta} \\ \dot{\psi} \end{bmatrix} = \begin{bmatrix} 1 & -S\psi C\varphi/C\psi & S\psi S\varphi/C\psi \\ 0 & C\varphi/C\psi & -S\varphi/C\psi \\ 0 & S\varphi & C\varphi \end{bmatrix} \begin{bmatrix} p \\ q \\ r \end{bmatrix} \quad (\text{B84})$$

## APPENDIX B

Roll-pitch-yaw sequence: The vector transformation matrix is:

$$\begin{bmatrix} D(\varphi) & D(\theta) & D(\psi) \end{bmatrix} = \begin{bmatrix} C\theta C\psi & -C\theta S\psi & S\theta \\ C\varphi S\psi + S\varphi S\theta C\psi & C\varphi C\psi - S\varphi S\theta S\psi & -S\varphi C\theta \\ S\varphi S\psi - C\varphi S\theta C\psi & S\varphi C\psi + C\varphi S\theta S\psi & C\varphi C\theta \end{bmatrix} \quad (\text{B85})$$

The Euler rates-to-body rates are:

$$\begin{bmatrix} p \\ q \\ r \end{bmatrix} = \begin{bmatrix} C\psi C\theta & S\psi & 0 \\ -S\psi C\theta & C\psi & 0 \\ S\theta & 0 & 1 \end{bmatrix} \begin{bmatrix} \dot{\varphi} \\ \dot{\theta} \\ \dot{\psi} \end{bmatrix} \quad (\text{B86})$$

The body rates-to-Euler rates are:

$$\begin{bmatrix} \dot{\varphi} \\ \dot{\theta} \\ \dot{\psi} \end{bmatrix} = \begin{bmatrix} C\psi/C\theta & -S\psi/C\theta & 0 \\ S\psi & C\psi & 0 \\ -C\psi S\theta/C\theta & S\psi S\theta/C\theta & 1 \end{bmatrix} \begin{bmatrix} p \\ q \\ r \end{bmatrix} \quad (\text{B87})$$

Roll-yaw-pitch sequence: The vector transformation matrix is:

$$\begin{bmatrix} D(\varphi) & D(\psi) & D(\theta) \end{bmatrix} = \begin{bmatrix} C\psi C\theta & -S\psi & C\psi S\theta \\ C\varphi S\psi C\theta + S\varphi S\theta & C\varphi C\psi & C\varphi S\psi S\theta - S\varphi C\theta \\ S\varphi S\psi C\theta - C\varphi S\theta & S\varphi C\psi & S\varphi S\psi S\theta + S\varphi C\theta \end{bmatrix} \quad (\text{B88})$$

The Euler rates-to-body rates are:

$$\begin{bmatrix} p \\ q \\ r \end{bmatrix} = \begin{bmatrix} C\theta C\psi & 0 & -S\theta \\ -S\psi & 1 & 0 \\ S\theta C\psi & 0 & C\theta \end{bmatrix} \begin{bmatrix} \dot{\varphi} \\ \dot{\theta} \\ \dot{\psi} \end{bmatrix} \quad (\text{B89})$$

## APPENDIX B

The body rates-to-Euler rates are:

$$\begin{bmatrix} \dot{\phi} \\ \dot{\theta} \\ \dot{\psi} \end{bmatrix} = \begin{bmatrix} C\theta/C\psi & 0 & S\theta/C\psi \\ C\theta S\psi/C\psi & 1 & S\theta S\psi/C\psi \\ -S\theta & 0 & C\theta \end{bmatrix} \begin{bmatrix} p \\ q \\ r \end{bmatrix} \quad (B90)$$

### Expanded Forms

This subsection presents the expanded or component forms of the vector equations required by the analog simulation and given in the subsections entitled Basic Equations of Motion and Equations of Motion for Hybrid Simulation. While some of the expanded forms are used in the digital program, it is not necessary to expand all terms in the detail required by the analog program. The digital program uses, as often as possible, subroutines that perform matrix multiplications, vector dot, or cross products, etc., for general matrices or vectors. Each time a matrix or vector operation is required in the vector equation, the subroutine is called to perform the operation. The necessity of writing all equations in component form for the digital simulation is thereby eliminated.

Spacecraft angular rate.- The spacecraft angular rate,  ${}_{s'}\bar{\omega}_{so}$ , was given by

$${}_{s'}\bar{\omega}_{so} = {}_s\bar{I}_s^{-1} \cdot \int \left[ {}_s\bar{M}_s - {}_{s'}\bar{\omega}_{so} \times ({}_s\bar{I}_s \cdot {}_{s'}\bar{\omega}_{so}) \right] dt \quad (B91)$$

Premultiplying each side of this equation by  ${}_s\bar{I}_s$  and replacing  ${}_s\bar{I}_s \cdot {}_{s'}\bar{\omega}_{so}$  by  ${}_s\bar{A}_s$  enables equation (B91) to be expressed by

$${}_s\bar{A}_s = \int \left( {}_s\bar{M}_s - {}_{s'}\bar{\omega}_{so} \times {}_s\bar{A}_s \right) dt \quad (B91a)$$

where

$${}_s\bar{A}_s = {}_s\bar{I}_s \cdot {}_{s'}\bar{\omega}_{so} \quad (B91b)$$

## APPENDIX B

The vectors in component form are denoted by

$$\left. \begin{aligned} {}_s\bar{\omega}_{so} &= {}_s p_{so} \bar{i}_s + {}_s q_{so} \bar{j}_s + {}_s r_{so} \bar{k}_s \\ {}_s\bar{M}_s &= {}_s M_{sx} \bar{i}_s + {}_s M_{sy} \bar{j}_s + {}_s M_{sz} \bar{k}_s \\ {}_s\bar{A}_s &= {}_s A_{sx} \bar{i}_s + {}_s A_{sy} \bar{j}_s + {}_s A_{sz} \bar{k}_s \end{aligned} \right\} \quad (B92)$$

and the spacecraft inertia dyadic\* by

$${}_s I_s = \begin{bmatrix} {}_s I_{sxx} & {}_s I_{sxy} & {}_s I_{sxz} \\ {}_s I_{syx} & {}_s I_{syy} & {}_s I_{syz} \\ {}_s I_{szx} & {}_s I_{szy} & {}_s I_{szz} \end{bmatrix} \quad (B93)$$

Expanding equation (B91b) and solving for the spacecraft angular rate components,

$$\begin{aligned} {}_s p_{so} &= \left[ {}_s A_{sx} - \left( {}_s q_{so} \right) \left( {}_s I_{sxy} \right) - \left( {}_s r_{so} \right) \left( {}_s I_{sxz} \right) \right] / {}_s I_{sxx} \\ {}_s q_{so} &= \left[ {}_s A_{sy} - \left( {}_s p_{so} \right) \left( {}_s I_{syx} \right) - \left( {}_s r_{so} \right) \left( {}_s I_{syz} \right) \right] / {}_s I_{syy} \\ {}_s r_{so} &= \left[ {}_s A_{sz} - \left( {}_s p_{so} \right) \left( {}_s I_{szx} \right) - \left( {}_s q_{so} \right) \left( {}_s I_{szy} \right) \right] / {}_s I_{szz} \end{aligned} \quad (B94)$$

and by expansion of equation (B91a),

$$\begin{aligned} {}_s A_{sx} &= \int \left[ {}_s M_{sx} + \left( {}_s r_{so} \right) \left( {}_s A_{sy} \right) - \left( {}_s q_{so} \right) \left( {}_s A_{sz} \right) \right] dt \\ {}_s A_{sy} &= \int \left[ {}_s M_{sy} + \left( {}_s p_{so} \right) \left( {}_s A_{sz} \right) - \left( {}_s r_{so} \right) \left( {}_s A_{sx} \right) \right] dt \\ {}_s A_{sz} &= \int \left[ {}_s M_{sz} + \left( {}_s q_{so} \right) \left( {}_s A_{sx} \right) - \left( {}_s p_{so} \right) \left( {}_s A_{sy} \right) \right] dt \end{aligned} \quad (B95)$$

---

\*The product of inertia terms are defined as positive quantities. Some authors define these as negative quantities.

## APPENDIX B

The expanded forms of equations (B91a) and (B91b) are solved simultaneously on the analog computer and  $\bar{M}_s$  is the forcing function given by equation (B42b) as

$$\bar{M}_s = \bar{M}_L + \bar{r}_a \times \bar{F}_L \quad (B42b)$$

The vector components are

$$\begin{aligned} M_{sx} &= M_{Lx} + \begin{pmatrix} s^y_a \end{pmatrix} \begin{pmatrix} F_{Lz} \end{pmatrix} - \begin{pmatrix} s^z_a \end{pmatrix} \begin{pmatrix} F_{Ly} \end{pmatrix} \\ M_{sy} &= M_{Ly} + \begin{pmatrix} s^z_a \end{pmatrix} \begin{pmatrix} F_{Lx} \end{pmatrix} - \begin{pmatrix} s^x_a \end{pmatrix} \begin{pmatrix} F_{Lz} \end{pmatrix} \\ M_{sz} &= M_{Lz} + \begin{pmatrix} s^x_a \end{pmatrix} \begin{pmatrix} F_{Ly} \end{pmatrix} - \begin{pmatrix} s^y_a \end{pmatrix} \begin{pmatrix} F_{Lx} \end{pmatrix} \end{aligned} \quad (B96)$$

where the components of  $\bar{M}_L$  and  $\bar{F}_L$  as determined by the individual load cell outputs have been previously defined.

Note that the components of  $\bar{r}_a$  and  $\bar{l}_s$  are constants selected after the specific simulation problem is defined.

Spacecraft attitude. - The spacecraft attitude is described by three Euler angles relating the spacecraft body axes to the inertial reference axes. The Euler angular rates were expressed by

$$\dot{\bar{e}}_s = D_{s\epsilon} \bar{\omega}_{so} \quad (B12)$$

A specific Euler angle sequence must be defined because  $D_{s\epsilon}$  is a function of the sequence. The selection of a sequence is quite arbitrary in this case. Therefore, a yaw, pitch, roll sequence is defined between the reference axes and the spacecraft body axes. The previous subsection (General Transformations) contains the transformation equation in matrix form, and by expanding equation (B12), the Euler rate components are

$$\left. \begin{aligned} \dot{\phi}_s &= s^p_{so} + \dot{\psi}_s \sin \theta_s \\ \dot{\theta}_s &= s^q_{so} \cos \phi_s - s^r_{so} \sin \phi_s \\ \dot{\psi}_s &= s^r_{so} \cos \phi_s \sec \theta_s + s^q_{so} \sin \phi_s \sec \theta_s \end{aligned} \right\} \quad (B97)$$



## APPENDIX B

and the Euler angles describing the spacecraft attitude are

$$\left. \begin{aligned} \varphi_s &= \int \dot{\varphi}_s dt \\ \theta_s &= \int \dot{\theta}_s dt \\ \psi_s &= \int \dot{\psi}_s dt \end{aligned} \right\} \quad (B98)$$

Astronaut's angular rate. - The angular rate of the astronaut's torso,  ${}_1\bar{\omega}_{10}$ , was given by equation (B30) as

$${}_1\bar{\omega}_{10} = {}_1\bar{\mathbf{I}}_m^{-1} \cdot \left\{ \int \left[ {}_1\bar{\mathbf{M}}_m - {}_1\bar{\omega}_{10} \times \left( {}_1\bar{\mathbf{I}}_m \cdot {}_1\bar{\omega}_{10} + {}_1\bar{\mathbf{J}}_m \right) \right] dt - {}_1\bar{\mathbf{J}}_m \right\} \quad (B30)$$

Equation (B30) was obtained by combining equations (B27) and (B29). It is convenient to use the latter two equations in expanded form. Referring to equations (B27) and (B29),

$${}_1\bar{\mathbf{H}}_{mm} = {}_1\bar{\mathbf{I}}_m \cdot {}_1\bar{\omega}_{10} + {}_1\bar{\mathbf{J}}_m \quad (B27)$$

$${}_1\bar{\mathbf{H}}_{mm} = \int \left[ {}_1\bar{\mathbf{M}}_m - {}_1\bar{\omega}_{10} \times {}_1\bar{\mathbf{H}}_{mm} \right] dt \quad (B29)$$

The vectors in component form are denoted by

$$\left. \begin{aligned} {}_1\bar{\omega}_{10} &= {}_1p_{10} \bar{\mathbf{i}}_1 + {}_1q_{10} \bar{\mathbf{j}}_1 + {}_1r_{10} \bar{\mathbf{k}}_1 \\ {}_1\bar{\mathbf{M}}_m &= {}_1M_{mx} \bar{\mathbf{i}}_1 + {}_1M_{my} \bar{\mathbf{j}}_1 + {}_1M_{mz} \bar{\mathbf{k}}_1 \\ {}_1\bar{\mathbf{H}}_{mm} &= {}_1H_{mmx} \bar{\mathbf{i}}_1 + {}_1H_{mmy} \bar{\mathbf{j}}_1 + {}_1H_{mmz} \bar{\mathbf{k}}_1 \\ {}_1\bar{\mathbf{J}}_m &= {}_1J_{mx} \bar{\mathbf{i}}_1 + {}_1J_{my} \bar{\mathbf{j}}_1 + {}_1J_{mz} \bar{\mathbf{k}}_1 \end{aligned} \right\} \quad (B99)$$

## APPENDIX B

and the astronaut's instantaneous inertia dyadic by

$${}_{1}\bar{\bar{I}}_m = \begin{bmatrix} {}_{1}I_{mxx} & {}_{1}I_{mxy} & {}_{1}I_{mxz} \\ {}_{1}I_{myx} & {}_{1}I_{myy} & {}_{1}I_{myz} \\ {}_{1}I_{mzx} & {}_{1}I_{mzy} & {}_{1}I_{mzz} \end{bmatrix} \quad (B100)$$

Expanding equation (B27) and solving for the torso angular rate components,

$$\left. \begin{aligned} {}_{1}p_{1o} &= \left[ {}_{1}H_{mmx} - {}_{1}J_{mx} - ({}_{1}q_{1o}) ({}_{1}I_{mxy}) - ({}_{1}r_{1o}) ({}_{1}I_{mxz}) \right] / {}_{1}I_{mxx} \\ {}_{1}q_{1o} &= \left[ {}_{1}H_{mmy} - {}_{1}J_{my} - ({}_{1}p_{1o}) ({}_{1}I_{myx}) - ({}_{1}r_{1o}) ({}_{1}I_{myz}) \right] / {}_{1}I_{myy} \\ {}_{1}r_{1o} &= \left[ {}_{1}H_{mmz} - {}_{1}J_{mz} - ({}_{1}p_{1o}) ({}_{1}I_{mzx}) - ({}_{1}q_{1o}) ({}_{1}I_{mzy}) \right] / {}_{1}I_{mzz} \end{aligned} \right\} \quad (B101)$$

and the expanded form of equation (B29) is

$$\left. \begin{aligned} {}_{1}H_{mmx} &= \int \left[ {}_{1}M_{mx} + ({}_{1}r_{1o}) ({}_{1}H_{mmy}) - ({}_{1}q_{1o}) ({}_{1}H_{mmz}) \right] dt \\ {}_{1}H_{mmy} &= \int \left[ {}_{1}M_{my} + ({}_{1}p_{1o}) ({}_{1}H_{mmz}) - ({}_{1}r_{1o}) ({}_{1}H_{mmx}) \right] dt \\ {}_{1}H_{mmz} &= \int \left[ {}_{1}M_{mz} + ({}_{1}q_{1o}) ({}_{1}H_{mmx}) - ({}_{1}p_{1o}) ({}_{1}H_{mmy}) \right] dt \end{aligned} \right\} \quad (B102)$$

The components of  ${}_{1}\bar{\bar{M}}_m$  are obtained from equation (B44) where

$${}_{1}\bar{\bar{M}}_m = D_{s1} {}_{s1}\bar{\bar{M}}_m \quad (B44)$$

The matrix,  $D_{s1}$ , transforms vectors in spacecraft coordinates to torso coordinates. The Euler sequence is selected to be compatible with the roll-pitch-yaw gimbal sequence of the SOS attitude head. Therefore,

$$D_{s1} = D^{-1}(\psi_{s1}) D^{-1}(\theta_{s1}) D^{-1}(\varphi_{s1}) \quad (B103)$$

## APPENDIX B

and equation (B44) in component form is

$$\left. \begin{aligned} {}_1M_{mx} &= \begin{pmatrix} d_{11} \\ s_{11} \end{pmatrix} {}_sM_{mx} + \begin{pmatrix} d_{12} \\ s_{12} \end{pmatrix} {}_sM_{my} + \begin{pmatrix} d_{13} \\ s_{13} \end{pmatrix} {}_sM_{mz} \\ {}_1M_{my} &= \begin{pmatrix} d_{21} \\ s_{21} \end{pmatrix} {}_sM_{mx} + \begin{pmatrix} d_{22} \\ s_{22} \end{pmatrix} {}_sM_{my} + \begin{pmatrix} d_{23} \\ s_{23} \end{pmatrix} {}_sM_{mz} \\ {}_1M_{mz} &= \begin{pmatrix} d_{31} \\ s_{31} \end{pmatrix} {}_sM_{mx} + \begin{pmatrix} d_{32} \\ s_{32} \end{pmatrix} {}_sM_{my} + \begin{pmatrix} d_{33} \\ s_{33} \end{pmatrix} {}_sM_{mz} \end{aligned} \right\} \quad (B104)$$

where the matrix elements,  $d_{s1}$ , are tabulated in the expanded forms of the transformation matrices. The contact moments on the astronaut in spacecraft coordinates,  $\bar{M}_s$ , were given by equation (B43b),

$$\bar{M}_s = -\bar{M}_s + \left( \bar{r}_{sm} \times \bar{F}_L \right) \quad (B43b)$$

Expanding,

$$\left. \begin{aligned} {}_sM_{mx} &= -{}_sM_{sx} + ({}_sy_{sm})F_{Lz} - ({}_sz_{sm})F_{Ly} \\ {}_sM_{my} &= -{}_sM_{sy} + ({}_sz_{sm})F_{Lx} - ({}_sx_{sm})F_{Lz} \\ {}_sM_{mz} &= -{}_sM_{sz} + ({}_sx_{sm})F_{Ly} - ({}_sy_{sm})F_{Lx} \end{aligned} \right\} \quad (B105)$$

Note the following:

- 1) The components of  $\bar{M}_s$  are contained in the expanded form of the spacecraft angular rate;
- 2) The components of  $\bar{F}_L$  were defined previously in the paragraph entitled Load Cell Array;
- 3) The components of  ${}_1\bar{I}_m$ ,  ${}_1\bar{J}_m$ , and  ${}_s\bar{r}_{sm}$  are determined in following expansions.

Astronaut's instantaneous inertia dyadic. - The astronaut's instantaneous inertia dyadic,  ${}_1\bar{I}_m$ , was shown to be

$${}_1\bar{I}_m = \sum_{i=1}^9 \left\{ {}_1\bar{I}_i + m_i \left[ ({}_1\bar{r}_i \cdot {}_1\bar{r}_i) \bar{E} - {}_1\bar{r}_i {}_1\bar{r}_i \right] \right\} \quad (B25)$$

# APPENDIX B

Denoting the inertia dyadic, as before, by

$${}_1\bar{\bar{I}}_m = \begin{bmatrix} {}_1I_{mxx} & {}_1I_{mxy} & {}_1I_{mxz} \\ {}_1I_{myx} & {}_1I_{myy} & {}_1I_{myz} \\ {}_1I_{mzx} & {}_1I_{mzy} & {}_1I_{mzz} \end{bmatrix} \quad (B100)$$

and the components of the position vector as

$${}_1\bar{r}_i = {}_1x_i \bar{i} + {}_1y_i \bar{j} + {}_1z_i \bar{k} \quad (B106)$$

the inertia components become

$$\left. \begin{aligned} {}_1I_{mxx} &= {}_1I_{lxx} + \sum_{i=2}^9 \left[ {}_1I_i \right]_{xx} + \sum_{i=1}^9 m_i ({}_1y_i^2 + {}_1z_i^2) \\ {}_1I_{myy} &= {}_1I_{lyy} + \sum_{i=2}^9 \left[ {}_1I_i \right]_{yy} + \sum_{i=1}^9 m_i ({}_1x_i^2 + {}_1z_i^2) \\ {}_1I_{mzz} &= {}_1I_{lzz} + \sum_{i=2}^9 \left[ {}_1I_i \right]_{zz} + \sum_{i=1}^9 m_i ({}_1x_i^2 + {}_1y_i^2) \\ {}_1I_{mxy} &= {}_1I_{myx} = \sum_{i=2}^9 \left[ {}_1I_i \right]_{xy} - \sum_{i=1}^9 m_i ({}_1x_i {}_1y_i) \\ {}_1I_{mxz} &= {}_1I_{mzx} = \sum_{i=2}^9 \left[ {}_1I_i \right]_{xz} - \sum_{i=1}^9 m_i ({}_1x_i {}_1z_i) \\ {}_1I_{myz} &= {}_1I_{mzy} = \sum_{i=2}^9 \left[ {}_1I_i \right]_{yz} - \sum_{i=1}^9 m_i ({}_1y_i {}_1z_i) \end{aligned} \right\} \quad (B107)$$

## APPENDIX B

The anthropometric data contained in Appendix D provides the components of the individual segment inertia dyadics,  ${}_i\bar{I}_i$ , in segment body coordinates where

$${}_i\bar{I}_i = \begin{bmatrix} {}_iI_{ixx} & 0 & 0 \\ 0 & {}_iI_{iyy} & 0 \\ 0 & 0 & {}_iI_{izz} \end{bmatrix} \quad (B108)$$

and  ${}_1\bar{I}_i$  is obtained by transforming  ${}_iI_i$  into the torso coordinate axes. Therefore,

$${}_1\bar{I}_i = D_{i1}({}_i\bar{I}_i)D_{1i} \quad (B109)$$

where  $D_{i1}$  and  $D_{1i}$  are the transformation matrices provided by the LIMS. Performing the indicated mathematical operations,

$$\left. \begin{aligned} \begin{bmatrix} {}_1I_i \end{bmatrix}_{xx} &= ({}_{11}d_{il})^2 {}_iI_{ixx} + ({}_{12}d_{il})^2 {}_iI_{iyy} + ({}_{13}d_{il})^2 {}_iI_{izz} \\ \begin{bmatrix} {}_1I_i \end{bmatrix}_{yy} &= ({}_{21}d_{il})^2 {}_iI_{ixx} + ({}_{22}d_{il})^2 {}_iI_{iyy} + ({}_{23}d_{il})^2 {}_iI_{izz} \\ \begin{bmatrix} {}_1I_i \end{bmatrix}_{zz} &= ({}_{31}d_{il})^2 {}_iI_{ixx} + ({}_{32}d_{il})^2 {}_iI_{iyy} + ({}_{33}d_{il})^2 {}_iI_{izz} \\ \begin{bmatrix} {}_1I_i \end{bmatrix}_{xy} &= ({}_{11}d_{il}) ({}_{21}d_{il}) {}_iI_{ixx} + ({}_{12}d_{il}) ({}_{22}d_{il}) {}_iI_{iyy} \\ &\quad + ({}_{13}d_{il}) ({}_{23}d_{il}) {}_iI_{izz} \\ \begin{bmatrix} {}_1I_i \end{bmatrix}_{xz} &= ({}_{11}d_{il}) ({}_{31}d_{il}) {}_iI_{ixx} + ({}_{12}d_{il}) ({}_{32}d_{il}) {}_iI_{iyy} \\ &\quad + ({}_{13}d_{il}) ({}_{33}d_{il}) {}_iI_{izz} \\ \begin{bmatrix} {}_1I_i \end{bmatrix}_{yz} &= ({}_{21}d_{il}) ({}_{31}d_{il}) {}_iI_{ixx} + ({}_{22}d_{il}) ({}_{32}d_{il}) {}_iI_{iyy} \\ &\quad + ({}_{23}d_{il}) ({}_{33}d_{il}) {}_iI_{izz} \end{aligned} \right\} \quad (B110)$$

## APPENDIX B

These expanded terms must be summed over  $i$  from 2 thru 9. Note the following:

- 1) The components of  ${}_1\bar{\mathbf{r}}_i$  are contained in the expanded form of the limb position vectors;
- 2) The matrix elements,  $d_{i1}$ , are contained in the expanded form of the transformation matrices.

Angular momentum term. - Equation (B26) defines the angular momentum term,  ${}_1\bar{\mathbf{J}}_m$ , by

$${}_1\bar{\mathbf{J}}_m = \sum_{i=1}^9 \left[ {}_1\bar{\mathbf{I}}_i \cdot {}_1\bar{\boldsymbol{\omega}}_{i1} + m_i ({}_1\bar{\mathbf{r}}_i \times {}_1\dot{\bar{\mathbf{r}}}_i) \right] \quad (\text{B26})$$

Denoting

$${}_1\bar{\mathbf{A}}_i = {}_1\bar{\mathbf{I}}_i \cdot {}_1\bar{\boldsymbol{\omega}}_{i1} \quad (\text{B111})$$

and recognizing  ${}_1\bar{\boldsymbol{\omega}}_{11} = 0$ , the expanded form of equation (B26) is

$$\left. \begin{aligned} {}_1J_{mx} &= \sum_{i=2}^9 {}_1A_{ix} + \sum_{i=1}^9 m_i ({}_1y_i {}_1\dot{z}_i - {}_1z_i {}_1\dot{y}_i) \\ {}_1J_{my} &= \sum_{i=2}^9 {}_1A_{iy} + \sum_{i=1}^9 m_i ({}_1z_i {}_1\dot{x}_i - {}_1x_i {}_1\dot{z}_i) \\ {}_1J_{mz} &= \sum_{i=2}^9 {}_1A_{iz} + \sum_{i=1}^9 m_i ({}_1x_i {}_1\dot{y}_i - {}_1y_i {}_1\dot{x}_i) \end{aligned} \right\} \quad (\text{B112})$$

The components of  ${}_1\bar{\mathbf{A}}_i$  are found using the transformation matrices,  $D_{i1}$ , given previously under the heading Limb Motion Sensor. Thus,

$${}_1\bar{\mathbf{A}}_i = {}_1\bar{\mathbf{I}}_i \cdot {}_1\bar{\boldsymbol{\omega}}_{i1} = D_{i1} \left[ {}_1\bar{\mathbf{I}}_i \cdot {}_1\bar{\boldsymbol{\omega}}_{i1} \right] \quad (\text{B113})$$

## APPENDIX B

and

$$\left. \begin{aligned} {}_1A_{ix} &= {}_{11}d_{il}({}_iI_{ixx}){}_ip_{il} + {}_{12}d_{il}({}_iI_{iyy}){}_iq_{il} + {}_{13}d_{il}({}_iI_{izz}){}_ir_{il} \\ {}_1A_{iy} &= {}_{21}d_{il}({}_iI_{ixx}){}_ip_{il} + {}_{22}d_{il}({}_iI_{iyy}){}_iq_{il} + {}_{23}d_{il}({}_iI_{izz}){}_ir_{il} \\ {}_1A_{iz} &= {}_{31}d_{il}({}_iI_{ixx}){}_ip_{il} + {}_{32}d_{il}({}_iI_{iyy}){}_iq_{il} + {}_{33}d_{il}({}_iI_{izz}){}_ir_{il} \end{aligned} \right\} \quad (B114)$$

These terms must be summed over  $i$  from 2 thru 9. Note that:

- 1) The components of  ${}_1\bar{r}_i$  are contained in the expanded form of the limb position vectors;
- 2) The matrix elements,  $d_{il}$ , are contained in the expanded form of the transformation matrices;
- 3) The components of  ${}_1\bar{\omega}_{il}$  are contained in the expanded form of the limb segment relative angular rates;
- 4) The components of  ${}_i\bar{I}_i$  are contained in Appendix D, Anthropometric Data.

Limb segment relative angular rates.- The angular momentum term,  ${}_1\bar{J}_m$ , requires expressions for the limb segment relative angular rates. The LIMS measures the Euler angles between connected segments. Differentiating these angles provides the Euler angular rates,  $\dot{\bar{e}}_{ij}$ . Knowing the Euler sequence associated with the angles, the Euler rates are transformed into segment body rates using the  $D_{\epsilon}^{-1}$  matrices contained in the subsection entitled General Transformations. For those segments directly connected to the torso (2, 3, 6, 7)

$$\dot{\bar{e}}_{ij} = \dot{\bar{e}}_{il} \quad (B115)$$

and

$${}_i\bar{\omega}_{il} = D_{il\epsilon}^{-1} \dot{\bar{e}}_{il} \quad (B116)$$

## APPENDIX B

For those segments not directly connected to the torso (4, 5, 8, 9), the Euler rate transformation determines the  $i$ th segment body rate relative to the  $j$ th segment,  ${}_i\bar{\omega}_{ij}$ . Therefore, for these segments,

$$\left. \begin{aligned} {}_i\bar{\omega}_{i1} &= {}_i\bar{\omega}_{ij} + {}_j\bar{\omega}_{j1} \\ &= D_{ij}^{-1} \dot{\bar{e}}_{ij} + D_{ji} {}_j\bar{\omega}_{j1} \end{aligned} \right\} \quad (B117)$$

where  $j = i - 2$ . Denoting,

$${}_i\bar{\omega}_{i1} = {}_i p_{i1} \bar{i}_i + {}_i q_{i1} \bar{j}_i + {}_i r_{i1} \bar{k}_i \quad (B118)$$

The components of the segment angular rates are given by:

Segment 2:

$$\left. \begin{aligned} {}_2p_{21} &= (S\psi_2) \dot{\theta}_2 + (C\psi_2 C\theta_2) \dot{\phi}_2 \\ {}_2q_{21} &= (C\psi_2) \dot{\theta}_2 - (S\psi_2 C\theta_2) \dot{\phi}_2 \\ {}_2r_{21} &= \dot{\psi}_2 + (S\theta_2) \dot{\phi}_2 \end{aligned} \right\} \quad (B119)$$

Segment 3:

$$\left. \begin{aligned} {}_3p_{31} &= (S\psi_3) \dot{\theta}_3 + (C\psi_3 C\theta_3) \dot{\phi}_3 \\ {}_3q_{31} &= (C\psi_3) \dot{\theta}_3 - (S\psi_3 C\theta_3) \dot{\phi}_3 \\ {}_3r_{31} &= \dot{\psi}_3 + (S\theta_3) \dot{\phi}_3 \end{aligned} \right\} \quad (B120)$$

Segment 4:

$$\left. \begin{aligned} {}_4p_{41} &= (C\theta_4) {}_2p_{21} - (S\theta_4) {}_2r_{21} \\ {}_4q_{41} &= \dot{\theta}_4 + {}_2q_{21} \\ {}_4r_{41} &= (S\theta_4) {}_2p_{21} + (C\theta_4) {}_2r_{21} \end{aligned} \right\} \quad (B121)$$

Segment 5:

$$\left. \begin{aligned} {}_5p_{51} &= (C\theta_5) {}_3p_{31} - (S\theta_5) {}_3r_{31} \\ {}_5q_{51} &= \dot{\theta}_5 + {}_3q_{31} \\ {}_5r_{51} &= (S\theta_5) {}_3p_{31} + (C\theta_5) {}_3r_{31} \end{aligned} \right\} \quad (B122)$$



# APPENDIX B

Segment 6:

$$\left. \begin{aligned} {}_6P_{61} &= (S\dot{\psi}_6) \dot{\theta}_6 + (C\dot{\psi}_6 C\theta_6) \dot{\phi}_6 \\ {}_6Q_{61} &= (C\dot{\psi}_6) \dot{\theta}_6 - (S\dot{\psi}_6 C\theta_6) \dot{\phi}_6 \\ {}_6R_{61} &= \dot{\psi}_6 + (S\theta_6) \dot{\phi}_6 \end{aligned} \right\} \quad (B123)$$

Segment 7:

$$\left. \begin{aligned} {}_7P_{71} &= (S\dot{\psi}_7) \dot{\theta}_7 + (C\dot{\psi}_7 C\theta_7) \dot{\phi}_7 \\ {}_7Q_{71} &= (C\dot{\psi}_7) \dot{\theta}_7 - (S\dot{\psi}_7 C\theta_7) \dot{\phi}_7 \\ {}_7R_{71} &= \dot{\psi}_7 + (S\theta_7) \dot{\phi}_7 \end{aligned} \right\} \quad (B124)$$

Segment 8:

$$\left. \begin{aligned} {}_8P_{81} &= (C\theta_8) {}_6P_{61} - (S\theta_8) {}_6R_{61} \\ {}_8Q_{81} &= \dot{\theta}_8 + {}_6Q_{61} \\ {}_8R_{81} &= (S\theta_8) {}_6P_{61} + (C\theta_8) {}_6R_{61} \end{aligned} \right\} \quad (B125)$$

Segment 9:

$$\left. \begin{aligned} {}_9P_{91} &= (C\theta_9) {}_7P_{71} - (S\theta_9) {}_7R_{71} \\ {}_9Q_{91} &= \dot{\theta}_9 + {}_7Q_{71} \\ {}_9R_{91} &= (S\theta_9) {}_7P_{71} + (C\theta_9) {}_7R_{71} \end{aligned} \right\} \quad (B126)$$

Limb position vectors. - The center-of-mass location of each segment with respect to the combined center of mass of the astronaut is denoted by the position vector  ${}_1\bar{r}_i$ , where

$${}_1\bar{r}_i = {}_1x_i \bar{i} + {}_1y_i \bar{j} + {}_1z_i \bar{k} \quad (B127)$$

With reference to the anthropometric data in Appendix D and the previously discussed LIMS transformations data, the components of the position vector for segments 2 thru 9 can be written in terms of segment 1 components as follows:

# APPENDIX B

Segment 2:

$$\left. \begin{aligned} {}_1x_2 &= {}_1x_1 + l_2 \ 13d_{21} \\ {}_1y_2 &= {}_1y_1 + l_2 \ 23d_{21} + S_1 \\ {}_1z_2 &= {}_1z_1 + l_2 \ 33d_{21} + S_2 - l_1 \end{aligned} \right\} \quad (B128)$$

Segment 3:

$$\left. \begin{aligned} {}_1x_3 &= {}_1x_1 + l_3 \ 13d_{31} \\ {}_1y_3 &= {}_1y_1 + l_3 \ 23d_{31} - S_1 \\ {}_1z_3 &= {}_1z_1 + l_3 \ 33d_{31} + S_2 - l_1 \end{aligned} \right\} \quad (B129)$$

Segment 4:

$$\left. \begin{aligned} {}_1x_4 &= {}_1x_1 + L_2 \ 13d_{21} + l_4 \ 13d_{41} \\ {}_1y_4 &= {}_1y_1 + L_2 \ 23d_{21} + l_4 \ 23d_{41} + S_1 \\ {}_1z_4 &= {}_1z_1 + L_2 \ 33d_{21} + l_4 \ 33d_{41} + S_2 - l_1 \end{aligned} \right\} \quad (B130)$$

Segment 5:

$$\left. \begin{aligned} {}_1x_5 &= {}_1x_1 + L_3 \ 13d_{31} + l_5 \ 13d_{51} \\ {}_1y_5 &= {}_1y_1 + L_3 \ 23d_{31} + l_5 \ 23d_{51} - S_1 \\ {}_1z_5 &= {}_1z_1 + L_3 \ 33d_{31} + l_5 \ 33d_{51} + S_2 - l_1 \end{aligned} \right\} \quad (B131)$$

Segment 6:

$$\left. \begin{aligned} {}_1x_6 &= {}_1x_1 + l_6 \ 13d_{61} \\ {}_1y_6 &= {}_1y_1 + l_6 \ 23d_{61} + S_3 \\ {}_1z_6 &= {}_1z_1 + l_6 \ 33d_{61} + L_1 - l_1 \end{aligned} \right\} \quad (B132)$$

# APPENDIX B

Segment 7:

$$\left. \begin{aligned} {}_1x_7 &= {}_1x_1 + l_7 {}_{13}d_{71} \\ {}_1y_7 &= {}_1y_1 + l_7 {}_{23}d_{71} - S_3 \\ {}_1z_7 &= {}_1z_1 + l_7 {}_{33}d_{71} + L_1 - l_1 \end{aligned} \right\} \quad (B133)$$

Segment 8:

$$\left. \begin{aligned} {}_1x_8 &= {}_1x_1 + L_6 {}_{13}d_{61} + l_8 {}_{13}d_{81} \\ {}_1y_8 &= {}_1y_1 + L_6 {}_{23}d_{61} + l_8 {}_{23}d_{81} + S_3 \\ {}_1z_8 &= {}_1z_1 + L_6 {}_{33}d_{61} + l_8 {}_{33}d_{81} + L_1 - l_1 \end{aligned} \right\} \quad (B134)$$

Segment 9:

$$\left. \begin{aligned} {}_1x_9 &= {}_1x_1 + L_7 {}_{13}d_{71} + l_9 {}_{13}d_{91} \\ {}_1y_9 &= {}_1y_1 + L_7 {}_{23}d_{71} + l_9 {}_{23}d_{91} - S_3 \\ {}_1z_9 &= {}_1z_1 + L_7 {}_{33}d_{71} + l_9 {}_{33}d_{91} + L_1 - l_1 \end{aligned} \right\} \quad (B135)$$

From the definition of man's combined center of mass written about the torso center of mass,

$${}_1\bar{r}_1 = (-1/m_m) \sum_{i=2}^9 m_i ({}_1\bar{r}_i - {}_1\bar{r}_1) \quad (B136)$$

Thus,

$$\left. \begin{aligned} {}_1x_1 &= (-1/m_m) \sum_{i=2}^9 m_i ({}_1x_i - {}_1x_1) \\ {}_1y_1 &= (-1/m_m) \sum_{i=2}^9 m_i ({}_1y_i - {}_1y_1) \\ {}_1z_1 &= (-1/m_m) \sum_{i=2}^9 m_i ({}_1z_i - {}_1z_1) \end{aligned} \right\} \quad (B137)$$

where the quantities in parentheses are formed from the component equations given above.

## APPENDIX B

Spacecraft/astronaut relative attitude.- The spacecraft/ astronaut relative attitude was given by the integral of the relative Euler rates of equation (B39),

$$\dot{\bar{\epsilon}}_{s1} = D_{s1\epsilon} \bar{\omega}_{1s} \quad (B39)$$

where

$${}_1\bar{\omega}_{1s} = {}_1\bar{\omega}_{1o} - D_{s1} {}_s\bar{\omega}_{so} \quad (B38)$$

Expanding equation (B38),

$$\left. \begin{aligned} {}_1p_{1s} &= {}_1p_{1o} - \left| \begin{pmatrix} {}_{11}d_{s1} \\ {}_{12}d_{s1} \\ {}_{13}d_{s1} \end{pmatrix} s^p_{so} + \begin{pmatrix} {}_{12}d_{s1} \\ {}_{22}d_{s1} \\ {}_{23}d_{s1} \end{pmatrix} s^q_{so} + \begin{pmatrix} {}_{13}d_{s1} \\ {}_{23}d_{s1} \\ {}_{33}d_{s1} \end{pmatrix} s^r_{so} \right| \\ {}_1q_{1s} &= {}_1q_{1o} - \left| \begin{pmatrix} {}_{21}d_{s1} \\ {}_{22}d_{s1} \\ {}_{23}d_{s1} \end{pmatrix} s^p_{so} + \begin{pmatrix} {}_{22}d_{s1} \\ {}_{32}d_{s1} \\ {}_{33}d_{s1} \end{pmatrix} s^q_{so} + \begin{pmatrix} {}_{23}d_{s1} \\ {}_{33}d_{s1} \\ {}_{33}d_{s1} \end{pmatrix} s^r_{so} \right| \\ {}_1r_{1s} &= {}_1r_{1o} - \left| \begin{pmatrix} {}_{31}d_{s1} \\ {}_{32}d_{s1} \\ {}_{33}d_{s1} \end{pmatrix} s^p_{so} + \begin{pmatrix} {}_{32}d_{s1} \\ {}_{33}d_{s1} \\ {}_{33}d_{s1} \end{pmatrix} s^q_{so} + \begin{pmatrix} {}_{33}d_{s1} \\ {}_{33}d_{s1} \\ {}_{33}d_{s1} \end{pmatrix} s^r_{so} \right| \end{aligned} \right\} \quad (B138)$$

The matrix components,  $d_{s1}$ , are given in the expanded form of the transformation matrices.

The Euler angle sequence in going from the spacecraft axes to the torso axes is the gimbal sequence of the SOS attitude head. This sequence is roll-pitch-yaw. Therefore, expanding equation (B39),

$$\left. \begin{aligned} \dot{\phi}_{s1} &= \left( C\psi_{s1} / C\vartheta_{s1} \right) {}_1p_{1s} - \left( S\psi_{s1} / C\vartheta_{s1} \right) {}_1q_{1s} \\ \dot{\vartheta}_{s1} &= \left( S\psi_{s1} \right) {}_1p_{1s} + \left( C\psi_{s1} \right) {}_1q_{1s} \\ \dot{\psi}_{s1} &= \left( - \frac{C\psi_{s1} S\vartheta_{s1}}{C\vartheta_{s1}} \right) {}_1p_{1s} + \left( \frac{S\psi_{s1} S\vartheta_{s1}}{C\vartheta_{s1}} \right) {}_1q_{1s} + {}_1r_{1s} \end{aligned} \right\} \quad (B139)$$

and the SOS attitude head servo-commands are given by

$$\begin{aligned} \phi_{s1} &= \int \dot{\phi}_{s1} dt \\ \vartheta_{s1} &= \int \dot{\vartheta}_{s1} dt \\ \psi_{s1} &= \int \dot{\psi}_{s1} dt \end{aligned} \quad (B140)$$

## APPENDIX B

Spacecraft/astronaut relative translation.- The spacecraft/ astronaut relative translational equations were described by equations (B33) thru (B37). Equation (B33) describes the relative acceleration as

$$\ddot{\bar{\mathbf{r}}}_{s\ sm} = \frac{-\bar{\mathbf{F}}_s}{Q} \quad (\text{B33})$$

and equation (B42a) indicates the load cell outputs,  $\mathbf{F}_L$ , equal the forces on the spacecraft,  $\bar{\mathbf{F}}_s$ . Therefore, denoting the components of  $\ddot{\bar{\mathbf{r}}}_{s\ sm}$  by

$$\ddot{\bar{\mathbf{r}}}_{s\ sm} = a_x \bar{\mathbf{i}}_s + a_y \bar{\mathbf{j}}_s + a_z \bar{\mathbf{k}}_s \quad (\text{B141})$$

then,

$$\left. \begin{aligned} a_x &= \frac{-F_{Lx}}{Q} \\ a_y &= \frac{-F_{Ly}}{Q} \\ a_z &= \frac{-F_{Lz}}{Q} \end{aligned} \right\} \quad (\text{B142})$$

where the components of  $\bar{\mathbf{F}}_L$  have previously been given and  $Q$  is the mass ratio term of equation (B34).

The relative velocity, equation (B35), was

$$\dot{\bar{\mathbf{r}}}_{s\ sm} = \int \left[ -\frac{\bar{\mathbf{F}}_s}{Q} - \left( \bar{\boldsymbol{\omega}}_{so} \times \dot{\bar{\mathbf{r}}}_{s\ sm} \right) \right] dt \quad (\text{B35})$$

Denoting,

$$\dot{\bar{\mathbf{r}}}_{s\ sm} = v_x \bar{\mathbf{i}}_s + v_y \bar{\mathbf{j}}_s + v_z \bar{\mathbf{k}}_s \quad (\text{B143})$$

## APPENDIX B

and expanding into component form,

$$\left. \begin{aligned} v_x &= \int \left| a_x + (s^r_{so}) v_y - (s^q_{so}) v_z \right| dt \\ v_y &= \int \left| a_y + (s^p_{so}) v_z - (s^r_{so}) v_x \right| dt \\ v_z &= \int \left| a_z + (s^q_{so}) v_x - (s^p_{so}) v_y \right| dt \end{aligned} \right\} \quad (B144)$$

The relative position vector,  ${}_s\bar{r}_{sm}$ , as given by equation (B36) is

$${}_s\bar{r}_{sm} = \int \left[ \dot{{}_s\bar{r}}_{sm} - ({}_s\bar{\omega}_{so} \times {}_s\bar{r}_{sm}) \right] dt \quad (B36)$$

In component form,

$$\left. \begin{aligned} s^x_{sm} &= \int \left| v_x + (s^r_{so}) s^y_{sm} - (s^q_{so}) s^z_{sm} \right| dt \\ s^y_{sm} &= \int \left| v_y + (s^p_{so}) s^z_{sm} - (s^r_{so}) s^x_{sm} \right| dt \\ s^z_{sm} &= \int \left| v_z + (s^q_{so}) s^x_{sm} - (s^p_{so}) s^y_{sm} \right| dt \end{aligned} \right\} \quad (B145)$$

The relative translational commands to drive the servo-driven moving base carriage of the SOS were given by equation (B37) as

$${}_s\bar{r}_{s1} = {}_s\bar{r}_{sm} + D_{1s} {}_1\bar{r}_1 \quad (B37)$$

The vector components are

$$\left. \begin{aligned} s^x_{s1} &= s^x_{sm} + ({}_{11}d_{1s}) {}_1x_1 + ({}_{12}d_{1s}) {}_1y_1 + ({}_{13}d_{1s}) {}_1z_1 \\ s^y_{s1} &= s^y_{sm} + ({}_{21}d_{1s}) {}_1x_1 + ({}_{22}d_{1s}) {}_1y_1 + ({}_{23}d_{1s}) {}_1z_1 \\ s^z_{s1} &= s^z_{sm} + ({}_{31}d_{1s}) {}_1x_1 + ({}_{32}d_{1s}) {}_1y_1 + ({}_{33}d_{1s}) {}_1z_1 \end{aligned} \right\} \quad (B146)$$

Note that:

- 1) The matrix elements,  $d_{1s}$ , are contained in the expanded form of the transformation matrices;
- 2) The components of  ${}_1\bar{r}_1$  are contained in the expanded form of the limb position vectors.

## APPENDIX B

Transformation matrices. - The elements of the transformation matrices are obtained from the discussion entitled General Transformations.

Spacecraft/astronaut:

$$D_{1s} = D(\varphi_{s1}) D(\theta_{s1}) D(\psi_{s1})$$

$$D_{s1} = D^{-1}(\psi_{s1}) D^{-1}(\theta_{s1}) D^{-1}(\varphi_{s1}) \quad (B147)$$

$${}_{11}d_{1s} = {}_{11}d_{s1} = C\theta_{s1} C\psi_{s1}$$

$${}_{12}d_{1s} = {}_{21}d_{s1} = -C\theta_{s1} S\psi_{s1}$$

$${}_{13}d_{1s} = {}_{31}d_{s1} = S\theta_{s1}$$

$${}_{21}d_{1s} = {}_{12}d_{s1} = C\varphi_{s1} S\psi_{s1} + S\varphi_{s1} S\theta_{s1} C\psi_{s1}$$

$${}_{22}d_{1s} = {}_{22}d_{s1} = C\varphi_{s1} C\psi_{s1} - S\varphi_{s1} S\theta_{s1} S\psi_{s1}$$

$${}_{23}d_{1s} = {}_{32}d_{s1} = -S\varphi_{s1} C\theta_{s1}$$

$${}_{31}d_{1s} = {}_{13}d_{s1} = S\varphi_{s1} S\psi_{s1} - C\varphi_{s1} S\theta_{s1} C\psi_{s1}$$

$${}_{32}d_{1s} = {}_{23}d_{s1} = S\varphi_{s1} C\psi_{s1} + C\varphi_{s1} S\theta_{s1} S\psi_{s1}$$

$${}_{33}d_{1s} = {}_{33}d_{s1} = C\varphi_{s1} C\theta_{s1}$$

# APPENDIX B

Segment 2, right upper arm:

$$\begin{aligned}
 D_{21} &= D(\psi = -45^\circ) D(\varphi_2) D(\vartheta_2) D(\psi_2) & (B148) \\
 {}_{11}d_{21} &= 0.7071 (C\vartheta_2 C\psi_2 + S\varphi_2 S\vartheta_2 C\psi_2 + C\varphi_2 S\psi_2) \\
 {}_{12}d_{21} &= 0.7071 (-C\vartheta_2 S\psi_2 + C\varphi_2 C\psi_2 - S\varphi_2 S\vartheta_2 S\psi_2) \\
 {}_{13}d_{21} &= 0.7071 (S\vartheta_2 - S\varphi_2 C\vartheta_2) \\
 {}_{21}d_{21} &= 0.7071 (-C\vartheta_2 C\psi_2 + S\varphi_2 S\vartheta_2 C\psi_2 + C\varphi_2 S\psi_2) \\
 {}_{22}d_{21} &= 0.7071 (C\vartheta_2 S\psi_2 + C\varphi_2 C\psi_2 - S\varphi_2 S\vartheta_2 S\psi_2) \\
 {}_{23}d_{21} &= 0.7071 (-S\vartheta_2 - S\varphi_2 C\vartheta_2) \\
 {}_{31}d_{21} &= -C\varphi_2 S\vartheta_2 C\psi_2 + S\varphi_2 S\psi_2 \\
 {}_{32}d_{21} &= S\varphi_2 C\psi_2 + C\varphi_2 S\vartheta_2 S\psi_2 \\
 {}_{33}d_{21} &= C\varphi_2 C\vartheta_2
 \end{aligned}$$

Segment 3, left upper arm:

$$\begin{aligned}
 D_{31} &= D(\psi = +45^\circ) D(\varphi_3) D(\vartheta_3) D(\psi_3) & (B149) \\
 {}_{11}d_{31} &= 0.7071 (C\vartheta_3 C\psi_3 - S\varphi_3 S\vartheta_3 C\psi_3 - C\varphi_3 S\psi_3) \\
 {}_{12}d_{31} &= 0.7071 (-C\vartheta_3 S\psi_3 - C\varphi_3 C\psi_3 + S\varphi_3 S\vartheta_3 S\psi_3) \\
 {}_{13}d_{31} &= 0.7071 (S\vartheta_3 + S\varphi_3 C\vartheta_3) \\
 {}_{21}d_{31} &= 0.7071 (C\vartheta_3 C\psi_3 + S\varphi_3 S\vartheta_3 C\psi_3 + C\varphi_3 S\psi_3) \\
 {}_{22}d_{31} &= 0.7071 (-C\vartheta_3 S\psi_3 + C\varphi_3 C\psi_3 - S\varphi_3 S\vartheta_3 S\psi_3) \\
 {}_{23}d_{31} &= 0.7071 (S\vartheta_3 - S\varphi_3 C\vartheta_3) \\
 {}_{31}d_{31} &= -C\varphi_3 S\vartheta_3 C\psi_3 + S\varphi_3 S\psi_3 \\
 {}_{32}d_{31} &= S\varphi_3 C\psi_3 + C\varphi_3 S\vartheta_3 S\psi_3 \\
 {}_{33}d_{31} &= C\varphi_3 C\vartheta_3
 \end{aligned}$$



# APPENDIX B

Segment 4, right lower arm:

$$D_{41} = D_{21} D_{42} \quad (B150)$$

where

$$D_{42} = D(\theta_4) \quad (B151)$$

$$\begin{aligned} {}_{11}d_{41} = 0.7071 [ & (C\theta_2 C\psi_2 + S\varphi_2 S\theta_2 C\psi_2 + C\varphi_2 S\psi_2) C\theta_4 \\ & - (S\theta_2 - S\varphi_2 C\theta_2) S\theta_4 ] \end{aligned}$$

$${}_{12}d_{41} = 0.7071 (-C\theta_2 S\psi_2 + C\varphi_2 C\psi_2 - S\varphi_2 S\theta_2 S\psi_2)$$

$$\begin{aligned} {}_{13}d_{41} = 0.7071 [ & (C\theta_2 C\psi_2 + S\varphi_2 S\theta_2 C\psi_2 + C\varphi_2 S\psi_2) S\theta_4 \\ & + (S\theta_2 - S\varphi_2 C\theta_2) C\theta_4 ] \end{aligned}$$

$$\begin{aligned} {}_{21}d_{41} = 0.7071 [ & (-C\theta_2 C\psi_2 + S\varphi_2 S\theta_2 C\psi_2 + C\varphi_2 S\psi_2) C\theta_4 \\ & + (S\theta_2 + S\varphi_2 C\theta_2) S\theta_4 ] \end{aligned}$$

$${}_{22}d_{41} = 0.7071 (C\theta_2 S\psi_2 + C\varphi_2 C\psi_2 - S\varphi_2 S\theta_2 S\psi_2)$$

$$\begin{aligned} {}_{23}d_{41} = 0.7071 [ & (-C\theta_2 C\psi_2 + S\varphi_2 S\theta_2 C\psi_2 + C\varphi_2 S\psi_2) S\theta_4 \\ & - (S\theta_2 + S\varphi_2 C\theta_2) C\theta_4 ] \end{aligned}$$

$${}_{31}d_{41} = (-C\varphi_2 S\theta_2 C\psi_2 + S\varphi_2 S\psi_2) C\theta_4 - (C\varphi_2 C\theta_2) S\theta_4$$

$${}_{32}d_{41} = S\varphi_2 C\psi_2 + C\varphi_2 S\theta_2 S\psi_2$$

$${}_{33}d_{41} = (-C\varphi_2 S\theta_2 C\psi_2 + S\varphi_2 S\psi_2) S\theta_4 + (C\varphi_2 C\theta_2) C\theta_4$$

# APPENDIX B

Segment 5, left lower arm:

$$D_{51} = D_{31} D_{53} \quad (B152)$$

where

$$D_{53} = D(\theta_5) \quad (B153)$$

$$\begin{aligned} {}_{11}d_{51} = 0.7071 [ & (C\theta_3 C\psi_3 - S\varphi_3 S\theta_3 C\psi_3 - C\varphi_3 S\psi_3) C\theta_5 \\ & - (S\theta_3 + S\varphi_3 C\theta_3) S\theta_5 ] \end{aligned}$$

$${}_{12}d_{51} = 0.7071 (-C\theta_3 S\psi_3 - C\varphi_3 C\psi_3 + S\varphi_3 S\theta_3 S\psi_3)$$

$$\begin{aligned} {}_{13}d_{51} = 0.7071 [ & (C\theta_3 C\psi_3 - S\varphi_3 S\theta_3 C\psi_3 - C\varphi_3 S\psi_3) S\theta_5 \\ & + (S\theta_3 + S\varphi_3 C\theta_3) C\theta_5 ] \end{aligned}$$

$$\begin{aligned} {}_{21}d_{51} = 0.7071 [ & (C\theta_3 C\psi_3 + S\varphi_3 S\theta_3 C\psi_3 + C\varphi_3 S\psi_3) C\theta_5 \\ & - (S\theta_3 - S\varphi_3 C\theta_3) S\theta_5 ] \end{aligned}$$

$${}_{22}d_{51} = 0.7071 (-C\theta_3 S\psi_3 + C\varphi_3 C\psi_3 - S\varphi_3 S\theta_3 S\psi_3)$$

$$\begin{aligned} {}_{23}d_{51} = 0.7071 [ & (C\theta_3 C\psi_3 + S\varphi_3 S\theta_3 C\psi_3 + C\varphi_3 S\psi_3) S\theta_5 \\ & + (S\theta_3 - S\varphi_3 C\theta_3) C\theta_5 ] \end{aligned}$$

$${}_{31}d_{51} = (-C\varphi_3 S\theta_3 C\psi_3 + S\varphi_3 S\psi_3) C\theta_5 - (C\varphi_3 C\theta_3) S\theta_5$$

$${}_{32}d_{51} = S\varphi_3 C\psi_3 + C\varphi_3 S\theta_3 S\psi_3$$

$${}_{33}d_{51} = (-C\varphi_3 S\theta_3 C\psi_3 + S\varphi_3 S\psi_3) S\theta_5 + (C\varphi_3 C\theta_3) C\theta_5$$

# APPENDIX B

Segment 6, right upper leg:

$$\begin{aligned}
 D_{61} &= D(\psi = -45^\circ) D(\varphi_6) D(\theta_6) D(\psi_6) & (B154) \\
 {}_{11}d_{61} &= 0.7071 (C\theta_6 C\psi_6 + S\varphi_6 S\theta_6 C\psi_6 + C\varphi_6 S\psi_6) \\
 {}_{12}d_{61} &= 0.7071 (-C\theta_6 S\psi_6 + C\varphi_6 C\psi_6 - S\varphi_6 S\theta_6 S\psi_6) \\
 {}_{13}d_{61} &= 0.7071 (S\theta_6 - S\varphi_6 C\theta_6) \\
 {}_{21}d_{61} &= 0.7071 (-C\theta_6 C\psi_6 + S\varphi_6 S\theta_6 C\psi_6 + C\varphi_6 S\psi_6) \\
 {}_{22}d_{61} &= 0.7071 (C\theta_6 S\psi_6 + C\varphi_6 C\psi_6 - S\varphi_6 S\theta_6 S\psi_6) \\
 {}_{23}d_{61} &= 0.7071 (-S\theta_6 - S\varphi_6 C\theta_6) \\
 {}_{31}d_{61} &= -C\varphi_6 S\theta_6 C\psi_6 + S\varphi_6 S\psi_6 \\
 {}_{32}d_{61} &= S\varphi_6 C\psi_6 + C\varphi_6 S\theta_6 S\psi_6 \\
 {}_{33}d_{61} &= C\varphi_6 C\theta_6
 \end{aligned}$$

Segment 7, left upper leg:

$$\begin{aligned}
 D_{71} &= D(\psi = +45^\circ) D(\varphi_7) D(\theta_7) D(\psi_7) & (B155) \\
 {}_{11}d_{71} &= 0.7071 (C\theta_7 C\psi_7 - S\varphi_7 S\theta_7 C\psi_7 - C\varphi_7 S\psi_7) \\
 {}_{12}d_{71} &= 0.7071 (-C\theta_7 S\psi_7 - C\varphi_7 C\psi_7 + S\varphi_7 S\theta_7 S\psi_7) \\
 {}_{13}d_{71} &= 0.7071 (S\theta_7 + S\varphi_7 C\theta_7) \\
 {}_{21}d_{71} &= 0.7071 (C\theta_7 C\psi_7 + S\varphi_7 S\theta_7 C\psi_7 + C\varphi_7 S\psi_7) \\
 {}_{22}d_{71} &= 0.7071 (-C\theta_7 S\psi_7 + C\varphi_7 C\psi_7 - S\varphi_7 S\theta_7 S\psi_7) \\
 {}_{23}d_{71} &= 0.7071 (S\theta_7 - S\varphi_7 C\theta_7) \\
 {}_{31}d_{71} &= -C\varphi_7 S\theta_7 C\psi_7 + S\varphi_7 S\psi_7 \\
 {}_{32}d_{71} &= S\varphi_7 C\psi_7 + C\varphi_7 S\theta_7 S\psi_7 \\
 {}_{33}d_{71} &= C\varphi_7 C\theta_7
 \end{aligned}$$

# APPENDIX B

Segment 8, right lower leg:

$$D_{81} = D_{61} D_{86} \quad (B156)$$

where

$$D_{86} = D(\theta_8) \quad (B157)$$

$$\begin{aligned} {}_{11}d_{81} = 0.7071 [ & (C\theta_6 C\psi_6 + S\varphi_6 S\theta_6 C\psi_6 + C\varphi_6 S\psi_6) C\theta_8 \\ & - (S\theta_6 - S\varphi_6 C\theta_6) S\theta_8 ] \end{aligned}$$

$${}_{12}d_{81} = 0.7071 (-C\theta_6 S\psi_6 + C\varphi_6 C\psi_6 - S\varphi_6 S\theta_6 S\psi_6)$$

$$\begin{aligned} {}_{13}d_{81} = 0.7071 [ & (C\vartheta_6 C\psi_6 + S\varphi_6 S\theta_6 C\psi_6 + C\varphi_6 S\psi_6) S\theta_8 \\ & + (S\vartheta_6 - S\varphi_6 C\theta_6) C\theta_8 ] \end{aligned}$$

$$\begin{aligned} {}_{21}d_{81} = 0.7071 [ & (-C\vartheta_6 C\psi_6 + S\varphi_6 S\theta_6 C\psi_6 + C\varphi_6 S\psi_6) C\theta_8 \\ & + (S\theta_6 + S\varphi_6 C\theta_6) S\theta_8 ] \end{aligned}$$

$${}_{22}d_{81} = 0.7071 (C\vartheta_6 S\psi_6 + C\varphi_6 C\psi_6 - S\varphi_6 S\theta_6 S\psi_6)$$

$$\begin{aligned} {}_{23}d_{81} = 0.7071 [ & (-C\theta_6 C\psi_6 + S\varphi_6 S\theta_6 C\psi_6 + C\varphi_6 S\psi_6) S\theta_8 \\ & - (S\vartheta_6 + S\varphi_6 C\vartheta_6) C\theta_8 ] \end{aligned}$$

$${}_{31}d_{81} = (-C\varphi_6 S\theta_6 C\psi_6 + S\varphi_6 S\psi_6) C\theta_8 - (C\varphi_6 C\theta_6) S\theta_8$$

$${}_{32}d_{81} = S\varphi_6 C\psi_6 + C\varphi_6 S\theta_6 S\psi_6$$

$${}_{33}d_{81} = (-C\varphi_6 S\vartheta_6 C\psi_6 + S\varphi_6 S\psi_6) S\vartheta_8 + (C\varphi_6 C\vartheta_6) C\vartheta_8$$

# APPENDIX B

Segment 9, left lower leg:

$$D_{\Theta 1} = D_{71} D_{\Theta 7} \quad (B158)$$

where

$$D_{\Theta 7} = D(\theta_{\Theta}) \quad (B159)$$

$$\begin{aligned} {}_{11}d_{\Theta 1} = 0.7071 [ & (C\theta_7 C\psi_7 - S\varphi_7 S\theta_7 C\psi_7 - C\varphi_7 S\psi_7) C\theta_{\Theta} \\ & - (S\theta_7 + S\varphi_7 C\theta_7) S\theta_{\Theta} ] \end{aligned}$$

$${}_{12}d_{\Theta 1} = 0.7071 (-C\theta_7 S\psi_7 - C\varphi_7 C\psi_7 + S\varphi_7 S\theta_7 S\psi_7)$$

$$\begin{aligned} {}_{13}d_{\Theta 1} = 0.7071 [ & C\theta_7 C\psi_7 - S\varphi_7 S\theta_7 C\psi_7 - C\varphi_7 S\psi_7) S\theta_{\Theta} \\ & + (S\theta_7 + S\varphi_7 C\theta_7) C\theta_{\Theta} ] \end{aligned}$$

$$\begin{aligned} {}_{21}d_{\Theta 1} = 0.7071 [ & C\theta_7 C\psi_7 + S\varphi_7 S\theta_7 C\psi_7 + C\varphi_7 S\psi_7) C\theta_{\Theta} \\ & - (S\theta_7 - S\varphi_7 C\theta_7) S\theta_{\Theta} ] \end{aligned}$$

$${}_{22}d_{\Theta 1} = 0.7071 (-C\theta_7 S\psi_7 + C\varphi_7 C\psi_7 - S\varphi_7 S\theta_7 S\psi_7)$$

$$\begin{aligned} {}_{23}d_{\Theta 1} = 0.7071 ( & C\theta_7 C\psi_7 + S\varphi_7 S\theta_7 C\psi_7 + C\varphi_7 S\psi_7) S\theta_{\Theta} \\ & + (S\theta_7 - S\varphi_7 C\theta_7) C\theta_{\Theta} ] \end{aligned}$$

$${}_{31}d_{\Theta 1} = (-C\varphi_7 S\theta_7 C\psi_7 + S\varphi_7 S\psi_7) C\theta_{\Theta} - (C\varphi_7 C\theta_7) S\theta_{\Theta}$$

$${}_{32}d_{\Theta 1} = S\varphi_7 C\psi_7 + C\varphi_7 S\theta_7 S\psi_7$$

$${}_{33}d_{\Theta 1} = (-C\varphi_7 S\theta_7 C\psi_7 + S\varphi_7 S\psi_7) S\theta_{\Theta} + (C\varphi_7 C\theta_7) C\theta_{\Theta}$$

## APPENDIX C

### DATA SMOOTHING PROCEDURE

The process of smoothing the digitized data is accomplished by fitting a polynomial to the test data, using the method of least squares. Because the data are sampled at equally spaced intervals, time may be replaced by an integer variable,  $k$ . Assuming  $N$  data points are being used for the curve fitting process, the variable  $k$  takes on  $N$  integrally spaced values, and is symmetric about  $k = 0$ , i.e.,  $-(N - 1)/2 \leq k \leq (N - 1)/2$ . It is assumed that a data point exists at  $k = 0$ , and therefore  $N$  is an odd number.

The desired curve approximating the test data may be defined as the linear combination of orthogonal polynomials,

$$y(k) = a_0 P_0(k) + a_1 P_1(k) + a_2 P_2(k) + \dots + a_n P_n(k) \quad (C1)$$

where the  $P_i$  are known orthogonal polynomials, and the  $a_i$  coefficients are to be determined such that  $y$  approximates the data in a least-squares sense.

Defining an error function

$$S = \sum_k [y(k) - x(k)]^2 \quad (C2)$$

where  $x$  represents values of the test data, the error can be minimized by setting the partial derivatives of  $S$  with respect to  $a_i$  equal to zero:

$$\frac{\partial S}{\partial a_i} = 2 \sum_k [y(k) - x(k)] P_i(k) = 0 \quad (C3)$$

# APPENDIX C

The  $a_i$  coefficients can then be found by solving the resulting matrix equation:

$$\begin{bmatrix} \sum_k (P_0 P_0) & \sum_k (P_1 P_0) & \dots & \sum_k (P_n P_0) \\ \sum_k (P_0 P_1) & \sum_k (P_1 P_1) & \dots & \sum_k (P_n P_1) \\ \vdots & \vdots & \ddots & \vdots \\ \sum_k (P_0 P_n) & \sum_k (P_1 P_n) & \dots & \sum_k (P_n P_n) \end{bmatrix} \begin{bmatrix} a_0 \\ a_1 \\ \vdots \\ a_n \end{bmatrix} = \begin{bmatrix} \sum_k (P_0 x) \\ \sum_k (P_1 x) \\ \vdots \\ \sum_k (P_n x) \end{bmatrix} \quad (C4)$$

However, because the  $P_i$  polynomials are orthogonal,

$$\sum_k P_i P_j = 0, \quad i \neq j \quad (C5)$$

the resulting matrix is diagonal. The  $a_i$  coefficients can therefore be found directly, eliminating the need for a time-consuming matrix inversion process.

Defining a new function,  $M_i$

$$M_i = \sum_k P_i(k) P_i(k) \quad i = 0, 1, 2, 3 \dots M \quad (C6)$$

the  $a_i$  coefficients then become

$$a_i = \sum_k \frac{P_i(k) x(k)}{M_i} \quad i = 0, 1, 2, 3 \dots M \quad (C7)$$

## APPENDIX C

To implement the data smoothing process, it is necessary to choose a certain number of test data points ( $N$ ) to be fit by a curve, and the highest order ( $M$ ) for the polynomial. To keep the highest order to a reasonable number, only a small portion of the test data points are fit with one curve. It has been determined that a combination of 31 test data points (at a sampling rate of 100/sec) and a fifth-order polynomial is sufficient to contain all the desired frequencies present in the test data.

Only one smoothed data point (the value at  $k = 0$ ) is obtained from each fifth-order curve fitted to the 31 consecutive test data points. The first data point is obtained from smoothing the first 31 test data points. Then a new curve is fitted to a new set of 31 consecutive test data points that are shifted in time by one data point from the first set. From this curve, the second smoothed data point is obtained. The procedure is continued until all test data points are smoothed. In this manner, a smooth set of data points result from which smooth numerical derivatives can be obtained.

The orthogonal polynomials used in this analysis are the Tschebycheff polynomials,  $P_i$ , which are listed in the following along with the respective weighting function,  $M_i$ ,

$$\begin{aligned}
 P_0(k) &= 1 \\
 P_1(k) &= k \\
 P_2(k) &= k^2 - (N^2 - 1)/12 \\
 P_3(k) &= k^3 - (3N^2 - 7)k/20 \\
 P_4(k) &= k^4 - (3N^2 - 13)k^2/14 + 3(N^2 - 1)(N^2 - 9)/560 \\
 P_5(k) &= k^5 - 5(N^2 - 7)k^3/18 + (15N^4 - 230N^2 + 407)k/1008
 \end{aligned}
 \quad \left. \vphantom{\begin{aligned} P_0(k) &= 1 \\ P_1(k) &= k \\ P_2(k) &= k^2 - (N^2 - 1)/12 \\ P_3(k) &= k^3 - (3N^2 - 7)k/20 \\ P_4(k) &= k^4 - (3N^2 - 13)k^2/14 + 3(N^2 - 1)(N^2 - 9)/560 \\ P_5(k) &= k^5 - 5(N^2 - 7)k^3/18 + (15N^4 - 230N^2 + 407)k/1008 \end{aligned}} \right\} \quad (C8)$$



# APPENDIX C

$$\begin{aligned}
 M_0 &= N \\
 M_1 &= N(N^2 - 1)/12 \\
 M_2 &= N(N^2 - 1)(N^2 - 4)/180 \\
 M_3 &= N(N^2 - 1)(N^2 - 4)(N^2 - 9)/2800 \\
 M_4 &= N(N^2 - 1)(N^2 - 4)(N^2 - 9)(N^2 - 16)/44\,100 \\
 M_5 &= N(N^2 - 1)(N^2 - 4)(N^2 - 9)(N^2 - 16)(N^2 - 25)/698\,544
 \end{aligned}
 \tag{C9}$$

APPENDIX D  
ANTHROPOMETRIC DATA

An analysis of the biomechanical properties of man has demonstrated that the segment masses, centers of gravity, pivot points, and moments of inertia may be expressed solely as linear functions of man's weight (refs. 2 and 3). The equations for these segment properties are given in the following. Tables D1 thru D9 present the results of a digital program that calculates anthropometric data as a function of man's weight. Number subscripts refer to segments labeled in figure D1.

Segment masses, slugs

$$m_1 = K_m (0.47W + 12.0) \quad (D1)$$

$$m_2 = m_3 = K_m (0.04W - 1.45) \quad (D2)$$

$$m_4 = m_5 = K_m (0.025W + 0.1) \quad (D3)$$

$$m_6 = m_7 = K_m (0.09W + 1.6) \quad (D4)$$

$$m_8 = m_9 = K_m (0.065W - 0.2) \quad (D5)$$

where  $W$  is the man's weight in pounds and  $K_m$  is given by

$$K_m = \frac{W}{29.3W + 389} \quad (D6)$$

Segment mass centers and pivot points, feet

With reference to figure D1, the segment mass and pivot point dimensions are

$$S_1 = 0.00196W + 0.388 \quad (D7)$$

$$S_2 = 0.00135W + 0.916 \quad (D8)$$

$$S_3 = 0.000422W + 0.208 \quad (D9)$$

$$L_1 = 0.0038W + 2.117 \quad (D10)$$

$$L_2 = L_3 = 0.00132W + 0.768 \quad (D11)$$

# APPENDIX D

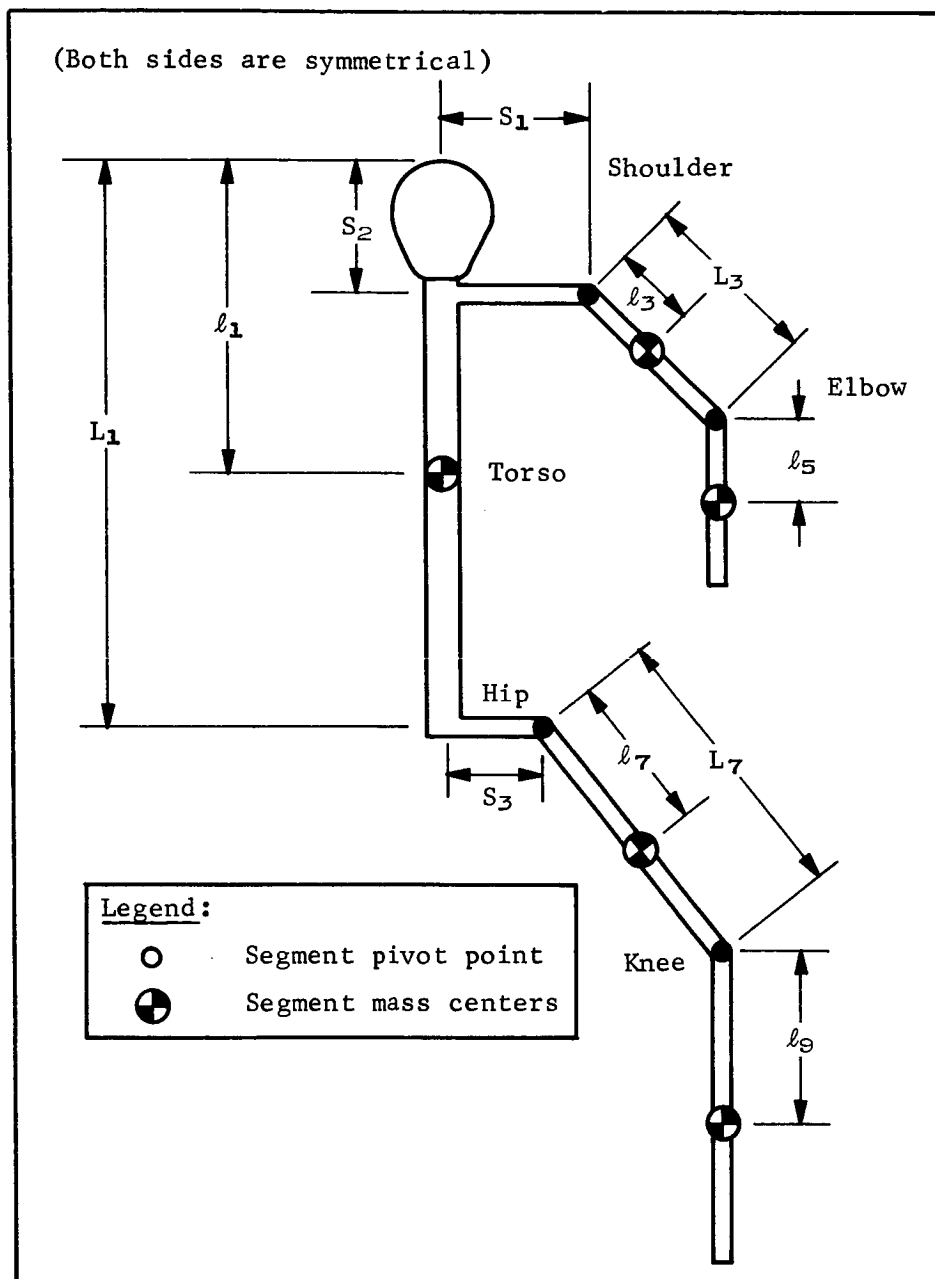


Figure D1.- Segmental Model of Man

# APPENDIX D

$$L_6 = L_7 = 0.000729W + 1.324 \quad (D12)$$

$$l_1 = 0.00145W + 1.55 \quad (D13)$$

$$l_2 = l_3 = 0.000145W + 0.355 \quad (D14)$$

$$l_4 = l_5 = 0.000658W + 0.456 \quad (D15)$$

$$l_6 = l_7 = -0.0004W + 0.828 \quad (D16)$$

$$l_8 = l_9 = 0.00106W + 0.597 \quad (D17)$$

## Segment inertias, slug-feet<sup>2</sup>

$${}_1I_{1xx} = 0.0146W - 0.576 \quad (D18)$$

$${}_1I_{1yy} = 0.0137W - 0.536 \quad (D19)$$

$${}_1I_{1zz} = 0.00331W - 0.243 \quad (D20)$$

$${}_2I_{2xx} = {}_2I_{2yy} = {}_3I_{3xx} = {}_3I_{3yy} = 0.00022W - 0.0172 \quad (D21)$$

$${}_2I_{2zz} = {}_3I_{3zz} = 0.0000268W - 0.00243 \quad (D22)$$

$${}_4I_{4xx} = {}_4I_{4yy} = {}_5I_{5xx} = {}_5I_{5yy} = 0.000159W - 0.00781 \quad (D23)$$

$${}_4I_{4zz} = {}_5I_{5zz} = 0.0000112W - 0.000768 \quad (D24)$$

$${}_6I_{6xx} = {}_6I_{6yy} = {}_7I_{7xx} = {}_7I_{7yy} = 0.000656W - 0.0373 \quad (D25)$$

$${}_6I_{6zz} = {}_7I_{7zz} = 0.00019W - 0.0142 \quad (D26)$$

$${}_8I_{8xx} = {}_9I_{9xx} = 0.000892W - 0.0544 \quad (D27)$$

$${}_8I_{8yy} = {}_9I_{9yy} = 0.000859W - 0.0534 \quad (D28)$$

$${}_8I_{8zz} = {}_9I_{9zz} = 0.0000797W - 0.00463 \quad (D29)$$

TABLE D1.-- SEGMENT PARAMETERS FOR 140-POUND MAN

SEGMENT	MASS (SLUGS)	INERTIA			L		<i>l</i> (FEET)
		IXX	IYY	IZZ	(FEET)	(FEET)	
1	2.425295	1.468000	1.382000	.220400	2.649000	1.753000	
2	.129370	.013600	.013600	.001336	.952800	.375300	
3	.129370	.013600	.013600	.001336	.952800	.375300	
4	.112224	.014450	.014450	.000800		.548120	
5	.112224	.014450	.014450	.000800		.548120	
6	.442663	.054540	.054540	.012400	1.426060	.772000	
7	.442663	.054540	.054540	.012400	1.426060	.772000	
8	.277444	.070480	.066860	.006528		.745400	
9	.277444	.070480	.066860	.006528		.745400	
S1 = .662400 FEET    S2 = 1.105000 FEET    S3 = .267080 FEET							

APPENDIX D

TABLE D2.- SEGMENT PARAMETERS FOR 150-POUND MAN

SEGMENT	MASS (SLUGS)	INERTIA			L		l
		IXX	IYY	IZZ	(FEET)	(FEET)	
1	2.586747	1.614000	1.519000	.253500	2.687000	1.767500	
2	.142663	.015800	.015800	.001605	.966000	.376750	
3	.142663	.015800	.015800	.001605	.966000	.376750	
4	.120715	.016040	.016040	.000912		.554700	
5	.120715	.016040	.016040	.000912		.554700	
6	.473453	.061100	.061100	.014300	1.433350	.768000	
7	.473453	.061100	.061100	.014300	1.433350	.768000	
8	.299436	.079400	.075450	.007325		.756000	
9	.299436	.079400	.075450	.007325		.756000	
S1 = .682000 FEET S2 = 1.118500 FEET S3 = .271300 FEET							

TABLE D3.- SEGMENT PARAMETERS FOR 160-POUND MAN

SEGMENT	MASS (SLUGS)	INERTIA			L		<i>l</i> (FEET)
		(SLUG-FT-FT)	(FEET)	(FEET)	(FEET)		
		IXX	IYY	IZZ			
1	2.748080	1.760000	1.656000	.286600	2.725000	1.782000	
2	.155998	.018000	.018000	.001874	.979200	.378200	
3	.155998	.018000	.018000	.001874	.979200	.378200	
4	.129210	.017630	.017630	.001024		.561280	
5	.129210	.017630	.017630	.001024		.561280	
6	.504235	.067660	.067660	.016200	1.440640	.764000	
7	.504235	.067660	.067660	.016200	1.440640	.764000	
8	.321450	.088320	.084040	.008122		.766600	
9	.321450	.088320	.084040	.008122		.766600	
S1 = .701600 FEET    S2 = 1.132000 FEET    S3 = .275520 FEET							

## APPENDIX D

TABLE D4.- SEGMENT PARAMETERS FOR 170-POUND MAN

SEGMENT	MASS (SLUGS)	INERTIA (SLUG-FT-FT)			L	
		IXX	IYY	IZZ	(FEET)	<i>l</i> (FEET)
1	2.909311	1.906000	1.793000	.319700	2.763000	1.796500
2	.169367	.020200	.020200	.002143	.992400	.379650
3	.169367	.020200	.020200	.002143	.992400	.379650
4	.137709	.019220	.019220	.001136		.567860
5	.137709	.019220	.019220	.001136		.567860
6	.535009	.074220	.074220	.018100	1.447930	.760000
7	.535009	.074220	.074220	.018100	1.447930	.760000
8	.343482	.097240	.092630	.008919		.777200
9	.343482	.097240	.092630	.008919		.777200
S1 = .721200 FEET		S2 = 1.145500 FEET		S3 = .279740 FEET		



TABLE D5.- SEGMENT PARAMETERS FOR 180-POUND MAN

SEGMENT	MASS (SLUGS)	INERTIA (SLUG-FT-FT)			L (FEET)	$\rho$ (FEET)
		IXX	IYY	IZZ		
1	3.070457	2.052000	1.930000	.352800	2.801000	1.811000
2	.182765	.022400	.022400	.002412	1.005600	.381100
3	.182765	.022400	.022400	.002412	1.005600	.381100
4	.146212	.020810	.020810	.001248		.574440
5	.146212	.020810	.020810	.001248		.574440
6	.565778	.080780	.080780	.020000	1.455220	.756000
7	.565778	.080780	.080780	.020000	1.455220	.756000
8	.365531	.106160	.101220	.009716		.787800
9	.365531	.106160	.101220	.009716		.787800
S1 = .740800 FEET		S2 = 1.159000 FEET		S3 = .283960 FEET		

## APPENDIX D

TABLE D6.- SEGMENT PARAMETERS FOR 190-POUND MAN

SEGMENT	MASS (SLUGS)	INERTIA			L	
		IXX	IYY	IZZ	(FEET)	(FEET)
1	3.231531	2.198000	2.067000	.385900	2.839000	1.825500
2	.196189	.024600	.024600	.002681	1.018800	.382550
3	.196189	.024600	.024600	.002681	1.018800	.382550
4	.154718	.022400	.022400	.001360		.581020
5	.154718	.022400	.022400	.001360		.581020
6	.596541	.087340	.087340	.021900	1.462510	.752000
7	.596541	.087340	.087340	.021900	1.462510	.752000
8	.387592	.115080	.109810	.010513		.798400
9	.387592	.115080	.109810	.010513		.798400
S1 = .760400 FEET    S2 = 1.172500 FEET    S3 = .288180 FEET						

TABLE D7.- SEGMENT PARAMETERS FOR 200-POUND MAN

SEGMENT	MASS (SLUGS)	INERTIA			L		$\rho$ (FEET)
		IXX	IYY	IZZ	(FEET)	(FEET)	
1	3.392543	2.344000	2.204000	.419000	2.877000	1.840000	
2	.209634	.026800	.026800	.002950	1.032000	.384000	
3	.209634	.026800	.026800	.002950	1.032000	.384000	
4	.163226	.023990	.023990	.001472		.587600	
5	.163226	.023990	.023990	.001472		.587600	
6	.627300	.093900	.093900	.023800	1.469800	.748000	
7	.627300	.093900	.093900	.023800	1.469800	.748000	
8	.409666	.124000	.118400	.011310		.809000	
9	.409666	.124000	.118400	.011310		.809000	
S1 = .780000 FEET    S2 = 1.186000 FEET    S3 = .292400 FEET							

APPENDIX D

TABLE D8.-- SEGMENT PARAMETERS FOR 210-POUND MAN

SEGMENT	MASS (SLUGS)	INERTIA (SLUG-FT-FT)			L (FEET)		<i>l</i> (FEET)
		IXX	IYY	IZZ			
1	3.553500	2.490000	2.341000	.452100	2.915000	1.854500	
2	.223097	.029000	.029000	.003219	1.045200	.385450	
3	.223097	.029000	.029000	.003219	1.045200	.385450	
4	.171736	.025580	.025580	.001584		.594180	
5	.171736	.025580	.025580	.001584		.594180	
6	.658056	.100460	.100460	.025700	1.477090	.744000	
7	.658056	.100460	.100460	.025700	1.477090	.744000	
8	.431749	.132920	.126990	.012107		.819600	
9	.431749	.132920	.126990	.012107		.819600	
S1 = .799600 FEET		S2 = 1.199500 FEET		S3 = .296620 FEET			

TABLE D9.- SEGMENT PARAMETERS FOR 220-POUND MAN

SEGMENT	MASS (SLUGS)	INERTIA			L	
		IXX	IYY	IZZ	(FEET)	(FEET)
1	3.714411	2.636000	2.478000	.485200	2.953000	1.869000
2	.236576	.031200	.031200	.003488	1.058400	.386900
3	.236576	.031200	.031200	.003488	1.058400	.386900
4	.180249	.027170	.027170	.001696		.600760
5	.180249	.027170	.027170	.001696		.600760
6	.688808	.107020	.107020	.027600	1.484380	.740000
7	.688808	.107020	.107020	.027600	1.484380	.740000
8	.453841	.141840	.135580	.012904		.830200
9	.453841	.141840	.135580	.012904		.830200
S1 = .819200 FEET    S2 = 1.213000 FEET    S3 = .300840 FEET						

## APPENDIX E

### DETERMINATION OF SAMPLING RATE FOR FLIGHT EXPERIMENT

An aperiodic real function,  $f(t)$ , can be represented in terms of its frequency components by taking the inverse of the Fourier transform of the function.

$$f(t) = \frac{1}{\pi} \int_0^{\infty} [A(\omega) \cos \omega t + B(\omega) \sin \omega t] d\omega \quad (E1)$$

where,

$$A(\omega) = \int_{-\infty}^{\infty} f(t) \cos \omega t dt \quad (E2)$$

$$B(\omega) = \int_{-\infty}^{\infty} f(t) \sin \omega t dt \quad (E3)$$

Assume  $f(t) = 0$  for  $t \leq 0$  and  $t > T$  (fig. E1).

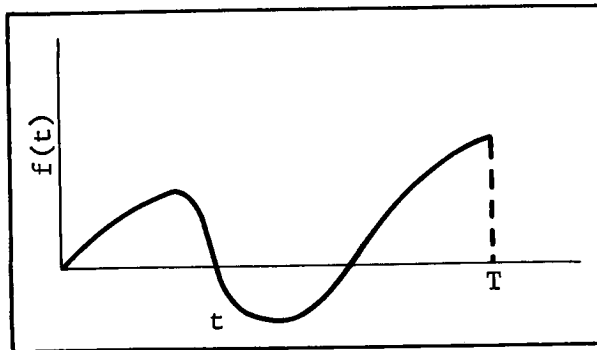


Figure E1.- Definition of T

# APPENDIX E

The integrals for  $A(\omega)$  and  $B(\omega)$  become

$$A(\omega) = \int_0^T f(t) \cos \omega t \, dt \quad (E4)$$

$$B(\omega) = \int_0^T f(t) \sin \omega t \, dt \quad (E5)$$

Assuming the integrations are to be performed numerically, using the trapezoidal rule,

$$A(\omega) = \tau \sum_{k=1}^{m-1} f(k\tau) \cos \omega k\tau + \frac{1}{2} \tau f(m\tau) \cos \omega m\tau \quad (E6)$$

$$B(\omega) = \tau \sum_{k=1}^{m-1} f(k\tau) \sin \omega k\tau + \frac{1}{2} \tau f(m\tau) \sin \omega m\tau \quad (E7)$$

where  $\tau$  is the sampling interval of  $f(t)$  and  $m\tau = T$ .

Selecting a fundamental frequency,  $\omega_o$ , and evaluating the  $A$  and  $B$  coefficients at discrete steps,  $n\omega_o$ , the resulting  $A$  and  $B$  coefficients are

$$A(n\omega_o) = \tau \sum_{k=1}^m f(k\tau) \cos n\omega_o k\tau \quad (E8)$$

$$B(n\omega_o) = \tau \sum_{k=1}^m f(k\tau) \sin n\omega_o k\tau \quad (E9)$$

## APPENDIX E

Using the same numerical integration process to evaluate the inversion integral, with  $\omega_o$  being the integration interval,  $f(t)$  is given as

$$f(t) = \frac{\omega_o}{\pi} \left[ \frac{A(o)}{2} + \sum_{k=1}^{\infty} A(k\omega_o) \cos k\omega_o t + \sum_{k=1}^{\infty} B(k\omega_o) \sin k\omega_o t \right] \quad (E10)$$

Assuming that the frequency components of the original function are negligible at frequencies above  $\omega = n\omega_o$  this summation reduces to

$$f(t) = \frac{\omega_o}{\pi} \left[ \frac{A(o)}{2} + \sum_{k=1}^n A(k\omega_o) \cos k\omega_o t + \sum_{k=1}^n B(k\omega_o) \sin k\omega_o t \right] \quad (E11)$$

This form is equivalent to the Fourier series that would be obtained if the original function,  $f(t)$ , was periodic, with a period of  $\pi/\omega_o$  sec. For this analysis, the selection of  $\omega_o$  is completely arbitrary, so long as  $\pi/\omega_o > T$ , because the only region of interest is the time period  $0 \leq t \leq T$ .

The original function may also be represented as a single summation of frequency components, by combining the two summations using trigonometric relations. When this is done, the summation reduces to

$$f(t) = \frac{\omega_o}{\pi} \sum_{k=0}^n C(k\omega_o) \cos (k\omega_o t + \phi_k) \quad (E12)$$

The  $C(k\omega_o)$  coefficients in this summation indicate the relative magnitude of the various frequency components that are contained in the original function.

The digitized data generated in the restrained crew activities simulation was analyzed for frequency content using the previously derived equations.



## APPENDIX E

Figure E2 is a plot of the  $C(\omega)$  coefficients of  $\text{PHI}(2)$  for run 19. The coefficients have been normalized to a maximum value of one. The plot indicates that the frequency components of the signal are insignificant above a frequency of 2 cps.

Figure E3 is a plot of the normalized  $C(\omega)$  coefficients of  $\text{THETA}(6)$  for run 17. This plot indicates that the frequency components of the signal are significant up to a frequency of 4 cps. The higher frequency content of this signal was expected, because run 19 involved only simple pendulum-type motion, whereas run 17, which is a console operation, involved a more complex motion. Figures A43 and A53 in Appendix A are plots of the two angles that were analyzed.

Figure E4 is a plot of the normalized  $C(\omega)$  coefficients of the measured force applied in the  $x$  direction (S/C axes) for run 19. This signal contains significant frequency components up to a frequency of 8.5 cps.

Based on the results of the frequency analysis, a sampling rate of 20 samples/sec was chosen for the experimental data. This sampling rate is sufficient for data that have no significant frequency components above 10 cps.

For use in the digital programs, a sampling rate of 100 samples/sec is desired. Therefore, it is necessary to interpolate between the points obtained at 20 samples/sec to obtain the additional points for the digital analysis. The interpolation is accomplished by using a  $\sin x/x$  ideal filter, which is implemented on the digital computer. With an input sample rate of 20 samples/sec the ideal filter will reproduce signals containing frequency components up to 10 cps. The output of the filter may then be obtained at any desired sampling rate. Figure E5 is a plot of the measured force applied in the  $x$  direction for run 19, first when sampled at 100 samples/sec, and second when sampled at 20 samples/sec and then passed through the ideal  $\sin x/x$  filter to obtain 100 samples/sec. Comparison of the two curves indicates negligible differences, as expected, because this is the signal that was previously analyzed and found to contain frequency components up to 8.5 cps.

The LIMS angles for run 19 were also passed through the digital  $\sin x/x$  filter, using an input sample rate of 20 samples/sec, and an output rate of 100 samples/sec. The data generated in this manner were smoothed and used as the input to the digital crew disturbance program. The resulting calculated forces are shown in figure E6 plotted over the corresponding calculated forces using the LIMS data sampled at 100 samples/sec. The plot shows negligible differences between the two sets of calculated forces.

APPENDIX E

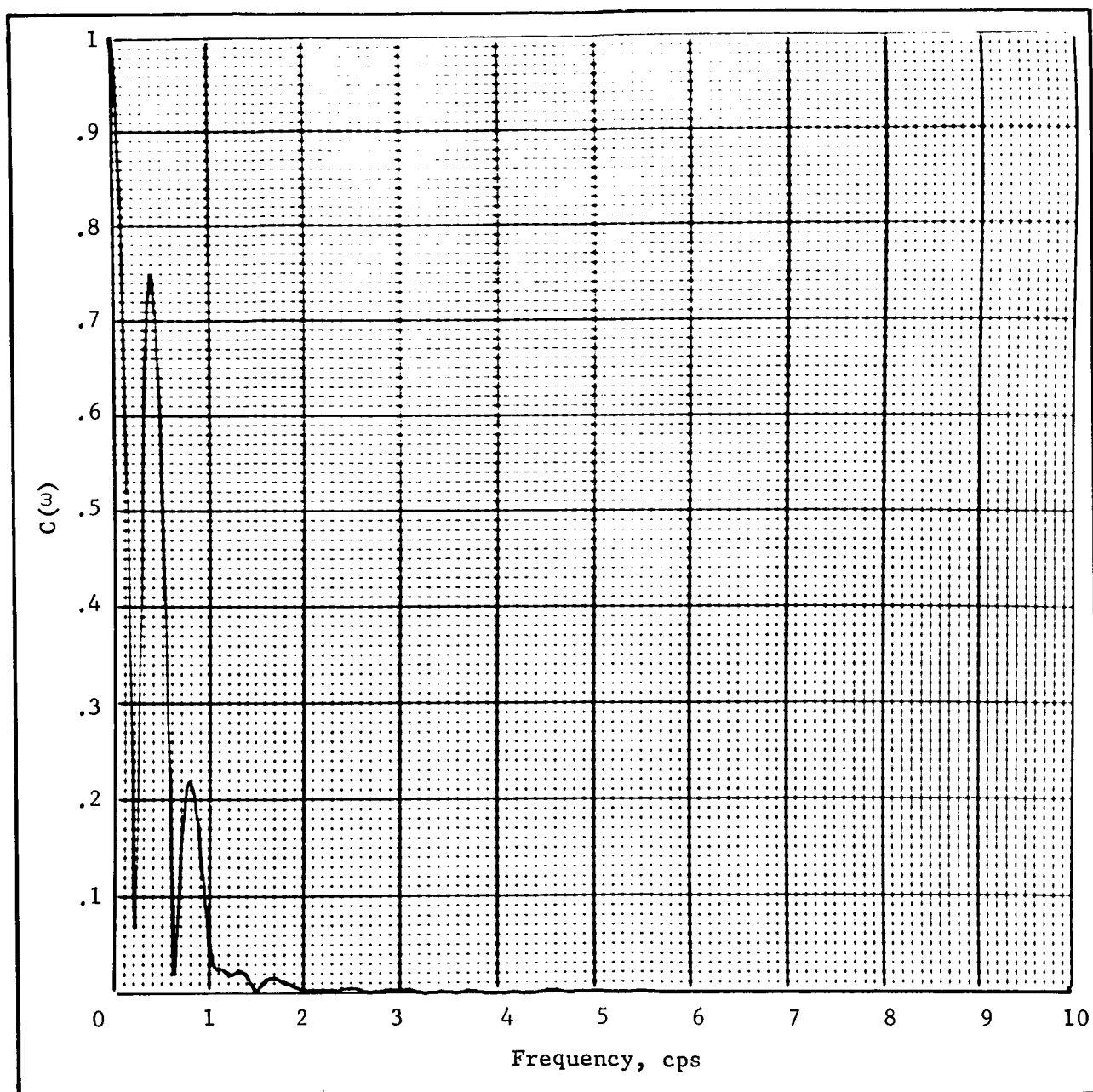


Figure E2.- Normalized Complex Fourier Integral for Run 19

# APPENDIX E

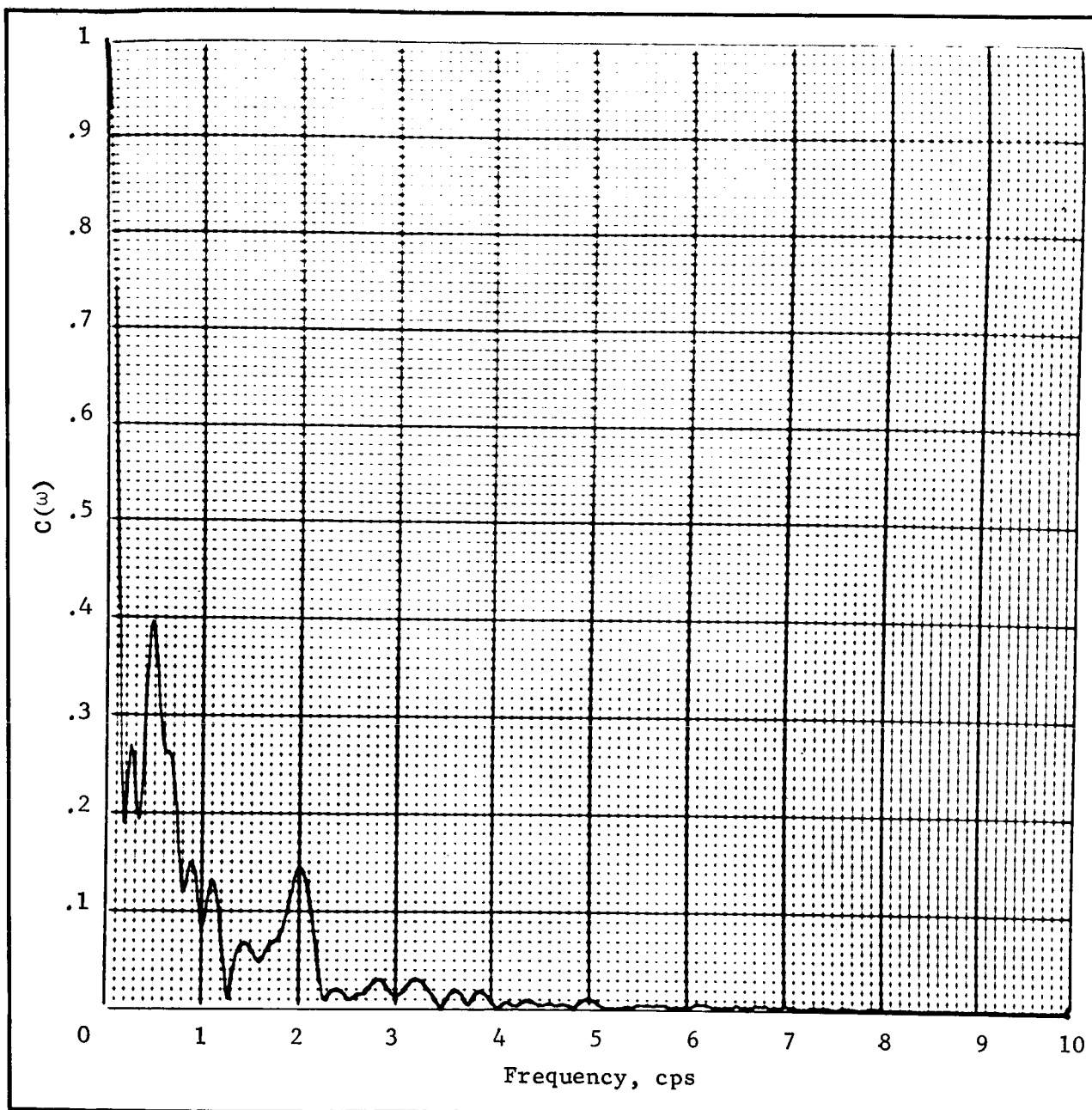


Figure E3.- Normalized Complex Fourier Integral for Run 17

# APPENDIX E

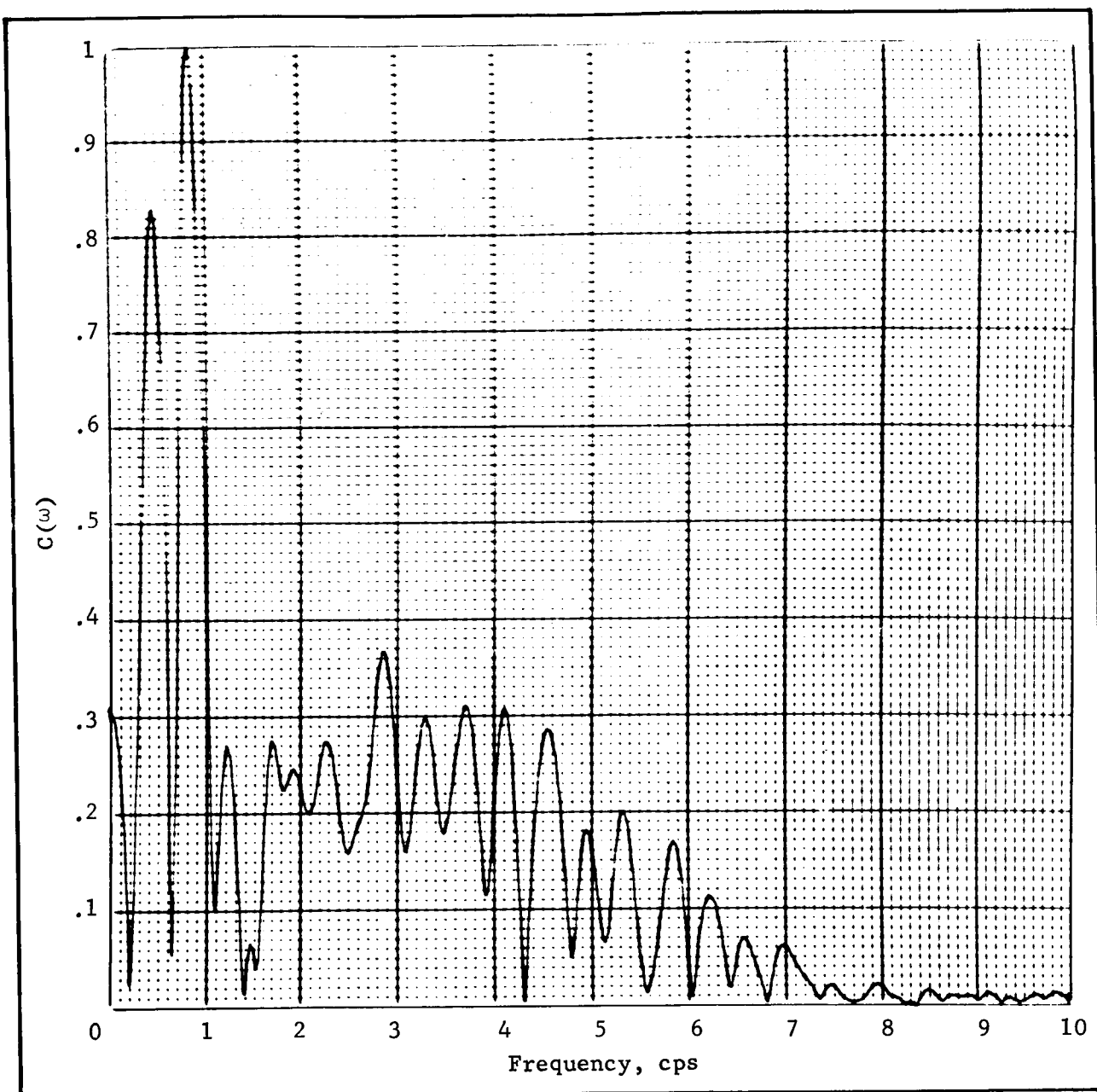
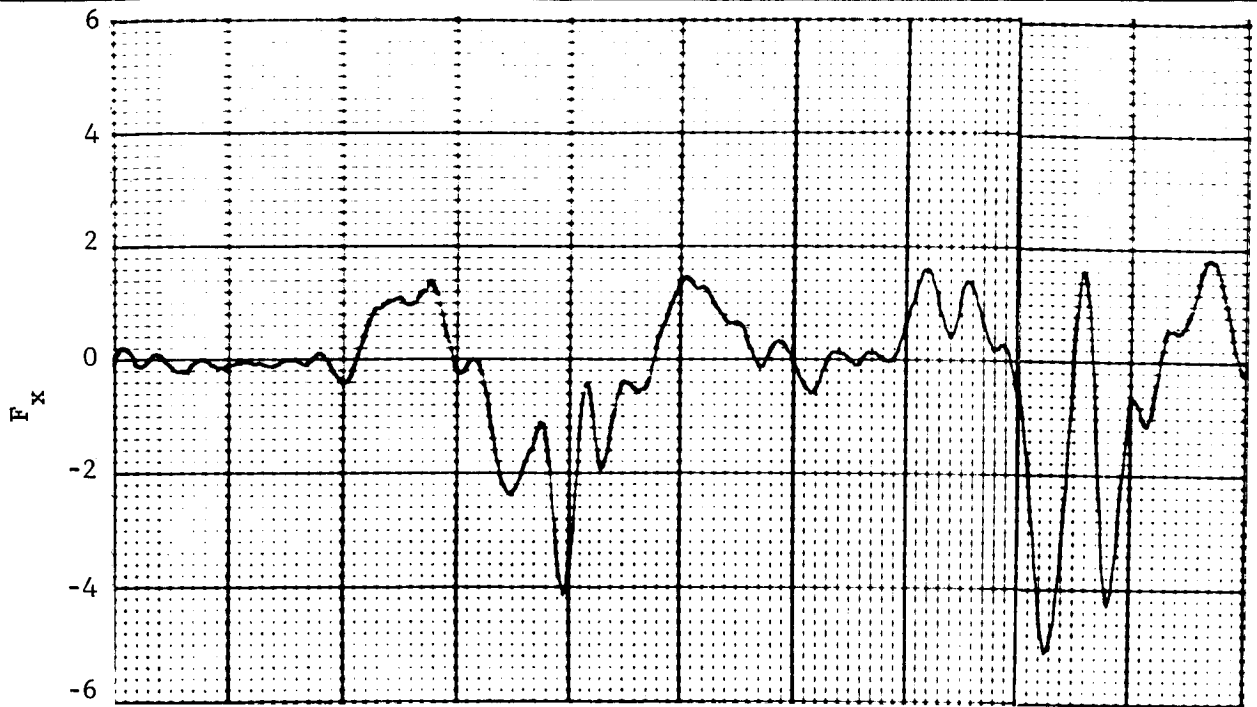
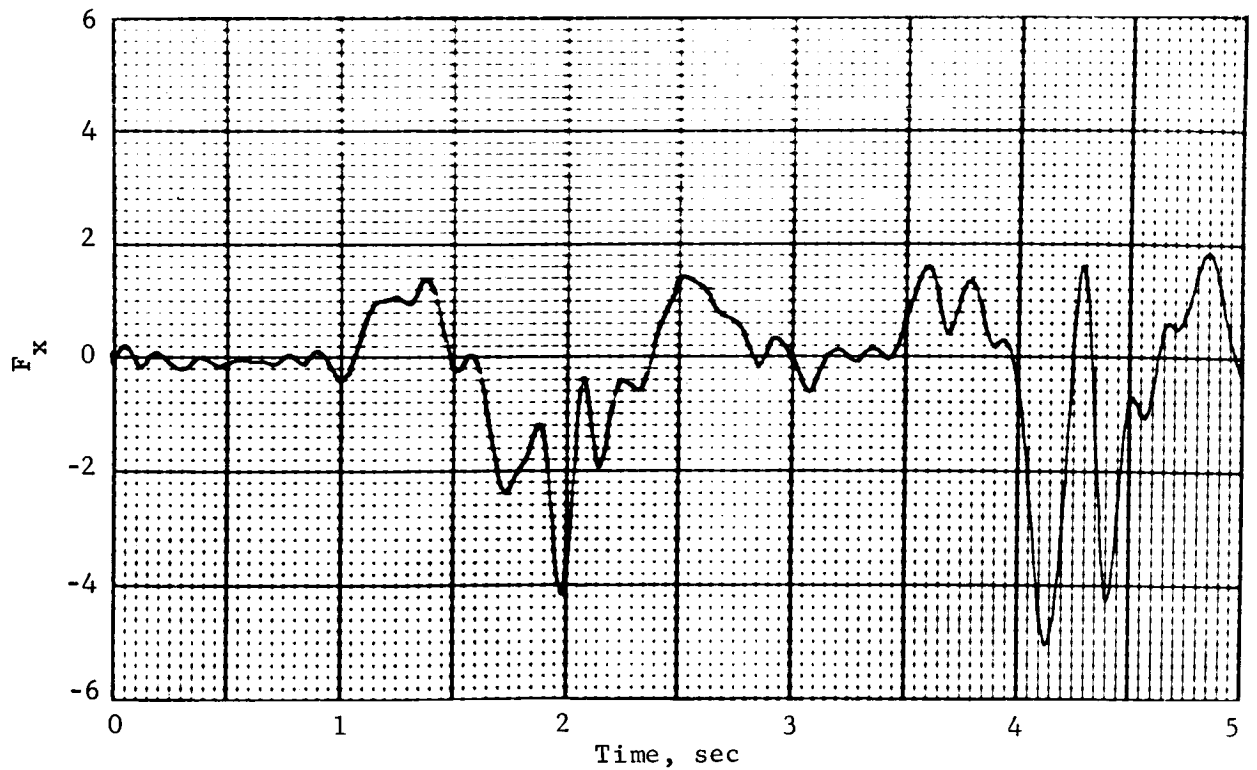


Figure E4.- Normalized Complex Fourier Integral for Run 19



(a) Original force from run 19



(b) Reconstructed data at 20 samples/sec

Figure E5.- Measured Force Applied in the x Direction, Run 19

# APPENDIX E

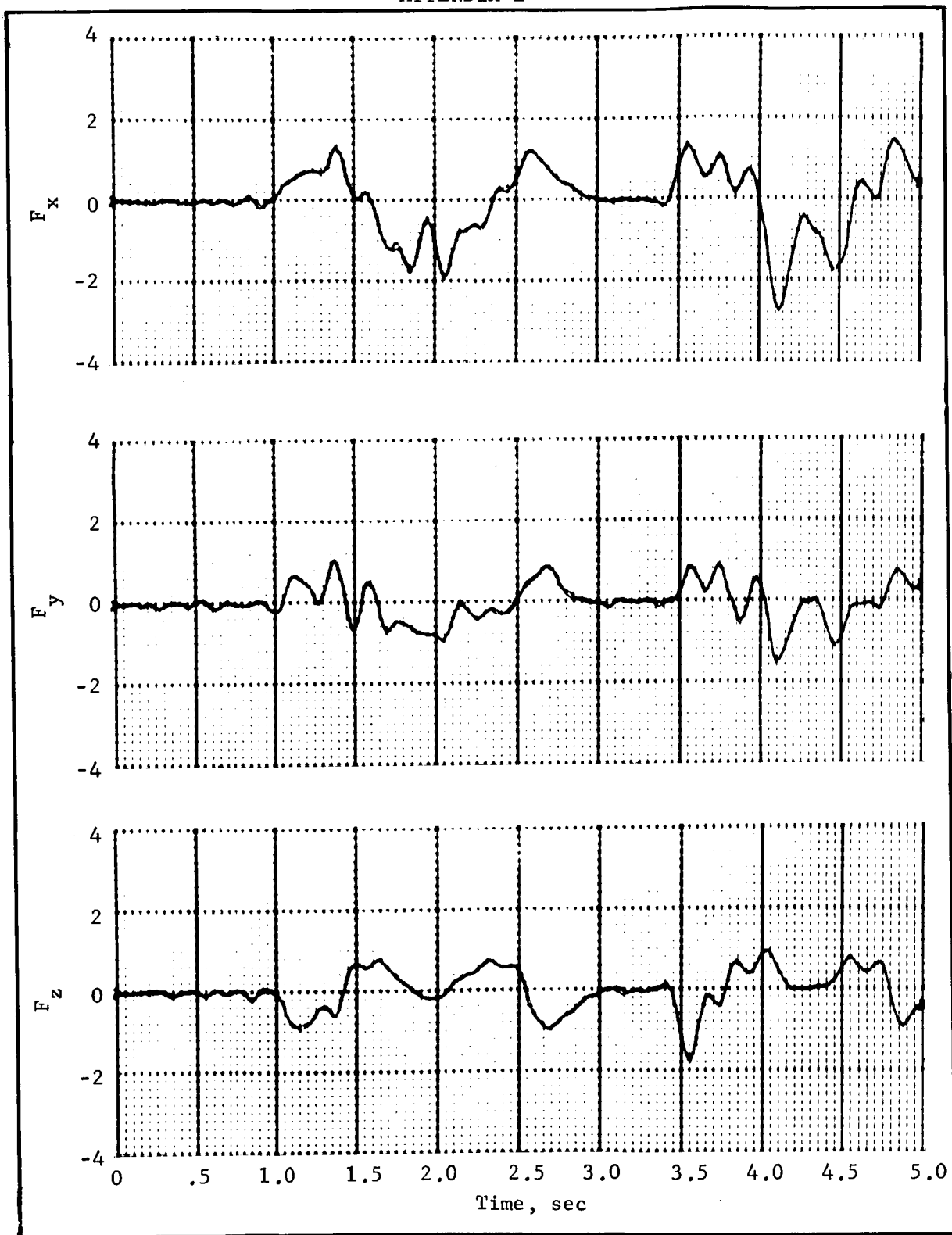


Figure E6.- Calculated Forces Using Reconstructed LIMS Data for Run 19

## APPENDIX F

### ANTHROPOMETRIC MEASUREMENTS OF TEST SUBJECTS

Tables F1 and F2 list the anthropometric measurements of the test subjects used in the simulation studies. The locations of those measurements not obvious by their titles are shown in figure F1. All dimensions are in inches.

TABLE F1.- ANTHROPOMETRIC MEASUREMENTS OF  
SUBJECT 1, WEIGHT, 144 POUNDS

Ankle circumference . . . . .	8.13
Axillary arm circumference . . . . .	11.75
Buttock depth . . . . .	8.75
Chest depth . . . . .	8.75
Chest breadth . . . . .	11.75
Elbow circumference . . . . .	9.88
Fist circumference . . . . .	10.5
Foot length . . . . .	9.88
Head circumference . . . . .	21.50
Hip breadth . . . . .	12.75
Knee circumference . . . . .	13.13
Lower arm length . . . . .	10.0
Shoulder height . . . . .	54.0
Sitting height . . . . .	34.5
Sphyrion height . . . . .	2.75
Stature . . . . .	66.25
Substernale height . . . . .	47.75
Thigh circumference . . . . .	18.0
Tibiale height . . . . .	18.25
Trochanteric height . . . . .	33.25
Upper arm length . . . . .	12.88
Waist breadth . . . . .	9.0
Waist depth . . . . .	7.25
Wrist circumference . . . . .	6.25

# APPENDIX F

TABLE F2.- ANTHROPOMETRIC MEASUREMENTS OF  
SUBJECT 2, WEIGHT, 157 POUNDS

Ankle circumference . . . . .	8.0
Axillary arm circumference . . . . .	12.0
Buttock depth . . . . .	9.1
Chest depth . . . . .	9.1
Chest breadth . . . . .	13.2
Elbow circumference . . . . .	10.5
Fist circumference . . . . .	10.9
Foot length . . . . .	10.2
Head circumference . . . . .	22.0
Hip breadth . . . . .	12.7
Knee circumference . . . . .	14.0
Lower arm length . . . . .	10.0
Shoulder height . . . . .	52.0
Sitting height . . . . .	34.0
Sphyrion height . . . . .	2.7
Stature . . . . .	64.7
Substernale height . . . . .	44.2
Thigh circumference . . . . .	21.5
Tibiale height . . . . .	17.0
Trochanteric height . . . . .	33.4
Upper arm length . . . . .	12.7
Waist breadth . . . . .	11.0
Waist depth . . . . .	8.0
Wrist circumference . . . . .	6.2



APPENDIX F

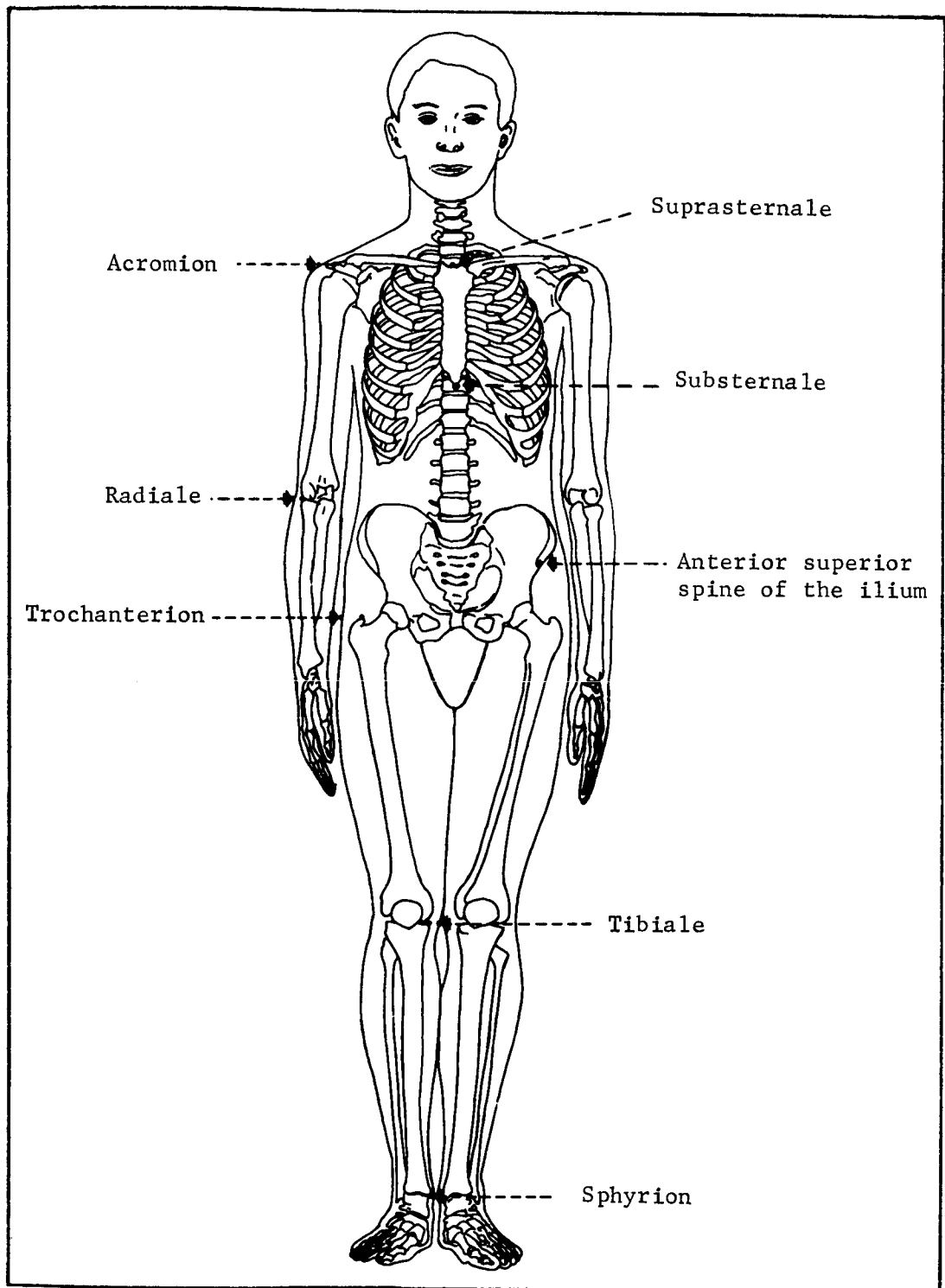


Figure F1.- Skeletal Anthropometric Points

## APPENDIX G

### MATHEMATICAL AND ERROR ANALYSIS OF APAS TECHNIQUES

#### Ultrasonic Triangulation

The basic concept from which the ultrasonic triangulation scheme is derived depends only on a set of sensors,  $\underline{S}_i$ , which are capable of measuring distance only. In general, these are sensors measuring distance in terms of elapsed time between the transmission and reception of a signal, or more fundamentally, the velocity of propagation of a signal. We thus consider a set of four sensors,  $\underline{S}_i$ ,  $i = 1, 2, 3, 4$ , and a target  $T$ , as indicated in figure G1.

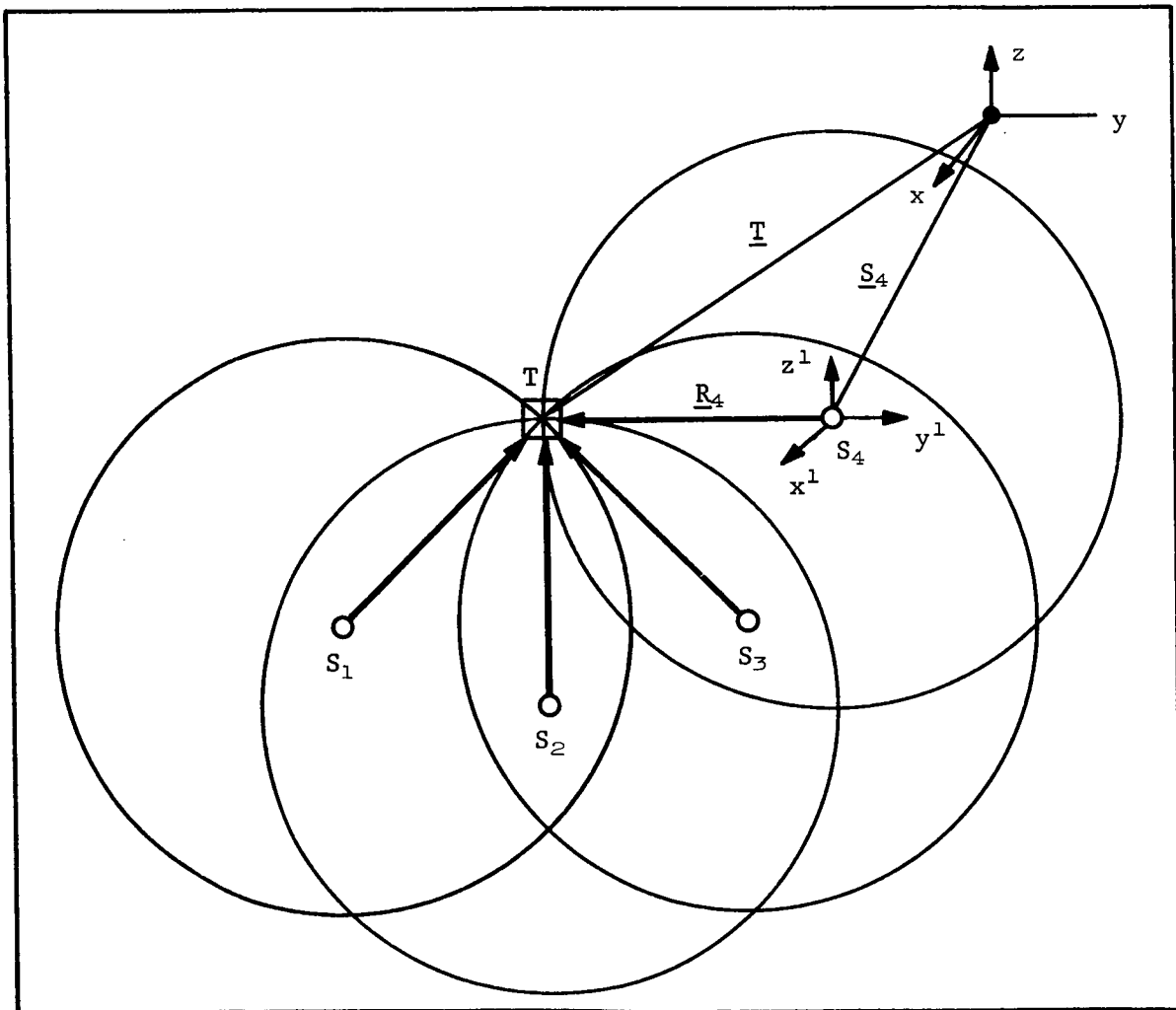


Figure G1.- Ultrasonic-RF APAS Geometry

# APPENDIX G

Shifting the origin of the reference coordinate system to one of the sensors, say  $\underline{S}_4$ , we construct a sphere centered on each of the sensors  $\underline{S}_i$  and intersecting the target,  $\underline{T}$ . The target coordinates are, with respect to the shifted origin,  $T_x^1$ ,  $T_y^1$ , and  $T_z^1$  and the sensor vectors are  $\underline{S}_i^1$ ,  $i = 1, 2, 3$ .

We can thus write:

$$\left(T_x^1 - S_{ix}^1\right)^2 + \left(T_y^1 - S_{iy}^1\right)^2 + \left(T_z^1 - S_{iz}^1\right)^2 = \left(R_i\right)^2 \quad i = 1, 2, 3, 4 \quad (G1)$$

Expanding equation (G1) and noting that

$$\begin{aligned} \left(T_x^1\right)^2 + \left(T_y^1\right)^2 + \left(T_z^1\right)^2 &= R_4^2 \\ \left(S_{ix}^1\right)^2 + \left(S_{iy}^1\right)^2 + \left(S_{iz}^1\right)^2 &= \left(S_i^1\right)^2 \end{aligned} \quad (G2)$$

we obtain

$$R_4^2 + \left(S_i^1\right)^2 + 2\underline{T}^1 \cdot \underline{S}_i^1 = R_i^2, \quad i = 1, 2, 3 \quad (G3)$$

or

$$\underline{T}^1 \cdot \underline{S}_i^1 = \frac{1}{2} \left[ R_i^2 - R_4^2 - \left(S_i^1\right)^2 \right], \quad i = 1, 2, 3 \quad (G4)$$

In matrix notation, equation (G4) may be written as:

$$\underline{S}^1 \underline{T} = \frac{1}{2} \begin{bmatrix} R_1^2 - R_4^2 - \left(S_1^1\right)^2 \\ R_2^2 - R_4^2 - \left(S_2^1\right)^2 \\ R_3^2 - R_4^2 - \left(S_3^1\right)^2 \end{bmatrix} \quad (G5)$$

where

$$\underline{S}^1 = \begin{bmatrix} S_{1x}^1 & S_{1y}^1 & S_{1z}^1 \\ S_{2x}^1 & S_{2y}^1 & S_{2z}^1 \\ S_{3x}^1 & S_{3y}^1 & S_{3z}^1 \end{bmatrix} \quad (G6)$$

# APPENDIX G

and

$$\underline{T}^1 = \begin{bmatrix} T_x^1 \\ T_y^1 \\ T_z^1 \end{bmatrix} \quad (G7)$$

Inverting the  $\underline{S}^1$  matrix and writing the  $\text{adj } \underline{S}^1$  in terms of the components of the vector products we have

$$\begin{bmatrix} T_x^1 \\ T_y^1 \\ T_z^1 \end{bmatrix} = \frac{1}{2\underline{S}_1^1 (\underline{S}_2^1 \times \underline{S}_3^1)} \begin{bmatrix} (\underline{S}_2^1 \times \underline{S}_3^1)_x & -(\underline{S}_1^1 \times \underline{S}_3^1)_x & (\underline{S}_1^1 \times \underline{S}_2^1)_x \\ -(\underline{S}_2^1 \times \underline{S}_3^1)_y & -(\underline{S}_1^1 \times \underline{S}_3^1)_y & (\underline{S}_1^1 \times \underline{S}_2^1)_y \\ (\underline{S}_2^1 \times \underline{S}_3^1)_z & -(\underline{S}_1^1 \times \underline{S}_3^1)_z & (\underline{S}_1^1 \times \underline{S}_2^1)_z \end{bmatrix} \cdot \begin{bmatrix} R_1^2 - R_4^2 - (\underline{S}_1^1)^2 \\ R_2^2 - R_4^2 - (\underline{S}_2^1)^2 \\ R_3^2 - R_4^2 - (\underline{S}_3^1)^2 \end{bmatrix} \quad (G8)$$

The components,  $T_x^1$ ,  $T_y^1$ , and  $T_z^1$  now define the vector  $\underline{R}_4$ . Reverting to the origin of the reference coordinate system, we find that

$$\underline{T} = \underline{S}_4 + \underline{R}_4 \quad (G9)$$

The fundamental accuracy of the two computational schemes depends on the accuracy with which the placement of the sensors can be made with respect to the reference coordinate systems and the known accuracy of the velocity of propagation of the signal used. As configured for the APAS, the target,  $\underline{T}$ , is the ultrasonic transmitter mounted on the astronaut. If the possibility of the intervention of signal attenuating or blocking objects between the target and any sensor exists, it is possible to employ additional sensors and develop a computer program to use the data from combinations of the sensors taken four at a time.

## APPENDIX G

A brief error analysis was conducted and is summarized, emphasizing the predominant error sources, in table G1.

TABLE G1.- ULTRASONIC ERROR ANALYSIS

Error source	Error contribution
Transmitting signal timing accuracy	Negligible
Transducer transient time effects	$1 \times 10^{-4}$ sec; 1 in. at 25 ft
Uncertainty of velocity of sound in media of OWS	15 fps; 4.5 in. at 25 ft
Placement accuracy of fixed ultrasonic receivers	Negligible
Counting accuracy	$0.5 \times 10^{-4}$ sec for 20 kHz clock frequency; 0.5 in. at 25 ft

Factors considered, but not fully analyzed, were reverberation effects resulting in spurious opening or closing of counting gates and the physiological effects of ultrasonics on the astronaut.

To further explain the error analysis, we consider that the radius vector magnitudes,  $|\underline{S}_i|$ ,  $i = 1, 2, 3, 4$  are determined by

$$|\underline{S}_i| = V_s t_i, \quad i = 1, 2, 3, 4 \quad (G10)$$

where  $V_s$  is the velocity of propagation of the ultrasonic wave and  $t_i$  the transit time of this same signal from the target transmitter to each of the four sensors as measured by the number of pulses stored in the register. Considering a single receiver pair, we can write

$$\Delta s_i = |\Delta \underline{S}_i| = V_s \Delta t_i + t_i \Delta V_s \quad (G11)$$

To separate velocity and timing effects, we can then write

$$\frac{\Delta S_i}{S_i} = \frac{\Delta t_i}{t_i} + \frac{\Delta v_s}{v_s} \quad (G12)$$

where the second order term has been neglected.

## APPENDIX G

Considering first the timing errors of table G1,  $\Delta t$ , and assuming a constant sound velocity of 1000 fps, we find that a  $\Delta t$  greater than  $2.5 \times 10^{-4}$  sec yields an error in  $s_i$  of 3 in. The RF signal transit time is of the order of  $10^{-6}$  sec, and thus contributes negligible errors in  $s_i$ . Transducer transient delays were estimated, through consideration of the reciprocal of the resonant frequency of the piezoelectric crystals of the ultrasonic transmitter/receiver, to be about  $5 \times 10^{-5}$  sec/transducer. The total transient time error for a single transmitter/receiver pair is thus of the order of  $10^{-4}$  sec assuming that no calibration and compensation techniques are employed. The transient delay times of ultrasonic transducers employing other than piezoelectric principles for the generation of the acoustic signal were deemed unsatisfactory. The clocking pulse generator storage register timing errors were considered, and assuming an uncertainty of one pulse at a repetition rate of 20 000 pulses/sec, results in an error,  $\Delta t$ , of 50  $\mu$ sec. Taking, as a worst case, an example wherein all of the timing errors are additive, the error in range,  $S_i$ , is approximately 1.5 in. at a nominal range of 25 ft.

Analyzing now the velocity effects above, the uncertainty in the velocity of sound in the OWS media occurs because of allowable variations in temperature, pressure, relative humidity, atmospheric composition, and atmospheric motion. Insufficient data were available to assess the effects of atmospheric motion and composition changes. Temperature and relative humidity effects were evaluated from the theoretical value for sound velocity

$$V_s = \sqrt{\gamma RT(1 + 2\beta\rho + 3C\rho^2 + \dots)} \quad (G13)$$

where  $\gamma$  is the ratio of specific heat at constant pressure to that at constant volume,  $R$  the universal gas constant,  $T$  the temperature in degrees Rankine  $\rho$  the density,  $\beta$  and  $C$  on the first virial coefficients of the gas. For the temperature range of interest, equation (G13) can be written

$$V_s = \sqrt{\gamma RT} \quad (G14)$$

# APPENDIX G

whence

$$\frac{\Delta V_s}{V_s} = \left( \sqrt{1 + \frac{\Delta T}{T+460}} - 1 \right) \quad (G15)$$

where  $T$  is in degrees Fahrenheit.

Taking  $T$  as the nominal temperature of the OWS we have  
 $T = 75^\circ \pm 10^\circ \text{F}$  and

$$\frac{\Delta V_s}{V_s} = 0.009 \quad (G16)$$

If we include the entire range of 40 to 100°F, we can write  
 $T = 70^\circ \pm 30^\circ \text{F}$  and about the nominal

$$\frac{\Delta V_s}{V_s} = 0.028 \quad (G17)$$

These velocity uncertainties lead to position uncertainties of the order of 2.75 and 8.4 in., respectively, in a nominal range of 25 ft. The humidity effects are assessed from

$$V_d = V_h \sqrt{1 - \frac{e}{p} \left( \frac{\gamma_w}{\gamma_a} - 5/8 \right)} \quad (G18)$$

where  $V_d$  is the velocity in dry air,  $V_h$  is the velocity in humid air,  $p$  is the barometric pressure,  $e$  is water vapor pressure, and  $\gamma_w$  and  $\gamma_a$  are the specific heat ratios for water vapor and air, respectively.

Thus for the OWS environment we have:

$$\frac{V_d}{V_h} = \sqrt{1 - 1.3 \frac{e}{p}} \quad (G19)$$

Again for the typical OWS environment, we obtain

$$V_h = 1.018 V_d \quad (G20)$$

## APPENDIX G

indicating that the specified variation in relative humidity could result and velocity could vary as much as 1.8% or the 3-in. position error upper bound would be exceeded at nominal range of 20 ft.

These effects can easily be eliminated by using a calibration procedure at the time of the performance of the experiment. This calibration would yield the actual effective velocity based on known ranges, and the timing errors would thereby be eliminated except for clock errors.

The errors considered herein were treated separately, and considered additive, a statistical treatment would yield more meaningful results; however, the use of the calibration technique would obviate the bulk of these errors and result in more accurate measurements. Thus, the statistical analysis was not carried out.

### Six-Accelerometer IMU

The accelerometer geometry and the defining equations for the six-accelerometer mechanization of the APAS is included in figure G2, where  $A_{mx1} A_{mx4}$  are the measured accelerations along the x-axis, etc.,  $A_I$  the inertial acceleration, and  $S$  is the position. The angular velocity  $\Omega_{mx}^2$  is the square of the angular velocity about the x-axis, etc.

The derivation of the mechanization equations developed in reference 6 will not be repeated here. Rather, only the error analysis since this technique, in all likelihood, will not be used for T013. Fundamental to the error analysis are certain assumptions and criteria to be met.

Assumptions.- We assume that the motion of the center of mass is linear with the x-axis along the direction of motion, that the acceleration when pushing off the wall,  $a$ , is equal in magnitude to the deceleration when encountering the opposite wall,  $a^1 = -a$ , that these accelerations are constant, and that the absolute value of their respective errors are less than some constant value. We define  $t_1$  and  $t_3-t_2$  to be the times of acceleration and deceleration, respectively and  $t_2-t_1$  the intervening time during which the velocity is constant.



# APPENDIX G

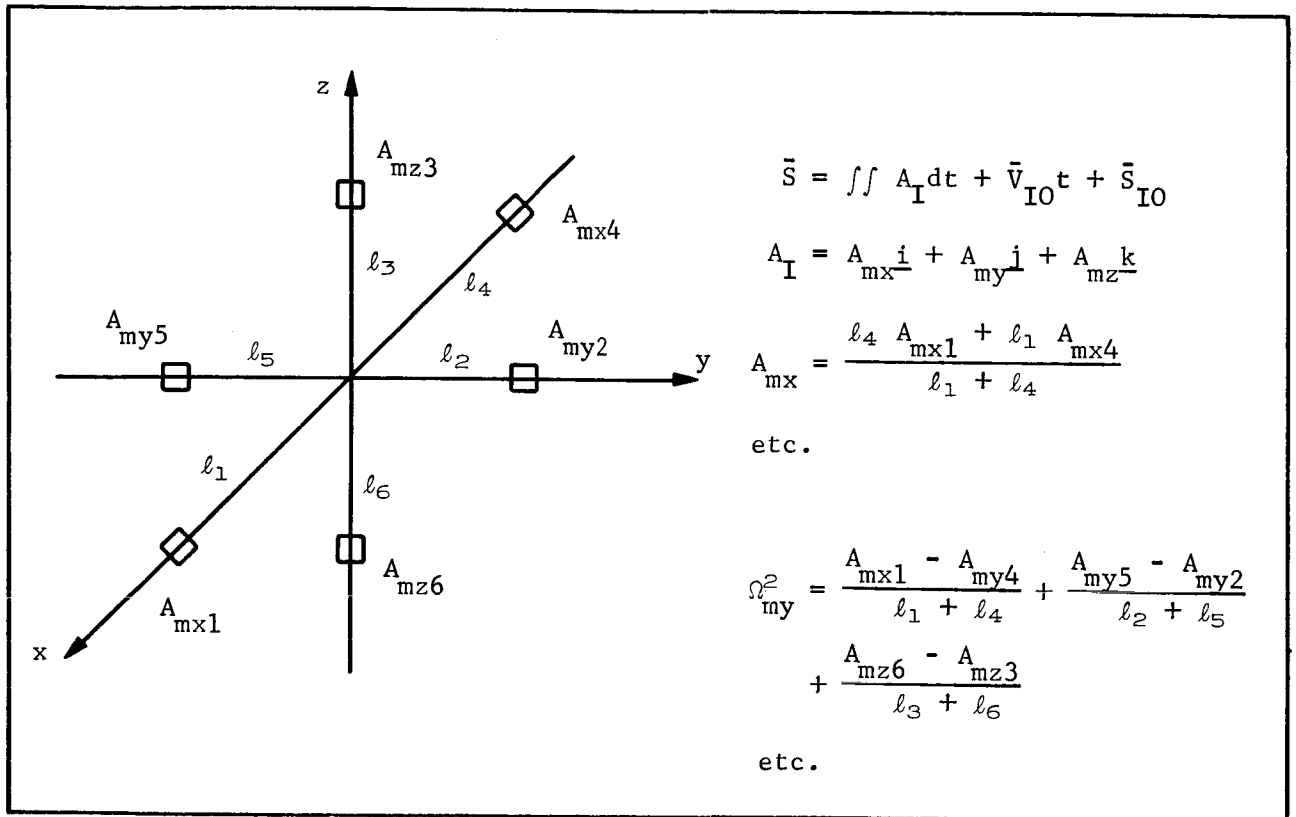


Figure G2.- Implementation of Six-Accelerometers for APAS

## APPENDIX G

In the accelerometer equations shown in figure G2, we assume that  $\ell_j = \ell$ ,  $j = 1, \dots, 6$ .

We define the "total rotation"  $R$  as

$$R = \max \sqrt{\omega_x^2 + \omega_y^2 + \omega_z^2}, \quad 0 \leq t \leq t_3 \quad (G21)$$

Equations and errors.- When these accelerations and their errors are integrated, we obtain the following equations for position, position error and velocity:

$$\underline{s}(t) = \left\{ \begin{array}{ll} \frac{1}{2} \underline{a} t^2 & t \in (0, t_1) \\ \frac{1}{2} \underline{a} t_1 (2t - t_1) & t \in (t_1, t_2) \\ \frac{1}{2} \underline{a} t_1 (2t - t_1) - \frac{1}{2} \underline{a} (t - t_2)^2 & t \in (t_2, t_3) \end{array} \right\} \quad (G22)$$

$$\Delta \underline{s}(t) = \left\{ \begin{array}{ll} \frac{1}{2} \underline{a} t^2 & t \in (0, t_1) \\ \frac{1}{2} \underline{a} t_1 (2t - t_1) & t \in (t_1, t_2) \\ \frac{1}{2} \underline{a} t_1 (2t - t_1) + \frac{1}{2} \underline{a}^1 (t - t_2)^2 & t \in (t_2, t_3) \end{array} \right\} \quad (G23)$$

$$\underline{v}(t) = \left\{ \begin{array}{ll} \underline{a} t & t \in (0, t_1) \\ \underline{a} t_1 & t \in (t_1, t_2) \\ \underline{a} t_1 - \underline{a} (t - t_2) & t \in (t_2, t_3) \end{array} \right\} \quad (G24)$$

Because  $v(t_3) = 0$ , we find that  $t_3 - t_2 = t_1$ , so that if  $\epsilon$  is an upper bound  $|\Delta \underline{a}|$ ,  $|\Delta \underline{a}^1|$ ,

$$\underline{s}(t_3) = \underline{a} t_1 (t_3 - t_1) \quad (G25)$$

$$|\Delta \underline{s}(t_3)| \leq \epsilon t_1 t_3 \quad (G26)$$

# APPENDIX G

We can also safely assume that  $t_1 \ll t_3$ , so that  $\underline{s}(t_3) \approx \underline{a}t_1t_3$ . Thus, we find that

$$\frac{|\Delta \underline{s}(t_3)|}{|\underline{s}(t_3)|} \leq \frac{\epsilon}{|\underline{a}|} \quad (G27)$$

The accelerometer equations are:

$$\underline{a} = \begin{bmatrix} \frac{\ell_4 A_{mx4} + \ell_1 A_{mx1}}{4 + 1} \\ \frac{\ell_5 A_{my5} + \ell_2 A_{my2}}{5 + 2} \\ \frac{\ell_6 A_{mz6} + \ell_3 A_{mz3}}{6 + 3} \end{bmatrix} \quad (G28)$$

$$\begin{bmatrix} \omega_x^2 \\ \omega_y^2 \\ \omega_z^2 \end{bmatrix} = \begin{bmatrix} -1 & 1 & 1 \\ 1 & -1 & 1 \\ 1 & 1 & -1 \end{bmatrix} \cdot \begin{bmatrix} \frac{A_{mx4} - A_{mx1}}{\ell_1 + \ell_4} \\ \frac{A_{my5} - A_{my2}}{\ell_2 + \ell_5} \\ \frac{A_{mz6} - A_{mz3}}{\ell_3 + \ell_6} \end{bmatrix} \quad (G29)$$

Upon differentiating the equation for  $\underline{a}$  and setting all the  $\ell_j$ 's equal we have:

$$\Delta \underline{a} = \begin{bmatrix} \frac{1}{2\ell} (A_{mx4} - A_{mx1}) \cdot \frac{1}{2} (\Delta \ell_4 - \Delta \ell_1) \\ \frac{1}{2\ell} (A_{my5} - A_{my2}) \cdot \frac{1}{2} (\Delta \ell_5 - \Delta \ell_2) \\ \frac{1}{2\ell} (A_{mz6} - A_{mz3}) \cdot \frac{1}{2} (\Delta \ell_6 - \Delta \ell_3) \end{bmatrix} + \frac{1}{2} \begin{bmatrix} \Delta A_{mx4} - \Delta A_{mx1} \\ \Delta A_{my5} - \Delta A_{my2} \\ \Delta A_{mz6} - \Delta A_{mz3} \end{bmatrix} \quad (G30)$$

# APPENDIX G

Now let

$$\underline{\varphi} = \begin{bmatrix} A_{mx4} - A_{mx1} \\ A_{my5} - A_{my2} \\ A_{mz6} - A_{mz3} \end{bmatrix} \quad (G31)$$

$$\left. \begin{aligned} \delta_\ell &= \max (|\Delta \ell_j|) \\ j &= 1, \dots, 6 \\ 0 &\leq t \leq t_3 \end{aligned} \right\} \quad (G32)$$

$$\left. \begin{aligned} \delta_A &= \max |\Delta A_{m\zeta j}| \\ \zeta &= x, y, z \\ j &= 1, \dots, 6 \\ 0 &\leq t \leq t_3 \end{aligned} \right\} \quad (G33)$$

Then we have:

$$\Delta \underline{a} \leq \frac{1}{2\ell} \delta_\ell |\underline{\varphi}| + 3\delta_A \leq \frac{1}{2\ell} \delta_\ell (|\varphi_1| + |\varphi_2| + |\varphi_3|) + 3\delta_A \quad (G34)$$

Note that from equations (G29) and (G31) one obtains

$$\underline{\varphi} = \ell \cdot \begin{bmatrix} \omega_y^2 + \omega_z^2 \\ \omega_x^2 + \omega_z^2 \\ \omega_y^2 + \omega_z^2 \end{bmatrix} \quad (G35)$$

so that

$$|\Delta \underline{a}| \leq \delta_\ell (\omega_x^2 + \omega_y^2 + \omega_z^2) + 3\delta_A R^2 \delta_\ell + 3\delta_A \quad (G37)$$

# APPENDIX G

If we let  $\epsilon = R^2 \delta_\ell + 3\delta_A$ , then

$$\frac{|\Delta s(t_3)|}{|\underline{s}(t_3)|} \leq \frac{\epsilon}{|\underline{a}|} = \frac{1}{|\underline{a}|} (R^2 \delta_\ell + 3\delta_A) \quad (G37)$$

and the position accuracy is now related to the instruments directly or

$$|\Delta \underline{s}(t_3)| \leq \epsilon t_1 t_3 = t_1 t_3 (R^2 \delta_\ell + 3\delta_A) \quad (G38)$$

We are also interested in the errors in attitude. These can be found by integrating  $\Delta R$ .

From equation (G30),

$$R^2 = \omega_x^2 + \omega_y^2 + \omega_z^2 = \frac{\varphi_1}{\ell_4 + \ell_1} + \frac{\varphi_2}{\ell_5 + \ell_2} + \frac{\varphi_3}{\ell_6 + \ell_3} \quad (G39)$$

$$2R\Delta R + (\Delta R)^2 = \frac{1}{4\ell^2} \sum_{j=1}^3 -(\Delta \ell_{j+3} + \Delta \ell_j) (\varphi_j + 2\ell \Delta \varphi_j) = \Delta(R^2) \quad (G40)$$

Solving the equation for  $\Delta R$  with  $R > 0$  and  $R^2 \gg |\Delta R^2|$ :

$$|\Delta R| = |-R + \sqrt{R^2 + \Delta(R^2)}| \leq \sqrt{|\Delta R^2|} \leq \frac{1}{2\ell} \sqrt{4\ell R^2 \delta_\ell + |2\ell \delta_A|} \quad (G41)$$

Thus for any  $R$ :

$$|\Delta R| \leq \frac{1}{\sqrt{\ell}} \sqrt{R^2 \delta_\ell + 3\delta_A} = \sqrt{\epsilon/\ell} \quad (G42)$$

and

$$|\Delta \theta(t_3)| \leq \frac{t_3}{\sqrt{\ell}} \sqrt{R^2 \delta_\ell + 3\delta_A} = t_3 \sqrt{\epsilon/\ell} \quad (G43)$$

One now has from equation (G27) that

$$\frac{|\Delta s|}{|\underline{s}|} \leq \frac{\epsilon}{|\underline{a}|} \quad (G44)$$

# APPENDIX G

where

$$\epsilon = R^2 \delta_\ell + 3\delta_A \quad (G45)$$

To satisfy the 5% accuracy criteria for position, it is then required that

$$\frac{\epsilon}{|a|} < 0.05 \quad (G46)$$

or

$$\epsilon < 0.05 |a| \quad (G47)$$

Using the lower limit of  $10^{-4}$  on acceleration,

$$\epsilon < 5 \times 10^{-6} \text{ g} \quad (G48)$$

Assuming that there is no angular velocity, then

$$\delta_A < 1.67 \times 10^{-6} \text{ g} \quad (G49)$$

With  $\delta_A$  defined as the  $\max |\Delta a_{\text{mci}}|$  the actual accelerometer itself must contribute an error less than  $10^{-6}$  g.

We now note that from equation (G42)

$$|\Delta R| = \sqrt{\epsilon/\ell} \quad (G50)$$

where

$$\frac{|\Delta R|}{R} \leq \frac{\sqrt{\epsilon/\ell}}{R} \quad (G51)$$

Imposing once again the 5% accuracy criterion, one obtains

$$\frac{\sqrt{\epsilon/\ell}}{R} \leq 5 \times 10^{-2} \quad (G52)$$

or

$$\frac{\epsilon/\ell}{R^2} \leq 25 \times 10^{-4} \quad (G53)$$

# APPENDIX G

Thus

$$\frac{R^2 \delta_{\ell} + 3\delta_A}{R^2 \ell} \leq 25 \times 10^{-4} \quad (G54)$$

or

$$\frac{\delta_{\ell}}{\ell} + \frac{3\delta_A}{R^2 \ell} \leq 25 \times 10^4 \quad (G55)$$

Assuming  $\ell = 0.5$  ft, one obtains that

$$\delta_{\ell} + \frac{3\delta_A}{R^2} \leq 1.25 \times 10^{-3} \text{ ft} \quad (G56)$$

which indicates that with zero accelerometer error there would be no problem in controlling  $\ell$  to the required accuracy.

Consider now the case where  $\delta_{\ell} = 0$ , whence for  $\ell = 0.5$  ft one has

$$\frac{3\delta_A}{R^2} \leq 1.25 \times 10^{-3} \text{ ft} \quad (G57)$$

Under the assumption that it is required to measure angular velocities of the order of  $10^{-2}$  rad/sec one finds

$$\delta_A \leq 4 \times 10^{-8} \text{ fps}^2 \quad (G58)$$

or

$$\delta_A \leq 1 \times 10^{-9} \text{ g} \quad (G59)$$

The assumed angular velocity of  $10^{-2}$  rad/sec is comparable to a linear velocity of the order of  $3 \times 10^{-2}$  fps, or about the same lateral impulse would be required to produce this angular velocity as the impulse required to produce the linear velocity. Equation (G36) is obviously very sensitive to the assumed value of angular velocity, and required range of angular velocities has significant importance in the accelerometer requirements, i.e., for angular velocities, smaller than  $10^{-2}$  rad/sec, accelerometer errors must be correspondingly smaller, and the requirements on the actual accelerometer more severe.

## APPENDIX G

### Photographic Technique

The performance of experiment T013 is planned for the experiment area adjacent to the crew quarters in the OWS. The cameras will be mounted near the outer shell of the OWS, about 4 to 5 ft apart and midway between the floor and ceiling. Assuming that the cameras are provided with 10-mm lenses, this placement will provide sufficient coverage of the maneuvering astronaut for the experiment as currently defined.

Definition of coordinate systems.- The focal points of the two camera lenses lie in a plane defined by the two focal points and the intersection of the line of sight from each camera. We denote this plane as the X-Y plane, and let the line of sight of camera 1 ( $C_1$ ) be  $Z_1$  and that of  $C_2$  be  $Z_2$ . The orthogonal reference coordinate system is centered at the focal point of  $C_1$  with the Z axis normal to the X-Y plane (see figure G3). Camera  $C_2$  focal point is then at ( $X_0$ ,  $Y_0$ , and  $Z = 0$ ) with the local reference coordinates of  $C_2$  parallel to those of  $C_1$ .

An arbitrary point ( $x, y, z$ ) within the field of view of both cameras is selected such that  $x > x_0 > 0$ ,  $y > 0$ ,  $y_0 > 0$ . Then

$$\left| \frac{y - y_0}{x - x_0} \right| < \frac{y_0}{x_0} < 1 \quad (G60)$$

and the angles  $\theta_1$  and  $\theta_2$  taken between  $x$  and  $Z_1$  and  $x$  and  $Z_2$ , respectively, are positive -- less than  $\pi/4$  and lie in the X-Y plane.

Coordinate transformations.- To show the relationship between the various coordinate systems, we examine figure G3 where the Z axis is assumed out of the paper.

We now define an arbitrary point ( $x, y, z$ ) in the reference coordinate system ( $X, Y, Z$ ). The vector  $\underline{R}$  ( $x, y, z$ ) is defined in the reference system and the vector  $\underline{R}_j$  ( $x_j, y_j, z_j$ ) in the respective camera coordinates. The vector  $\rho$  joining the two camera focal points is defined in the reference system. Then for convenience we define a  $\underline{\rho}_j$  ( $x, y, z$ ) as whence

$$\underline{\rho}_j = \begin{cases} \underline{\rho} & j = 1 \\ \underline{\rho} = (x_0, y_0, z_0) & j = 2 \end{cases} \quad (G61)$$



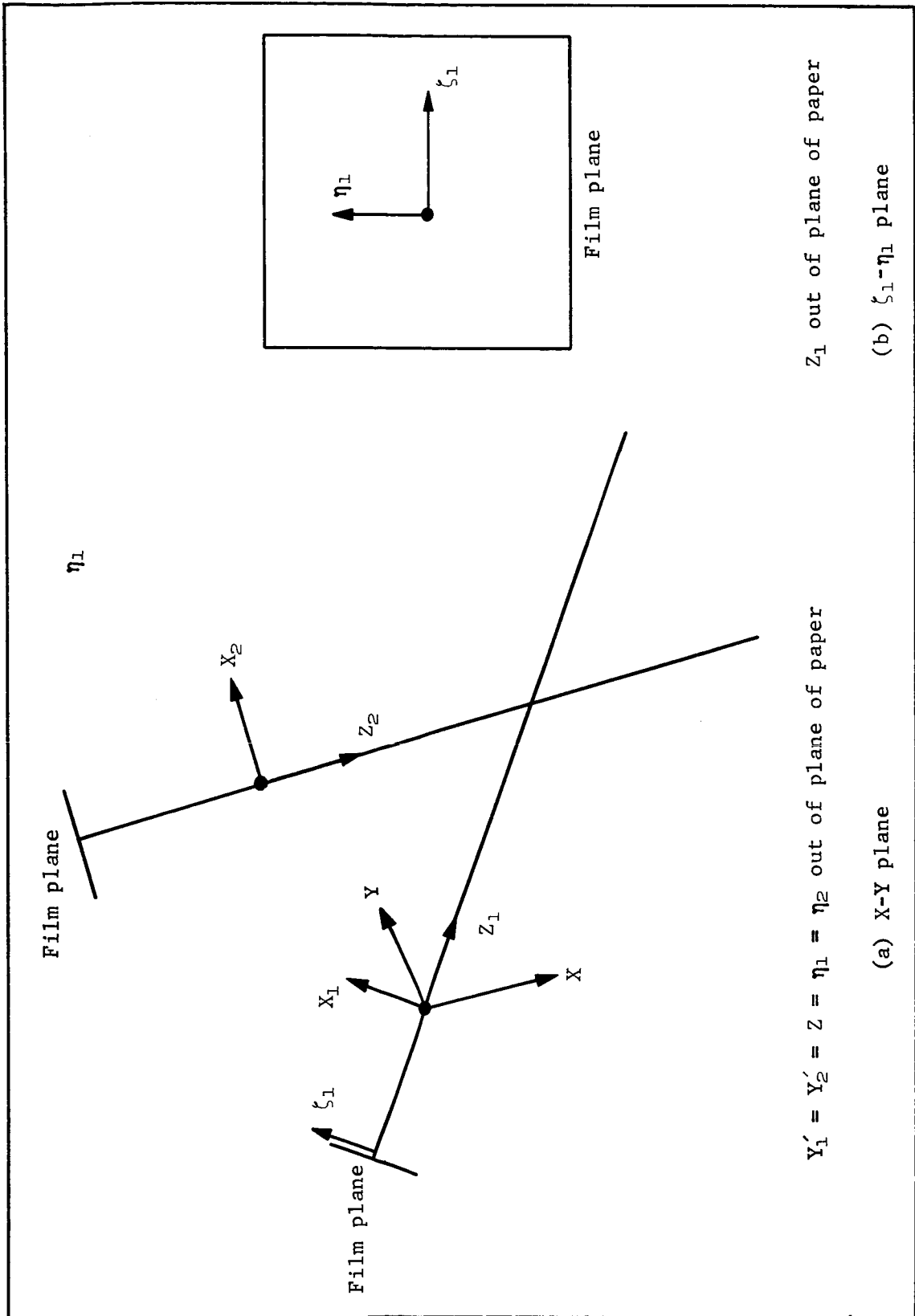


Figure G3.- Camera Coordinate Systems

# APPENDIX G

Defining the coordinate transformation rotating the reference  $(X,Y,Z)$  system into the respective camera systems  $(x_j, y_j, z_j)$   $j = 1, 2$  as  $\underline{\underline{A}}_j$ , we have

$$\underline{R}_1 = \begin{bmatrix} x_1 \\ y_1 \\ z_1 \end{bmatrix} = \underline{\underline{A}}_1 \underline{R} = \underline{\underline{A}}_1 \begin{bmatrix} x \\ y \\ z \end{bmatrix} \quad (G62)$$

$$\underline{R}_2 = \begin{bmatrix} x_2 \\ y_2 \\ z_2 \end{bmatrix} = \underline{\underline{A}}_2 \underline{r} = \underline{\underline{A}}_2 \begin{bmatrix} x \\ y \\ z \end{bmatrix} \quad (G63)$$

and

$$\underline{R} = \underline{\rho} + \underline{r} \quad (G64)$$

Thus,

$$\underline{R}_1 = \underline{\underline{A}}_1 \underline{R} \quad (G65)$$

$$\underline{R}_2 = \underline{\underline{A}}_2 (\underline{R} - \underline{\rho}) \quad (G66)$$

By virtue of the definition of  $\underline{\rho}_j$  we can generalize and write

$$\underline{R}_j = \underline{\underline{A}}_j (\underline{R} - \underline{\rho}_j) \quad (G67)$$

where

$$\underline{\underline{A}}_j = \begin{bmatrix} -\sin \theta_j & \cos \theta_j & 0 \\ 0 & 0 & 1 \\ \cos \theta_j & \sin \theta_j & 0 \end{bmatrix} ; j = 1, 2 \quad (G68)$$

The relationship between the object coordinates  $(x_j, y_j, z_j)$  and the image coordinates  $(\xi_j, \eta_j)$ ,  $j = 1, 2$  can be obtained through consideration of

# APPENDIX G

$$\frac{\xi_j}{x_j} = \frac{\eta_j}{y_j} = -\frac{f}{z_j}, \quad \begin{cases} j = 1, 2 \\ y_j = z \end{cases} \quad (G69)$$

where  $f$  is the focal length of the camera lens.

Solution of the equations.— Equating the right and left sides of operation (G69), we have

$$\left. \begin{aligned} \xi_1 z_1 + f x_1 &= 0 \\ \xi_2 z_2 + f x_2 &= 0 \end{aligned} \right\} \quad (G70)$$

From equation (G67) the set (G70) becomes

$$\begin{bmatrix} -f \sin \theta_1 + \xi_1 \cos \theta_1 & f \cos \theta_1 + \xi_1 \sin \theta_1 \\ -f \sin \theta_2 + \xi_2 \cos \theta_2 & f \cos \theta_2 + \xi_2 \sin \theta_2 \end{bmatrix} \begin{bmatrix} x \\ y \end{bmatrix}$$

$$\mathcal{S} = \begin{bmatrix} 0 \\ 1 \end{bmatrix} \quad (G71)$$

Solving now for  $\underline{R}$  we have

$$\begin{bmatrix} x \\ y \end{bmatrix} = \frac{\mathcal{S}}{K} \cdot \underline{V} \quad (G72)$$

where

$$\underline{V} = \begin{bmatrix} (-f \cos \theta_1 - \xi_1 \sin \theta_1) \\ (-f \sin \theta_1 + \xi_1 \cos \theta_1) \end{bmatrix} \quad (G73)$$

and

$$K = (f^2 + \xi_1 \xi_2) \sin(\theta_2 - \theta_1) + (\xi_1 - \xi_2) \cos(\theta_2 - \theta_1) \quad (G74)$$

from equation (G69) we obtain

$$z = y_2 = \frac{-h_1 z_2}{f} = \frac{-h_1}{f} (x \cos \theta_1 + y \sin \theta_1) = \frac{\mathcal{S} \eta_1}{K} \quad (G75)$$

# APPENDIX G

therefore,

$$\underline{R} = \frac{\mathcal{L}}{K} \begin{bmatrix} (-f \cos \theta_1 - \zeta_1 \sin \theta_1) \\ (-f \sin \theta_1 + \zeta_1 \cos \theta_1) \\ \eta_1 \end{bmatrix} \quad (G76)$$

Error analysis. - We begin by repeating the system for  $\begin{bmatrix} x \\ y \end{bmatrix}$  :

$$\begin{bmatrix} -f \sin \theta_1 + \zeta_1 \cos \theta_1 & f \cos \theta_1 + \zeta_1 \sin \theta_1 \\ -f \sin \theta_2 + \zeta_2 \cos \theta_2 & f \cos \theta_2 + \zeta_2 \sin \theta_2 \end{bmatrix} \begin{bmatrix} x \\ y \end{bmatrix} = \Delta \mathcal{L} \begin{bmatrix} 0 \\ 1 \end{bmatrix} \quad (G77)$$

Then we differentiate both sides and solve for  $\begin{bmatrix} \Delta x \\ \Delta y \end{bmatrix}$  :

$$\begin{aligned} & \begin{bmatrix} -f \sin \theta_1 + \zeta_1 \cos \theta_1 & f \cos \theta_1 + \zeta_1 \sin \theta_1 \\ -f \sin \theta_2 + \zeta_2 \cos \theta_2 & f \cos \theta_2 + \zeta_2 \sin \theta_2 \end{bmatrix} \begin{bmatrix} \Delta x \\ \Delta y \end{bmatrix} \\ &= \mathcal{L} \begin{bmatrix} 0 \\ 1 \end{bmatrix} - \begin{bmatrix} (\Delta \zeta_1) \cos \theta_1 & (\Delta \zeta_1) \sin \theta_1 \\ (\Delta \zeta_2) \cos \theta_2 & (\Delta \zeta_2) \sin \theta_2 \end{bmatrix} \cdot \begin{bmatrix} x \\ y \end{bmatrix} \\ &- \begin{bmatrix} (-f \cos \theta_1 - \zeta_1 \sin \theta_1) \Delta \theta_1 & (-f \sin \theta_1 + \zeta_1 \cos \theta_1) \Delta \theta_1 \\ (-f \cos \theta_2 - \zeta_2 \sin \theta_2) \Delta \theta_2 & (-f \sin \theta_2 + \zeta_2 \cos \theta_2) \Delta \theta_2 \end{bmatrix} \begin{bmatrix} x \\ y \end{bmatrix} \quad (G78) \end{aligned}$$

where

$$\begin{aligned} \Delta \mathcal{L} &= (-f \sin \theta_2 + \zeta_2 \cos \theta_2) \Delta x_0 + (\zeta_2 \sin \theta_2 + f \cos \theta_2) \Delta y_0 \\ &+ (y_0 \sin \theta_2 + x_0 \cos \theta_2) \Delta \zeta_2 \\ &+ -x_0 (\zeta_2 \sin \theta_2 + f \cos \theta_2) + y_0 (-f \sin \theta_2 + \zeta_2 \cos \theta_2) \Delta \theta_2 \quad (G79) \end{aligned}$$

We can simplify equation (G79) by letting  $\theta_1 = \theta_2$  and remembering from (G61) and (G63) that:

$$\zeta_1 = -\frac{fx_1}{z_1} = -f \left[ \frac{-x \sin \theta + y \cos \theta}{x \cos \theta + y \sin \theta} \right] \quad (G80)$$

# APPENDIX G

$$\zeta_2 = -\frac{fx_2}{z_2} = -f \left[ \frac{-(x - x_0) \sin \theta + (y - y_0) \cos \theta}{(x - x_0) \cos \theta + (y - y_0) \sin \theta} \right] \quad (G81)$$

$$\eta_1 = -\frac{fz}{z_1} \quad (G82)$$

Then the equation (G79) can be simplified as follows:

$$f \begin{bmatrix} -\frac{y}{z_1} & \frac{x}{z_1} \\ -\frac{y - y_0}{z_2} & \frac{x - x_0}{z_2} \end{bmatrix} \begin{bmatrix} \Delta x \\ \Delta y \end{bmatrix} = \Delta \mathcal{L}' \begin{bmatrix} 0 \\ 1 \end{bmatrix} - \begin{bmatrix} z_1 \Delta \zeta_1 \\ z_2 \Delta \zeta_2 \end{bmatrix} \quad (G83)$$

$$+ f \begin{bmatrix} +\frac{x}{z_1} \Delta \theta_1 & +\frac{y}{z_1} \Delta \theta_1 \\ +\frac{(x - x_0)}{z_2} \Delta \theta_2 & +\frac{(y - y_0)}{z_2} \Delta \theta_2 \end{bmatrix} \begin{bmatrix} x \\ y \end{bmatrix}$$

where

$$\Delta \mathcal{L}' = -\frac{f}{z_2} (y - y_0) \Delta x_0 + \frac{f}{z_2} (x - x_0) \Delta y_0 \quad (G84)$$

$$- \frac{f}{z_2} x_0 (x - x_0) + y_0 (y - y_0) \Delta \theta_2$$

First, let us consider the effects of  $\Delta \zeta$ . Let  $\epsilon = \text{maximum} (|\Delta \zeta_1|, |\Delta \zeta_2|, |\Delta \eta_1|)$ . Then we let the other errors be zero in equation (G55) and solve for  $\begin{bmatrix} \Delta x \\ \Delta y \end{bmatrix}$ .

$$|\Delta x|_{\zeta} \leq \frac{1}{f(xy_0 - yx_0)} (z_1^2 |x - x_0| + z_2^2 x) \epsilon \quad (G85)$$

$$|\Delta y|_{\zeta} \leq \frac{1}{f(xy_0 - yx_0)} (z_1^2 |y - y_0| + z_2^2 y) \epsilon \quad (G86)$$

From equation (G67) since we used  $\eta_1$

$$\Delta z = \frac{1}{f} \Delta(z_1 \eta_1) = \frac{-1}{f} (z_1 \Delta \eta_1 + \eta_1 \Delta z_1) = -\frac{z_1}{f} \Delta \eta_1 + \frac{z}{z_1} \Delta z_1 \quad (G87)$$

# APPENDIX G

Since by equation (G61)

$$\Delta z_1 = \Delta x \cos \theta + \Delta y \sin \theta - (x \sin \theta - y \cos \theta) \Delta \theta_1 \quad (G88)$$

$$|\Delta z|_{\zeta} \leq \frac{1}{f} \left[ z_1 + \frac{|z|}{xy_0 - yx_0} (z_1 + z_2) \right] \epsilon \quad (G89)$$

Similarly, if  $\epsilon_R = \max (|\Delta x_0|, |\Delta y_0|)$ ,

$$|\Delta x|_R \leq \frac{x}{xy_0 - yx_0} (x - x_0 + |y - y_0|) \epsilon_R \quad (G90)$$

$$|\Delta y|_R \leq \frac{y}{xy_0 - yx_0} (x - x_0 + |y - y_0|) \epsilon_R \quad (G91)$$

$$|\Delta z|_R \leq \frac{z}{xy_0 - yx_0} (x - x_0 + |y - y_0|) \epsilon_R \quad (G92)$$

and if  $\epsilon_\theta = \max (|\Delta \theta_1|, |\Delta \theta_2|)$

$$|\Delta x|_\theta \leq \frac{1}{xy_0 - yx_0} \left[ (x - x_0) (x^2 + y^2) + x(x - x_0)^2 + (y - y_0)^2 \right] \epsilon_\theta \quad (G93)$$

$$|\Delta y|_\theta \leq \frac{1}{xy_0 - yx_0} \left[ (y - y_0) (x^2 + y^2) + y(x - x_0)^2 + (y - y_0)^2 \right] \epsilon_\theta \quad (G94)$$

$$|\Delta z|_\theta \leq \frac{z}{z_1} \frac{1}{zy_0 - yx_0} \left[ (z_2 (x^2 + y^2) + z_1 (x - x_0)^2 + (y - y_0)^2 \right] \epsilon_\theta \quad (G95)$$

Now we would like to combine the  $x, y, z$ , component to find  $|\Delta \underline{R}|$

$$\begin{aligned} |\Delta \underline{R}|_{\zeta} &\leq \frac{z_1}{f} \epsilon + \frac{1}{f(xy_0 - yx_0)} \left\{ z_1^2 \begin{bmatrix} x - x_0 \\ |y - y_0| \\ \frac{|z|}{z_1} z_2 \end{bmatrix} + z_2^2 \begin{bmatrix} x \\ y \\ \frac{|z|}{z_1} \end{bmatrix} \right\} \epsilon \\ &\leq \frac{z_1}{f} \epsilon + \frac{1}{f(xy_0 - yx_0)} (z_1^2 R_2 + z_2^2 R_1) \epsilon \end{aligned} \quad (G96)$$

# APPENDIX G

where

$$R_j = |\underline{R} - \underline{c}_j|, \quad j = 1, 2 \quad (G97)$$

Note that the last inequality is true because  $z_2/z_1 < 1$ .

$$|\underline{\Delta R}|_R \leq \frac{R_1}{xy_c - yx_c} (x - x_c + |y - y_c|) \epsilon_R \quad (G98)$$

$$|\underline{\Delta R}|_\theta \leq \frac{1}{xy_c - yx_c} \left\{ (x^2 + y^2) R_2 + \left[ (x - x_c)^2 + (y - y_c)^2 \right] R_1 \right\} \epsilon_\theta \quad (G99)$$

We can simplify this still further by realizing that

$$z_1^2 \leq x^2 + y^2 \leq R_1^2 \quad \text{and} \quad z_2^2 \leq (x - x_c)^2 + (y - y_c)^2 \leq R_2^2 \quad (G100)$$

Then,

$$|\underline{\Delta R}|_\epsilon \leq \frac{R_1}{f} \left[ 1 + \frac{R_2}{(xy_c - yx_c)} (R_1 + R_2) \right] \epsilon \quad (G101)$$

$$|\underline{\Delta R}|_R \leq \frac{\sqrt{2 R_1 R_2}}{xy_c - yx_c} \epsilon_R \quad (G102)$$

$$|\underline{\Delta R}|_\theta \leq \frac{R_1 R_2}{xy_c - yx_c} (R_1 + R_2) \epsilon_\theta \quad (G103)$$

Further clarification is achieved by noting that

$$xy_c - yx_c = r_c r_1 \sin (\phi_0 - \phi) \quad (G104)$$

where  $r_c = \sqrt{x_c^2 + y_c^2}$  the distance between the cameras;  $r_1 = \sqrt{x^2 + y^2}$ , the length of the projection of  $\underline{R}$  on to the camera plane;  $\phi_0 = \arctan (y_c/x_c)$ , the angle from the x-axis to the line between the two cameras; and  $\phi = \arctan (y/x)$ , the angle from the x-axis to the  $\underline{R}$  projection. For completeness, we repeat that  $R_1$  is the distance from camera 1 to the point of interest ( $|\underline{R}|$ ), and  $R_2$  is the distance from camera 2 to this point. Also,  $f$  is the focal length of both cameras. Let  $R_m = \max (R_1, R_2)$ . Then  $|\underline{\Delta R}|$  becomes:

# APPENDIX G

$$|\Delta \underline{R}|_t \leq \frac{R_m}{f} \left[ 1 + \frac{2R_m^2}{r_0 r_1 \sin(\varphi_0 - \varphi)} \right] \epsilon \quad (G105)$$

$$|\Delta \underline{R}|_R \leq \frac{2R_m^2}{r_0 r_1 \sin(\varphi_0 - \varphi)} \epsilon_R \quad (G106)$$

$$|\Delta \underline{R}|_\theta \leq \frac{2R_m^3}{r_0 r_1 \sin(\varphi_0 - \varphi)} \epsilon_\theta \quad (G107)$$

Typical values.- Along the path under consideration, with the cameras positioned approximately as previously indicated, the values that concern us vary from

$$(R_1 r_1, \varphi_0 - \varphi) = (19, 18.5, \frac{\pi}{3}) \quad (G108)$$

to

$$(R, r, \varphi_0 - \varphi) = (16, 15.5, \frac{\pi}{6}) \quad (G109)$$

These are very rough estimates, but they will give us a good idea of what our error term will be.

At the first point (near the right-hand corner of the room), from equation (G14), with  $f = 0.05$  and  $r_0 = 5$ :

$$|\Delta \underline{R}|_t \leq \frac{19}{0.05} \left[ 1 + \frac{(2)(361)}{(5)(18.5)(0.87)} \right] \epsilon \approx 3800\epsilon \quad (G110)$$

$$|\Delta \underline{R}|_R \leq \frac{(1.4)(361)}{(5)(18.5)(0.87)} \epsilon_R \approx 6.3\epsilon_R \quad (G111)$$

$$|\Delta \underline{R}|_\theta \leq \frac{(7.19)(361)}{(5)(18.5)(0.87)} \epsilon_\theta \approx 170\epsilon_\theta \quad (G112)$$

At the second point (near the other end of the path to be traversed):

$$|\Delta \underline{R}|_t \leq \frac{16}{0.5} \left[ 1 + \frac{(2)(256)}{(5)(15.5)(0.50)} \right] \epsilon \approx 4500\epsilon \quad (G113)$$

$$|\Delta \underline{R}|_R \leq \frac{(1.4)(256)}{(5)(15.5)(0.50)} \epsilon_R \approx 9.3\epsilon_R \quad (G114)$$



# APPENDIX G

$$|\Delta R|_{\theta} \leq \frac{(2.16)(256)}{(5)(15.5)(0.50)} \varepsilon_{\theta} \approx 220 \varepsilon_{\theta} \quad (G115)$$

Recommendations.- It is apparent from the previous discussion that a better relative positioning of  $C_2$  would be with  $x_0 = 0$  (actually moving  $C_1$  to the right so that  $\varphi_0 = \pi/2$ ). This change would not only make  $\sin(\varphi_0 - \varphi)$  larger but would make  $R$  smaller for a given point. The error terms would then become:

$$|\Delta R|_{\zeta} \leq \frac{R}{f} m \left[ 1 + \frac{2R^2}{r_0 r_1 \cos \varphi} \right] \varepsilon \quad (G116)$$

$$|\Delta R|_R \leq \frac{\sqrt{2} R_m^2}{r_0 r_1 \cos \varphi} \varepsilon_R \quad (G117)$$

$$|\Delta R|_{\theta} \leq \frac{2 R_m^3}{r_0 r_1 \cos \varphi} \varepsilon_{\theta} \quad (G118)$$

The points considered in equation (G108) would then become (roughly)

$$(R, r, \varphi_0 - \varphi) = (18, 17.5, \frac{9\pi}{20}) \quad (G119)$$

and

$$(R, r_1, \varphi_0 - \varphi) = (15, 14.5, \frac{\pi}{3}) \quad (G120)$$

respectively. Also  $R$  becomes 4.2. Then for the first point,

$$|\Delta R|_{\zeta} \leq \frac{18}{0.05} \left[ 1 + \frac{(2)(324)}{(4.2)(17.5)(0.98)} \right] \varepsilon \approx 2900 \varepsilon \quad (G121)$$

$$|\Delta R|_R \leq \frac{(1.4)(324)}{(4.2)(17.5)(0.98)} \varepsilon_R = 6.4 \varepsilon_R \quad (G122)$$

$$|\Delta R|_{\theta} \leq \frac{(2.18)(324)}{(4.2)(17.5)(0.98)} \varepsilon_{\theta} = 160 \varepsilon_{\theta} \quad (G123)$$

For the second point:

$$|\Delta R|_{\zeta} \leq \frac{15}{0.05} \left[ 1 + \frac{(2)(225)}{(4.2)(14.5)(0.87)} \right] \varepsilon = 2800 \varepsilon \quad (G124)$$

# APPENDIX G

$$|\Delta R|_R \leq \frac{(1.4)(225)}{(4.2)(14.5)(0.87)} \delta_R = 6.0 \delta_R \quad (G125)$$

$$|\Delta R|_\theta \leq \frac{(2)(3375)}{(4.2)(14.5)(0.87)} \delta_\theta = 10 \delta_\theta \quad (G126)$$

Comparison of these results with those for the original positioning of the camera seems to indicate a significant reduction of error, especially for object positions with large  $y$  values. One might think that making  $x_0 = 0$  would further reduce the error, but space and camera field angle limitations tend to limit the distance we could move  $C_1$  to the right or  $C_2$  to the left. The basic recommendation is, then, to make  $\varphi_0$  as near  $\pi/2$  as possible with respect to the above limitations.

More accurate measurements and use of the more accurate bounds, equations (G12) and G13) give somewhat larger values for the corner point and somewhat smaller ones for the point near the top middle of the room. However, the conclusion is the same. The following upper bounds can be safely assumed with the recommended placement of the cameras:

$$|\Delta R|_z \leq 4000 \text{ } \epsilon \quad (G127)$$

$$|\Delta R|_R \leq 10 \delta_R \quad (G128)$$

$$|\Delta R|_\theta \leq 200 \delta_\theta \quad (G129)$$

To maintain  $|\Delta R|$  less than 1 in., the following conditions must exist:

$$\left. \begin{aligned} t\epsilon &\leq 25 \times 10^{-5} \text{ in.} \\ \delta_R &\leq 0.1 \text{ in.} \\ \delta_\theta &\leq 5 \times 10^{-4} \text{ rad} \end{aligned} \right\} \quad (G130)$$

The conditions (G130) can easily be achieved with modern photogrammetric techniques.

A crude approximation for attitude can be obtained by assuming that the spatial coordinates of two points located on the maneuvering astronaut and placed 1 ft apart have been obtained by

# APPENDIX G

reducing the photographic data as previously assessed. The accuracy of measurement of this system is easily of the order of  $10^{-4}$  in., whence  $|\Delta R|_{\zeta}$  is approximately 0.4 in. for each of the two points and

$$\Delta\theta \leq \tan^{-1} \frac{0.8}{12} = 4^{\circ} \quad (G131)$$

Experimental results.- For the particular experiment conducted with the Martin Marietta Space Operations Simulator (fig. G4), the general equations above reduce to:

$$x = \frac{d}{K}(-f \cos \theta_1 - \zeta_1 \sin \theta_1) \quad (G132)$$

$$y = \frac{d}{K}(-f \sin \theta_1 + \zeta_1 \cos \theta_1) \quad (G133)$$

$$z = \frac{d}{K} \eta_1 \quad (G134)$$

$$d = (-fx_0 + \zeta_2 y_0) \sin \theta_2 + (\zeta_2 x_0 + fy_0) \cos \theta_2 \quad (G135)$$

$$K = (f^2 + \zeta_1 \zeta_2) \sin(\theta_2 - \theta_1) + f(\zeta_1 - \zeta_2) \cos(\theta_2 - \theta_1) \quad (G136)$$

The initial conditions were:

$$\left. \begin{aligned} \theta_1 &= 8.25^{\circ} \\ \theta_2 &= -8.35^{\circ} \\ x_0 &= 0 \\ y_0 &= 48.4 \text{ in.} \\ f &= 0.394 \text{ in.} \\ x &= 166.67 \text{ in.} \\ y &= 24.125 \text{ in.} \end{aligned} \right\} \text{initial distances from camera 1 to target} \quad (G137)$$

The scale factors for the particular X-Y plotter used were established as follows:

$$\zeta_{1s} = f \tan \frac{\theta}{2} = 0.394 \tan 27.45^{\circ} = 0.20448 \text{ in.} \quad (G138)$$

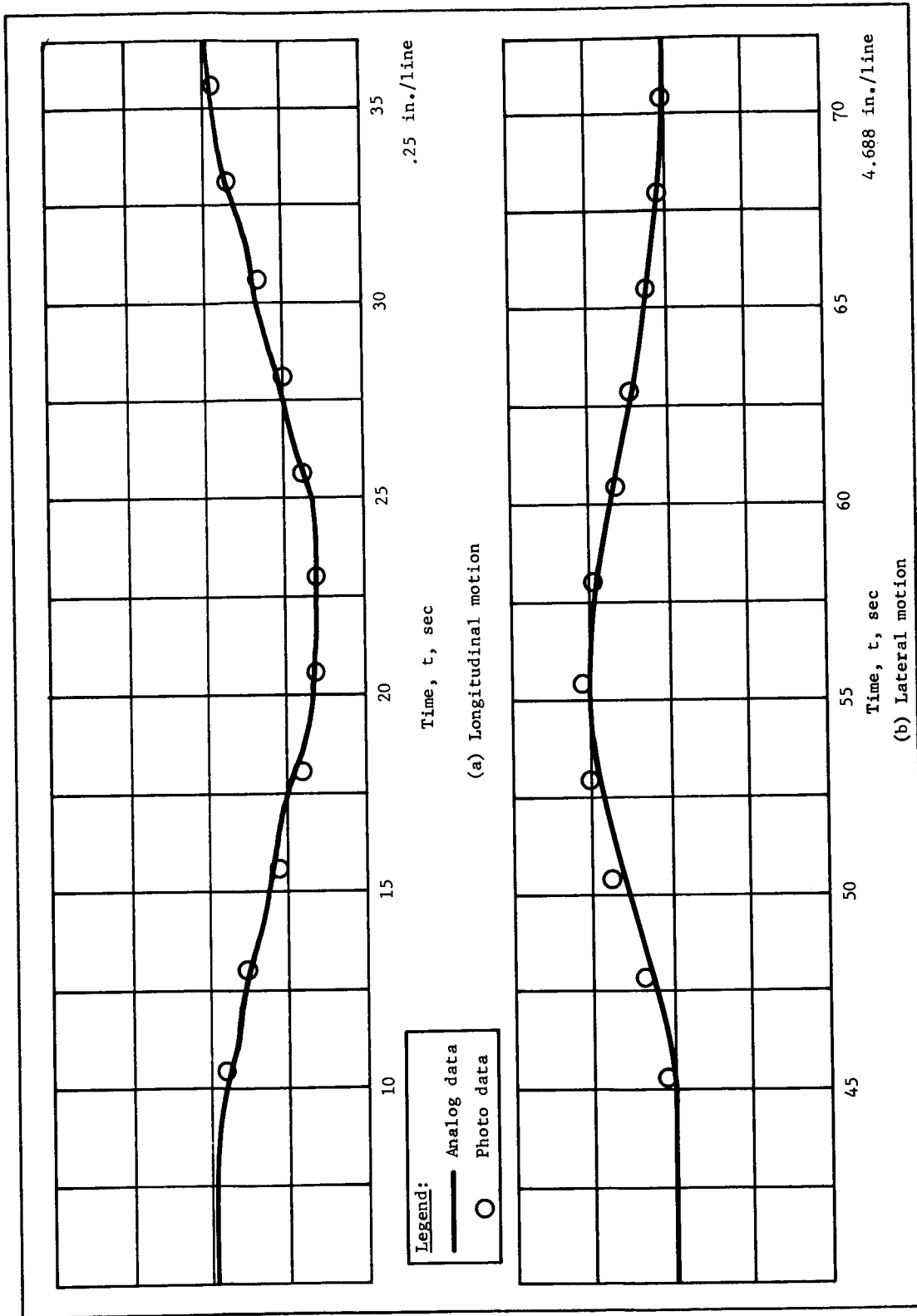


Figure G4.- Simulator-Photo Data Comparison

# APPENDIX G

which is the distance from the optical center to the edge of the film projection in the x direction. The digital readout of the plotter allotted 3000 counts for this distance, thus

$$\zeta_{1s} = \frac{0.20448}{3000} = 682 \times 10^{-7} \text{ in./count} \quad (\text{G139})$$

$$\eta_{1s} = 0.394 \tan 20.45^\circ = 0.147 \text{ in.} \quad (\text{G140})$$

which is the optical center to edge distance in the y direction for which 2205 counts were allotted giving

$$\eta_{1s} = 667 \times 10^{-7} \text{ in./count} \quad (\text{G141})$$

Substituting initial conditions (G137), we obtain

$$\left. \begin{aligned} \mathcal{L} &= 18.9 - 7.03\zeta_2 \\ K &= 0.0443 - 0.2857\zeta_1\zeta_2 + 0.378(\zeta_1 - \zeta_2) \\ x &= \frac{\mathcal{L}}{K} (-0.3905 - 0.1433\zeta_1) \\ y &= \frac{\mathcal{L}}{K} (-0.0565 + 0.989\zeta_1) \\ z &= \frac{\mathcal{L}}{K} \eta_1 \end{aligned} \right\} \quad (\text{G142})$$

A static check with  $\zeta_i = \eta_i = 0$ , yielding

$$\left. \begin{aligned} x_1 &= 166.5 \text{ in.} \\ y_1 &= 24.1 \text{ in.} \\ z_1 &= 0 \end{aligned} \right\} \quad (\text{G143})$$

was made. A direct comparison of the set (G142) with that of (G137) yields a difference

# APPENDIX G

$$\left. \begin{aligned} \epsilon_x &= \frac{0.170}{166.67} \times 100 = 0.102\% \\ \epsilon_y &= \frac{0.025}{24.125} \times 100 = 0.104\% \\ \epsilon_z &= 0 \end{aligned} \right\} \quad (G144)$$

A second static check was made using maximum excursion of the simulator in the lateral direction wherein

$$\left. \begin{aligned} \zeta_1 &= -563 \text{ counts} = 0.0384 \text{ in.} \\ \zeta_2 &= -585 \text{ counts} = 0.0399 \text{ in.} \end{aligned} \right\} \quad (G145)$$

Thus

$$\left. \begin{aligned} x_{LM} &= 166.9 \text{ in.} \\ y_{LM} &= 40.6 \text{ in.} \end{aligned} \right\} \quad (G146)$$

Removing the 24.125-in. initial distance from  $y_{LM}$ , we obtain

$$\left. \begin{aligned} x_{LM} &= 166.9 \text{ in.} \\ y_{LM} &= 16.5 \text{ in.} \end{aligned} \right\} \quad (G147)$$

The analog output data as determined by the simulator was

$$\left. \begin{aligned} x_{LMA} &= 166.5 \text{ in.} \\ y_{LMA} &= 16 \text{ in.} \end{aligned} \right\} \quad (G148)$$

The difference in this case was

$$\left. \begin{aligned} \epsilon_{xm} &= \frac{0.4}{166.5} \times 100 = 0.24\% \\ \epsilon_{ym} &= \frac{15}{16} \times 100 = 3.125\% \end{aligned} \right\} \quad (G149)$$

## APPENDIX G

A final static check using maximum excursion of the simulator in the longitudinal direction yielded the following:

$$\left. \begin{aligned} \zeta_1 &= 128 \text{ counts} \rightarrow 8.73 \times 10^{-3} \text{ in.} \\ \zeta_2 &= -119 \text{ counts} \rightarrow -8.12 \times 10^{-3} \text{ in.} \\ \mathcal{L} &= 18.95 \\ K &= -0.380 \end{aligned} \right\} \frac{\mathcal{L}}{K} = 498 \quad (G150)$$

Thus

$$\left. \begin{aligned} x_M &= (194 - 166.5) = 27.5 \text{ in.} \\ y_M &= 23.9 \text{ in.} \end{aligned} \right\} \quad (G151)$$

and

$$\left. \begin{aligned} x_{MA} &= 27.2 \text{ in.} \\ y_{MA} &= 24.1 \text{ in.} \end{aligned} \right\} \quad (G152)$$

$$\left. \begin{aligned} \epsilon_x &= \frac{0.3}{27.5} \times 100 = 1.09\% \\ \epsilon_y &= \frac{0.2}{23.9} \times 100 = 0.837\% \end{aligned} \right\} \quad (G153)$$

The static checks serve to illustrate the manner in which the data are used with the equations to compute target position and to indicate the level of computation involved as well as to give an estimate on the accuracy obtainable, which in every case was within the required 1 in. or 5%.

The photographic data recorded were subsequently reduced for every 2.5 sec. Figure G4 compares these data with the position data derived from the analog output of the simulator.

Although the experimental results do not appear to be as accurate as the analysis might suggest, there are several reasons giving rise to this difference:

## APPENDIX G

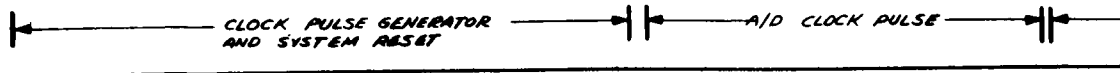
- 1) The initial position coordinates were measured with a steel tape resulting in possible errors in  $\delta_R$  in excess of 0.1 in. Thus,  $\left| \Delta_R \right|_R$  could exceed 1 in.
- 2) There was a slight, but unmeasured, tilt upward of the camera plane (X-Y plane) which was not included in the analysis resulting in errors, in particular for the longitudinal excursion;
- 3) The analog recorder time scale was unduly compressed making direct comparison with photographic data difficult and inaccurate;
- 4) The target identification marker used did not have enough contrast with its surroundings to render it easily identifiable on the film record, which in several instances made accurate interpretation of the photographic data difficult;
- 5) Slide rule accuracy was used on all computations.

These five error sources were not extensively treated nor compensated for because, at this stage of the development, the primary concern was to establish feasibility of the concept only. The fact that despite these obvious error sources the resulting data were better than 95% accurate certainly does serve to establish the feasibility of the photographic technique to obtain APAS data.



APPENDIX H  
DESIGN DRAWINGS REFERENCED IN TEXT

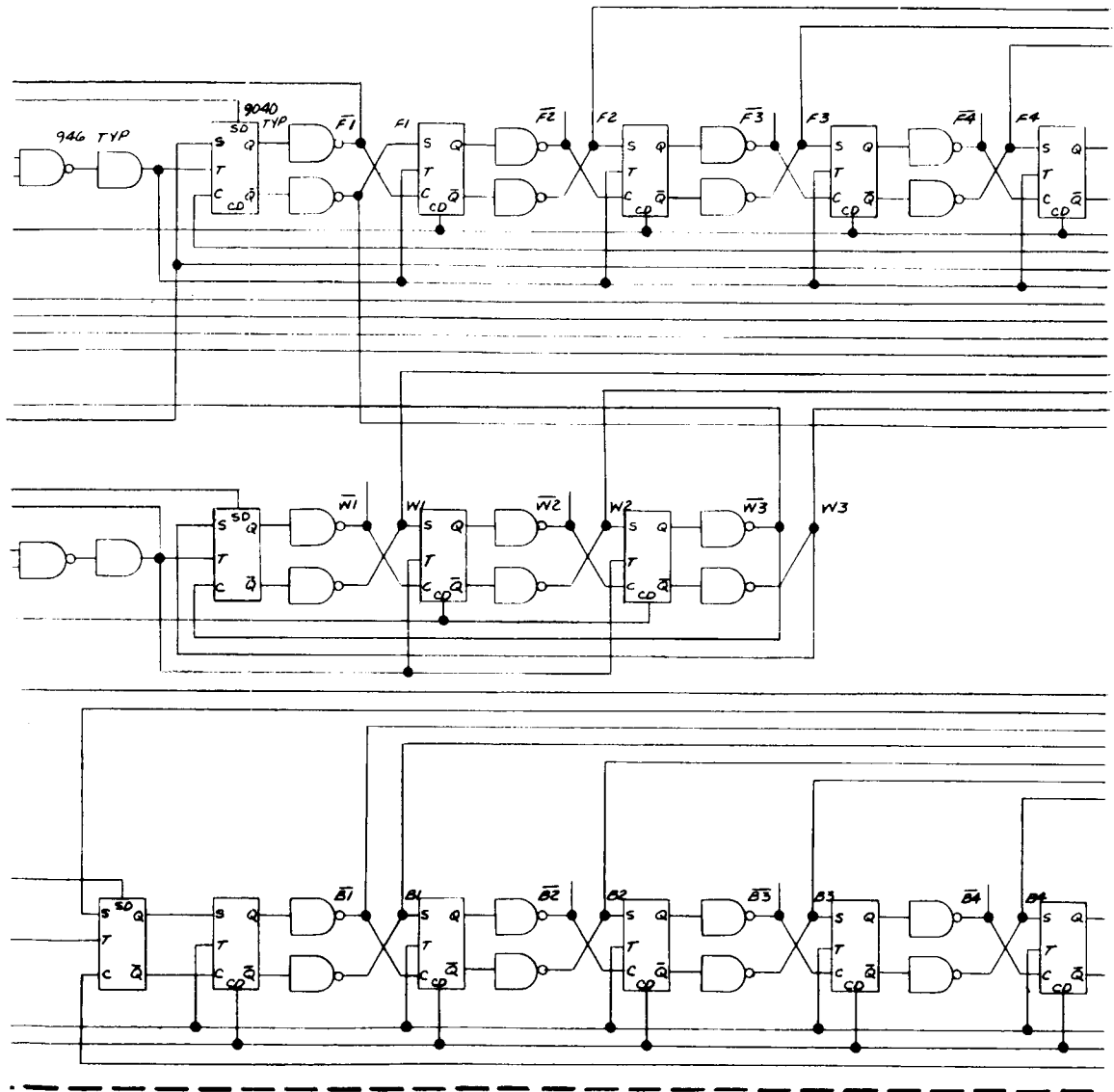
## APPENDIX H



(a)

**SRD727613000**

# APPENDIX H



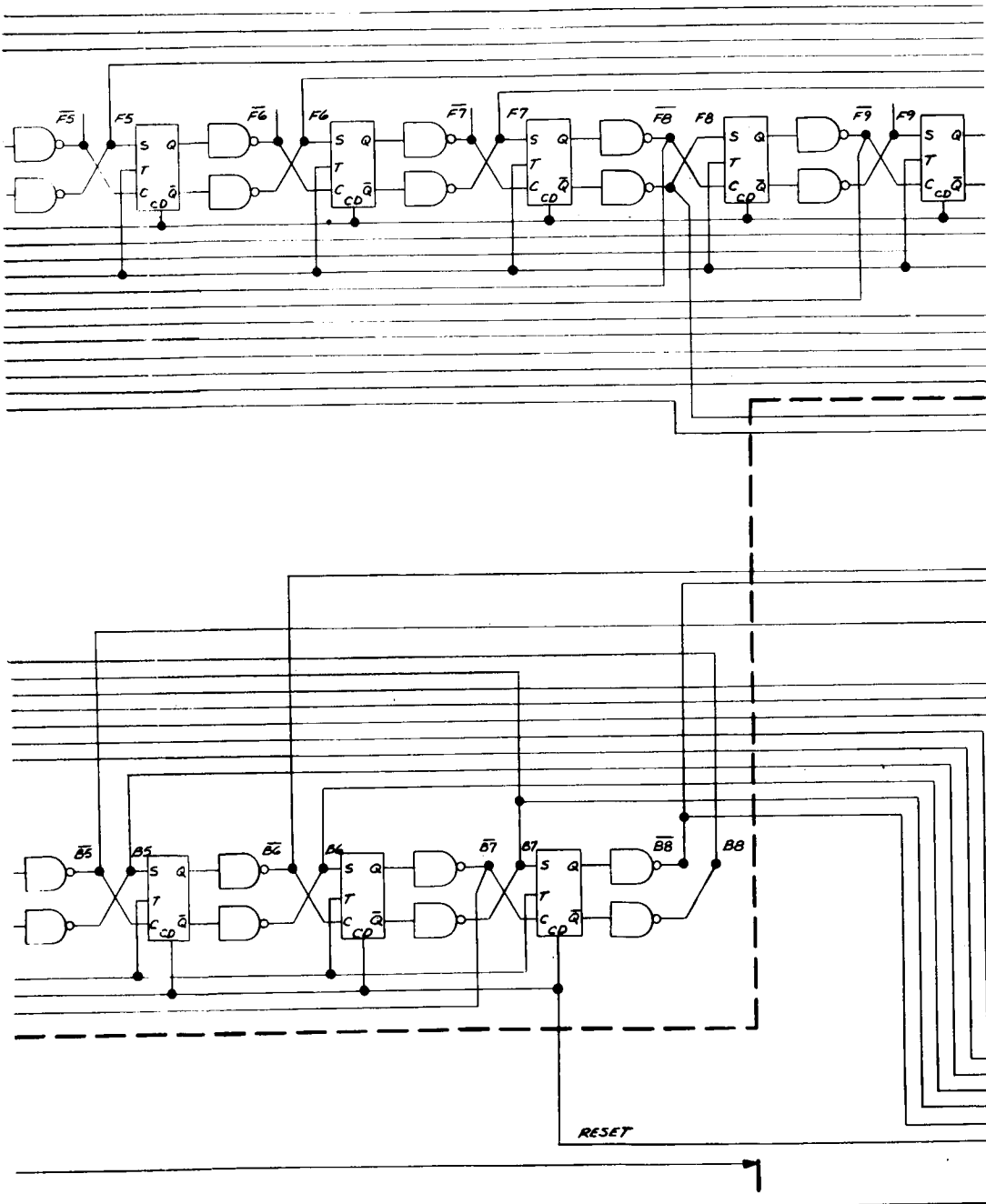
ALL FF LPDTL 9040  
ALL GATES DTL 946

PROGRAMMER

(b)

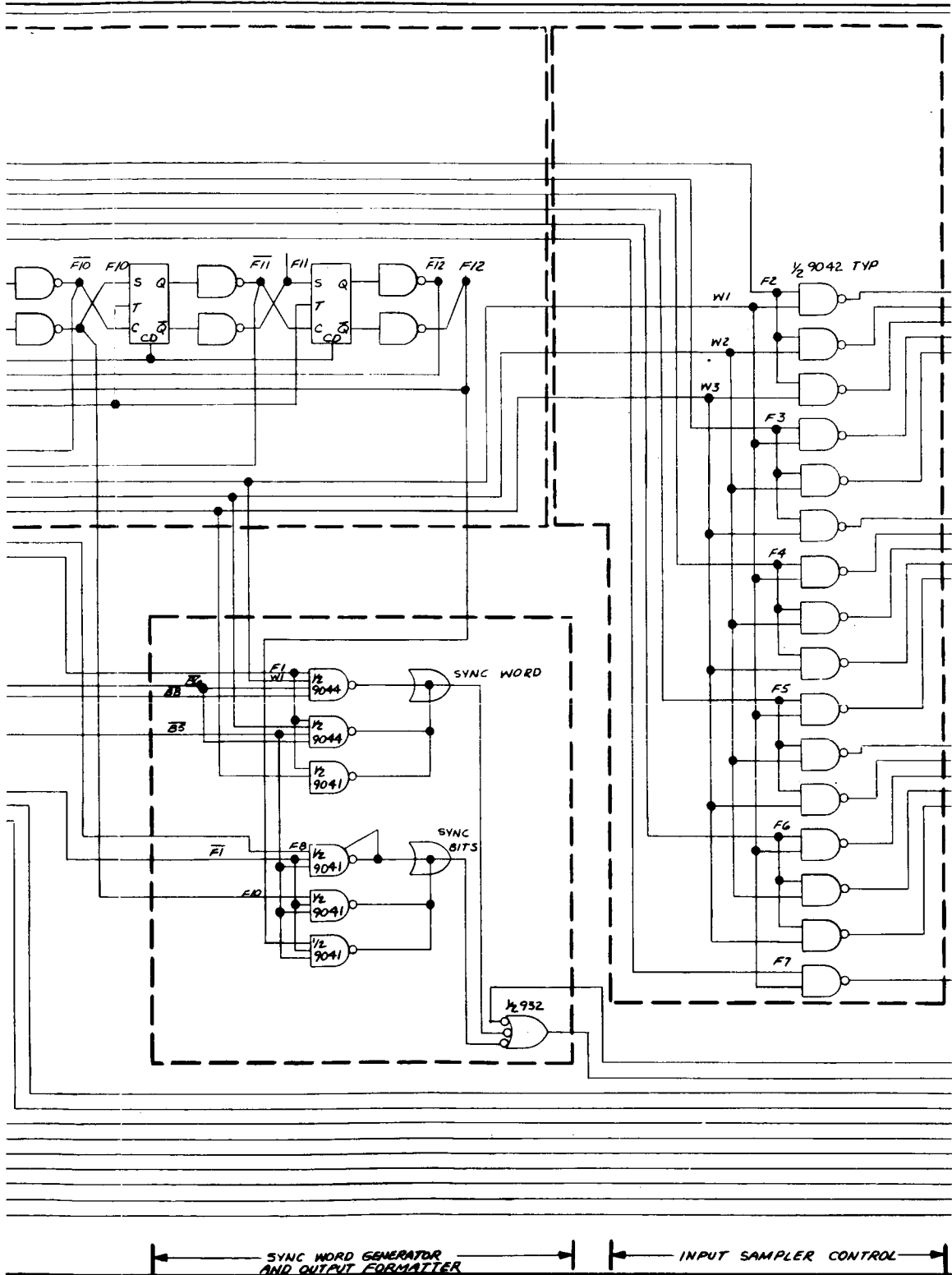
SRD727613000

# APPENDIX H



(c)

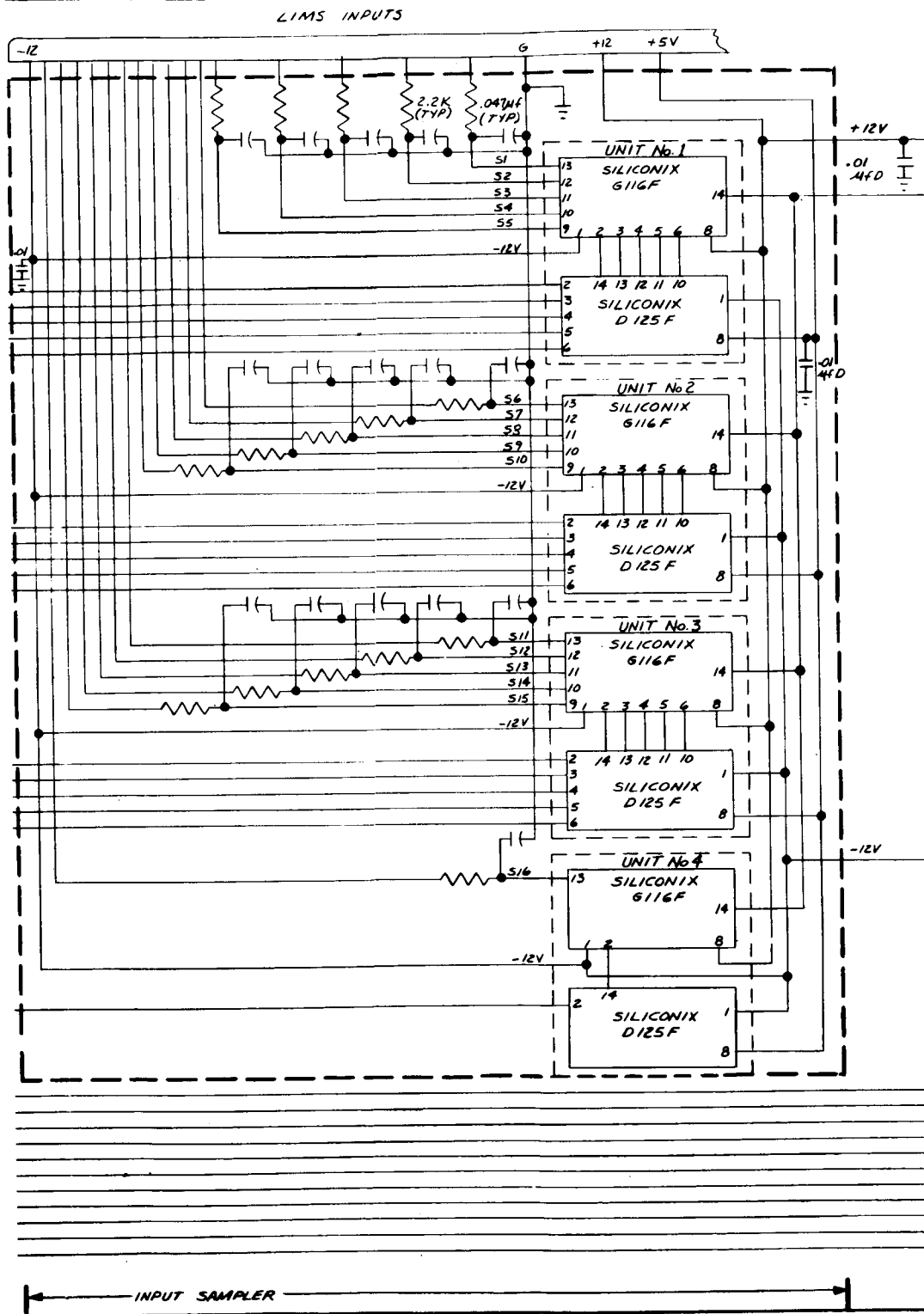
SRD727613000



(d)

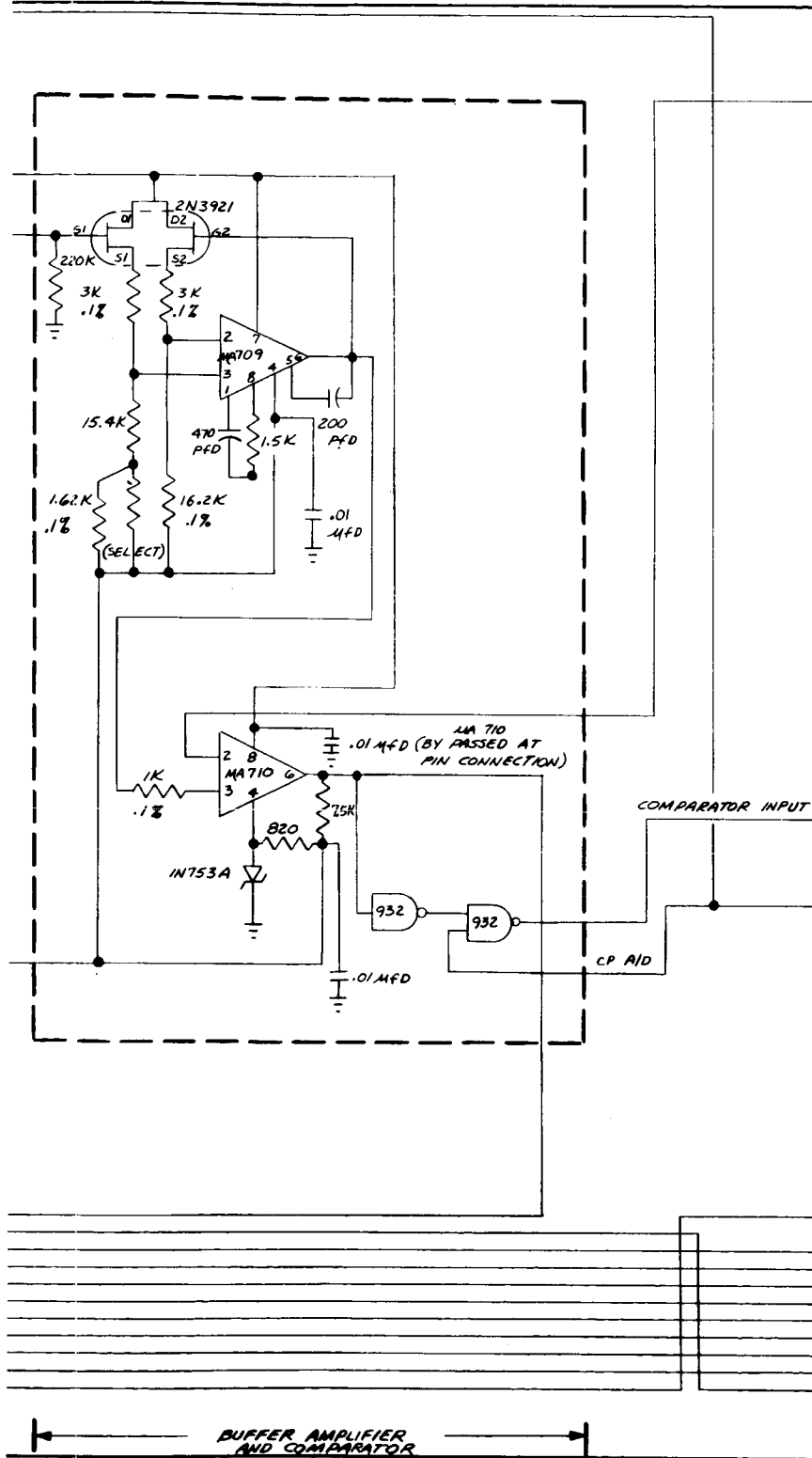
SRD727613000

# APPENDIX H



(e)

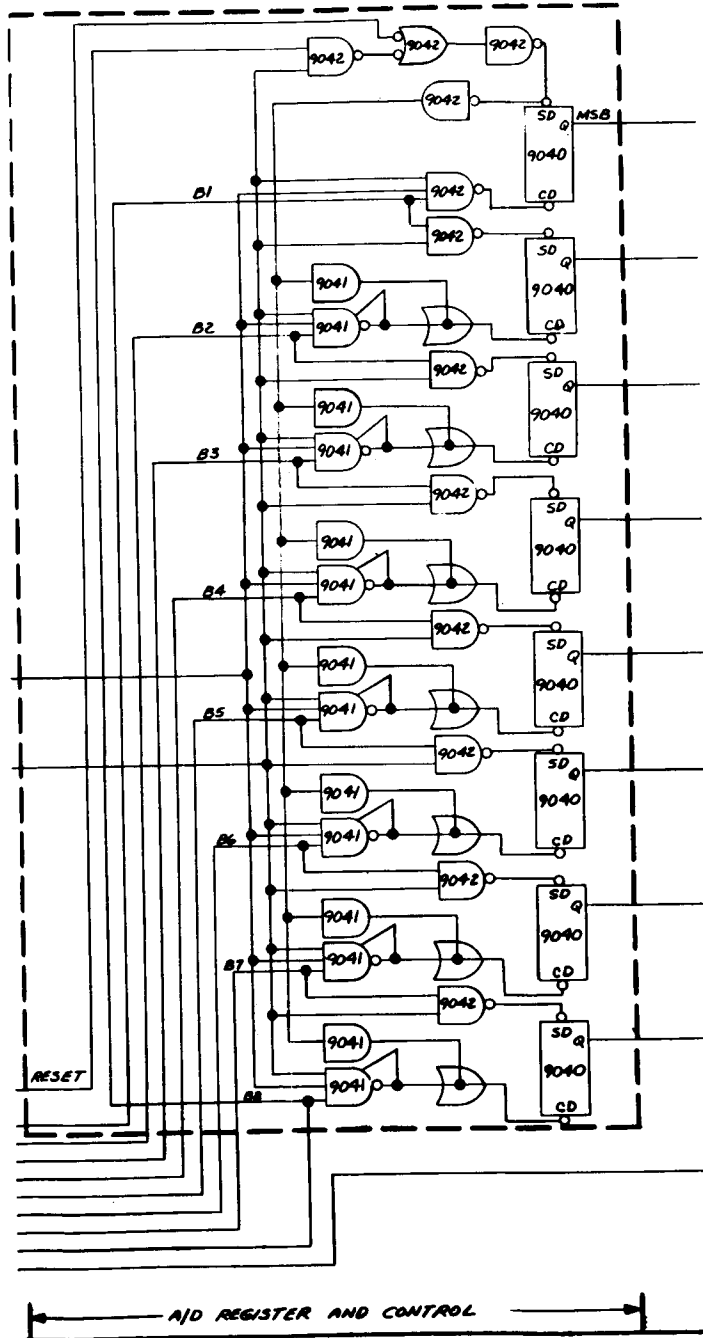
SRD727613000



(f)

SRD727613000

# APPENDIX H

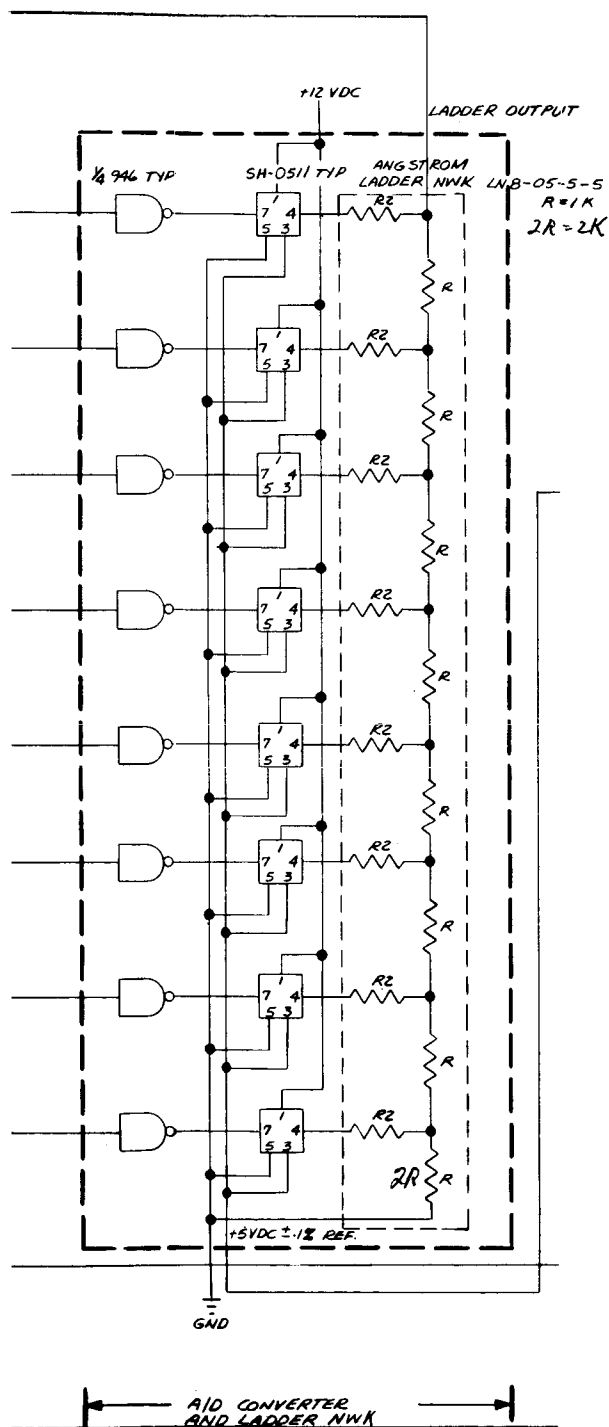


(g)

SRD727613000



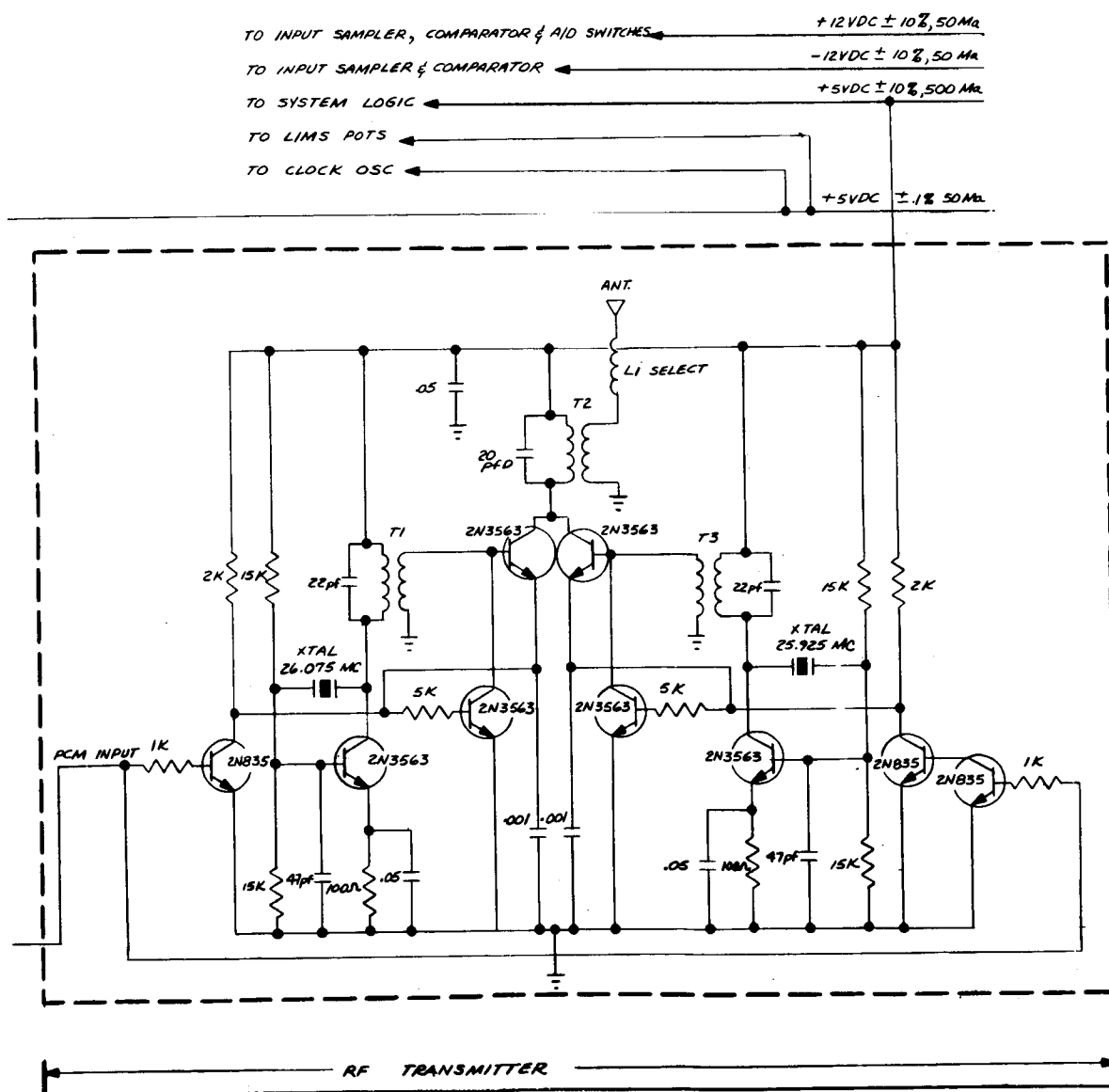
# APPENDIX H



(h)

SRD727613000

## APPENDIX H



(i)

SRD727613000

# APPENDIX H

REVISIONS				
REV	ZONE	DESCRIPTION	DATE	APPROVED

YARDNEY HR-1  
Ag 2a  
BATTERY PACK

## NOTES:

UNLESS SPECIFIED

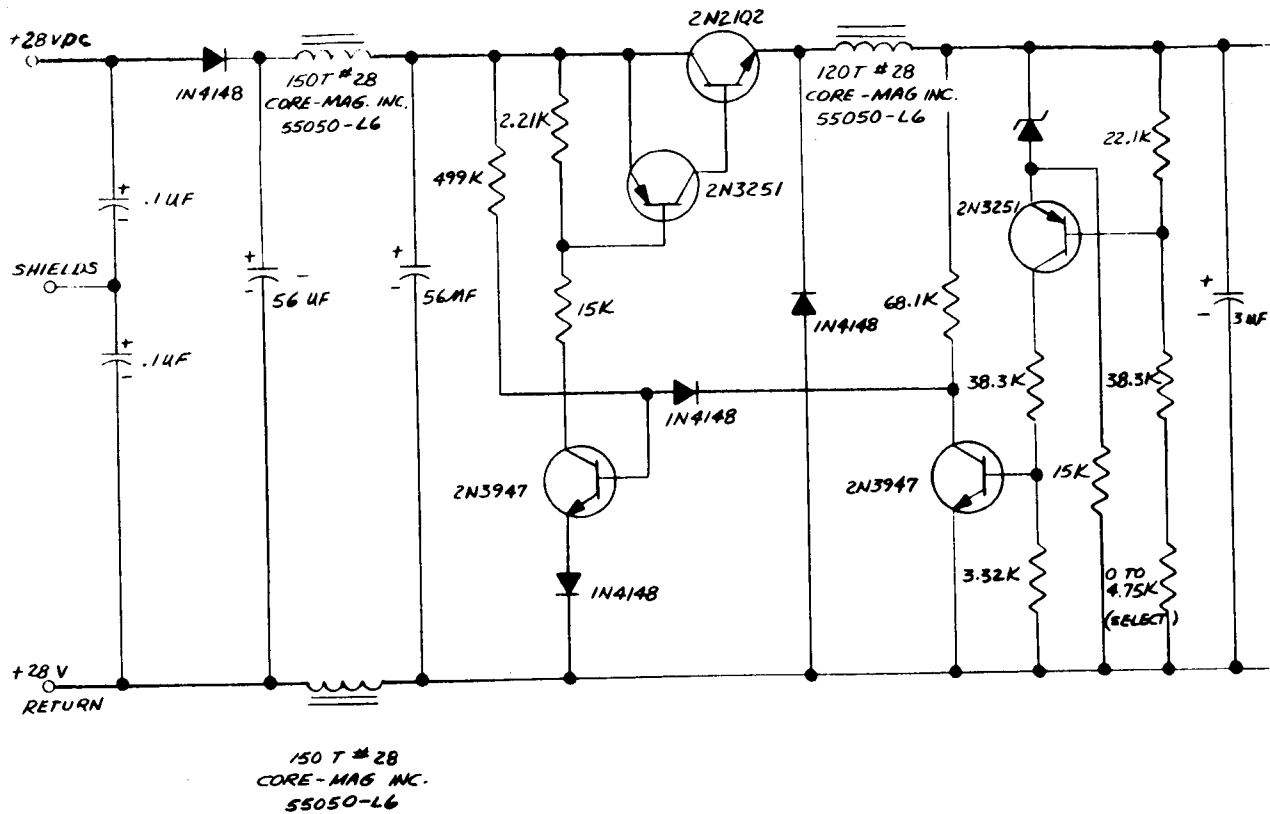
1. ALL RESISTORS 1/4W, 5%
2. ALL CAPACITORS IN MFD.
3. T1, T2 & T3 - PRIMARY 15 TURNS # 32 WIRE  
SECONDARY 4 TURNS # 32 WIRE  
WOUND ON PERMACOR X-7889.
4. XMTR ANTENNA - LOOP ON ASTRONAUT SUIT.
5. L1 LOADING COIL ADJUSTED IN FINAL PACKAGE.
6. +5 VDC MUST BE CONNECTED TO SYSTEM LOGIC.  
REFER TO MFR DATA SHEET.
7. ALL FLAT PACKS ARE FAIRCHILD DTL & LPDTL.  
UNIDENTIFIED FLAT PACK PIN INTERCONNECTIONS  
WILL BE SPECIFIED WHEN PACKAGING BOARD  
LAYOUT IS COMPLETED.

DESIGNED BY <b>E. MARTINEZ 1620</b>	DATE <b>11-1-67</b>	MARTIN BARRITT CORPORATION DENVER DIVISION P.O. BOX 170 DENVER, COLORADO	
CHECKED BY <b>H. J. MARR</b>	SYNOPSIS CHG.	ASTRONAUT DATA ACQUISITION AND TRANSMISSION SUBSYSTEM	
BY NAME	BY NAME		
RELIABILITY	RELIABILITY		
MR. ENGINEER <b>H. J. MARR</b>	MR. ENGINEER <b>H. J. MARR</b>		
DATE <b>11-1-67</b>	DATE <b>11-1-67</b>	SIZE <b>04236</b>	CODE IDENT NO. <b>SRD727613000</b>
CUST. REQ.	CUST. REQ.	SCALE	UNIT <b>1001</b>

(j)

SRD727613000

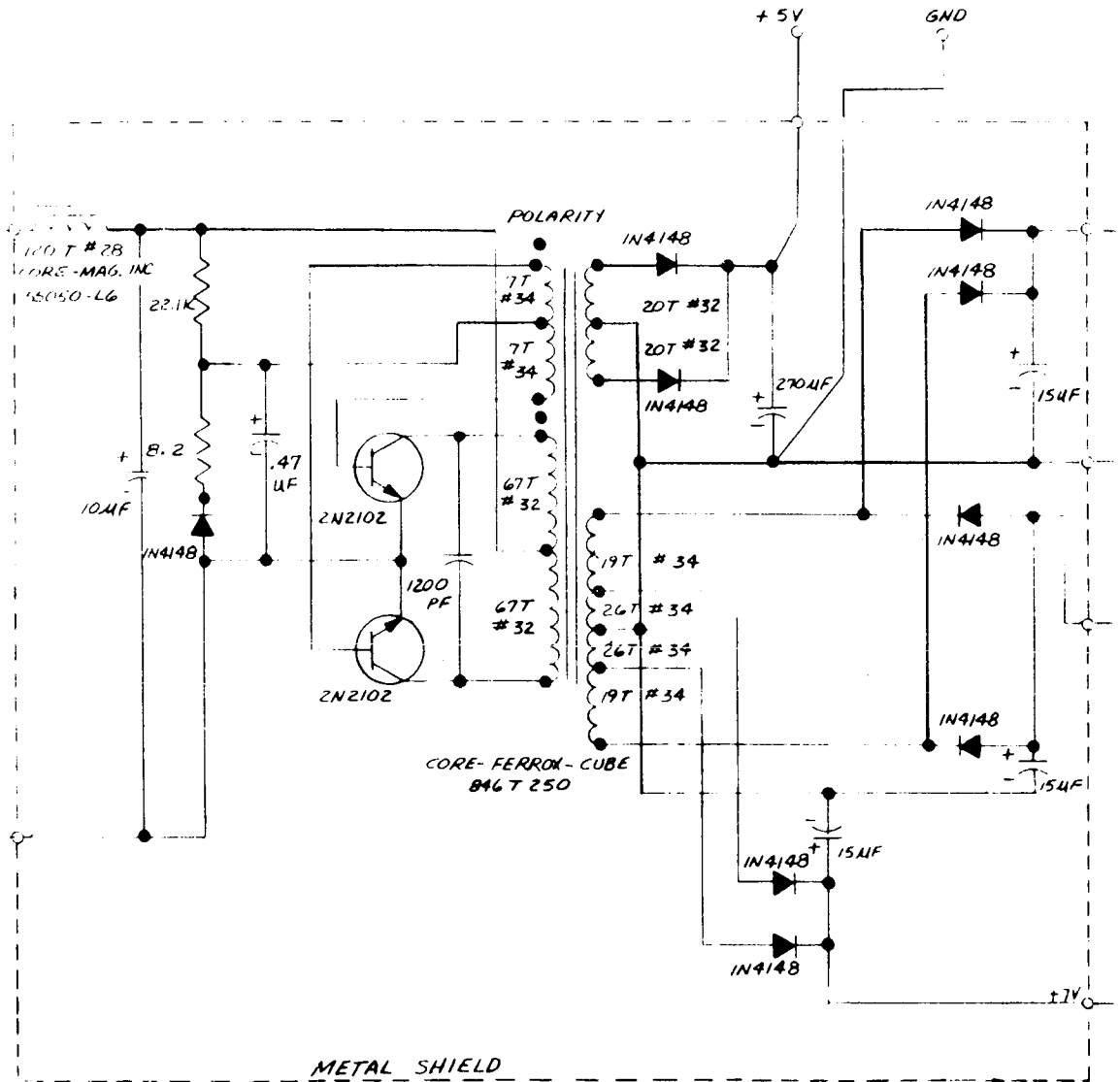
# APPENDIX H



(a)

SRD727613600

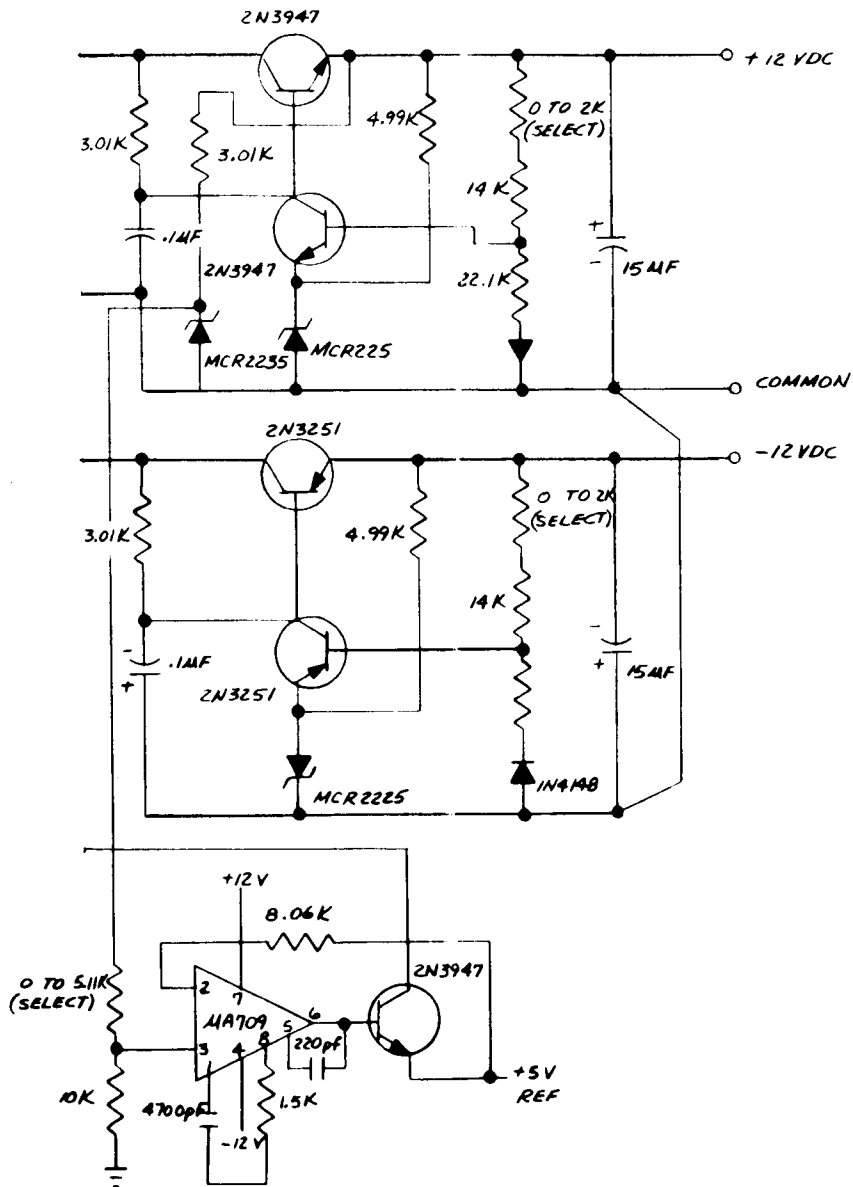
# APPENDIX H



(b)

SRD727613600

# APPENDIX H



(c)

SRD727613600

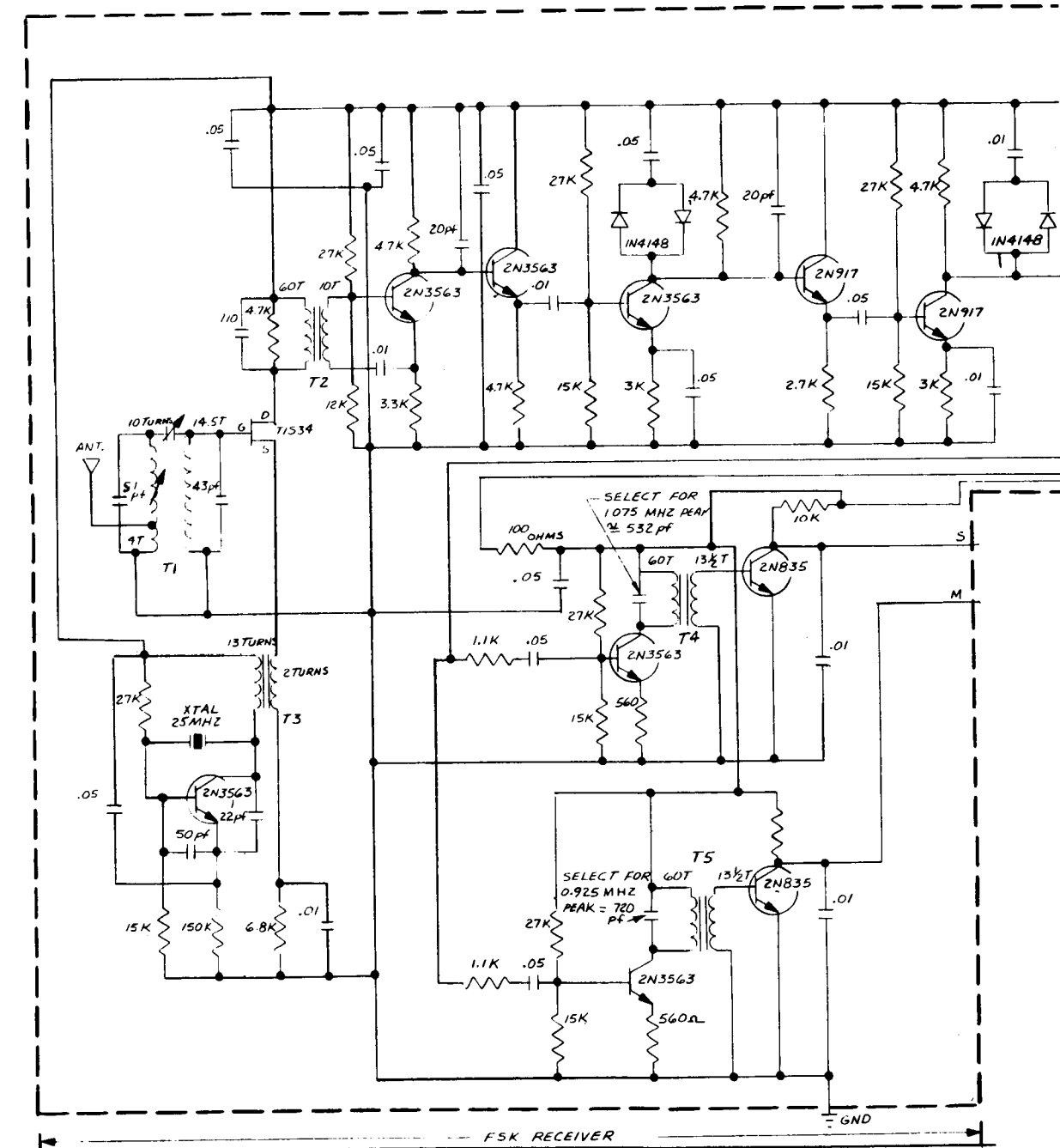
# APPENDIX H

NOTE:  
ALL RESISTORS  $\frac{1}{8}$  W 1% METAL FILM.

DRAWN BY <b>E. MARTINEZ KEO 11-1-67</b>		DEPT.		DATE		MARTIN MARIETTA CORPORATION DENVER DIVISION P.O. BOX 170 DENVER, COLORADO	
CHECKER						SYSTEM DATA SYNTHESIZER - POWER SUPPLY	
STRESS ENGR.							
ST. ENGR.							
MATH. ENGR.							
RELIABILITY							
DR. ENGR. <b>The J. M. M. PE.</b>		SIZE		CODE IDENT. NO.		PART NO.	
PREPARED BY <b>C. H. M. 11-8-67</b>				<b>04226</b>		<b>SRD727613600</b>	
COPY. REP.		SCALE				TOLER.	

(d)

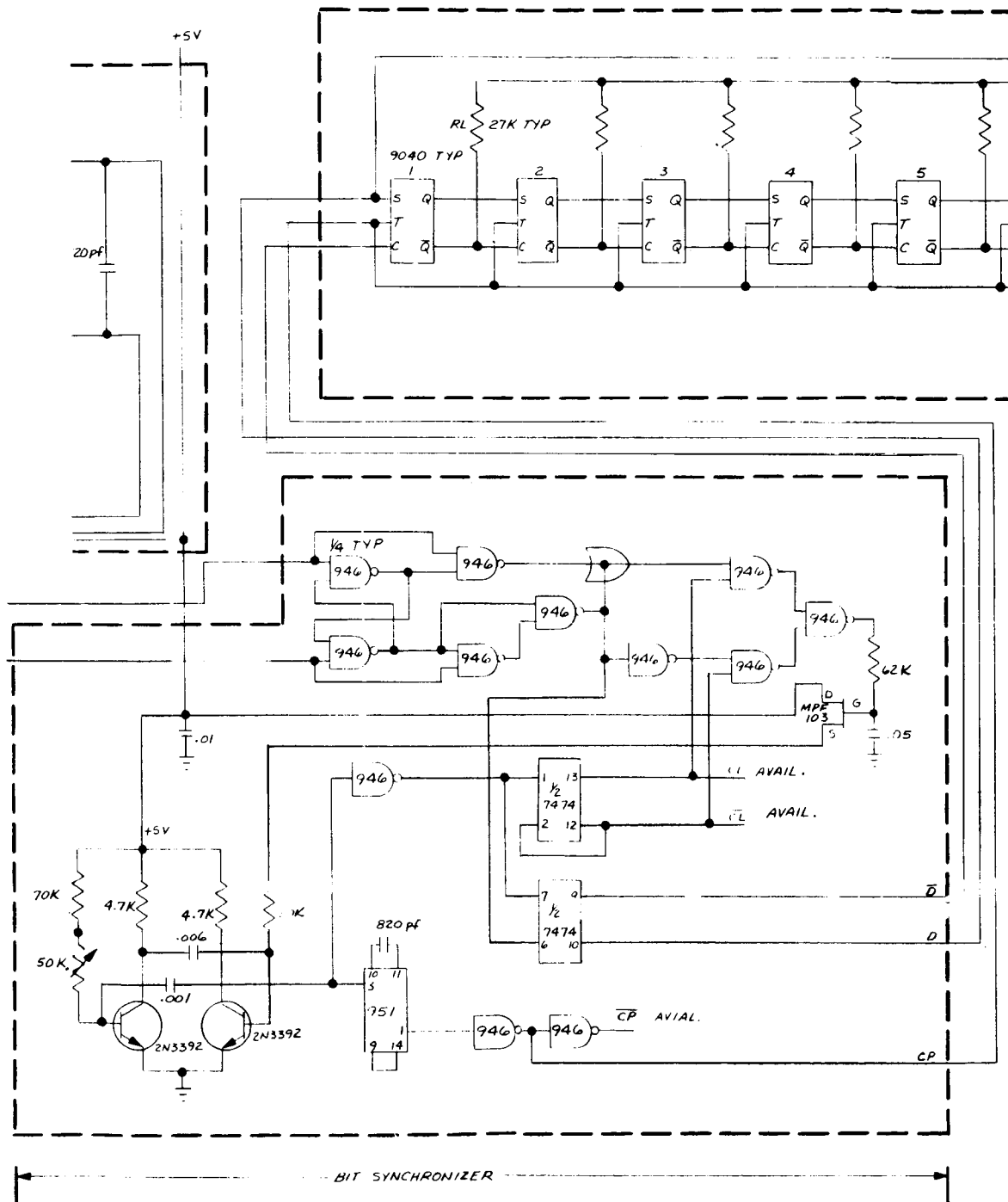
SRD727613600



(a)

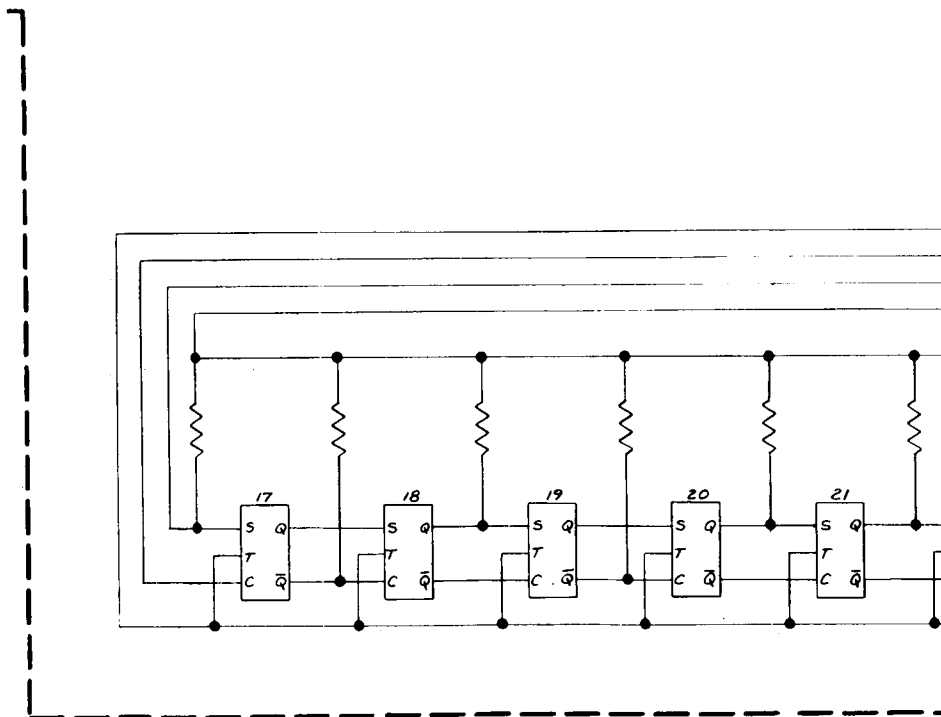
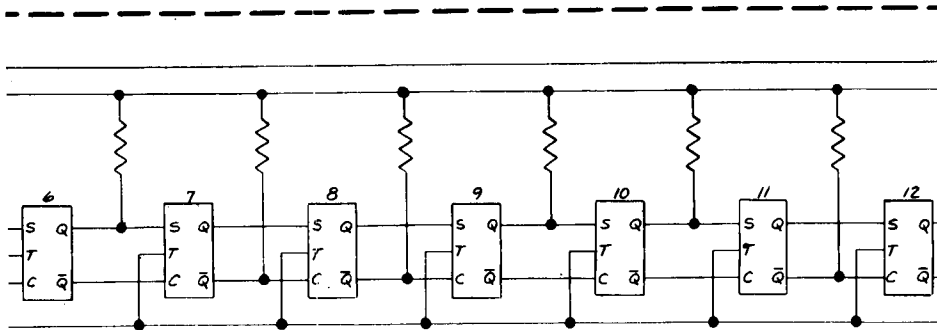
SRD727613800, sheet 1 of 2





(b)

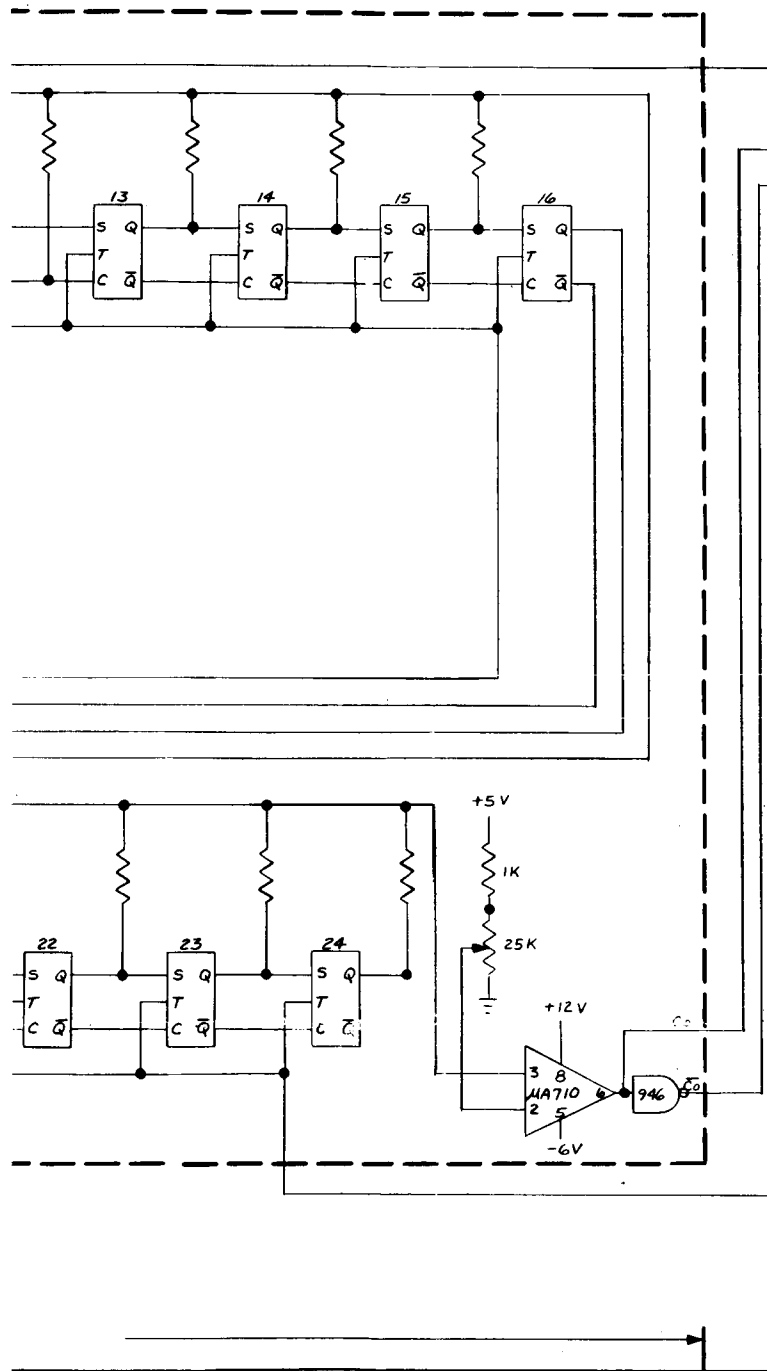
# APPENDIX H



← FRAME SYNCHRONIZER

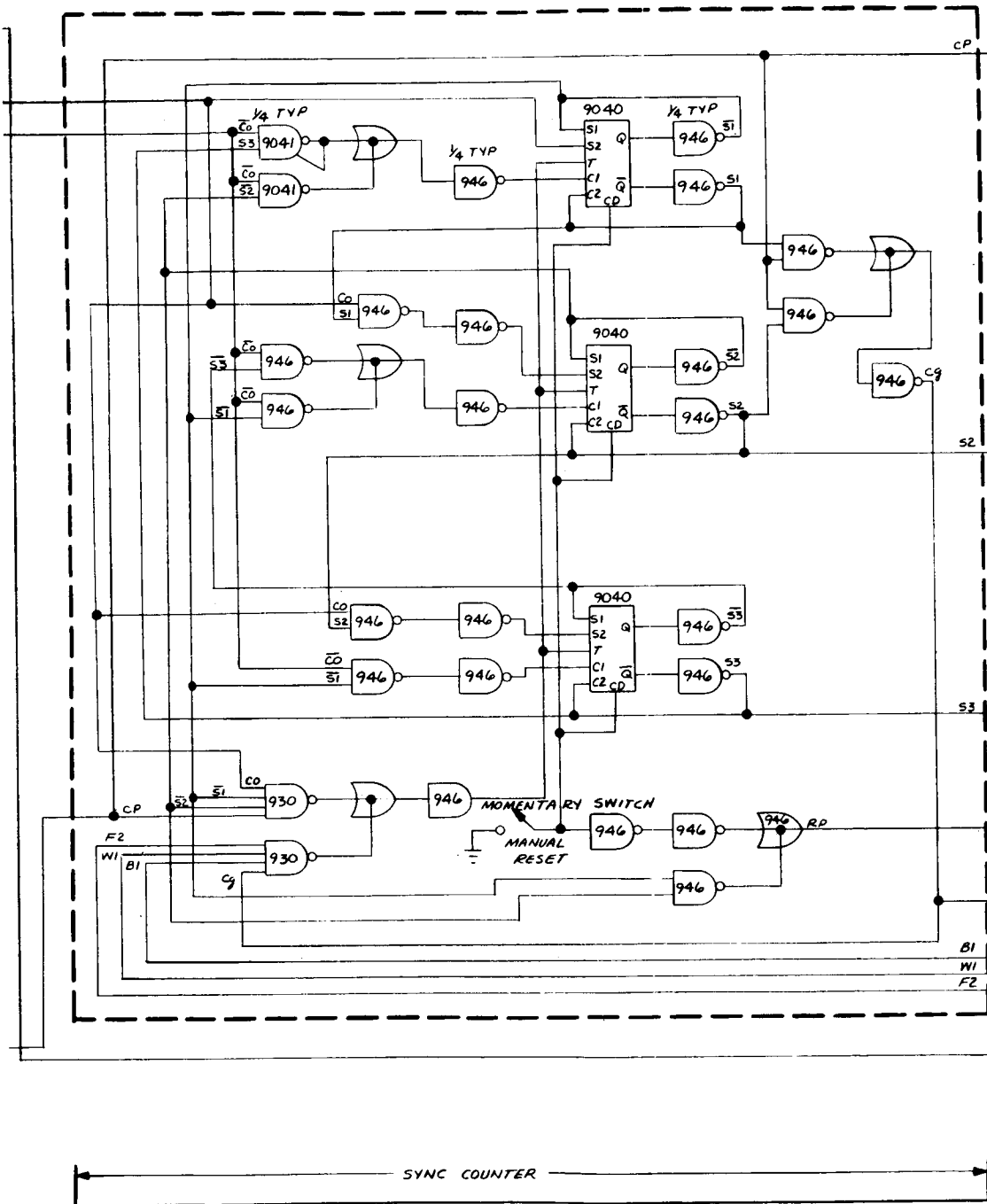
(c)

SRD727613800, sheet 1 of 2



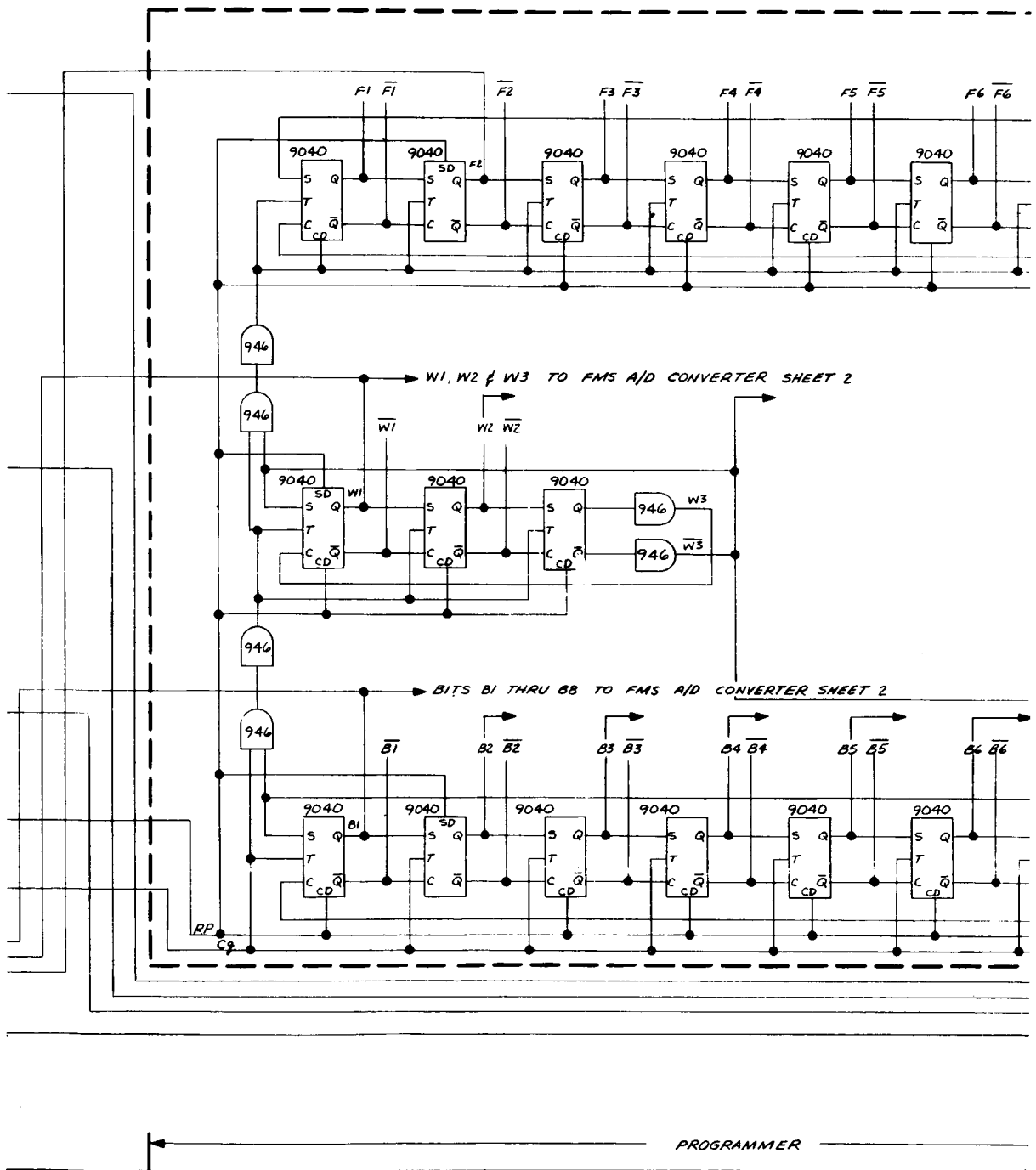
(d)

# APPENDIX H



(e)

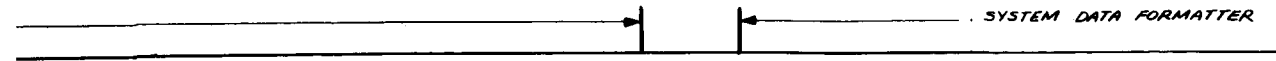
SRD727613800, sheet 1 of 2



(f)

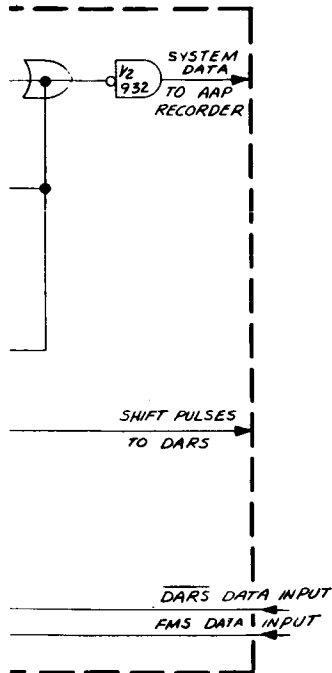
SRD727613800, sheet 1 of 2

\_\_\_\_\_



# APPENDIX H

REVISIONS				
SYM	DATE	DESCRIPTION	DATE	APPROVED



## NOTES:

UNLESS SPECIFIED

1. ALL RESISTORS  $\frac{1}{8}$  W, 5%.
2. ALL CAPACITORS IN MFD.
3. T1, T2, T3, T4 & T5 TURNS REQ'D INDICATED IN DWG. T1 WOUND ON CAMBRIDGE THERMIONIC FORM 1304-A, T2 THRU T5 WOUND ON PERMCOR FORM X-7889.
4. RCVR ANTENNA DESIGN IS CROSSED SLOT CIRCULAR POLARIZATION
5. A/D CONVERTER FOR FORCE MEASURING UNIT ON SEPARATE SHEET SIGNALS TO A/D CONVERTER FROM SHEET 3 ARE BITS B1 THRU B8, W1, W2 & W3, F9 THRU F12 AND CP.
6. ALL FLAT PACKS ARE FAIRCHILD DTL & LPDTL
7. UNIDENTIFIED FLAT PACK PIN INTERCONNECTIONS WILL BE SPECIFIED WHEN PACKAGING BOARD LAYOUT IS COMPLETED.
8. +5 VDC MUST BE CONNECTED TO SYSTEM LOGIC, REFER TO MFR DATA SHEET.

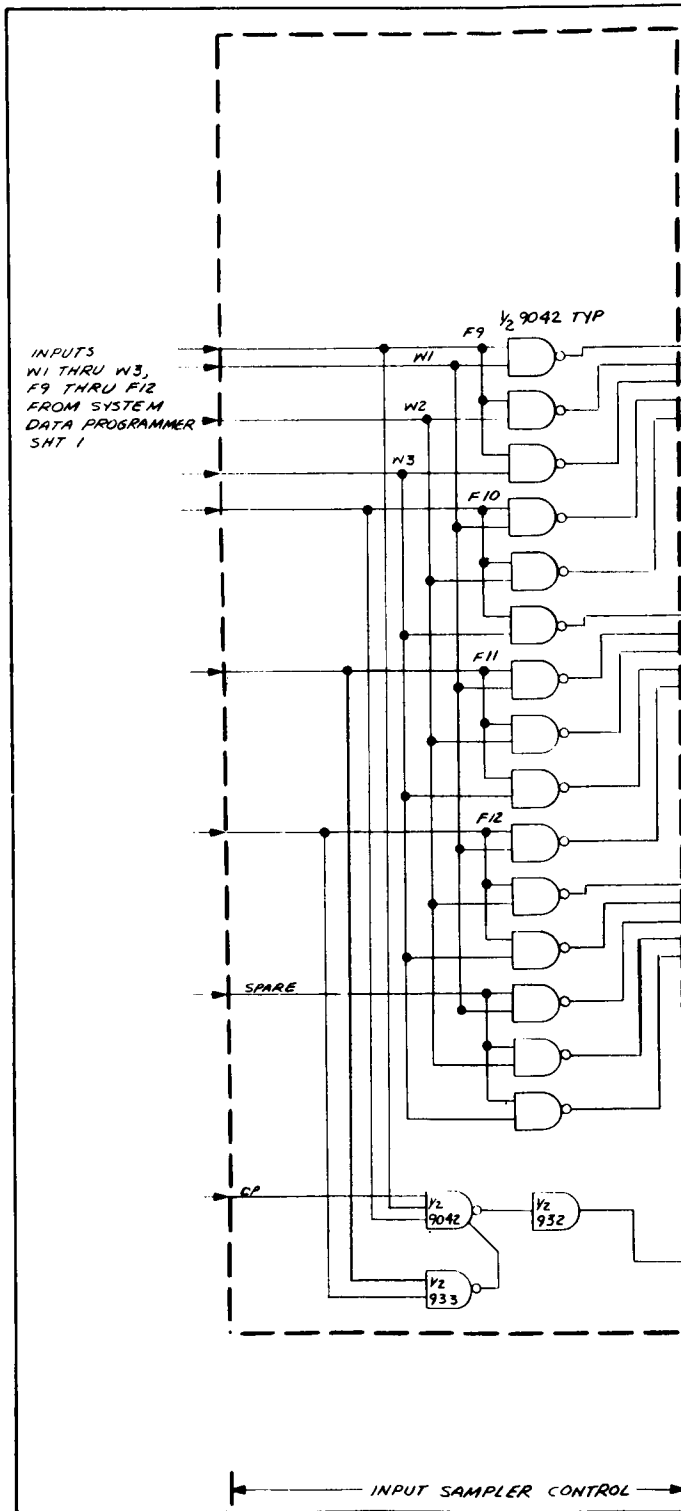
SHEET 2

DRAWN BY <b>E. MARTINEZ</b>		DATE <b>14-67</b>	
CHECKED BY 			
STRESS ENGR 			
WY. ENGR 			
MATH. ENGR 			
RELIABILITY 			
DR. ENGR <b>H. J. NIEL, P.E.</b>			
PROJECT <b>CN Models 11-N-67</b>			
CUST. REP. 			
MARTIN COMPANY THE AEROSPACE DIVISION OF MARTIN MARIETTA CORPORATION FRIENDSHIP INTERNATIONAL AIRPORT, MARYLAND		RF RECEIVER AND SYSTEM DATA SYNTHESIZER	
CODE IDENT NO <b>38507</b>	SIZE <b>SRD727613800</b>		
SCALE 	SHEET 1 of 2		

(h)

SRD727613800, sheet 1 of 2

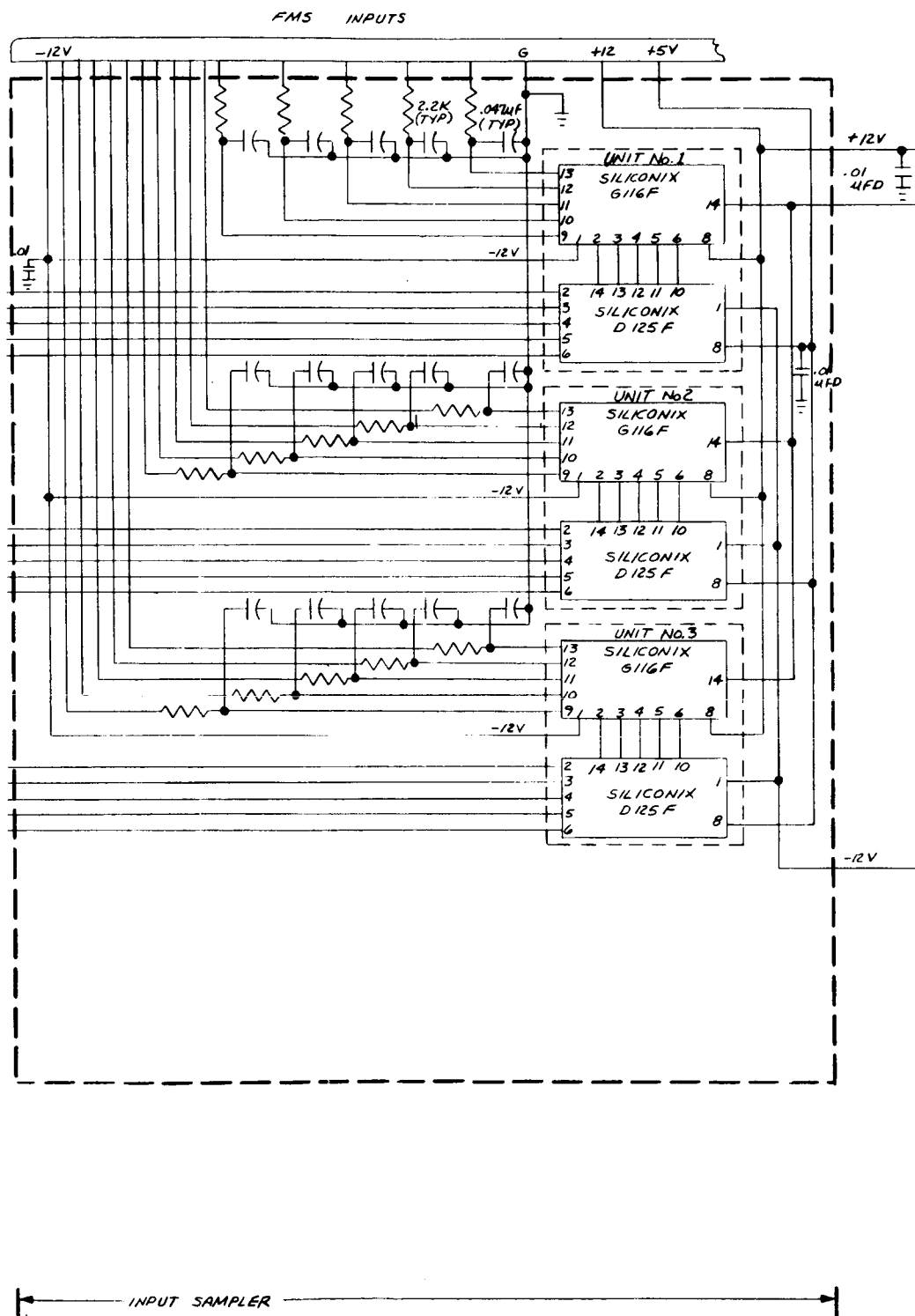
# APPENDIX H



SRD727613800, sheet 2 of 2



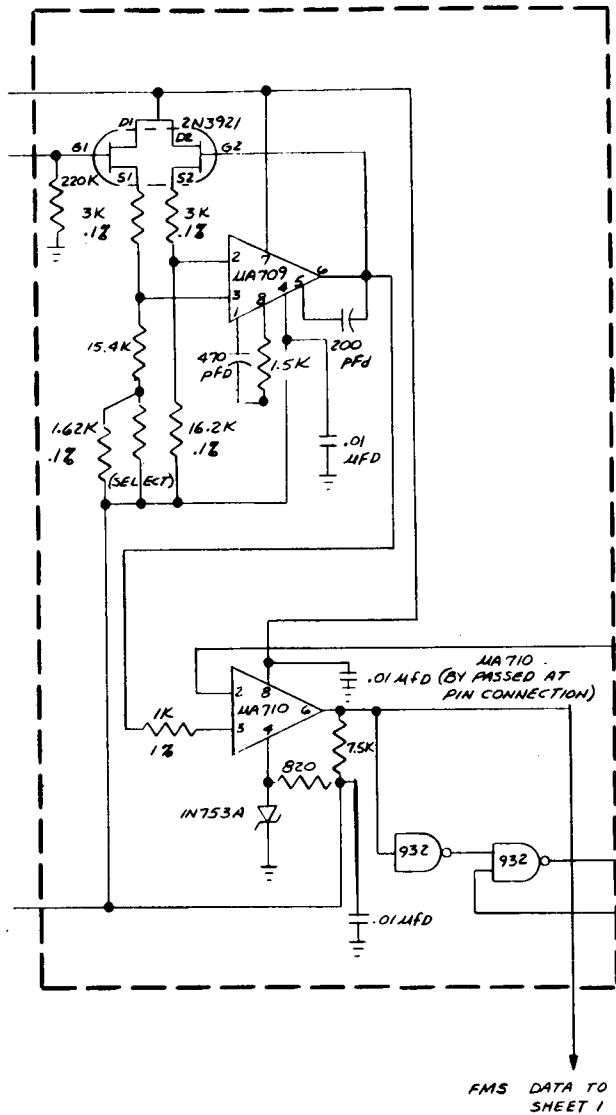
# APPENDIX H



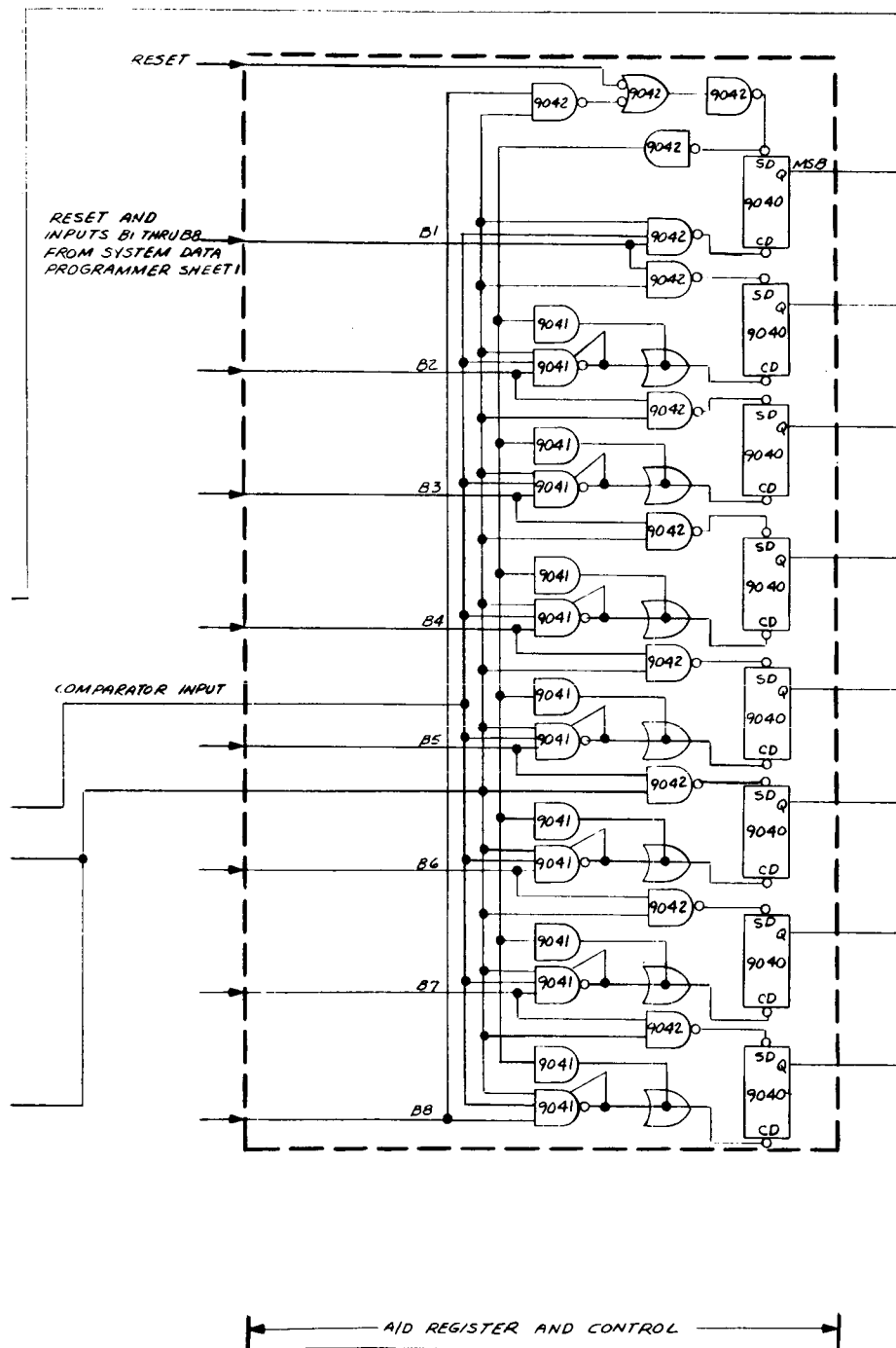
(b)

SRD727613800, sheet 2 of 2

# APPENDIX H



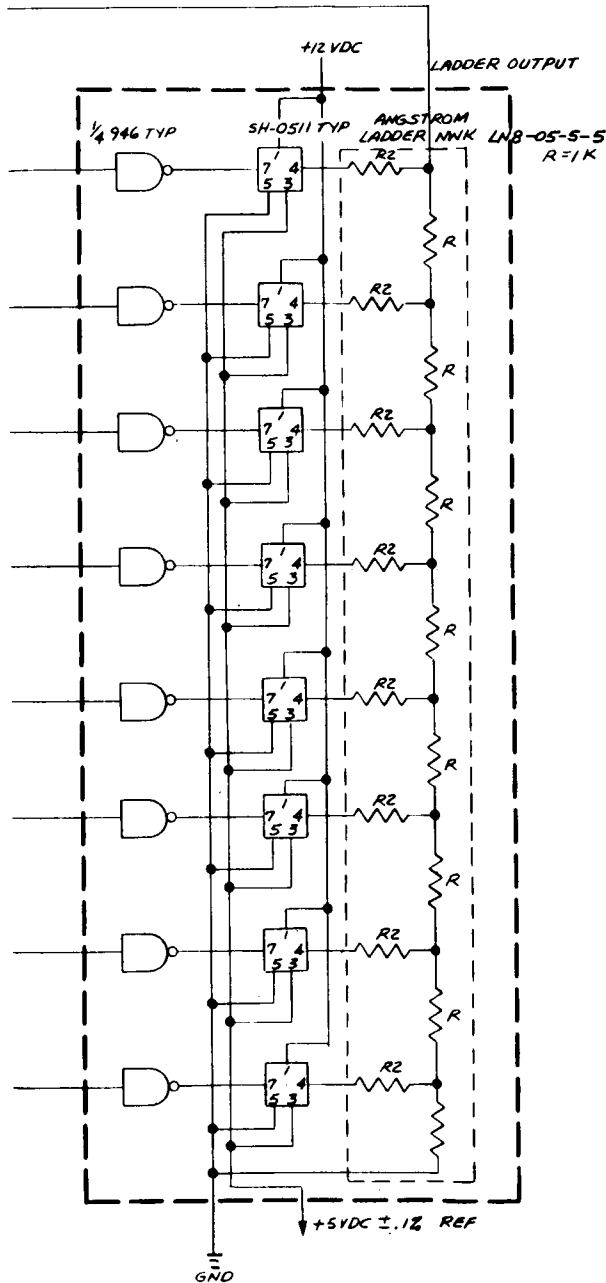
BUFFER  
 (c)



(d)

SRD727613800, sheet 2 of 2

# APPENDIX H



A/D CONVERTER AND LADDER NWK  
(e)

SYB		ROW	DESCRIPTION	DATE	APPROVED

NOTE;  
ALL POWER SUPPLY VOLTAGES COME  
FROM SRD727613600.

RF RECEIVER AND  
SYSTEM DATA SYNTHESIZER  
FMS A/D CONV.

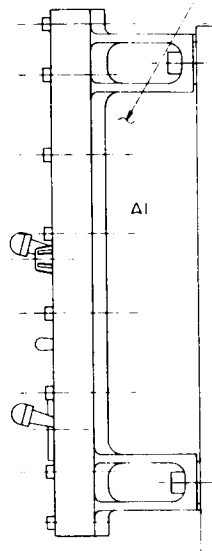
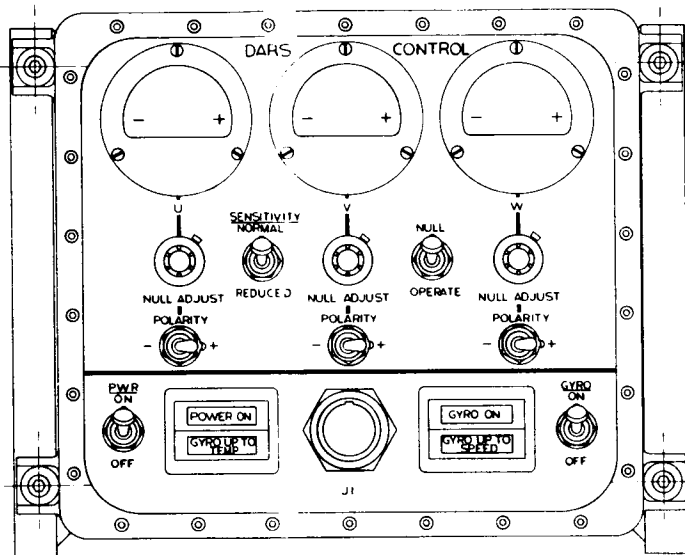
SRD727613800	2
--------------	---

(f)

SRD727613800, sheet 2 of 2

# APPENDIX H

①  
② 4 REQD



(a)

SRD727610000

Technical drawing of a mechanical assembly, showing three views: front, top, and side.

**Front View (Top):** Shows a rectangular block with a central cutout. The cutout is labeled **A4**. The block has a flange on the left side. A dimension line indicates a width of **100**. A callout **② 4 REQD** points to the top surface.

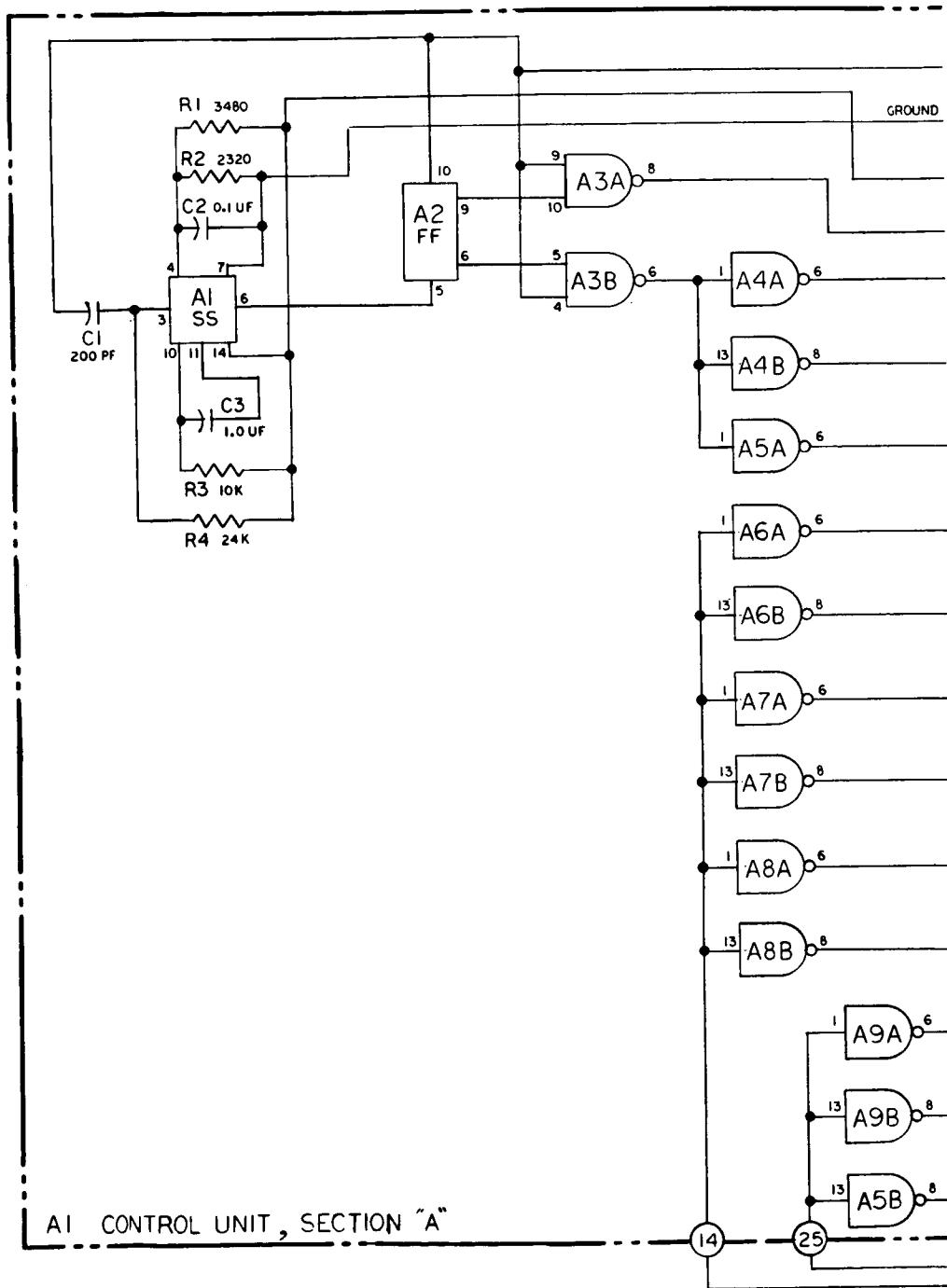
**Top View (Bottom):** Shows a trapezoidal shape with a central rectangular area. The central area is labeled **A3**. The shape has a flange on the left side. A dimension line indicates a width of **100**. A callout **⑤** points to the bottom surface.

**Side View (Right):** Shows a rectangular block with a central cutout. The cutout is labeled **A4**. The block has a flange on the left side. A dimension line indicates a width of **100**. A callout **③ 4 REQD** points to the top surface.

[illegible]

SRD727610000

# APPENDIX H

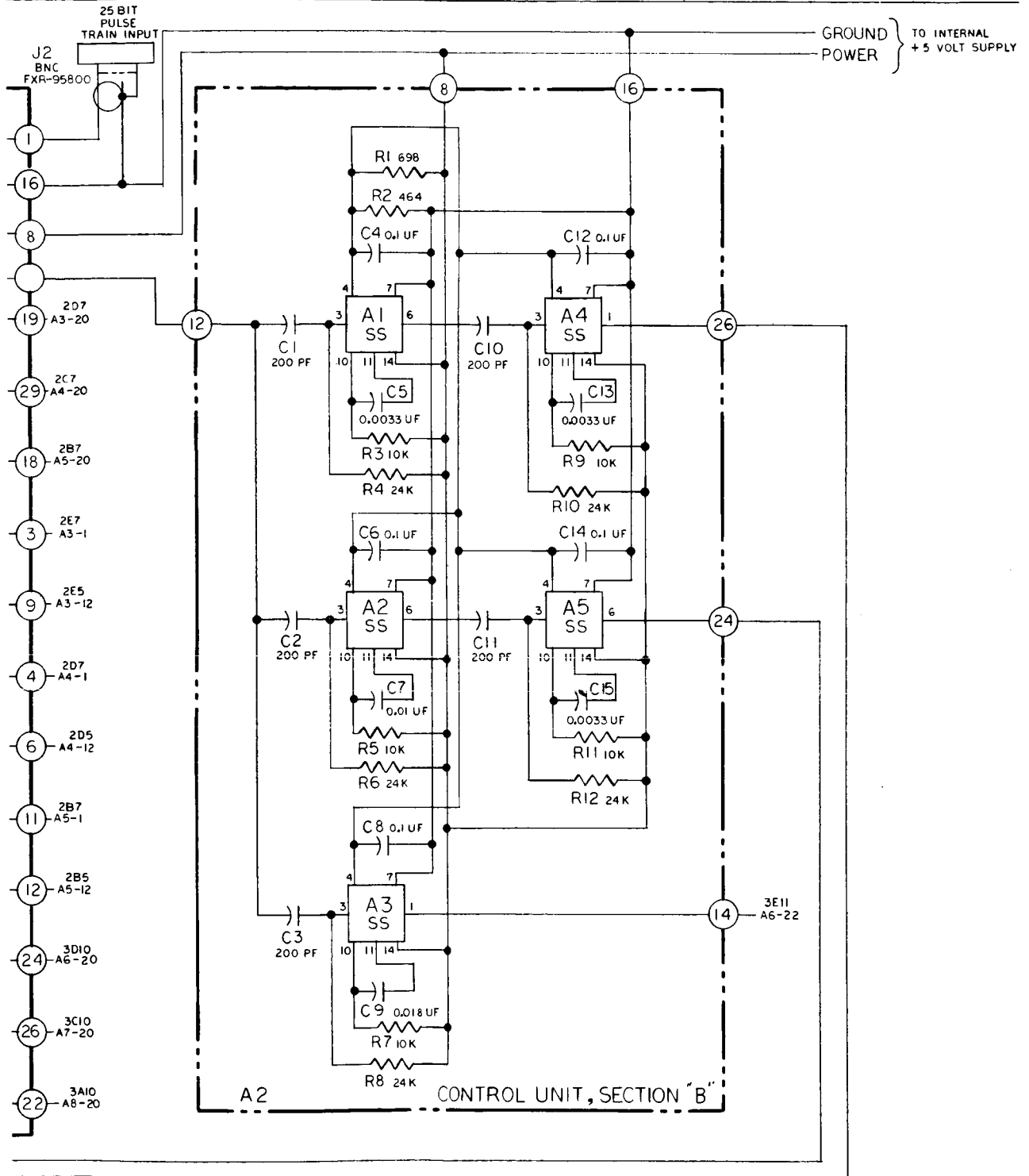


(a)

SRD727610101, sheet 1 of 4



# APPENDIX H



(b)

(The reverse of this page is blank.)

PRECEDING PAGE BLANK NOT FILMED.

APPENDIX H

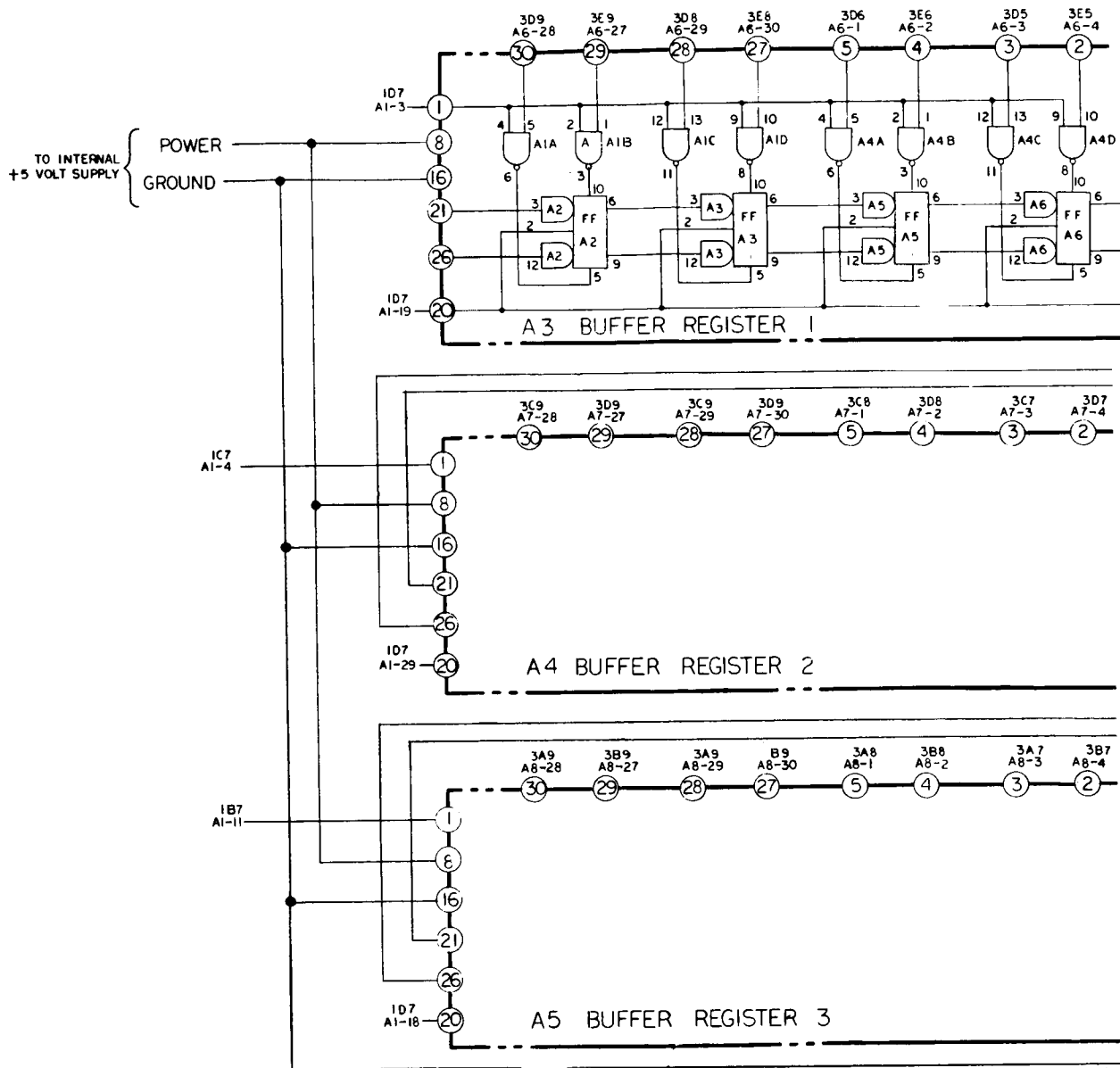
SCHEMATIC  
ELECTRONIC UNIT

CNO.	CODE IDENT NO.	SIZE	SRD727610101	
	38597		<i>R. Szepesky 11-8-67 C.H. Mennick 11-1-67</i>	
SCALE	SHEET		1 OF 4	PAGE

(c)

SRD727610101, sheet 1 of 4

# APPENDIX H

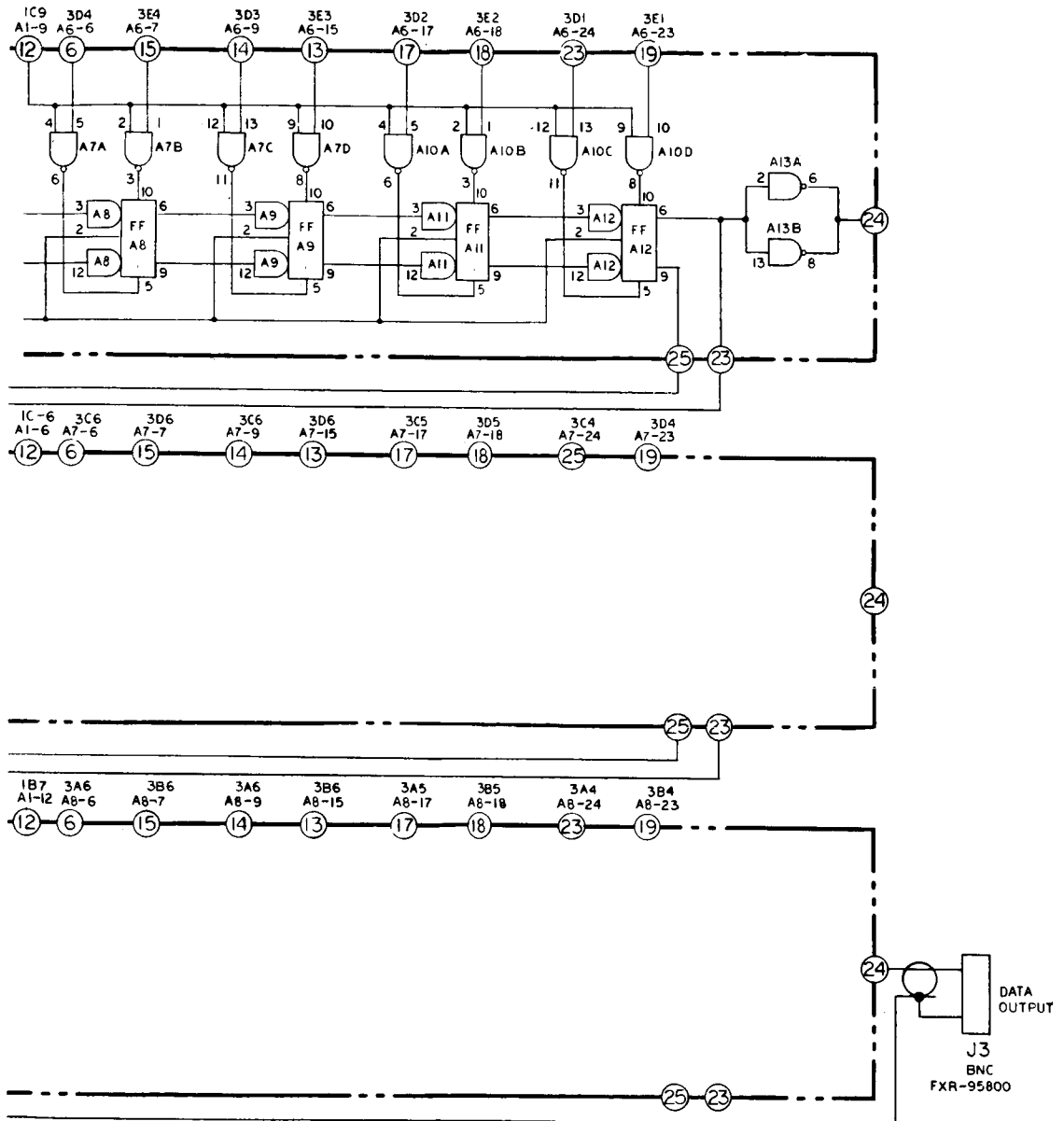


## SCHEMATIC ELECTRONIC UNIT

(a)

SRD727610101, sheet 2 of 4

# APPENDIX H



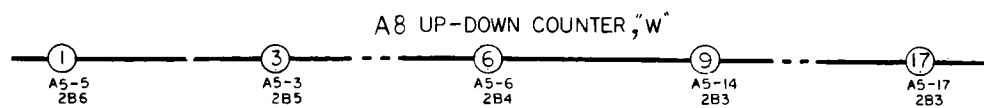
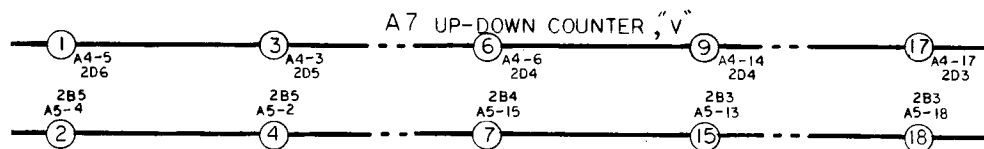
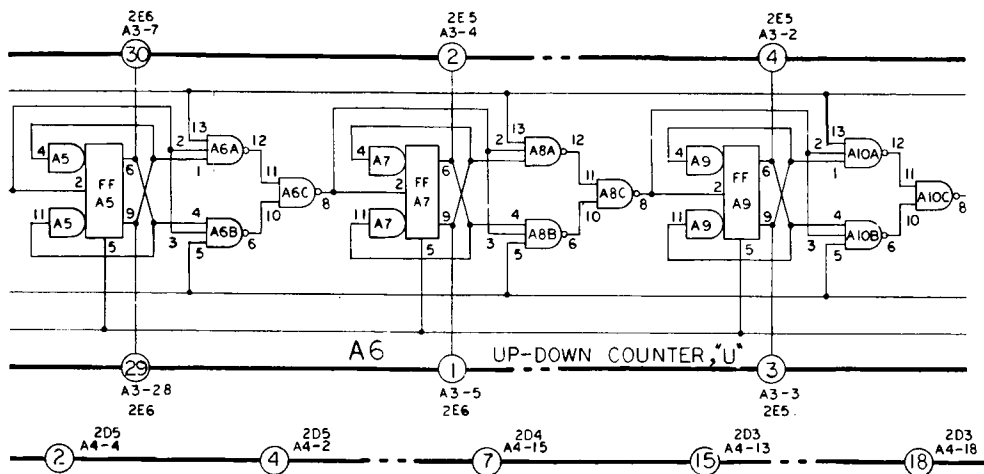
CHG.	CODE IDENT NO.	SIZE	<b>SRD727610101</b> <i>R. Steppensky 11-8-67</i> CH Manual 1A447
	38597		
SCALE	SHEET	PAGE	
	2 OF 4		

(b)

SRD727610101, sheet 2 of 4

SRD727610101, sheet 3 of 4

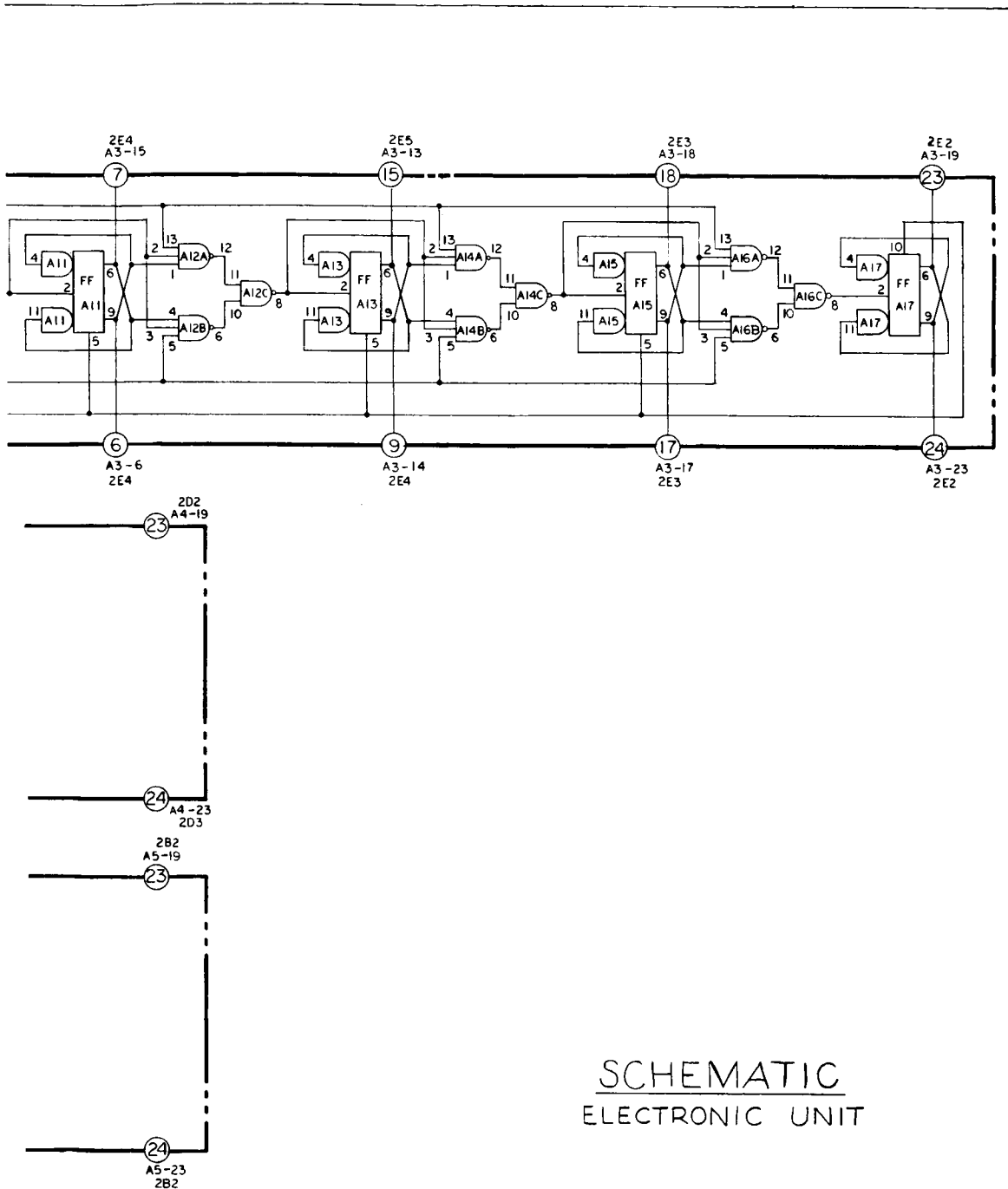
# APPENDIX H



(b)

(The reverse of this page is blank.)

APPENDIX H



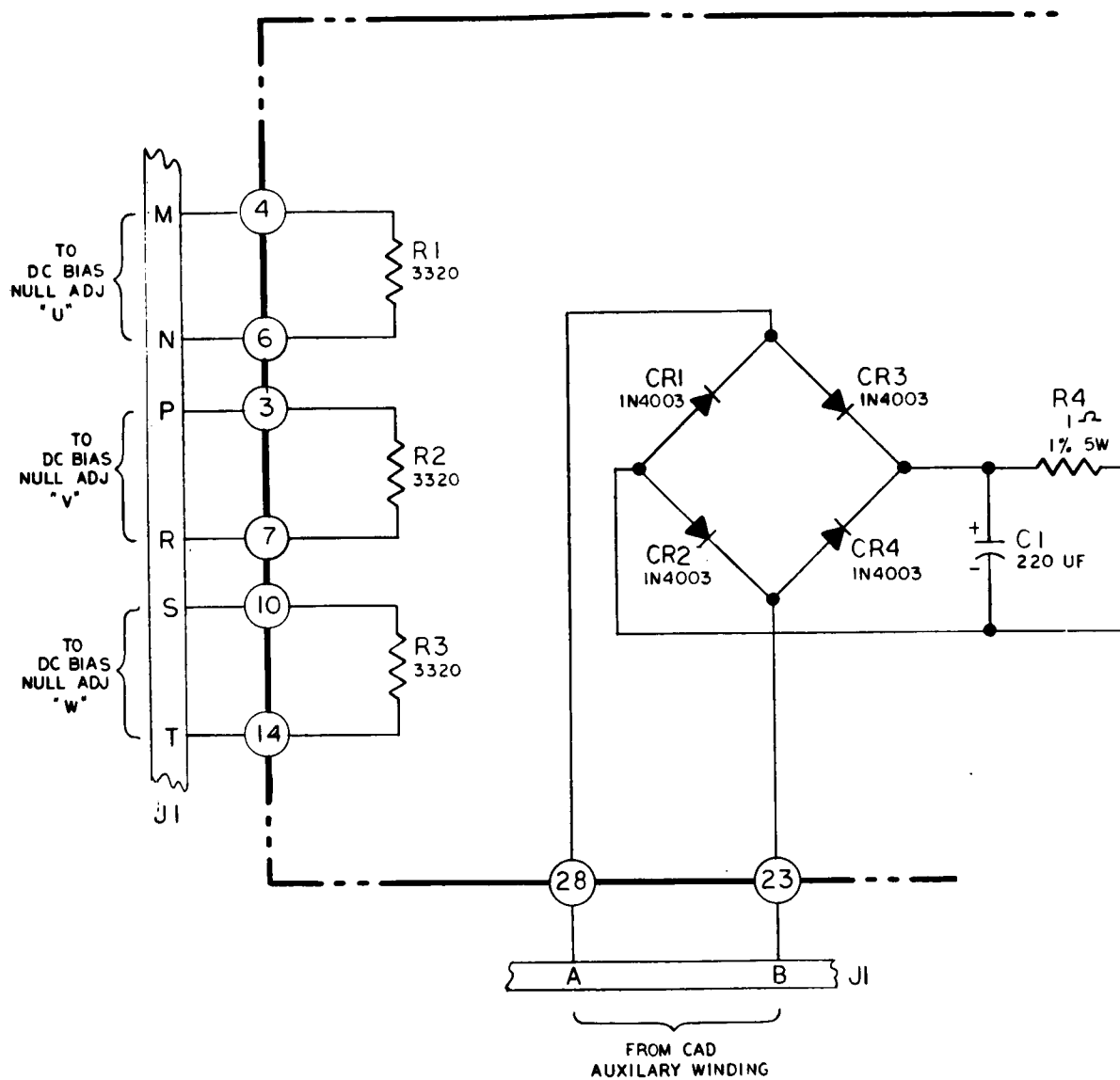
SCHEMATIC  
ELECTRONIC UNIT

CND.	CODE IDENT NO.	SIZE	<b>SRD727610101</b> <i>P. Sappachy 11-8-67 C.H. Munn 11-8-67</i>
	<b>38597</b>		
SCALE	SHEET	PAGE	
	3 OF 4		

(c)

SRD727610101, sheet 3 of 4

# APPENDIX H

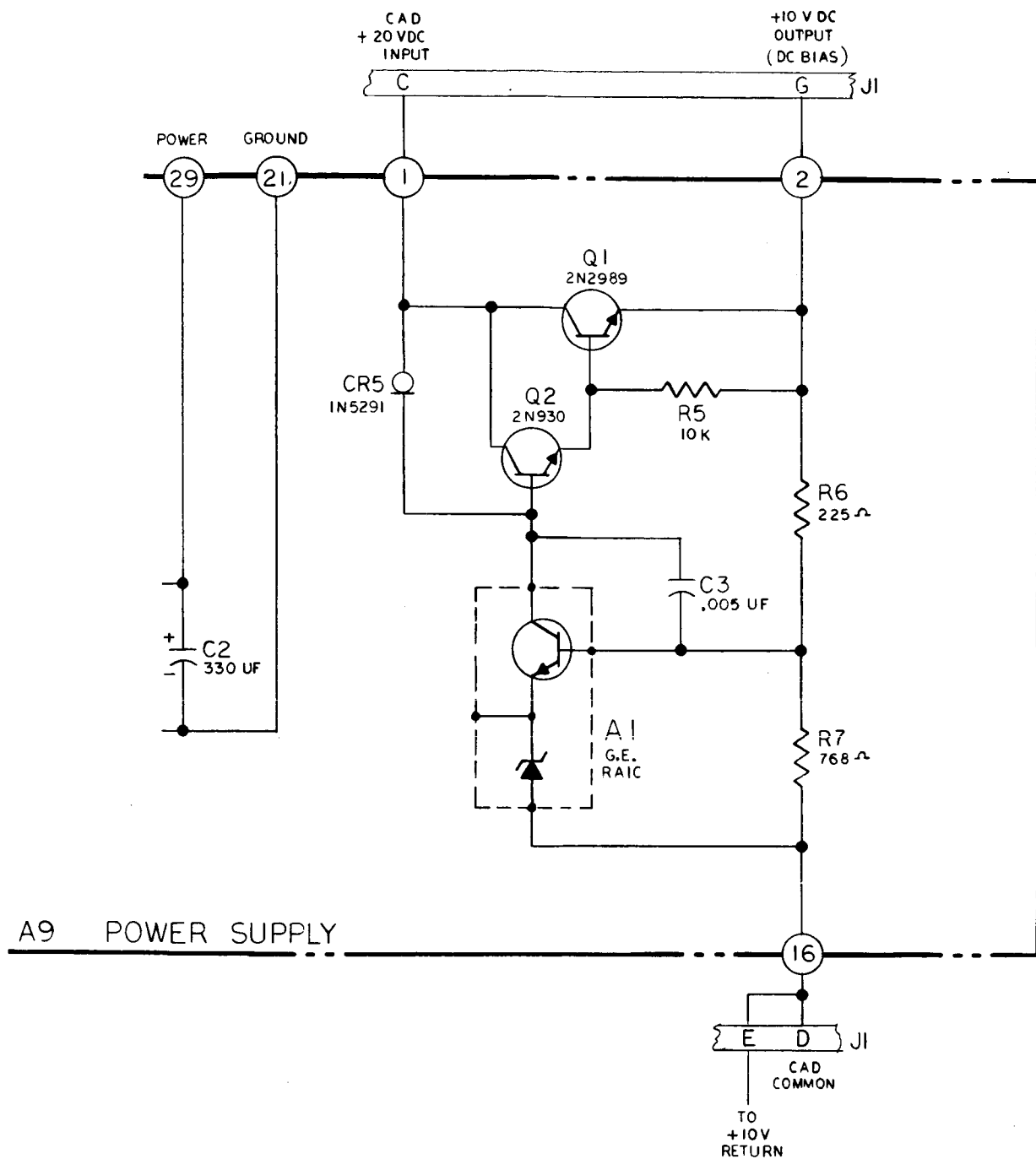


(a)

SRD727610101, sheet 4 of 4



# APPENDIX H



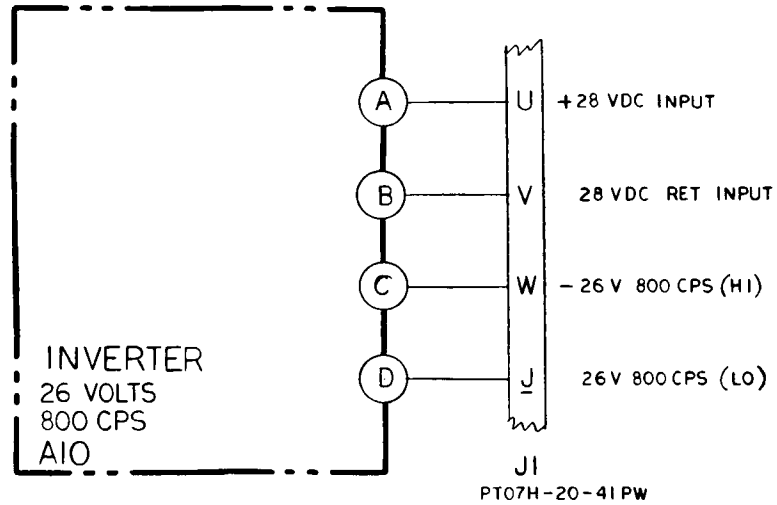
(b)

SRD727610101, sheet 4 of 4

(The reverse of this page is blank.)

PRECEDING PAGE BLANK NOT FILMED.

# APPENDIX H



## SCHEMATIC ELECTRONIC UNIT

CHG.	CODE IDENT NO.	SIZE	SRD727610101	
	38597		<i>R. Boyarsky 11-7-67 CH Manual 11-8-67</i>	
	SCALE	SHEET	PAGE	
	NONE	4 OF 4		

(c)

SRD727610101, sheet 4 of 4

# APPENDIX I

## GYROSCOPE SYSTEMS

In the development of the Digital Attitude and Rate Systems, the decision was made very early in the Crew Motion Program to base the system on an existing inertial sensing package.

The Martin Marietta Corporation had previously developed a basic guidance and control system based on the use of two gyroscopic sensor systems. These, in Martin Marietta terminology, are the three-axis reference systems (TARS) and the rate gyro system (RGS) employed in the radio guidance loop for Titan missiles. Figure 11 shows the interrelationship of these systems. Associated with each of the gyro systems are amplifiers used to provide proper scaling of the gyro outputs for use in the vehicle system. The TARS gyros are of the displacement type deriving an output proportional to the angular displacement of the gyro case about the input axis with respect to inertial space. The RGS gyros are of the rate type deriving an output proportional to the integral of the angular rate of the gyro case about the input axis with respect to inertial space. Table 11 delineates the basic properties of the gyros used in each system. Simple modification in the feedback torquer circuit result in a change of threshold and saturation levels of the gyro system rendering it capable of meeting the T013 system requirements.

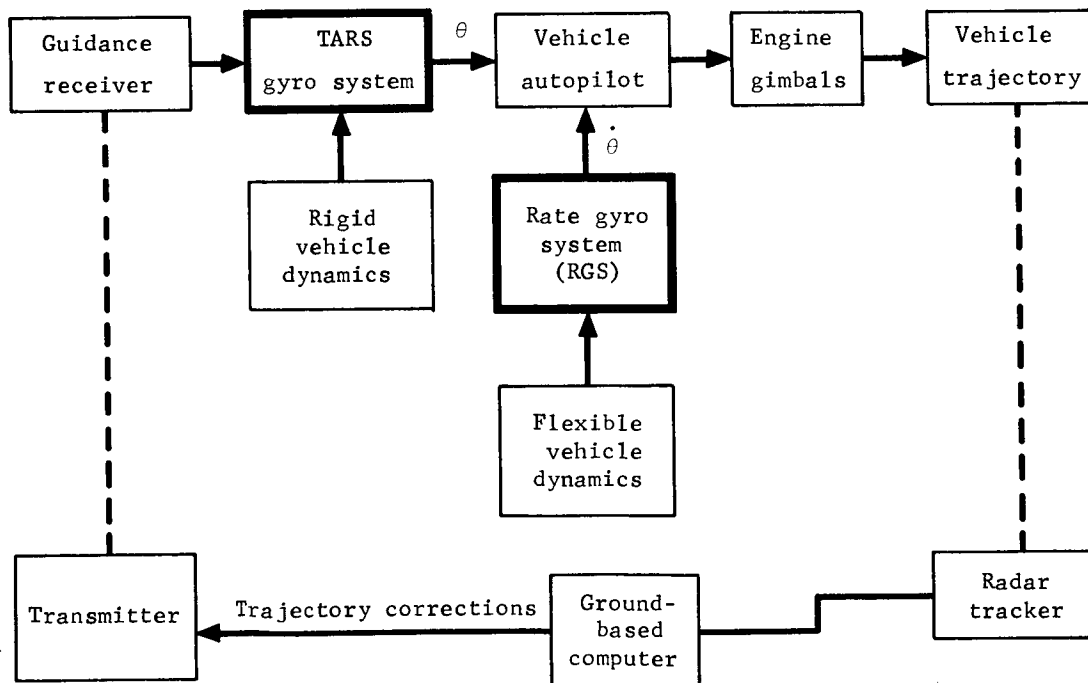


Figure 11.- Block Diagram Illustrating TARS-RGS Interrelationship

# APPENDIX I

TABLE II.- CANDIDATE GYRO PARAMETERS

Parameter	TARS gyro (PD9600010-010)	RGS gyro (PD96S0008-019)
Non-g-sensitivity at null, deg/hr	Less than 3	Less than 3°
Non-g-sensitivity off null, deg/hr/deg off null	Less than 2	Less than 5
G-sensitivity, deg/hr/g	Less than 10	Less than 10
G <sup>2</sup> -sensitivity deg/hr/g <sup>2</sup>	Less than 0.08	Less than 0.08
Non-g-sensitivity drift, deg/hr	Less than 0.75	
G-sensitive drift, deg/hr/g		
Along input axis	Less than 0.75	5°/hr for 48-hr run
Along spin axis	Less than 0.75	
Short-term random drift (1σ value for a 1-hr continuous run in deg/hr-output axis vertical, input axis last)	Less than 0.05	--
Input axis vertical, 1-hr continuous run	Less than 0.1	
Open loop gain, mV/deg displacement	28.5 mV rms ± 15%	400 mV rms ± 15%
Input angle freedom, gyro uncaged, deg	±9 to ±13	±0.65 to ±1.4
Output angle freedom, deg	±1.44	--
Characteristic time (gimbal moment of inertia about output axis divided by damping coefficient), msec	0.26 ± 0.040	3.6 ± 0.6
Angular momentum of gyro wheel, dyn-cm-sec	5.13 x 10 <sup>4</sup> ± 2%	5.13 x 10 <sup>4</sup> ± 2%
Damping coefficient of output axis, dyn-cm-sec, at 160°F	82.3 ± 3%	82.3 ± 3%
Open loop gyro output null level	Less than 1 mV runs	Less than 5 mV runs
Wheel natural frequency, Hz	Greater than 2200	Greater than 2200
Rate resolution, deg/hr	Less than 5	Less than 1
Threshold		
Displacement	0.025°	--
Rate	0.01°/sec	Less than 1°/hr
Stiction-gyro gimbal torqued about output axis, deg/hr	±1	--
Signal generator sensitivity, mV/deg gimbal displacement	178 ± 10%	178 ± 10%
Torque scale factor, deg/sec/mA inputs from 0.1 to 20 deg/sec	0.15 ± 1%	0.15 ± 2%
Life, hr	2000	2000

## REFERENCES

1. Tewell, J. R.; and Murrish, C. H.: Engineering Study and Experiment Definition for an Apollo Applications Program Experiment on Vehicle Disturbance Due to Crew Activity. NASA CR-66277, 1966.
2. Barter, J. T.: Estimation of the Mass of Body Segments. WADC Technical Report 57-620, Wright Air Development Center, Wright-Patterson Air Force Base, Ohio, Apr. 1957.
3. Wooley, C. T.: Segment Masses, Centers of Gravity, and Local Moments of Inertia for an Analytical Model of Man. LWP-228, Langley Research Center, Langley Station, Hampton, Va.
4. Tewell, J. R.; and Johnson, C. H.: EVA/IVA Simulation Dynamics. R-67-8, Martin Marietta Corporation, Denver, Colo., Feb. 1967.
5. Hanavan, E. P.: Mathematical Model of the Human Body. AMRL-TR-64-102, 6570th Aerospace Medical Research Laboratories, Wright-Patterson Air Force Base, Ohio, Oct. 1964. (Available from ASTIA as AD 605487.)
6. Di Napoli, Louis D.: The Measurement of Angular Velocities without the Use of Gyros. M. S. Thesis, Univ. of Pennsylvania, 1965.
7. Anon.: High Reliability Requirements for Resistance Welding of Electronic Modules. TOS 7069-443,871, Martin Marietta Corporation, Denver, Colo., Dec. 1966.
8. Fullerton, J.; McElroy, James; and Villyard, Kenneth: Value Engineering Study on Derived Rate and a Miniature Rate System. TM 0451-17-65, Martin Marietta Corporation, Denver, Colo., Aug. 1965.
9. Anon.: Apollo Operation Handbook. SM2A-03-SC012, North American Aviation, Inc, Space and Information Systems Division, Downey, Cal. (NAS9-150)